

Diastereoselective and Enantioselective Catalysis for Sustainable Synthesis of Carbohydrates and Heterocycles

by

Oleksii Zhelavskiy

A dissertation submitted in partial fulfillment
of the requirements for the degree of
Doctor of Philosophy
(Chemistry)
in the University of Michigan
2024

Doctoral Committee:

Professor Pavel Nagorny, Co-Chair
Professor Paul M. Zimmerman, Co-Chair
Assistant Professor Timothy Cernak
Professor Adam Matzger
Professor Corey Stephenson

Oleksii Zhelavskyi

ozhelavs@umich.edu

ORCID iD: 0000-0002-9240-8446

© Oleksii Zhelavskyi 2024

Dedication

I dedicated this thesis to all people who shaped me as a person and a scientist: my family, my friends and my mentors.

Acknowledgments

I can express only the part of all gratitude without turning this acknowledgments section into another hundred-page thesis. First and foremost, I would like to express my greatest gratitude to my advisors, Dr. Pavel Nagorny and Dr. Paul Zimmerman. I greatly appreciate the mentorship and guidance during the research that Dr. Nagorny gave me for the past five years and I am honored to have been a member of his research group at the University of Michigan. I am glad that I experienced the great environment and atmosphere of the deepest chemical knowledge, openness to new ideas, and opportunity to grow as an independent researcher in his laboratory. I am extremely grateful to Dr. Paul Zimmerman for accepting me for the co-advising Ph.D. program and providing me with an opportunity to develop myself as a computational chemist. His advice, patience, and kindness helped me to overcome all hardships while mastering the field of quantum chemistry. I am thankful to both of my advisors for this long and interesting journey during the multidisciplinary research experience that made it possible to advance through multiple research projects.

I wouldn't be able to accomplish even a fraction of the current research work and build up a knowledge of chemistry without help from my teachers and mentors. First, I am thankful to my school teacher Elena Rusanova who introduced me to the beautiful world of chemistry in middle school and guided me on the first steps in it. I am extremely grateful for the help and lessons from my International Chemistry Olympiad mentors Dr. Mykyta Onizhuk, Dr. Iryna Zaporozhets, Dr. Oleg Borodin, Dr. Yekaterina Goloviznina and Dr. Ievgen Zviagin. I would like to express my

sincere gratitude to Dr. Ievgen Zviagin as he also became my first research advisor and mentor during my undergraduate research work at SSI “Institute for Single Crystals”. I am also thankful to all the researchers of this institute and, especially, Dr. Valentyn Chebanov for being my first scientific advisor on my way to becoming a scientist.

Since I came to the University of Michigan, I have been thoroughly grateful for help and assistance from my graduate mentors Dr. Siyuan Sun, Dr. Sibin Wang, and Dr. Michael Robo who guided me during my first year in Nagorny and Zimmerman groups. I am thankful alumni Dr. Alonso Argüelles, Dr. Sibin Wang, and Dr. Yaroslav Khomutnyk who started and contributed a lot as co-authors to research projects described in this dissertation. I want to acknowledge my current and former labmates who also became friends during my Ph.D. studies: Dr. Zachary Fejedelem. Dr. Nolan Carney, Dr. Exequiel Punzalan, Dr. Kevin Enrique Rivera Cruz, Dr. Sunjin Kim, Dr. Ryan Rutkoski, Natasha Perry, Zoey Surma, Soumik Das and Dr. Volodymyr Hiiuk. I also want to recognize my mentees and amazing students Yin-Jia Zhang and Seren Parikh who significantly contributed to my research projects.

I am truly lucky to have my amazing best friends Oleksandr Vozhov, Den Martymianov, and Dmytro Tsarenko. Even though life has brought us to different locations, I am glad that through time we forged a true and strong friendship helping me to overcome any obstacles in life.

Finally, my deepest gratitude to my family for their unconditional support and help. I am thankful to my grandfather Anantolyi, grandmother Galina, and my mom Yuliia for their guidance and love. My special thanks to my brother Andrey and sister Yekaterina for their kindness and great time spent together. Despite a huge turmoil in my country, I am grateful for all of their help and dedication to keep in touch with me during all these five years.

Table of Contents

Dedication.....	ii
Acknowledgments.....	iii
List of Tables	ix
List of Figures.....	xi
List of Schemes.....	xiii
List of Appendices	xviii
List of Abbreviations	xix
Abstract.....	xxi
Chapter 1 Introduction to Catalytic Methods.....	1
1.1 Catalysis and Sustainable Chemistry	1
1.2 Introduction to flow chemistry.....	2
1.3 Photocatalysis principles.....	7
1.4 Overview of Chiral Phosphoric Acid Catalysis	14
1.4.1 Chiral Phosphoric Acids Immobilization.....	20
1.5 References.....	29
Chapter 2 Regioselective Acetalization of Carbohydrates	34
2.1 Introduction to carbohydrates	34
2.2 Overview of non-chiral catalytic methods for regioselective carbohydrate modifications.....	39
2.2.1 Stannylene acetal catalysis.....	39
2.2.2 Borinate and boronate esters	41

2.3 Asymmetric catalytic methods of regioselective carbohydrate modifications	45
2.3.1 Cinchona Alkaloid Catalysts and Hydrogen bonding effect.....	46
2.3.2 Chiral copper catalysis.....	48
2.3.3 Benzotetramisole Catalysts.....	51
2.3.4 covalent bond-forming chiral catalysis	53
2.3.5 Chiral Phosphoric Acid Catalysis	55
2.3.6 One-pot approach for the synthesis of differentially protected monosaccharides...	59
2.4 Development of the scalable regioselective CPA-catalyzed method for regioselective carbohydrate acetalization	62
2.4.1 Chiral Phosphoric Acids Immobilization.....	63
2.4.2 Immobilized CPAs testing for regioselective monosaccharides acetalization.	64
2.5 Computational mechanistic investigations of carbohydrate regioselective acetalization under CPA catalysis.....	68
2.6 Experimental evaluation of potential mechanisms	77
2.6.1 Experiments for covalent-phosphate detection.....	77
2.6.2 Determining stereospecificity of the hydroxyl group addition to enol ether double bond.....	81
2.6.3 Analysis of room temperature NMR spectra of nondeuterated and deuterated MOC-protected glucoside.	83
2.6.4 The analysis of nondeuterated MOC-protected glucose derivative using low temperature NMR (–80 °C).....	86
2.6.5 Analysis of d-labeled MOC-protected glucoside using low temperature NMR (–80 °C)	95
2.7 Conclusions.....	100
2.8 Experimental information	102
2.8.1 Compounds characterization data	108
2.9 Computational details	113
2.10 References.....	117

Chapter 3 Asymmetric Transfer Hydrogenation of Heterocyclic Compounds in a Continuous Flow	123
3.1 Introduction.....	123
3.2 Initial conditions optimization and substrate scope screening.....	130
3.3 Transfer hydrogenation in a continuous flow	135
3.4 Conclusions.....	141
3.5 Experimental information	142
3.5.1 Products characterization data	146
3.6 References.....	171
Chapter 4 Photochemical Alkynylation of Aziridinoquinoxalines Through the Intermediacy of Azomethine Ylides.....	175
4.1 Introduction to aziridine chemistry	175
4.2 Fused aziridinoquinoxalines as potential precursors for ylides generation	181
4.3 Overview of copper(I)-catalyzed asymmetric addition reactions of alkynes	184
4.3.1 Overview of mechanistic principles.....	184
4.3.2 Photoinduced copper-catalyzed enantioselective alkynylations.....	188
4.4 Generation and alkynylation of ylides from aziridinoquinoxalines under thermal conditions.....	191
4.5 Photochemical activation and alkynylation of aziridinoquinoxalines	197
4.5.1 Functionalization of alkynylated aziridines	212
4.6 Mechanistic studies of photocatalytic aziridinoquinoxalines alkynylation	214
4.7 Conclusions.....	221
4.8 Experimental information	222
4.8.1 General procedures	223
4.8.2 Mechanistic studies experimental details.....	228
4.8.3 Computational details	234

4.8.4 Compounds characterization data	236
4.9 References	260
Chapter 5 Closing Remarks and Future Directions	265
Appendices.....	270

List of Tables

Table 2.1. Recyclability of PS-SPINOL	68
Table 2.2. Comparing TS structures enthalpy and free energy barriers calculated relatively to lowest energy reactants complex for both 223K and 273K	74
Table 2.3. Comparing concerted and phosphate-mediated mechanisms at 223K and 273K.....	75
Table 3.1. Initial evaluation of immobilized CPAs 3a and 3c for the in batch transfer hydrogenation of 2-substituted quinolines.....	131
Table 3.2. Recyclability test of immobilized CPA PS-AdTRIP in batch	134
Table 3.3. Optimization of the continuous flow transfer hydrogenation	136
Table 4.1. Reaction conditions optimization for thermal activation of aziridinoquinoxalines...	193
Table 4.2. Chiral ligand screening for thermal alkylation of aziridinoquinoxalines.	195
Table 4.3. Copper source screening for enantioselective alkylation	197
Table 4.4. Computed data for aziridinoquinoxaline substrate models.....	198
Table 4.5. Initial screening of photochemical conditions	200
Table 4.6. Photochemical conditions screening under activation by Green LED	205
Table 4.7. Development of the enantioselective alkyne addition under photochemical conditions.	210
Table 4.8. Thermodynamic data for elementary steps of Mechanism B.	216
Table 4.9 Thermodynamic data for potential decomposition pathway on Scheme 4.22	220
Appendix Table A.1. Chiral Phosphoric Acid catalyst optimization performed by Yin-Jia Jhang	283
Appendix Table B.1. Optimization of regioselective acetalization in continuous flow	307
Appendix Table B.2. Conditions screening for the <i>O</i> -MOC protection group installation.....	307

Appendix Table B.3. Optimization of regioselective acetalization in a continuous flow using <i>O</i> -MOC enol as a protecting group	308
--	-----

List of Figures

Figure 1.1. Comparing parameters used for batch and flow reactions setup.....	3
Figure 1.2. Elements of the standard two-feed continuous flow setup.....	4
Figure 1.3. Flow reactor types.	6
Figure 2.1. Selectivity versus temperature profile for the MOC and MOP protection of 2-60b, and theoretically predicted selectivity profile for a reaction with no mechanism switch using Arrhenius model.....	69
Figure 2.2. Noncovalent interaction analysis for regiocontrolling transition states.	77
Figure 2.3. ^1H and ^{13}C NMR in benzene- d_6 of MOC and deuterium diphenylphosphate, and their mixture.	79
Figure 2.4. ^{31}P NMR in benzene- d_6 of starting reagents and reaction solution.	80
Figure 2.5. NMR in benzene of the $(\text{PhO})_2\text{P}(=\text{O})\text{OD}$ and MOC reaction mixture.	80
Figure 2.6. Preliminary NMR studies of compounds 2-65b and d_3 -2-65b.	84
Figure 2.7. 2D NMR studies of compound 2-65b at $-80\text{ }^\circ\text{C}$	88
Figure 2.8. Computational conformers screening and analysis of compound x.	90
Figure 2.9. NMR shifts calculations (B3LYP/6-31G*) of compound 2-65b	92
Figure 2.10. - SPh rotation PES scan and its impact on the NMR shifts (B97-D3/6-31++G**).	94
Figure 2.11. 2D NMR studies of compound d_3 -2-65b and d_3 -2-65b -rt at $-80\text{ }^\circ\text{C}$	98
Figure 3.1. Photo of the pump setup for synthesis in-flow	146
Figure 4.1. Computed energy barriers (electronic energy) for photoinduced ring-opening of aziridinoquinoxalines.....	198
Figure 4.2. Excited states of aziridine 4-27a calculated via TD-DFT	201
Figure 4.3. Fluorescence spectrum for S_0 - S_1 transition of compound 4-27a.....	201
Figure 4.4. Fluorescence spectrum for S_0 - T_1 transition of compound 4-27a.....	202

Figure 4.5. Absorption (blue line) and fluorescence (dotted line) of Ir(4-CF ₃ -ppy) ₃ photocatalyst and used Green LED emission (green line)	215
Figure 4.6. Cyclic voltammetry measurements of compound 4-27a in acetonitrile	218
Figure 4.7. Emission Spectrum of Blue LED	229
Figure 4.8. Emission Spectrum of Green LED	229
Figure 4.9. UV-Vis absorption spectrum of compound 4-27a.....	230
Figure 4.10. UV-Vis absorption spectrum of compound 4-27b	230
Figure 4.11. Fluorescence spectrum of Ir(4-CF ₃ -ppy) ₃	231
Figure 4.12. Excitation (absorption) spectrum of Ir(4-CF ₃ -ppy) ₃	232
Figure 4.13. Cyclic voltammetry scan of compound 4-27a, range -3.0 V to 3.0 V, 50 mV/s	233

List of Schemes

Scheme 1.1. General Jablonski diagram for molecule electronic states.	9
Scheme 1.2. General mechanism and catalytic cycles for photoredox catalysis.	10
Scheme 1.3. General catalytic cycle and mechanisms of EnT processes	11
Scheme 1.4. Examples of EnT reactions proceeding via Dexter EnT mechanism.	13
Scheme 1.5. The general structure of CPA catalysts and most common chiral backbones.	15
Scheme 1.6. The pKa dependence on structural elements of CPAs (theoretical studies).	16
Scheme 1.7. Modes of substrate activation by CPAs.	18
Scheme 1.8. Reactivity and general strategy of BINOL scaffold modifications.	19
Scheme 1.9. Approaches to CPA immobilization by Rueping and co-workers.	21
Scheme 1.10. Synthesis of the immobilized CPA PS-2 by Blechert.	23
Scheme 1.11. Immobilization of CPA via its installation into Merrifield resin.	24
Scheme 1.12. Friedel-Crafts reaction in continuous flow using a reaction with immobilized CPA PS-3.	25
Scheme 1.13. Improved synthesis of the polymeric TRIP CPA by Pericas and co-workers and its application for the allylation in continuous flow.	26
Scheme 1.14. SPINOL-based CPA immobilization and application for desymmetrization of 3,3-Disubstituted Oxetanes in a continuous flow by Pericas.	28
Scheme 1.15. Preparation of embedded BINOL to the porous aromatic framework by Sanchez.	29
Scheme 2.1. Example of synthetic approach towards synthesis of the complex carbohydrates. .	35
Scheme 2.2. One-pot regioselective functionalization of D-glucose by Hung and coworkers. ...	37
Scheme 2.3. Steric effects controlling the reactivity of hydroxyl groups.	38
Scheme 2.4. Stannyl oxide-mediated regioselective carbohydrate functionalization.	40

Scheme 2.5. Dialkyltin(IV) dichloride catalysis.....	41
Scheme 2.6. Catalytic alkylation and benzylation using borinate esters catalysis	42
Scheme 2.7. The postulated mechanism of borinate-catalyzed regioselective functionalization of carbohydrates.....	43
Scheme 2.8. Boronic acid catalysis.....	44
Scheme 2.9. Shimada's Lewis base-bearing boronic acid catalysis	45
Scheme 2.10. Examples of utilizing the counter anion effect and H-bonding for controlling the regioselectivity of carbohydrate acylation.....	47
Scheme 2.11. Chiral Cu(II) Ph-Box-catalyzed regioselective acylation of carbohydrates.....	49
Scheme 2.12. Regiodivergent benzylation with PyBox complexes by Dong et al.....	50
Scheme 2.13. Regioselective acylation of 1,2-trans-diols by benzotetramisole catalyst.....	52
Scheme 2.14. Regioselective functionalization of carbohydrates through reversible covalent catalysis.....	54
Scheme 2.15. CPA controlled regioselective acetalization of carbohydrates.....	58
Scheme 2.16. The one-pot strategy of monosaccharides modification using CPA catalysis.	60
Scheme 2.17. Regiodivergent acetalization catalyzed by SPINOL-based CPA.....	63
Scheme 2.18. Routes for preparing immobilized CPA catalysts	64
Scheme 2.19. Catalyst controlled regioselective acetalization using immobilized CPAs ^a	66
Scheme 2.20. Proposed mechanism for the regioselective acetalization.....	70
Scheme 2.21. Computational model with QM/MM setup and mixed basis set for transition states search.	71
Scheme 2.22. Computed free energy profiles of concerted and phosphate-mediated mechanisms	73
Scheme 2.23. Experiment design for covalent phosphate detection.....	78
Scheme 2.24. Proposed Equilibrium Leading to D/H Exchange.....	81
Scheme 2.25. Synthesis of the deuterated MOC acetals d ₃ -2-65b and d ₃ -2-65b-rt, and reference acetal 2-65b.....	83
Scheme 2.26. Analysis of potential outcomes for diol 2-60b reaction with deuterated d ₃ -MOC	97

Scheme 2.27. ^1H and $^2\text{H(D)}$ NMR in benzene- d_6 or benzene for the deuterium-exchanged DPPA	105
Scheme 2.28. QM/MM setup for geometry optimization, frequencies, and growing string computations.	114
Scheme 2.29. Molecular alignment (distances constraints) for conformer generation in the concerted mechanism.	114
Scheme 2.30. Molecular alignment (distances constraints) for conformer generation in the phosphate mechanism.	116
Scheme 3.1. Important chiral heterocycles.	124
Scheme 3.2. Approaches towards asymmetric hydrogenation of heterocycles.	126
Scheme 3.3. Mechanism of asymmetric transfer hydrogenation.	127
Scheme 3.4. Reduction of 1,4-benzoxazines.	129
Scheme 3.5. Continuous flow reduction of quinolines and benzoxazines.	130
Scheme 3.6. Exploration of catalyst PS-AdTRIP (3a) for the in-batch asymmetric reduction of quinolines, 2H-1,4-benzoxazines, and 2H-1,4-benzoxazin-2-ones.	133
Scheme 3.7. Continuous flow transfer hydrogenation of nitrogen-containing heterocyclic compounds.	139
Scheme 3.8. Control experiments to determine the origins of enantioselectivity erosion at low flow rates.	141
Scheme 3.9. General procedure for the asymmetric reduction in batch	144
Scheme 3.10. General scheme of continuous flow setup for the transfer hydrogenation of heterocycles.	145
Scheme 4.1. Reactivity trends of aziridines.	176
Scheme 4.2. Stereochemical control of aziridine ring-opening.	178
Scheme 4.3. Aziridine ring opening via a direct photoexcitation with UV-C light.	179
Scheme 4.4. SET oxidation of aziridine for activating ring for nucleophilic substitution.	179
Scheme 4.5. Photoredox generation of aziridine ylides and their [3+2] cycloaddition reactions.	180
Scheme 4.6. Synthesis and reactivity of aziridinoquinoxalines.	182

Scheme 4.7. Investigation of photochemical properties of aziridinoquinoxalines.	183
Scheme 4.8. Two modes of metal-alkyne complexes formation.	185
Scheme 4.9. General mechanism of a copper(I)-catalyzed alkyne addition to electrophilic π -bonds.	186
Scheme 4.10. Asymmetric alkynylation of isoquinolinium and quinolinium-based cations.	188
Scheme 4.11. Three types of copper catalysis in photochemical transformations.	189
Scheme 4.12. Photocatalyzed C-C cross-coupling with alkynes.	190
Scheme 4.13. Asymmetric photocatalyzed alkynylation of tetrahydroisoquinolines.	191
Scheme 4.14. Proposed reaction design based on copper-catalyzed alkynylation of azomethine ylides.	192
Scheme 4.15. Chiral ligands used for conditions screening in Table 4.2.	196
Scheme 4.16. Summary of the excited state analysis for aziridine forms and ylides of compounds 4-27a, 4-60-4-62.	203
Scheme 4.17. The substrate scope of Green LED promoted alkynylation of aziridinoquinoxalines. ^a	207
Scheme 4.18. Substrate scope for enantioselective alkyne addition.	211
Scheme 4.19. Asymmetric functionalization of quinoxalinium salts by Karimov and heteroarenium salts synthesis via alkylation reactions.	213
Scheme 4.20. Further modifications of aziridinoquinoxalines and alkynylated aziridines.	214
Scheme 4.21. Two photochemical mechanisms of ylide generation.	216
Scheme 4.22. Mechanistic studies of alkyne addition to ylides	219
Scheme 4.23. Potential decomposition pathway through SET reduction.	220
Scheme 4.24. Structures and the properties of used photocatalyst	234
Appendix Scheme A.1. Examples of aziridine-containing and quinoxaline-based pharmaceuticals.	272
Appendix Scheme A.2. Regiodivergent modifications of aziridinoquinoxalines.	272
Appendix Scheme A.3. Synthesis of racemic aziridinoquinoxalines 5-1 with following chiral resolution during nucleophilic addition.	274

Appendix Scheme A.4. Types of kinetic resolutions.....	275
Appendix Scheme A.5. Kinetic resolution of indolines and tetrahydroquinolines.....	276
Appendix Scheme A.6. Kinetic resolution of atropoisomers.	277
Appendix Scheme A.7. Example of DKR reaction catalyzed by CPA.	278
Appendix Scheme A.8. PKR resolution of ferrocene derivatives.	278
Appendix Scheme A.9. Reduction under non-chiral conditions.....	279
Appendix Scheme A.10. CPA-catalyzed reduction of aziridinoquinoxaline 5-1a.	280
Appendix Scheme A.11. Synthesis of reduced aziridinoquinoxalines and X-Ray characterization performed by Yin-Jia Jhang.....	281
Appendix Scheme A.12. Detailed analysis of the parallel kinetic resolution reduction of 5-1a.	282
Appendix Scheme A.13. Relative stabilities of all possible diastereomers of tetrahydroazirino[1,2-a]quinoxalines.....	285
Appendix Scheme A.14. Nucleophilic ring-opening of tetrahydroazirino[1,2-a]quinoxalines..	286

List of Appendices

Appendix A: Studies of Enantioselective Kinetic Resolution of Aziridine-Containing Quinoxalines	271
A.1 Introduction	271
A.2 Chiral Phosphoric Acid catalyzed kinetic resolution	274
A.3 Chiral resolution of aziridinoquinoxalines	279
A.4 Ring-opening of the tetrahydroazirino[1,2-a]quinoxalines	284
A.5 Results and conclusions	287
A.6 Experimental information	288
A.7 Characterization data	290
A.8 Computational details	302
A.9 References	302
Appendix B: Regioselective Acetalization of Carbohydrates in a Continuous Flow	306
B.1 Continuous flow conditions development	306
B.2 Summary	309

List of Abbreviations

Å	angstrom
Ac	acetyl
Acac	acetylacetone
Ad	adamantyl
Aq	aqueous
Ar	aryl
Atm	atmosphere (unit)
BINOL	1,1'-bi-2-naphthol
Bn	benzyl
Boc	tert-butyloxycarbonyl
BOM	benzyloxymethyl
Br	broad
Bu	butyl
Bz	benzoyl
Calcd	calculated
COSY	correlation spectroscopy
CPA	chiral phosphoric acid
CSA	camphorsulfonic acid
Cy	cyclohexyl
d	days
DBU	1,8-diazabicyclo[5.4.0]undec-7-ene
DCM	dichloromethane
DCE	1,2-dichloroethane
DDQ	2,3-Dichloro-5,6-dicyano-1,4-benzoquinone
DFT	Density Functional Theory
DMAP	4-dimethylaminopyridine
DMF	dimethylformamide
DPPA	diphenylphosphoric acid
dr	diastereomeric ratio
ee	enantiomeric excess
equiv	equivalent
ESI-MS	electrospray ionization mass spectrometry
Et	ethyl
EtOAc	ethyl acetate
GSM	growing string method

h	hours
HMBC	heteronuclear multiple bond correlation
HOMO	highest occupied molecular orbital
HPLC	high-performance liquid chromatography
HRMS	high resolution mass spectrometry
HSQC	heteronuclear single quantum correlation
Hz	hertz
<i>i</i> Pr	<i>isopropyl</i>
IR	infrared
<i>J</i>	coupling constant
kcal	kilocalorie
LUMO	lowest unoccupied molecular orbital
M	molar
Me	Methyl
mg	milligrams
min	minutes
mL	milliliters
mmol	millimoles
MS	mass spectrometry
MS	molecular sieves
MW	molecular weight
NMR	nuclear magnetic resonance
NOESY	nuclear Overhauser effect spectroscopy
o/n	overnight
PG	protecting group
Ph	Phenyl
PhMe	Toluene
ppm	parts per million
R	alkyl group (generic)
rac	racemic
R _f	retention factor
RDS	rate determining step
r.r.	regioisomeric ratio
rt	room temperature
S _{N1}	unimolecular nucleophilic substitution
S _{N2}	bimolecular nucleophilic substitution
SPINOL	1,1'-spirobiindane-7,7'-diol
t	time
T	temperature

Abstract

The development of new catalytic methods has undoubtedly played a crucial role in the recent rapid growth of chemical industries, especially in the pharmaceutical research and process development. Novel chiral catalytic methods have drastically improved the access to complex chiral organic molecules such as oxygen- and nitrogen-based heterocyclic compounds. These compounds have a long history of being essential building blocks for medicinal chemistry and numerous therapeutic agents contain chiral heterocyclic motifs including carbohydrates. This dissertation is focused on the development and mechanistic studies of regioselective modifications of *trans*-2,3-equatorial diols in carbohydrate molecules under immobilized CPA catalysis. Chiral Phosphoric Acids (CPAs) represent a particularly prospective subclass of chiral catalysts due to their versatility in catalyzing a broad spectrum of organic reactions. Combining stereoselective catalysis with immobilized CPAs and continuous flow methods we managed to improve the sustainability and achieve streamlined generation of chiral nitrogen-containing heterocycles with efficient catalyst recycling. Finally, based on theoretical mechanistic studies we explored the reactivity of fused previously pure studied aziridinoquinoxalines as useful precursors for the generation of aromatic aziridine ylides under photochemical energy transfer catalysis.

Chapter 1 introduces various “green”-chemistry methods such as flow chemistry and photochemical catalysis used in this dissertation for developing sustainable catalytic protocols. In addition, this chapter describes the principles of CPA catalysis and recent progress toward the synthesis and application of immobilized CPA catalysts.

Chapter 2 describes the application of (*R*)-BINOL- and (*S*)-SPINOL-based CPA catalysts incorporated into a polymer matrix for regioselective acetalization of monosaccharides with enol ethers. The QM/MM model based on the CHARMM force field and DFT method is developed for reaction potential energy surface exploration to investigate potential mechanisms of CPA-catalyzed regioselective acetalization. In combination with the experimental NMR studies two possible temperature-dependent mechanisms controlling regioselectivity of the acetalization were postulated.

Chapter 3 details our efforts to improve the sustainability of the CPA-catalyzed transfer hydrogenation of aromatic heterocycles with Hantzsch esters. We designed the continuous flow system with immobilized CPA placed in the packed-bed reactor for performing enantioselective reduction of quinolines and 1,4-benzoxazines. The developed protocol allows large-scale and effective transfer hydrogenation with easily recyclable catalysts as well as improve enantioselectivity of the process.

Chapter 4 provides an overview of the aziridinoquinoxalines properties and their application for ylide generation via the ring-opening reaction of the aziridine cycle. Theoretical investigations using DFT and TD-DFT methods assisted in the development of a photochemical energy transfer catalytic system to perform *in-situ* azomethine ylides synthesis. As a result, we demonstrated that cooperative Ir(III)/Cu(I) dual catalysis can be effectively used for generation and trapping generated ylides via asymmetric alkynylation reaction.

Appendix A describes the initial development of enantioselective transfer hydrogenation with Hantzsch esters under CPA catalysis to achieve parallel kinetic resolution of aziridinoquinoxalines.

Chapter 1 Introduction to Catalytic Methods

1.1 Catalysis and Sustainable Chemistry

Chiral molecules are one of the keystones of all life existing on our planet and there is no surprise that the development and production of such molecules is of great importance to the modern pharmaceutical industry. According to the modern state of all chemical industry fields, the pharmaceutical field still remains the most cost-demanding, non-efficient, and waste-producing industry. The synthesis of pharmaceuticals commonly requires a synthetic route involving multiple steps that is disadvantageous due to the large amount of material loss, waste generation and the usage of costly catalysts for performing chiral synthesis.¹ Paul Anastas and John Warner postulated the 12 principles of Green Chemistry in 1998² that provide common guidelines for developing more ecologically friendly and effective processes for the chemical industry. There are three main categories:

1. Preventing the generation of chemical waste
2. Minimization of use of the toxic and dangerous chemicals
3. Optimization of current protocols for higher efficiency and less waste generation.³

Catalysis is one of the most significant advances toward the development of green chemical processes stated above. The use of catalyst have enabled chemists to design more efficient syntheses of complex molecules (such as chiral heterocycles) without the use of stoichiometric chiral reagents. Catalytic processes usually proceed under milder conditions due to lowering of the activation barriers for the reaction. Additionally, catalysts increase reaction selectivity and yields, and minimize costs and waste generation during purification. Despite these advantages

most developed catalytic processes are still not widely used in industry due to the high cost of the catalysts and the need for their recycling.⁴

Another important direction currently on the rise is the development of new methods of reaction activation. Photochemical methods provide a more effective way to activate substrates as light generation and transfer to reaction media has higher energy conversion efficiency rather than thermal heating (due to less energy dissipation). On the other hand, flow chemistry allow the minimization of safety risks associated with large-volume batch reactors and provide higher efficiency of energy transfer to reaction media. A more detailed discussion of these approaches will be described later in the chapter.^{3,4}

1.2 Introduction to flow chemistry

Flow chemistry is an area of synthesis focused on performing reactions in a continuous stream under the conditions when reagents are introduced to the continuous reactor and the reaction is happening during the fluid pumping through the system. Compared to conventional batch processing which are carried out in round-bottom flasks, it offers several advantages such as enhanced mass and heat transfer, improved safety, increased reaction efficiency, reduced waste, better scalability, and improved reproducibility. Mostly, flow chemistry is of particular interest of industrial applications due to the almost unlimited scalability of the process. While batch-reactors have fixed volume and reaction scale is limited to their size, flow reactors with smaller volumes can provide continuous generation of the product as reagents constantly pumped into the reactor while products are removed from it. Decreasing the reaction volume results in shortened reaction time and allows for more efficient heat transfer to and from the reactor. Smaller reactor size also mitigates potential safety concerns, such as explosions or leaks while the reaction is progressing

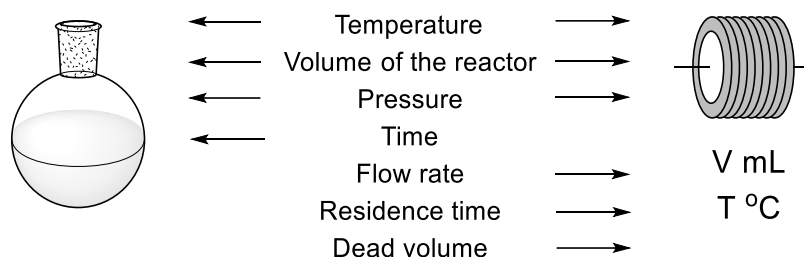
because the system is limited to a small portion of the tubing rather a thousand-liter reaction vessel.⁵

Despite all the advantages flow processes are still viewed with skepticism and this area of chemistry still undergoes continuous development. Among limitations, we can postulate these ones:⁶

- Difficulties implementing heterogeneous reactions (with solids precipitations or heterogeneous catalysts clogging tubes)
- A more complex reaction setup is usually required.
- Reaction time is relatively long (> 24 hours)
- Reaction scale is small (less than 1 mmol).

Both batch and flow reaction setups possess the same parameters that we can use to characterize the reaction protocols (Figure 1.1). This includes temperature, reactor size, and pressure in the system. However, in terms of the reaction time flow systems should be characterized differently.

Figure 1.1. Comparing parameters used for batch and flow reactions setup.



In addition to the parameters above, flow systems should be characterized in terms of the flow rate used to stream fluid through the system and the dead volume of the system consisting of all tubing volume not related to the flow reactor (connection lines, flow pump lines, and pump heads, etc.).

Flow rate simply is defined as the volume of fluid that passes per unit of time (eq. 1):

$$q = \frac{dV}{dt} \quad (1)$$

, and usually expressed in mL/min or other ratio of volume to time.

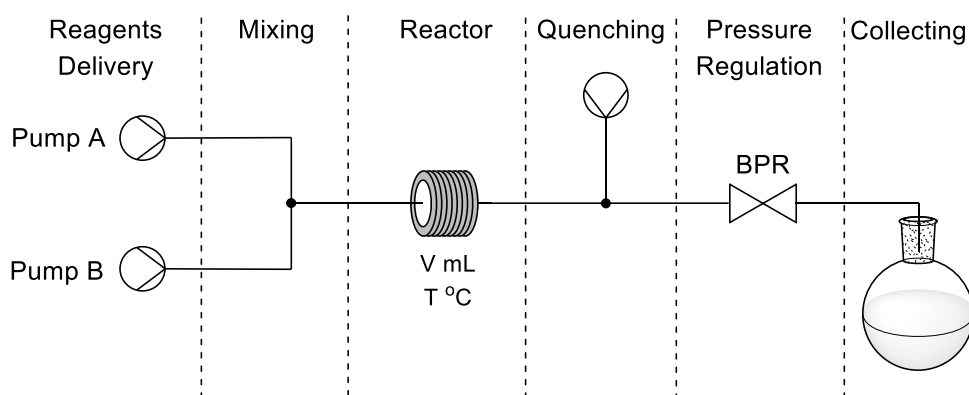
The reaction time is defined as the time a compound spends in the flow reactor. This leads to the expression of the residence time τ (s, min or hours, equation 2):

$$\tau = \frac{V}{q} \quad (2)$$

, where V – is the volume of the flow reactor and q – is the flow rate.

For classical tube reactors, residence time depends on the length of the tube and flow rate. The stoichiometry of the reaction is not defined as the molar ratio of the used reagents as it is for the in-batch conditions but in terms of the flow rate of the reagents that are being pumped into the system (mol/min, mmol/min). Therefore, reaction stoichiometry can be regulated by altering the flow rates of solutions that are being pumped into the system.⁷After defining specific characteristics used to describe flow system it's worth to discuss the general setup of the flow reactions (Figure 1.2).

Figure 1.2. Elements of the standard two-feed continuous flow setup.

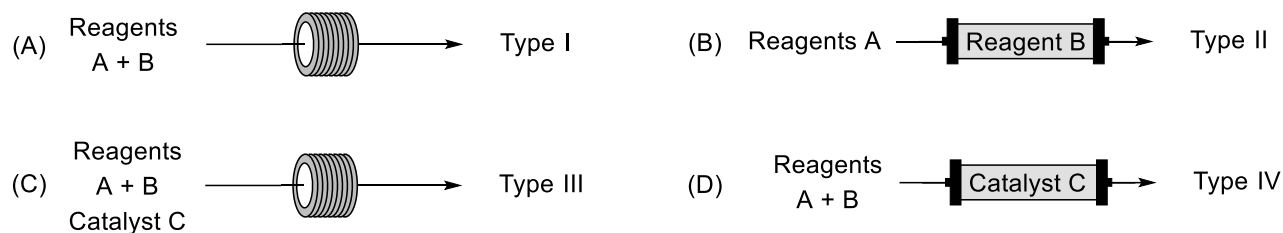


Reagent delivery is usually performed via syringe pumps for small-scale flow reactions or HPLC and/or specialized pumps for large-scale reactions which allow continuous pumping of the fluid to the system. If reagents are supplied via two or more flow pumps, a mixer module is usually required before feeding the stream into the flow reactor. In the case of multiple solvent pumps

being used, the flow rate of the system will be equal to the total sum of the flow rates of each pump. If the reaction does not require heating or other activation, reagents may start reacting as soon as they are mixed. Otherwise, the mixed solutions are pumped into the flow reactor where the reaction occurs. After the reaction mixture exits the reactor, an additional flow stream can provide a quenching solution if needed. An important part of the flow system is pressure regulation usually achieved by installing a Back Pressure Regulator (BPR). This device defines and maintains stable pressure in the system. For example, to prevent solvents from boiling in the tubing by setting the pressure higher than needed for evaporation. BPR serves as a back valve that facilitates fluid stream out of the system to alleviate pressure in the system if it surpasses the desired pressure, while the flow pump provides pressure in the system. Lastly, the fluid stream reaches the collection point and exits the system. This general flow setup can be modified by additional modules for in-flow extraction, introducing gases, in-stream reaction monitoring, etc.⁸

There are 4 commonly used flow reactor types/setups (Figure 1.3). Type I is the most common flow reactor, usually consisting of tubing of a certain length where the reaction occurs between two or more reagents pumped as a homogenous solution (Figure 1.3A). It is similar to the type III flow reactions that use homogeneous catalysts in addition to substrates (Figure 1.3C). However, this type is limited to catalysts' availability and price. In the case of expensive and rare catalysts, such as transition metal complexes, and chiral catalysts there are no significant benefits in running the reaction in flow or batch conditions. Two other reaction setups are based on heterogeneous flow reactors.

Figure 1.3. Flow reactor types.



Type II features a setup that involves passing one of the substrates through a packed-bed reactor with one of the substrates covalently immobilized on some inert media, such as polymer (Figure 1.3B). Reagent A reacts with immobilized reagent B while being passed through the reactor and the products are isolated afterward. This approach has advantages such as the stabilization of otherwise labile reagent B on the polymer support that prolongs its half-life. However, eventually, such a flow reactor will require regeneration to restore consumed reagent B. The most effective, but often difficult to set up is the Type IV flow system (Figure 1.3D). This setup takes advantage of immobilized catalysts to achieve heterogeneous catalysis in flow. During the reaction, the catalyst is immobilized on an insoluble matrix in a packed-bed reactor while catalyzing the reaction between the substrates being passed by flow. Even though this is a most ideal scenario to perform catalytic reactions without any scale limitations as the catalyst remains intact in packed bed reactors, there are only a few examples of such transformations. First, the immobilized catalyst in a packed bed reactor should be easily regenerated or reactivated, preferably without disassembling the reactor. Second, the catalyst should have a high turnover number to achieve efficient large-scale synthesis. Third, heterogeneous flow systems such as Type IV reactors are hard to design due to various undesirable processes such as clogging of fluid lines due to the presence of insoluble components or large back pressure build-up. Back pressure occurs when flow of liquid should pass through some heterogeneous media with low porosity, such as polymer materials used for catalyst immobilization. If these issues are properly addressed, type IV reactors could be employed to

achieve highly efficient synthetic protocols utilizing only small quantities of catalysts. Therefore, the synthesis of recyclable immobilized catalysts for continuous flow applications represents the importance of this field.^{5,9}

1.3 Photocatalysis principles

One of the important aims of catalysis is to investigate new methods for molecular activation. Using light as the energy source for catalysis has become increasingly popular over recent decades as photons are the form of energy that could provide reactivity unobservable under thermal conditions. Historically, the majority of photochemical organic transformations rely on high-energy light sources, such as UV-B or UV-C light. The efficiency is limited by the formation of numerous side products due to the decomposition of starting materials and products under UV-B and UV-C irradiation. The use of high-energy light sources requires special equipment, and safety precautions and is often hard to reproduce. Many of these problems have been addressed after the development of photocatalysts (PC) that can be activated with low-energy photons to promote further transformations of the organic molecules.¹⁰

Before describing the principles of photocatalysis, we should review the general principle of molecular photoactivation. Most of the organic molecules have a multiplicity of 1 in their ground state (i.e. there are no unpaired electrons, and the total spin is 0) which is called ground singlet state (S_0). Multiplicity can be calculated using the formula (eq. 3) where S – is the total spin of electrons:

$$M = 2S + 1 \quad (3)$$

It is worth noting that changes in electronic state can happen with a change in the total spin of electrons. However, in general, such transitions have a low probability of occurrence and are rendered as “forbidden”. The probability of transition could be established using quantum

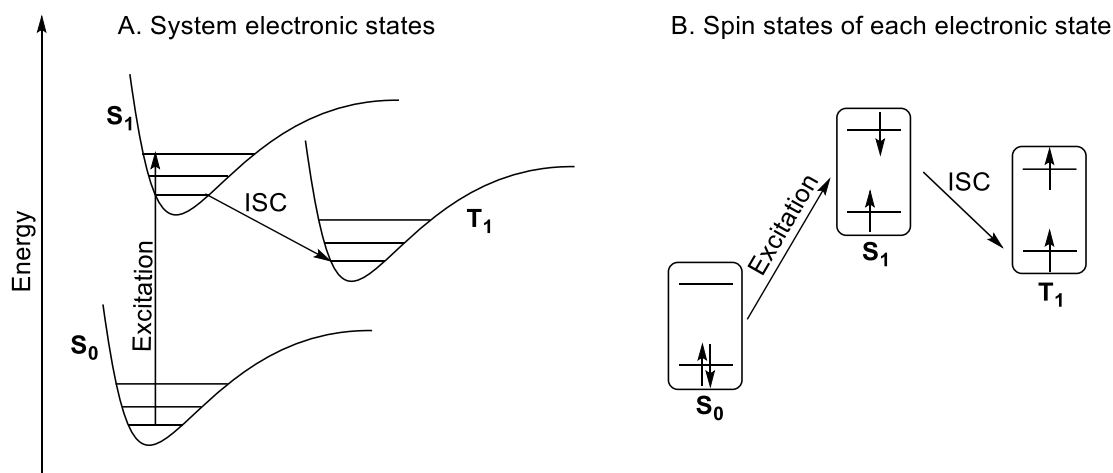
chemistry selection rules. These rules are based on the calculating transition moment integral (eq.4) where ψ_1 and ψ_2 – wave functions of the two states, μ – transition moment operator:

$$m_{1,2} = \int \psi_1 \mu \psi_2 d\tau \quad (4)$$

The transition is forbidden if the value of the integral is 0 which can often be established by looking at the symmetry of wavefunctions without actual integral calculation. If anti-symmetric or odd, then it will have a value of 0. In the case of electronic transitions under photoexcitation, a change of the spin represents an anti-symmetric case $\psi_1(\alpha) = -\psi_2(\beta)$ and will have the transition moment integral equal to 0. Therefore, light-induced transitions are forbidden if happening with a concurrent change in total spin S.¹¹

The molecular electronic transitions are typically described using the Jablonski diagram (Scheme 1.1A). As discussed above, absorbing photons will lead to a photoexcitation from the ground S_0 energy level to the first excited state S_1 (or higher states depending on the photon energy). Such transitions are also more likely to happen between the most similar in symmetry vibrational states of molecules. According to Franck–Condon principle¹² such transitions result in almost no change in the molecular geometry. However, they will lead to a higher energetic vibrational state S_1 which can then relax to a lower vibrational state with some non-irradiative energy loss. Relaxation back to S_0 with a photon release is called fluorescence. In some cases, molecules can undergo intersystem crossing to the triplet state T_1 . Relaxation from T_1 to S_1 is called phosphorescence, which is a spin-forbidden process and explains why triplet states typically have longer lifetimes (10^{-9} to 10^{-6} sec for fluorescence, 10^{-3} to >100 sec for phosphorescence). The changes in spin states during the described processes are also represented in Scheme 1.1B.¹¹

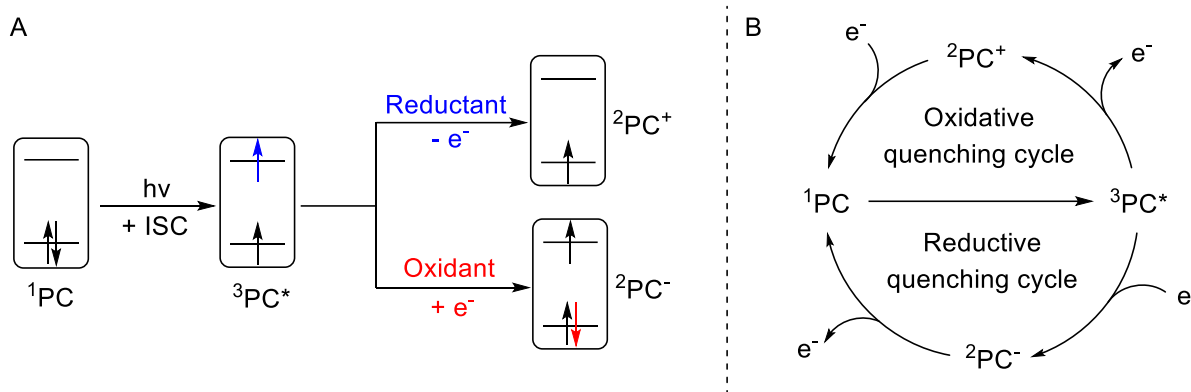
Scheme 1.1. General Jablonski diagram for molecule electronic states.



For further discussion in this thesis, we will introduce and distinguish two ways by which the excited photocatalyst can interact with a substrate: (1) single electron transfer (SET) and change in oxidation states (photoredox catalysis) and (2) energy transfer (EnT) with no concurrent change in oxidation states.¹³

Photoredox catalysis has received an enormous amount of attention from the synthetic community in the last two decades. Photoredox catalysis may be applied to almost all types of organic reactions: from direct SET-promoted cyclization to metal-catalyzed cross-coupling reactions. Currently a wide range of Ru- and Ir- photocatalysts have been developed and they have dominated the field of photoredox reactions. The key feature of these photocatalysts is the effective photoexcitation under mild photo conditions (370-450 nm light sources). Scheme 1.2 depicts the principles of photocatalysis described above.¹⁴

Scheme 1.2. General mechanism and catalytic cycles for photoredox catalysis.

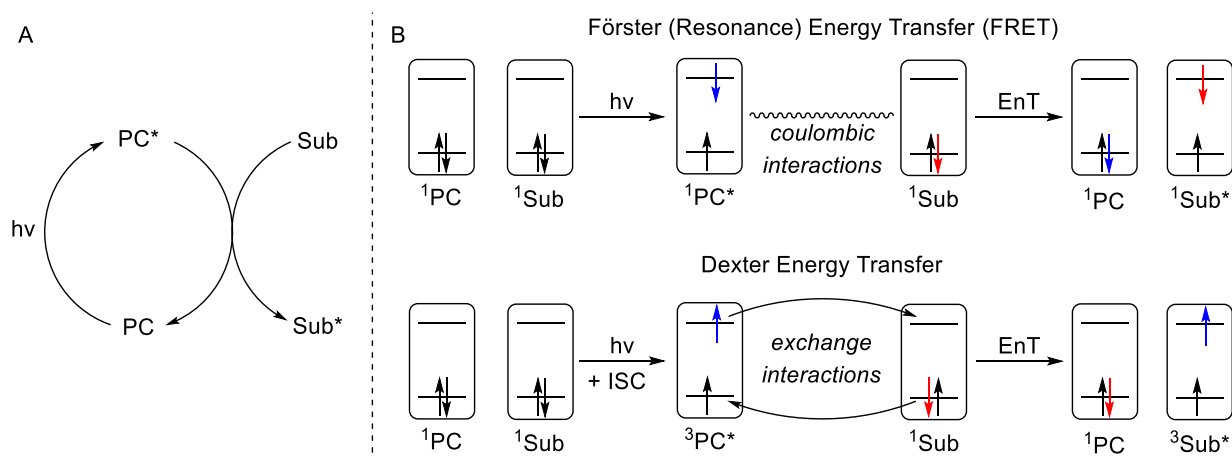


The general mechanism for the photoredox catalytic cycle is as follows (Scheme 1.2A). First, the photocatalyst is excited by UV-A or visible light to its long-living triplet state ($^3\text{PC}^*$). In contrast to the ground state, the excited triplet state ($^3\text{PC}^*$) has two unpaired electrons on different orbitals making it suitable for both reduction and oxidation processes. The higher energy electron in the ^3PC triplet state serves as a better reductive agent than ^1PC in its ground state, while the lower SOMO (Single Occupied Molecular Orbital) in the ^3PC triplet state has an increased oxidative property compared to ^1PC . Excited ^3PC may either perform a SET oxidation or a SET reduction. Regeneration of the photocatalyst occurs via either oxidation or reduction with different reaction substrates, intermediate or sacrificial reagents. Depending on what type of process leads to the PC regeneration, photocatalytic cycles may be classified as reductive quenching cycle or oxidative quenching cycle (Scheme 1.2B). As discussed above, an enormous amount of protocols using photoredox catalytic cycles have already been published leaving energy transfer photocatalysis underdeveloped.^{15,16} Photoredox catalysis has been widely implemented for reactions requiring SET processes, for example, oxidations/reductions,¹⁷ anion-radical cyclizations,¹⁸ and more.

In comparison to the large number of photoredox-based catalytic cycles that have been published to date, the discussed below energy transfer photocatalysis is significantly less

developed. There are reactions proceeding without change in oxidation states and requiring direct excitation of molecules. For many organic molecules, direct excitation is not effective due to their large $S_0 - S_1$ energy gap which requires using high-energy light sources that may also decompose starting materials. This obstacle can be overcome by introducing energy transfer (EnT) catalysts which serve as mediators for indirect photoexcitation of the substrate (Scheme 1.3A). Such photocatalysts typically possess an efficient $S_0 - S_1$ transition and are excited using longer wavelengths of light that are compatible with organic substrates. An excited photocatalyst (PC*) interacts with the substrate and donates the energy to the substrate and returns to its ground state. In contrast to SET processes, there are no electron transfers only energy exchange, but energy carried by photons is transferred to the substrate indirectly.¹⁹

Scheme 1.3. General catalytic cycle and mechanisms of EnT processes



The first mechanism of energy transfer is called as referred to as Förster (Resonance) Energy transfer or FRET and proceeds through a dipole-dipole (columbic) interaction between the excited photocatalyst (called donor) and substrate (acceptor). The photocatalyst first is excited to the S_1 state, and then electronic oscillations in the excited state induce a dipole in the ground state of the acceptor through the electromagnetic field. This interaction promotes the excitation of the acceptor to the first excited singlet state ($^1Sub^*$) while energy for this transition is taken during the

relaxation of the donor ($^1\text{PC}^*$ to ^1PC). This mechanism plays an essential role in natural photosynthesis as well as in fluorescence labeling and bioimaging. Additionally, due to the nature of an energy transfer of a substrate through space, these processes may occur with significant separation in space (10-100 Å).²⁰

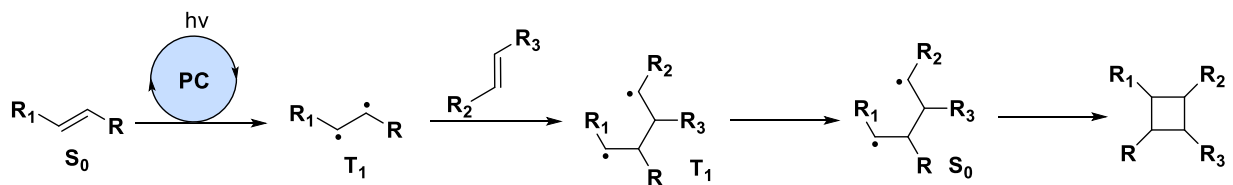
However, the typical EnT processes from PC excited triplet state ($^3\text{PC}^*$) to a substrate (^1Sub) cannot be described by the Förster mechanism. It would require two separate electronic transitions with spin change forbidden by the Wigner spin-conservation rule.²¹ Considering this, the second EnT mechanism proposed is called Dexter energy transfer (Scheme 1.3B).²² This the main mechanism through which energy transfer happens between the PC and substrate in solution. First, the photocatalyst is excited by the light source to its T_1 state ($^3\text{PC}^*$) via intersystem crossing. Eventually, the photocatalyst and substrate approach each other via diffusion and form a solvent-shared encounter complex. Within this complex, collisions occur which result in orbital overlap. Having proximity to each other and efficient orbital overlap facilitates two-electron transfers resulting in a higher energy electron from the $^3\text{PC}^*$ SOMO orbital transferring to the LUMO of the substrate (^1Sub). At the same time electron from the substrate HOMO orbital transfers to the lower energy SOMO orbital in $^3\text{PC}^*$. As a result of this electron exchange, the photocatalyst returns to its ground state ^1PC by losing an excited electron while the substrate receives a high-energy electron from the PC and loses one of the ground-state electrons resulting in the formation of a triplet state ($^3\text{Sub}^*$). It should also be noted that all the mechanistic steps of Dexter energy transfer described above compete with uni- or bimolecular excited state deactivation processes, such as phosphorescence or static quenching. For photocatalysts with relatively shorter triplet state lifetimes, triplet deactivation can become a limitation for the overall EnT process. Dexter EnT process is usually effective when the orbital overlap between donor and acceptor is significant,

meaning that they are similar in energy and symmetry in space. Generally, when the energy of the triplet state of the donor is higher than the acceptor ($E_T(D) > E_T(A)$), energy transfer should be fast and the kinetics should be close to the diffusion limit. In the case of reverse energy gap when $E_T(D) < E_T(A)$, energy transfer can occur, but it is limited to specific high-energy vibrational or rotational levels of the donor T_1 state that can effectively couple with energy levels of the acceptor.²⁰

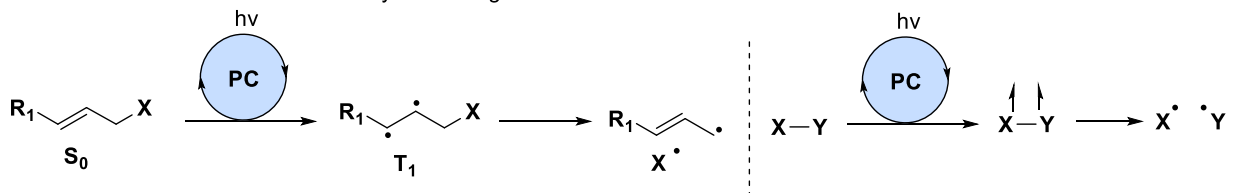
Most of the time EnT processes are used to unlock thermally forbidden transformations such as $[2\pi+2\pi]$ cyclization (Scheme 1.4). For example, an olefine can be excited to its triplet state via the photocatalytic EnT mechanism which can subsequently undergo radical addition with another alkene molecule (Scheme 1.4, A) resulting in another bi-radical species. This bi-radical intermediate relaxes back to its singlet state and rapidly dimerizes leading to a cyclobutane ring as the product of formal $[2\pi+2\pi]$ cycloaddition. Another application of EnT alkene activation through the triplet state is its E/Z isomerization as in the bi-radical state there are no rotational barrier existing in comparison to the ground state which is locked by the π -bond. Also, the excited triplet states behave as typical bi-radical species and can undergo a radical bond scission or homolytic cleavage to form new radical intermediates (Scheme 1.4, B).¹⁹

Scheme 1.4. Examples of EnT reactions proceeding via Dexter EnT mechanism.

A. Excitation of olefines and $[2+2]$ cycloadditions



B. Radical bond scissions and homolytic cleavage



Considering that there is less development in the area of EnT processes in comparison to a wide scope of photoredox reactions, our work will be focused on exploring new types of transformations promoted by excitations to molecules' triplet state via photocatalytic processes.

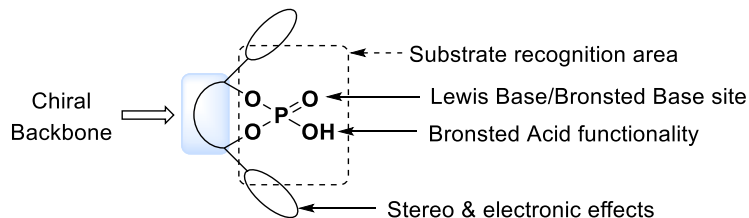
1.4 Overview of Chiral Phosphoric Acid Catalysis

In 2004 Akiyama²³ and Terada²⁴ independently reported using BINOL-based chiral phosphoric acids (CPA) as catalysts for asymmetric Mannich reactions. Since that CPAs have emerged as versatile catalysts for a wide range of organic reactions.²⁵

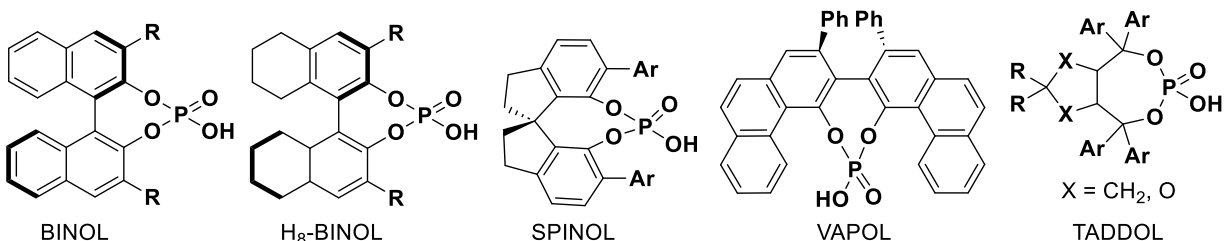
In general, the CPA structure consists of several elements depicted in general Scheme 1.5A. These elements include the chiral backbone skeleton serving as the structural element controlling the stereoselectivity of the reaction, tunable substituents on the chiral backbone that could be used to adjust the steric and electronic environment of the catalyst cavity, and the phosphoric acid group that serves as the binding site and is essential for the Bronsted acid activity. It is worth noting that hydrogen phosphate moiety has two functional centers, one of which is the hydroxyl (OH) group serving as the Bronsted acid (proton donor), and the second one is phosphate oxygen (=O) that can act as a Lewis or Bronsted base site. Since the original publications by Akiyama and Terada, a great number of different chiral scaffolds have been developed to diversify the catalytic activity of CPAs. The most common ones are represented on the Scheme 1.5B. Among them are BINOL, H₈-BINOL, and SPINOL scaffolds which are the most frequently used due to their excellent ability to stereocontrol and tunability of the substituents in the chiral backbone.²⁵

Scheme 1.5. The general structure of CPA catalysts and most common chiral backbones.

A. Chiral Phosphoric Acids general structure

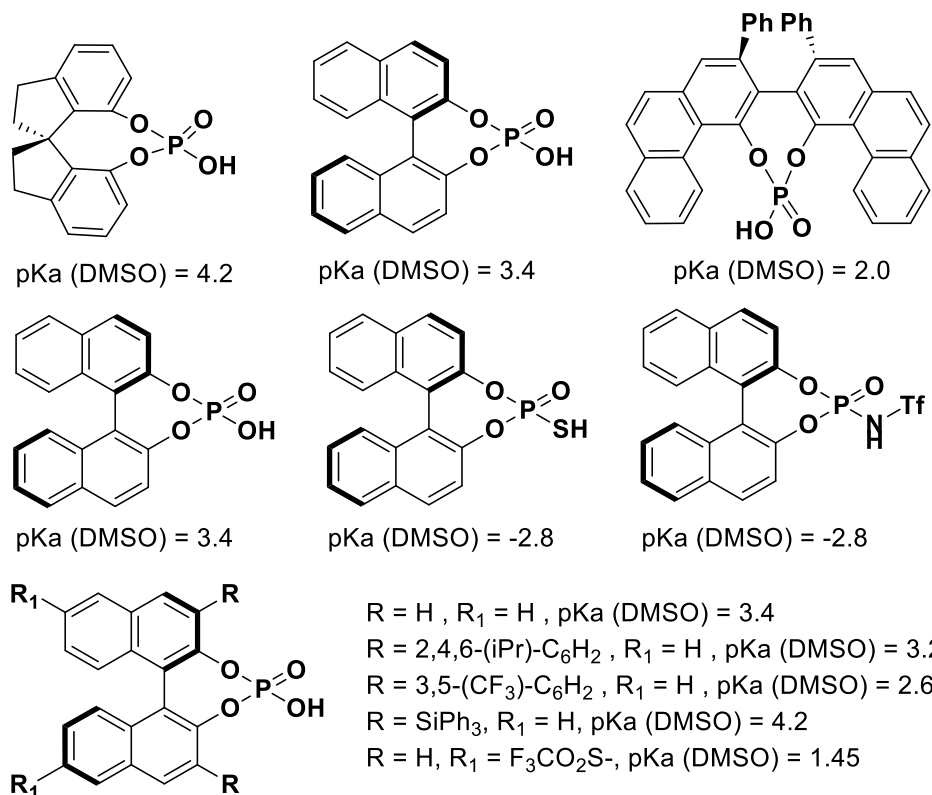


B. Common CPA scaffolds



The structure of the chiral scaffold and substituents significantly impact the catalytic activity and enantioselectivity of a CPA. While the chiral backbone defines the size of the CPA catalytic pocket, the side substituents on it serve as a finer tool to tune the chiral environment of the catalyst. Usually, bulky groups are required to achieve high enantiomeric excess, however, an excessive steric hindrance may retard the reaction and lead to diminished stereocontrol, especially in the case of bulky or conformationally restricted substrates. In addition to the steric control, both the scaffold and its substituents may impact the acidity of the CPAs (Scheme 1.6). For example, the SPINOL has only one aromatic ring in the chiral scaffold. Decreasing the conjugated system leads to lower stability of the CPA anion and therefore to higher values of the pK_a of CPA. In contrast, due to more conjugated aromatic system, VAPOL CPA demonstrates higher acidity.^{26,27}

Scheme 1.6. The pKa dependence on structural elements of CPAs (theoretical studies).

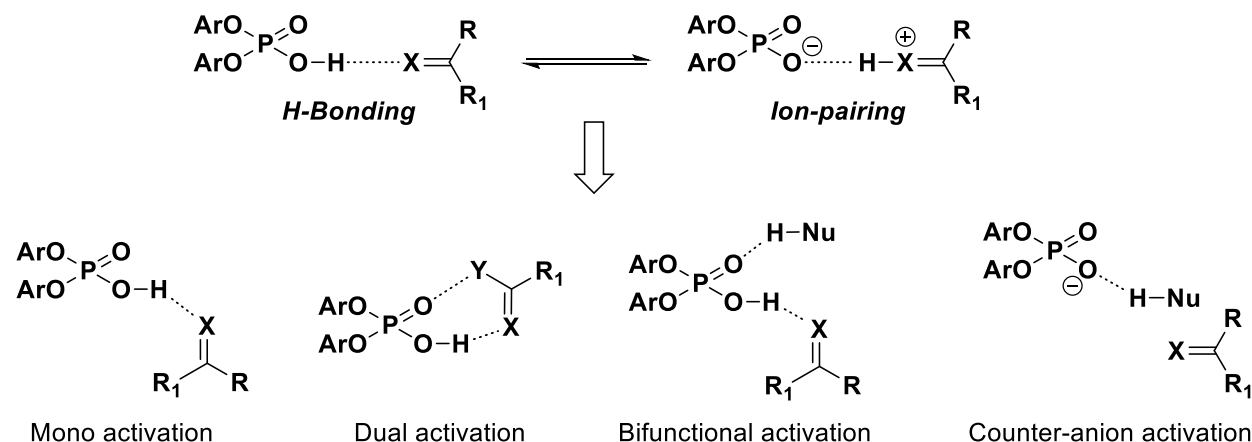


The acidity of CPAs is also strongly dependent on the presence of heteroatoms attached to the phosphoric acid group. Replacing the phosphate hydroxyl group (OH) group to thiol SH increases the acidity of the resulting catalyst by almost 6 pKa units scale due to the lower strength of the S-H bond and higher polarizability of the sulfur atom.²⁷ In 2006 Yamamoto and co-workers²⁸ explored asymmetric Diels-Alder of silyl enol ethers and cyclopentadiene and found that the acidity of chiral phosphate significantly impacts the reaction yields this consequently led to the development of *N*-Triflyl phosphoramides as more acidic variants of CPAs. Electronic effects of substituents can also impact the pKa of a CPA. For example, 3,3'-BINOL-aryl substituents with electron-withdrawing groups lowers pKa from 3.4 (non-substituted BINOL CPA) to 2.6 in the case of BINOL CPA.^{27,29} Introducing triphenylsilyl group has an opposite effect and increases pKa to the value 4.2. Recent theoretical studies by Gennisson and Gaspard also suggest that (*R*)-BINOL-

6,6'-bistriflone CPA derivatives should have significantly lower pKa values than other CPAs due to the presence of strong electron-withdrawing groups. Consequently, such catalysts can be used as alternative to *N*-Triflyl Phosphoramides.³⁰

The acidity of CPA and substrate properties are the most important factors in determining the mode of catalytic activation during the reaction. CPA catalysis is based on a well-known strategy of lowering the LUMO of an electrophile via protonation and activation of the substrate toward reaction with nucleophiles. However, the interaction of a CPA and substrate cannot always be clearly defined as either binding by H-bonding or as a complete protonation with anion coordination. Rather some combination of these two modes on a continuous scale is observed (Scheme 1.7).³¹ Whether the proton is fully transferred to the substrate, or the protonation event happens only partially can be dependent on various factors, such as the pKa of the CPA and the basicity of the functional group interacting with hydrogen phosphate. We will review various modes of the activation on the example of CPA-catalyzed additions to C=X bonds (carbonyls, imines, enamines, enols, etc.).^{31,32} A simple mono-activation can occur when CPA is engaged in H-bonding or protonation of the nucleophile. In some cases, multiple non-covalent interactions may happen at the same time if there are additional sites that can coordinate with hydrogen phosphate via H-bonds.²⁹

Scheme 1.7. Modes of substrate activation by CPAs.



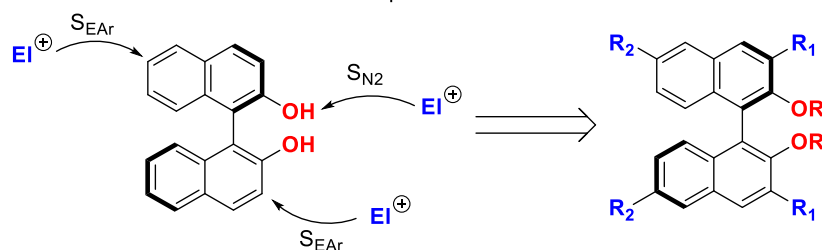
However, the most common mode observed for CPA catalysis is Bifunctional activation, when both electrophile and nucleophile are coordinated to CPA. This is possible due to the both acidic and basic nature of hydrogen phosphate which can serve both as the donor and the acceptor of H-bonds. In this case, in addition to H-bonding to electrophile which activates it by lowering LUMO energy, an additional hydrogen bonding with the nucleophile with oxygen of the CPA facilitates simultaneous nucleophile deprotonation. In addition, bifunctional activation features more restricted electrophile and nucleophile alignment in the TS resulting in higher stereocontrol in the addition reactions.^{31,33} Finally, Benjamin List introduced the concept of the counter anion-directed reactions where the CPA anion, deprotonated by a base before the reaction was used to direct the nucleophilic addition to imine double bonds.³⁴ This approach uses the CPA salts as chiral anions that do not activate electrophiles but rather interact with nucleophiles via an H-bonding framework. Such anion activation has been widely used in combination with Lewis acid catalysis such as metal cations.³⁵⁻³⁷

The synthesis and modification of commonly used CPAs are usually done starting with the commercially available chiral scaffolds such as BINOL, SPINOL, TADDOL, etc. Most commonly, synthetic approaches rely on the activated aromatic systems (for example for BINOL,

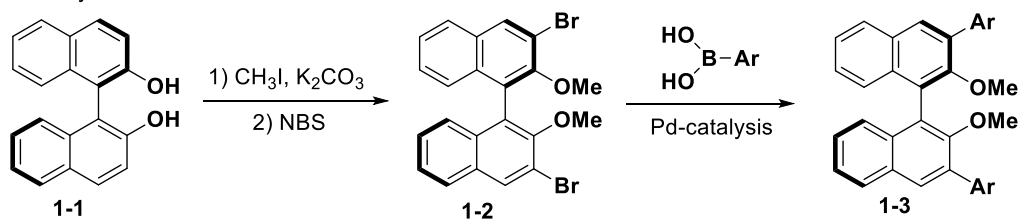
Scheme 1.8A). The hydroxyl group-containing rings in the BINOL scaffold act as classical phenol moieties which may readily react with various electrophiles. The hydroxyl groups activate the aromatic system of BINOL making its modification via the S_{EAr} reaction mechanism much easier relative to benzene. BINOL can easily undergo such reactions as bromination and ortho-lithiation that are used for the subsequent Suzuki cross-coupling reactions to install the substituents at the 3,3'-positions.^{38,39}

Scheme 1.8. Reactivity and general strategy of BINOL scaffold modifications.

A. Selective functionalization of BINOL with electrophiles



B. General way for modification of BINOL Scaffold



A typical strategy for the BINOL-based CPA synthesis is depicted in Scheme 1.8, B. First, hydroxyl groups are protected (for example, as methyl ethers). The resultant BINOL is brominated via a direct reaction with bromine, NBS or iodinated through ortho-lithiation/iodine quench sequence. Thus, obtained intermediate **1-2** is then used in a Pd-catalyzed cross-coupling reaction such as Suzuki coupling to install aryl substituents at the 3,3'-positions of the BINOL skeleton. Finally, hydroxyl groups are deprotected and converted into hydrogen phosphate or its derivatives.³⁸

Although rather simple and well-established transformations are used for the BINOL CPA synthesis, the overall process is not always high-yielding. There are limitations to the cross-coupling reaction substrate scope and outlined above strategy does not allow late-stage modifications of the chiral scaffolds. Due to these reasons, a substantial number of known CPAs remain non-commercialized. This limits the use of CPAs as catalysts for large-scale reactions as CPAs recycling is a challenging task because of their high polarity and acidity. Therefore, an increasing number of recent studies have been focused on making easily recyclable CPAs, with improved post-reaction recovery.

1.4.1 Chiral Phosphoric Acids Immobilization

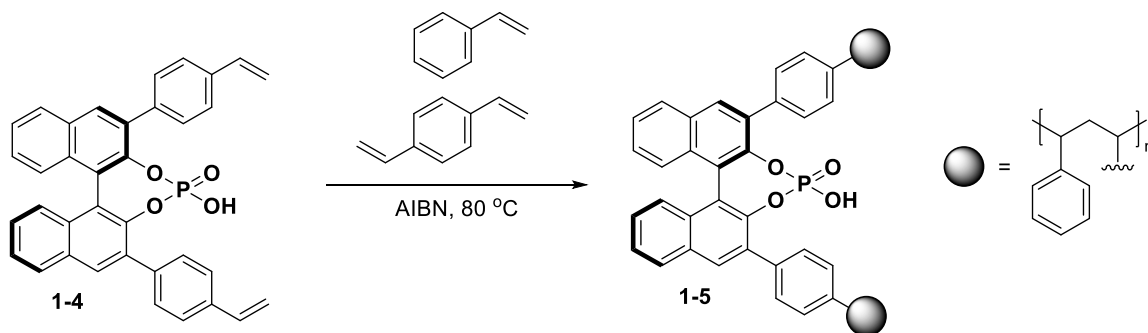
Chiral phosphoric acid catalysis is a well-known and established area in organocatalysis; however, as mentioned above, their availability and problems with recyclability significantly limit the wide-spread application of CPA catalysts, especially in industrial settings (*vide supra*). One of the ways to address this issue is by performing reactions with heterogeneous CPA catalysts. Such catalyst features easier recovery and can potentially be utilized in packed-bed reactors for large-scale synthesis in continuous flow.

In 2010 Rueping and co-workers were the first group to introduce the concept of CPAs immobilization onto insoluble in organic solvents polymeric matrix (Scheme 1.9). The main idea of this approach is to perform heterogeneous catalysis using immobilized CPAs with convenient and easy-to-execute catalyst separation from the reaction mixture by filtration or centrifugation. The initial route (Scheme 1.9, A) started with CPA intermediate **1-4** where the styrene moieties were introduced to the BINOL scaffold into 3,3'-positions. These alkenes were then used to perform a co-polymerization of CPA to form polymeric material representing polystyrene matrix installed catalytic CPA units. Divinyl benzene was added to create additional cross-linkage in the

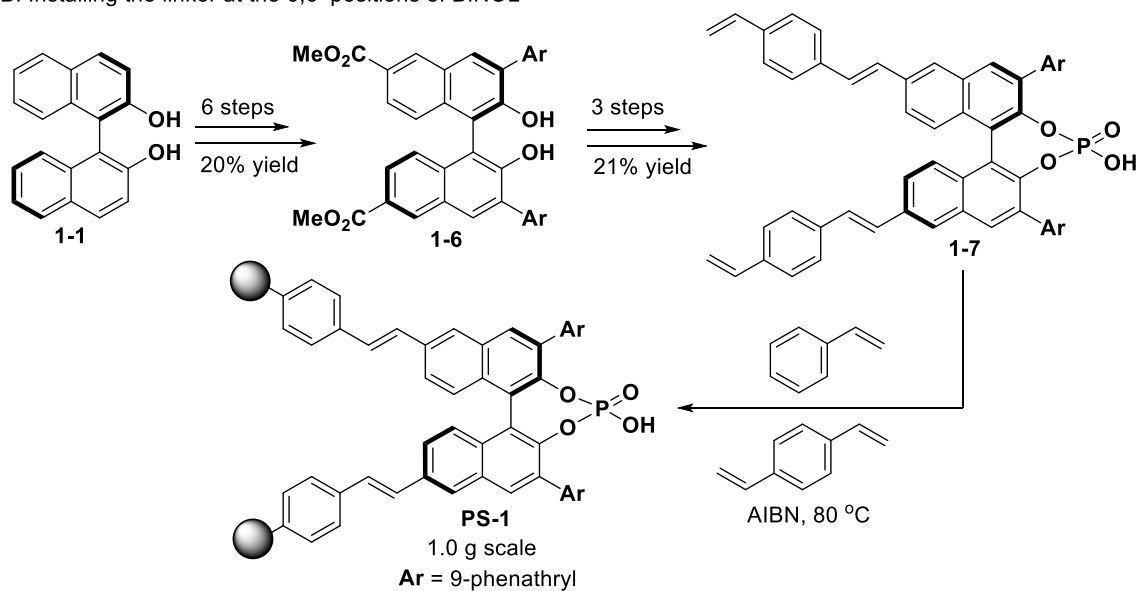
polymer matrix with a more porous and rigid structure. However, even though the immobilization of the CPA was successful, the obtained material **1-5** had inferior catalytic activity in the control reaction (asymmetric transfer hydrogenation) resulting in only 65% ee vs the standard protocol with the monomeric CPA that provided 92% ee. This was explained by the difference in the size of the 3,3'-substituents, as the previously published methods used CPA with 9-phenanthryl substituents, which gave different stereoenviroment in comparison to the synthesized immobilized CPA **1-5**.⁴⁰

Scheme 1.9. Approaches to CPA immobilization by Rueping and co-workers.

A. Installing the linker at the 3,3'-positions of BINOL



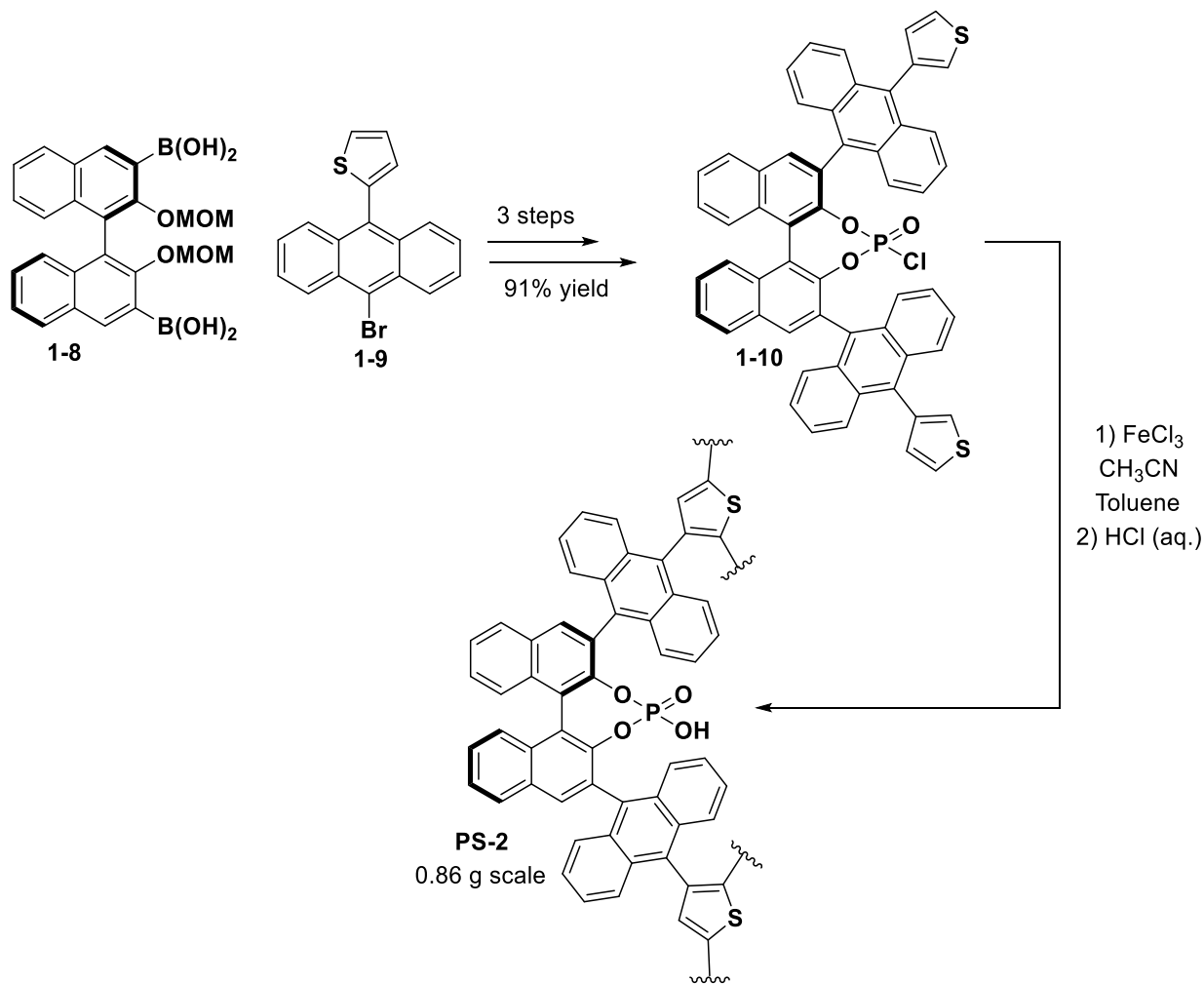
B. Installing the linker at the 6,6'-positions of BINOL



Considering this, the authors implemented a different approach to the synthesis of immobilized CPAs. Starting with (*R*)-BINOL **1-1**, in 6 steps they synthesized intermediate **1-6** containing ester groups in 6,6'-positions and 9-phenanthryl substituents at the 3,3'-positions. Then ester groups were converted into styrene-based linkages giving intermediate **1-7** (3 steps, 21% yield) which was co-polymerized with styrene to generate material **PS-1** (1.0 g scale). This immobilized CPA demonstrated high catalytic activity in the reactions similar to standard homogenous catalysis and the authors were able to recycle the polymeric catalyst with no catalytic activity loss for more than 10 reaction cycles.⁴⁰

In a subsequent study in 2011, the Blechert group proposed a different method for CPA immobilization that was also based on installing the linker groups into the 3,3'-positions of the BINOL skeleton (Scheme 1.10).

Scheme 1.10. Synthesis of the immobilized CPA PS-2 by Blechert.

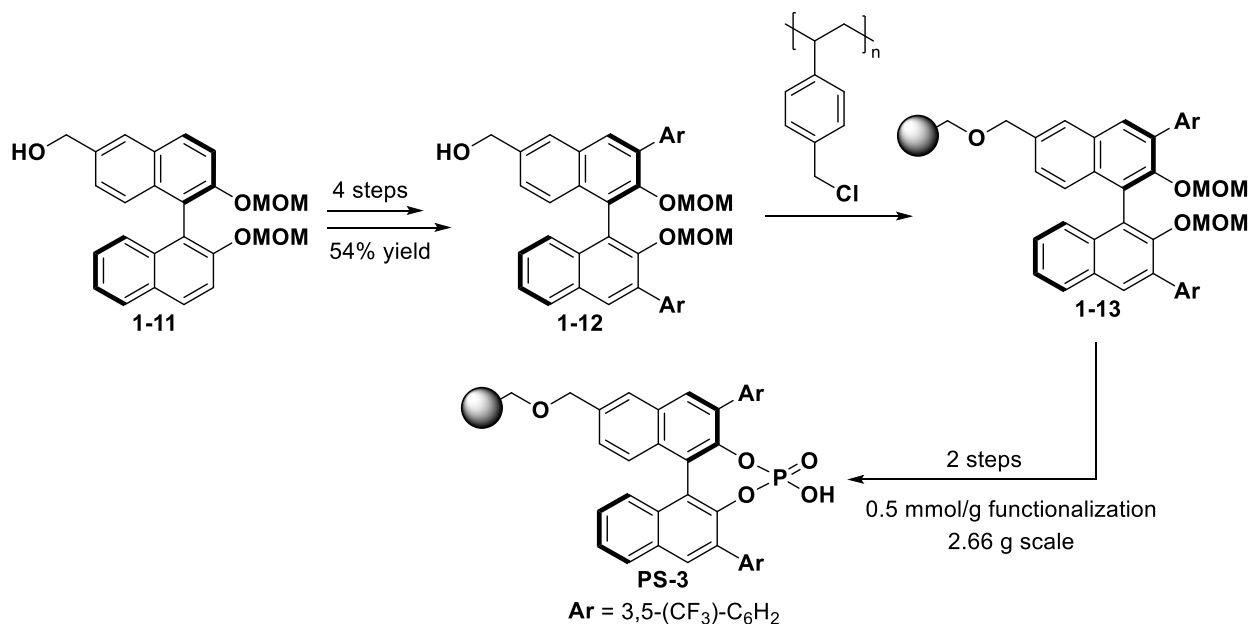


In this approach, they started with the known MOM-protected BINOL derivative **1-8** containing preinstalled boronic acid groups at the 3,3'-positions. Following the Suzuki cross-coupling with compounds **1-9**, the hydroxyl groups were deprotected and converted to phosphoryl chloride derivatives **1-10**. Subsequently, **1-10** was subjected to mild oxidative conditions (FeCl₃) which induced cross-coupling at the thiophene moieties thus creating a polymer matrix. Finally, the phosphoryl chloride was hydrolyzed giving the polymeric material **PS-2** with installed CPA centers. Even though the obtained material **PS-2** demonstrates high catalytic activity and recyclability in asymmetric transfer hydrogenation reactions (see Chapter 3 for more details), this

synthetic route is limited to thiophene derivatives required for polymerization and it is challenging to tune the CPA chiral environment by modifying its 3,3'-substituents.^{41,42}

Significant improvements in the area of CPA immobilization and catalysis have been made by the Pericas group. In 2014 Pericas and co-workers reported an alternative way of installing CPA into the polymer matrix (Scheme 1.11). Instead of co-polymerization of CPA with other monomers, the authors synthesized building block **1-12** containing free primary hydroxyl group from the intermediate **1-11** (4 steps, 54% yield). The alcohol moiety was then used to couple intermediate **1-12** with already existing commercially available Merrifield resin via a nucleophilic substitution reaction. Subsequently, polymeric material **1-13** was deprotected and hydroxyl groups converted to hydrogen phosphate providing polymeric catalyst **PS-3** in 7 overall steps.

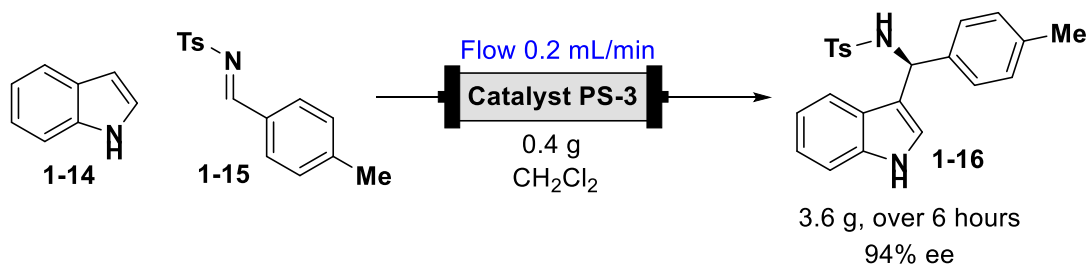
Scheme 1.11. Immobilization of CPA via its installation into Merrifield resin.



Notably, the Pericas group demonstrated that **PS-3** is suitable for the reactions in continuous flow (Scheme 1.12). Their flow system consisted of a flow pump and packed-bed reactors holding 0.4 g of polymeric catalyst **PS-3**. At the 0.2 mL/min flow rate, 3.6 g of Friedel-Crafts product **1-16**

was obtained in 94% enantiomeric excess. The reaction in-batch demonstrated catalytic activity loss after 8 reaction cycles, however, the catalyst was successfully regenerated by wash with HCl.⁴³

Scheme 1.12. Friedel-Crafts reaction in continuous flow using a reaction with immobilized CPA PS-3.

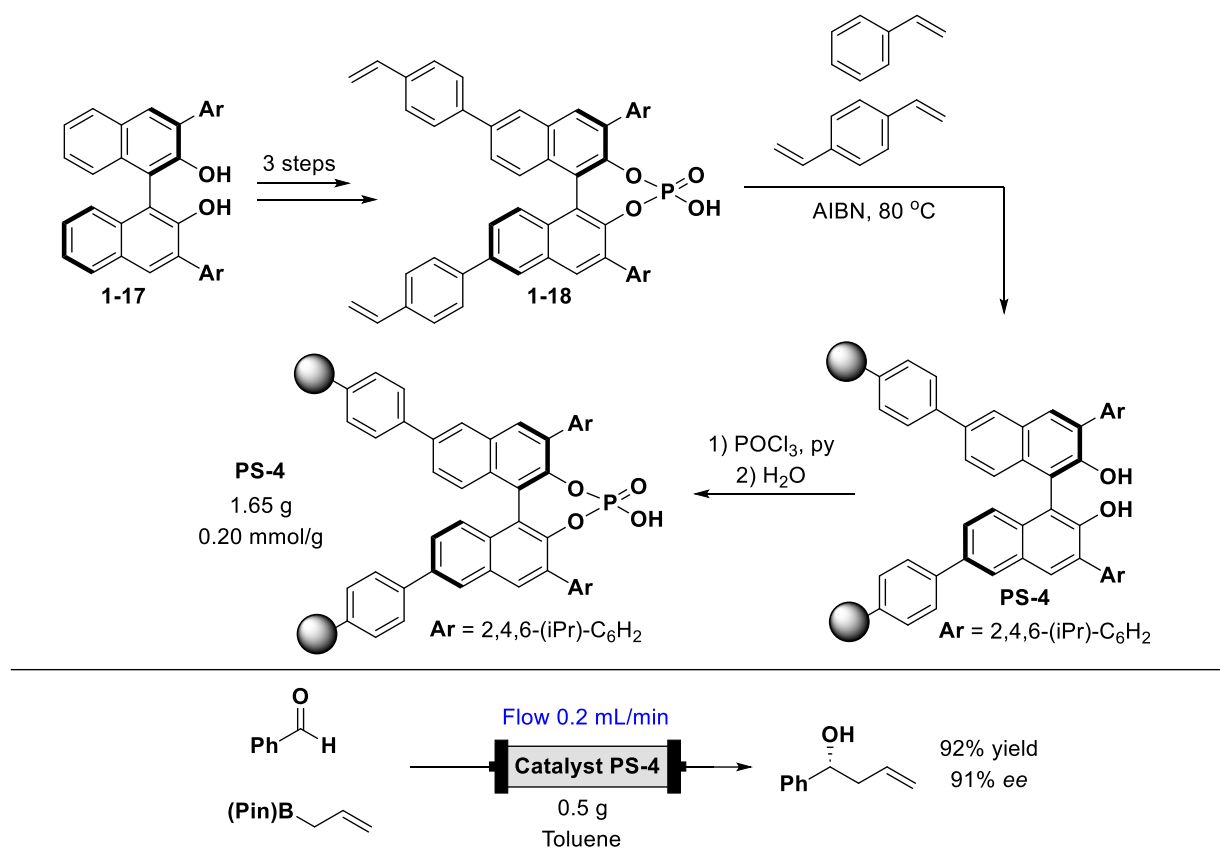


Despite the aforementioned successful application of immobilized CPA **PS-3** in continuous flow, the preparation of catalyst **PS-3** requires many synthetic steps and starts with unavailable intermediate **1-11**.

To address these issues, the Pericas group 2016 proposed a different route based on the immobilization pathway published by the Rueping group in 2010. The authors were able to shorten the linker installation by synthesizing intermediate **1-18** from the commercially available BINOL **1-17** with already pre-installed substituents at the 3,3'-positions. BINOL derivative **1-17** was brominated at the 6,6'-positions and then cross-coupled with vinylboronic acid to produce intermediate **1-18** (2 steps, 65% yield) which was ready for co-polymerization with styrene (Scheme 1.13). Similar to Rueping's protocol, divinyl benzene was added as a cross-linker to create a polymer with a suitable structure. As a result, the immobilized CPA **PS-4** can be produced in only 5 steps from the commercially available compound **1-17**. Catalyst **PS-4** was then explored in aldehyde allylation using allylpinacol borane both in batch and continuous flow (Scheme 1.13). With a combined flow rate of 0.2 mL/min, the allylation product can be obtained in 92% yield and 91% ee. The total operation time for the flow system was 28 hours before the catalytic activity of the immobilized CPA dropped and had to be reactivated by washing with HCl in EtOAc. Based

on this, the authors calculated the TON (turnover number) of the catalyst to be 282 and the productivity was determined to be 2.22 mmol/(h×gram of resin).⁴⁴ The developed immobilized catalyst **PS-4** can also be successfully used to promote a Pictet-Spengler cyclization with a continuous flow setup as well.⁴⁵

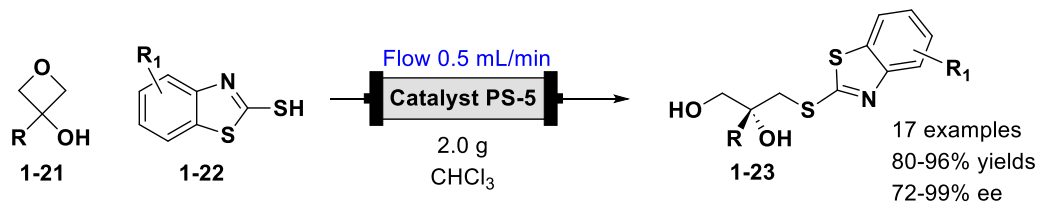
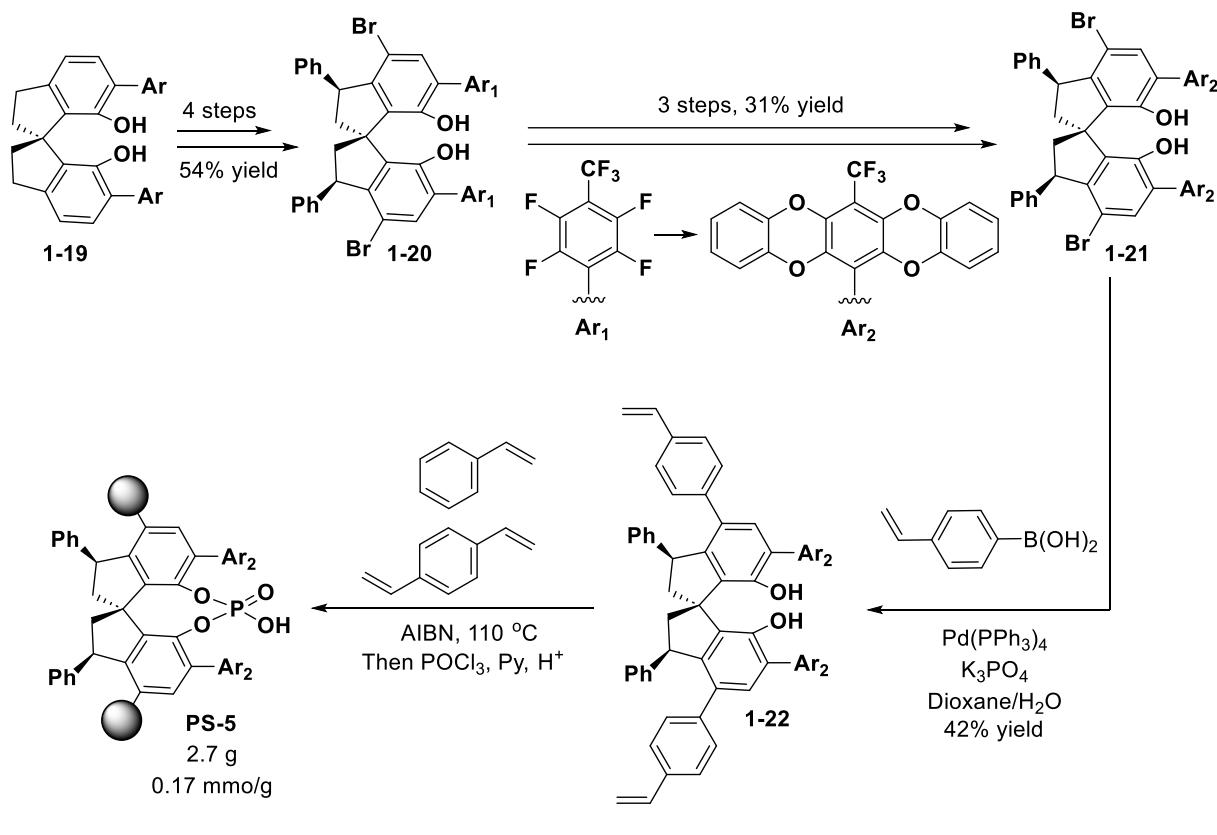
Scheme 1.13. Improved synthesis of the polymeric TRIP CPA by Pericas and co-workers and its application for the allylation in continuous flow.



Contemporaneously with our work in this area, Pericas and co-workers established the same pathway for the immobilization of the SPINOL-based CPAs (Scheme 1.14). Their synthesis started with the SPINOL intermediate **1-19** containing fluorinated aryl substituents (Ar₁). A four-step sequence was needed to install the bromine atoms at the 4,4'-positions of the SPINOL scaffold to get intermediate **1-20**. Then, via 3 steps aryl substituents (2 steps for protection and deprotection of hydroxyl groups) were modified to create more steric hindrance in the catalytic center (Ar₂).

The authors utilized the same procedure for installing styrene cross-linkers into a molecule and performing immobilization of the SPINOL scaffold into a polymeric matrix via co-polymerization. Phosphoric acid group installation was performed on already polymerized material giving immobilized catalyst **PS-5**. The developed catalyst was successfully applied to perform a desymmetrization reaction of 3,3-substituted oxetanes **1-21** (Scheme 1.14). A procedure was developed to perform the transformation in a continuous flow using 2.0 g of immobilized resin **PS-5** packed into a glass Omnifit column. The flow system allowed to perform reactions with 0.5 mL/min flow rate to prepare desymmetrized products **1-23** on the gram scale. In total, 17 substrates were synthesized in 80-96% yields and moderate to perfect enantioselectivity (72-99 % ee).⁴⁶

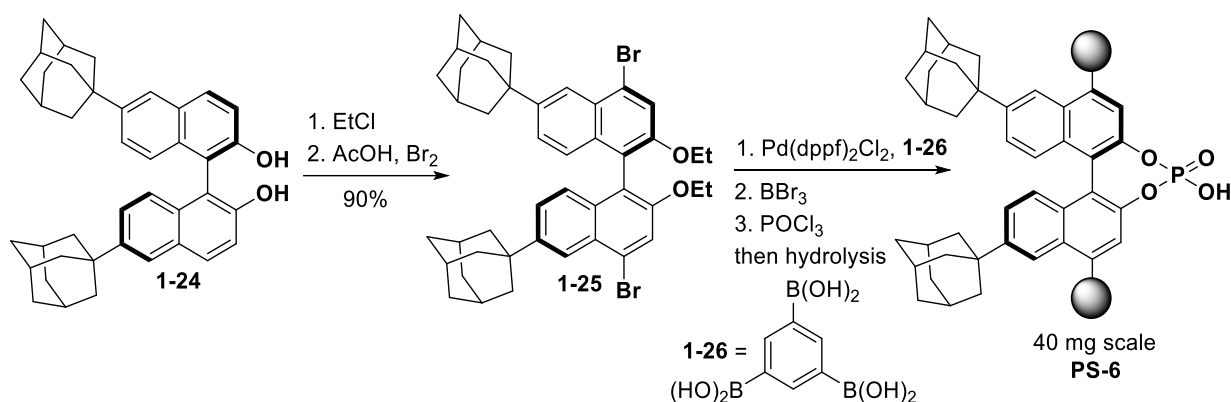
Scheme 1.14. SPINOL-based CPA immobilization and application for desymmetrization of 3,3-Disubstituted Oxetanes in a continuous flow by Pericas.



An alternative polymeric framework with an installed CPA catalyst was developed by the Sanchez group in 2019 (Scheme 1.15). The precursor **1-24** can be easily obtained from commercial BINOL and 1-adamantanol. Protection and bromination of **1-24** in acetic acid gave intermediate **1-25** which then was cross-coupled with triboronic acid **1-27** to obtain a porous framework containing BINOL functional groups (after deprotection with BBr₃). The authors used synthesized material to perform diethylzinc addition to aldehydes where immobilized BINOL served as a chiral ligand. The reaction proceeded with high yields (> 90%) and perfect enantioselectivities (87-91 %

ee). After that, this material was subjected to phosphorylation with POCl_3 and hydrolysis to install the phosphoric acid group into BINOL. Unfortunately, the obtained polymeric material **PS-6** demonstrated poor catalytic activity in asymmetric transfer hydrogenation reactions (see Chapter 3) producing chiral heterocycles only with 35% ee.

Scheme 1.15. Preparation of embedded BINOL to the porous aromatic framework by Sanchez.



This can be explained by the absence of bulky substituents in 3,3' BINOL positions needed to achieve significant stereocontrol in tested reactions.⁴⁷

In summary, we can say that several published works describe successful protocols for CPA immobilization and further applications for the reactions in continuous flow. However, the scope of the reactions as well as the scope of the synthesized immobilized CPAs still quite small and not well developed despite the perspectives to use such catalysts as novel and sustainable method to perform catalytic transformations on large scale.

1.5 References

- (1) STEPHEN K. RITTER. EPA Data Suggest Green Success. *Chemical & Engineering News Archive* **2015**, 93 (5), 32–33. <https://doi.org/10.1021/CEN-09305-SCITECH1>.
- (2) Paul T Anastas; John Charles Warner. *Green Chemistry: Theory and Practice*: Paperback: Paul Anastas. **1998**, 148.
- (3) Ganesh, K. N.; Zhang, D.; Miller, S. J.; Rossen, K.; Chirik, P. J.; Kozłowski, M. C.; Zimmerman, J. B.; Brooks, B. W.; Savage, P. E.; Allen, D. T.; Voutchkova-Kostal, A. M. *Green*

- Chemistry: A Framework for a Sustainable Future. *Organic Process Research and Development*. American Chemical Society July 16, 2021, pp 1455–1459. <https://doi.org/10.1021/acs.oprd.1c00216>.
- (4) de Marco, B. A.; Rechelo, B. S.; Tótolí, E. G.; Kogawa, A. C.; Salgado, H. R. N. Evolution of Green Chemistry and Its Multidimensional Impacts: A Review. *Saudi Pharmaceutical Journal*. Elsevier B.V. January 1, 2019, pp 1–8. <https://doi.org/10.1016/j.jsps.2018.07.011>.
- (5) Porta, R.; Benaglia, M.; Puglisi, A. Flow Chemistry: Recent Developments in the Synthesis of Pharmaceutical Products. *Organic Process Research and Development*. American Chemical Society January 15, 2016, pp 2–25. <https://doi.org/10.1021/acs.oprd.5b00325>.
- (6) Plutschack, M. B.; Pieber, B.; Gilmore, K.; Seeberger, P. H. The Hitchhiker's Guide to Flow Chemistry. *Chemical Reviews*. American Chemical Society September 27, 2017, pp 11796–11893. <https://doi.org/10.1021/acs.chemrev.7b00183>.
- (7) Capaldo, L.; Wen, Z.; Noël, T. A Field Guide to Flow Chemistry for Synthetic Organic Chemists. *Chemical Science*. Royal Society of Chemistry 2023. <https://doi.org/10.1039/d3sc00992k>.
- (8) Hone, C. A.; Kappe, C. O. Towards the Standardization of Flow Chemistry Protocols for Organic Reactions. *Chemistry-Methods*. John Wiley and Sons Inc November 1, 2021, pp 454–467. <https://doi.org/10.1002/cmtd.202100059>.
- (9) Hayes, H. L. D.; Mallia, C. J. Continuous Flow Chemistry with Solids: A Review. *Organic Process Research and Development*. American Chemical Society 2023. <https://doi.org/10.1021/acs.oprd.3c00407>.
- (10) Reischauer, S.; Us Pieber, B. Emerging Concepts in Photocatalytic Organic Synthesis. *iScience* **2021**, *24*, 102209. <https://doi.org/10.1016/j.isci>.
- (11) Harris, D. C.; Bertolucci, M. D. Symmetry and Spectroscopy: An Introduction to Vibrational and Electronic Spectroscopy. **1989**, 550.
- (12) Franck, J.; Dymond, E. G. Elementary Processes of Photochemical Reactions. *Transactions of the Faraday Society* **1926**, *21* (February), 536–542. <https://doi.org/10.1039/TF9262100536>.
- (13) Srivastava, V.; Singh, P. K.; Singh, P. P. Recent Advances of Visible-Light Photocatalysis in the Functionalization of Organic Compounds. *Journal of Photochemistry and Photobiology C: Photochemistry Reviews*. Elsevier B.V. March 1, 2022. <https://doi.org/10.1016/j.jphotochemrev.2022.100488>.
- (14) Koike, T.; Akita, M. Visible-Light Radical Reaction Designed by Ru- and Ir-Based Photoredox Catalysis. *Inorg Chem Front* **2014**, *1* (8), 562–576. <https://doi.org/10.1039/c4qi00053f>.
- (15) Prier, C. K.; Rankic, D. A.; MacMillan, D. W. C. Visible Light Photoredox Catalysis with Transition Metal Complexes: Applications in Organic Synthesis. *Chemical Reviews*. July 10, 2013, pp 5322–5363. <https://doi.org/10.1021/cr300503r>.
- (16) Shaw, M. H.; Twilton, J.; MacMillan, D. W. C. Photoredox Catalysis in Organic Chemistry. *Journal of Organic Chemistry*. American Chemical Society August 19, 2016, pp 6898–6926. <https://doi.org/10.1021/acs.joc.6b01449>.
- (17) Teegardin, K.; Day, J. I.; Chan, J.; Weaver, J. Advances in Photocatalysis: A Microreview of Visible Light Mediated Ruthenium and Iridium Catalyzed Organic Transformations. *Organic Process Research and Development*. American Chemical Society July 15, 2016, pp 1156–1163. <https://doi.org/10.1021/acs.oprd.6b00101>.

- (18) Sivanandan, S. T.; Bharath Krishna, R.; Baiju, T. V.; Mohan, C. Visible-Light-Mediated Ring-Opening Reactions of Cyclopropanes. *European Journal of Organic Chemistry*. John Wiley and Sons Inc December 28, 2021, pp 6781–6805. <https://doi.org/10.1002/ejoc.202100986>.
- (19) Strieth-Kalthoff, F.; Glorius, F. Triplet Energy Transfer Photocatalysis: Unlocking the Next Level. *Chem*. Elsevier Inc August 6, 2020, pp 1888–1903. <https://doi.org/10.1016/j.chempr.2020.07.010>.
- (20) Strieth-Kalthoff, F.; James, M. J.; Teders, M.; Pitzer, L.; Glorius, F. Energy Transfer Catalysis Mediated by Visible Light: Principles, Applications, Directions. *Chem Soc Rev* **2018**, *47* (19), 7190–7202. <https://doi.org/10.1039/c8cs00054a>.
- (21) *Spin Conservation Rule (Wigner Rule)*. <https://www.degruyter.com/database/IUPAC/entry/iupac.60.0344/html> (accessed 2024-05-30).
- (22) Dexter, D. L. A Theory of Sensitized Luminescence in Solids. *J Chem Phys* **1953**, *21* (5), 836–850. <https://doi.org/10.1063/1.1699044>.
- (23) Akiyama, T.; Itoh, J.; Yokota, K.; Fuchibe, K.; Akiyama, T.; Itoh, J.; Yokota, K.; Fuchibe, K. Enantioselective Mannich-Type Reaction Catalyzed by a Chiral Brønsted Acid. *Angewandte Chemie International Edition* **2004**, *43* (12), 1566–1568. <https://doi.org/10.1002/ANIE.200353240>.
- (24) Uraguchi, D.; Terada, M. Chiral Brønsted Acid-Catalyzed Direct Mannich Reactions via Electrophilic Activation. *J Am Chem Soc* **2004**, *126* (17), 5356–5357. https://doi.org/10.1021/JA0491533/SUPPL_FILE/JA0491533SI20040216_011316.PDF.
- (25) Rahman, A.; Lin, X. Development and Application of Chiral Spirocyclic Phosphoric Acids in Asymmetric Catalysis. *Organic and Biomolecular Chemistry*. Royal Society of Chemistry 2018, pp 4753–4777. <https://doi.org/10.1039/c8ob00900g>.
- (26) Gashaw, A.; Debeli, D. K. Recent Progress on Asymmetric Multicomponent Reactions via Chiral Phosphoric Acid Catalysis. *Journal of the Iranian Chemical Society*. Springer Science and Business Media Deutschland GmbH May 1, 2022, pp 1593–1611. <https://doi.org/10.1007/s13738-021-02435-1>.
- (27) Yang, C.; Xue, X. S.; Jin, J. L.; Li, X.; Cheng, J. P. Theoretical Study on the Acidities of Chiral Phosphoric Acids in Dimethyl Sulfoxide: Hints for Organocatalysis. *Journal of Organic Chemistry* **2013**, *78* (14), 7076–7085. https://doi.org/10.1021/JO400915F/SUPPL_FILE/JO400915F_SI_001.PDF.
- (28) Nakashima, D.; Yamamoto, H. Design of Chiral N-Triflyl Phosphoramidate as a Strong Chiral Brønsted Acid and Its Application to Asymmetric Diels-Alder Reaction. *J Am Chem Soc* **2006**, *128* (30), 9626–9627. https://doi.org/10.1021/JA062508T/SUPPL_FILE/JA062508TSI20060613_014339.PDF.
- (29) Parmar, D.; Sugiono, E.; Raja, S.; Rueping, M. Complete Field Guide to Asymmetric BINOL-Phosphate Derived Brønsted Acid and Metal Catalysis: History and Classification by Mode of Activation; Brønsted Acidity, Hydrogen Bonding, Ion Pairing, and Metal Phosphates. *Chemical Reviews*. American Chemical Society September 24, 2014, pp 9047–9153. <https://doi.org/10.1021/cr5001496>.
- (30) Mouhtady, O.; Castellan, T.; André-Barrès, C.; Gornitzka, H.; Fabing, I.; Saffon-Merceron, N.; Génisson, Y.; Gaspard, H.; Mouhtady, O.; Gornitzka, H.; Gaspard, H. BINOL-6,6'-Bistriflone: Shortened Synthesis, Characterization, and Enantioselective Catalytic Applications. *European J Org Chem* **2021**, No. 48. <https://doi.org/10.1002/ejoc.202101137i>.
- (31) del Corte, X.; Martínez de Marigorta, E.; Palacios, F.; Vicario, J.; Maestro, A. An Overview of the Applications of Chiral Phosphoric Acid Organocatalysts in Enantioselective

Additions to C=O and C=N Bonds. *Organic Chemistry Frontiers*. Royal Society of Chemistry September 7, 2022, pp 6331–6399. <https://doi.org/10.1039/d2qo01209j>.

(32) Jiménez, E. I. An Update on Chiral Phosphoric Acid Organocatalyzed Stereoselective Reactions. *Organic and Biomolecular Chemistry*. Royal Society of Chemistry April 5, 2023, pp 3477–3502. <https://doi.org/10.1039/d3ob00212h>.

(33) Grayson, M. N. Chiral Phosphoric Acid Catalysis: The Terada Model Revisited. *Journal of Organic Chemistry* **2021**, *86* (19), 13631–13635. <https://doi.org/10.1021/acs.joc.1c01665>.

(34) Mayer, S.; List, B. Asymmetric Counteranion-Directed Catalysis. *Angewandte Chemie International Edition* **2006**, *45* (25), 4193–4195. <https://doi.org/10.1002/ANIE.200600512>.

(35) Phipps, R. J.; Hamilton, G. L.; Toste, F. D. The Progression of Chiral Anions from Concepts to Applications in Asymmetric Catalysis. *Nature Chemistry* **2012**, *4* (8), 603–614. <https://doi.org/10.1038/nchem.1405>.

(36) Li, F.; Korenaga, T.; Nakanishi, T.; Kikuchi, J.; Terada, M. Chiral Phosphoric Acid Catalyzed Enantioselective Ring Expansion Reaction of 1,3-Dithiane Derivatives: Case Study of the Nature of Ion-Pairing Interaction. *J Am Chem Soc* **2018**, *140* (7), 2629–2642. https://doi.org/10.1021/JACS.7B13274/SUPPL_FILE/JA7B13274_SI_005.CIF.

(37) Brodt, N.; Niemeyer, J. Chiral Organophosphates as Ligands in Asymmetric Metal Catalysis. *Organic Chemistry Frontiers*. Royal Society of Chemistry March 29, 2023, pp 3080–3109. <https://doi.org/10.1039/d3qo00206c>.

(38) Pu, L. Regioselective Substitution of BINOL. *Chemical Reviews*. American Chemical Society 2024. <https://doi.org/10.1021/acs.chemrev.4c00132>.

(39) Woldegiorgis, A. G.; Han, Z.; Lin, X. Recent Advances in Chiral Phosphoric Acid Catalyzed Asymmetric Organic Reactions: An Overview. *Journal of Molecular Structure*. Elsevier B.V. February 5, 2024. <https://doi.org/10.1016/j.molstruc.2023.136919>.

(40) Rueping, M.; Sugiono, E.; Steck, A.; Theissmann, T. Synthesis and Application of Polymer-Supported Chiral Brønsted Acid Organocatalysts. *Adv Synth Catal* **2010**, *352* (2–3), 281–287. <https://doi.org/10.1002/adsc.200900746>.

(41) Bleschke, C.; Schmidt, J.; Kundu, D. S.; Blechert, S.; Thomas, A. A Chiral Microporous Polymer Network as Asymmetric Heterogeneous Organocatalyst. *Adv Synth Catal* **2011**, *353* (17), 3101–3106. <https://doi.org/10.1002/adsc.201100674>.

(42) Kundu, D. S.; Schmidt, J.; Bleschke, C.; Thomas, A.; Blechert, S. A Microporous Binol-Derived Phosphoric Acid. *Angewandte Chemie - International Edition* **2012**, *51* (22), 5456–5459. <https://doi.org/10.1002/anie.201109072>.

(43) Osorio-Planes, L.; Rodríguez-Escrich, C.; Pericàs, M. A. Enantioselective Continuous-Flow Production of 3-Indolylmethanamines Mediated by an Immobilized Phosphoric Acid Catalyst. *Chemistry - A European Journal* **2014**, *20* (8), 2367–2372. <https://doi.org/10.1002/chem.201303860>.

(44) Clot-Almenara, L.; Rodríguez-Escrich, C.; Osorio-Planes, L.; Pericàs, M. A. Polystyrene-Supported TRIP: A Highly Recyclable Catalyst for Batch and Flow Enantioselective Allylation of Aldehydes. *ACS Catal* **2016**, *6* (11), 7647–7651. https://doi.org/10.1021/ACSCATAL.6B02621/SUPPL_FILE/CS6B02621_SI_001.PDF.

(45) Chaudhari, M. B.; Gupta, P.; Llanes, P.; Pericàs, M. A. Polymer-Supported Phosphoric-Acid Catalysed Enantioselective Pictet-Spengler Cyclisation for the Synthesis of Quaternary Tryptolines in Batch/Continuous Flow. *Adv Synth Catal* **2023**, *365* (4), 527–534. <https://doi.org/10.1002/ADSC.202201275>.

- (46) Lai, J.; Fianchini, M.; Pericas, M. A. Development of Immobilized Spinol-Derived Chiral Phosphoric Acids for Catalytic Continuous Flow Processes. Use in the Catalytic Desymmetrization of 3,3-Disubstituted Oxetanes. *ACS Catal* **2020**, *10* (24), 14971–14983. https://doi.org/10.1021/ACSCATAL.0C04497/SUPPL_FILE/CS0C04497_SI_002.CIF.
- (47) Monterde, C.; Navarro, R.; Iglesias, M.; Sánchez, F. Adamantyl-BINOL as Platform for Chiral Porous Polymer Aromatic Frameworks. Multiple Applications as Recyclable Catalysts. *J Catal* **2019**, *377*, 609–618. <https://doi.org/10.1016/J.JCAT.2019.07.059>.

Chapter 2 Regioselective Acetalization of Carbohydrates¹

2.1 Introduction to carbohydrates

Carbohydrates are an essential part of our lives as they are involved in a wide range of biological processes in our bodies. Structurally diverse, these compounds are even more complex than other biological polymers. Carbohydrates can exist as oligo- and polysaccharides or as parts of other molecules (aglycons of peptides, lipids, etc.). Besides their role in metabolism and as structural building blocks, they are fundamental parts of every cell structure. Being overlooked in drug discovery previously, carbohydrates represent an unexplored potential source of new drugs and vaccines drug discovery previously, carbohydrates represent an unexplored potential source of new drugs and vaccines.^{1,2}

However, in many instances, gaining access to complex oligosaccharides and glycoconjugates has been the bottleneck for the exploration of their biological and medicinal properties. Complex oligosaccharides are comprised of simpler monosaccharides, and, not surprisingly, modern synthetic approaches to oligosaccharides strongly rely on the ability to access differentially protected building blocks.³

¹ Authors and Contributions:

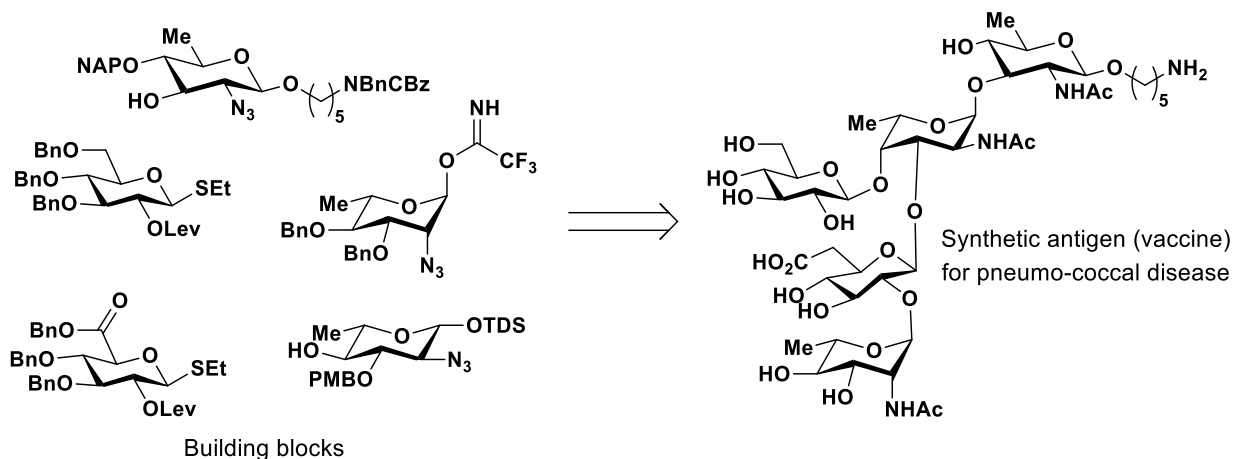
This chapter partially is adapted from: Wang S.*, **Zhelavskiy O.***, Lee J., Arguellas A.*, Khomutnyk Y. Y., Mensah E., Guo H., Hourani R., Zimmerman P., Nagorny P, *JACS* **2021** *143* (44), 18592-18604. * - equal contribution.

Dr. J Lee developed the one-pot protocol for carbohydrate modifications

Dr. Sibin Wang and Dr. Yaroslav Khomutnyk performed catalyst immobilization

Dr. Alonso J. Argüelles contributed to preliminary mechanistic studies

Scheme 2.1. Example of synthetic approach towards synthesis of the complex carbohydrates.

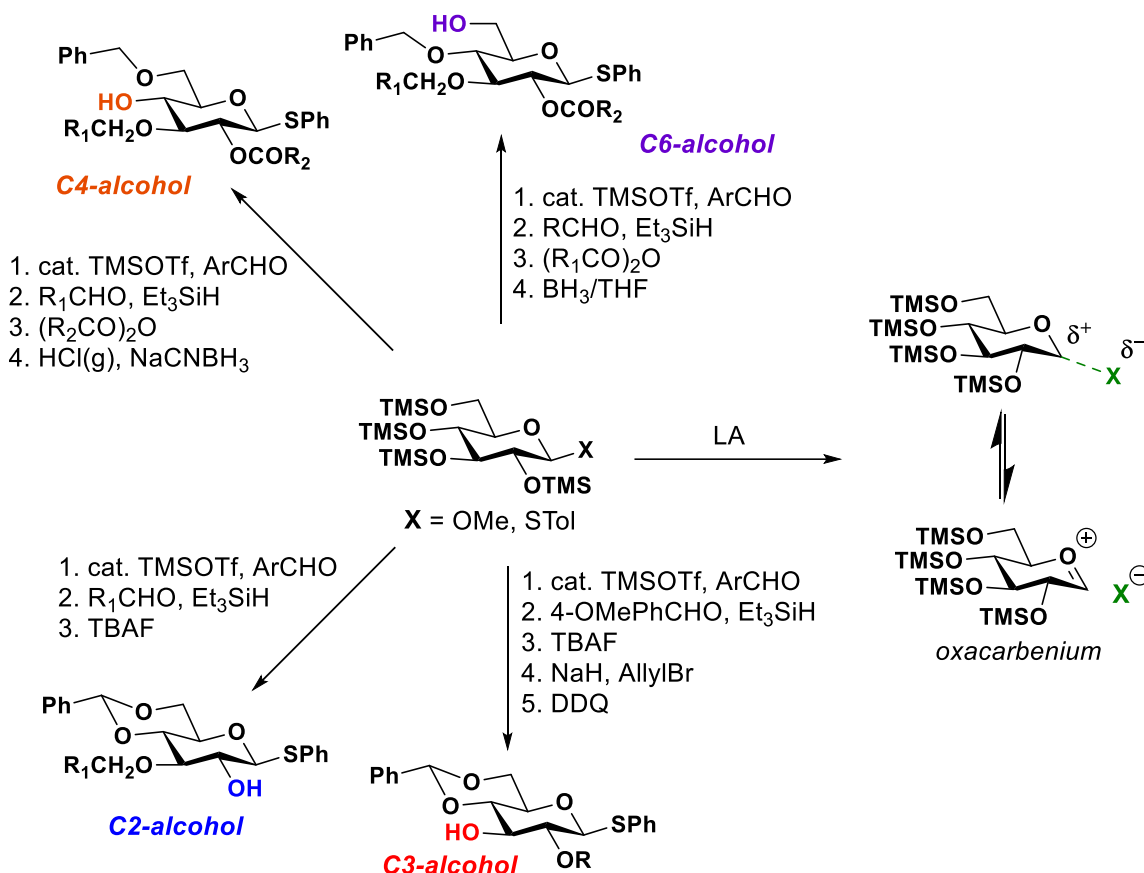


For example, Seeberger describes the synthesis of the carbohydrate vaccine that can be used for preventing pneumococcal disease from 5 different monosaccharide building blocks (Scheme 2.1). More complex carbohydrates can require an even bigger variety of the starting building blocks that should be selectively modified prior to the assembly of the glycan oligomer.⁴ Synthesis of such differentially protected monosaccharides often requires multiple-step sequences to differentiate numerous hydroxyl groups and may suffer from low yields and tedious purifications due to the formation of undesirable regioisomers throughout these sequences.

Most of the approaches towards regioselective monosaccharides modifications are based on protecting group manipulation. The chemistry of hydroxyl groups protection and deprotection is well known; however, the biggest challenge is being able to differentiate between the hydroxyl groups in similar steric and electronic environments. For certain carbohydrates, the C1-position is the only one that can be well distinguished in terms of reactivity as most transformations for the C1-modifications proceed through oxocarbenium cation generated via acid catalysis (Scheme 2.2).² For the other hydroxyl groups, the nucleophilic substitution is the dominant mechanism of functionalization reactions. To date, a plethora of methods exists for the regioselective synthesis of protected monosaccharides; however, such syntheses suffer from a significant number of linear

steps. Recent efforts have focused on developing tandem procedures to access functionalized carbohydrates. In 2007, the Hung group demonstrated a general method for achieving multistep single-pot functionalizations of *D*-glucose (Scheme 2.2). Starting with pertrimethylsilylated *D*-glucose derivative, several different sequences of the steps were performed in “single-pot” way to generate four different types of protected monosaccharides. The final monosaccharides have only one free hydroxyl group available for further transformation, while the other three hydroxyl groups are orthogonally protected. This approach also outlines the strategies for the protection of the specific hydroxyl positions. For example, the C4- and C6-hydroxyl groups are usually protected as a cyclic benzylidene acetal, which then can be selectively reductively open by using hydrides BH_3 or NaBH_3CN .⁵ Although very convenient for the expedient synthesis of several different classes of protected *D*-glucose, Hung’s approach has significant limitations and cannot be easily extended beyond the synthesis of the specified *D*-glucose derivatives. Following the original report by Hung, several other studies focused on extending this work to other monosaccharides; however, the application of this one-pot protocol beyond the functionalization of *D*-glucose has significant challenges.^{6–10}

Scheme 2.2. One-pot regioselective functionalization of D-glucose by Hung and coworkers.

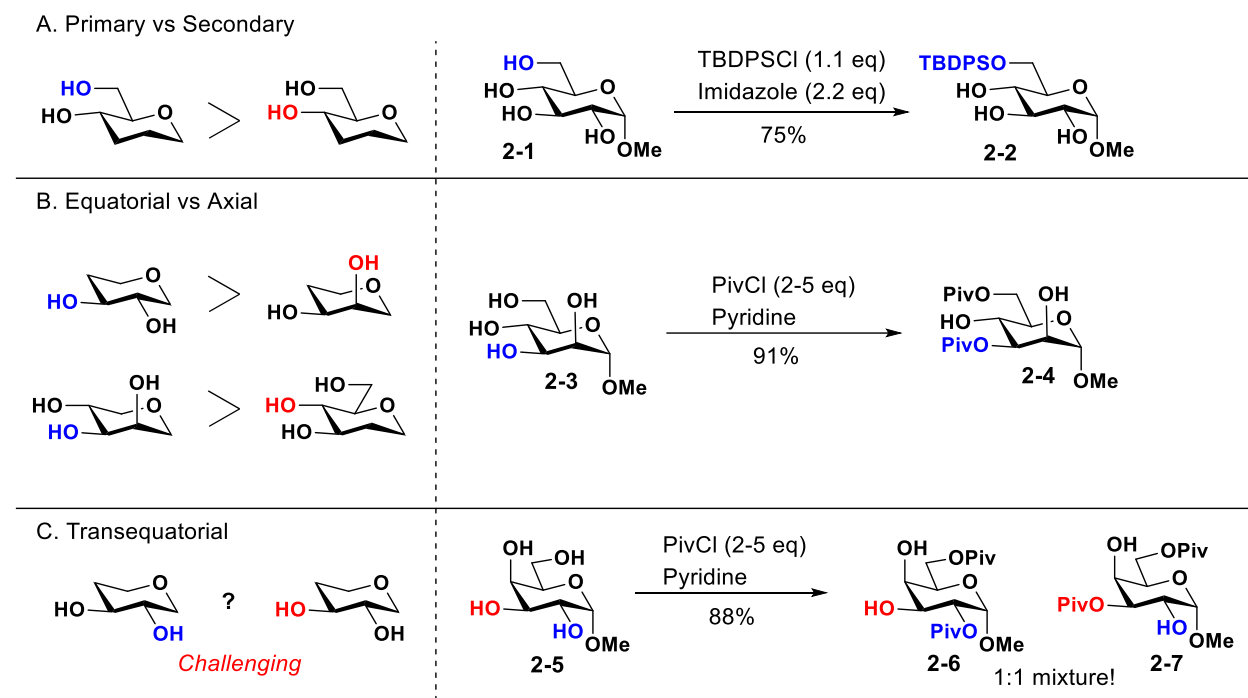


There are several factors A–D outlined below that are important for the analysis of the intrinsic reactivity of carbohydrates.¹¹ The steric hindrance of the hydroxyl groups is of great importance for their nucleophilicity. B) The acidity of the hydroxyl group may affect the selectivity with the base-promoted reactions. C) The hydrogen bonding network between the hydroxyl groups may significantly enhance or diminish the hydroxyl acidity and facilitate the coordination of the electrophiles during reactions. D) The nearby protecting groups may impact the steric environment around the hydroxyl group or enhance its reactivity through reagent coordination.

The steric hindrance around the hydroxyl group translates into its nucleophilicity, and it is the primary factor responsible for much higher reactivity of the primary vs secondary alcohols. For example, the C6 hydroxyl group of methyl α -D-glucopyranoside **2-1** can be selectively

protected with TBDPS in 75% yield (Scheme 2.3, A). Other bulky protecting groups such as triphenylmethyl ether or pivaloyl ester can be introduced for the selective protection of the C-6 alcohol.¹²

Scheme 2.3. Steric effects controlling the reactivity of hydroxyl groups



The secondary hydroxyl groups may also exhibit different reactivity due to the differences in their steric environments; however, such reactivity differences are typically less profound than in the case of primary vs secondary hydroxyls. For two hydroxyls in a similar electronic environment, the equatorial one is usually more reactive than an axial alcohol. Between the two equatorial hydroxyls, the one with the axially oriented neighbor is typically more reactive (Scheme 2.3B). This can be exemplified by the reaction of methyl α -D-mannoside **2-3** with pivaloyl chloride in pyridine. First, the C-6 primary hydroxyl group is protected, and then the second equivalent of pivaloyl chloride undergoes selective acylation of the equatorial C3-alcohol to afford 3,6-bispivaloylated product **2-4** in 91% yield.¹³ It must be noted that selective functionalization of one

secondary hydroxyl in the presence of the others is often a challenging task, and frequently such reaction proceed with low selectivity and produce regioisomeric side-products. It is particularly hard to achieve a site-selective functionalization of one equatorial hydroxyl group in the presence of the other ones, especially if these equatorial hydroxyls are in similar steric and electronic environments (Scheme 2.3C). For many sugars, the equatorial hydroxyls at the C2 and C3 positions have similar reactivity, and their protection typically leads to ~1:1 mixture of two inseparable regioisomeric products (*cf.* Scheme 2.3C).¹⁴ Consequently, there is a significant demand in new selective catalytic methods for the differentiation of similar hydroxyl groups in carbohydrates, and the next subchapter provides an overview of the recent developments in this area.

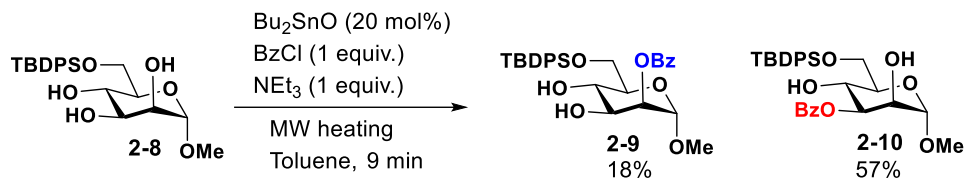
2.2 Overview of non-chiral catalytic methods for regioselective carbohydrate modifications

2.2.1 Stannylene acetal catalysis.

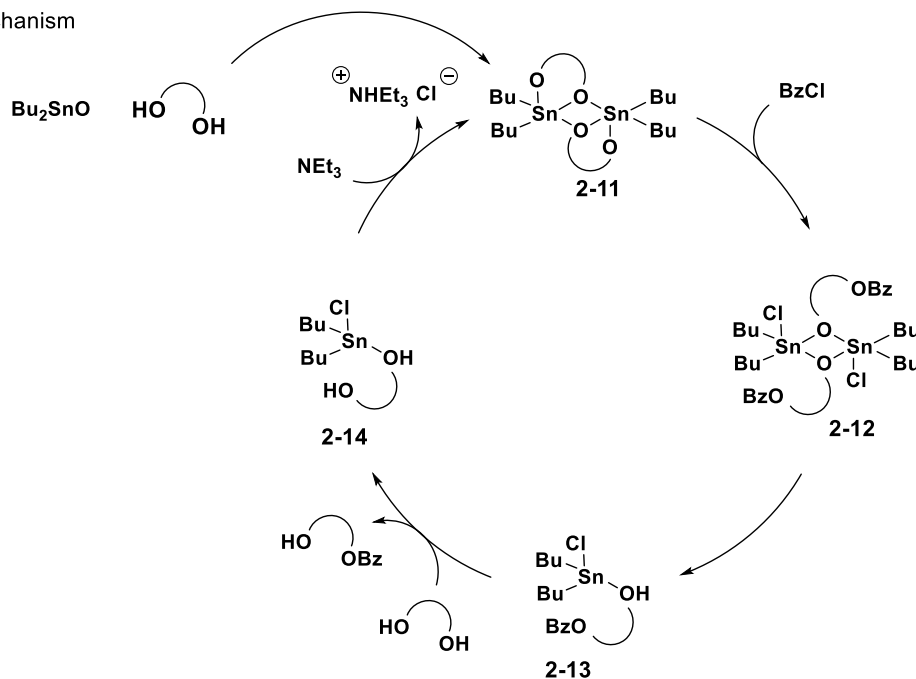
Stoichiometric formation of cyclic stannylene acetal followed by an electrophilic attack on one of the protected hydroxyl groups represents an early strategy that has become routine for the monofunctionalization of 1,2-diols.^{15,16} However, the use of Sn(IV)-based reagents, in particular on a large scale, imposes health hazards and requires tedious purification of the products.¹⁷

Scheme 2.4. Stannyl oxide-mediated regioselective carbohydrate functionalization

A. Stannylene oxide-catalyzed regioselective benzylation



B. Mechanism

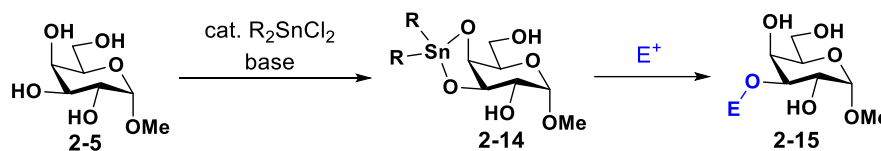


In 1994 Valverde and coworkers developed a catalytic approach using dibutyltin oxide and microwave heating leading to C3-selective benzylation of mannopyranoside **2-8** (Scheme 2.4, A). In this reaction, catalytically generated stannylene acetal from two cis-OH groups controls the benzylation of the more sterically accessible alcohol group.¹⁸ Later, the mechanism of this transformation was studied using ^{119}Sn NMR spectroscopy revealing the formation of dimeric species **2-11** from initial tin oxide (Scheme 2.4, B). This cyclic stannylene acetal formation prefers a five-membered ring over a six-membered ring and a cis diol over a trans diol. Further reaction with benzoyl chloride cleaves dimeric species and ligand exchange with not yet reacted diol leads to expelling the reaction product from the catalytic cycle.¹⁹

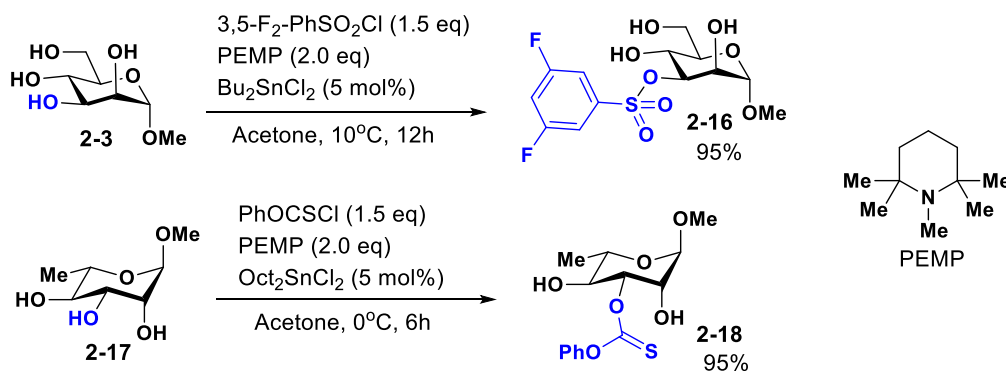
After this pioneering work, Matsumura found that the reaction can be carried out more effectively and without MW irradiation with more reactive dimethyltin dichloride (Scheme 2.5A). In this case, tin catalysis allowed selectively sulfonylate and thiocarbonylate mannose **2-3** at C- and galactose **2-17** at C3-position respectively (Scheme 2.5B).

Scheme 2.5. Dialkyltin(IV) dichloride catalysis

A. Mechanism of reaction with dialkyltin dichloride



B. Selected examples of reaction scope



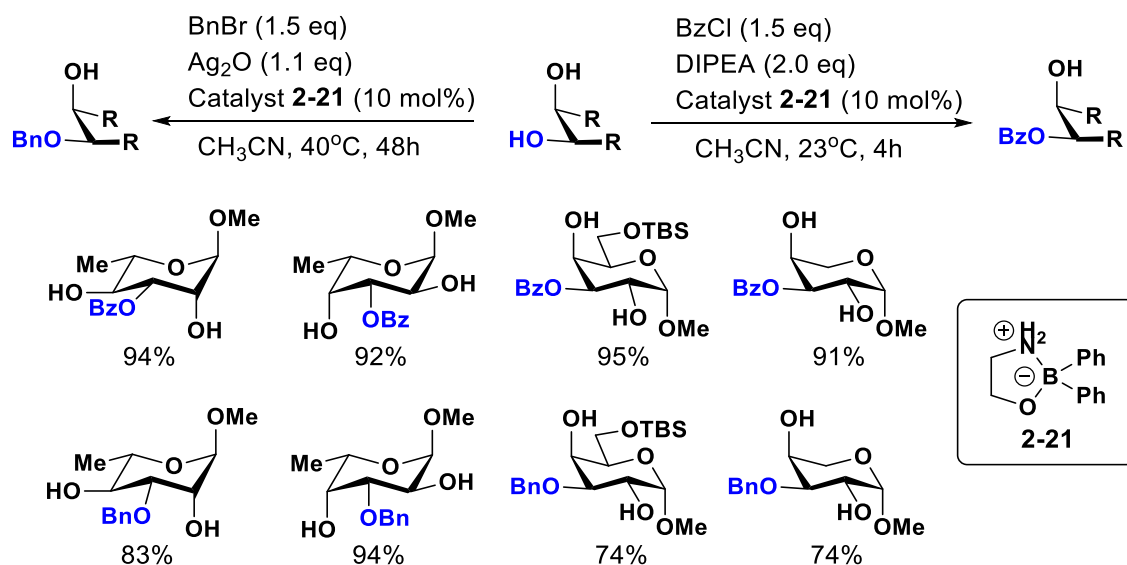
This methodology allows selective modification of the specified non-protected sugars at their C3-positions. As before, cyclic stannylene acetal forms at the *cis*-1,2-diol moiety, and the less hindered C3-hydroxyl group reacts with the electrophiles.^{20,21}

2.2.2 Borinate and boronate esters

Boron(III) compounds are well known to form tetracoordinate complexes with oxygen-based compounds. Unsurprisingly, displaying similar ability to complex *cis*-1,2-diols as Sn(IV) compounds, organoboronic acids were viewed as safer and non-toxic surrogates to tin. The work of Aoyama in 1997 described the use of stoichiometric arylboronic acids to form cyclic intermediates with the hydroxyl groups in carbohydrates.²² Although this approach provided a

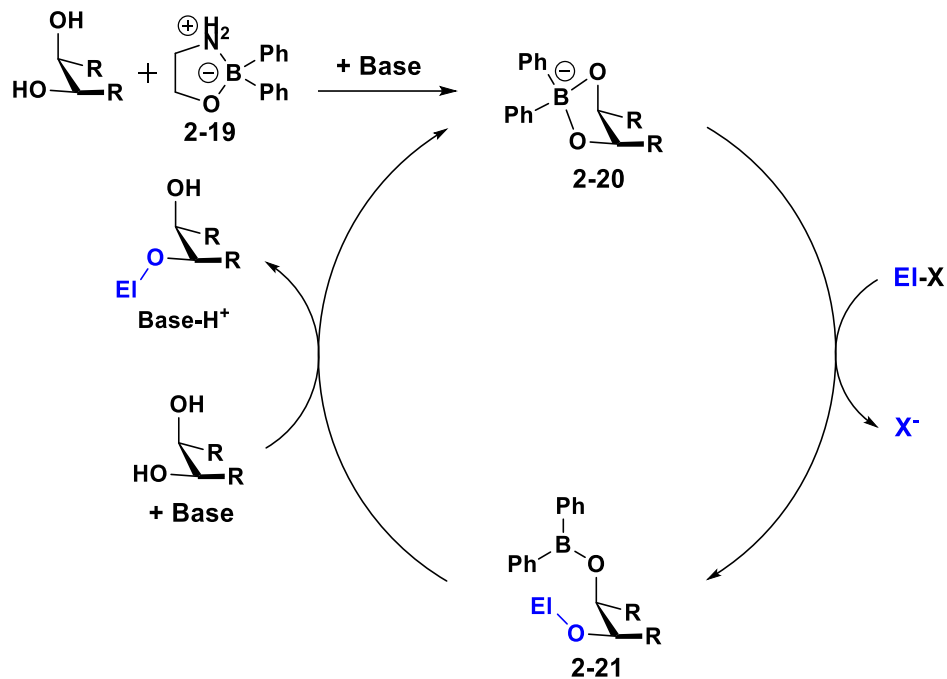
great alternative to traditional tin chemistry, the requirement of using a stoichiometric amount of the boron reagents was not optimal for applications. In the search to address this, borinate ester catalysis was introduced by Taylor and coworkers in 2011. Using borinate ester **2-21** as the pre-catalyst, acylation, benzylation, benzoylation, and sulfonylation of the C3-position of various carbohydrates was achieved (Scheme 20).^{23–25}

Scheme 2.6. Catalytic alkylation and benzoylation using borinate esters catalysis



The mechanism of these transformations is depicted in Scheme 21. The catalytic cycle begins with the reaction of pre-catalyst **2-19**, which loses ethanolamine and binds to *cis*-1,2 diol moiety of the carbohydrate (Scheme 2.7). Cyclic and negatively charged borinate ester **2-20** then reacts with the electrophile and, again, the less sterically hindered hydroxyl group reacts to form the protected product **2-21** with excellent regioselectivity. Tricoordinated boron intermediate then reacts with a new substrate molecule, restoring the initial resting state of catalyst **2-20**.

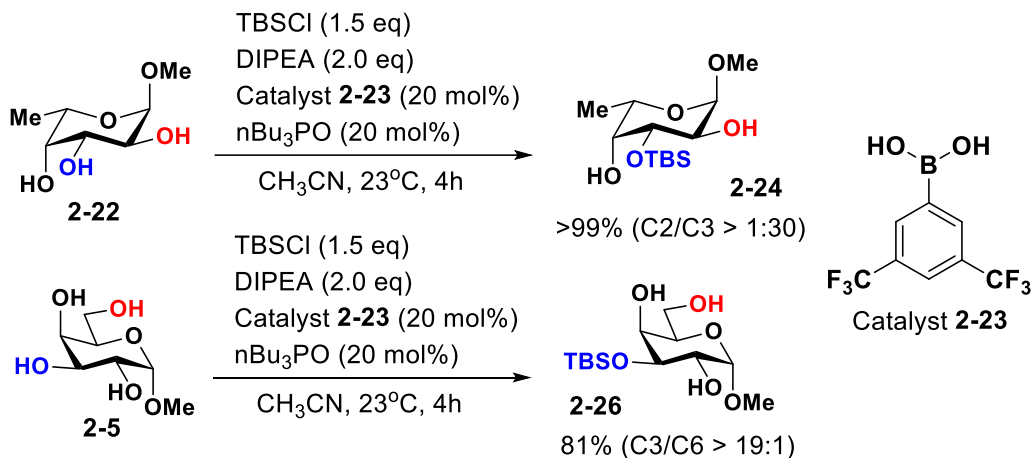
Scheme 2.7. The postulated mechanism of borinate-catalyzed regioselective functionalization of carbohydrates.



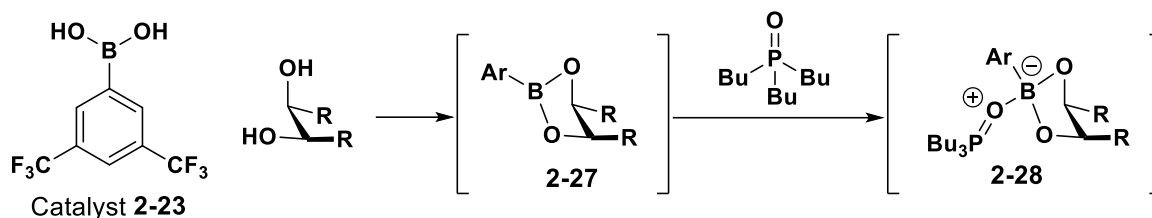
As mentioned before, the original Aoyama's method required using stoichiometric amounts of cyclic boronate esters made from boronic acids. However, in 2013 Taylor disclosed a modified protocol that employed electron deficient 3,5-*bis*-trifluoromethylphenyl boronic acid **2-23** as the catalyst in combination with tributylphosphine oxide as the co-catalyst for regioselective silylation reactions (Scheme 2.8A).²⁶ The treatment of methyl α -L-fucopyranoside **2-22** with TBSCl under these conditions provides the C3-silylated product with complete regioselectivity. This reaction protocol is also compatible with fully unprotected carbohydrates, as silylation of α -D-galactopyranoside **2-5** provides mostly the C3-silylated product **2-26** despite the presence of more active primary C6-hydroxyl group (C3/C6 = 19:1).

Scheme 2.8. Boronic acid catalysis.

A. Catalysis with boronic acids



B. Mechanism

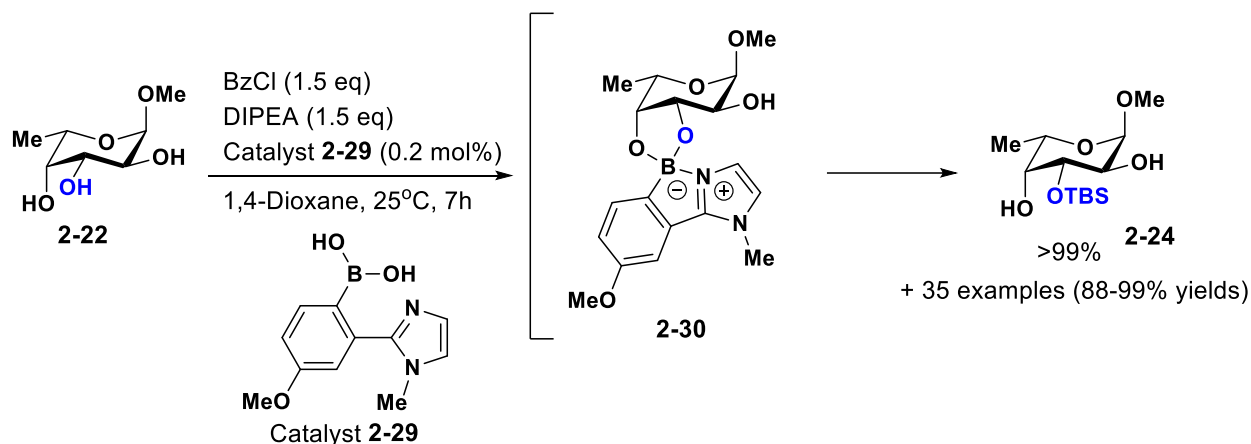


The postulated reaction mechanism for this dual catalytic transformation is presented in Scheme 2.8B. While boronic acid **2-23** forms non-active tricoordinated boronate ester **2-27**, tributylphosphine oxide co-catalyst acts as Lewis base to activate intermediate **2-27** by coordinating to boron and forming active borinate ester **2-28** with more nucleophilic and sterically accessible equatorial oxygen.

Alternatively, as reported by Shimada and coworkers in 2019, 2-(*N*-methyl-2-imidazolyl)phenylboronic acid **2-29** (Scheme 2.9) can serve as a catalyst for C3-benzoylation of minimally protected carbohydrates. This reaction also utilizes previous findings, that tetracoordinated boronate ester works as an activator of *cis*-1,2 diols and provides selective modification of less hindered OH groups. It is worth noting, that treating α -L-fucopyranoside **2-22** with only 0.2 mol % of catalyst **2-29** and 1.5 equivalents of benzoyl chloride affords C3-

benzoylated product **2-24** in over 99% yield with complete regioselectivity. Their work described the synthesis of 35 monosaccharides using this approach with excellent yields (88-99%).²⁷

Scheme 2.9. Shimada's Lewis base-bearing boronic acid catalysis



Using boronic and borinic acid derivatives for catalysis may provide high selectivities and helps to minimize the toxicity and challenges with waste-handling associated with using the tin(IV) reagents. However, the described above methods rely on the presence of the *cis*-1,2 diol moiety to achieve a successful cyclic acetal formation and cannot be generally used for selective functionalization of *trans*-1,2-diol moiety. This limits the substrate scope to carbohydrates containing at least one axial hydroxyl groups, and are only effective for the protection of the equatorial alcohols that are next to the axial hydroxyl.

2.3 Asymmetric catalytic methods of regioselective carbohydrate modifications

Boron- and tin-based reagents and catalysts overviewed above contained no chirality, but their use allowed to achieve high selectivities for carbohydrate modification albeit with significant limitations in scope. The described above protocols worked well with 1,2-*cis*-diol moieties, and the reagents/catalysts directed the functionalization of the less hindered equatorial hydroxyl group. However, more general catalysts, which would enable access to all possible regioisomers for a

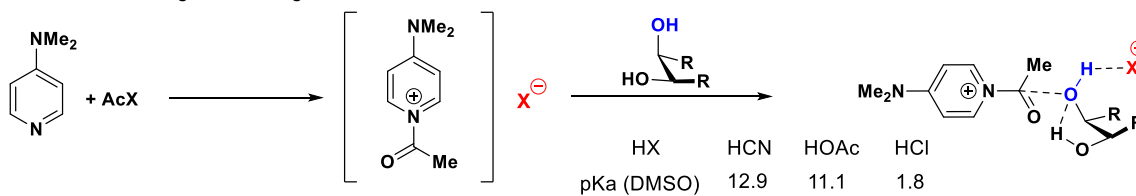
diverse set of sugars are strongly desired for carbohydrate synthesis. The use of chiral catalysts may significantly expand the scope of the site-selective transformations since the chirality of the catalyst may be sensitive to subtle steric differences between otherwise similar hydroxyl groups in a sugar. In addition, simple switch in the catalyst chirality may lead to the opposite regioselectivity and make the reaction protocol to be more general in terms of the substrate scope. Therefore, applying chiral catalysis was a logical direction of researchers after establishing non-chiral catalytic methods.¹¹

2.3.1 Cinchona Alkaloid Catalysts and Hydrogen bonding effect

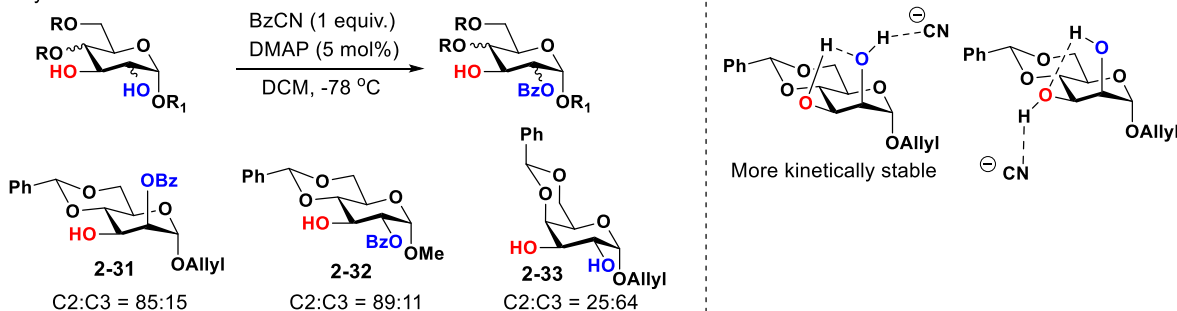
Unprotected carbohydrates form complex intramolecular networks of hydrogen bonds and that can affect reactivity of specific OH groups even without any catalysts. The hydroxyl group that serves as an H-bond donor demonstrates higher nucleophilicity than groups accepting H-bonds since increasing the partial negative charge on the oxygen. That can be used for selective acylation of specific OH groups with classical DMAP catalysis (Scheme 2.10, A). Counter anions, produced in the reaction also can impact hydrogen bonding. First, anions can serve as H-bond acceptors, impacting the nucleophilicity of the OH group. Second, the pKa of conjugated acid determines how strength of counter anion X as a base.^{11,14}

Scheme 2.10. Examples of utilizing the counter anion effect and H-bonding for controlling the regioselectivity of carbohydrate acylation.

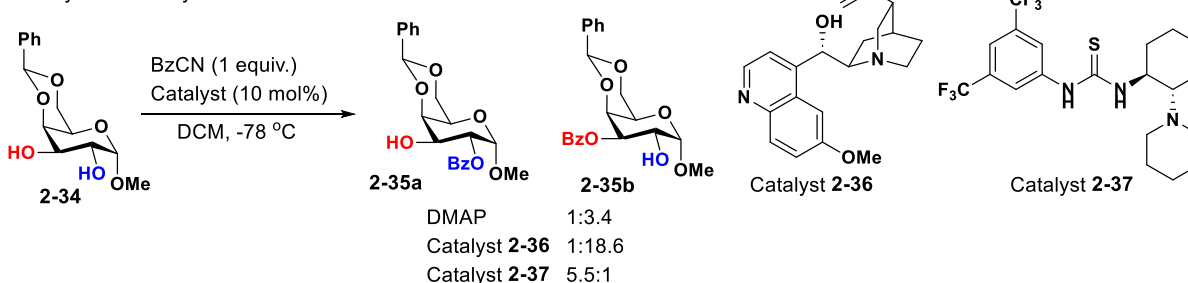
A. Anion effect through H-bonding



B. Cyanide effect



C. Asymmetric catalysis with alkaloids and thiourea



Moderately selective anion-directed benzoylation of carbohydrates was known since 1975 from the work of Haines,²⁸ and further exploration of the anion effect was carried by Yoshida in 1999.²⁹ It was discovered that using benzoyl cyanide can provide moderate selectivity towards the C2-protection of carbohydrates (Scheme 2.10B). The reaction with a cyanide anion proceeds faster than when benzoyl chloride or acetate was used, confirming the presented above postulate of base catalysis (as the cyanide counter anion has the highest pKa, it is the most effective base to deprotonate the hydroxyl group during the acylation). Mechanistic studies performed by Schmidt using both experimental and computational methods allowed to explain the observed selectivity

under cyanide anion catalysis by kinetic stabilities of the H-bond networks forming with different OH in carbohydrates (Scheme 2.10B).³⁰

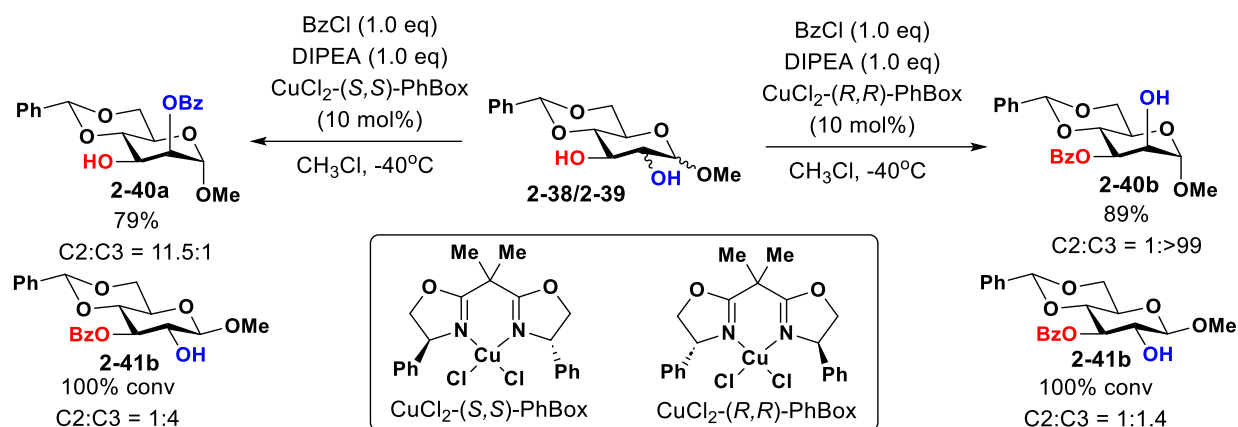
These mechanistic findings were used to develop catalytic system to intervene with the H-bonding network by using chiral catalysis. Peng and Schmidt applied quinidine **2-36** instead of DMAP to achieve higher selectivity for benzoylation of 4,6-*O*-benzylidene-methyl- α -*D*-galactopyranoside **2-34** with benzoyl cyanide (Scheme 2.10C). In contrast, the use of thiourea catalyst **2-37** resulted in overturned selectivity and favored the C2-protection product. Therefore, developing an organocatalytic system with a chiral catalyst interacting with the substrate via H-bond framework is a promising direction.

2.3.2 Chiral copper catalysis

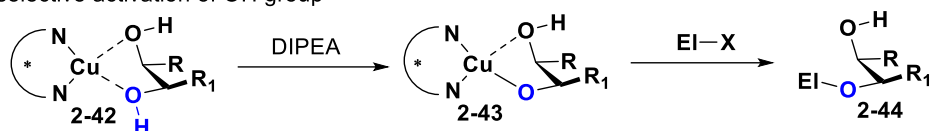
Copper cations are well known to form stable complexes with hydroxyl groups, especially under chelate control. Matsumura and Onomura used this for their advantage to utilize chiral copper complexes and their coordination to 1,2-*cis*-diols for selective activation of one of the OH group. Under chiral copper catalysis, they reported kinetic resolution of *meso* 1,2-diols, where chiral ligand of the complex dictated the selection of the hydroxyl group to react with electrophiles.³¹

Following work of the enantioselective resolution of *meso* diols, Miller and coworkers reported the chiral Ph-Box-Copper(II) complex (both enantiomers) to control regioselective acylation of both *cis*- and *trans*-diol moieties in carbohydrates (Scheme 2.11).

Scheme 2.11. Chiral Cu(II) Ph-Box-catalyzed regioselective acylation of carbohydrates.



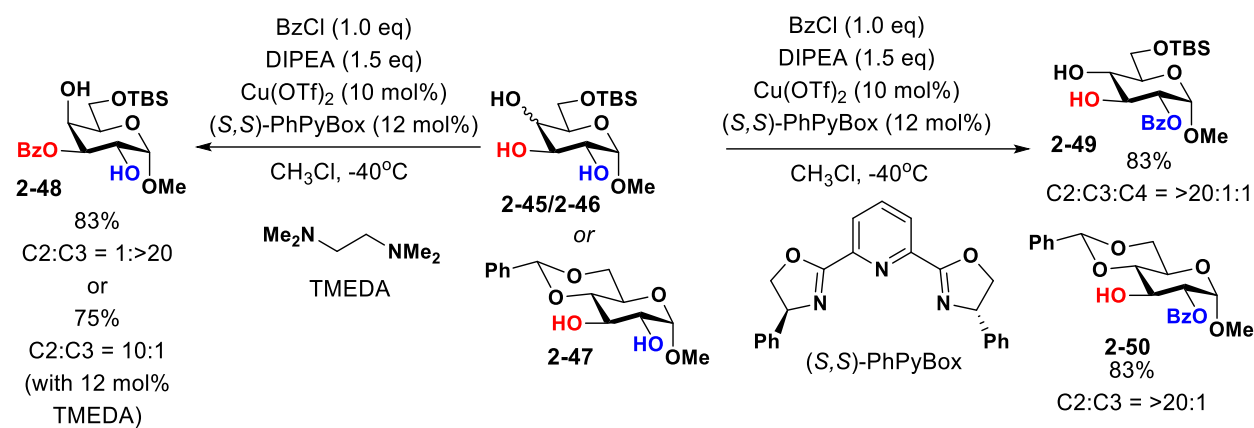
Mechanism of selective activation of OH group



The treatment of 4,6-*O*-protected methyl α -*D*-mannose derivative **2-38** with benzoyl chloride and DIPEA in the presence of (*S,S*)-PhBox catalyst led to the formation of the C2-protected product **2-40a** in 79% yield (C2:C3 = 11.5:1). Remarkably, the use of the enantiomeric (*R,R*)-PhBox catalyst successfully overturned this selectivity and provided the C3-protected product as a single isomer in >99:1 regioisomer ratio, (r.r.). In a control experiment without the catalyst, the reaction product was formed in C2:C3 = 1: 4.5 ratio, demonstrating mediocre substrate control in this reaction. The proposed reaction mechanism consists of two key steps: (1) Copper complex coordinates to the diol, (2) base deprotonates the more accessible hydroxyl group to form copper(II)-alkoxide **2-43**, which then reacts with the electrophile. Even though this mode of activation is similar to the previously described non-chiral methods (such as borinate ester catalysis), the selectivity of this process demonstrates significant dependence on the stereochemistry of the employed catalyst. This led to the conclusion that noncovalent interactions with the chiral catalyst rather than the substrate were detrimental to the selectivity of this process. Despite promising results, selective modification of *trans*-1,2-diols, such as β -*D*-glucose

derivative **2-39**, was beyond the capabilities of this catalytic system. Only moderate selectivity for the C3-protection product **2-41b** was observed (C2:C3 = 1:4) with CuCl₂-(*S,S*)-PhBox, while the use of its enantiomer led to a completely unselective reaction. This observation can be explained by the significantly less favored complexation between the copper (II) catalyst and *trans*-1,2 diols.³²

Scheme 2.12. Regiodivergent benzylation with PyBox complexes by Dong et al.



Independently from the Miller group, Dong and co-workers³³ developed a similar protocol relying on (*S,S*)-PhPuBox•Cu(OTf)₂ complex (Scheme 2.12) to perform regiodivergent benzylations of carbohydrates. Similar to the observation by Miller, carbohydrates with *cis*-1,2-diol motif, such as galactose **2-45**, underwent a highly selective C3-protection. It was also discovered that when the chiral ligand was replaced with a small non-chiral ligand such as TMEDA, moderate C2-selectivity was achieved (C2:C3 = 10:1). More importantly, (*S,S*)-PhPuBox•Cu(OTf)₂ complex could be used beyond the cases of monosaccharides with *cis*-1,2-hydroxyl groups if these saccharides feature α -configuration at the anomeric position. Benzoylation of both C6-silylated glucose **2-46** and 4,6-benzylidene-protected glucose **2-47** proceeded with excellent selectivity and yields towards the C2-position despite presence of additional hydroxyl groups. This demonstrates a significant improvement in substrate scope when selective protections

are run with chiral copper(II) Box complexes as the catalysts in comparison to the traditional methods. Same catalytic system was used by Ren to perform regioselective alkylation of carbohydrates.³⁴

Although the specified methods based on the use of chiral copper(II) complexes had extended the substrate scope to some substrates featuring *trans*-1,2-diols moiety, the requirement for the α -anomeric chelating groups in the substrate limits the scope of these reactions. In addition, dealing with moisture-sensitive Cu(II) complexes is not ideal and further attention of researchers shifted to more versatile chiral organocatalysis.

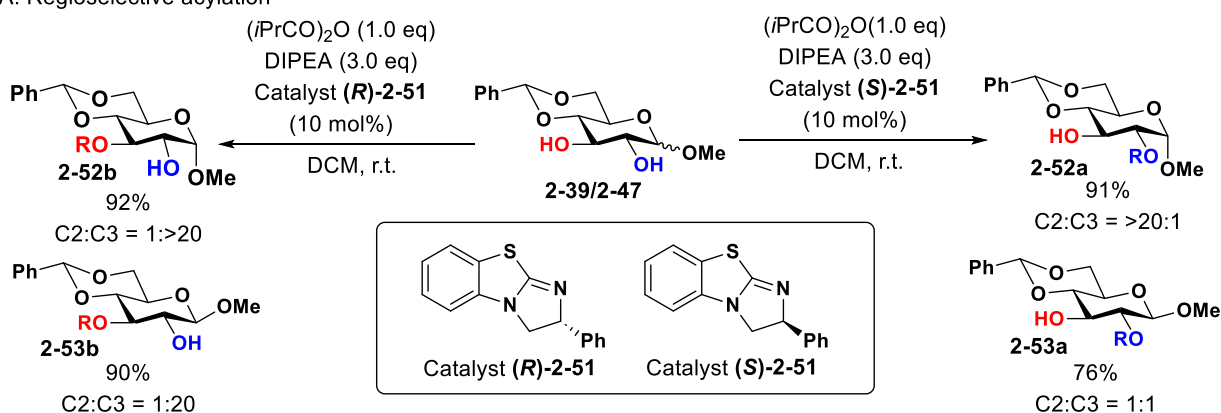
2.3.3 Benzotetramisole Catalysts

Following the work of Peng and Schmidt, Tang's research group³⁵ reported that a pair of enantiomeric benzotetramisole catalysts (**R**)-**2-51** and (**S**)-**2-51** can be used for regioselective acylation of *trans*-1,2-equatorial diol moieties in carbohydrate molecules (Scheme 2.13A). The reaction of 2.5 equivalents of isobutyric anhydride with 4,6-*O*-benzylidene- α -D-glucose methyl glycoside **2-39** catalyzed by (**R**)-**2-51** led to the C3-acylated product **2-52b** in 92% yield and >1:20 rr. Perfectly following the intended principle of catalyst-controlled regioselectivity, the use of (**S**)-**2-51** resulted in the formation of product **2-52a** in 91% yield and opposite selectivity of >20:1 rr. Same trend was observed for 4,6-*O*-benzylidene- β -D-galactose methyl glycoside as well as for derivatives of xylose and rhamnose. Unfortunately, β -D-glucose methyl glycoside derivatives such as **2-47**, demonstrated high regioselectivity only with catalyst (**R**)-**2-51**, while the use of the opposite enantiomer of the catalyst provided no selectivity at all. The following mechanistic studies, performed by DFT computations, allowed them to identify the transition states of the transformations and capture the interactions leading to the C2 or C3 selectivity. The catalytic cycle begins with an anhydride reaction with a catalyst leading to the reactive intermediate **2-52** (the

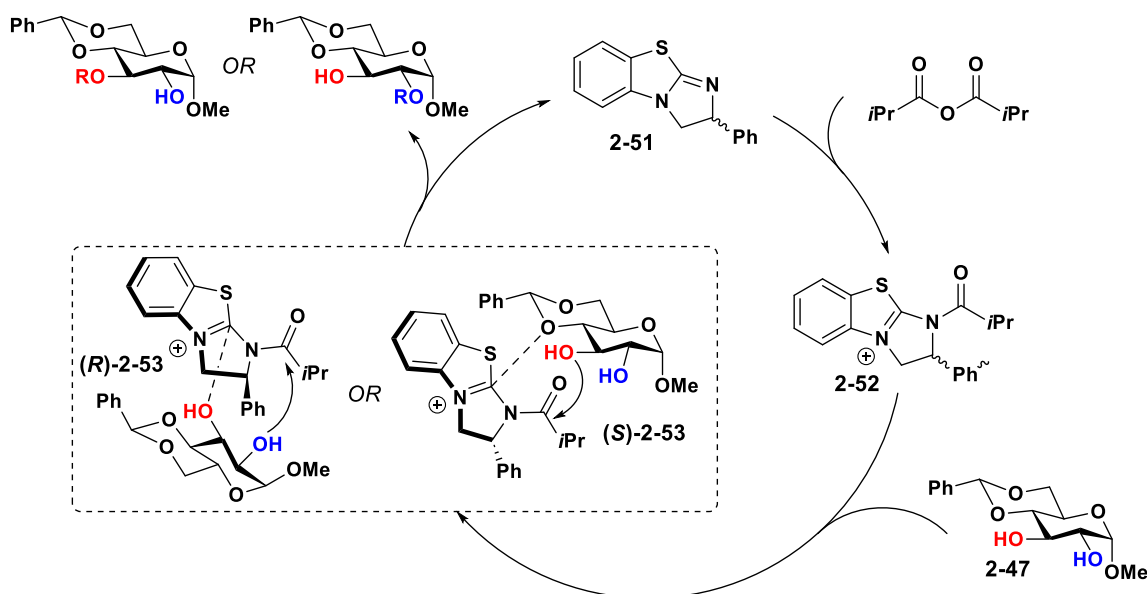
analog of DMAP-Acyl complex). Subsequently, this intermediate coordinates to the substrate through noncovalent cation/n interaction between the acylated catalyst and the lone pair on one of the substrate oxygens. In the case of the C2 protection, the C3 hydroxyl group interacts with the cationic center on the catalyst, thus positioning the C2 hydroxyl group for nucleophilic attack of the acyl group.

Scheme 2.13. Regioselective acylation of 1,2-trans-diols by benzotetramisole catalyst

A. Regioselective acylation



B. Reaction mechanism and TS controlling selectivity



For the C3-protection, the O4 of the benzylidene acetal coordinates to intermediate 2-52 to form the most stable TS. That also provides an explanation for why there is no selectivity for the

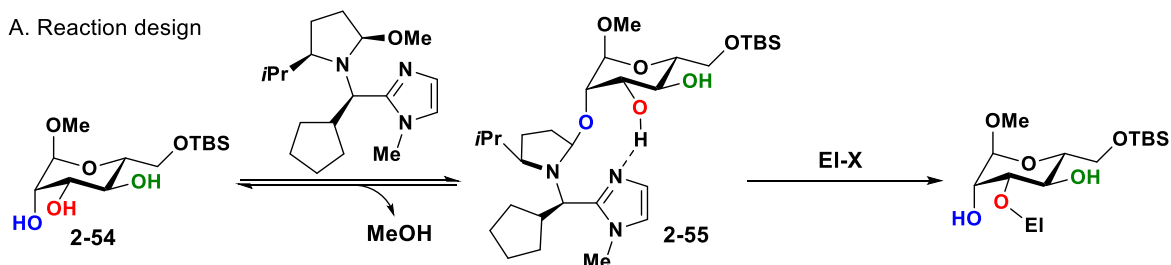
acylation of β -anomers as coordination to both the benzylidene acetal O4 and to O1 of the anomeric methoxy group is possible in this case. Even though Tang and co-workers have developed a reliable method for achieving catalyst-controlled acylation, this approach has some limitations with respect to the substrate scope, and moderate selectivities for some of the galactose and mannose substrates were observed.

2.3.4 covalent bond-forming chiral catalysis

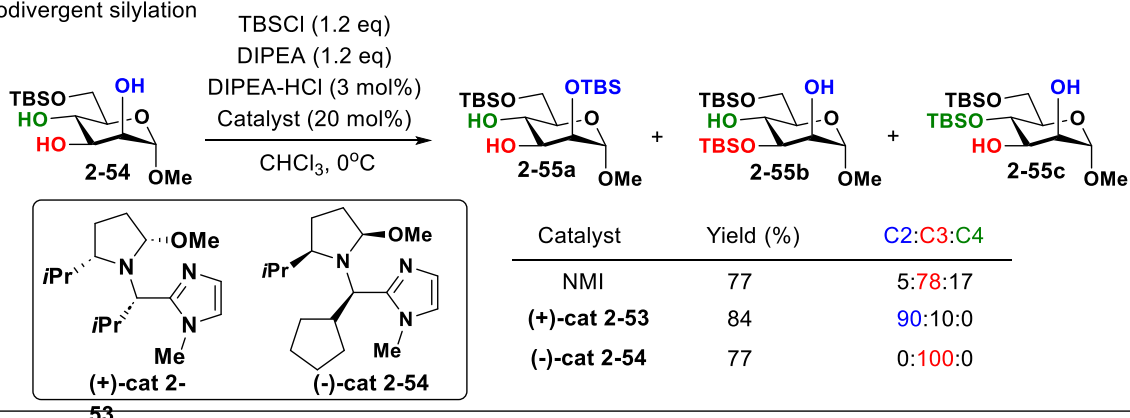
The cases above highlighted regioselective carbohydrate modification using chiral catalysts interacting through either noncovalent interactions (hydrogen bonding, cation- π interactions) or through the formation of reactive complexes (chiral copper (II) catalysts). Alternative to these mechanisms, Tan and co-workers demonstrated the possibility of a different type of catalysis that involved reversible covalent bond formation between the organic catalyst and H-bond acceptors. This might be advantageous since the covalent intermediate formed in the catalytic cycle may have a closer distance between the reacting centers, which may result in stronger noncovalent interaction between the chiral backbone of the catalyst and substrate. This concept was brought to life by designing a chiral organocatalyst containing 2-alkoxyoxazolidine moiety as a substrate binding site and an imidazole group as a catalytically active site engaged in making an H-bond (Scheme2.14A).³⁶

Scheme 2.14. Regioselective functionalization of carbohydrates through reversible covalent catalysis.

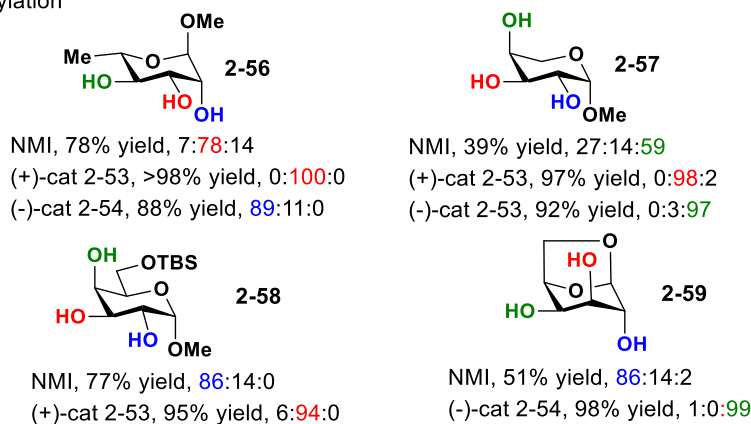
A. Reaction design



B. Regiodivergent silylation



C. Substrate scope for silylation



The selected catalyst, 2-alkoxyoxazolidine, may undergo a reversible iminium ion followed by the reversible covalent binding to one of the substrate hydroxyl groups to form a hemiaminal intermediate. This brings the hydrogen bond acceptor, imidazole, into proximity of the remaining substrate hydroxyl groups, one of which is activated towards the nucleophilic attack through the formation of an intramolecular H-bond with imidazole. This catalytic system demonstrates good substrate tolerance and could be easily adjusted by tuning the size of the alkyl group on the catalyst.

The authors discovered that the direct silylation of the C6-protected mannose derivative **2-54** with NMI (*N*-methylimidazole) as the catalyst led to good C3-selectivity, but other regioisomers were also observed in significant amounts (Scheme 2.14B). The use of catalyst (-)-**cat 2-54** instead of NMI resulted in enhanced silylation selectivity and provided only the C3-protected product in full conversion. In contrast, the use of (+)-**cat 2-53** overrode the substrate-dictated preference for the C3-product and resulted in the C2 regioisomer as the major product (84% yield, C2:C3 = 90:10 r.r.).³⁷

This approach was applied to 8 different monosaccharides to achieve regioselective protection with high yields and selectivity (Scheme 2.14C).³⁸ For example, methyl α -L-rhamnoside **2-56**, methyl β -L-arabinoside **2-57**, and methyl α -D-galactoside **2-58** followed the observed above trend for the C2/C3-protection exhibited by catalysts (-)-**cat 2-54** and (+)-**cat 2-53**. At the same time, 1,6-anhydro- β -D-galactose **2-59** exhibited a different reactivity profile and underwent highly selective C4-protection with (-)-**cat 2-54**. It is worth mentioning, that some selectivity was also achieved using achiral NMI as the catalyst, but such reactions had lower yields and produced other regioisomeric side-products. Of note was also the observation that inconsistent regioselectivity trends were observed with β -anomeric substrates. Covalent binding which was key to these transformations has its own drawbacks. The covalent attachment of the catalyst to substrate may restrict free movements in the transition state, which may impose limitations on substrate size as substrates with bulky substituents require more flexible conformational movement during TS.

2.3.5 Chiral Phosphoric Acid Catalysis

Chiral Phosphoric Acids (CPAs) have emerged as powerful and versatile tools for asymmetric synthesis. As it was overviewed in Chapter 1, their catalytic site bears bifunctional hydrogen

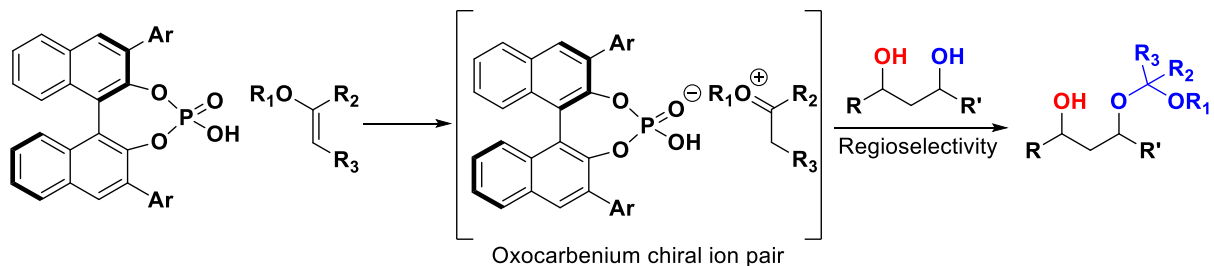
phosphate moiety that may serve as both the H-bond donor and acceptor as well as Brønsted acid. It is known that the main mode of substrate activation by CPA is protonation, and stereocontrol of such reactions is dictated by noncovalent interactions with the chiral phosphate anion. These properties make CPAs to be promising catalysts for achieving regiocontrol in carbohydrate chemistry.³⁹

Acid-catalyzed acetal formation is known to proceed through the highly reactive intermediates— oxocarbenium ions, which are known to react with nucleophiles indiscriminately. In 2012 Nagorny group demonstrated the application of CPA catalysis towards diastereoselective and enantioselective spiroketalizations in different carbohydrate molecules proceeding via an asynchronous concerted mechanism featuring oxocarbenium-like transition state.⁴⁰ Utilizing CPA catalysis, the following principle of regioselective acetalization of sugars as a method of hydroxyl group protection (Scheme 2.15A) can be proposed. The CPA protonates enol ether to form a highly reactive oxocarbenium cation, which then reacts with a polyol to form a mixed ketal. Based on the spiroketalization precedent, this intermolecular variant may proceed via an asynchronous concerted mechanism. The regioselectivity here would be dictated by the chirality of the chiral phosphate anion, which may impact its binding to the substrate via H-bonding. As part of these studies, Mensah and Nagorny in 2013 disclosed selective functionalization of monosaccharides using 1,1'-bi-2-naphthol (BINOL)-derived chiral phosphoric acids (CPAs) as the catalysts to direct regioselective acetalization of carbohydrate-derived 2,3-diols (Scheme 2.15B). After screening various CPAs, this study demonstrated that (*R*)-AdTRIP CPA catalyst **2-62e** bearing sterically bulky 4-(1-adamantyl)-2,6-(*i*-Pr)₂C₆H₂- substituents promoted C2-selective protection of D-galactose derivative **2-60a** with moderate selectivity of 8:1 r.r. using tetrahydropyran (THP) as a protecting group. While the reaction with the (*R*)-enantiomer of AdTRIP provided moderate

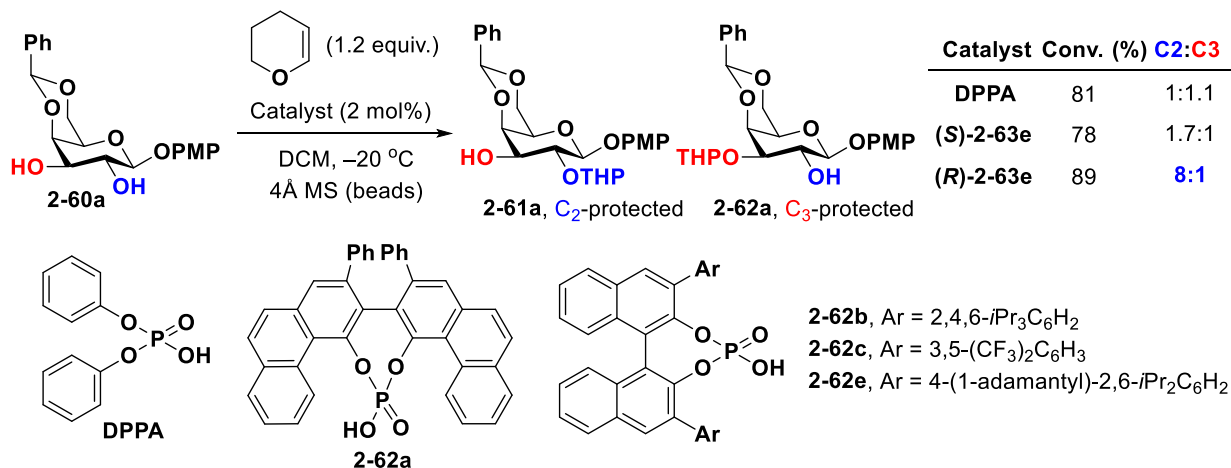
selectivity for the C2-protection of *D*-glucose, *D*-galactose, and *D*-mannose-derived diols, the (*S*)-enantiomer exhibited no selectivity at all. Further optimization included testing more reactive enols, such as 2-methoxypropene (**MOP**), and 1-methoxycyclohexene (**MOC**). Both enols (**MOP** and **MOC**) required much lower reaction temperatures (−78 and −55 °C, respectively), but their use led to significant improvement in regioselectivity allowing to obtain C2-protected products with 20:1 to 25:1 r.r. values (Scheme 2.15C).⁴¹

Scheme 2.15. CPA controlled regioselective acetalization of carbohydrates

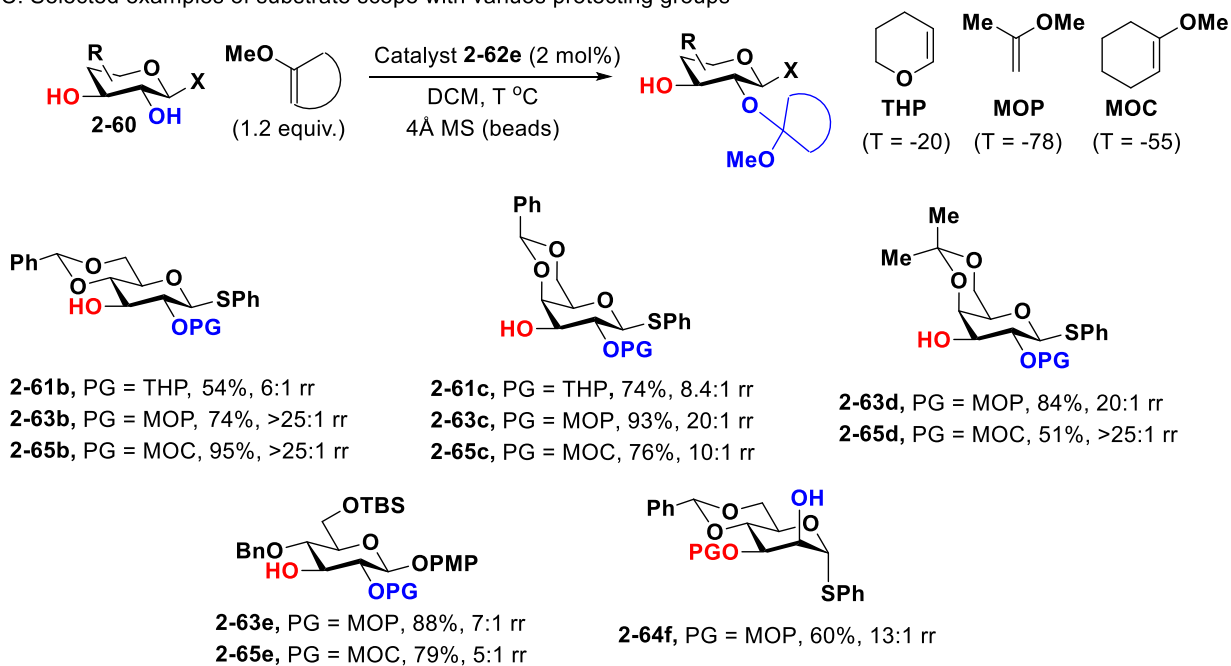
A. Proposed reaction design



B. Regioselective acetalization with THP



C. Selected examples of substrate scope with various protecting groups

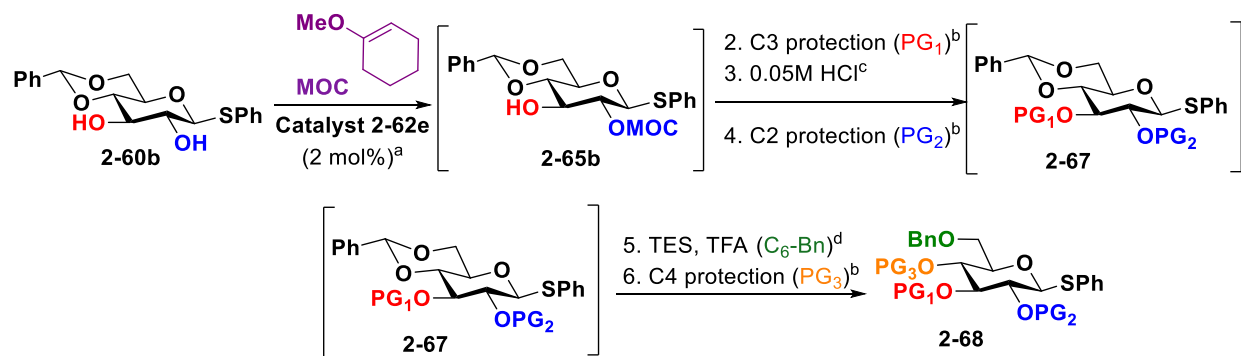


The reactions of D-glucose and D-galactose derivatives proceeded at the sites that cannot be directly functionalized with achiral reagents such as n-dibutyltin(IV) oxide. These transformations tolerated various modifications of the C6/C4 protection (substrates **x** and **x**). The only exception was mannose derivative **2-60f**, which gives C3-protected product **2-64f**. Importantly, these transformations featured mild reaction conditions and the use of easily available and non-toxic substrates and catalysts.

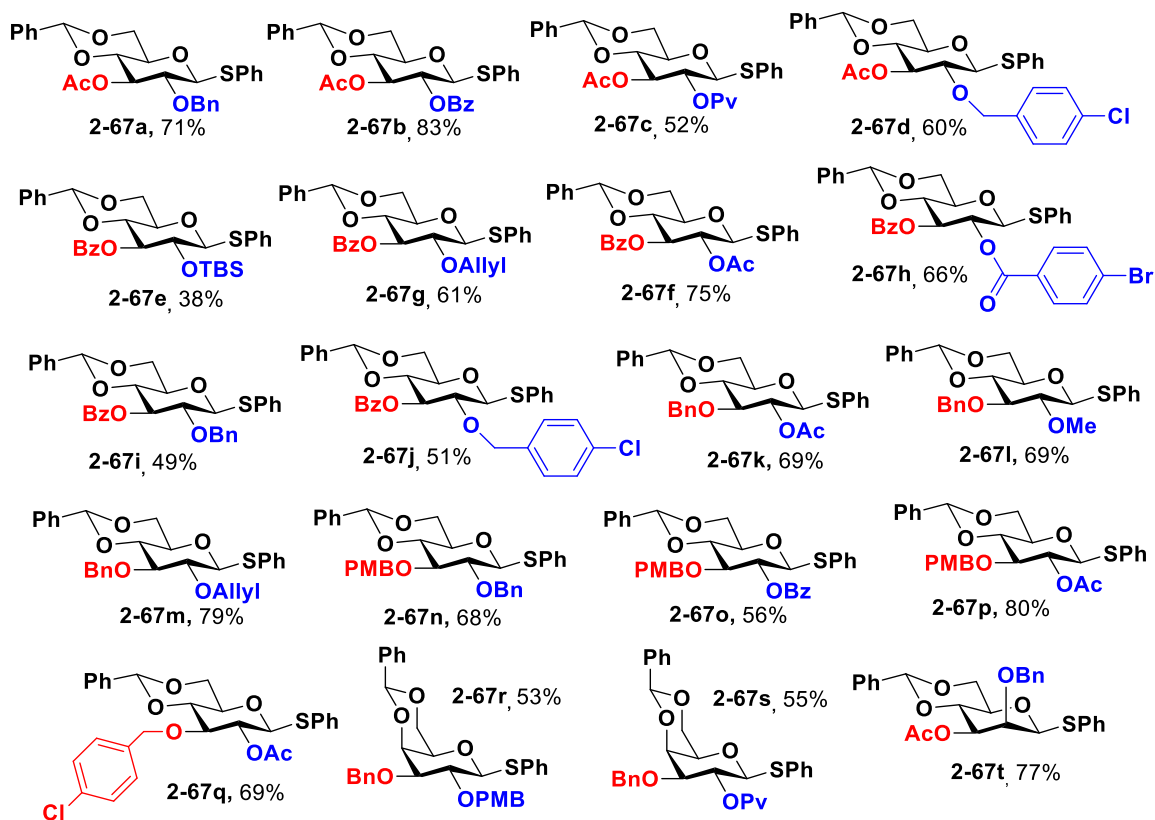
2.3.6 One-pot approach for the synthesis of differentially protected monosaccharides

While mixed acetal protecting groups are less common in carbohydrate synthesis than acyl or benzyl protection, their stability to bases and significant liability under mildly acidic conditions offer excellent opportunities for carrying out the subsequent functionalizations in a single operation. Following the concept of a streamlined single-pot synthesis of various *D*-glucose derivatives by Hung and coworkers (*vide supra*),⁵ Dr. Jeonghyo Lee investigated one-pot derivatizations of **2-60** (Scheme 2.16).⁴² The one-pot transformations leading to differentially protected C2/C3 products **2-67a-2-67t** (Scheme 2.16, A) commenced with CPA-directed regioselective acetalization, and the resultant C2-acetal **2-65b** (or **2-65c** and **2-66g**) was successfully obtained in full conversion.

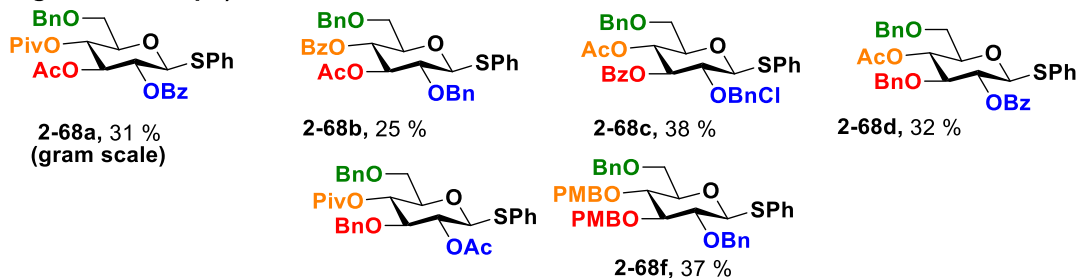
Scheme 2.16. The one-pot strategy of monosaccharides modification using CPA catalysis.



A. (Single Pot, 4 steps)



B. (Single Pot, 6 steps)



^aExperiments were carried out on a 0.056 mmol scale, using DCM as a solvent and 4Å molecular sieves, -50°C, 24h. ^bAcylation was carried using Ac₂O (1.1 equiv), DMAP (10 mol%), Et₃N (5.0 equiv) or BzCl (1.2 equiv), DMAP (20 mol%), Py (10 equiv). Alkylation was accomplished by addition of NaH (1.2 equiv), alkyl halide (1.1 equiv), TBAI (0.1 equiv) and DM. ^cThe MOC cleavage was achieved by addition of 0.05M HCl in CH₂Cl₂ (pH=5). ^dBenzylidene acetal cleavage was accomplished using Et₃SiH (5 equiv), CF₃CO₂H (5 equiv), DCM, 0 °C, 2h.

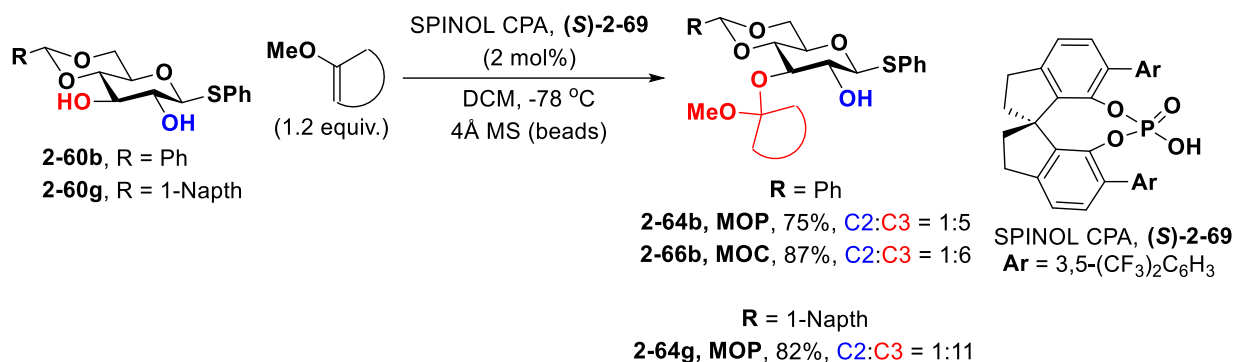
The regioselective acylation of the C3-OH was accomplished using (RCO)₂O/Py or RCOCl/Et₃N in the presence of catalytic DMAP (substrates **2-67a** – **2-67j**). Alternatively, the C3-alkylation was accomplished using alkyl halides and sodium hydride as the base in the presence of catalytic TBAI (**2-67k** – **2-67t**). The C2-acetal was removed by adding excess of HCl solution in DCM to the reaction mixture and then concentrated crude oils were subjected to the C2-protection to provide products **6a-6t** in good yields (49-83% overall yield). This method was also successfully applied to generate D-galactose-based substrates **2-67r** and **2-67s**. D-mannose-derived substrate **2-67t** required reverse order of modification, as CPA-catalyzed acetalization led to C3-MOP acetal **2-66g**. These transformations could be further combined with benzylidene acetal opening/C4 protection steps to accomplish single-pot generation of differentially protected D-glucose derivatives **2-68a–2-68f** depicted in Scheme 2.16, B. Thus, the previously developed protocol included regioselective benzylidene acetal reduction with CF₃CO₂H/Et₃SiH leading to a product containing free C4 alcohol that was subsequently protected. These single-pot transformations proceeded in 25-38% overall yield (~85% yield per operation) with high levels of overall regiocontrol. These procedures were scalable, and the derivative **8a** was made on a 1.0 g scale (31% yield) with the same yield as on a 0.056 mmol scale. While this method allows to expand the repertoire of sugar derivatives and transformations developed by Hung⁵, it suffers from the obligatory use of expensive chiral acid AdTRIP CPA **2-62e**. We surmised that the costs associated with the use of **2-62e** could be dramatically reduced if the catalyst is immobilized on a solid support as numerous recent studies suggest that such catalysts could be readily recovered and recycled.

2.4 Development of the scalable regioselective CPA-catalyzed method for regioselective carbohydrate acetalization

Usage of (*R*)-AdTRIP CPA **2-62e** can provide perfect selectivity for C2-acetalization of trans-equatorial moieties in carbohydrates with more than 25:1 regioselective ratio of products and can be applied across various range of monosaccharides. However, as mentioned before, the opposite enantiomer of the catalyst did not revert the regioselectivity as it is desired in an ideal case scenario. Before performing the immobilization studies, we pursued the search for an alternative CPA catalysts that would revert the regioselectivity and provide C3, rather than C2, regioisomers. .

As Miller³² and Dong³³ demonstrated in their work of chiral copper(II) catalyzed reactions, if the opposite enantiomer of the catalyst does not work effectively for switching the mode of regiocontrol, this can be achieved by tuning the chiral catalyst scaffold and using a structurally different catalyst of the same kind. Guided by that, we investigated another popular, but more expensive and less available SPINOL CPAs (Scheme 2.17). Delightfully, these studies identified **2-69** as the catalyst that is capable to overturn the selectivity and provide a C3 rather than C2 product. Thus, when carried under the same conditions, **2-69** catalyzed acetal protection of substrate **2-60b** provided product **2-64b** in good yields and C2:C3 = 1:5 selectivity with MOP and product **2-66b** (C2:C3 = 1:6) with MOC as an electrophile. Assuming that steric factors play a significant role in controlling the regioselectivity of this reaction, we also tested glucose **2-60g** with 4,6-naphthalen-1-yl acetal protecting group and were able to obtain the corresponding product in 82% yield and improved selectivity for the C3-protection product (C2:C3 = 1:11).

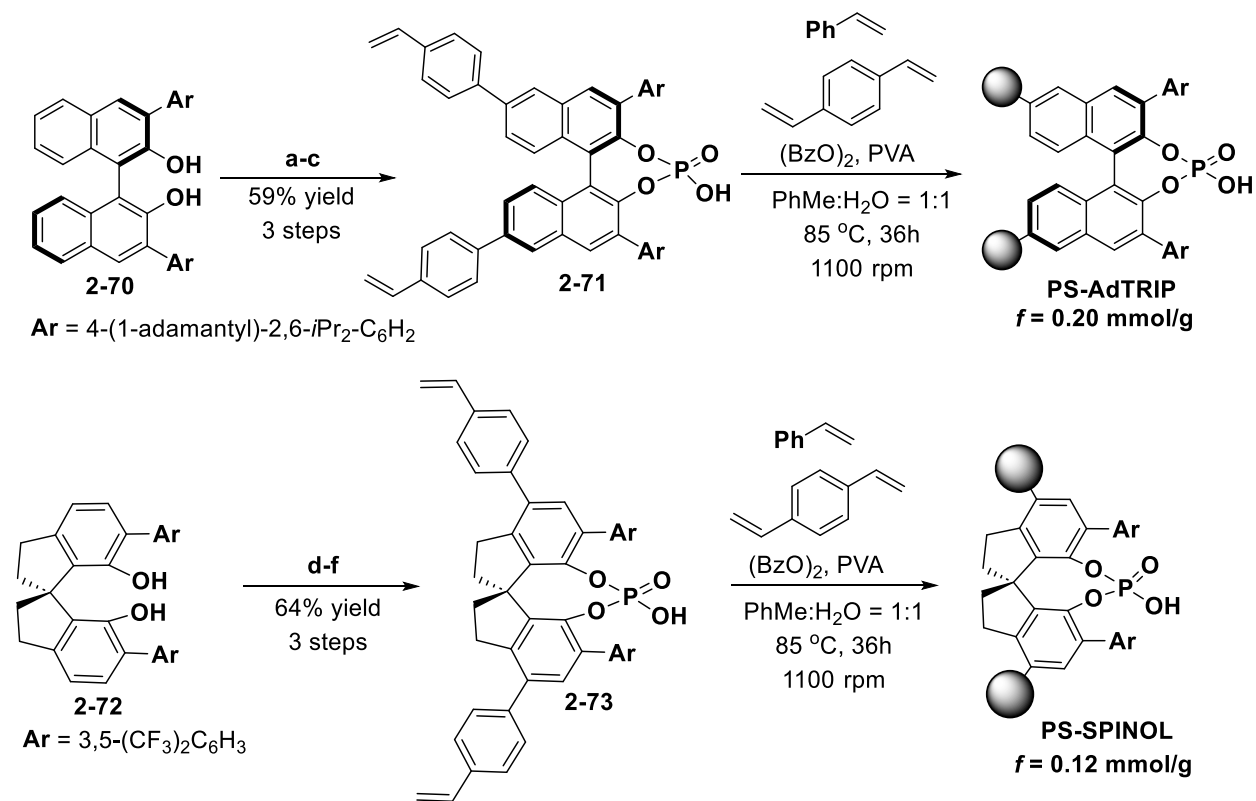
Scheme 2.17. Regiodivergent acetalization catalyzed by SPINOL-based CPA.



2.4.1 Chiral Phosphoric Acids Immobilization.

Our subsequent efforts were focused on developing a catalytically active immobilized version of AdTRIP CPA **2-62e** and SPINOL CPA **2-69** catalysts into the polymer matrix. Based on the previously developed strategies for CPA immobilization discussed in Chapter 1,⁴³ Dr. Sibin Wang explored the synthesis of polystyrene supported catalyst **PS-AdTRIP** (Scheme 2.18). After synthesizing precursor **2-70** containing installed 4-(1-adamantyl)-2,6-(*i*-Pr)₂C₆H₂- substituents, Dr. Sibin Wang was able to modify the previously published by Rueping and Pericas approaches,⁴² as these previously published routes did not lead to catalytically active materials. Dr. Yaroslav Khomutnyk also pursued the preparation of new immobilized **PS-SPINOL**⁴⁴ depicted in Scheme **2.18**, using the approach developed for the synthesis of **PS-AdTRIP** CPA. Remarkably, the gram scale synthesis of **PS-SPINOL** was accomplished in only 4 steps from **2-72** that is a commercially available derivative of (*S*)-SPINOL.

Scheme 2.18. Routes for preparing immobilized CPA catalysts



(a) **2-70** (1 equiv), Br₂ (2.2 equiv), DCM (0.16 M), -78 °C, 2.5 h, 92%; (b) 4-vinylphenylboronic acid (2.4 equiv), K₂CO₃ (4.0 equiv), EtOH:THF = 1:1 (0.1 M), Pd(PPh₃)₄ (15 mol%), reflux, 12h, 65%; (c) POCl₃ (2.0 equiv), pyridine (0.1 M), 70 °C, 12 h, then H₂O (0.1 M) 100 °C, 16 h, 57%; (d) **2-72** (1 equiv), Br₂ (2.2 equiv), DCM (0.16 M), -78 °C, 2.5 h, 97%; (e) 4-vinylphenylboronic acid (5 equiv), K₂CO₃ (5.0 equiv), dioxane:water=2:1 ratio (0.066 M), Pd(PPh₃)₄ (5 mol%), 70 °C, 5h, 88% yield; (f) POCl₃ (5.0 equiv), pyridine (0.1 M), 70 °C, 12 h, then H₂O (0.1 M) 100 °C, 16h, 75%.

2.4.2 Immobilized CPAs testing for regioselective monosaccharides acetalization.

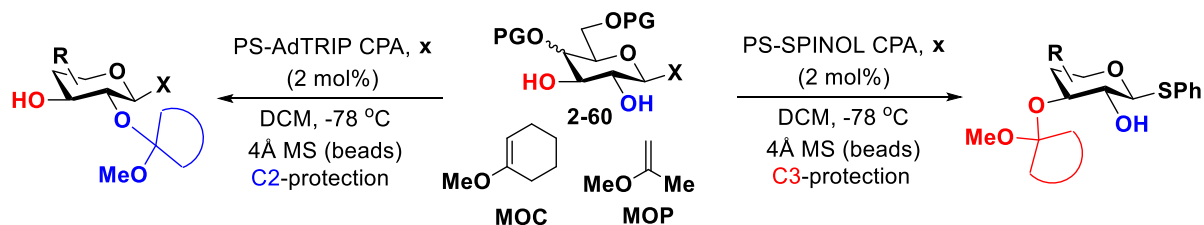
After the immobilization of both catalysts **2-62e** and **2-69** was developed, we used these polymeric materials as the catalysts of regioselective carbohydrate acetalization (Scheme 2.19, A). Dr. Sibin Wang demonstrated that **PS-AdTRIP** catalyst has an excellent selectivity profile for the generation of the corresponding 2-MOP protected derivatives, and with the exception of one case (**5n**), the resultant products were obtained in excellent C2-selectivity (Scheme 2.19, A). It is noteworthy that the selectivities and yields for substrates **2-63b**, **2-65d**, and **2-65f** obtained with

the immobilized catalyst **PS-AdTRIP** matched the corresponding results previously obtained for CPA **2-62e**. Remarkably, in three instances (**2-63e**, **2-63g**, and **2-63h**), PS-supported CPA provided significantly higher regioselectivities than the monomeric acid **2-62e** (25:1 rr vs 3:1 rr for **2-63g**, 25:1 rr vs. 7:1 rr for **2-63e**, and 19:1 rr vs 12:1 rr for **2-63h**). Finally, in instances of **2-64k** and **2-63c**, the selectivities obtained with **PS-AdTRIP** were lower than the selectivities obtained with **2-62e** (1:1 rr vs 6:1 rr for **2-64k** and 20:1 rr vs 15:1 rr for **2-63c**).

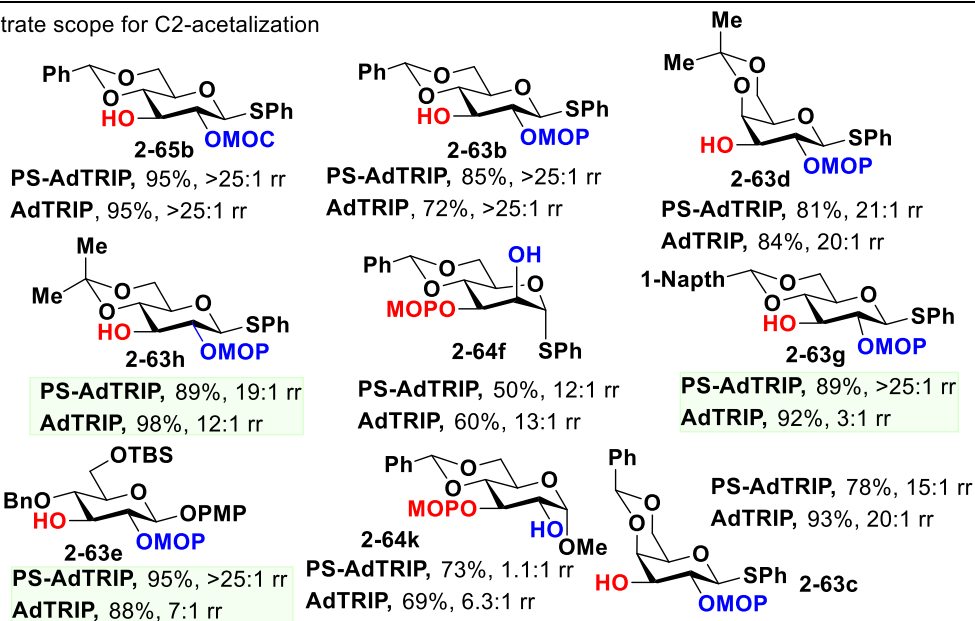
Subsequently, we evaluated (**S**)-**PS-SPINOL** resulted in regio divergent acetalization of substrates **2-60b**, **2-60d**, **2-60g**, and **2-60h**, leading to the regioisomeric C₃-acetals in good to excellent selectivities. However, in the case of products **2-63e** and **2-64k**, the same regioisomers as with (**R**)-Ad-TRIP CPA **2-62e** and **PS-AdTRIP** were observed. The selectivities improved with increasing steric size of the O4/O6 acetal (from 6:1 to 8:1 to 10:1 rr for **2-66b**, **2-64g**, and **2-64h**). Similarly, increasing the steric size of electrophile (i.e. 1-MOC vs. 2-MOP) consistently resulted in an improvement of the reaction selectivities (from 10:1 for **2-64g** to 14:1 for **2-66g** and from 8:1 for **2-64b** to 9:1 for **2-66b**). To demonstrate the scalability of the process, the synthesis of **2-66b** with **PS-SPINOL** was successfully carried on 1.0 g (2.78 mmol) scale with improved 94% yield and 8:1 rr.

Scheme 2.19. Catalyst controlled regioselective acetalization using immobilized CPAs^a

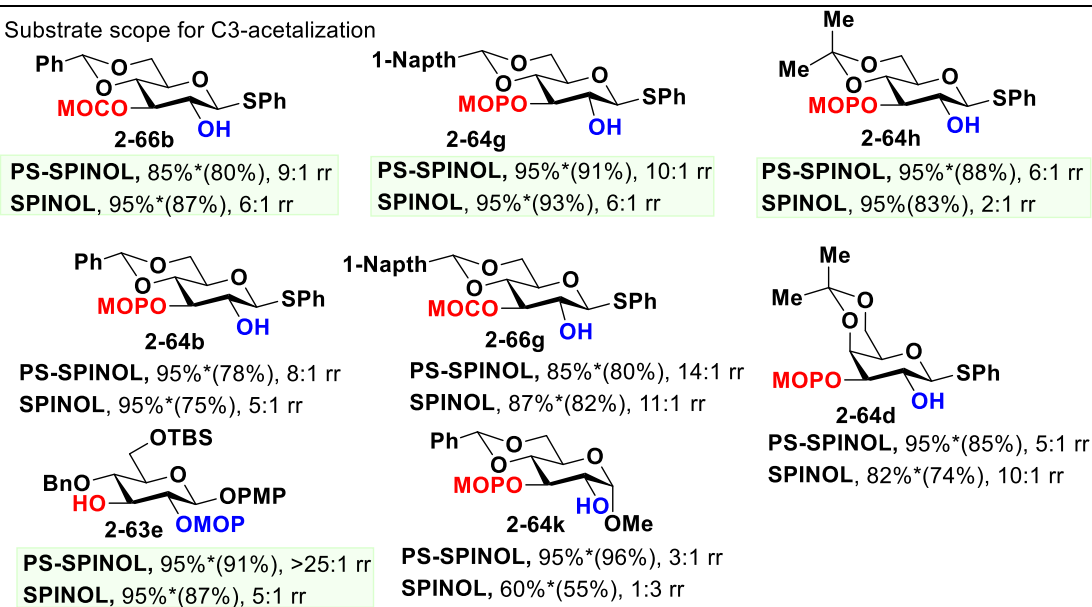
A. Catalyst-controlled regioselective acetalization



B. Substrate scope for C2-acetalization



C. Substrate scope for C3-acetalization



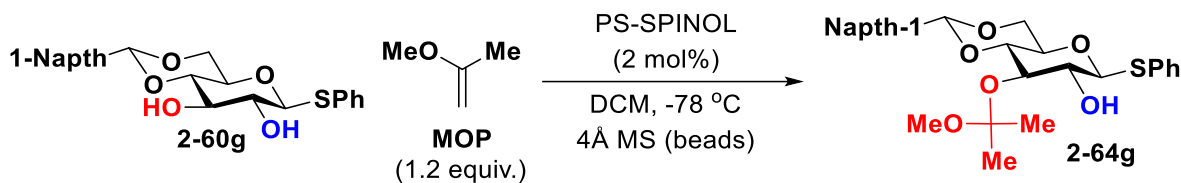
^aResults in Scheme 2.19B were obtained by Dr. Sibin Wang.

It is noteworthy that as in the case of the **PS-AdTRIP**, the use of **(S)-PS-SPINOL** may lead to significant improvement in the reaction selectivity in comparison to the monomeric catalyst **2-69**. Such improvements in selectivity were observed for substrates **2-64b**, **2-66b**, **2-64h** and **2-63e** although for **2-64d** polymeric catalyst was inferior to SPINOL CPA **2-69**. Remarkably, complete switch in selectivity was observed in the case of substrate **2-64k**, and while polymeric **PS-SPINOL** resulted in moderately selective formation of the C3-protected product **2-64k** (3:1 rr), monomeric **(S)-2-69** resulted in the formation of the C2 regioisomer **2-63k** (1:3 rr). These observations suggest that the additional structural features present in **PS-AdTRIP** and **PS-SPINOL** that are not present in **(R)-2-62e** and **(S)-2-69** such as the linker and polystyrene matrix may impact the steric interactions between the CPA and substrate. This could have both positive or negative consequences for the reaction outcome although in the majority of cases presented in Schemes 34A and 34B improvements in the selectivity were observed.

As a next step, we performed recyclability tests (Table 2.1). Reactions were performed using substrate **2-60g** and the same amount of the **PS-SPINOL** (18 mg), that was isolated after each reaction by filtration and used in the next cycle. Due to partial decomposition of product **2-64g** during filtration at room temperature, before isolation reaction was quenched with 0.5 M NH₃ solution in methanol. Due to partial quenching of catalyst with ammonia solution in methanol, erosion of selectivity was noted at cycles 4–6. This could be easily addressed by resin reactivation by washing with 6M HCl and then DCM (cycle 7). Alternatively, resin can be washed and reactivated each time after the reaction to prevent catalytic activity erosion. In parallel, Dr. Sijin Wang also performed recyclability tests for **PS-AdTRIP** showing catalyst can be used repeatedly to run nine consecutive 1.0 g scale MOP-protections of **2-60b** with only 0.5 mol% (50 mg) of

resin. These results indicate that significant catalyst economy was achieved as the same 50 mg of PS-AdTRIP CPA were used to convert the total of 14.0 g of **2-60b** into **2-63b**.

Table 2.1. Recyclability of PS-SPINOL



Cycle	Wash	C2:C3 (r.r.)	Conversion (% , NMR)
1	–	11.2	88
2	–	10.9	95
3	–	10.6	95
4	–	9.6	95
5	–	9.5	92
6	–	6.4	94
7 ^a	6N HCl	10.3	93

^aCatalyst PS-SPINOL was washed with 6N HCl and then CH₂Cl₂, and dried before running the experiment in entry 7 to regenerate its activity and selectivity that erodes due to NH₃ workup.

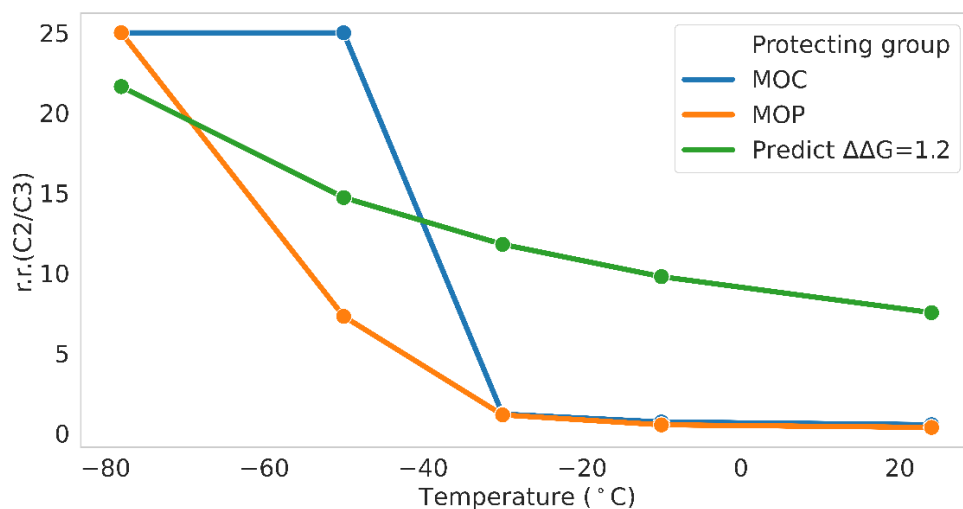
2.5 Computational mechanistic investigations of carbohydrate regioselective acetalization under CPA catalysis

Even though CPA-catalysis is a well-defined field now and mechanisms of CPA-catalysis were studied using both experimental and computational methods, in most cases these studies were related to enantioselective transformations, such as addition to C=X double bonds, transfer hydrogenations, chiral resolutions, etc. However, applications of CPA as a catalyst for regioselective differentiation of hydroxyl groups in polyols remain a new area with no stereomodels developed, especially in carbohydrate chemistry.³⁹

Our subsequent studies were focused on experimental and computational exploration of the mechanism for the regioselective acetalizations and development of a stereochemical model

explaining the observed selectivity trends. Experiment performed by Dr. Jeonghyo Lee demonstrated that both MOC and MOP acetalizations show unusual selectivity versus temperature profiles (Figure 2.1). Thus, both types of acetalization were unselective at temperatures above -30 °C but demonstrated significant jump in selectivity once cooled below -50 °C. These unusual temperature vs. selectivity profiles are not consistent with the theoretically predicted ones obtained using the Arrhenius model of regioselectivity as a function of temperature computed for $\Delta\Delta G^\circ=1.2$ kcal/mol. The regioselectivity should be exponentially dependent on temperature, and the profiles in Figure 2.1 should not involve an abrupt increase of selectivity at some threshold temperature. The observed temperature dependence suggests that the acetalization may happen through competing mechanisms and that the mechanism prevailing at temperatures below -50 °C might be different from the reaction mechanism at higher temperatures.

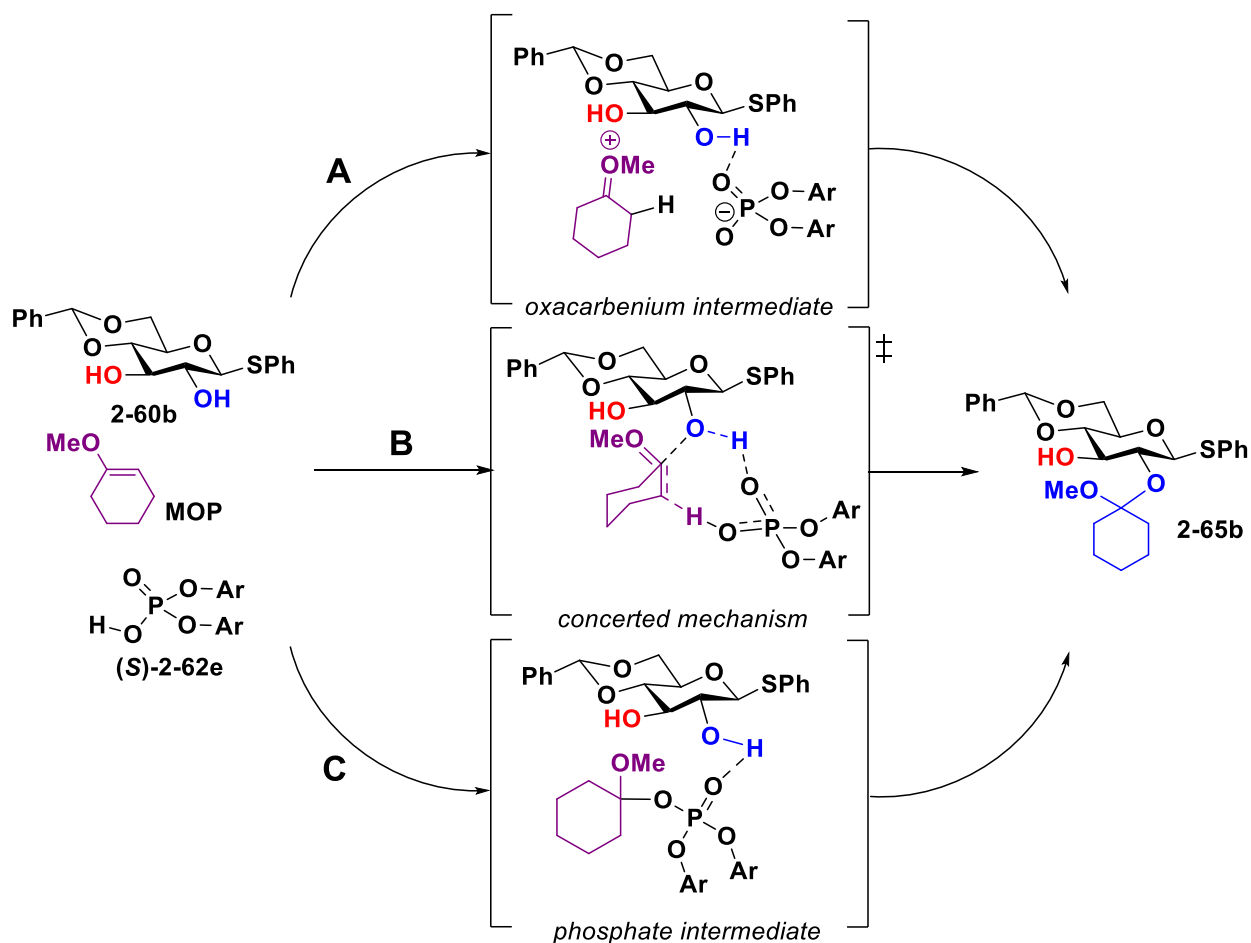
Figure 2.1. Selectivity versus temperature profile for the MOC and MOP protection of 2-60b, and theoretically predicted selectivity profile for a reaction with no mechanism switch using Arrhenius model.



With these observations in mind, three different reaction mechanisms depicted in Scheme 2.20 were proposed by Dr. Alonso J. Arguelles. These involved the conventional mechanism

proceeding through the oxocarbenium ion (Path A), as well as direct synchronous or asynchronous concerted addition, as previously proposed by the Nagorny group for the CPA-catalyzed spiroketalizations (path B)⁴⁰. Alternatively, the catalyst may react with the MOC or MOP enol ethers to form a phosphate intermediate, which then proceeds through SN₁ or SN_i mechanisms that were observed by Nagorny and co-workers for the CPA-catalyzed glycosylation of 6-dEB (path C)⁴⁵.

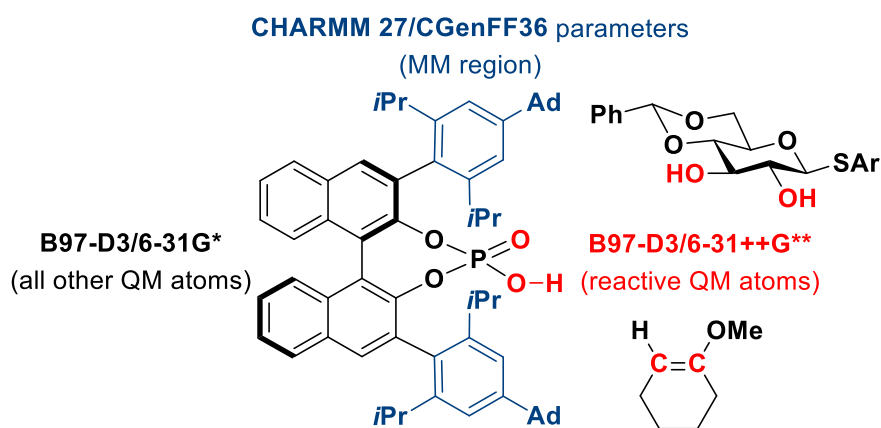
Scheme 2.20. Proposed mechanism for the regioselective acetalization.



Differentiating these mechanistic options computationally represents a challenging task as it requires finding and optimizing conformationally flexible transition state structures. To address some of these challenges, our computational studies used the reaction-path and transition-state

search tool called the Growing String Method (GSM). The large size of the system (207 atoms) motivated a Quantum Mechanics/Molecular Mechanics (QM/MM) approach to make the reaction path analysis feasible. The QM/MM borders were set on the C-C bond at the 3,3'-positions of the chiral catalyst **2-62e** placing bulky hydrocarbon moieties in the MM region (Scheme 2.21, details are in Chapter 2.9). The reaction pathways were determined using GSM for the 20 lowest energy conformers for each path.

Scheme 2.21. Computational model with QM/MM setup and mixed basis set for transition states search.



The concerted mechanism was investigated first, beginning from the complex involving the substrate H-bonded to (*R*)-**2-62e** (Scheme 2.22). The reaction pathway shows an asynchronous concerted transformation: the CPA protonates the enol ether (PG) to generate an oxocarbenium cation that then reacts with the hydroxyl group of the sugar substrate **2-60b** (TS₁ for C2-path and TS₂ for C3-path). The resultant CPA anion deprotonates the hydroxyl group synchronously with oxygen nucleophilic attack on the oxocarbenium cation. The lowest energy activation barriers among the 20 conformers of each TS favor C2-protected product **2-65b** formation at 223K ($\Delta\Delta G^\ddagger_{223} = -1.2$ kcal/mol) and 273K ($\Delta\Delta G^\ddagger_{273} = -1.0$ kcal/mol) (Table 2.2). Activation energies (ΔG^\ddagger , kcal/mol) for this mechanism (21.1 and 22.3 kcal/mol for C2- and C3-pathways respectively)

are slightly higher than expected from the experimental data (18-19 kcal/mol for overnight reaction at $-50\text{ }^{\circ}\text{C}$). This concerted mechanism, which does not show an oxocarbenium intermediate (Scheme 2.20, Path A), does bear similarities with the oxocarbenium mechanism. In particular, the oxocarbenium ion appears along the reaction path at the transition state structure, which identifies the concerted mechanism as asynchronous (Scheme 2.20, Path B). The two elementary step phosphate-mediated mechanism (Scheme 2.20, Path C) was investigated next. To do so, 20 conformationally distinct reaction pathways involving (**R**)-**2-62e** and 1-methoxycyclohexene (PG) were examined. The phosphate intermediate is reached via asynchronous protonation of the enol ether PG followed by a nucleophilic attack with the same phosphoric acid oxygen that participated in substrate protonation. The activation energy for the lowest barrier phosphate formation step is 14.7 kcal/mol (Scheme 2.22, Table 2.2). Unlike our previous studies of the CPA-catalyzed glycosylations, the covalent phosphate intermediate formation was not directly observed by low-temperature ^{31}P , ^{13}C or ^1H NMR studies (see discussion in Chapter 2.6). This is not surprising, however, as the computational studies indicate that covalent phosphate is 4.4 kcal/mol less stable than the reactant complex. Keeping in mind the low energy barrier for its formation and dissociation back, this step should be considered as being in equilibrium. During the reaction, the phosphate acetal would be formed only in trace quantities and exist as a steady-state intermediate, which could be observed in a deuterium-exchange experiment with deuterium-labeled phosphoric acid (see discussion in Chapter 2.6).

Scheme 2.22. Computed free energy profiles of concerted and phosphate-mediated mechanisms

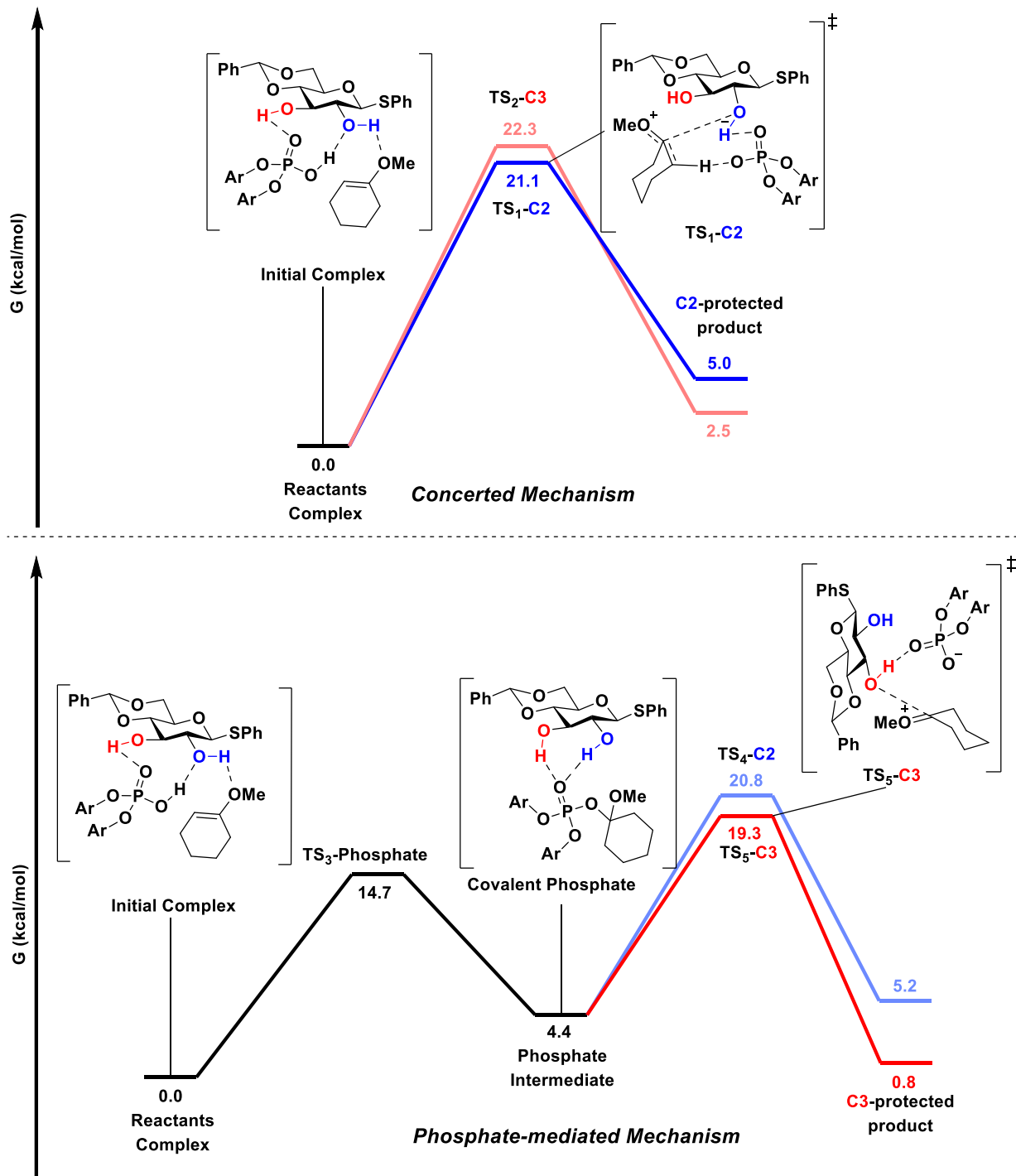


Table 2.2. Comparing TS structures enthalpy and free energy barriers calculated relatively to lowest energy reactants complex for both 223K and 273K

Step	ΔH^\ddagger (kcal/mol)	ΔG^\ddagger (kcal/mol)	$\Delta\Delta G^\ddagger$ (kcal/mol)
Concerted mechanism at 223K			
C2-protection	20.6	21.1	-1.2
C3-protection	22.7	22.3	
Phosphate-mediated mechanism at 223K			
Phosphate formation	15.3	14.7	-
C2-protection via phosphate S_{Ni} reaction	21.3	20.8	1.5
C3-protection via phosphate S_{Ni} reaction	19.7	19.3	
Concerted mechanism at 273K			
C2-protection	20.6	21.4	-1.0
C3-protection	22.8	22.4	
Phosphate-mediated mechanism at 273K			
Phosphate formation	15.1	14.3	-
C2-protection via phosphate S_{Ni} reaction	21.5	20.8	1.6
C3-protection via phosphate S_{Ni} reaction	19.8	19.2	

The second step of the phosphate-mediate pathway (Path C) has a reaction energy profile more consistent with a concerted S_{Ni} mechanism rather than an S_{N1} mechanism, as no stable carbocation intermediates were detected (Scheme 2.22). In this step the hydroxyl group of 2,3-diol 4a attacks the carbon atom of the methoxy cyclohexane fragment of the phosphate intermediate at the same time as the C-O phosphate bond cleaves. This second step is rate-limiting and shows the opposite regioselectivity compared to the concerted mechanism. That is, at both temperatures of interest (Table 2.2) the C3-protection was favored over the C2-protection ($\Delta\Delta G^\ddagger_{223} = 1.5$ kcal/mol and $\Delta\Delta G^\ddagger_{273} = -1.6$ kcal/mol). Surprisingly, the activation energies of the rate-limiting step were also close to the ones computed for the concerted mechanism (Scheme 38).

The energy diagram summarizing our computational studies is provided in Scheme 38 as well as energy values for rate-determining steps (RDS) are given in Table 2.3. As it can be seen,

for both concerted and phosphate-mediated pathways C2-protection activation energies are extremely close (the difference is less than 1 kcal/mol). The regioselectivity reversion is caused by the energy of the transition state leading to a C3-protected product: in the case of the phosphate mechanism, TS is 3.2 kcal/mol more stable than TS leading to C3-product via concerted mechanism. Even though there was a slight preference for the phosphate mechanism, an obvious assignment of operating mechanism is not possible due to the energy difference being within the errors of the model. Accounting such a small energy gap (1-2 kcal/mol), it is not possible to distinguish between concerted and phosphate mechanisms at both 223K and 273K, making them both possible to be happening in competitive or temperature-dependent mode. This situation, however, allows us to postulate that the concerted mechanism is preferred at low temperatures and the phosphate mechanism at high temperatures. Invoking this switch in mechanism comes with a change in regioselectivity that nicely explains the experimental results depicted in Figure 2.1. At low temperatures, the concerted mechanism (Path B) would therefore give rise to high C2-selectivity ($\Delta\Delta G^\ddagger$ (C2-C3) = -1.2 kcal/mol). At higher temperatures the phosphate mechanism (Path C) likely results in increased amounts of the C3 acetalization product ($\Delta\Delta G^\ddagger$ (C2-C3) = 1.5 kcal/mol).

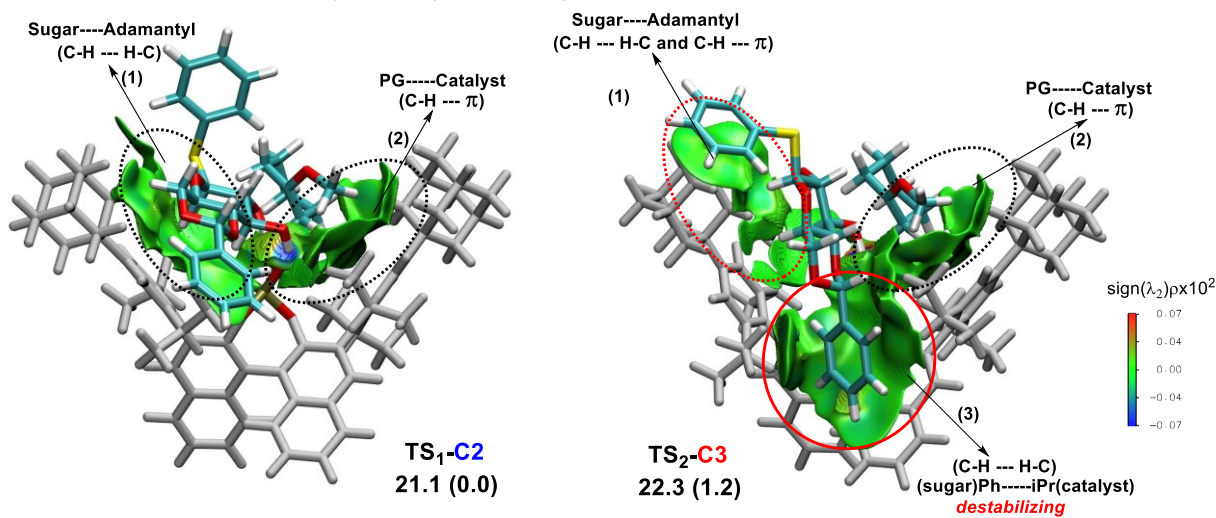
Table 2.3. Comparing concerted and phosphate-mediated mechanisms at 223K and 273K.

Path	ΔG^\ddagger (phosphate), kcal/mol	ΔG^\ddagger (concerted), kcal/mol	$\Delta\Delta G^\ddagger_{\text{RDS}}$ (concerted - phosphate), kcal/mol
223 K			
C2	20.8	21.1	0.3
C3	19.3	22.3	3.0
Lowest	-	21.1 (C2)	1.8
	19.3 (C3)	-	
273K			
C2	20.8	21.4	0.6
C3	19.2	22.4	3.2
Lowest	-	21.4 (C2)	2.2
	19.2 (C3)	-	

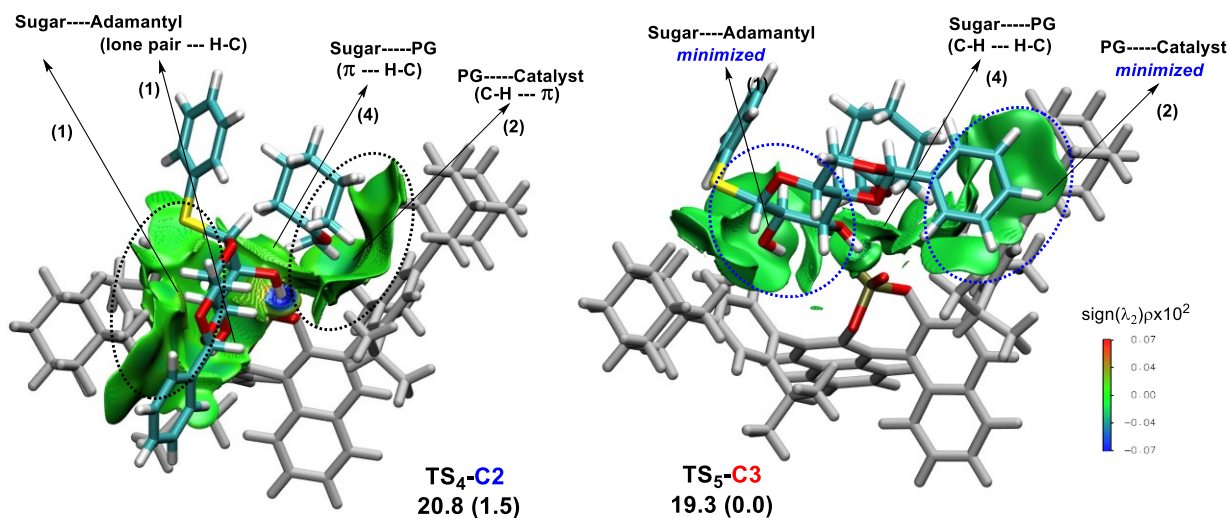
With the mechanistic picture in hand, transition state analysis was performed to identify the key structural features leading to different selectivities in each mechanism. The non-covalent interactions (NCIs) are known to be crucial in stabilizing or destabilizing the transition states when changes in energy by 1-2 kcal/mol can dramatically change the reaction selectivity. The graphical analysis delineates NCI into three categories: blue, strong attraction; green, weak interaction; and red, strong repulsion. For the concerted mechanism (Figure 2.2) there are two common regions of non-covalent interactions: (1) C-H van-der-Waals interactions of sugar backbone with catalyst adamantyl group and (2) enol ether C-H interaction with π -system of catalyst 3-aryl system. The most important interaction (3) is between the 4,6-benzaldine group and CPA isopropyl groups (circled for TS₂). The presence of such inter-action can destabilize the transition state and make the C3-protection less favorable than the corresponding C2-pathway that lacks such steric repulsion (3). Remarkably, during the C2-protection via the phosphate-mediated mechanism, reactants, and catalyst in TS₄ are aligned almost in the same ways as for the concerted reaction (TS₁). There are some weak $\pi\cdots\text{H-C}$ interactions (4) that appear between the substrate 4a and the MOC protecting group PG, but interactions (1) and (2) with the catalyst skeleton also are present. These similarities in NCI patterns for the TS₁ and TS₄ are in good agreement with almost identical TS energies for the C2-acetylation for both mechanisms. In contrast, the molecular alignment in TS₅ (C3-protection) is significantly different from the concerted mechanism. The reactants are aligned in a more compact way and positioned further away from the catalytic pocket. The NCIs (1) and (2) arising from the 2,3-diol **2-60b**, MOC enol ether PG and the catalyst are minimized, and only interaction (4) between the reactants are clearly present. The absence of these NCIs in TS₅ leads to its higher stability and, thus, the C3-protection prevails for the phosphate-mediated mechanism.

Figure 2.2. Noncovalent interaction analysis for regiocontrolling transition states.

A. Noncovalent interaction analysis of regiocontrolling transition states for concerted mechanism at 223K



B. Noncovalent interaction analysis of regiocontrolling transition states for phosphate-mediated mechanism at 223K



2.6 Experimental evaluation of potential mechanisms

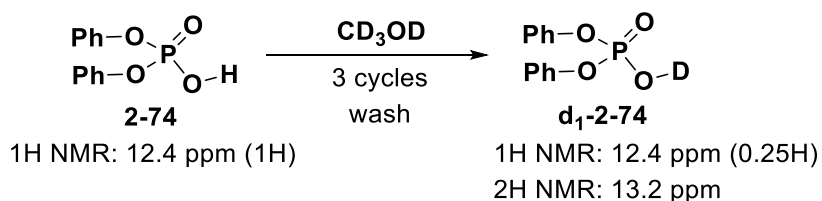
2.6.1 Experiments for covalent-phosphate detection

To observe possible covalent phosphate **2-75** formation, diphenyl deuterium phosphate **d₁-2-74** (**d-DPPA**) was used as a model. Isotope exchange was performed via diphenyl hydrogen phosphate wash with methanol- d_4 (3 times, see Chapter 2.8 for details). Deuterium exchange was

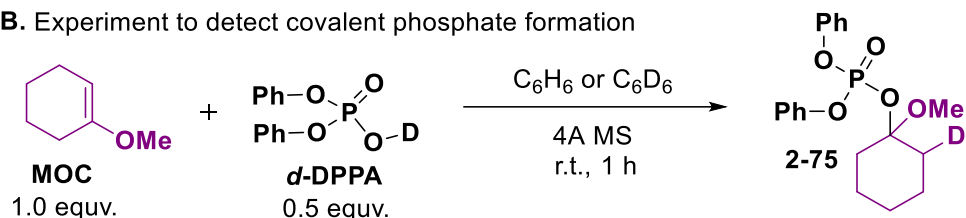
confirmed with ^1H NMR by observing the reduction of the acidic proton signal integral, and $^2\text{H(D)}$ NMR by observing the appearance of the acidic deuterium signal at 13 ppm (Scheme 2.23). The test reaction was performed in the oven-dried vial, where deuterated phosphoric acid **d₁-2-74** was mixed with 1-methoxycyclohexene (MOC) in the presence of molecular sieves. Benzene- d_6 (or non-deuterated benzene for $^2\text{H(D)}$ NMR studies) was used as a solvent (Scheme 2.23).

Scheme 2.23. Experiment design for covalent phosphate detection.

A. Diphenyl phosphoric acid deuteration



B. Experiment to detect covalent phosphate formation



Analysis of the ^{13}C NMR spectrum didn't provide any evidence for the covalent phosphate formation as no new carbon signals can correspond to the acetal phosphate carbon. Under the acidic conditions, MOC partially hydrolyzed to cyclohexanone and new hydrogen signals in aliphatic region 1-2 ppm and new carbon signals in ^{13}C NMR (Figure 2.3). While the ^{31}P NMR spectrum (Figure 2.4) contains only one strong signal of deuterated diphenyl phosphoric acid at -9.5 ppm, several low intensity signals were observed in -11 to -12.5 ppm region. These species may potentially belong to the depicted in Figure 2.4 mixed phosphates; however, further structural assignments were not possible.

Figure 2.3. ^1H and ^{13}C NMR in benzene- d_6 of MOC and deuterium diphenylphosphate, and their mixture.

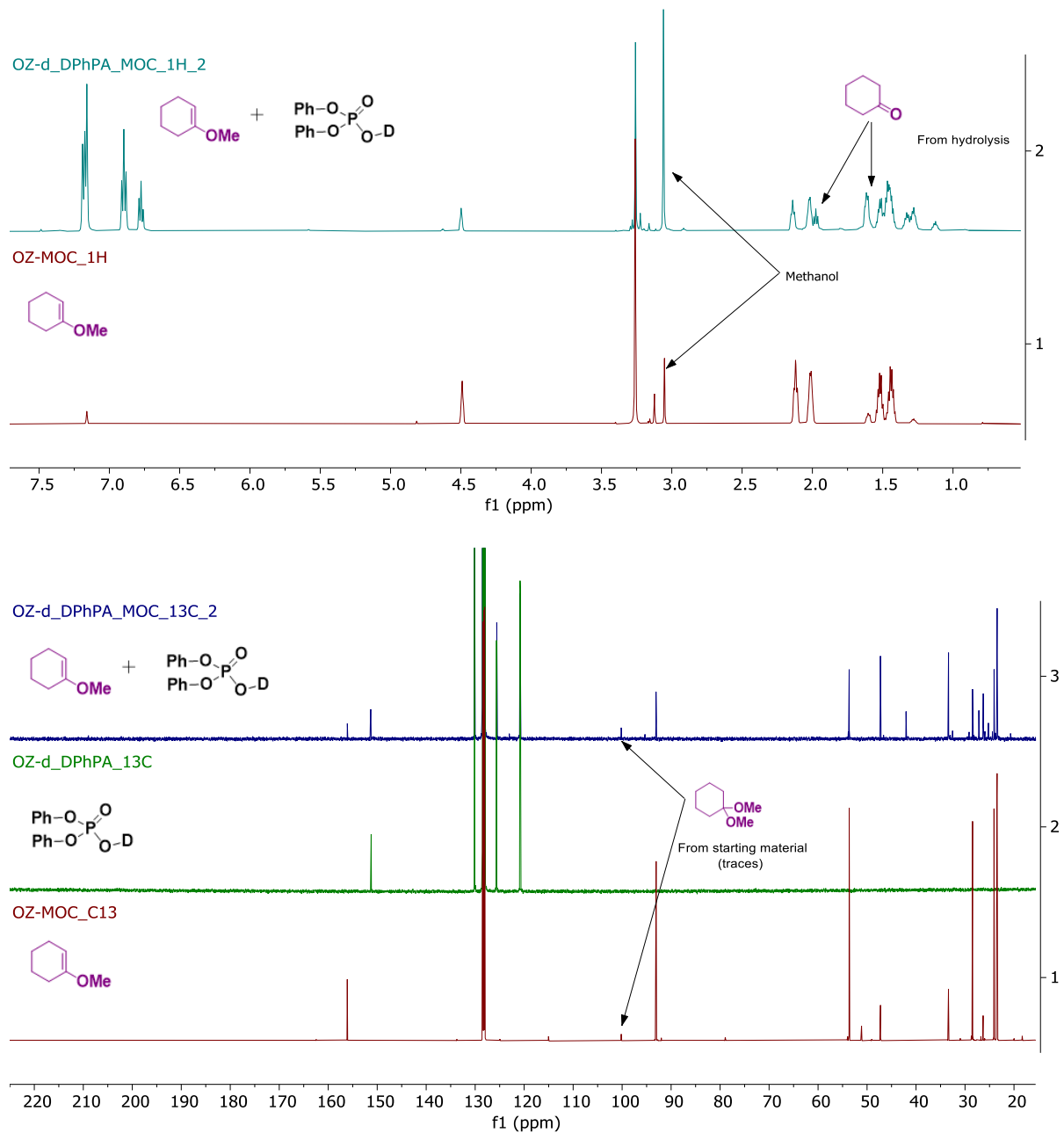
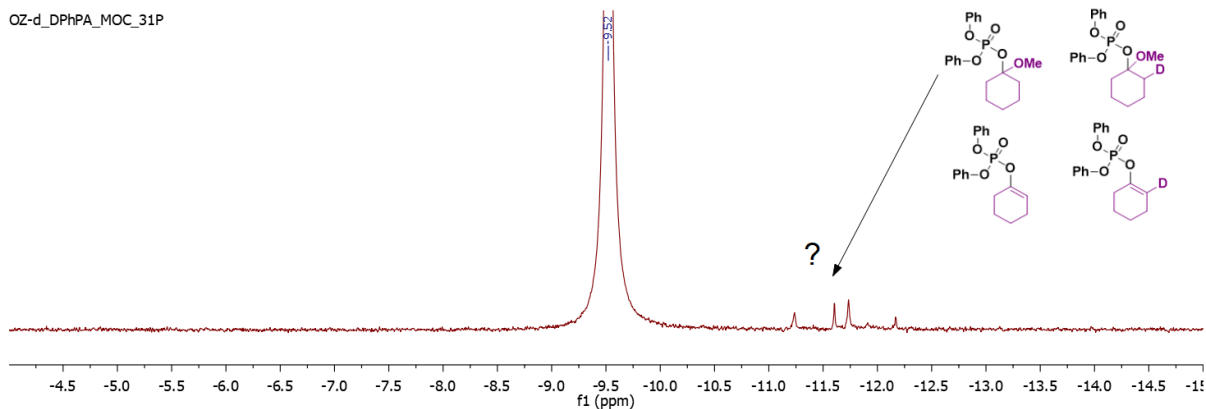
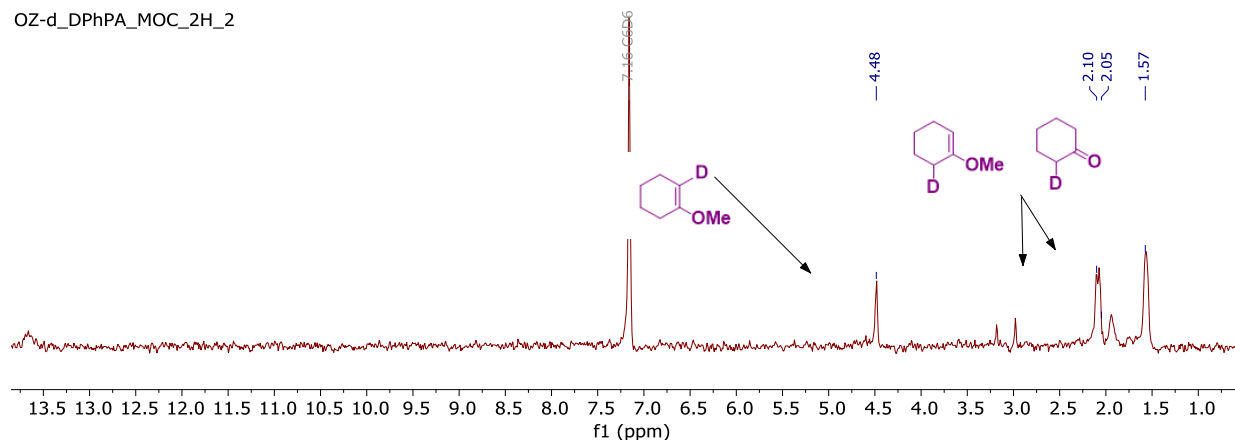


Figure 2.4. ^{31}P NMR in benzene- d_6 of starting reagents and reaction solution.



Finally, the analysis by $^2\text{H(D)}$ NMR demonstrated deuterium exchange leading to the disappearance of the acidic deuterium bound to the phosphoric acid and the appearance of new signals rising in the higher field region (Figure 2.5). The signal at 4.49 ppm is likely due to the C2-deuterated 1-methoxycyclohexene, while other downfield signals may correspond to the deuterium incorporation into cyclohexanone (the MOC hydrolysis product) or deuterium being introduced in the allylic position of MOC starting material.

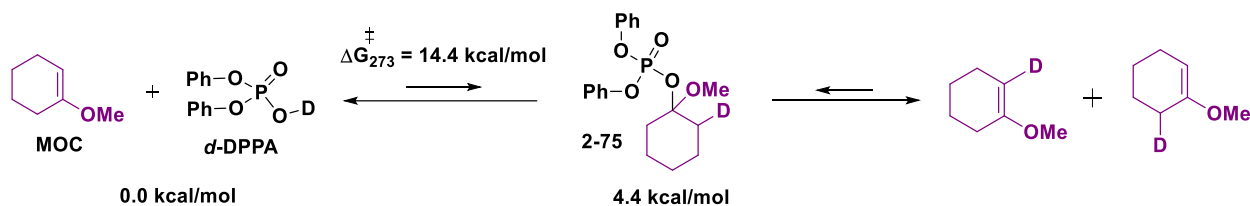
Figure 2.5. NMR in benzene of the $(\text{PhO})_2\text{P(=O)OD}$ and MOC reaction mixture.



The formation of the C2-deuterated MOC derivatives and no significant accumulation of the covalent phosphate intermediate are consistent with the results previously obtained by

computational studies (Chapter 2.5). The covalent phosphate acetal intermediate is 4.4 kcal/mol less stable than the starting reagents, but the activation energy barrier is low enough for the fast equilibrium to be established (Scheme 2.24). As a result, no significant amounts of the intermediate phosphate acetal should be observed, but its formation in trace quantities would lead to the observed proton (deuterium) exchange.

Scheme 2.24. Proposed Equilibrium Leading to D/H Exchange.



The same NMR studies were performed after reaction mixture was steered for 24h. However, there were no changes in NMR spectra except for observing higher degree of MOC decomposition (hydrolysis).

2.6.2 Determining stereospecificity of the hydroxyl group addition to enol ether double bond

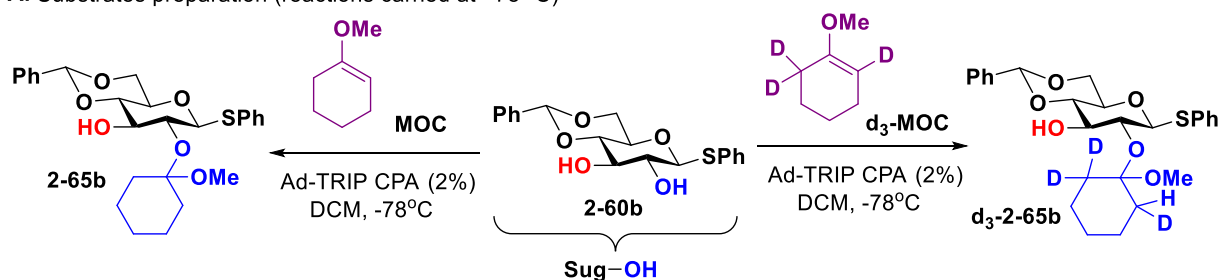
Computational analysis (Chapter 2.5) suggested that if the acetalization proceeds via the concerted addition at -78°C , then the monosaccharide hydroxyl group should undergo exclusive *syn*-addition to the MOC alkene. In contrast, the reaction proceeding through a phosphate intermediate should lead to both *syn*- and *anti*-addition of the hydroxyl group to the double bond due to fast equilibration through covalent phosphate.

To investigate the stereoselectivity of OH (of the carbohydrate diol) addition to alkene during the acetalization steps, series of experiments described below and involving the reaction of α -deuterated 1-methoxycyclohex-1-ene-2,6,6-d₃ (**d₃-MOC**), substrate **2-60b** and (*R*)-Ad-TRIP catalyst and leading to various diastereomeric products **d₃-2-65b** depending on the choice of temperature (-78°C or r.t.) were carried. The sample of **d₃-2-65b** was generated by the C2-

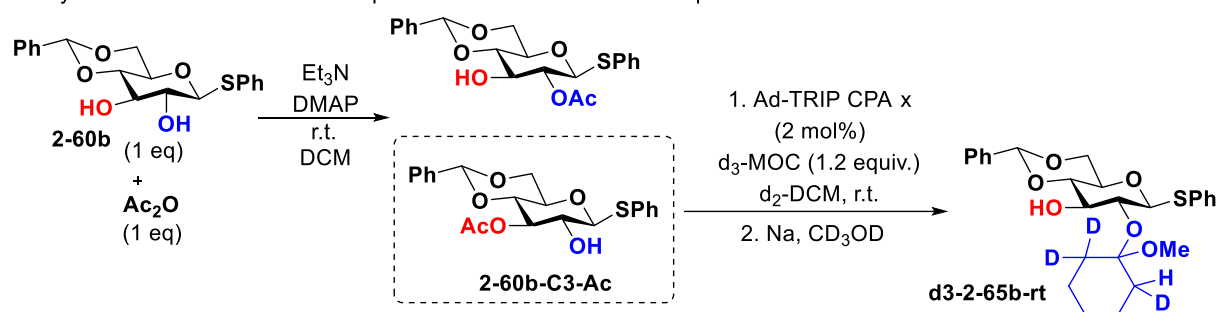
selective acetalization at $-78\text{ }^{\circ}\text{C}$ with (*R*)-**Ad-TRIP 2-62e** using the standard procedure (Scheme 2.25). To obtain the C2-protected product **d₃-2-65b-rt** at room temperature for comparison, acetalization was carried out. However, the direct reaction between **2-60b** and **d₃-MOC** at room temperature was complicated by the formation of a hardly separable C3-regioisomer. To circumvent this, the acylation of the **2-60b** at room temperature was performed followed by separation of C2- and C3-acylated products. Then C3-acylated compound **2-60b-C3-Ac** was acetalized with **d₃-MOC** and acetyl group was cleaved under basic conditions. This provided us with a sample of C2-protected product **d₃-2-65b-rt** generated at room temperature (Scheme 2.25). In total, addition of OH group of **2-60b** to enol double bond should produce $\sim 1:1:1:1$ mixture of two *syn*- and two *anti*-isomers (Scheme 2.25C). Subsequent NMR studies focused on interpreting the diastereotopic ^1H and ^{13}C NMR signals of the MOC group at positions next to the acetal group (Scheme 2.25, D).

Scheme 2.25. Synthesis of the deuterated MOC acetals **d₃-2-65b and **d₃-2-65b-rt**, and reference acetal **2-65b**.**

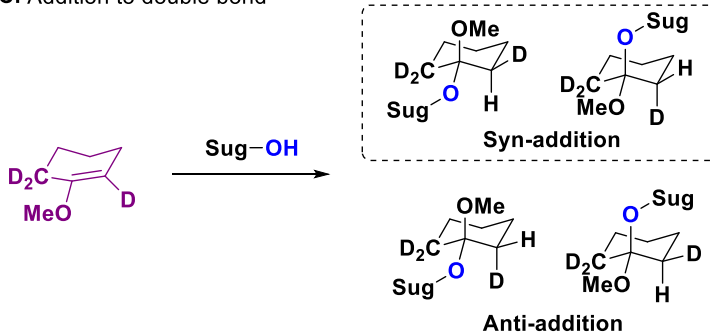
A. Substrates preparation (reactions carried at -78°C)



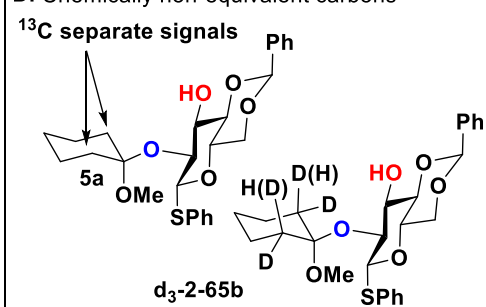
B. Synthetic route to obtain the C2-protected substrate at room temperature



C. Addition to double bond



D. Chemically non-equivalent carbons



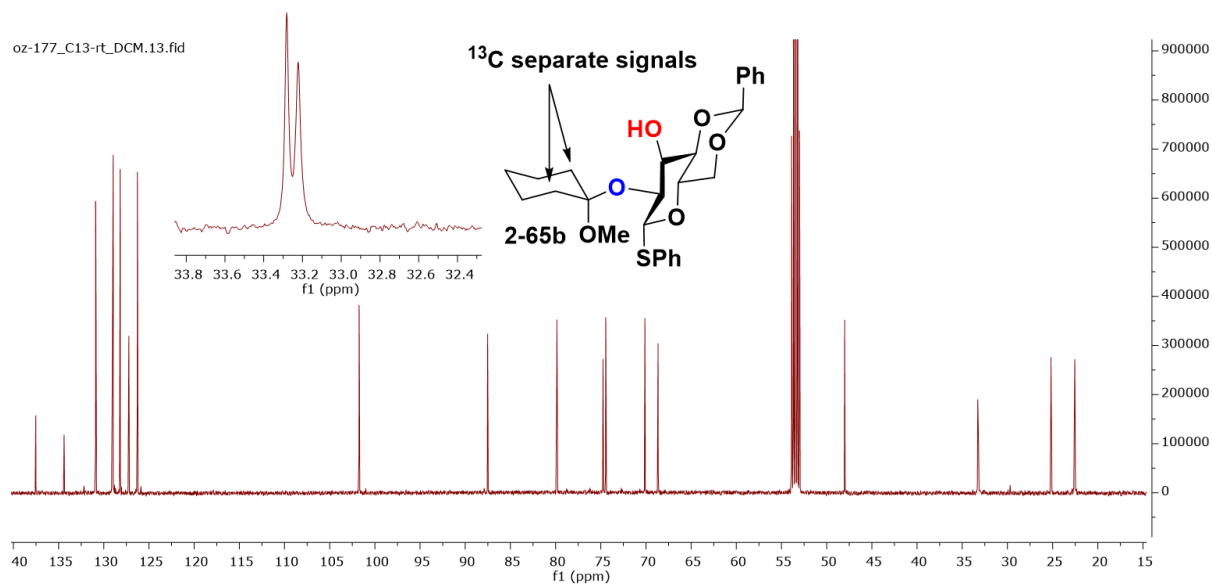
2.6.3 Analysis of room temperature NMR spectra of nondeuterated and deuterated MOC-protected glucoside.

Our preliminary NMR studies indicated that α -carbons (i.e. CH_2 groups next to the acetal carbon) in **2-65b** are not chemically equivalent in ^{13}C NMR spectrum (Figure 2.6). Rapid axil/equatorial conformer interconversion at room temperature did not allow to distinguish between the protons and their relative position in products **2-65b** and **d₃-2-65b** (Figure 2.6, B). $^1\text{H}/^{13}\text{C}$ HSQC spectrum contained two cross-peaks (positive, CH_2) for α -hydrogens of **2-65b** and

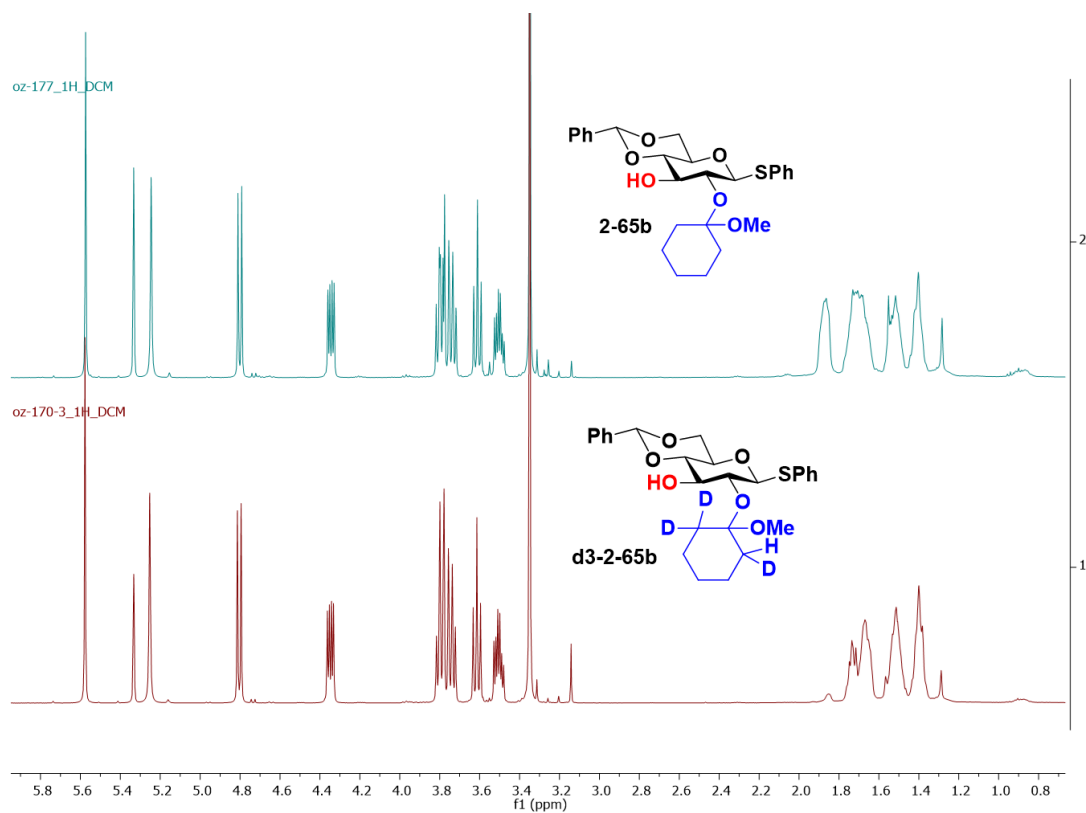
one (negative, CH) for **d₃-2-65b** (Figures 2.6C and 2.6D). As anticipated, the ¹H/¹³C HSQC NMR spectra of **d₃-2-65b** demonstrated full disappearance of one of the CH₂ cross peaks in comparison to **2-65b**, and the presence of small proton signal at {1.87, 32.7} is attributed to the diastereomer arising from the diastereoselective addition to Si- and Re- faces of **MOC** alkene. In this latter case, the proton added to **d₃-MOC** may end up being attached to two different chemically non-equivalent α-carbons, **Scheme 2.25-D**).

Figure 2.6. Preliminary NMR studies of compounds 2-65b and d₃-2-65b.

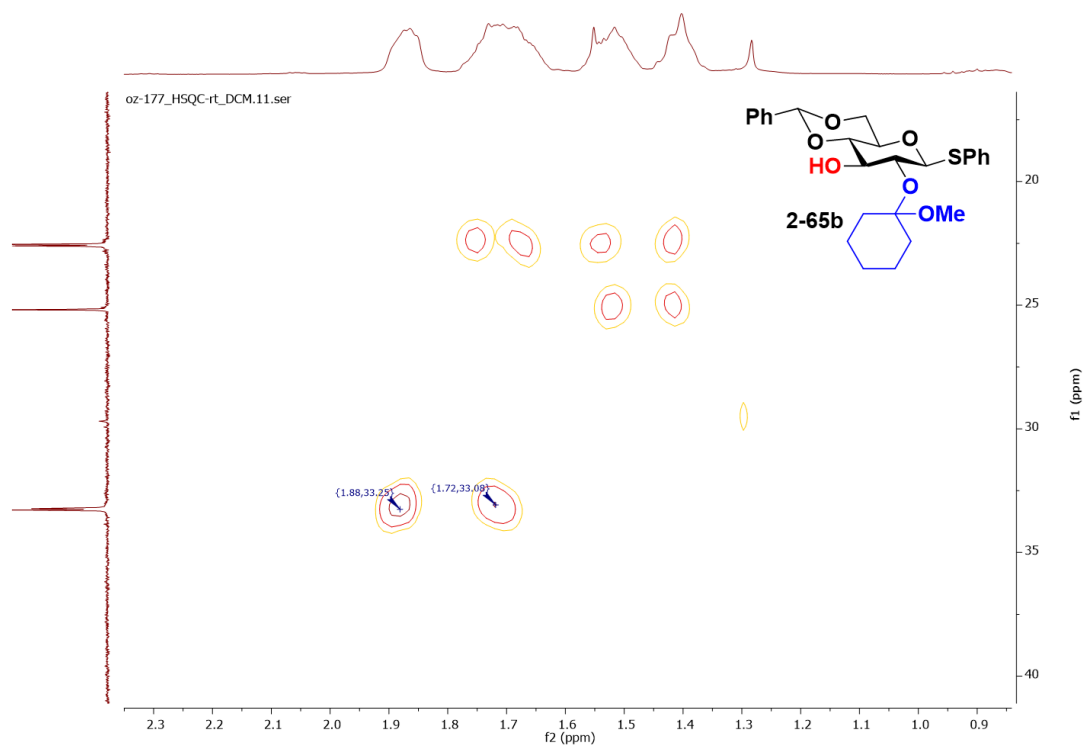
A. ¹³C NMR (CD₂Cl₂) of 5a demonstrating non-equivalence of α-carbons.



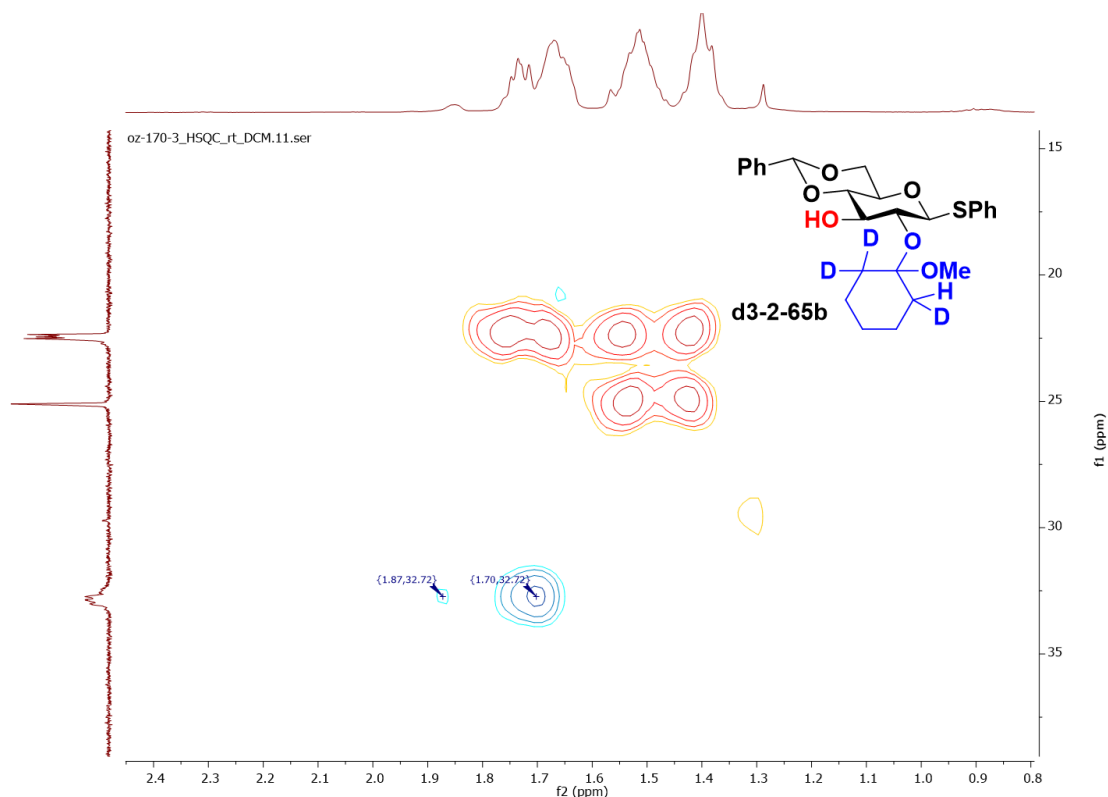
B. ^1H NMRs (CD_2Cl_2) of **2-65b** and **d₃-2-65b**.



C. HSQC (CD_2Cl_2) of **2-65b**



D. HSQC (CD₂Cl₂) of **d₃-2-65b**



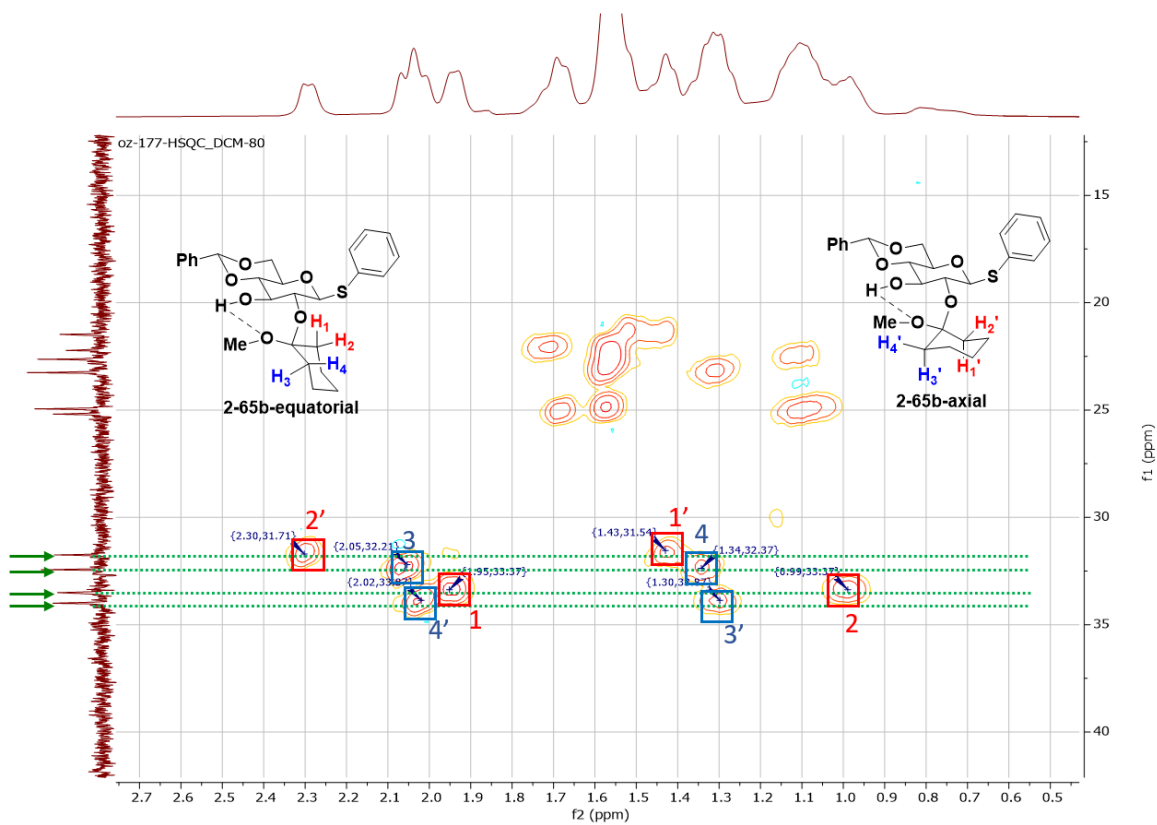
2.6.4 The analysis of nondeuterated MOC-protected glucose derivative using low temperature NMR (−80 °C)

Arguing that axial/equatorial conformer exchange could be significantly slowed down at lower temperatures, the NMR spectra of **2-65b** and **d₃-2-65b** were carried at −80 °C. Indeed, lowering the NMR acquisition temperature allowed to distinguish two conformers of cyclohexane ring flip. As evident from the ¹³C and ¹H/¹³C HSQC NMR spectra of compound **2-65b** (Figure 2.7A) – lowering the temperature to −80 °C causes each of the two signals of α-carbons to split into a pair of signals (i.e. a pair of axial and equatorial conformers). Consequently, the ¹H/¹³C HSQC spectrum of **2-65b** now has 4 pairs of ¹H/¹³C correlation cross peaks – 2 pairs belong to the CH₂ groups of one **2-65b** conformer (equatorial), the other two are due to the axial conformer of **2-65b**. In each pair of cross peaks correlating with a specific ¹³C signal, one proton signal

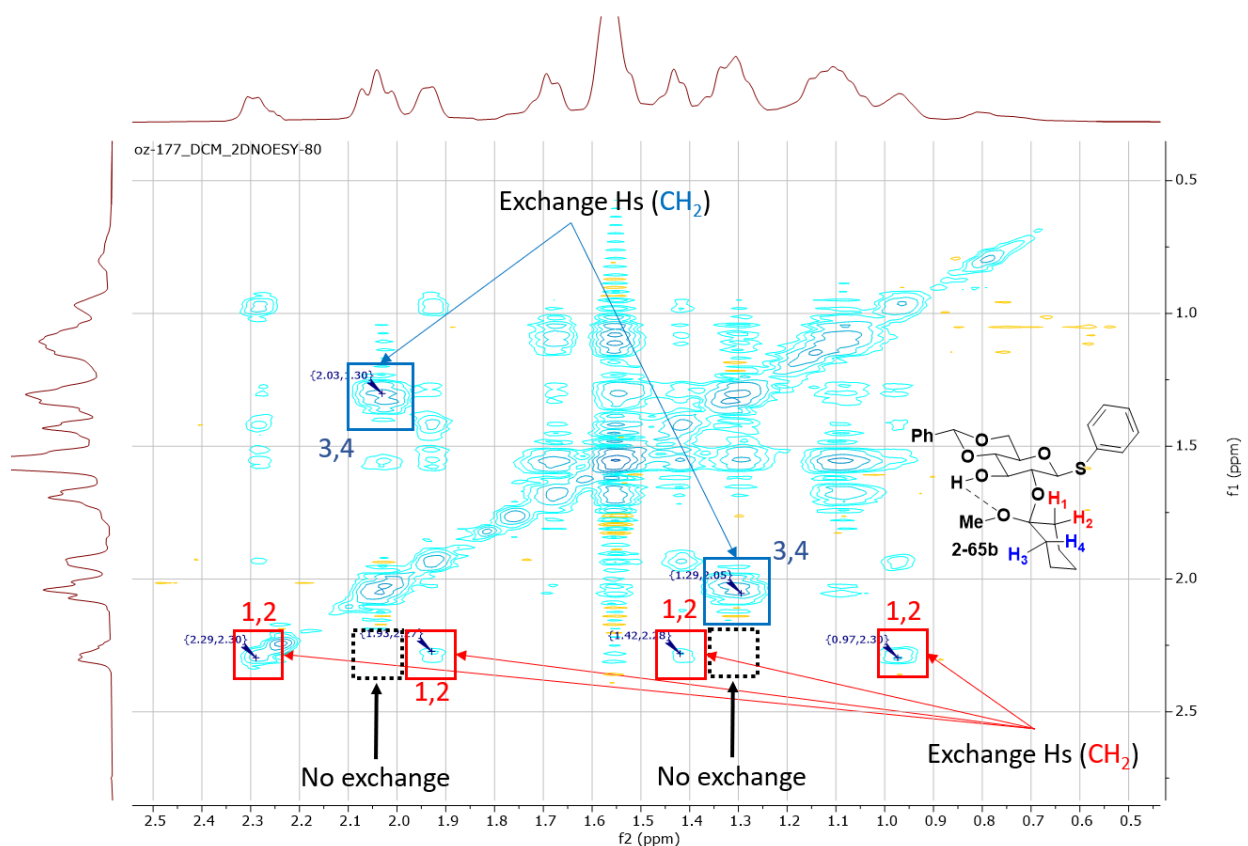
(downfield) is due to the correlation with an equatorial proton of CH₂ groups, and another (upfield) arises due to the correlation with an axial H. To accomplish the relative signal assignment and to prove the hypothesis that proton pairs 1-2 and 3-4 arise from different α -CH₂ groups, NOESY-EXCY experiment was performed (Figure 2.7B). The observed correlation cross-peaks indicate that protons with ¹H NMR signals at 2.05 and 2.02 ppm are conformationally exchangeable with protons with ¹H NMR signals at 1.34 and 1.30 ppm (the positive signs of these correlations are due to the large distance between the axial and equatorial protons). The signals at 2.30, 1.95, 1.43 and 0.99 ppm are also exchangeable with each other but show no correlation peaks with previously mentioned protons (i.e. Hs with signals at 2.05, 2.02, 1.34, and 1.30 ppm). These studies allowed to accomplish the assignment of proton groups to different carbons (i.e. assign the α -CH₂ pairs) as shown in Figure 2.7A.

Figure 2.7. 2D NMR studies of compound 2-65b at $-80\text{ }^{\circ}\text{C}$

A. HSQC NMR (CD_2Cl_2) of compound 2-65b acquired at $-80\text{ }^{\circ}\text{C}$



B. 2D NOESY-EXCY NMR (CD_2Cl_2) of compound **2-65b** at -80°C

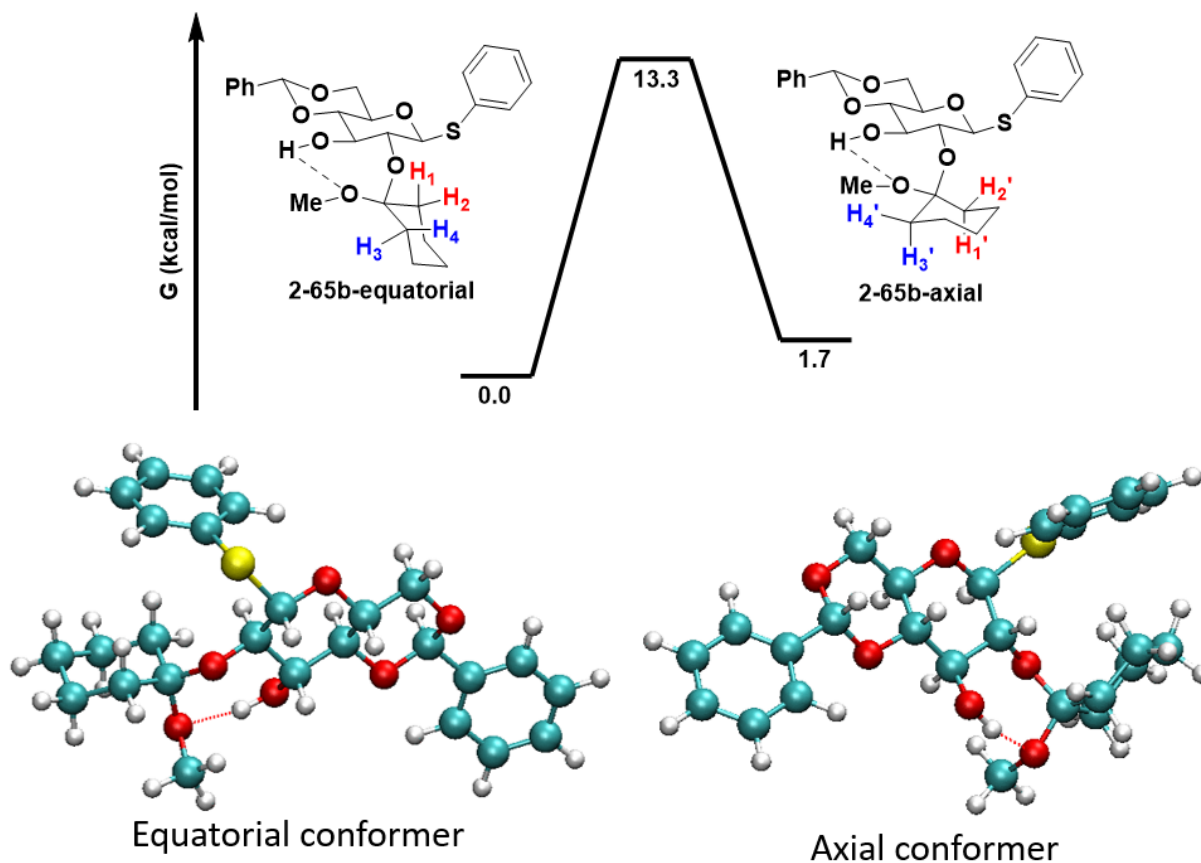


To further corroborate these experimental observations, additional computational studies were performed. First, we investigated the hypothesis that the cyclohexane ring rotational conformers make the α -carbons of MOC acetal non-equivalent in ^{13}C NMR, even at room temperature. Using the computed structure of **2-65b** the barrier for chair-to-chair transition was estimated by GSM (SMD(DCM)/ ω B97X-D3/cc-pVTZ//B97-D3/6-31++G**) to be 13.3 kcal/mol. At -80°C , the conversion between the equatorial (**2-65b -equatorial**) or axial (**2-65b -axial**) conformations of the sugar molecule is therefore sufficiently slow to distinguish the two (Figure 2.8A). The two conformer types were further sampled using the Self-guided Langevin Dynamic method at 298K. The 60 resulting structures revealed hydrogen bonds in all conformers, with an almost constant distance (approximately 1.8 Å) between the C3-OH hydrogen and oxygen of the methoxy group of MOC (Figure 2.8B). This intermolecular hydrogen bonding fixes the position

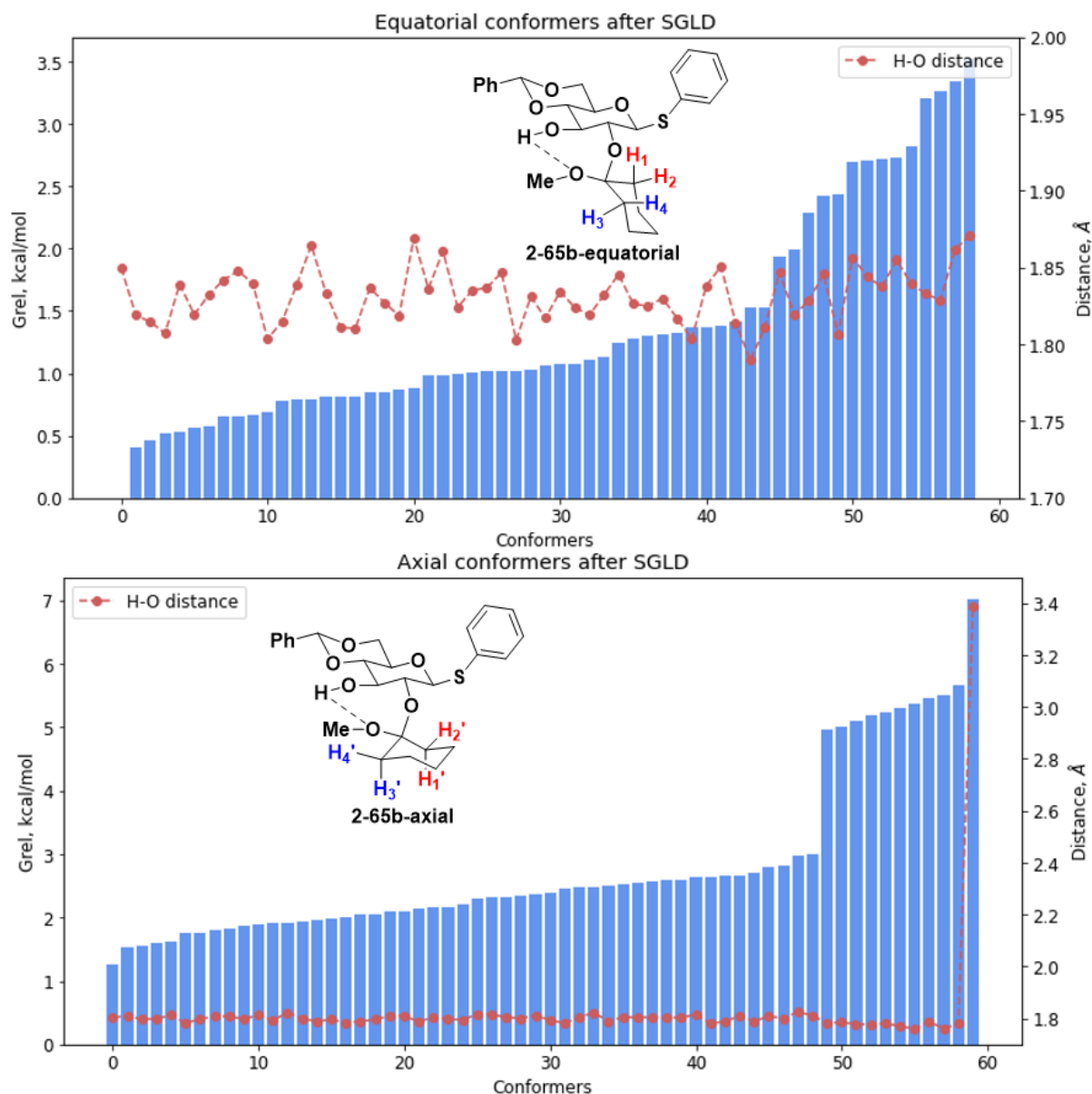
of the cyclohexane ring making the α -carbon atoms chemically non-equivalent in ^{13}C NMR. Only after raising the sample temperature to 100 °C the conformers lacking intermolecular H-bonds were generated (these were higher in energy by 5-8 kcal/mol). These calculations suggest that the hydrogen bond forming between the C3-hydroxyl hydrogen and oxygen of the methoxy group of MOC locks the MOC groups and prevents its rotation around the C–O bond during the NMR experiments at room temperature and –80 °C.

Figure 2.8. Computational conformers screening and analysis of compound x.

A. Conformational flip of the cyclohexane ring at 298K, SMD(DCM)/ ω B97X-D3/cc-pVTZ//B97-D3/6-31++G**))



B. Relative energies of generated conformers of **2-65b-equatorial** and **2-65b-axial** with interatomic distances between H (C3-OH group) and O (OMe group).

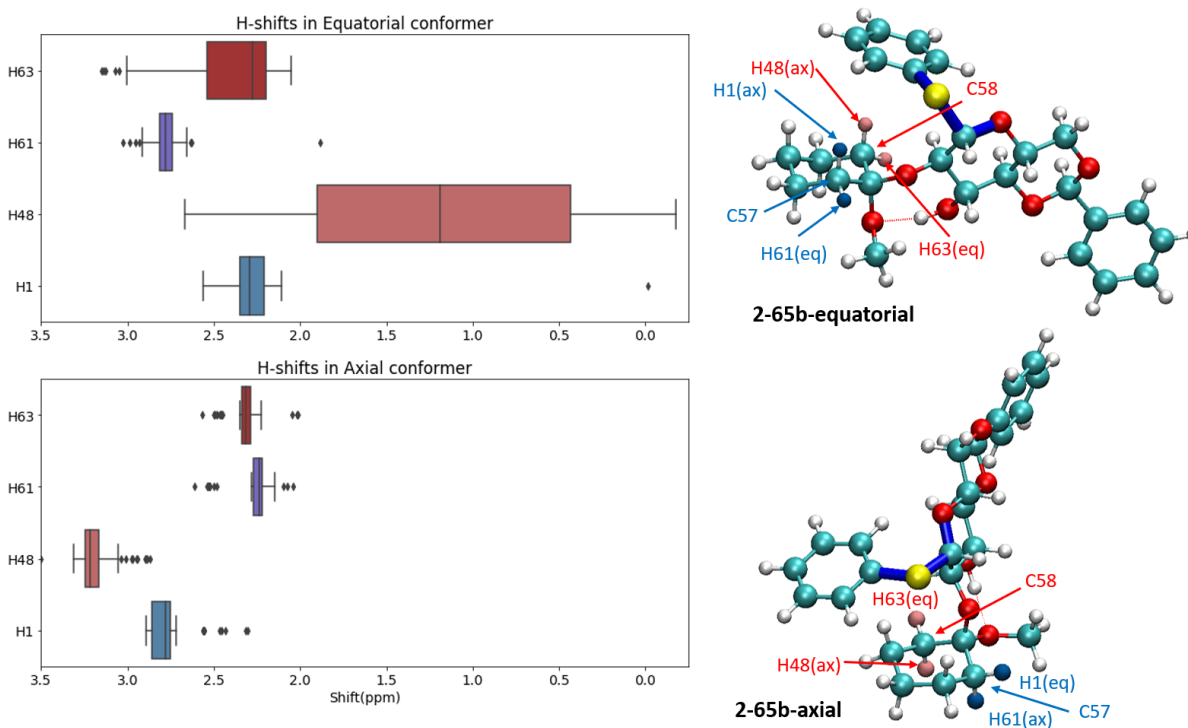


Subsequently, ^1H and ^{13}C NMR shifts were calculated at the B3LYP/6-31G* theory level for both the equatorial and axial conformers. First, the proton shift of H48 (the axial H₂ of the red CH₂ group, Figure 2.9A) in **2-65b-equatorial** structures varies throughout the conformer ensemble (Figure 2.9A). The equatorial hydrogen (H₁ which is H63 on Figure 2.9A) of the red CH₂ also has notable variation of the chemical shift. This suggests that one of the MOC acetal $\alpha\text{-CH}_2$ groups

has a stronger shift variation due to the conformational interconversions. This is indeed observed in the $^1\text{H}/^{13}\text{C}$ HSQC spectrum of **2-65b** (Figure 2.7) where two signal pairs have broader shift ranges (H1 and H2, 0.9-2.3 ppm). In addition, these calculations confirmed the relative ^1H NMR shift positions of the equatorial (more down-field, 1.9-2.3 ppm) and axial (more up-field, 0.9-1.4 ppm) protons.

Figure 2.9. NMR shifts calculations (B3LYP/6-31G*) of compound 2-65b

A. Predicted ^1H NMR shifts

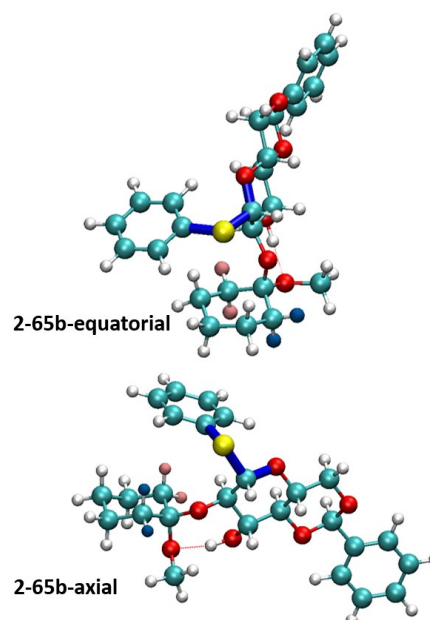
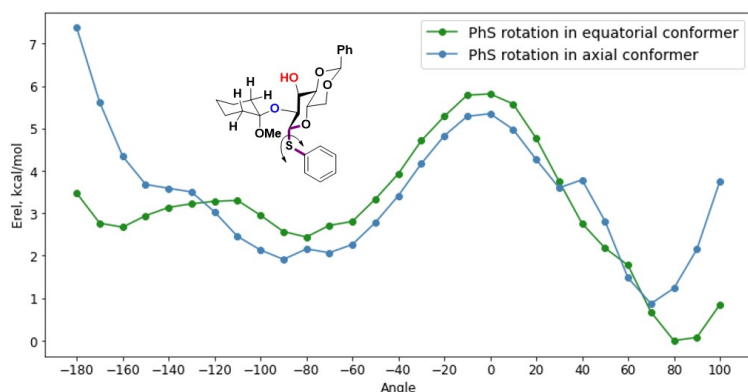


Subsequently, we investigated the unusual high-shielding phenomenon for the hydrogen with a ^1H NMR signal at 0.9 ppm that is observed both experimentally and computationally. This shielding can be explained by the anisotropic effects due to the SPh group positioning over the axial Hs (H48 and H1), specifically by examining the potential energy surface (PES) over the Ph-S-C-O torsion rotation (**Figure 2.9A**). As the diagram shows, there are two major rotamers present for both axial and equatorial conformers. However, one of the equatorial rotomers is approximately

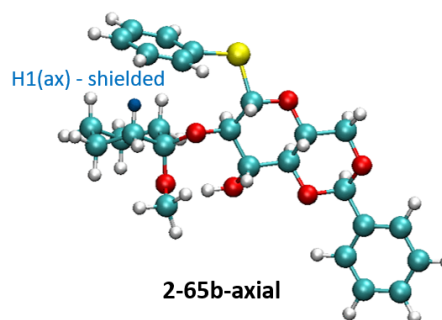
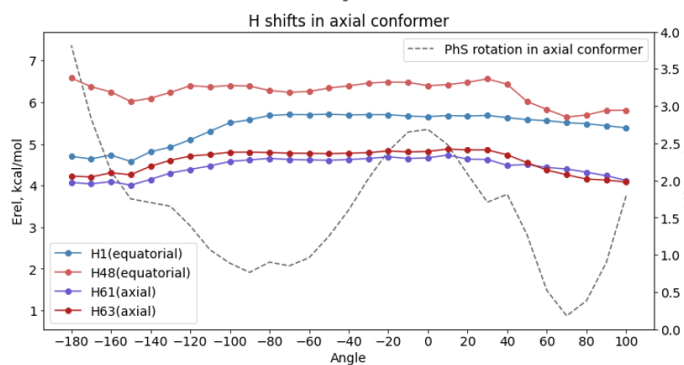
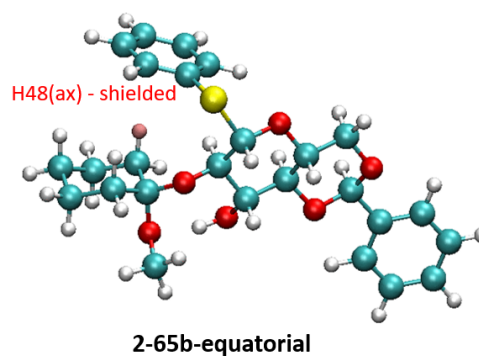
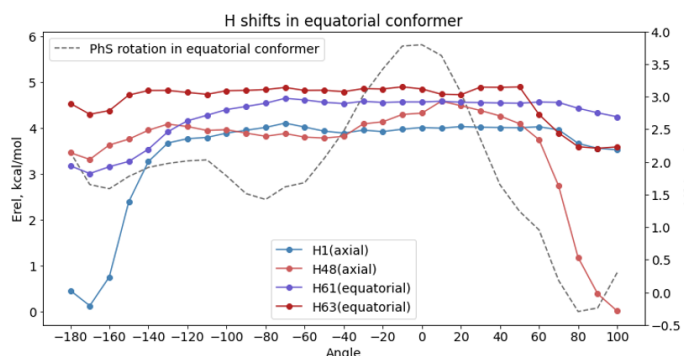
3 kcal/mol more stable, and, therefore, one of the α -CH₂ groups is more affected by the SPh group magnetic anisotropy than the other. This is also evident from the low temperature ¹H/¹³C HSQC spectrum (one of the α -CH₂ groups has greater NMR shifts distribution due to the phenyl group magnetic anisotropy, Figure 2.7), and in chemical shifts distribution computed in conformers ensemble (Figure 2.7). In contrast, two major rotamers in axial conformer **2-65b-axial** are almost the same in energy. Further analysis indicates strong dependence of chemical shift of the axial protons in **2-65b-equatorial** conformer on the torsion angle parameter (Figure 2.10). At certain torsion angle values where, aromatic ring is positioned at the top of axial protons, it results in high shielding bringing chemical shift to values of 0.0-0.9 ppm. Considering that one rotamer of SPh in **2-65b-equatorial** will be dominant at low temperature, only one axial proton should be dominantly shielded. This is again in excellent agreement with the ¹H/¹³C HSQC spectrum of **2-65b** where one hydrogen (H2 at 0.9 ppm, Figure 2.10C) is significantly shielded relative to the other three hydrogens (H1', H3' and H4 at 1.3-1.4 ppm). The same is true for the equatorial H, however, the shielding effect is smaller in magnitude due to the higher distance to the phenyl ring of the aromatic system. For the **2-65b-axial** conformer, the distance between the SPh group and the α -CH₂ groups is greater, which leads to much lower chemical shift dependence on the phenyl ring position.

Figure 2.10. - SPh rotation PES scan and its impact on the NMR shifts (B97-D3/6-31++G)**

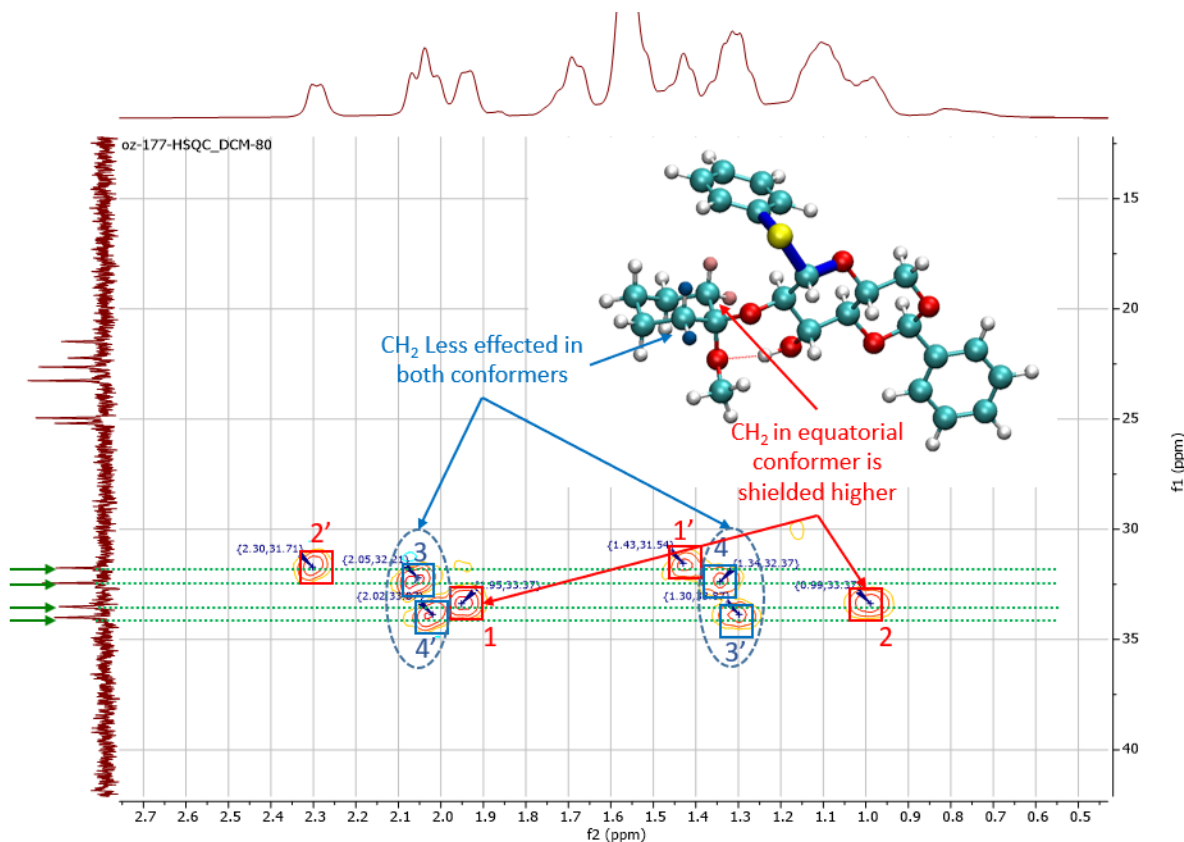
A. PES scan profiles (torsion rotation is highlighted in blue)



B. α -protons shift dependence on the -SPh position (torsion rotation). Structures at the right represents shielding of axial protons due to aromatic currents of -SPh.



C. $^1\text{H}/^{13}\text{C}$ HSQC (CD_2Cl_2) spectrum indicates good agreement between the observed and computed variation in ^1H NMR shift of **2-65b**.

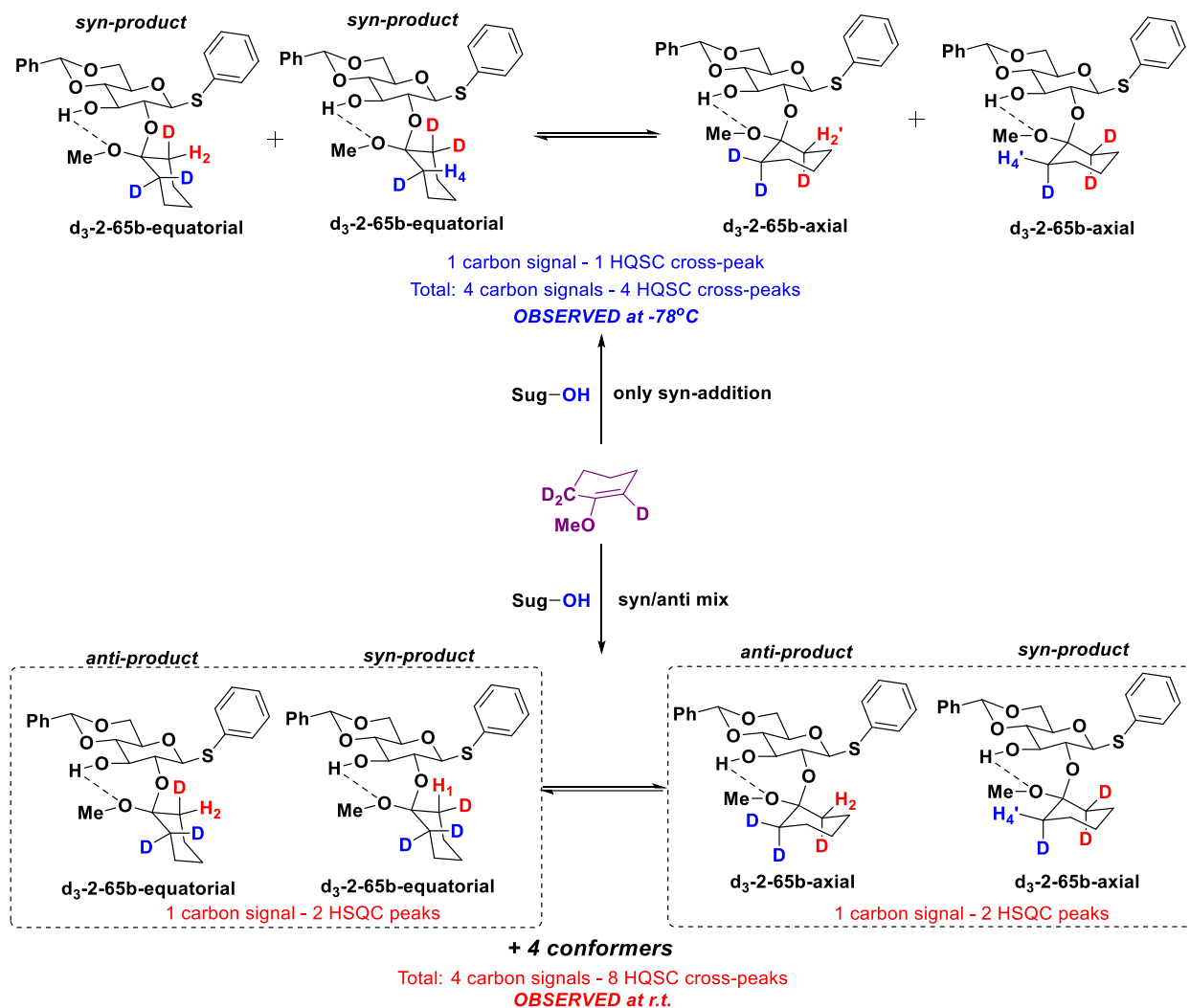


2.6.5 Analysis of d-labeled MOC-protected glucoside using low temperature NMR ($-80\text{ }^\circ\text{C}$)

After the assignment of the MOC acetal $\alpha\text{-CH}_2$ group NMR signals, the same set of low temperature NMR experiments was performed for substrate **d₃-2-65b** obtained by the (*R*)-AdTRIP-catalyzed reaction of **d₃-MOC** and substrate **2-60b** at $-78\text{ }^\circ\text{C}$ (Scheme 2.25). As lowering the temperature during the NMR acquisition helps to differentiate the protons of the MOC cyclohexane ring, we observed almost complete disappearance of ^1H NMR signals at 2.05 and 1.95 ppm (traces, 0.3H integration), but the signals at 2.30 and 0.99 ppm remain intact (1.0H integration). $^1\text{H}/^{13}\text{C}$ HSQC spectrum of **d₃-2-65b** (Figure 14A) demonstrated full disappearance of the proton pairs 2 (H_1 and $\text{H}_{1'}$) and 3 (H_3 and $\text{H}_{3'}$). The signals of MOC acetal $\alpha\text{-CH}_2$ group carbons were not clearly visible due to deuterium spin-spin coupling. It is also obvious, that in contrast to

substrate **2-65b**, there is no equatorial/axial H cross peaks in $^1\text{H}/^{13}\text{C}$ HSQC related to the same carbon atom signal (like 1 and 2 and 1' and 2' cross peaks pairs at Figure 2.7A). Each of the remaining 4 signals (2 major and 2 minor) correlates with the different carbon atom signals meaning that they belong to different conformers. The analysis of the NOESY-EXCY of **d₃-2-65b** also confirmed conformational exchange between the protons at 2.27 and 0.97 ppm (major CHD group) and exchange between 2.00 and 1.30 ppm signals of the minor CHD group (Figure 2.11B). However, there are no EXCY cross-peaks between these pairs of CHD signals, indicating that these signals belong to different carbons. Based on this, we can conclude that **d₃-2-65b** product was formed as a ~3:1 mixture of two diastereomers arising from *syn*- (or *anti*-) addition to two different (Si- or Re-) faces of 1-methoxycyclohexene (MOC) alkene moiety. One pair of the cross-peaks belongs to the major product's CHD group, while the second pair is arising from the minor diastereomer's CHD group (different carbon from the second α -CH₂ position of cyclohexane resulting from the fixed by H-bond cyclohexane ring position and diastereoselective addition from one double bond side). Considering that for each carbon signal (for each conformer of equatorial/axial sugar part position) there could be only one H cross-peak due to either an axial or an equatorial hydrogen, this addition is stereospecific in the direction of addition to double bond can be either *syn*- or *anti*-. In the case of competitive *syn*-/*anti*- addition (that is not observed here), the mixture of *syn*- and *anti*-products should give rise to two cross-peaks for each conformer carbon signal (one would come from an equatorial hydrogen, and another comes from an axial hydrogen attached to the same carbon atom) (Scheme 2.26). Considering the -SPh group magnetic anisotropy effects discussed above (Figures 2.9 and 2.10), the observed NMR spectra for **d₃-2-65b** are consistent with a mixture of two *syn*- (rather than two *anti*-) diastereomers.

Scheme 2.26. Analysis of potential outcomes for diol 2-60b reaction with deuterated d3-MOC

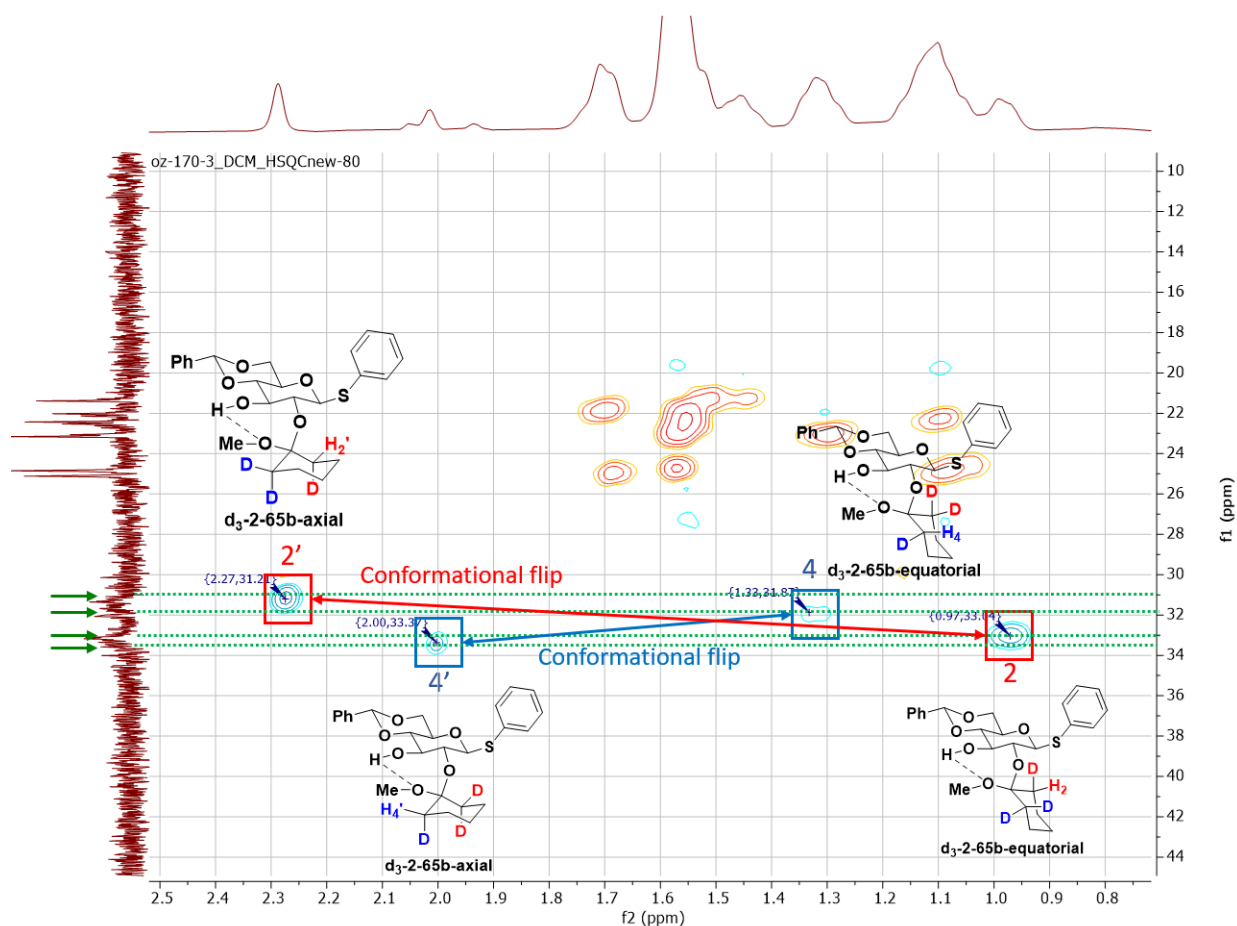


To confirm that **d₃-2-65b** obtained by the reaction catalyzed by (*R*)-AdTRIP at -78°C is in fact a mixture of two *syn*-diastereomers (obtained in $\sim 3:1$ d.r.), we pursued a control acetalization with (*R*)-AdTRIP at room temperature (Scheme 2.25B). The resultant acetal product **d₃-2-65b-rt** was subjected to the same set of NMR experiments at -80°C . As it is clear from its $^1\text{H}/^{13}\text{C}$ HSQC spectrum (Figure 2.11C), this compound has all 8 $^1\text{H}/^{13}\text{C}$ HSQC cross-peaks in contrast to only 4 cross-peaks observed for the substrate **d₃-2-65b** (for which **d₃-MOC** moiety was installed at -78°C). The analysis of this $^1\text{H}/^{13}\text{C}$ HSQC reveals that for each ^{13}C signal there are two ^1H peaks belonging to both the axial and equatorial positions. Therefore, for each conformer

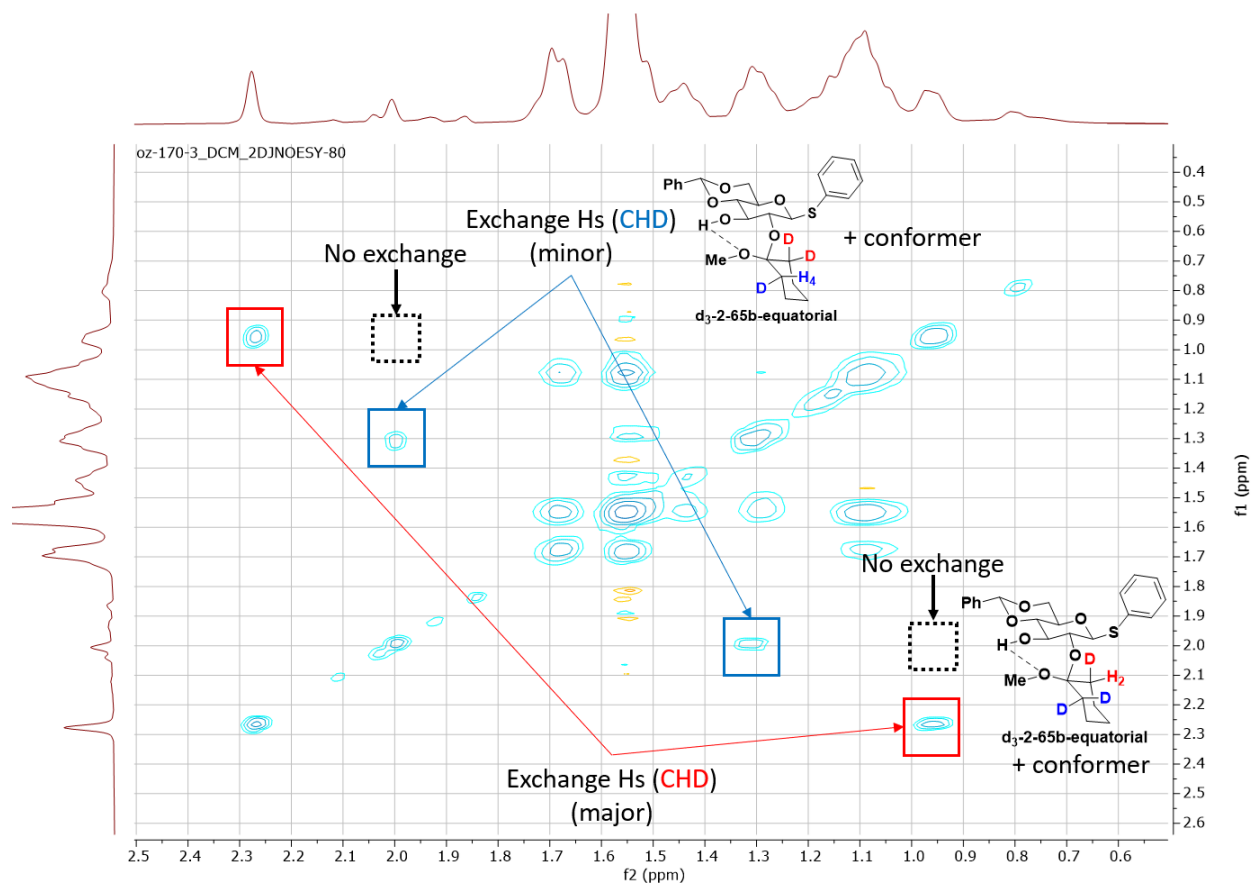
that has -OMe group in either axial or equatorial position there are both axial and equatorial hydrogens ^1H observed, indicating that this compound represents the mixture of $\sim 1:1:1:1$ *syn*- and *anti*-addition products. This confirms that the reaction at $-78\text{ }^\circ\text{C}$ is diastereoselective (i.e. *syn*-selective). This observation is consistent with the computed reaction mechanism, as it is predicted that room temperature acetalization may proceed through the equilibrating phosphate intermediate, which would react to provide both *syn*- and *anti*-products.

Figure 2.11. 2D NMR studies of compound d_3 -2-65b and d_3 -2-65b-rt at $-80\text{ }^\circ\text{C}$

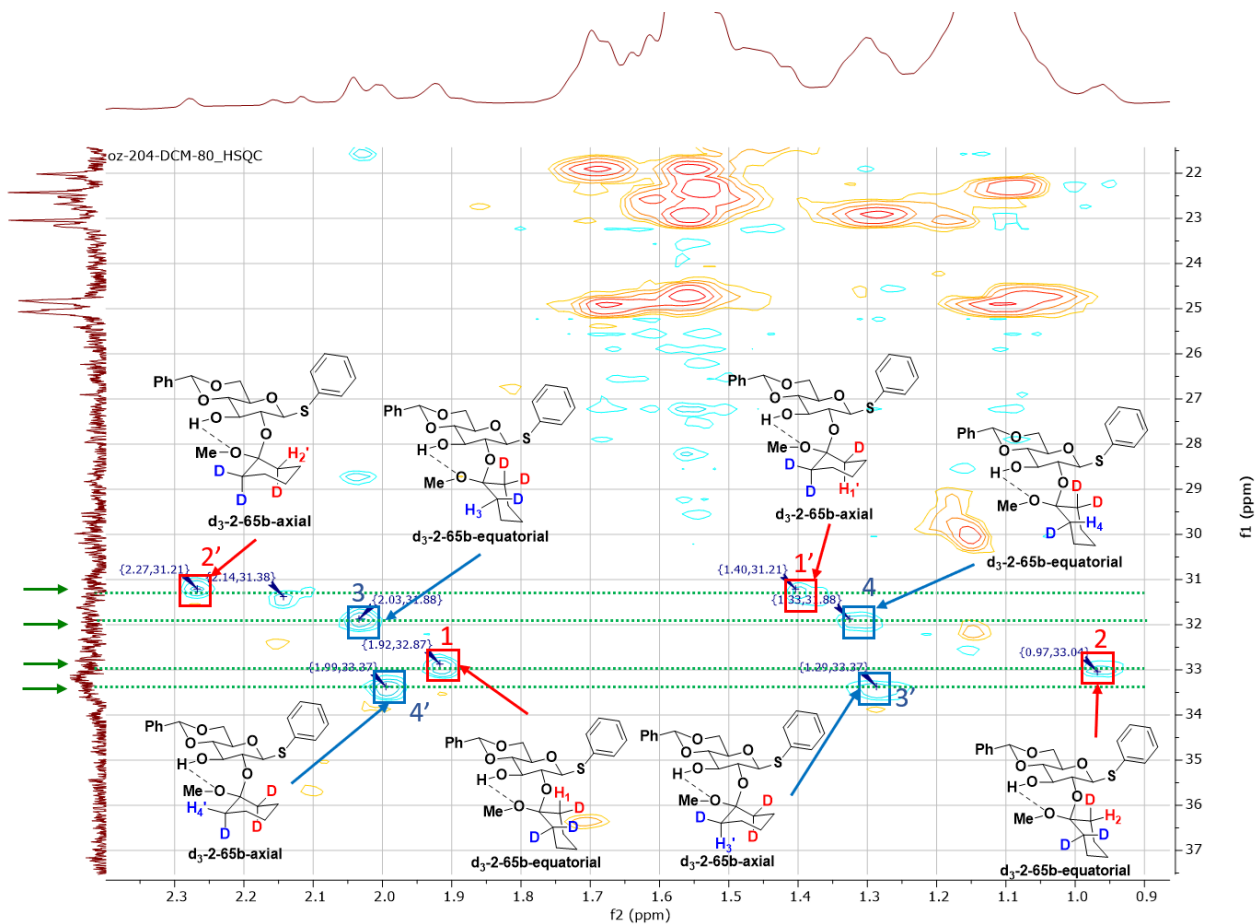
A. HSQC (CD_2Cl_2) shifts at $-80\text{ }^\circ\text{C}$ of d_3 -2-65b (*syn*-addition at $-78\text{ }^\circ\text{C}$, concerted mechanism)



B. 2D NOESY-EXCY NMR (CD_2Cl_2) of compound **d₃-2-65b** at -80°C



C. HSQC (CD_2Cl_2) shifts at -80°C of **d₃-2-65b-rt** (syn-/anti-addition at r.t., phosphate mechanism)



In summary, both experimental and computational (Chapter 2.5) results support *syn*-addition to the alkene moiety of **MOC** during the regioselective acetalization. As a result, this provides strong evidence for the concerted mechanism as the major reaction pathway operating at -78°C .

2.7 Conclusions

In conclusion, this chapter provides an overview of the challenges in regioselective modification of monosaccharides. An increasing number of publications dedicated to this topic have recently emerged as the problems associated with the regioselective synthesis of glycosylated molecules significantly impede the discovery of new therapeutic agents. There are methods for

effective synthesis of polysaccharide molecules, however availability of monosaccharide building block limits their applications. Many useful methods for the regioselective modification of carbohydrates have been developed to date; however, these methods have significant limitations due to their strong reliance on substrate control and electrophile properties. Many of these challenges can be addressed by applying asymmetric catalysis to differentiate hydroxyl groups that are similar in electronic effects.

This chapter demonstrates the utility of CPAs as the catalysis that directs highly regioselective acetalizations of carbohydrates through H-bonding interactions and steric effects arising from the interactions with the chiral catalyst backbone. Previously developed catalyst **AdTRIP CPA 2-62e** promotes highly regioselective protection of the C2-position in monosaccharide 2,3-diols. This method enabled the development of single-pot protocol for the synthesis of 34 regioisomerically pure differentially functionalized mono- and disaccharide derivatives by Dr. Jenghyuo Lee. In parallel, it was discovered that **SPINOL CPA 2-69** may revert the regioselectivity of the acetalization leading to the C3-modified products. To further improve the utility of the CPA-catalysis, both **AdTRIP CPA 2-62e** and **SPINOL CPA 2-69** were immobilized into a polymer matrix by Dr. Sibin Wand and Dr. Yaroslav Khomutnyk. The exploration of the immobilized CPAs was carried in collaboration with Dr. Sibin Wang, and it demonstrated good-to-excellent selectivities and yields for the desired products. Remarkably, the use of **PS-AdTRIP** and **PS-SPINOL** has improved the regioisomer ratios in most cases, and the origins of this effect are yet to be understood. The immobilized catalysts demonstrated superior to monomeric CPAs catalytic performance and selectivity, could be readily recycled by filtration and wash, and reused multiple times on 1.0 to 5.0 g scale acetalizations with loadings as low as 0.5 to 0.1 mol%.

The computational and mechanistic studies indicate complex temperature-dependent interplay of two reaction mechanisms. The dominant at low temperatures concerted asynchronous mechanism favors the formation of the C2 isomer due to destabilizing the TS leading to the C3 isomer interactions between the benzylidene acetal moiety of **2-60b** and catalyst **2-62e**. This mechanism should lead to the stereospecific addition of ROH resulting in syn-product, which is confirmed through the reaction of **x** with deuterium-labeled d₃-1-methoxycyclohexene (d₃-MOC).

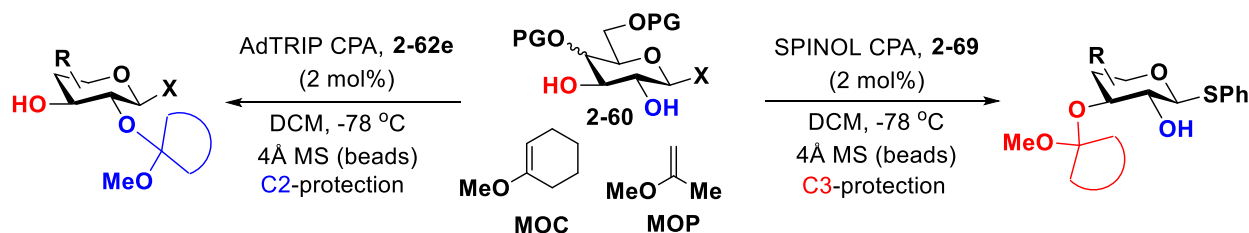
2.8 Experimental information

Methods and reagents: Unless otherwise noted, all reagents were purchased from commercial suppliers and used without further purification. Tetrahydrofuran (THF), dichloromethane (DCM), and diethyl ether (Et₂O) were filtered through a column (Innovative Technology PS-MD-5) of activated alumina under a nitrogen atmosphere. All reactions were carried out under an atmosphere of nitrogen in flame- or oven-dried glassware with magnetic stirring. Reactions were cooled using Neslab Cryocool CB-80 immersion cooler (0 to -60 °C) and Neslab Cryocool immersion cooler CC-100 II, or via external cooling baths: ice water (0 °C), sodium chloride/ ice water (-10 °C), or dry ice/acetone (-78°C). Heating was achieved by use of a silicone bath with heating controlled by electronic contact thermometer. Deionized water was used in the preparation of all aqueous solutions and for all aqueous extractions. Solvents used for extraction and chromatography were ACS or HPLC grade. Purification of reactions mixtures was performed by flash column chromatography on SiO₂ using SiliCycle SiliaFlash P60 (230-400 mesh). Diastereomeric ratios were determined by ¹H NMR analysis. Enantiomeric excess was determined by HPLC analysis using a Waters e2695 Separations Module with a Waters 2998 photodiode array detector.

Instrumentation: All spectra were recorded on Varian vnmrs 700 (700 MHz), Varian vnmrs 500 (500 MHz), Varian MR400 (400 MHz), Varian Inova 500 (500 MHz) spectrometers and chemical

shifts (δ) are reported in parts per million (ppm) and referenced to the ^1H signal of the internal tetramethylsilane according to IUPAC recommendations. Data are reported as (br = broad, s = singlet, d = doublet, t = triplet, q = quartet, qn = quintet, sext = sextet, m = multiplet; coupling constant(S) in Hz; integration). High resolution mass spectra (HRMS) were recorded on MicromassAutoSpecUltima or VG (Micromass) 70-250-S Magnetic sector mass spectrometers in the University of Michigan mass spectrometry laboratory. Infrared (IR) spectra were recorded as thin films on NaCl plates on a Perkin Elmer Spectrum BX FT-IR spectrometer. Absorption peaks were reported in wavenumbers (cm^{-1}).

Procedure for the regioselective acetalization of monohydrates **x using homogeneous CPA catalysts (Protocol A)**



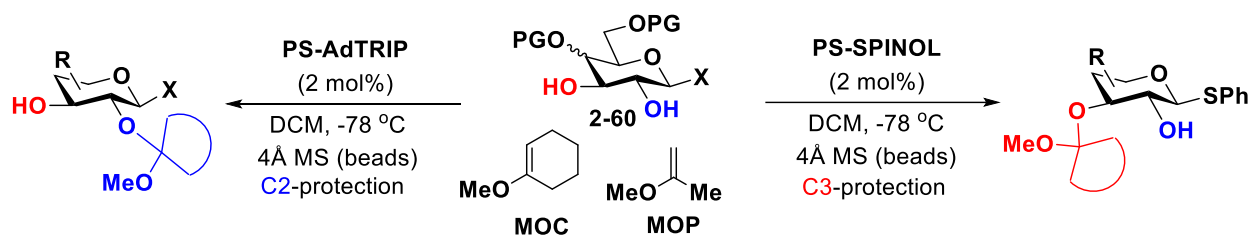
Protocol A: A one-dram vial was oven-dried and purged with nitrogen. Then substrate diol **4** (1.0 equiv.), which was previously dried by azeotropic removal of moisture with toluene was added. Then, activated 4Å molecular sieves (beads), AdTRIP CPA **2-62e** or SPINOL CPA **2-69** (2 mol%) and anhydrous dichloromethane (0.04 M) were added to the flask. The resultant reaction mixture was submerged in dry ice-acetone ($-78\text{ }^\circ\text{C}$) bath, and enol ether electrophile MOP or MOC (1.2 equiv.) was added. The reaction mixture was transferred to Neslab CB 80 immersion cooler and stirred at $-78\text{ }^\circ\text{C}$ for 24 h. After the reaction completion was indicated by TLC, 1 mL of NH_3 solution in MeOH (0.5M) was added to assist filtration and prevent product decomposition. The crude mixture was concentrated under reduced pressure to obtain the regioisomerically enriched acetal-containing product, which was purified by flash chromatography and characterized.

C2-protected products were previously characterized by Nagorny group.^{41,42}

The assessment of the regioselectivity (for C3-protected products): was accomplished using a previously published procedure.^{41,42} The obtained crude product from CPA-catalyzed acetalization was subjected directly to acetyl protection by being treated with triethylamine (5.0 equiv) and anhydrous dichloromethane (0.3 M). Then anhydrous acetic anhydride (1.1 equiv), and 4-dimethylaminopyridine (DMAP) (0.1 equiv.) were added to the mixture. The reaction was stirred at room temperature until the reaction completion, which was judged by TLC. After the reaction was completed, the mixture was completely dried by gentle N₂ flow followed by a high vacuum. The crude reaction mixture was analyzed by COSY NMR to determine the regioselective of C2 and C3. The acetylation results in a significant shift of the proton next to the acetoxy group to the 4.2–4.6 ppm region.

C₃-protected product characterization data is provided below in Chapter 2.8.1.

Procedure for the regioselective acetalization of monohydrates x using homogeneous CPA catalysts (Protocol B)



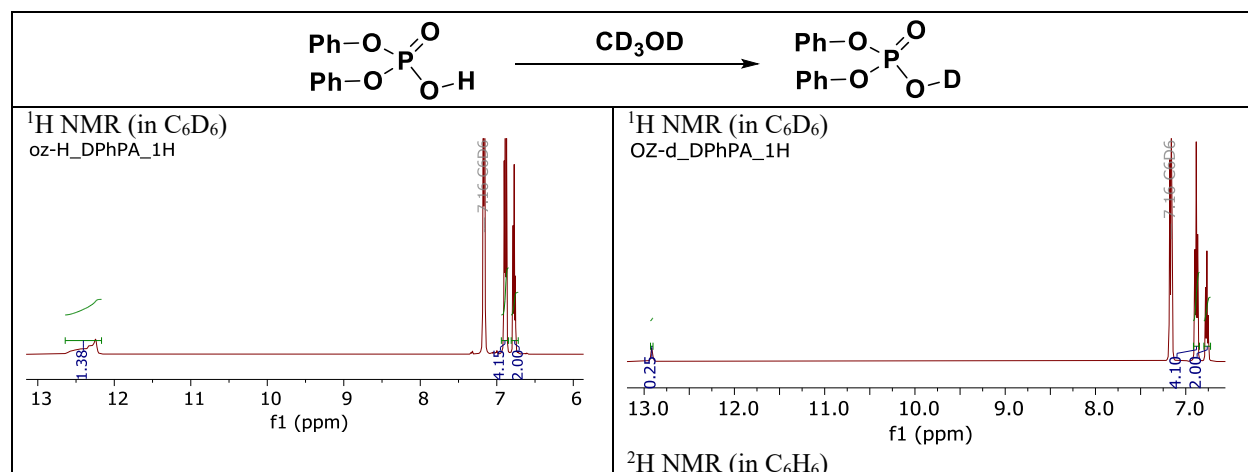
Protocol B: A one-dram vial was oven-dried and purged with nitrogen. Then substrate diol (1.0 equiv.), which was previously dried by azeotropic removal of moisture with toluene was added. Then, activated 4Å molecular sieves (beads), PS-AdTRIP or PS-SPINOL (2 mol% or 0.5 mol% for large-scale experiment) and anhydrous dichloromethane (0.04 M) were added to the flask. The resultant reaction mixture was submerged in dry ice-acetone (-78 °C) bath, and enol ether electrophile (1.2 equiv.) was added. The reaction mixture was transferred to Neslab CB 80

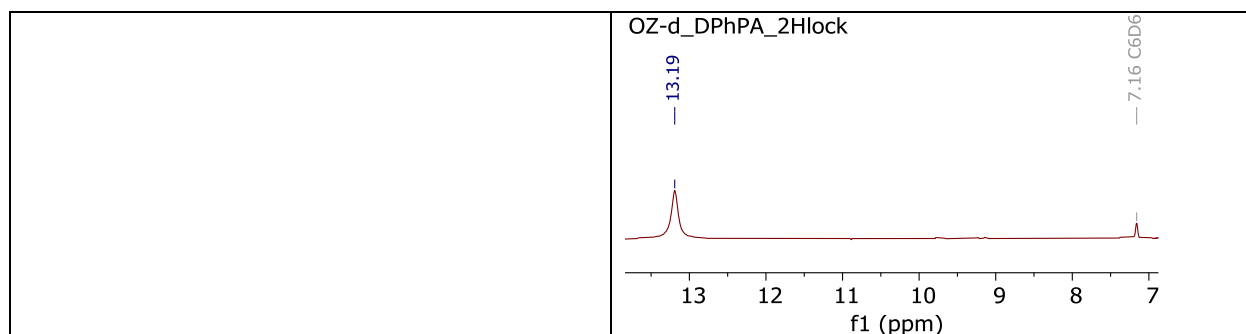
immersion cooler and stirred at $-78\text{ }^{\circ}\text{C}$ for 24 h. After the reaction completion was indicated by TLC, 1 mL of NH_3 solution in MeOH (0.5M) was added to assist filtration and prevent product decomposition. Then, the reaction mixture was filtered through a fritted funnel via vacuum filtration. The filtrate was concentrated under reduced pressure to obtain the regioisomerically enriched acetal-containing product, which was purified by flash chromatography and characterized.

Synthesis of diphenyl deuterium phosphate $\text{d}_1\text{-2-74}$ (d-DPPA)

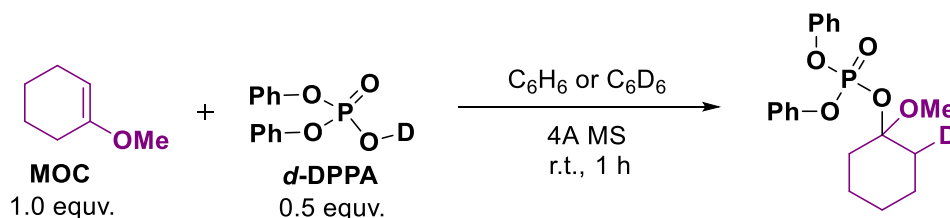
Isotope exchange was performed via diphenyl hydrogen phosphate wash with methanol- d_4 . Diphenyl hydrogen phosphate (50 mg) was dissolved in 5 mL of deuterated methanol, stirred for 1 h and then deuterated methanol was evaporated under the reduced pressure. The procedure was repeated 3 times. Deuterium exchange was confirmed by ^1H NMR by observing the reduction of the acidic proton signal integral, and ^2H (D) NMR by observing the appearance of the acidic deuterium signal at 13 ppm (Scheme 2.27).

Scheme 2.27. ^1H and ^2H (D) NMR in benzene- d_6 or benzene for the deuterium-exchanged DPPA



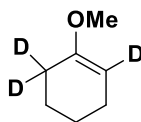


Procedure for detection of covalent phosphate detection



To an oven-dried vial, 12.5 mg (0.05 mmol) of deuterated above phosphoric acid **d₁-2-74**, 4Å MS (25 mg) and a stir bar was added. To this 1 mL of benzene-*d*₆ (or non-deuterated benzene for ²H(D) NMR studies) was added, and upon dissolution, 12 μL (0.1 mmol) of 1-methoxycyclohexene (**MOC**) was added to the resultant mixture. After stirring for 1 h, the solution was transferred to a NMR tube to record spectra.

Synthesis of 1-methoxycyclohex-1-ene-2,6,6-d₃ (**d₃-MOC**)



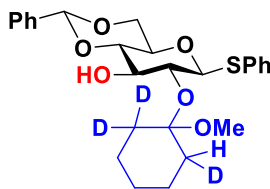
The compound was synthesized according to the procedure by K. Shishido.⁴⁶ To 2.0 ml (19.3 mmol, 1.0 eq.) of cyclohexan-1-one-2,2,6,6-d₄ 2.54 ml (23.2 mmol, 1.2 eq.) of trimethyl orthoformate was added followed by 36 mg (0.193 mmol, 0.01 eq.) of *p*-toluenesulfonic acid monohydrate. The reaction mixture was stirred at room temperature for 2 hours. Then the reaction mixture was distilled at atmospheric pressure and product **d₃-MOC** was collected at a temperature 140-145 °C (1.21 g, 54%).

$^1\text{H NMR}$ (500 MHz, Benzene- d_6) δ 3.3 (s, 3H), 2.0 (t, J = 6.0 Hz, 2H), 1.5 – 1.5 (m, 2H), 1.5 – 1.4 (m, 2H).

$^{13}\text{C NMR}$ (125 MHz, Benzene- d_6) δ 155.4, 92.2 (t, J = 23.8 Hz), 53.1, 27.4 – 26.9 (m), 23.3, 22.7.

$^2\text{H NMR}$ (77 MHz, Benzene- d_6) δ 4.3 (s, 1D), 1.9 (s, 2D).

Synthesis of the diol **d₃-2-65b** for NMR studies



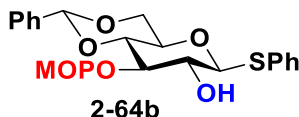
Using diol **2-60b** (36 mg, 0.1 mmol, 1.0 equiv.) as the starting material, preparation of **d₃-2-65b** was accomplished following the **Protocol A** using 1-methoxycyclohex-1-ene-2,6,6- d_3 **d₃-MOC** (1.2 eq, 0.12 mmol, 15 μL) as the electrophile. This product was purified by flash column chromatography on SiO_2 (8/2 Hexanes/Ethyl acetate + 2% triethylamine) to afford **d₃-2-65b** as a colorless oil (44.8 mg, 94%, C2:C3 = >25:1).

$^1\text{H NMR}$ (500 MHz, Benzene- d_6) δ 7.68-7.64 (m, 2H), 7.57-7.52 (m, 2H), 7.17-7.14 (m, 2H) 7.11-7.07 (m, 1H), 7.04 (dd, J = 8.4, 7.0 Hz, 2H), 6.99-6.94 (m, 1H), 5.38 (s, 1H), 5.30 (s, 1H), 4.72 (d, J = 9.5 Hz, 1H), 4.10 (dd, J = 10.3, 5.0 Hz, 1H), 3.92 (ddd, J = 9.3, 7.6, 1.4 Hz, 1H), 3.82 (ddd, J = 8.8, 7.6, 1.1 Hz, 1H), 3.62 (t, J = 9.3 Hz, 1H), 3.50 (t, J = 10.2 Hz, 1H), 3.20 (td, J = 9.8, 5.0 Hz, 1H), 2.95 (s, 3H), 1.71 (s, 0.5H), 1.62-1.49 (m, 2.5H), 1.42 – 1.35 (m, 1H), 1.30-1.23 (m, 1H), 1.21-1.12 (m, 2H).

$^{13}\text{C NMR}$ (125 MHz, Benzene- d_6) δ 138.1, 134.8, 131.4(2C), 128.8(2C), 128.6, 127.1, 126.6(2C), 101.4, 87.5, 80.2, 75.4, 74.7, 70.2, 68.5, 47.4, 47.4, 32.9(2C) (t, J = 18.5 Hz), 25.0, 22.4, 22.4, 22.3, 22.3.

HRMS (ESI+) (m/z): $[\text{M}+\text{Na}]^+$ calcd for $\text{C}_{26}\text{H}_{29}\text{D}_3\text{O}_6\text{SNa}$ 498.2000, found 498.1985.

2.8.1 Compounds characterization data



18 mg scale experiment:

Using diol **2-60b** (18mg, 0.05 mmol, 1.0 equiv.) as the starting material, preparation of **2-64b** was accomplished following **General Protocol B**. This product was purified by flash column chromatography on SiO₂ (4/1 Hexanes/Ethyl acetate + 1% triethylamine) to afford **2-64b** as a pale yellow oil (16.9 mg, 78%, C2:C3 = 1:8).

1.0 g scale experiment:

Using diol **2-60b** (1.0 g, 3.0 mmol, 1.0 eq.) as the starting material and 2-methoxypropene (1.2 eq., 4.0 mmol, 383 μ l), preparation of **2-64b** was accomplished by following **General Protocol B** using 0.5 mol% of catalyst loading (125 mg of **PS-SPINOL**). After the reaction completion was indicated by TLC (36 h), 20 ml of NH₃ solution in MeOH (0.5M) was added to assist filtration and prevent product decomposition. Then the reaction mixture was filtered through a fritted funnel via vacuum filtration. The filtrate was evaporated under reduced pressure to obtain **2-64b** as a white solid (1.22 g, 94%, C2:C3 = 1:8) that can be further used without purification. The **PS-SPINOL** as partitioned in DCM to separate it from 4 Å MS beads, washed with THF, 1N HCl, H₂O, acetone, and dichloromethane. Then the **PS-SPINOL** was dried under reduced pressure and then recycled.

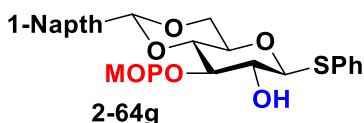
¹H NMR (500 MHz, Methanol-*d*₄) δ 7.55–7.53 (m, 2H), 7.51–7.48 (m, 1H), 7.46–7.44 (m, 2H), 7.34 (dt, *J* = 5.5, 2.2 Hz, 5H), 5.60 (s, 0.2 H), 5.53 (s, 1H), 4.81 (d, *J* = 9.2 Hz, 0.2H), 4.74 (d, *J* = 9.8 Hz, 1H), 4.27 (dd, *J* = 10.5, 5.0 Hz, 1H), 3.92 (dd, *J* = 9.2, 8.2 Hz, 1H), 3.73 (t, *J* = 10.2 Hz, 1H), 3.52 (dt, *J* = 9.8, 4.8 Hz, 1H), 3.45 (t, *J* = 9.3 Hz, 1H), 3.36 (s, 0.6H), 3.29 (dd, *J* = 9.1, 8.3 Hz, 1H) 3.19 (s, 3H), 1.46 (s, 0.6H), 1.42 (s, 0.6H), 1.39 (s, 3H), 1.38 (s, 3H).

¹³C NMR (125 MHz, Chloroform-*d*) δ 137.7, 132.8, 132.2, 131.1, 128.5, 127.6, 127.4, 126.3, 101.8, 101.6, 88.3, 79.8, 75.7, 72.3, 70.3, 68.2, 49.2, 24.5, 23.8.

IR (FTIR-ATR, cm⁻¹): 3368, 2989, 2925, 1583, 1456, 1439, 1266, 1237, 1203, 1147, 1086, 1044, 1026, 849.

HRMS (ESI+) (*m/z*): [M+Na]⁺ calcd for C₂₃H₂₈O₆SNa 455.1499, found 455.1492.

$[\alpha]^{24}_{\text{D}}$ = -39.2° (c 0.03 M, CH₂Cl₂).



Using diol **2-60g** (20.5 mg, 0.05 mmol, 1.0 equiv.) as the starting material, preparation of **2-64g** was accomplished following the **General Protocol B**. This product was purified by flash column chromatography on SiO₂ (4/1 Hexanes/Ethyl acetate + 1% triethylamine) to afford **2-64g** as a colorless oil (22.0 mg, 91%, C2:C3 = 1:10).

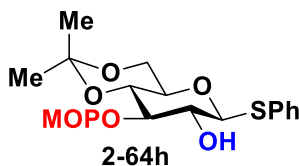
¹H NMR (500 MHz, Methanol-*d*₄) δ 8.20 (d, *J* = 8.1 Hz, 1H), 7.86 (d, *J* = 8.5 Hz, 2H), 7.73 (d, *J* = 7.2 Hz, 1H), 7.59 – 7.54 (m, 2H), 7.53 – 7.42 (m, 4H), 7.34 (m, 2H), 6.17 (s, 0.08H), 6.10 (s, 1H), 4.77 (d, *J* = 9.7 Hz, 1H), 4.36 (dd, *J* = 10.4, 4.2 Hz, 1H), 3.95 (t, *J* = 8.3 Hz, 1H), 3.87 (t, *J* = 9.8 Hz, 1H), 3.66 – 3.59 (m, 2H), 3.37 – 3.32 (m, 1H), 3.14 (s, 3H), 1.46 (s, 0.4H), 1.43 (s, 0.4H), 1.35 (s, 3H), 1.25 (s, 3H).

¹³C NMR (125 MHz, Methanol-*d*₄) δ 133.8, 132.9, 132.2(2C), 131.0, 130.5, 129.1, 128.6, 128.5(2C), 128.0, 127.4, 125.6, 125.3, 124.3, 123.7, 101.8, 100.3, 88.3, 80.1, 75.6, 72.4, 70.4, 68.4, 49.2, 24.4, 23.7.

IR (FTIR-ATR, cm⁻¹): 3386, 3053, 2989, 2927, 2872, 1583, 1479, 1465, 1384, 1373, 1238, 1173, 1109, 1072, 1043, 1024, 790

HRMS (ESI+) (*m/z*): [M+Na]⁺ calcd for C₂₇H₃₀O₆SNa 505.1655, found 505.1651.

[α]²⁴_D = -6.8° (c 0.03 M, CH₂Cl₂).



Using diol **2-60h** (15.6 mg, 0.05 mmol, 1.0 equiv.) as the starting material and 2-methoxypropene (1.2 eq., 0.06 mmol, 6 μl), preparation of **2-64h** was accomplished following the **General Protocol B**. This product was purified by flash column chromatography on SiO₂ (8/2 Hexanes/Ethyl acetate + 2% triethylamine) to afford **2-64h** as a pale-yellow oil (16.9 mg, 88%, C2:C3 = 1:6). C2 and C3 selectivity was determined based on the NMR analysis.

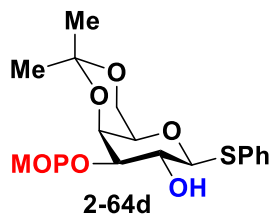
¹H NMR (500 MHz, Methanol-*d*₄) δ 7.51 (d, *J* = 7.3 Hz, 2H), 7.47 (d, *J* = 7.6 Hz, 0.42H), 7.32 (t, *J* = 7.3 Hz, 3H), 4.75 (d, *J* = 9.3 Hz, 0.17H), 4.67 (d, *J* = 9.8 Hz, 1H), 3.87 (dd, *J* = 10.7, 5.3 Hz, 1H), 3.73 (t, *J* = 8.7 Hz, 2H), 3.47 (t, *J* = 9.4 Hz, 1H), 3.35 (d, *J* = 3.4 Hz, 1H), 3.28 (s, 3H), 3.24 (t, *J* = 9.0 Hz, 1H), 1.46 (s, 3H), 1.40 (s, 6H), 1.35 (s, 3H).

¹³C NMR (125 MHz, Methanol-*d*₄) δ 133.0, 132.0(2C), 128.5(2C), 127.3, 101.7, 99.2, 88.4, 76.0, 72.5, 72.4, 71.3, 61.8, 49.1, 28.1, 24.6, 24.0, 17.9.

IR (FTIR-ATR, cm^{-1}): 3394, 3058, 2991, 2940, 2886, 1583, 1497, 1463, 1382, 1373, 1263, 1201, 1172, 1149, 1084, 1025, 862, 745

HRMS (ESI+) (m/z): $[\text{M}+\text{Na}+\text{MeOH}]^+$ calcd for $\text{C}_{19}\text{H}_{28}\text{O}_6\text{SNaCH}_3\text{OH}^+$ 439.1761, found 439.1752.

$[\alpha]^{24}_{\text{D}} = -51.4^\circ$ (c 0.022 M, CH_2Cl_2).



Using D-galactose diol **2-60d** (15.6 mg, 0.05 mmol, 1.0 eq.) as the starting material and 2-methoxypropene (1.2 eq., 0.06 mmol, 6 μL), preparation of **2-64d** was accomplished following the **General Protocol B**. This product was purified by flash column chromatography on SiO_2 (8/2 Hexanes/Ethyl acetate + 2% triethylamine) that results in full separation of C_2 - and C_3 -protected products: 13.1 mg (68%) of major C_3 -acetalized **2-64d** and 3.8 mg (20%) of minor C_2 -acetalized **5r** (total yield is 88%). C_2 and C_3 selectivity was determined based on the NMR analysis.

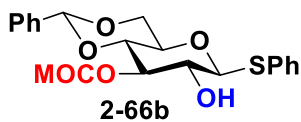
^1H NMR (500 MHz, Benzene- d_6) δ 7.55 (d, $J = 7.8$ Hz, 2H), 7.29 (t, $J = 7.5$ Hz, 2H), 7.28 – 7.21 (m, 1H), 4.59 (d, $J = 10.0$ Hz, 1H), 4.26 – 4.23 (m, 1H), 4.05 (t, $J = 6.2$ Hz, 1H), 3.96 (ddd, $J = 7.3, 4.1, 1.9$ Hz, 1H), 3.66 (t, $J = 9.0$ Hz, 1H), 3.59 (dd, $J = 10.1, 4.2$ Hz, 1H), 3.51 (dd, $J = 10.1, 6.9$ Hz, 1H), 3.18 (s, 3H), 1.43 (s, 3H), 1.33 (s, 9H).

^{13}C NMR (125 MHz, Benzene- d_6) δ 134.1, 130.9, 128.4, 126.8, 109.7, 100.0, 87.0, 80.0, 75.5, 74.1, 71.4, 60.5, 27.0, 25.2, 23.4, 23.3

IR (FTIR-ATR, cm^{-1}): 3432, 3058, 2988, 2935, 1584, 1480, 1458, 1380, 1371, 1243, 1215, 1165, 1149, 1080, 1051, 873, 839, 745

HRMS (ESI+) (m/z): $[\text{M}+\text{Na}]^+$ calcd for $\text{C}_{19}\text{H}_{28}\text{O}_6\text{SNa}$ 407.1499, found 407.1496.

$[\alpha]^{24}_{\text{D}} = +12.0^\circ$ (c 0.023 M, CH_2Cl_2).



Using diol **2-60b** (18 mg, 0.05 mmol, 1.0 equiv.) as the starting material and 1-methoxycyclohexene (1.2 eq., 0.06 mmol, 7 μL), preparation of **2-66b** was accomplished by following the **General Protocol B**. This product was purified by flash column chromatography on

SiO₂ (7/3 Hexanes/Ethyl acetate + 2% triethylamine) to afford **2-66b** as a colorless oil (19.8 mg, 84%, C₂:C₃ = 1:9). C₂ and C₃ selectivity was determined based on the NMR analysis.

¹H NMR (500 MHz, Methanol-*d*₄) δ 7.56 – 7.53 (m, 2H), 7.50 – 7.48 (m, 1H), 7.46 (dd, J = 6.7, 3.0 Hz, 2H), 7.33 (td, J = 5.6, 4.5, 2.4 Hz, 5H), 5.55 (s, 1H), 4.75 (d, J = 9.7 Hz, 1H), 4.27 (dd, J = 10.4, 4.3 Hz, 1H), 3.98 (t, J = 8.3 Hz, 1H), 3.73 (t, J = 9.8 Hz, 1H), 3.54 – 3.47 (m, 2H), 3.29 (t, J = 7.1 Hz, 1H), 3.19 (s, 3H), 1.79 – 1.71 (m, 4H), 1.65 – 1.58 (m, 2H), 1.48 – 1.34 (m, 4H).

¹³C NMR (125 MHz, Methanol-*d*₄) δ 137.8, 132.8, 132.2, 128.5, 128.5, 127.62, 127.4, 126.0, 101.7, 101.4, 87.5, 79.6, 75.0, 72.6, 70.3, 69.0, 33.9, 33.0, 25.0, 22.7.

IR (FTIR-ATR, cm⁻¹): 3359, 3060, 2936, 2861, 1584, 1479, 1456, 1374, 1259, 1156, 1085, 1022, 918, 749, 697

HRMS (ESI+) (*m/z*): [M+Na]⁺ calcd for C₂₆H₃₂O₆SNa 495.1812, found 495.1807.

[α]²⁴_D = -33.9° (c 0.027, CH₂Cl₂).



Using diol **2-60g** (20.5 mg, 0.05 mmol, 1.0 equiv.) as the starting material and 1-methoxycyclohexene (1.2 eq., 0.06 mmol, 7 μl), preparation of **2-66g** was accomplished by following the **General Protocol B**. This product was purified by flash column chromatography on SiO₂ (7/3 Hexanes/Ethyl acetate + 2% triethylamine) to afford **2-66g** as a white solid (18.3 mg, 70%, C₂:C₃ = 1:14). C₂ and C₃ selectivity was determined based on the NMR analysis.

Characterization of this compound is shown below.

¹H NMR (500 MHz, Benzene-*d*₆) δ 8.13 (d, J = 8.5 Hz, 1H), 7.89 (d, J = 7.1 Hz, 1H), 7.75 – 7.71 (m, 2H), 7.58 (d, J = 8.2 Hz, 1H), 7.53 (d, J = 8.2 Hz, 1H), 7.39 – 7.35 (m, 1H), 7.27 – 7.24 (m, 1H), 7.22 (d, J = 7.8 Hz, 1H), 7.04 (t, J = 7.6 Hz, 2H), 6.99 – 6.97 (m, 1H), 5.70 (s, 1H), 4.64 (d, J = 9.6 Hz, 1H), 4.12 (dd, J = 10.4, 5.0 Hz, 1H), 3.86 (t, J = 8.5 Hz, 1H), 3.58 – 3.53 (m, 1H), 3.48 (t, J = 10.2 Hz, 1H), 3.40 (t, J = 9.4 Hz, 1H), 3.12 (td, J = 9.9, 5.1 Hz, 1H), 2.93 (s, 3H), 1.72 – 1.67 (m, 1H), 1.60 – 1.56 (m, 1H), 1.55 – 1.51 (m, 1H), 1.45 – 1.41 (m, 1H), 1.40 – 1.36 (m, 2H), 1.17 – 1.12 (m, 2H), 0.94 – 0.88 (m, 2H)

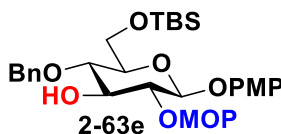
¹³C NMR (125 MHz, Benzene-*d*₆) δ 133.9, 133.6, 133.5(2C), 133.3, 130.9, 129.5, 128.7(2C), 128.1-127.1(hidden under solvent peak), 128.5, 125.7, 125.4, 124.9, 124.9, 123.8, 101.5, 100.1, 88.3, 79.2, 76.3, 73.1, 70.5, 68.7, 47.7, 33.6, 32.7, 24.9, 22.7, 21.9.

¹³C NMR (125 MHz, DCM-*d*₂) δ 133.0, 132.1, 131.6(2C), 129.9, 128.9, 128.2(2C), 127.8, 127.0, 125.5, 125.0, 124.3, 123.6, 123.0, 101.2, 99.5, 87.4, 78.6, 75.5, 72.2, 70.1, 68.3, 47.6, 33.1, 32.1, 28.7, 24.4, 22.2, 21.4

IR (FTIR-ATR, cm⁻¹): 3358, 3053, 2929, 2858, 1583, 1512, 1439, 1347, 1264, 1171, 1109, 1076, 1038, 1022, 803, 790.

HRMS (ESI+) (*m/z*): [M+Na]⁺ calcd for C₃₀H₃₄O₆SNa 545.1968, found 545.1965.

$[\alpha]_D^{24} = -12.2^\circ$ (c 0.014 M, CH₂Cl₂).



Using diol **2-60e** (24.5 mg, 0.05 mmol, 1.0 eq.) as the starting material and 2-methoxypropene (1.2 eq., 0.06 mmol, 6 μ l), preparation of **2-63e** was accomplished by following **General Protocol B**.

This product was purified by flash column chromatography on SiO₂ (7/3 Hexanes/Ethyl acetate + 2% triethylamine) to afford **2-63e** as a colorless oil (23.0 mg, 85 % yield, C2:C3 > 25:1). C2 and C3 selectivity was determined based on the NMR analysis.

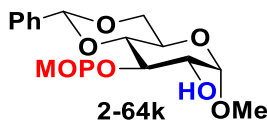
¹H NMR (700 MHz, Methanol-*d*₄) δ 7.36 (d, *J* = 7.5 Hz, 2H), 7.32 (t, *J* = 7.6 Hz, 3H), 7.29 – 7.24 (m, 1H), 7.05 – 6.91 (m, 1H), 6.83 – 6.76 (m, 2H), 4.95 (d, *J* = 11.1 Hz, 1H), 4.82 – 4.77 (m, 1H), 4.67 (d, *J* = 11.1 Hz, 1H), 3.85 (dd, *J* = 11.5, 1.9 Hz, 1H), 3.78 – 3.69 (m, 6H), 3.66 (t, *J* = 8.6 Hz, 1H), 3.53 – 3.46 (m, 1H), 3.46 – 3.38 (m, 1H), 1.51 (s, 3H), 1.46 (s, 3H), 0.90 (s, 3H), 0.88 (s, 9H), 0.03 (s, 3H), -0.01 (s, 3H).

¹³C NMR (176 MHz, Methanol-*d*₄) δ 155.2, 151.6, 138.6, 128.0, 127.5, 127.3, 117.6, 114.1, 101.8, 100.7, 77.8, 76.3, 75.6, 74.60, 74.35, 62.3, 54.6, 49.1, 25.0, 23.8, 17.8, -6.4, -6.6.

IR (thin film, cm⁻¹): 3402, 2928, 2855, 1506, 1462, 1372, 1226, 1056, 1034, 833, 776, 698, 670.

HRMS (ESI+) (*m/z*): [M+Na]⁺ calcd for C₃₀H₄₆O₈SiNa 585.2854, found 585.2847.

$[\alpha]_D^{26} = -9.9^\circ$ (c=2.6, DCM).



Using *D*-mannose derivative **2-60k** (18 mg, 0.04 mmol, 1.0 equiv.) as the starting material, synthesis of **2-64k** was accomplished following **General Protocol B**. This product was purified by flash column chromatography on SiO₂ (3/1 Hexanes/Ethyl acetate + 1% triethylamine) to afford **2-64k** as a pale-yellow oil (8.6 mg, 50%, C2:C3 = 1:12).

¹H NMR (500 MHz, Methanol-*d*₄) δ 7.54 – 7.43 (m, 4H), 7.39 – 7.25 (m, 6H), 5.58 (s, 1H), 5.48 (s, 1H), 4.29 (td, *J* = 9.8, 4.8 Hz, 1H), 4.22 (d, *J* = 3.0 Hz, 1H), 4.19 (dd, *J* = 10.0, 3.1 Hz, 1H), 4.11 (dd, *J* = 10.2, 4.8 Hz, 1H), 4.05 (at, *J* = 9.7 Hz, 1H), 3.82 (at, *J* = 10.3 Hz, 1H), 3.21 (s, 3H), 1.40 (d, *J* = 12.0 Hz, 3H), 1.37 (s, 3H).

¹³C NMR (125 MHz, Methanol-*d*₄) δ 137.9, 133.7, 131.6, 128.8, 128.5, 127.6, 127.3, 126.0, 102.0, 101.5, 89.5, 77.3, 72.5, 68.1, 65.7, 48.6, 47.1, 24.5, 24.2.

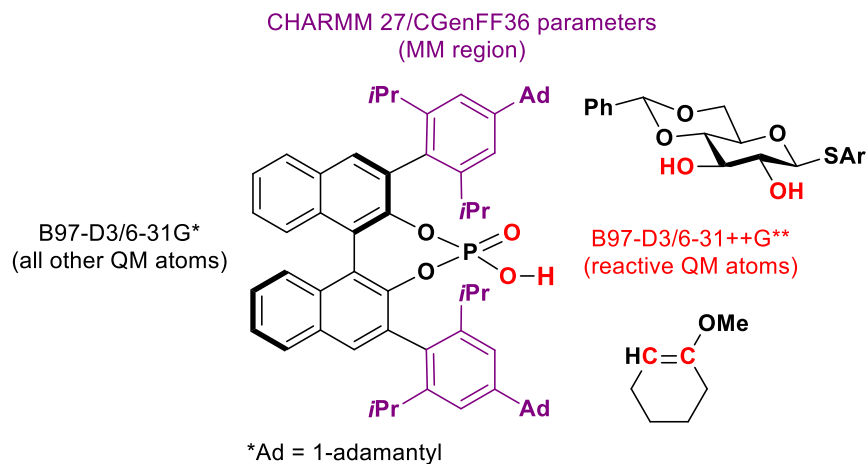
IR (thin film, cm⁻¹): 3433, 2985, 2923, 2853, 1456, 1373, 1211, 1169, 1095, 1031, 970.

HRMS (ESI+) (m/z): $[M+Na]^+$ calcd for $C_{23}H_{28}O_6SNa$ 455.1499, found 455.1513.
 $[\alpha]_D^{26} = +48.9^\circ$ ($c=0.51$, DCM).

2.9 Computational details

All molecular mechanics calculations and molecular dynamics simulations were performed in CHARMM (v. 45a2)⁴⁷ software package. CGenFF⁴⁸ was used for automatic atom typing and assigning parameters and charges from the CHARMM General Force Field (CGenFF36)⁴⁹. All quantum (QM) and quantum mechanics/molecular mechanics (QM/MM) computations were performed using development version of QChem 5.2.0⁵⁰ and electrostatically embedded QM/MM model with H link atoms⁵¹. The QM region is described by the B97-D3 DFT functional⁵² (with Grimme D3BJ dispersion correction) and a mixed double- ζ -quality basis sets 6-31++G**(reactive atoms)/6-31G*(all other atoms)⁵³. The MM region was treated with the CHARMM27-type⁵⁴ force field using CGenFF36 parameters as described above. The QM/MM borders were set on the C-C bond at the 3,3'-positions of the chiral catalyst (**R**)-**2-62e** placing bulky hydrocarbon parts of catalyst to MM region (Scheme 2.28). The 3,3'-substituents should participate only in steric interactions with substrates that will minimize possible artefacts during computing QM/MM interactions. Reaction pathways were optimized using the growing string method^{55,56} developed by Zimmerman group, using the just-described QM/MM approach (CHARMM27/CGenFF36//B97-D3/6-31++G**/6-31G*, Scheme X). After the GSM run, TS structures were further refined using an eigenvector TS optimizer. Visualization of transition state structures was performed in VMD software package⁵⁷. To analyze non-covalent interactions the NCIPLOT program⁵⁸ was used to calculate reduced density gradient (RDG) and create VMD cube files for isosurface visualization (density cut-off $r1 = 0.07$ a.u., RDG cut-off $r2 = 0.3$ a.u.). Single point energies were evaluated at ω B97X-D3/cc-pVTZ^{59,60} level of theory for the whole system in QM with SMD⁶¹ solvation model (DCM as a solvent).

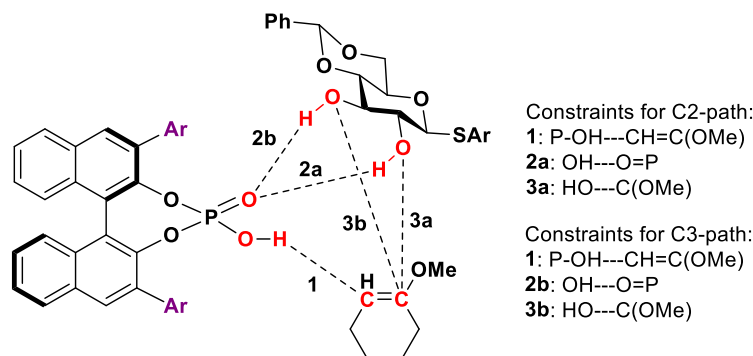
Scheme 2.28. QM/MM setup for geometry optimization, frequencies, and growing string computations.



Conformers generation and molecule alignment

Conformers of reacting molecules and their alignment were performed using Self-Guided Langevin Dynamics in the OpenMM/CHARMM45a2 interface. Catalyst (**R**)-**2-62e** (**R-CPA**), compound **2-60b** (**sugar**), and 1-methoxycyclohexene (protecting group, **PG**) were placed in a 50Å cubic box with periodic boundary conditions. Three general restraint distances with target values of 2.0Å and 10 kcal/mol force harmonic constant were set to keep three molecules approximately oriented for a concerted mechanism (individually for C2 and C3 pathways) during conformer generation (Scheme X).

Scheme 2.29. Molecular alignment (distances constraints) for conformer generation in the concerted mechanism.



Self-Guided Langevin Dynamics were run with Particle Mesh Ewald algorithm (pmEwald), 0.2 ps local average time (TSGAVG) and self-guided factor 1.0 (SGFT). An integration time step of 0.002 ps was chosen for both systems, with equilibration (2 ns run) and sampling (20 ns run) at 298K. Full MD parameters list is given below:

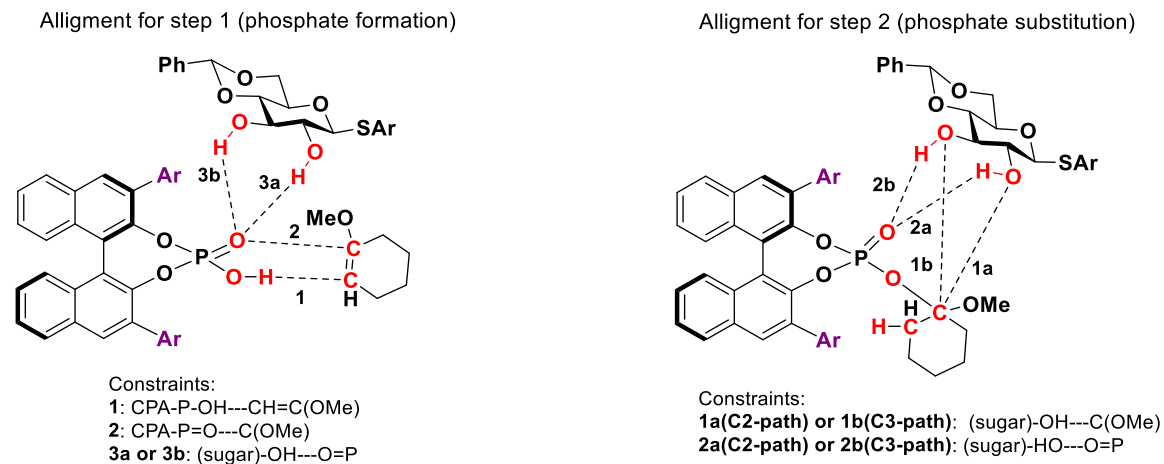
CHARMM MD parameters:

cdie eps 1 - !! Set constant dielectric value of 1
vdw vswitch - !! Set non-bonded VDW using switching function
cutnb 12.0 - !! 12.0Å non-bonding interactions cutoff
ctonnb 10.0 ctofnb 12.0 - !! VDW switching functions from 10.0Å to 12.0Å
Ewald - !! Use Ewald electrostatics
kappa 0.320 - !! Gaussian distribution central to the Ewald method
pmEwald - !! Particle Mesh Ewald algorithm
order 6 - !! Interpolation order
sgld tsgavg 0.2 sgft 1.0 - !! self-guided LD with constant guiding factor

Trajectory files were split into 2000 frames to produce conformers with further MM-optimization in CHARMM. The 20 lowest-MM-energy conformers were chosen for each C2- and C3-path.

The same SGLD procedure was used with different constraints to generate alignments for the competing phosphate-mediated pathway (Scheme 9S). For step 1 the sugar was explicitly added to system to account for specific molecular interactions such as H-bonds that can stabilize the starting complex, transition states or intermediates. The 20 lowest conformers were taken for TS computations for both step 1 and step 2 in phosphate mechanism.

Scheme 2.30. Molecular alignment (distances constraints) for conformer generation in the phosphate mechanism.



Growing string computations

For the single-ended growing string (SE-GSM) runs, 30 nodes were set as the maximum limit, though this limit was not reached. During the growth phase, new nodes were added when the RMS gradient was less than 0.005 Hartree/Å. An initial maximum optimization step size of 0.1 was used. When the total perpendicular gradient magnitude over all nodes, F , reached $F < 0.3$, the climbing image search was initiated. When $F < 0.1$, or when the highest energy node had an RMS gradient below double the nodal convergence criterion and $F < 0.2$, the exact transition state search was initiated within the string. The string is considered completely converged when an RMS gradient < 0.0003 Hartree/Å was obtained for the transition state node. After string optimization, the TSs were further optimized to higher tolerances (0.0015 gradient tolerance, 0.0002 energy tolerance). Further computational details can be found in references^{62,63}.

Conformers from SGLD were further re-optimized at the QM/MM level of theory (CHARMM27/CGenFF36//B97-D3/6-31++G**/6-31G*) without any restrained distances and then used as initial geometries for SE-GSM runs. For the C2 and C3 pathways, 20 possible reaction pathways each were calculated. In several runs, the formation of oxocarbenium-like species

(involved in asynchronous mechanism) was observed before the TS. Attempts to identify and optimize a stable oxocarbenium intermediate were not successful.

Computational data (XYZ files, energies breakdown of all computed structures and transition states) available in Supplementary Information of a paper published by Nagorny et. al.⁴²

<https://doi.org/10.1021/jacs.1c08448>

2.10 References

- (1) Ernst, B.; Magnani, J. L. From Carbohydrate Leads to Glycomimetic Drugs. *Nature Reviews Drug Discovery*. 2009, pp 661–677. <https://doi.org/10.1038/nrd2852>.
- (2) Filice, M.; Palomo, J. M. Monosaccharide Derivatives as Central Scaffolds in the Synthesis of Glycosylated Drugs. *RSC Advances*. March 7, 2012, pp 1729–1742. <https://doi.org/10.1039/c2ra00515h>.
- (3) Krasnova, L.; Wong, C. H. Oligosaccharide Synthesis and Translational Innovation. *J Am Chem Soc* **2019**, *141* (9), 3735–3754. https://doi.org/10.1021/JACS.8B11005/ASSET/IMAGES/LARGE/JA-2018-110052_0007.JPEG.
- (4) Seeberger, P. H. Discovery of Semi- And Fully-Synthetic Carbohydrate Vaccines against Bacterial Infections Using a Medicinal Chemistry Approach. *Chem Rev* **2021**, *121* (7), 3598–3626. https://doi.org/10.1021/ACS.CHEMREV.0C01210/ASSET/IMAGES/LARGE/CR0C01210_0024.JPEG.
- (5) Wang, C. C.; Lee, J. C.; Luo, S. Y.; Kulkarni, S. S.; Huang, Y. W.; Lee, C. C.; Chang, K. L.; Hung, S. C. Regioselective One-Pot Protection of Carbohydrates. *Nature* **2007**, *446* (7138), 896–899. <https://doi.org/10.1038/nature05730>.
- (6) Wang, C. C.; Kulkarni, S. S.; Lee, J. C.; Luo, S. Y.; Hung, S. C. Regioselective One-Pot Protection of Glucose. *Nat Protoc* **2008**, *3* (1), 97–113. <https://doi.org/10.1038/NPROT.2007.493>.
- (7) Huang, T. Y.; Zulueta, M. M. L.; Hung, S. C. Regioselective One-Pot Protection, Protection–Glycosylation and Protection–Glycosylation–Glycosylation of Carbohydrates: A Case Study with D-Glucose. *Org Biomol Chem* **2013**, *12* (2), 376–382. <https://doi.org/10.1039/C3OB42097C>.
- (8) Zulueta, M. M. L.; Janreddy, D.; Hung, S. C. One-Pot Methods for the Protection and Assembly of Sugars. *Isr J Chem* **2015**, *55* (3–4), 347–359. <https://doi.org/10.1002/IJCH.201400171>.
- (9) Français, A.; Urban, D.; Beau, J. M. Tandem Catalysis for a One-Pot Regioselective Protection of Carbohydrates: The Example of Glucose. *Angewandte Chemie International Edition* **2007**, *46* (45), 8662–8665. <https://doi.org/10.1002/ANIE.200703437>.
- (10) Beau, J.-M.; Bourdreux, Y.; Despras, G.; Gouasmat, A.; Jose, G. S.; Urban, D.; Vauzeilles, B. One-Pot Multistep Regioselective Protection of Carbohydrates Catalyzed by Acids. *Protecting Groups* **2019**, 201–226. <https://doi.org/10.1002/9783527697014.CH7>.

- (11) Yamatsugu, K.; Kanai, M. Catalytic Approaches to Chemo- and Site-Selective Transformation of Carbohydrates. *Chemical Reviews*. American Chemical Society May 24, 2023, pp 6793–6838. <https://doi.org/10.1021/acs.chemrev.2c00892>.
- (12) Hanessian, S.; Lavallee, P.; LAVALLEE Can Chem, P. J. The Preparation and Synthetic Utility of Tert-Butyldiphenylsilyl Ethers. <https://doi.org/10.1139/v75-419> **2011**, *53* (19), 2975–2977. <https://doi.org/10.1139/V75-419>.
- (13) Jeanloz, R. W.; Jeanloz, D. A. Partial Esterification of Methyl 4, 6-O-Benzylidene- α -D-Glucopyranoside in Pyridine Solution. *J Am Chem Soc* **1957**, *79* (10), 2579–2583. https://doi.org/10.1021/JA01567A058/ASSET/JA01567A058.FP.PNG_V03.
- (14) Taylor, M. S. Catalyst-Controlled, Regioselective Reactions of Carbohydrate Derivatives. *Top Curr Chem* **2015**, *372*, 125–156. https://doi.org/10.1007/128_2015_656/SCHEMES/31.
- (15) David, S.; Hanessian, S. Regioselective Manipulation of Hydroxyl Groups via Organotin Derivatives. *Tetrahedron* **1985**, *41* (4), 643–663. [https://doi.org/10.1016/S0040-4020\(01\)96443-9](https://doi.org/10.1016/S0040-4020(01)96443-9).
- (16) Munavu, R. M.; Szmant, H. H. Selective Formation of 2 Esters of Some Methyl α -D-Hexopyranosides via Dibutylstannylene Derivatives. *Journal of Organic Chemistry* **1976**, *41* (10), 1832–1836. https://doi.org/10.1021/JO00872A033/ASSET/JO00872A033.FP.PNG_V03.
- (17) Gordon, R. G.; Prescia, J. W. Implications of the Toxicity of Tetramethyltin, Dimethyl Tin Dichloride, and Tin Tetrachloride in Selecting a Suitable Tin Precursor in the Chemical Vapor Deposition of Tin Oxide. *AIP Conf Proc* **1988**, *166* (1), 1–9. <https://doi.org/10.1063/1.37122>.
- (18) Herradón, B.; Morcuende, A.; Valverde, S. Microwave Accelerated Organic Transformations: Dibutylstannylene Acetal Mediated Selective Acylation of Polyols and Amino Alcohols Using Catalytic Amounts of Dibutyltin Oxide. Influence of the Solvent and the Power Output on the Selectivity. *Synlett* **1995**, *1995* (5), 455–458. <https://doi.org/10.1055/S-1995-4988/BIB>.
- (19) Martinelli, M. J.; Vaidyanathan, R.; Pawlak, J. M.; Nayyar, N. K.; Dhokte, U. P.; Doecke, C. W.; Zollars, L. M. H.; Moher, E. D.; Khau, V. Van; Košmrlj, B. Catalytic Regioselective Sulfonylation of α -Chelatable Alcohols: Scope and Mechanistic Insight. *J Am Chem Soc* **2002**, *124* (14), 3578–3585. https://doi.org/10.1021/JA016031R/SUPPL_FILE/JA016031R_S1.PDF.
- (20) Muramatsu, W. Chemo- and Regioselective Monosulfonylation of Nonprotected Carbohydrates Catalyzed by Organotin Dichloride under Mild Conditions. *Journal of Organic Chemistry* **2012**, *77* (18), 8083–8091. https://doi.org/10.1021/JO301353K/SUPPL_FILE/JO301353K_SI_001.PDF.
- (21) Muramatsu, W.; Tanigawa, S.; Takemoto, Y.; Yoshimatsu, H.; Onomura, O. Organotin-Catalyzed Highly Regioselective Thiocarbonylation of Nonprotected Carbohydrates and Synthesis of Deoxy Carbohydrates in a Minimum Number of Steps. *Chemistry – A European Journal* **2012**, *18* (16), 4850–4853. <https://doi.org/10.1002/CHEM.201104007>.
- (22) Oshima, K.; Kitazono, E. I.; Aoyama, Y. Complexation-Induced Activation of Sugar OH Groups. Regioselective Alkylation of Methyl Fucopyranoside via Cyclic Phenylboronate in the Presence of Amine. *Tetrahedron Lett* **1997**, *38* (28), 5001–5004. [https://doi.org/10.1016/S0040-4039\(97\)01070-8](https://doi.org/10.1016/S0040-4039(97)01070-8).
- (23) Jäger, M.; Minnaard, A. J. Regioselective Modification of Unprotected Glycosides. *Chemical Communications* **2015**, *52* (4), 656–664. <https://doi.org/10.1039/C5CC08199H>.
- (24) Lee, D.; Taylor, M. S. Borinic Acid-Catalyzed Regioselective Acylation of Carbohydrate Derivatives. *J Am Chem Soc* **2011**, *133* (11), 3724–3727. https://doi.org/10.1021/JA110332R/SUPPL_FILE/JA110332R_SI_001.PDF.

- (25) Chan, L.; Taylor, M. S. Regioselective Alkylation of Carbohydrate Derivatives Catalyzed by a Diarylborinic Acid Derivative. *Org Lett* **2011**, *13* (12), 3090–3093. https://doi.org/10.1021/OL200990E/SUPPL_FILE/OL200990E_SI_001.PDF.
- (26) Lee, D.; Taylor, M. S. Regioselective Silylation of Pyranosides Using a Boronic Acid/Lewis Base Co-Catalyst System. *Org Biomol Chem* **2013**, *11* (33), 5409–5412. <https://doi.org/10.1039/C3OB40981C>.
- (27) Shimada, N.; Nakamura, Y.; Ochiai, T.; Makino, K. Catalytic Activation of Cis-Vicinal Diols by Boronic Acids: Site-Selective Acylation of Carbohydrates. *Org Lett* **2019**, *21* (10), 3789–3794. https://doi.org/10.1021/ACS.ORGLETT.9B01231/ASSET/IMAGES/LARGE/OL-2019-01231K_0002.JPEG.
- (28) Abbas, S. A.; Haines, A. H. Benzoyl Cyanide as a Selective Acylating Agent. *Carbohydr Res* **1975**, *39* (2), 358–363. [https://doi.org/10.1016/S0008-6215\(00\)86148-0](https://doi.org/10.1016/S0008-6215(00)86148-0).
- (29) Kurahashi, T.; Mizutani, T.; Yoshida, J. I. Effect of Intramolecular Hydrogen-Bonding Network on the Relative Reactivities of Carbohydrate OH Groups†. *J Chem Soc Perkin 1* **1999**, No. 4, 465–474. <https://doi.org/10.1039/A808798I>.
- (30) Peng, P.; Linseis, M.; Winter, R. F.; Schmidt, R. R. Regioselective Acylation of Diols and Triols: The Cyanide Effect. *J Am Chem Soc* **2016**, *138* (18), 6002–6009. https://doi.org/10.1021/JACS.6B02454/ASSET/IMAGES/LARGE/JA-2016-02454V_0004.JPEG.
- (31) Matsumura, Y.; Maki, T.; Murakami, S.; Onomura, O. Copper Ion-Induced Activation and Asymmetric Benzoylation of 1,2-Diols: Kinetic Chiral Molecular Recognition. *J Am Chem Soc* **2003**, *125* (8), 2052–2053. https://doi.org/10.1021/JA0289402/SUPPL_FILE/JA0289402SI20030112_111533.PDF.
- (32) Allen, C. L.; Miller, S. J. Chiral Copper(II) Complex-Catalyzed Reactions of Partially Protected Carbohydrates. *Org Lett* **2013**, *15* (24), 6178–6181. https://doi.org/10.1021/OL4033072/SUPPL_FILE/OL4033072_SI_001.PDF.
- (33) Chen, I. H.; Kou, K. G. M.; Le, D. N.; Rathbun, C. M.; Dong, V. M. Recognition and Site-Selective Transformation of Monosaccharides by Using Copper(II) Catalysis. *Chemistry – A European Journal* **2014**, *20* (17), 5013–5018. <https://doi.org/10.1002/CHEM.201400133>.
- (34) Ren, B.; Wang, J.; Zhang, M.; Chen, Y.; Zhao, W. A Chiral Copper Catalyzed Site-Selective O-Alkylation of Carbohydrates. *Adv Synth Catal* **2022**, *364* (3), 665–670. <https://doi.org/10.1002/ADSC.202101121>.
- (35) Xiao, G.; Cintron-Rosado, G. A.; Glazier, D. A.; Xi, B. M.; Liu, C.; Liu, P.; Tang, W. Catalytic Site-Selective Acylation of Carbohydrates Directed by Cation- π Interaction. *J Am Chem Soc* **2017**, *139* (12), 4346–4349. https://doi.org/10.1021/JACS.7B01412/ASSET/IMAGES/LARGE/JA-2017-01412H_0004.JPEG.
- (36) Sun, X.; Worthy, A. D.; Tan, K. L. Scaffolding Catalysts: Highly Enantioselective Desymmetrization Reactions. *Angewandte Chemie International Edition* **2011**, *50* (35), 8167–8171. <https://doi.org/10.1002/ANIE.201103470>.
- (37) Worthy, A. D.; Sun, X.; Tan, K. L. Site-Selective Catalysis: Toward a Regiodivergent Resolution of 1,2-Diols. *J Am Chem Soc* **2012**, *134* (17), 7321–7324. https://doi.org/10.1021/JA3027086/SUPPL_FILE/JA3027086_SI_002.PDF.
- (38) Sun, X.; Lee, H.; Lee, S.; Tan, K. L. Catalyst Recognition of Cis-1,2-Diols Enables Site-Selective Functionalization of Complex Molecules. *Nature Chemistry* **2013**, *5* (9), 790–795. <https://doi.org/10.1038/nchem.1726>.

- (39) Parmar, D.; Sugiono, E.; Raja, S.; Rueping, M. Complete Field Guide to Asymmetric BINOL-Phosphate Derived Brønsted Acid and Metal Catalysis: History and Classification by Mode of Activation; Brønsted Acidity, Hydrogen Bonding, Ion Pairing, and Metal Phosphates. *Chemical Reviews*. American Chemical Society September 24, 2014, pp 9047–9153. <https://doi.org/10.1021/cr5001496>.
- (40) Sun, Z.; Winschel, G. A.; Borovika, A.; Nagorny, P. Chiral Phosphoric Acid-Catalyzed Enantioselective and Diastereoselective Spiroketalizations. *J Am Chem Soc* **2012**, *134* (19), 8074–8077. https://doi.org/10.1021/JA302704M/SUPPL_FILE/JA302704M_SI_003.CIF.
- (41) Mensah, E.; Camasso, N.; Kaplan, W.; Nagorny, P. Chiral Phosphoric Acid Directed Regioselective Acetalization of Carbohydrate-Derived 1,2-Diols. *Angewandte Chemie International Edition* **2013**, *52* (49), 12932–12936. <https://doi.org/10.1002/ANIE.201304298>.
- (42) Wang, S.; Zhelavskiy, O.; Lee, J.; Argüelles, A. J.; Khomutnyk, Y. Y.; Mensah, E.; Guo, H.; Hourani, R.; Zimmerman, P. M.; Nagorny, P. Studies of Catalyst-Controlled Regioselective Acetalization and Its Application to Single-Pot Synthesis of Differentially Protected Saccharides. *J Am Chem Soc* **2021**, *143* (44), 18592–18604. https://doi.org/10.1021/JACS.1C08448/SUPPL_FILE/JA1C08448_SI_019.PDF.
- (43) Clot-Almenara, L.; Rodríguez-Escrich, C.; Osorio-Planes, L.; Pericas, M. A. Polystyrene-Supported TRIP: A Highly Recyclable Catalyst for Batch and Flow Enantioselective Allylation of Aldehydes. *ACS Catal* **2016**, *6* (11), 7647–7651. https://doi.org/10.1021/ACSCATAL.6B02621/SUPPL_FILE/CS6B02621_SI_001.PDF.
- (44) Lai, J.; Fianchini, M.; Pericas, M. A. Development of Immobilized Spinol-Derived Chiral Phosphoric Acids for Catalytic Continuous Flow Processes. Use in the Catalytic Desymmetrization of 3,3-Disubstituted Oxetanes. *ACS Catal* **2020**, *10* (24), 14971–14983. https://doi.org/10.1021/ACSCATAL.0C04497/SUPPL_FILE/CS0C04497_SI_002.CIF.
- (45) Tay, J. H.; Argüelles, A. J.; Demars, M. D.; Zimmerman, P. M.; Sherman, D. H.; Nagorny, P. Regiodivergent Glycosylations of 6-Deoxy-Erythronolide B and Oleandomycin-Derived Macrolactones Enabled by Chiral Acid Catalysis. *J Am Chem Soc* **2017**, *139* (25), 8570–8578. https://doi.org/10.1021/JACS.7B03198/SUPPL_FILE/JA7B03198_SI_002.PDF.
- (46) Shishido, K.; Hiroya, K.; Ueno, Y.; Fukumoto, K.; Kametani, T.; Honda, T. An Efficient Synthesis of Functionalized Tricyclo[6.3.1.0^{1,6}]Dodec-4-Enes by a Stereoselective Intramolecular Diels–Alder Reaction. *J Chem Soc Perkin 1* **1986**, No. 0, 829–836. <https://doi.org/10.1039/P19860000829>.
- (47) Brooks, B. R.; Brooks, C. L.; Mackerell, A. D.; Nilsson, L.; Petrella, R. J.; Roux, B.; Won, Y.; Archontis, G.; Bartels, C.; Boresch, S.; Caflisch, A.; Caves, L.; Cui, Q.; Dinner, A. R.; Feig, M.; Fischer, S.; Gao, J.; Hodoscek, M.; Im, W.; Kuczera, K.; Lazaridis, T.; Ma, J.; Ovchinnikov, V.; Paci, E.; Pastor, R. W.; Post, C. B.; Pu, J. Z.; Schaefer, M.; Tidor, B.; Venable, R. M.; Woodcock, H. L.; Wu, X.; Yang, W.; York, D. M.; Karplus, M. CHARMM: The Biomolecular Simulation Program. *J Comput Chem* **2009**, *30* (10), 1545–1614. <https://doi.org/10.1002/JCC.21287>.
- (48) Vanommeslaeghe, K.; Mackerell, A. D. Automation of the CHARMM General Force Field (CGenFF) I: Bond Perception and Atom Typing. *J Chem Inf Model* **2012**, *52* (12), 3144–3154. https://doi.org/10.1021/CI300363C/SUPPL_FILE/CI300363C_SI_001.ZIP.
- (49) Vanommeslaeghe, K.; Hatcher, E.; Acharya, C.; Kundu, S.; Zhong, S.; Shim, J.; Darian, E.; Guvench, O.; Lopes, P.; Vorobyov, I.; Mackerell, A. D. CHARMM General Force Field: A Force Field for Drug-like Molecules Compatible with the CHARMM All-Atom Additive

Biological Force Fields. *J Comput Chem* **2010**, *31* (4), 671–690. <https://doi.org/10.1002/JCC.21367>.

(50) Shao, Y.; Gan, Z.; Epifanovsky, E.; Gilbert, A. T. B.; Wormit, M.; Kussmann, J.; Lange, A. W.; Behn, A.; Deng, J.; Feng, X.; Ghosh, D.; Goldey, M.; Horn, P. R.; Jacobson, L. D.; Kaliman, I.; Khaliullin, R. Z.; Kuš, T.; Landau, A.; Liu, J.; Proynov, E. I.; Rhee, Y. M.; Richard, R. M.; Rohrdanz, M. A.; Steele, R. P.; Sundstrom, E. J.; Woodcock, H. L.; Zimmerman, P. M.; Zuev, D.; Albrecht, B.; Alguire, E.; Austin, B.; Beran, G. J. O.; Bernard, Y. A.; Berquist, E.; Brandhorst, K.; Bravaya, K. B.; Brown, S. T.; Casanova, D.; Chang, C. M.; Chen, Y.; Chien, S. H.; Closser, K. D.; Crittenden, D. L.; Diedenhofen, M.; Distasio, R. A.; Do, H.; Dutoi, A. D.; Edgar, R. G.; Fatehi, S.; Fusti-Molnar, L.; Ghysels, A.; Golubeva-Zadorozhnaya, A.; Gomes, J.; Hanson-Heine, M. W. D.; Harbach, P. H. P.; Hauser, A. W.; Hohenstein, E. G.; Holden, Z. C.; Jagau, T. C.; Ji, H.; Kaduk, B.; Khistyayev, K.; Kim, J.; Kim, J.; King, R. A.; Klunzinger, P.; Kosenkov, D.; Kowalczyk, T.; Krauter, C. M.; Lao, K. U.; Laurent, A. D.; Lawler, K. V.; Levchenko, S. V.; Lin, C. Y.; Liu, F.; Livshits, E.; Lochan, R. C.; Luenser, A.; Manohar, P.; Manzer, S. F.; Mao, S. P.; Mardirossian, N.; Marenich, A. V.; Maurer, S. A.; Mayhall, N. J.; Neuscamman, E.; Oana, C. M.; Olivares-Amaya, R.; Oneill, D. P.; Parkhill, J. A.; Perrine, T. M.; Peverati, R.; Prociuk, A.; Rehn, D. R.; Rosta, E.; Russ, N. J.; Sharada, S. M.; Sharma, S.; Small, D. W.; Sodt, A.; Stein, T.; Stück, D.; Su, Y. C.; Thom, A. J. W.; Tsuchimochi, T.; Vanovschi, V.; Vogt, L.; Vydrov, O.; Wang, T.; Watson, M. A.; Wenzel, J.; White, A.; Williams, C. F.; Yang, J.; Yeganeh, S.; Yost, S. R.; You, Z. Q.; Zhang, I. Y.; Zhang, X.; Zhao, Y.; Brooks, B. R.; Chan, G. K. L.; Chipman, D. M.; Cramer, C. J.; Goddard, W. A.; Gordon, M. S.; Hehre, W. J.; Klamt, A.; Schaefer, H. F.; Schmidt, M. W.; Sherrill, C. D.; Truhlar, D. G.; Warshel, A.; Xu, X.; Aspuru-Guzik, A.; Baer, R.; Bell, A. T.; Besley, N. A.; Chai, J. Da; Dreuw, A.; Dunietz, B. D.; Furlani, T. R.; Gwaltney, S. R.; Hsu, C. P.; Jung, Y.; Kong, J.; Lambrecht, D. S.; Liang, W.; Ochsenfeld, C.; Rassolov, V. A.; Slipchenko, L. V.; Subotnik, J. E.; Van Voorhis, T.; Herbert, J. M.; Krylov, A. I.; Gill, P. M. W.; Head-Gordon, M. *Advances in Molecular Quantum Chemistry Contained in the Q-Chem 4 Program Package. Mol Phys* **2015**, *113* (2), 184–215. <https://doi.org/10.1080/00268976.2014.952696>.

(51) Zimmerman, P. M.; Head-Gordon, M.; Bell, A. T. Selection and Validation of Charge and Lennard-Jones Parameters for QM/MM Simulations of Hydrocarbon Interactions with Zeolites. *J Chem Theory Comput* **2011**, *7* (6), 1695–1703. <https://doi.org/10.1021/CT2001655>.

(52) Grimme, S.; Ehrlich, S.; Goerigk, L. Effect of the Damping Function in Dispersion Corrected Density Functional Theory. *J Comput Chem* **2011**, *32* (7), 1456–1465. <https://doi.org/10.1002/JCC.21759>.

(53) Hehre, W. J.; Ditchfield, K.; Pople, J. A. Self—Consistent Molecular Orbital Methods. XII. Further Extensions of Gaussian—Type Basis Sets for Use in Molecular Orbital Studies of Organic Molecules. *J Chem Phys* **1972**, *56* (5), 2257–2261. <https://doi.org/10.1063/1.1677527>.

(54) *All-atom empirical force field for nucleic acids: I. Parameter optimization based on small molecule and condensed phase macromolecular target data - Foloppe - 2000 - Journal of Computational Chemistry - Wiley Online Library.* [https://onlinelibrary.wiley.com/doi/10.1002/\(SICI\)1096-987X\(20000130\)21:2%3C86::AID-JCC2%3E3.0.CO;2-G](https://onlinelibrary.wiley.com/doi/10.1002/(SICI)1096-987X(20000130)21:2%3C86::AID-JCC2%3E3.0.CO;2-G) (accessed 2024-05-01).

(55) Zimmerman, P. M. Growing String Method with Interpolation and Optimization in Internal Coordinates: Method and Examples. *J Chem Phys* **2013**, *138* (18). <https://doi.org/10.1063/1.4804162>.

- (56) Zimmerman, P. M. Automated Discovery of Chemically Reasonable Elementary Reaction Steps. *J Comput Chem* **2013**, *34* (16), 1385–1392. <https://doi.org/10.1002/JCC.23271>.
- (57) Humphrey, W.; Dalke, A.; Schulten, K. VMD: Visual Molecular Dynamics. *J Mol Graph* **1996**, *14* (1), 33–38. [https://doi.org/10.1016/0263-7855\(96\)00018-5](https://doi.org/10.1016/0263-7855(96)00018-5).
- (58) Contreras-García, J.; Johnson, E. R.; Keinan, S.; Chaudret, R.; Piquemal, J. P.; Beratan, D. N.; Yang, W. NCIPLLOT: A Program for Plotting Noncovalent Interaction Regions. *J Chem Theory Comput* **2011**, *7* (3), 625–632. https://doi.org/10.1021/CT100641A/SUPPL_FILE/CT100641A_SI_001.PDF.
- (59) Lin, Y. S.; Li, G. De; Mao, S. P.; Chai, J. Da. Long-Range Corrected Hybrid Density Functionals with Improved Dispersion Corrections. *J Chem Theory Comput* **2013**, *9* (1), 263–272. https://doi.org/10.1021/CT300715S/SUPPL_FILE/CT300715S_SI_001.PDF.
- (60) Kendall, R. A.; Dunning, T. H.; Harrison, R. J. Electron Affinities of the First-row Atoms Revisited. Systematic Basis Sets and Wave Functions. *J Chem Phys* **1992**, *96* (9), 6796–6806. <https://doi.org/10.1063/1.462569>.
- (61) Marenich, A. V.; Cramer, C. J.; Truhlar, D. G. Universal Solvation Model Based on Solute Electron Density and on a Continuum Model of the Solvent Defined by the Bulk Dielectric Constant and Atomic Surface Tensions. *Journal of Physical Chemistry B* **2009**, *113* (18), 6378–6396. <https://doi.org/10.1021/jp810292n>.
- (62) Zimmerman, P. Reliable Transition State Searches Integrated with the Growing String Method. *J Chem Theory Comput* **2013**, *9* (7), 3043–3050. <https://doi.org/10.1021/CT400319W>.
- (63) Zimmerman, P. M. Single-Ended Transition State Finding with the Growing String Method. *J Comput Chem* **2015**, *36* (9), 601–611. <https://doi.org/10.1002/JCC.23833>.

Chapter 3 Asymmetric Transfer Hydrogenation of Heterocyclic Compounds in a Continuous Flow²

3.1 Introduction

For more than a century, the chemistry of heterocyclic compounds has attracted great interest from the synthetic community due to their significance to biomedicine and material science. Various heterocycles were used for the synthesis of commercial materials, fluorescent probes, etc. Many nitrogen-containing heterocyclic compounds are widely distributed in nature and usually possess biochemical and pharmacological properties determining their broad use as vitamins, pharmaceuticals, dyes, and agrochemicals (Scheme 3.1, A).¹ Recent data suggests that more than 85% of all biologically active compounds contain heterocyclic motifs embedded in their structures. Analysis of the US FDA-approved pharmaceuticals highlights the importance of nitrogen-containing heterocycles as 59% of unique drugs contain at least one nitrogen heterocycle.² A further look at statistics demonstrates that among all existing heterocycles, six-membered motifs such as piperidine and pyridine are the most abundant and represent 40% of all six-membered heterocycles skeletons in pharmaceutical compounds. For example, tetrahydroquinoline which incorporates piperidine moiety is a core for several natural products. Saturated six-membered heterocycles with one or several stereocenters are also widely present in different pharmaceuticals (Scheme 3.1, B).² The continuously increasing interest in nitrogen-containing heterocyclic

² Authors and Contributions:

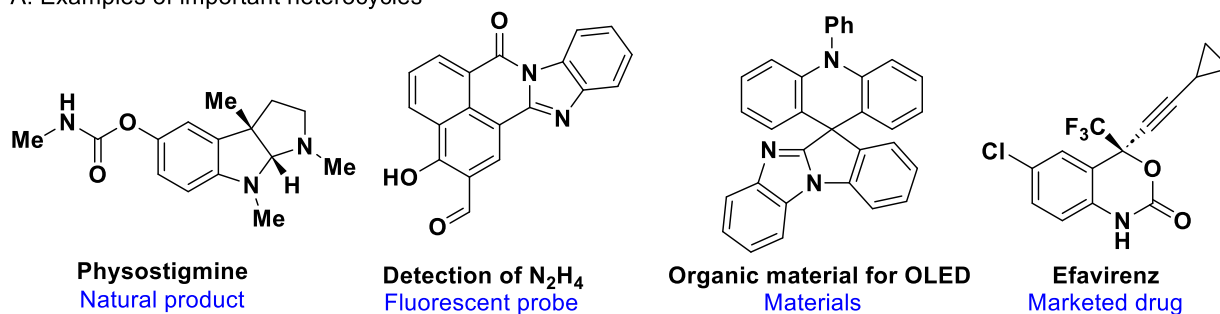
This chapter is adapted from: **Zhelavskiy O.**, Jhang Y.-J., Nagorny P. *Synthesis* **2023**, 55(15): 2361-2369

Y.-J. Jhang contributed to the synthesis of starting materials for the substrate scope screening

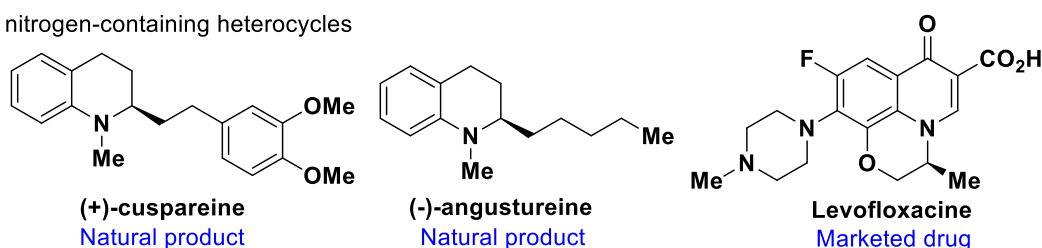
compounds has fueled the development of many creative synthetic methodologies to access various nitrogen-containing scaffolds, particularly in their enantiopure forms. These studies have been enabled by the recent advances in asymmetric catalysis, photocatalysis, transition metal catalysis and organocatalysis.³

Scheme 3.1. Important chiral heterocycles.

A. Examples of important heterocycles



B. Chiral nitrogen-containing heterocycles

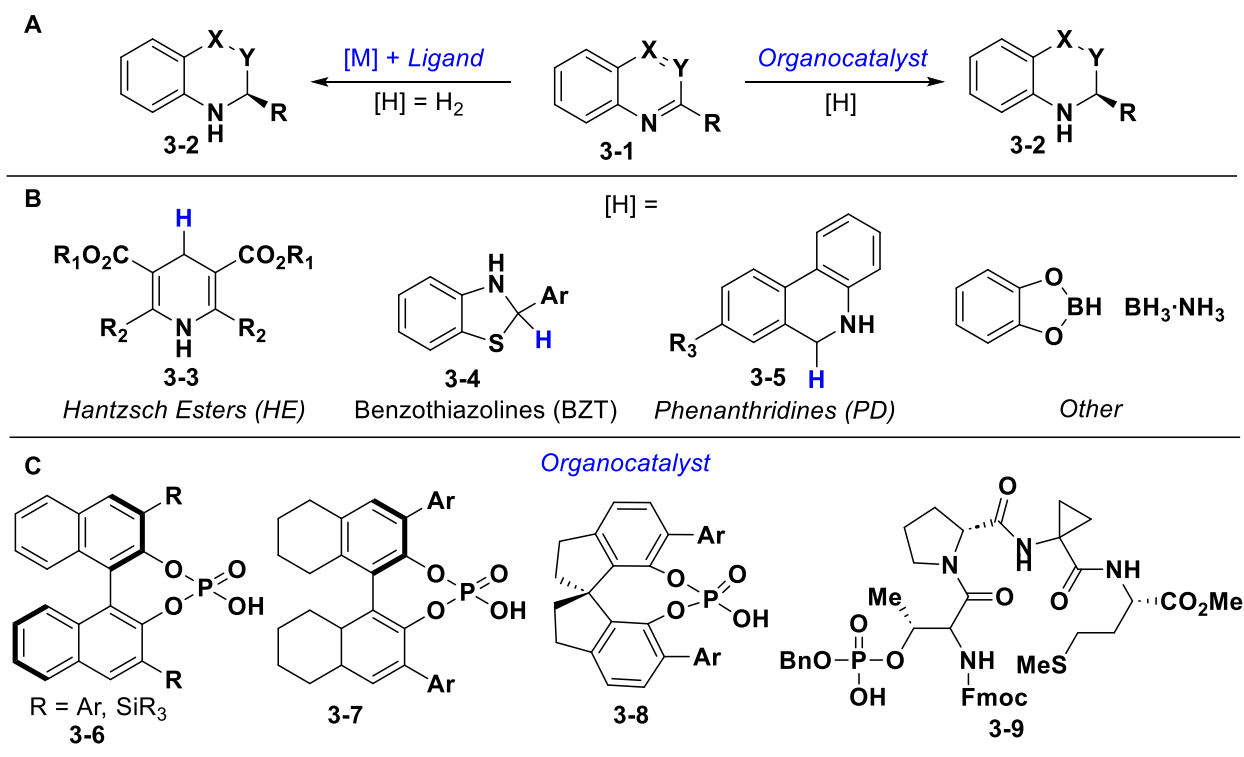


Arguably, among various routes for the synthesis of chiral heterocyclic compounds, dearomative reduction with a chiral catalyst has been one of the most important methods. Starting with broadly accessible and easily modifiable heteroarenes, one or multiple stereocenters can be installed via one step of reduction. Despite many methods developed for asymmetric reduction of unsaturated compounds, such as olefines, imines, ketones, etc., the asymmetric hydrogenation of arenes/heteroarenes is a much less explored area. This can be explained by the high stability of aromatic compounds that demand much harsher conditions for reduction and affect enantioselectivity. In general, two approaches are used for enantioselective reduction: direct hydrogenation with hydrogen with transition metal catalysis and organocatalytic transfer hydrogenation where another organic molecule is used as a reducing agent (Scheme 3.2, A).⁴

Asymmetric hydrogenation with transition metals is well established and can provide high selectivity and yields while using simple hydrogen gas for reduction. Despite the listed above advantages, the following four major challenges involving arene hydrogenation still exist.⁵

- **Safety and scale up.** Using hydrogen gas and pressurized reactions can create significant danger during the scale-up processes.
- **Catalyst poisoning.** Heteroatoms such as Sulphur or Nitrogen are Lewis basic and tend to coordinate strongly with transition metals. This can result in a total shutdown of reactivity.
- **Substrate scope.** In general, chiral ligands are suitable for only specific scaffolds, and the hydrogenation methods are not necessarily transferable to all heterocyclic systems.
- **Selectivity.** The *cis*-configured product is generally favored according to the Horiuti-Polanyi mechanism.⁶ Trans-hydrogenation is underdeveloped and challenging. Competing side reactions affecting other reductively labile groups (nitriles, ketones, double bonds) also create the problem of overreduction and side reactions.

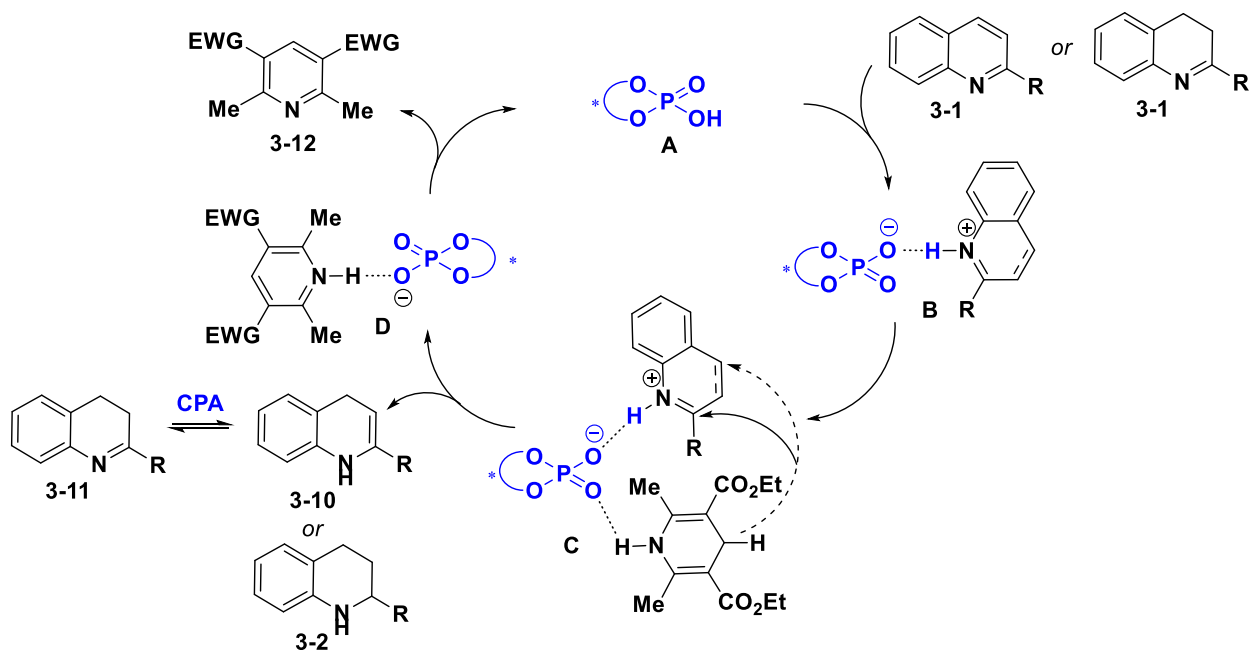
Scheme 3.2. Approaches towards asymmetric hydrogenation of heterocycles.



An alternative route to accomplishing asymmetric dearomative hydrogenation is using organic molecules as reductants and catalysts (Scheme 3.2A). Introduced by MacMillan and inspired by natural oxidoreductases, Hantzsch esters (HEs) facilitated the development of a new type of asymmetric reduction via a hydrogen transfer mechanism (Scheme 3.3).^{7,8} The pioneering work of Rueping demonstrated that chiral phosphoric acids (CPAs) can be used as effective catalysts for the asymmetric transfer hydrogenation of heterocyclic compounds with Hantzsch esters.⁹ The general mechanism of such transformation is depicted in Scheme 3.3. For the first cycle, CPA **A** coordinates the substrate, quinoline **3-1**, and protonates it leading to complex **B**. The second oxygen atom of the CPA coordinates HE **3-3**, to form catalytic complex **C**. The protonated quinoline ring is activated now for a hydride transfer from HE to the C4-position of quinoline, which leads to dihydroquinoline **3-10** in its enamine form that can be tautomerized to imine form **3-11**. After the HE is oxidized to pyridine **3-12**, it reprotonates the CPA thus completing the

catalytic cycle. The second reduction of dihydroquinoline **3-11** proceeds with the same catalytic cycle; however, in this case, complex **C** formed between the CPA, substrate and HE is crucial for enantioselectivity as it controls the face, from which the hydride is transferred from HE to imine **3-11**. Before developing this protocol for quinolines reduction, Rueping and Macmillan groups also demonstrated that HEs can be tuned to improve the enantioselectivity of asymmetric reduction of imines by varying the substituents at the C2- and C6- positions of the 1,4-dihydropyridine ring (R_2) and the ester groups (R_1). That provides an additional way to enhance the enantioselectivity and helps to adapt this method to a larger subset of substrates.^{10,11} The formation of the stable pyridine ring in oxidized HE represents the thermodynamic driving force that promotes the hydride transfer to quinolines or imines. Using this approach, alternative reduction agents, such as Benzothiazoles **3-4** (BZTs)¹² and Phenanthridines **3-5** (PD)^{13,14} were developed and effectively used in asymmetric hydrogenations (Scheme 3.2B). Catalytic systems based on borane hydrides were also reported.¹⁵

Scheme 3.3. Mechanism of asymmetric transfer hydrogenation.

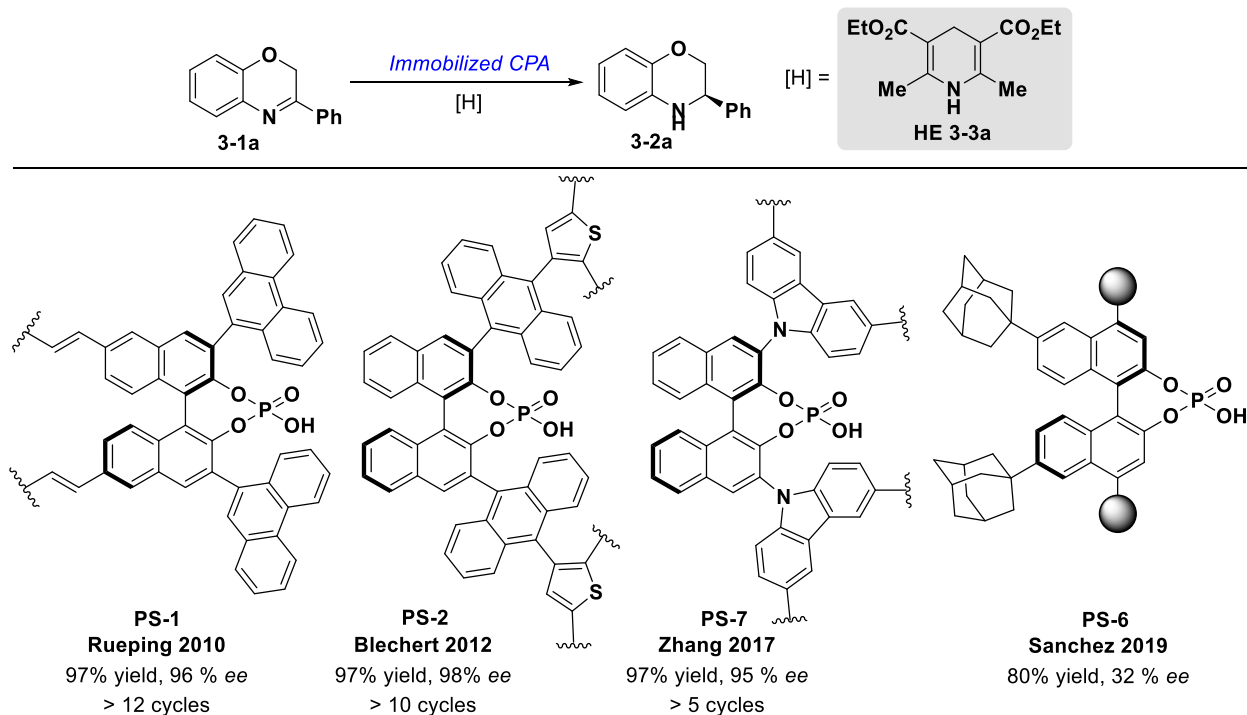


Since such transformation requires neither the usage of hydrogen gas nor expensive and toxic transition metals and the reactions show great air and moisture tolerance, which results in operational simplicity and safer processes. Due to this, a significant number of publications utilizing various CPA catalysts arose in the last two decades. While the majority of these studies utilized classical BINOL-, H₈-BINOL- and SPINOL-based CPAs, other types of CPAs could be also effective in promoting such transformations.¹⁶ For example, Miller and coworkers¹⁷ used phosphothreonine **3-9** as the chiral Brønsted acid demonstrating that the versatility of the asymmetric transfer hydrogenation is not limited to classical BINOL-type CPA scaffolds.

While these and related transfer hydrogenations often proceed with excellent enantioselectivities under mild conditions and involve safe-to-handle reagents, such reactions often require high loadings of expensive CPAs, which are not easy to recover and recycle.¹⁸ As discussed before in Chapter 1, some of these issues could be addressed by immobilizing the CPA catalyst. Continuing developing the methods for the asymmetric reductions, Rueping and coworkers¹⁹ synthesized polymeric CPA **PS-1** and successfully used for the reduction of 3-phenyl-2H-benzo-[1,4]oxazine **3-1a** in excellent yield and enantioselectivity (Scheme 3.4). Catalyst **PS-1**, immobilized in polymer matrix was used in unusual “teabag” setup when the polymer sticks were immersed into the reaction mixture and then removed when the reaction reached its completion. Studies demonstrated that a polymer stick could be recovered, washed, and recycled more than 12 times without the erosion in yields or selectivity. Following Rueping’s study, Blechert^{20,21} and Zhang²² groups have described the synthesis of immobilized CPA catalysts which were connected to polymer chain at 3,3’-positions. Immobilized CPA catalysts **PS-2** and **PS-7** were successfully used for asymmetric transfer hydrogenation of substituted quinolines and substituted 2H-benzo-[1,4]oxazines providing products in high yields (97%) and excellent

enantioselectivities (95 and 98% *ee*) and were recycled multiple times. Recently, the same reaction was investigated by the Sanchez group²³ using a porous polymer containing adamantyl-BINOL motif (**PS-6**) as the catalyst. Even though the product of the catalyzed reaction was isolated in 80% yield, this polymeric catalyst demonstrated low enantioselectivity.

Scheme 3.4. Reduction of 1,4-benzoxazines.

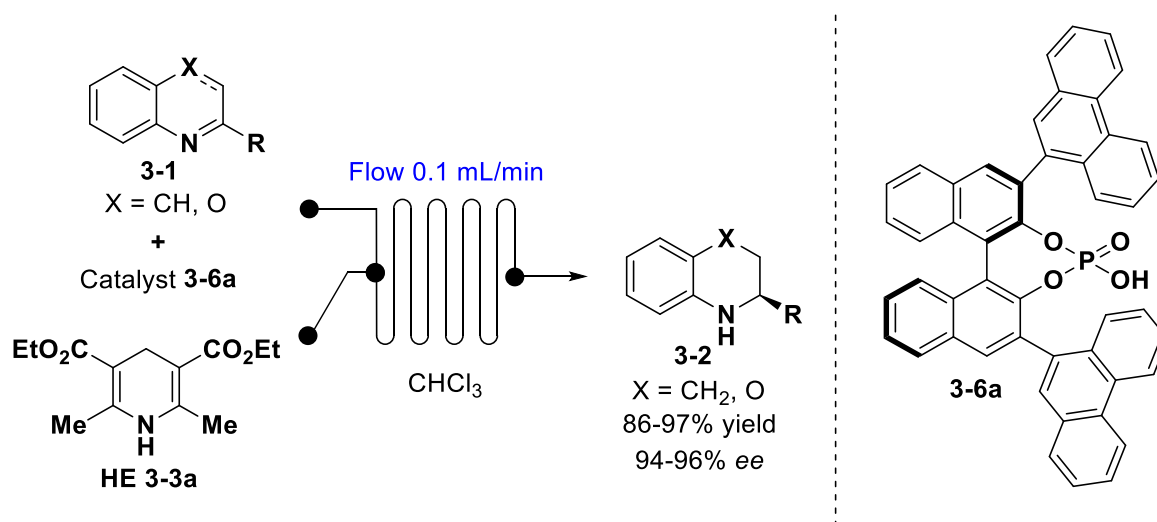


Metal-organic frameworks (MOFs) may also provide a nice alternative for the heterogenization of chiral Brønsted acids resulting in a highly porous catalyst framework as it was discovered by Jiang²⁴ and Liu²⁵ research groups who applied these catalysts towards hydrogenations of imines and benzoxazines. Finally, BINOL CPAs can also be immobilized onto polystyrene brush grafted on SiO₂ nanoparticles, but the applications of such catalysts are limited to enantioselective allylation reactions with allylboronic acid pinacol ester²⁶.

However, despite its great potential, the use of immobilized CPA catalysts for catalysis in continuous flow was not previously explored. The most closely related example of continuous

flow reduction of quinolines and benzoxazines with non-immobilized CPA catalysts was developed by Rueping (Scheme 3.5).²⁷ The flow reaction was performed in a commercial flow microreactor and with the reaction control using a ReactIR flow cell to monitor reaction progress, which allows fast and convenient optimization of reaction parameters. The reaction was homogeneously catalyzed by CPA **3-6a**, resulting in high product yields and selectivity. Despite that, the potential scale-up of such a protocol is limited due to the low flow rate required to achieve high conversions (0.1 mL/min) and the application of homogeneous CPA catalysis that will require large quantities of CPA to be used for big-scale reactions.

Scheme 3.5. Continuous flow reduction of quinolines and benzoxazines.



Therefore, the current chapter is focused on the development of an effective method of continuous flow asymmetric transfer hydrogenation of heterocycles.

3.2 Initial conditions optimization and substrate scope screening

Our initial studies commenced with evaluating the potential of polymeric acids **PS-AdTRIP** and **PS-SPINOL** as well as their monomeric counterparts **3-6b** and **3-8a** for the reduction of quinolines **3-1b** and **3-1c** with various reducing agents (Table 3.1).

Table 3.1. Initial evaluation of immobilized CPAs 3a and 3c for the in batch transfer hydrogenation of 2-substituted quinolines

PS-AdTRIP
Ar = 4-(1-adamantyl)-2,6-(iPr)₂C₆H₂

AdTRIP CPA, **3-6b**

PS-SPINOL
Ar = 3,5-(CF₃)₂C₆H₃

SPINOL CPA, **3-8a**

3-3a, R₁ = Me, R₂ = Et
3-3b, R₁ = Me, R₂ = *t*Bu
3-3c, R₁ = *i*Pr, R₂ = Me

3-4a

3-5a

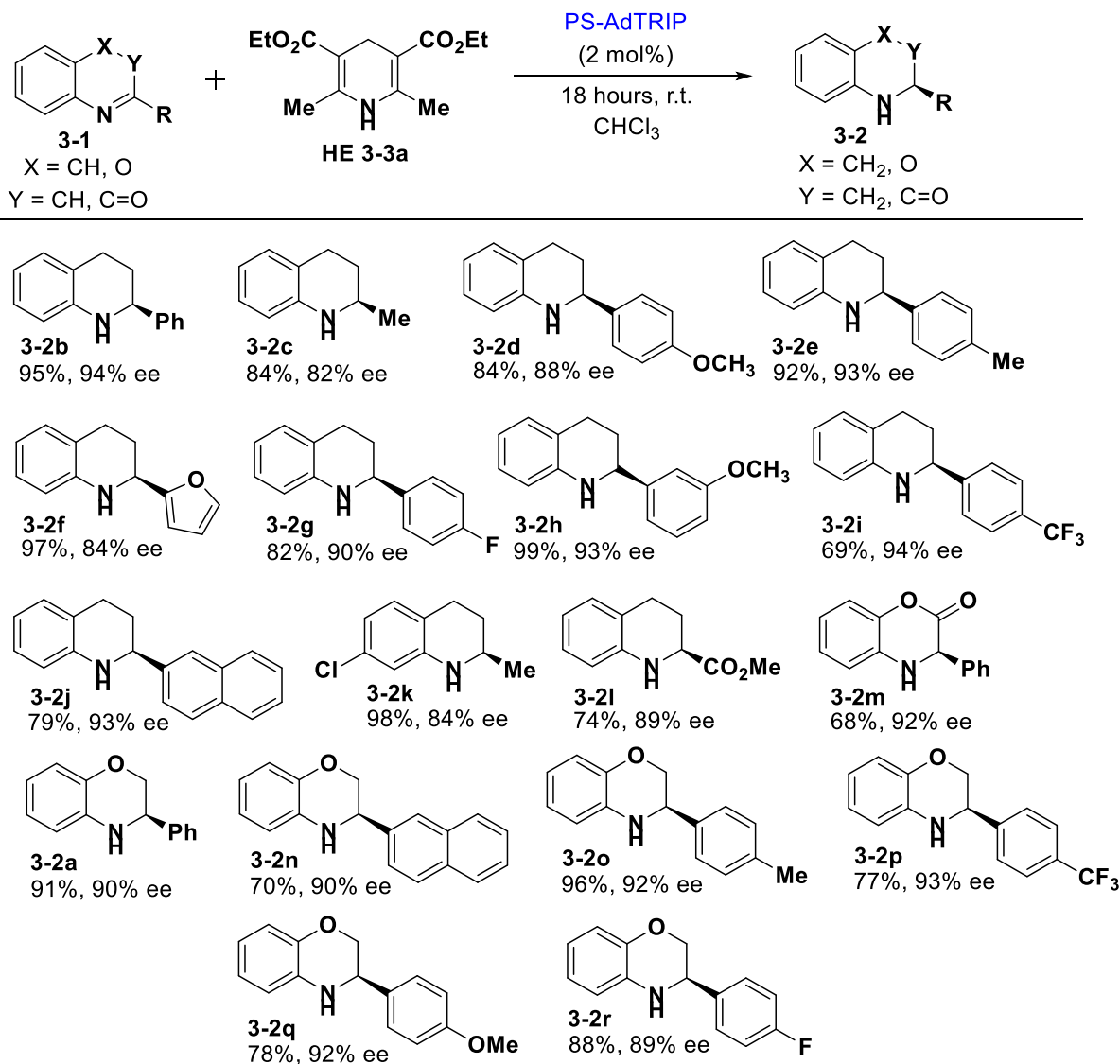
Entry	Catalyst	R	[H]	T, °C	Time, h	Yield, %	ee, %
1	PS-AdTRIP	Ph	3-3a	60	4	90	92
2	PS-AdTRIP	Ph	3-3a	r.t.	18	92	94
3	3-6b	Ph	3-3a	r.t.	18	88	96
4	PS-SPINOL	Ph	3-3a	60	48	71	-42
5	3-8a	Ph	3-3a	60	48	61	-35
6	PS-AdTRIP	Me	3-3a	r.t.	18	84	82
7	3-6b	Me	3-3a	r.t.	18	85	82
8	PS-AdTRIP	Me	3-3b	r.t.	18	86	81
9	PS-AdTRIP	Me	3-3c	60	24	0	-
10	PS-AdTRIP	Me	3-4a	60	24	0	-
11	PS-AdTRIP	Me	3-5a	60	24	0	-

Subjecting **3-1b** to the reduction with Hantzsch ester **3-3a** catalyzed by **PS-AdTRIP** (2 mol%) under the standard conditions developed by Rueping and coworkers¹⁹ (entry 1) resulted in

formation of chiral product **3-2b** in excellent yield and enantioselectivity (90%, 92% ee). The selectivity was further improved to 94% ee by reducing the reaction temperature to r.t. although this increased the reaction time to 18 h (entry 2). Monomeric **Ad-TRIP** catalyst **3-6b** was similarly active under the reaction conditions and provided the chiral product **3-2b** in 88% yield and 98% ee (entry 3). In contrast, SPINOL-based CPAs **PS-SPINOL** and **3-8a** did not demonstrate good catalytic profiles in this reaction, and the formation of **3-2** proceeded with low selectivities and required prolonged reaction times even at 60 °C (entries 4 and 5). Considering that a general catalyst should demonstrate good substrate tolerance, the reduction of 2-methylquinoline (**3-1c**) leading to **3-1c** was evaluated next (entries 6-11). Subjecting **3-1c** to the optimal reduction conditions with **PS-AdTRIP** as the catalyst resulted in the formation of **3-1c** in 84% yield and 82% ee (entry 6). Similar results were also observed with the monomeric catalyst **Ad-TRIP (3-6b)** (entry 7). As demonstrated in the pioneering work by MacMillan¹¹, Hantzsch ester substitution may have a significant impact on the reduction of enantioselectivity. However, further attempts to improve the selectivity by using bulkier Hantzsch esters such as **3-3b** and **3-3c** either resulted in a similar outcome (**3-3b**, entry 8) or no formation of **3-2b** was observed (**3-3c**, entry 9). Similarly, the use of alternative reducing agents **3-4a**¹² and **3-5a**^{13,14} did not result in the formation of **3-2c** (entries 10 and 11).

Based on these studies above, the most optimal reaction conditions from Table 3.1, entry 2 were selected and used to evaluate the scope of the reduction with the polymeric catalyst **PS-AdTRIP** (Scheme 3.6).

Scheme 3.6. Exploration of catalyst PS-AdTRIP (3a) for the in-batch asymmetric reduction of quinolines, 2H-1,4-benzoxazines, and 2H-1,4-benzoxazin-2-ones.

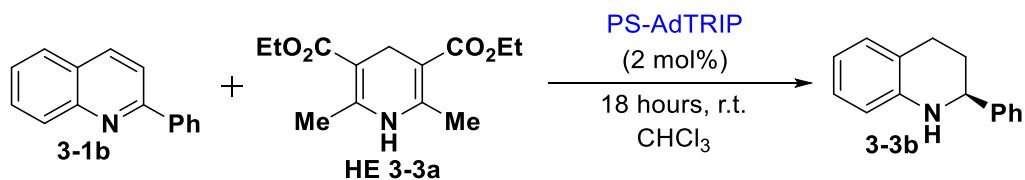


The variation in the C2-aromatic substitution of quinoline **3-1b** was found to be well-tolerated, and chiral products with the phenyl group containing both electron-donating (**3-2d**, **3-2e**, **3-2h**) and electron-withdrawing (**3-2g**, **3-2i**) substituents as well as the 2-furanyl (**3-2f**) and C₂-naphthyl (**3-2j**) groups were obtained with excellent enantioselectivities (84-94% ee). Similarly, modification in the structure of 2-methylquinoline led to minor improvements in enantioselectivities and yields and reduced 7-chloro derivative **3-2k** and 2-carbomethoxy

derivative **3-2l** were obtained in 84% ee and 89% ee, correspondingly. Considering that 2H-1,4-benzoxazines have been previously used as the substrates for the Hantzsch ester transfer hydrogenation with polymeric CPAs, the reduction of various 1,4-benzoxazines was investigated next. When compared side-by-side with their quinoline counterparts, 2H-1,4-benzoxazines **3-2a** **3-2n**, **3-2o**, **3-2p**, and **3-2r** were formed in 1-3% lower ee; however, in the case of the 4-methoxy-group substituted substrate, the formation of 2H-1,4-benzoxazine **3-2q** proceeded with 4% higher enantioselectivity. Finally, to demonstrate that other modifications are tolerated, chiral 2H-1,4-benzoxazin-2-one **3-2m** was produced in 68% yield and 92% ee.

Importantly, catalyst **PS-AdTRIP** was successfully recovered by filtration, washed, and recycled without the loss in activity in all of these studies. Furthermore, to prove the recyclability of the immobilized catalyst, we ran five consecutive reactions of the substrate **3-1b** with the same batch of polymer resin (10 mg). The reaction was performed in a glass funnel with an extra fine glass frit that allowed to run a reaction with the following liquid phase filtration under applied nitrogen pressure (see the experimental section for additional details). This way, 10 mg of the polymer resin stayed in the reaction vessel all the time, and the loss of immobilized CPA due to polymer transfer and filtration was eliminated. All 5 reaction cycles demonstrated no catalytic activity loss of the resin in terms of conversion and enantiomeric excess of product **3-2b** obtained (Table 3.2).

Table 3.2. Recyclability test of immobilized CPA PS-AdTRIP in batch

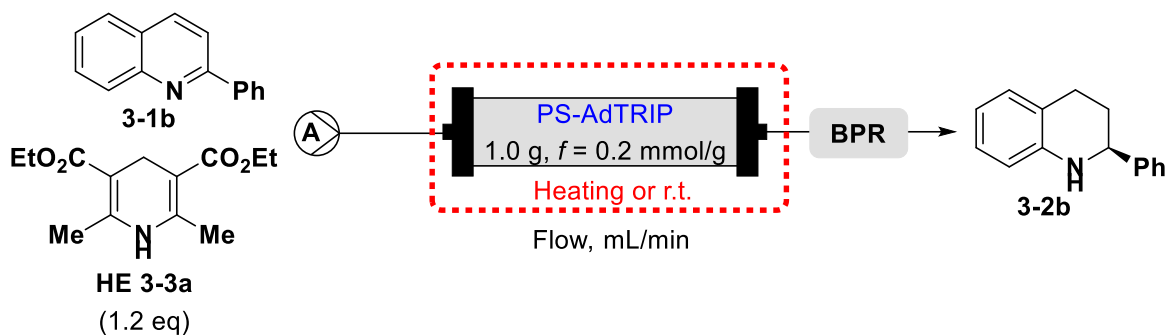


Run #	NMR conv., %	ee, %
1	> 95	94.9
2	> 95	94.4
3	> 95	93.7
4	> 95	94.3
5	> 95	93.8

3.3 Transfer hydrogenation in a continuous flow

With the successful demonstration that **PS-AdTRIP** could be generally employed for the enantioselective synthesis of chiral heterocycles such as **3-2a-r**, we investigated the possibility of carrying such transformations in a continuous flow using a fluidized bed reactor packed with **PS-AdTRIP** (Table 3.3). The initial flow system was assembled with a dual-piston HPLC pump (see Chapter 3.5 for the experimental details) capable of providing flow rates from 0.01 mL/min to 12 mL/min and operating in the 0-12000 psi pressure range. The first attempts to run chloroform as the solvent through the stainless steel HPLC columns (with I.D. of 2.1 and 4.6 mm) packed with 0.5 g of immobilized resin were unsuccessful due to significant back pressure buildup in the system (> 2000 psi). This observation can be explained by the fact that dry polymer resin swells when solubilized thus clogging the column outlets. Another possible reason is that the small column diameter contributed to the pressure build up inside of the system. To minimize these effects, we employed Omnifit® glass column with I.D 10 mm and two adjustable end pieces. After packing the column with 1.0 g of **PS-AdTRIP** resin and starting the flow of the solvent, the packed-bed reactor size was adjusted to accommodate a bigger volume of swelled polymeric resin.

Table 3.3. Optimization of the continuous flow transfer hydrogenation



Entry	T, °C	Flow, mL/min	Residence time, min	BPR, psi	NMR conv, %	ee, %
1	60	0.05	31.4	50	Full	78
2	60	0.1	15.7	50	Full	78
3	60	0.15	10.5	50	Full	80
4	60	0.2	7.9	50	Full	80
5	45	0.1	15.7	-	Full	88
6	45	0.2	7.9	-	Full	90
7	r.t.	0.2	7.9	-	Full	90
8	r.t.	0.5	3.14	-	Full	97
9	r.t.	0.75	2.1	-	Full	98
10	r.t.	1.0	1.6	-	Full	98
11	r.t.	1.5	1.0	-	Full	98
12	r.t.	2.0	0.8	-	Full	98
13	r.t.	2.5	0.6	-	Full	98
14	r.t.	3.0	0.5	-	96%	98

This setup allowed us to operate the flow system with 0.01-2.5 mL/min flow rate with minimal back pressure build-up (<350 psi). To perform the reaction, a solution of **3-1b** (50 mM) and **3-3a** (120 mM) in CHCl₃ was pumped through the packed column. A back pressure regulator (BPR) was used in the system to allow heating and maintain stable pressure (and as a result – stable flow rate) in the system without solvent vaporization in flow lines. Our initial studies focused on

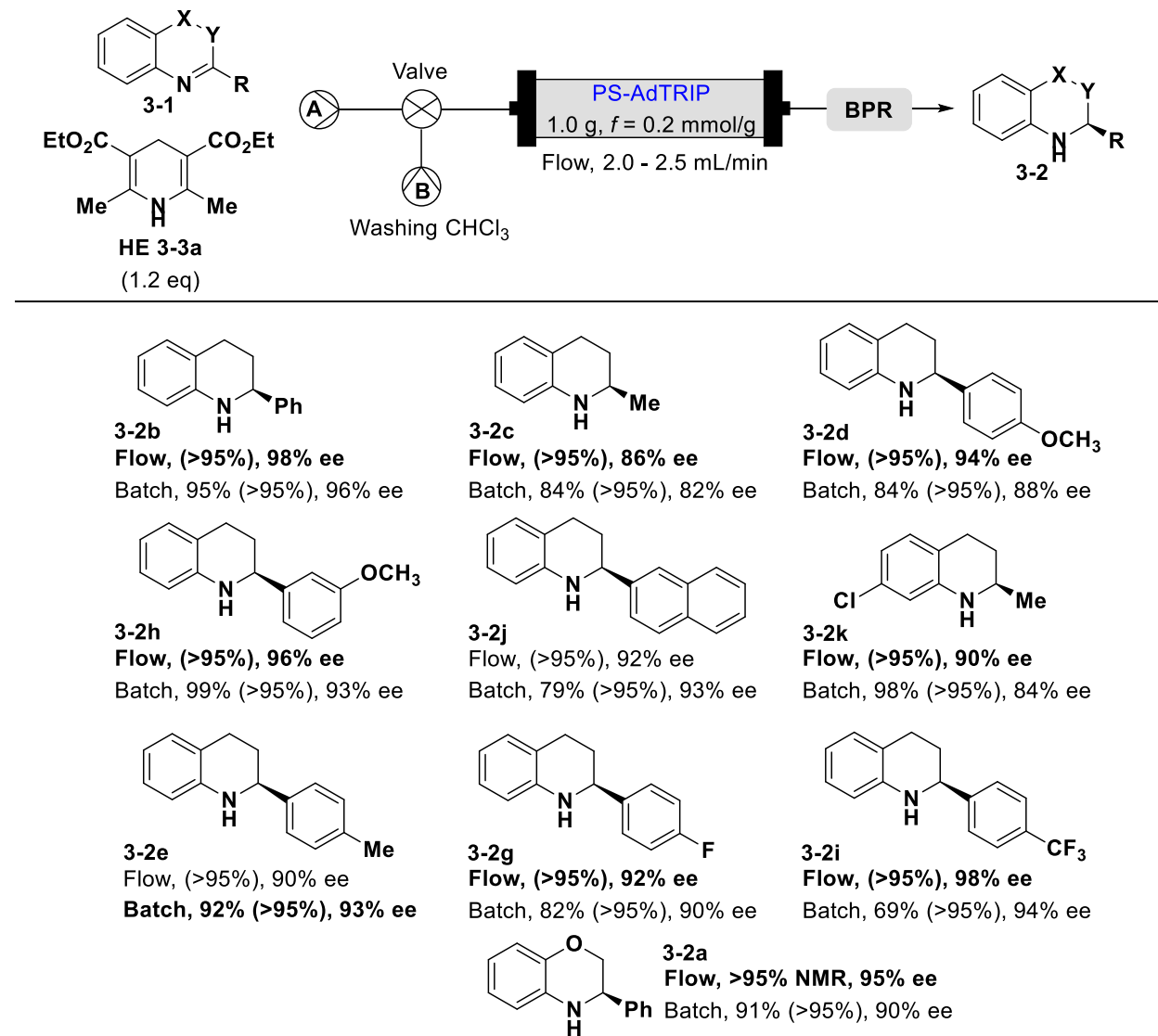
identifying the optimal temperature and flow rate. The related studies on CPA-catalyzed continuous flow allylation and thiol addition reactions by the Pericas group²⁸⁻³⁰ utilized flow rates in the range of 0.2-0.5 mL/min, and we initially evaluated similar flow rates (0.05 to 0.2 mL/min) at 60 °C (entries 1-4)

While the formation of **3-2b** proceeded with full conversion in all these cases, the observed enantioselectivities were significantly lower than the observed 92% ee value for the in-batch reduction at 60 °C carried earlier (Table 3.1, entry 1). Lowering the reaction temperature to 45 °C led to a significant improvement in enantioselectivity, and **3-2b** was obtained in 88% ee at flow rates equal to 0.1 mL/min (entry 5) and 90% ee with the flow rates of 0.2 mL/min (entry 6). Further decreasing temperature to room temperature (r.t.) did not result in diminished conversion; however, no increase in enantioselectivity was observed (entry 7). The results above suggest that the reduction of **3-1b** over the bed of **PS-AdTRIP** in continuous flow is a fast process even at room temperature; however, improved enantioselectivity is consistently observed at higher flow rates. This may result from the reduction becoming reversible in the presence of the excess of catalyst **PS-AdTRIP**, which leads to the epimerization of the product.^{31,32} Such epimerization process should be suppressed if **3-2b** residual time on the surface of **PS-AdTRIP** is lowered, which may be achieved at higher flow rates. Indeed, increasing the flow rate has led to a significant increase in enantioselectivity for the formation of **3-2b** (entries 8-14). Remarkably, the reaction was found to proceed to a significant extent even at flow rates as high as 2.5 mL/min, and the product **3-2b** was obtained in 98% ee and 94% conversion (entry 13). Further increase in the flow rate to 3.0 mL/min resulted in slightly lower conversion (91%), but similar enantioselectivity 98% ee (entry 14).

It should be noted that the overall increase of the flow rate from 0.2 mL/min to 2.5 mL/min has led to +8% increase in enantioselectivity, and the enantioselectivity in continuous flow (98% ee) is higher than in batch (94% ee). It is also noteworthy that achieving high flow rates of 2.5 mL/min enables generating ~1.5 g (7.5 mmol) of **3-2b** per hour, which is a significant improvement in terms of the throughput when compared to the related processes.

With the optimized conditions in hand, our subsequent studies focused on demonstrating that the same Omnifit® column containing **PS-AdTRIP** catalyst could be used continuously to generate multiple chiral products **3-2b** (Scheme 3.7).

Scheme 3.7. Continuous flow transfer hydrogenation of nitrogen-containing heterocyclic compounds.



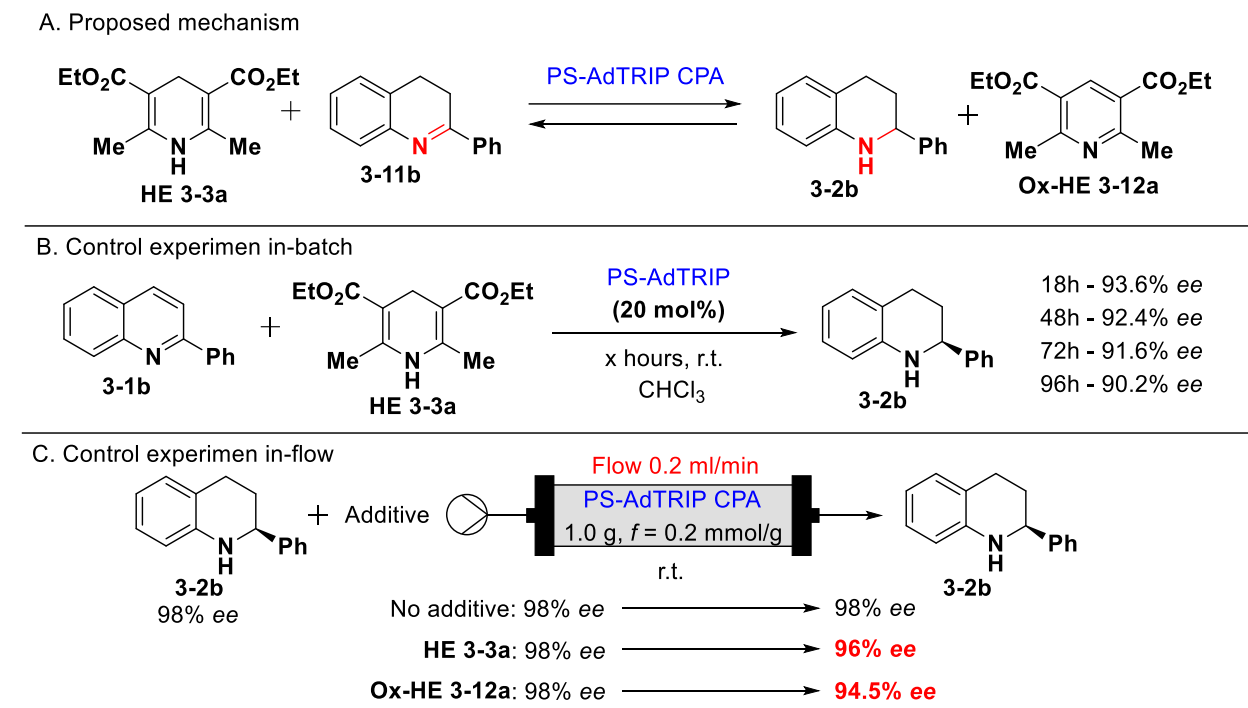
Thus, the original continuous flow set up was modified to introduce a line with washing solvent (CHCl_3) that was used to wash the reactor containing **PS-AdTRIP** between the runs. After the consumption of the reaction mixture containing heterocycle (1.0 mmol) and **3-3a** (2.4 mmol), the resin **PS-AdTRIP** was washed for 10 minutes, and then the next reaction mixture containing a different heterocyclic compound was introduced. Remarkably, in almost all the evaluated cases, a significant improvement in enantioselectivity for the continuous flow process in comparison to

the reduction in the batch was observed (Scheme 3.7). Thus, substrates **3-2a-3-2d**, **3-2h-3-2k**, **3-2e**, **3-2g**, and **3-2i** were generated with the improvement in the range of +4-6% ee. It should be noted that for substrates **3-2e** and **3-2j**, minor erosion in the ee was noted (-3% and -1%, correspondingly); however, further optimization of the flow rate for **3-2e** and **3-2j** may improve the enantioselectivity of the flow process. Importantly, all of the chiral substrates in Scheme 3.7 were generated using the same reactor containing **PS-AdTRIP** in less than 48 h.

To confirm the hypothesis that lower product enantiopurities observed at lower flow rates are due to the epimerization arising from the oxidation of chiral product **3-2b** with the oxidized Hantzsch ester Ox-HE **3-12a** (Scheme 3.8), the controlled experiments summarized in Schemes 3.8B and 3.8C were performed. The reaction of substrate **3-1b** and Hantzsch ester **3-3a** was carried in batch in the presence of 20 mol% of **PS-AdTRIP**, and the enantioselectivity was monitored at different times (Scheme 3.8B). As previously observed, the formation of product **3-2b** was complete after 18 h (93.6% ee). However, the continued exposure of the reaction mixture to catalyst **PS-AdTRIP** indeed resulted in lower enantiopurity, and 90.2% ee was observed after 96 h. Subsequently, the continuous flow experiments in Scheme 3.8C were performed with the flow rate of 0.2 mL/min. When enantioenriched product **3-2b** (98% ee) was passed through the column containing **PS-AdTRIP**, no change in enantiopurity was detected. At the same time, when the mixture of **3-2b** (98% ee) and Hantzsch ester **3-3a** was passed through the reactor containing **PS-AdTRIP**, a minor reduction of enantiopurity of **3-2b** to 96% ee was observed. Finally, when the mixture of **3-2b** (98% ee) and oxidized Hantzsch ester Ox-HE **3-12a** was passed through **PS-AdTRIP**, more significant epimerization was observed, and **3-2b** was isolated with 94.5% ee. These studies shed light onto the origins of the observed enantioselectivity dependence on flow

rates and highlight the improvements in enantioselective catalysis obtained with continuous flow setup.

Scheme 3.8. Control experiments to determine the origins of enantioselectivity erosion at low flow rates.



3.4 Conclusions

Simple aromatic heterocycles are employed as the feedstock building blocks for the synthesis of more complex heterocycle-containing therapeutics. Therefore, developing reliable methods for the asymmetric hydrogenation of some simple and common heterocycles, such as pyridines, quinolines, indoles, benzoxazines, etc. represents an important challenge in asymmetric catalysis. While there are various methods available for achieving highly enantioselective hydrogenation of aromatic compounds with direct usage of H₂ gas, the approaches relying on transition metal-catalyzed hydrogenation may suffer from different drawbacks, such as scalability, safety, and catalyst poisoning/recyclability. On the other hand, the methods based on using

organocatalysts and simple organic molecules as reducing agents may provide safer alternatives. In the past two decades, multiple research groups described protocols for enantioselective transfer hydrogenation catalyzed by CPAs and relying on Hantzsch esters as the reducing agent. Despite precedents of using immobilized CPAs that addressed issue of catalyst recycling and recovering, no cases of applying flow chemistry methods for heterogeneous heterocycles hydrogenation was described.

In summary, this chapter described the transfer hydrogenation of nitrogen-containing heterocycles with polymeric chiral phosphoric acid **PS-AdTRIP** both in batch and in continuous flow. **PS-AdTRIP** was used as a recyclable catalyst for in-batch enantioselective reduction of various quinolines, *2H*-1,4-benzoxazines, and *2H*-1,4-benzoxazin-2-ones using Hantzsch ester **3-3a** as the reducing agent. A continuous flow variant of this protocol features generally improved enantioselectivity when carried at high flow rates (2.0-2.5 mL/min or 7.5 mmol/h) and enables highly selective asymmetric reduction of ten different chiral heterocyclic products in less than 48 hours using the same fluidized bed reactor containing **PS-AdTRIP**. High flow rates and no need of catalyst regeneration during these studies demonstrated advantages of using flow chemistry methods for asymmetric reduction of heterocycles in comparison to previously published work dealing with in-batch conditions. Further studies revealed possible mechanisms of epimerization of reduced quinolines and benzoxazines promoted by immobilized **PS-AdTRIP**. The subsequent experiments suggested that improvements in stereoselectivity at high flow rates may stem from less significant epimerization in continuous flow than in batch.

3.5 Experimental information

Methods and reagents: Unless otherwise noted, all reagents were purchased from commercial suppliers and used without further purification. Chloroform (CHCl₃) was filtered through a column

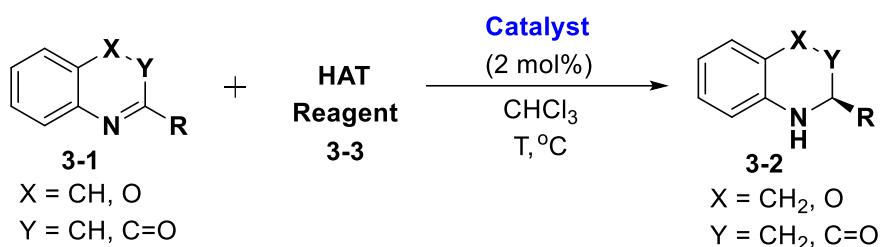
(Innovative Technology PS-MD-5) of activated alumina under a nitrogen atmosphere. All reactions were carried out under an atmosphere of nitrogen in oven-dried glassware with magnetic stirring. Heating was achieved by the use of a metal heating block with heating controlled by an electronic contact thermometer. Reactions were monitored by nuclear magnetic resonance (NMR) or thin layer chromatography (TLC) on silica gel precoated glass plates (0.25 mm, SiliCycle, SiliaPlate). TLC plate visualization was accomplished by irradiation with UV light at 254 nm or by staining with a cerium ammonium molybdate (CAM) solution. Continuous flow experiments were performed using Masterflex Constant Pressure Dual Piston Pump, Diba Omnifit EZ Solvent Plus Glass Column (10x100 mm, with two adjustable endpieces) and Zaiput Back-Pressure Regulator BPR-10. Column heating was performed using an aluminum beads bath. Deionized water was used in the preparation of all aqueous solutions and for all aqueous extractions. Solvents used for chromatography were ACS or HPLC grade. Purification of reaction mixtures was performed by flash column chromatography on SiO₂ using SiliCycle SiliaFlash P60 (230-400 mesh) to pack the columns for the Teledyne ISCO CombiFlash Rf+ purification system. Enantiomeric excess was determined by HPLC analysis using a Waters e2695 Separations Module with a Waters 2998 photodiode array detector.

Instrumentation: All spectra were recorded on Bruker Avance Neo 500 (500 MHz) spectrometer and chemical shifts (δ) are reported in parts per million (ppm) and referenced to the ¹H signal of the internal tetramethylsilane according to IUPAC recommendations. Data are reported as (br = broad, s = singlet, d = doublet, t = triplet, q = quartet, qn = quintet, sext = sextet, m = multiplet; coupling constant(S) in Hz; integration). High-resolution mass spectra (HRMS) were recorded on MicromassAutoSpecUltima or VG (Micromass) 70-250-S Magnetic sector mass spectrometers in

the University of Michigan mass spectrometry laboratory. Optical rotations were measured at room temperature in a solvent of choice on a JASCO P-2000 digital polarimeter at 589 nm (D-line).

Procedure A. Asymmetric HAT with Polymer-Supported Chiral Phosphoric Acid.

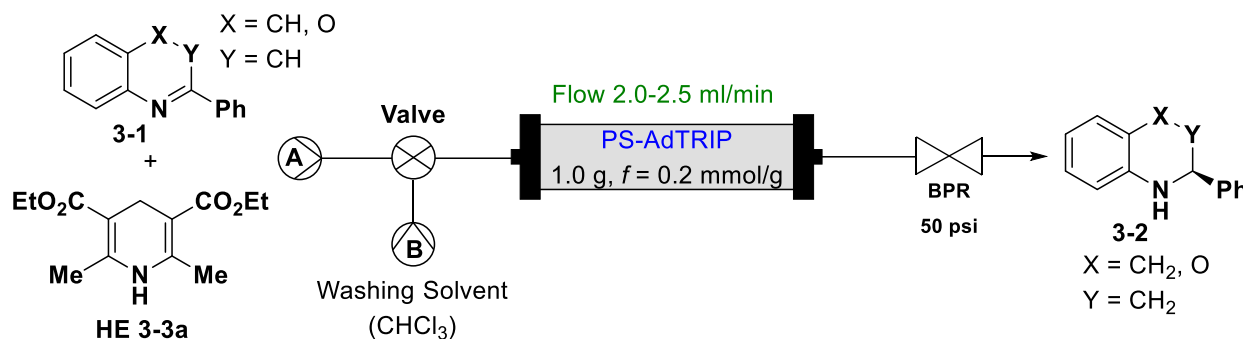
Scheme 3.9. General procedure for the asymmetric reduction in batch



An oven-dried vial was charged with a magnetic stir bar, polymer-supported catalyst **PS-AdTRIP CPA** (10 mg, $f = 0.2$ mmol/g, 200 μmol , 2 mol%), the corresponding substrate **3-1** (0.1 mmol) and the appropriate amount of reducing agent **HAT** (0.12 mmol or 0.24 mmol depending on substrate **3-1**). The vial was capped with a septum, attached to the Schlenk line using a 22G needle, and then evacuated and refilled with nitrogen 3 times. After that, 2 mL of CHCl_3 was added through the septum, and the vial was placed on the stir plate (a metal heating block was used when the heating was required). The reaction mixture was stirred for 18 hours after which TLC indicated the full consumption of the starting material. After that reaction mixture was filtered to isolate the immobilized catalyst that was subsequently washed with 2-3 mL of DCM. Filtrate was concentrated under reduced pressure and crude was analyzed via NMR to determine conversion. Purification was performed using a CombiFlash Chromatograph system on SiO_2 using Hexane and EtOAc as solvents and gradient from 95:5 to 80:20 over 15 minutes. The identity of the purified product was confirmed by NMR and ESI-HRMS and its enantiomeric excess was analyzed by HPLC (using the appropriate chiral column, see details below). **Note:** In the case of immobilized catalyst **PS-SPINOL**, 17 mg (204 μmol , 2 mol%) of resin was used due to lower functionality $f = 0.12$ mmol/g.

Procedure B. Continuous flow setup for Asymmetric Transfer Hydrogenation using Polymer-Supported Chiral Phosphoric Acid catalyst.

Scheme 3.10. General scheme of continuous flow setup for the transfer hydrogenation of heterocycles.

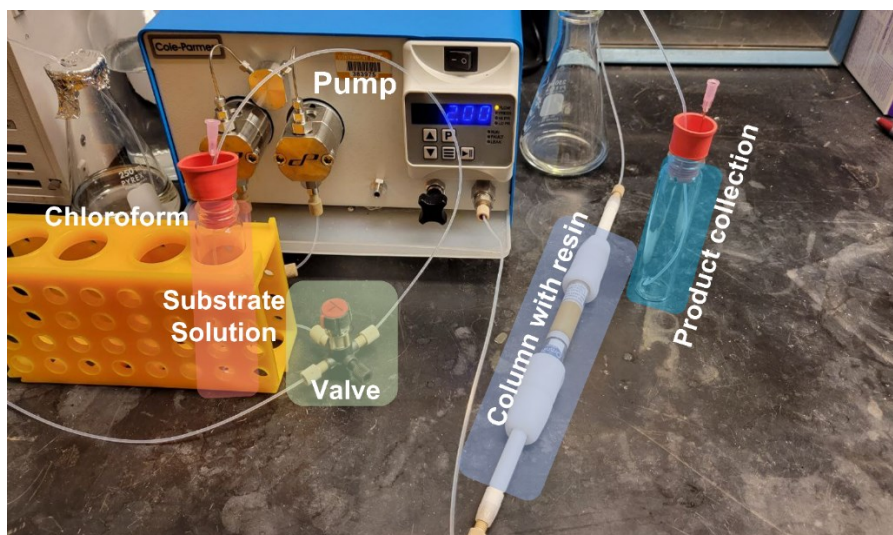


Assembly: A Masterflex Constant Pressure Dual Piston Pump was used to pump the solvents and reaction solutions through the system. A 4-way T-Valve was connected to the pump input line to switch the flow input between the reactant solution (**A**) and washing solvent (**B**) to prime and wash the system between runs. The output of the piston pump was connected to the Diba Omnifit EZ Solvent Plus Glass Column (10x100 mm, with two adjustable endpieces). The column can be heated if needed using an aluminum-beads heating bath and Zaiput Back-Pressure Regulator BPR-10 can be added to the flow system to maintain the constant pressure during the run.

Reaction setup: Polymer-supported catalyst (**PS-AdTRIP**, 1.0 g, $f = 0.2$ mmol/g) was placed in Omnifit Glass Column and the stream of the CHCl₃ was pumped at 0.5 mL/min for 2 hours to swell the resin inside the column. After that column endpieces were adjusted to fit the volume of swelled polymer. The reaction solution containing 1 mmol of the corresponding heterocycle **3-1** and 2.4 mmol of the Hantzsch ester **3-3a** (1.2 mmol if only mono reduction is needed) in 20 mL of CHCl₃ was placed in a 40-mL glass vial and connected to the pump input **A**. Reactants solution was pumped through the system at required flow rate and reaction products were collected in 40-

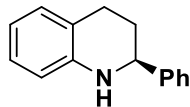
mL glass vial. After full consumption of the reagents solution, the valve was switched to position **B**, and the CHCl_3 was pumped through the system with the same flow rate for 10 minutes to wash out all reaction products from the pump lines and column and was collected into the vial with products. After that system is ready for the new run and the next reagent solution is plugged into position **A**. The Collected solution after the flow run was concentrated under reduced pressure and purified using the CombiFlash Chromatograph system on SiO_2 using Hexane and EtOAc as solvents and gradient from 95:5 to 80:20 over 15 minutes.

Figure 3.1. Photo of the pump setup for synthesis in-flow



3.5.1 Products characterization data

(S)-2-phenyl-1,2,3,4-tetrahydroquinoline (3-2b)



Known compound³³, white solid, 19.8 mg, 95% yield, >95% NMR conv. in-flow (2.5 mL/min), 94% ee (batch), 98% ee (in-flow)

$^1\text{H NMR}$ (500 MHz, Chloroform- d) δ 7.44 – 7.38 (m, 2H), 7.37 (dd, $J = 8.5, 6.6$ Hz, 2H), 7.34 – 7.27 (m, 1H), 7.03 (t, $J = 7.5$ Hz, 2H), 6.67 (td, $J = 7.4, 1.2$ Hz, 1H), 6.58 – 6.53 (m, 1H), 4.46 (dd, $J = 9.4, 3.3$ Hz, 1H), 4.05 (s, 1H), 2.94 (ddd, $J = 16.3, 10.7, 5.5$ Hz, 1H), 2.75 (dt, $J = 16.3, 4.8$ Hz, 1H), 2.18 – 2.10 (m, 1H), 2.01 (dddd, $J = 12.9, 10.6, 9.3, 5.0$ Hz, 1H).

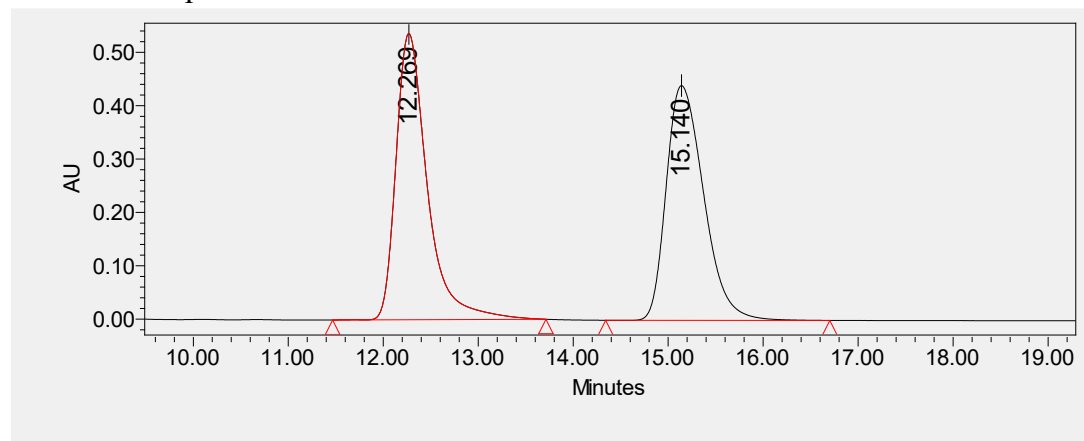
^{13}C NMR (126 MHz, Chloroform- d) δ 144.94, 144.86, 129.43, 128.70, 127.57, 127.03, 126.67, 121.00, 117.28, 114.10, 77.41, 77.16, 76.91, 56.39, 31.11, 26.51.

HRMS (ESI+) (m/z): $[\text{M}+\text{H}]^+$ calcd for $\text{C}_{15}\text{H}_{15}\text{NH}^+$ 210.1277, found 210.1273;

$[\alpha]^{24}_{\text{D}} = -38.8^\circ$ ($c = 0.05\text{M}$, CH_3Cl).

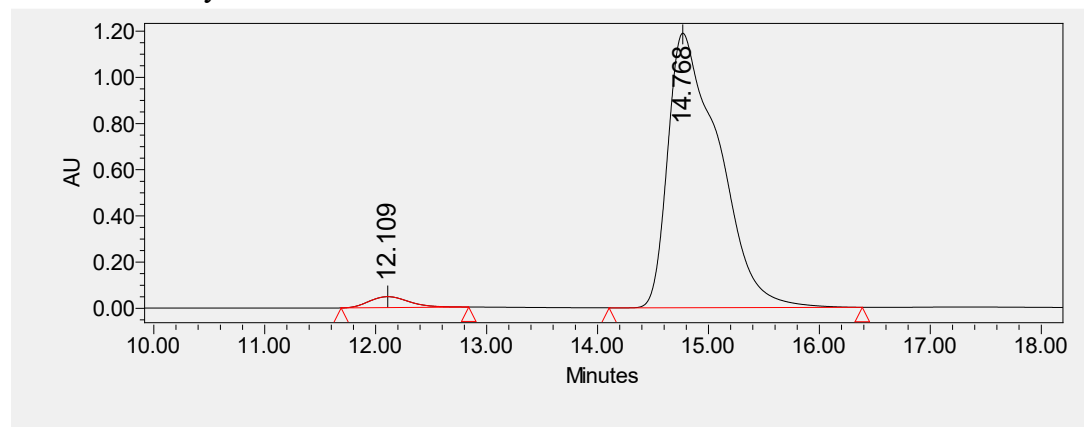
HPLC: Chiralpak IA column, 98:2 hexanes/isopropanol, 0.5 ml/min, $t_r = 12.1$ min (minor, R), 15.1 min (major, S)

Racemic compound HPLC Traces:



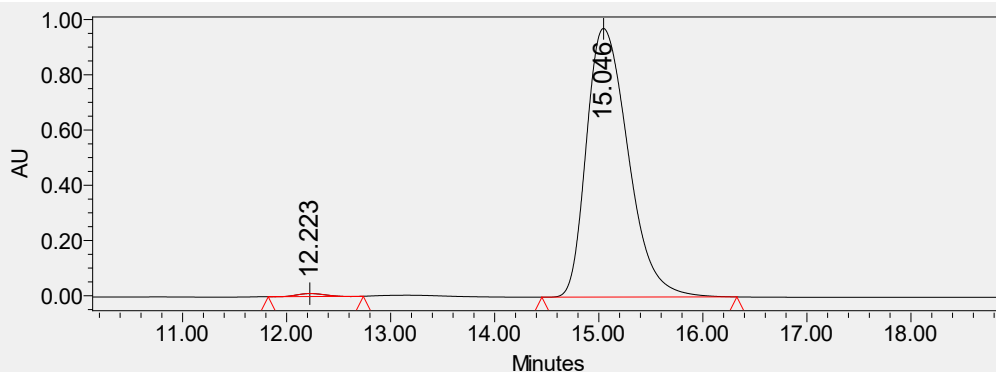
	Retention Time	Area	% Area	Height
1	12.269	12284705	50.49	536431
2	15.140	12048497	49.51	439937

Enantiomeric synthesis in-batch HPLC Traces:



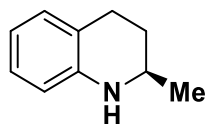
	Retention Time	Area	% Area	Height
1	12.109	1186144	3.02	47247
2	14.768	38049168	96.98	1188404

Enantiomeric synthesis in-flow HPLC Traces:



	Retention Time	Area	% Area	Height
1	12.223	196587	0.72	10671
2	15.046	27181156	99.28	972900

(R)-2-methyl-1,2,3,4-tetrahydroquinoline (3-2c)



Known compound³⁴, yellow oil, 12.4 mg, 84% yield, 94% NMR conv. in flow (2.5 mL/min), 82% ee (batch), 86% ee (in-flow)

¹H NMR (500 MHz, Chloroform-d) δ 6.97 (tdd, $J = 6.5, 2.4, 1.3$ Hz, 2H), 6.62 (td, $J = 7.4, 1.2$ Hz, 1H), 6.48 (dd, $J = 8.4, 1.3$ Hz, 1H), 3.68 (s, 1H), 3.41 (dtd, $J = 12.6, 6.3, 2.9$ Hz, 1H), 2.90 – 2.80 (m, 1H), 2.74 (ddd, $J = 16.4, 5.4, 3.5$ Hz, 1H), 1.98 – 1.90 (m, 1H), 1.60 (dddd, $J = 12.8, 11.6, 9.9, 5.3$ Hz, 1H), 1.22 (d, $J = 6.2$ Hz, 3H).

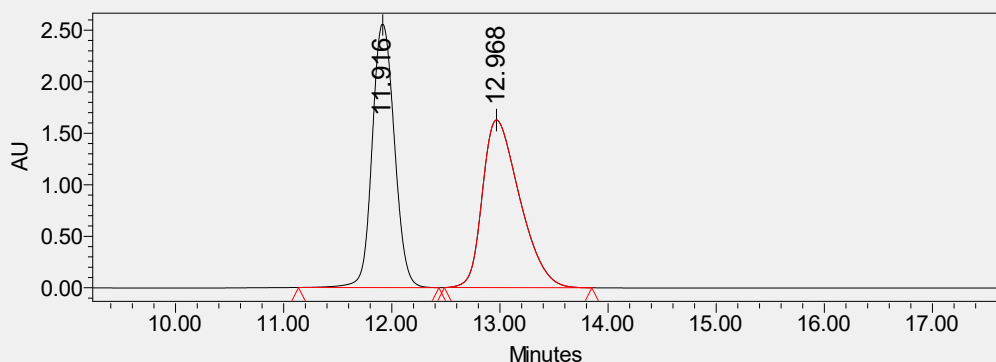
¹³C NMR (126 MHz, Chloroform-d) δ 144.90, 129.40, 126.82, 121.23, 117.10, 114.12, 77.41, 77.16, 76.91, 47.29, 30.26, 26.73, 22.75.

HRMS (ESI+) (m/z): $[M+H]^+$ calcd for C₁₀H₁₃NH⁺ 148.1121, found 148.1117;

$[\alpha]^{24}_D = +83.3^\circ$ ($c = 0.04M$, CH₃Cl).

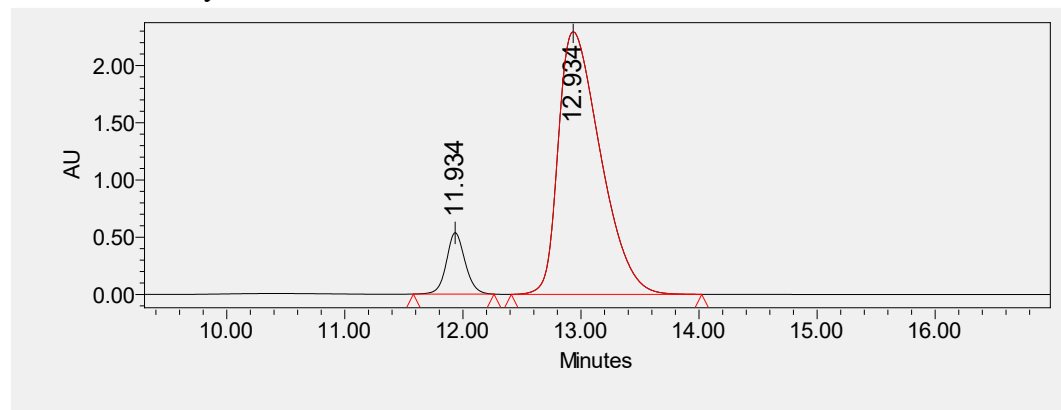
HPLC: Chiralpak OJ-H column, 95:5 hexanes/isopropanol, 1.0 ml/min, tr = 11.9 min (minor, *S*), 12.9 min (major, *R*)

Racemic compound HPLC Traces:



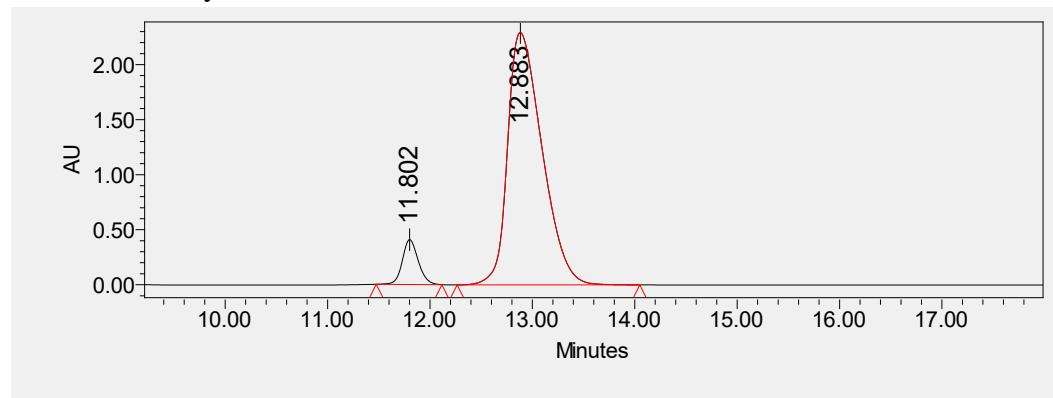
	Retention Time	Area	% Area	Height
1	11.916	36511269	48.43	2553729
2	12.968	38880775	51.57	1626345

Enantiomeric synthesis in-batch HPLC Traces:



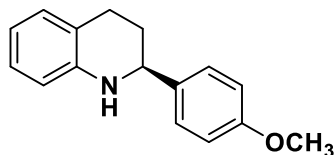
	Retention Time	Area	% Area	Height
1	11.934	5680868	9.05	535891
2	12.934	57091154	90.95	2293638

Enantiomeric synthesis in-flow HPLC Traces:



	Retention Time	Area	% Area	Height
1	11.802	4001534	6.89	407376
2	12.883	53991725	93.11	2291974

(S)-2-(4-methoxyphenyl)-1,2,3,4-tetrahydroquinoline (3-2d)



Known compound³³, white solid, 20.1 mg, 84% yield, >95% NMR conv. in flow (2.0 mL/min), 88% ee (batch), 94% ee (in-flow)

¹H NMR (500 MHz, Chloroform-d) δ 7.36 – 7.29 (m, 2H), 7.02 (tt, J = 7.2, 1.2 Hz, 2H), 6.94 – 6.87 (m, 2H), 6.66 (td, J = 7.4, 1.2 Hz, 1H), 6.54 (dd, J = 8.4, 1.2 Hz, 1H), 4.39 (dd, J = 9.6, 3.2

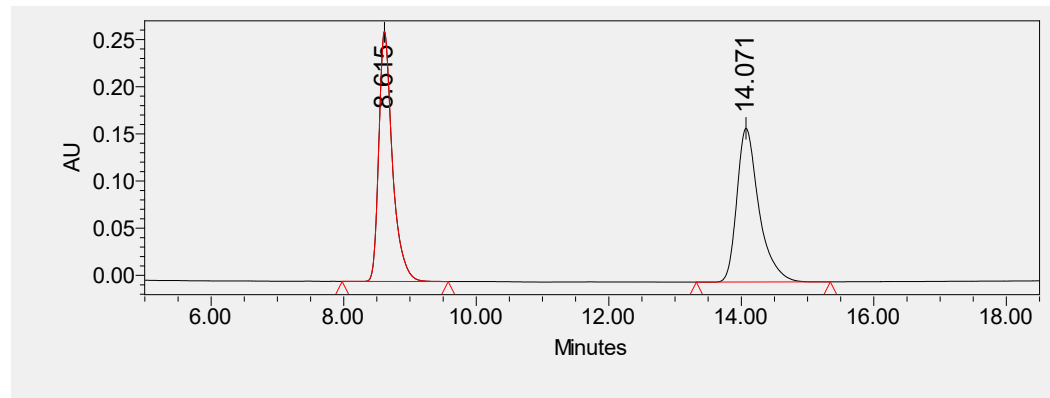
Hz, 1H), 3.99 (s, 1H), 3.82 (s, 3H), 2.94 (ddd, $J = 16.4, 11.0, 5.5$ Hz, 1H), 2.75 (dt, $J = 16.3, 4.6$ Hz, 1H), 2.10 (dddd, $J = 12.9, 5.5, 4.2, 3.2$ Hz, 1H), 1.98 (dddd, $J = 12.9, 10.9, 9.6, 5.0$ Hz, 1H).
 ^{13}C NMR (126 MHz, Chloroform- d) δ 159.08, 144.95, 137.01, 129.41, 127.76, 126.98, 121.00, 117.23, 114.08, 114.04, 77.41, 77.16, 76.91, 55.85, 55.45, 31.23, 26.68.

HRMS (ESI+) (m/z): $[\text{M}+\text{H}]^+$ calcd for $\text{C}_{16}\text{H}_{17}\text{NOH}^+$ 240.1383, found 240.1375;

$[\alpha]^{24}_{\text{D}} = -21.3^\circ$ ($c = 0.04\text{M}$, CH_3Cl).

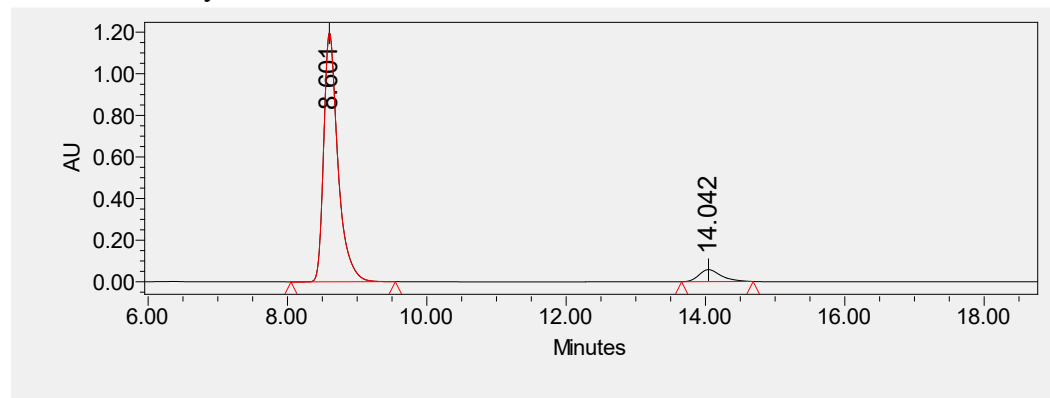
HPLC: Chiralpak OD-H column, 90:10 hexanes/isopropanol, 1.0 ml/min, $t_r = 8.6$ min (major, R), 14.0 min (minor, S)

Racemic compound HPLC Traces:



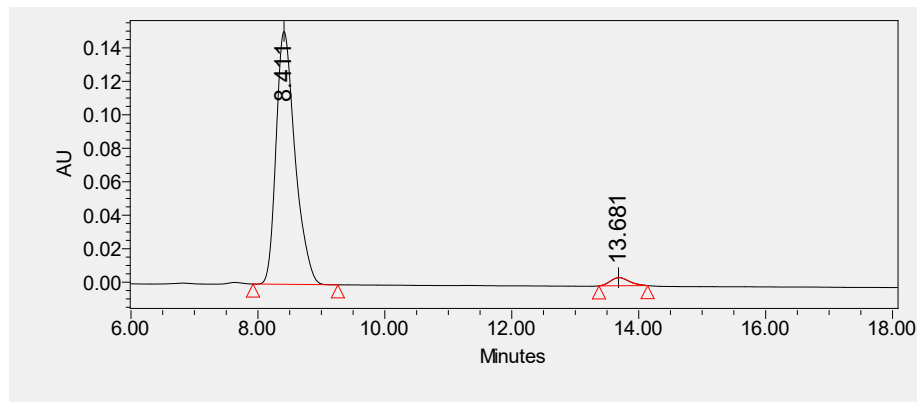
	Retention Time	Area	% Area	Height
1	8.615	3767635	50.03	265021
2	14.071	3763313	49.97	163011

Enantiomeric synthesis in-batch HPLC Traces:



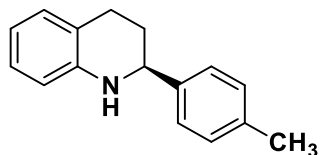
	Retention Time	Area	% Area	Height
1	8.601	16952618	93.00	1196833
2	14.042	1275881	7.00	57668

Enantiomeric synthesis in-flow HPLC Traces:



	Retention Time	Area	% Area	Height
1	8.411	3136025	96.93	151064
2	13.681	99361	3.07	4877

(S)-2-(p-tolyl)-1,2,3,4-tetrahydroquinoline (3-2e)



Known compound³³, white solid, 20.5 mg, 92% yield, 92% NMR conv in-flow (2.5 mL/min), 93% ee (batch), 90% ee (in-flow)

¹H NMR (500 MHz, Chloroform-d) δ 7.33 – 7.28 (m, 2H), 7.19 (d, J = 7.8 Hz, 2H), 7.03 (t, J = 7.2 Hz, 2H), 6.67 (td, J = 7.4, 1.2 Hz, 1H), 6.57 – 6.52 (m, 1H), 4.42 (dd, J = 9.5, 3.2 Hz, 1H), 4.02 (s, 1H), 2.94 (ddd, J = 16.3, 10.8, 5.5 Hz, 1H), 2.76 (dt, J = 16.3, 4.7 Hz, 1H), 2.38 (s, 3H), 2.12 (dddd, J = 13.0, 5.4, 4.3, 3.2 Hz, 1H), 2.00 (dddd, J = 12.9, 10.7, 9.5, 5.0 Hz, 1H).

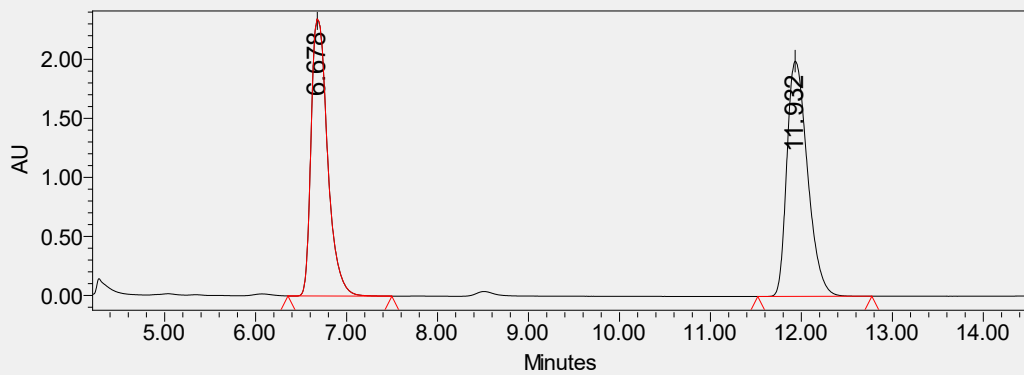
¹³C NMR (126 MHz, Chloroform-d) δ 144.93, 141.95, 137.21, 129.40, 129.36, 126.99, 126.58, 121.00, 117.20, 114.06, 77.41, 77.16, 76.91, 56.14, 53.56, 31.15, 26.61, 21.23.

HRMS (ESI+) (m/z): $[M+H]^+$ calcd for C₁₆H₁₇NH⁺ 224.1434, found 224.1431;

$[\alpha]^{24}_D = -25.5^\circ$ ($c = 0.05M$, CH₃Cl).

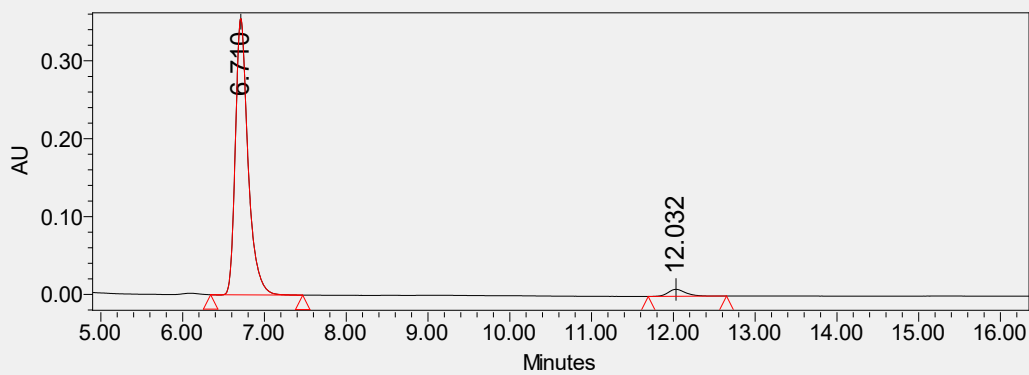
HPLC: Chiralpak OD-H column, 90:10 hexanes/isopropanol, 1.0 ml/min, tr = 6.7 min (major, *S*), 11.9 min (minor, *R*)

Racemic compound HPLC Traces:



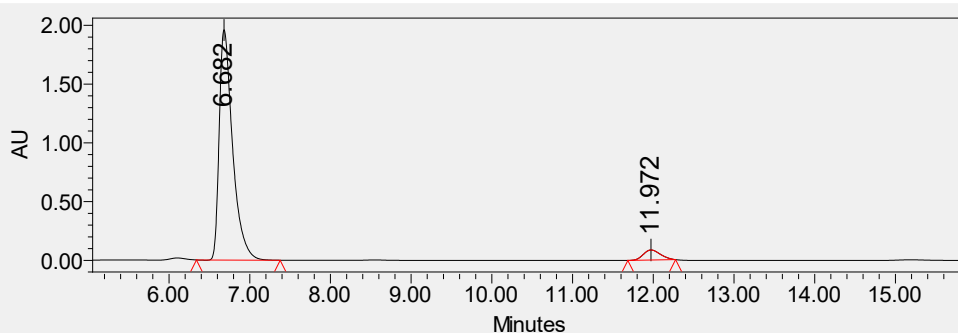
	Retention Time	Area	% Area	Height
1	6.678	29502261	48.47	2347538
2	11.932	31370104	51.53	1991519

Enantiomeric synthesis in-batch HPLC Traces:



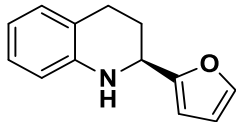
	Retention Time	Area	% Area	Height
1	6.710	3819669	96.60	354915
2	12.032	134298	3.40	8918

Enantiomeric synthesis in-flow HPLC Traces:



	Retention Time	Area	% Area	Height
1	6.682	22540651	94.70	1960042
2	11.972	1262344	5.30	85755

(S)-2-(furan-2-yl)-1,2,3,4-tetrahydroquinoline (3-2f)



Known compound³⁵, yellow solid, 19.3 mg, 97% yield, 84% ee (batch).

¹H NMR (500 MHz, Chloroform-d) δ 7.38 (d, $J = 2.0$ Hz, 1H), 7.04 – 6.96 (m, 2H), 6.66 (td, $J = 7.4, 1.2$ Hz, 1H), 6.56 (dd, $J = 7.9, 1.2$ Hz, 1H), 6.34 (dd, $J = 3.3, 1.8$ Hz, 1H), 6.21 (d, $J = 3.2$ Hz, 1H), 4.54 (dd, $J = 8.4, 3.5$ Hz, 1H), 4.14 (s, 1H), 2.87 (ddd, $J = 15.4, 9.4, 5.6$ Hz, 1H), 2.76 (dt, $J = 16.4, 5.5$ Hz, 1H), 2.26 – 2.09 (m, 2H).

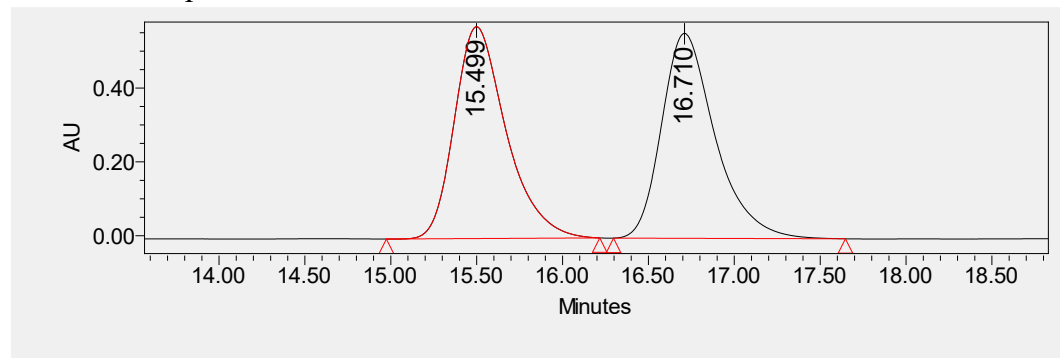
¹³C NMR (126 MHz, Chloroform-d) δ 156.97, 143.78, 141.64, 129.29, 126.90, 121.00, 117.58, 114.37, 110.20, 105.23, 49.71, 26.92, 25.55.

HRMS (ESI+) (m/z): $[M+H]^+$ calcd for C₁₃H₁₃NOH⁺ 200.1070, found 200.1067;

$[\alpha]^{24}_D = +31.2^\circ$ ($c = 0.039M$, CH₃Cl).

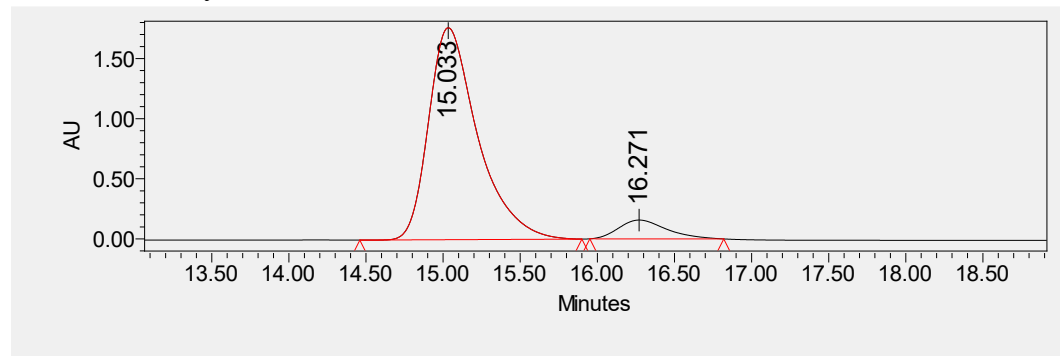
HPLC: Chiralpak OD-H column, 90:10 hexanes/isopropanol, 0.5 ml/min, $t_r = 15.5$ min (major, S), 16.7 min (minor, R)

Racemic compound HPLC Traces:



	Retention Time	Area	% Area	Height
1	15.499	12034623	50.04	573888
2	16.710	12013937	49.96	555274

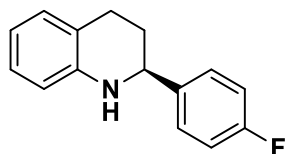
Enantiomeric synthesis in-batch HPLC Traces:



	Retention Time	Area	% Area	Height
--	----------------	------	--------	--------

1	15.033	39003943	92.02	1762589
2	16.271	3380915	7.98	156712

(S)-2-(4-fluorophenyl)-1,2,3,4-tetrahydroquinoline (3-2g)



Known compound³³, white solide, 18.6 mg, 82% yield, 93% NMR conv. in-flow (2.0 mL/min), 90% ee (batch), 92% ee (in-flow)

¹H NMR (500 MHz, Chloroform-*d*) δ 7.40 – 7.33 (m, 2H), 7.09 – 6.99 (m, 4H), 6.67 (td, *J* = 7.4, 1.2 Hz, 1H), 6.58 – 6.53 (m, 1H), 4.44 (dd, *J* = 9.4, 3.2 Hz, 1H), 4.01 (s, 1H), 2.93 (ddd, *J* = 16.3, 10.7, 5.5 Hz, 1H), 2.74 (dt, *J* = 16.4, 4.8 Hz, 1H), 2.11 (dddd, *J* = 13.1, 5.4, 4.5, 3.2 Hz, 1H), 1.97 (dddd, *J* = 12.9, 10.6, 9.3, 5.0 Hz, 1H).

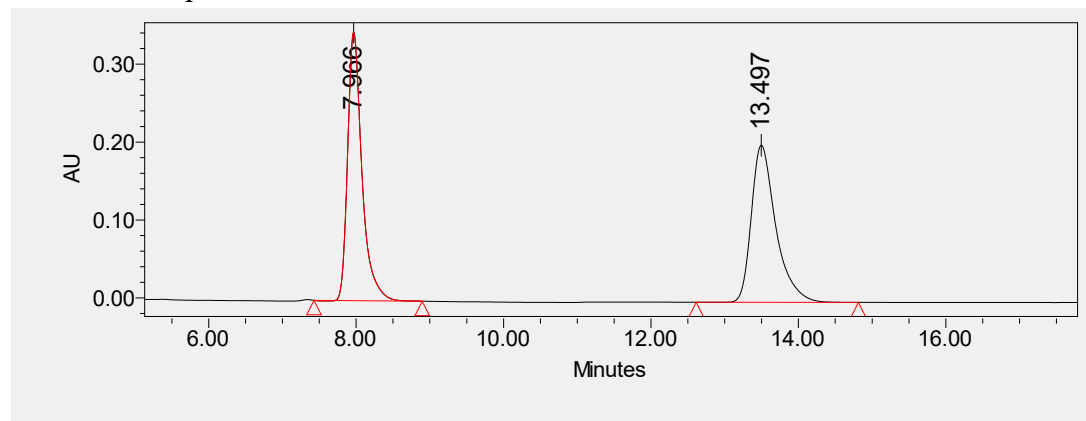
¹³C NMR (126 MHz, Chloroform-*d*) δ 162.13 (d, *J* = 245.3 Hz), 144.58, 140.53 (d, *J* = 3.1 Hz), 129.34, 128.10 (d, *J* = 8.0 Hz), 126.97, 120.85, 117.38, 115.36 (d, *J* = 21.3 Hz), 114.07, 55.62, 31.15, 26.32.

HRMS (ESI+) (*m/z*): [M+H]⁺ calcd for C₁₅H₁₄NFH⁺ 228.1183, found 228.1179;

[α]²⁴_D = -25.47° (c = 0.044M, CH₃Cl).

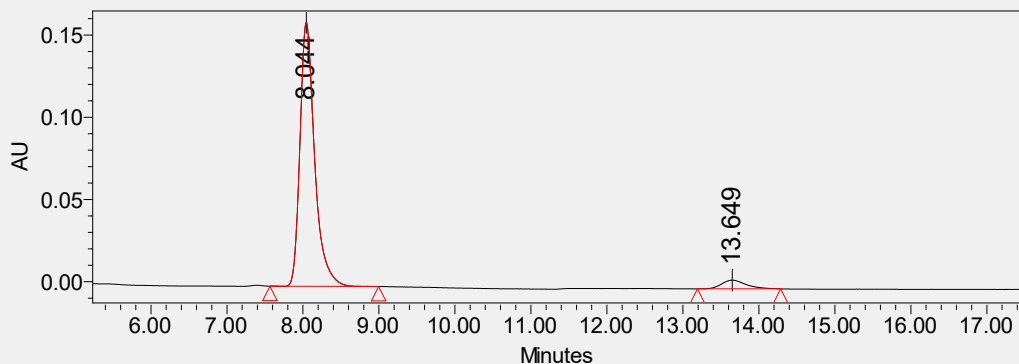
HPLC: Chiralpak OD-H column, 90:10 hexanes/isopropanol, 1.0 ml/min, tr = 8.0 min (major, *S*), 13.5 min (minor, *R*)

Racemic compound HPLC Traces:



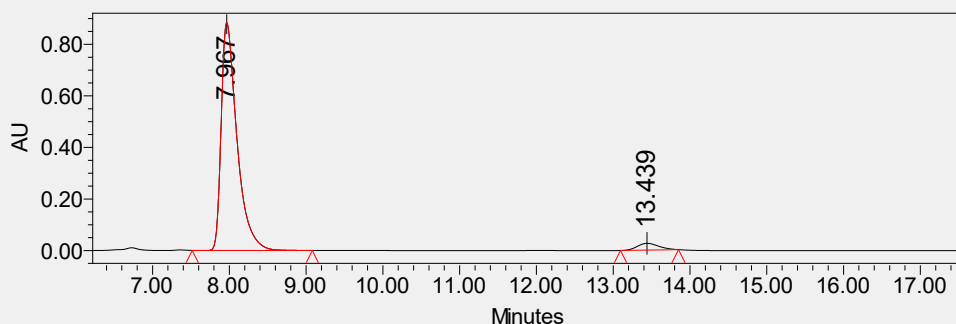
	Retention Time	Area	% Area	Height	Int Type
1	7.966	4661777	50.09	344471	bb
2	13.497	4644386	49.91	201598	bb

Enantiomeric synthesis in-batch HPLC Traces:



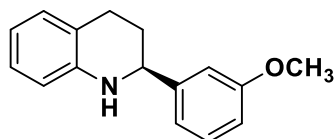
	Retention Time	Area	% Area	Height
1	8.044	2154003	94.79	160526
2	13.649	118333	5.21	5305

Enantiomeric synthesis in-flow HPLC Traces:



	Retention Time	Area	% Area	Height
1	7.967	12576483	96.09	883216
2	13.439	512316	3.91	26405

(S)-2-(3-methoxyphenyl)-1,2,3,4-tetrahydroquinoline (3-2h)



Known compound³⁶, colorless oil, 23.7 mg, 99% yield, 91% NMR conv. in-flow (2.5 mL/min), 93% ee (batch), 96% ee (in-flow).

¹H NMR (500 MHz, Chloroform-d) δ 7.28 (t, J = 7.8 Hz, 1H), 7.06 – 6.95 (m, 4H), 6.84 (ddd, J = 8.3, 2.6, 1.0 Hz, 1H), 6.66 (td, J = 7.4, 1.2 Hz, 1H), 6.58 – 6.52 (m, 1H), 4.43 (dd, J = 9.6, 3.1 Hz, 1H), 4.04 (s, 1H), 3.82 (s, 3H), 2.94 (ddd, J = 16.3, 10.8, 5.5 Hz, 1H), 2.75 (dt, J = 16.3, 4.7 Hz, 1H), 2.13 (dddd, J = 13.0, 5.4, 4.4, 3.2 Hz, 1H), 2.00 (dddd, J = 13.0, 10.8, 9.4, 5.0 Hz, 1H).

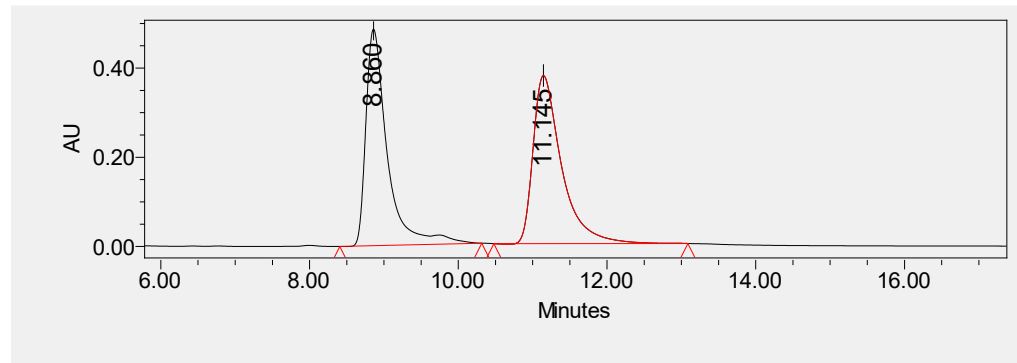
¹³C NMR (126 MHz, Chloroform-d) δ 159.88, 146.58, 144.68, 129.60, 129.31, 126.92, 120.89, 118.91, 117.21, 114.01, 112.81, 112.08, 56.28, 55.27, 31.03, 26.46.

HRMS (ESI+) (m/z): $[M+H]^+$ calcd for C₁₆H₁₇NOH⁺ 240.1383, found 240.1368;

$[\alpha]^{24}_D = -40.5^\circ$ ($c = 0.58M$, CH_3Cl).

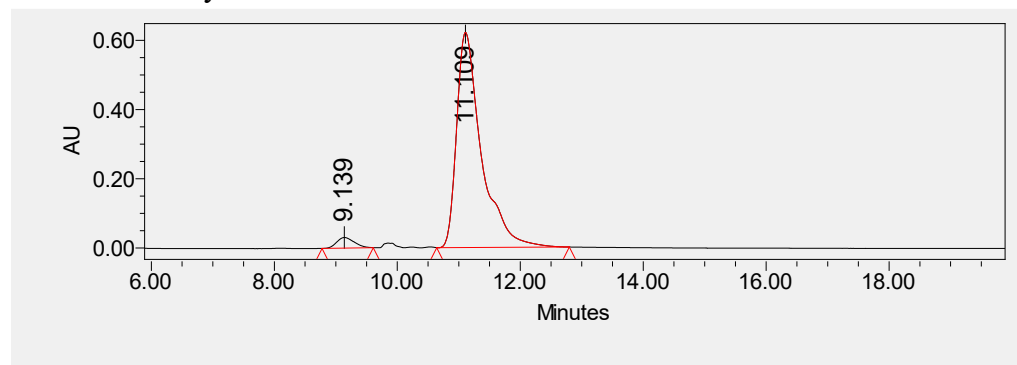
HPLC: Chiralpak IA column, 98:2 hexanes/isopropanol, 1.0 ml/min, $t_r = 8.9$ min (minor, *R*), 11.1 min (major, *S*)

Racemic compound HPLC Traces:



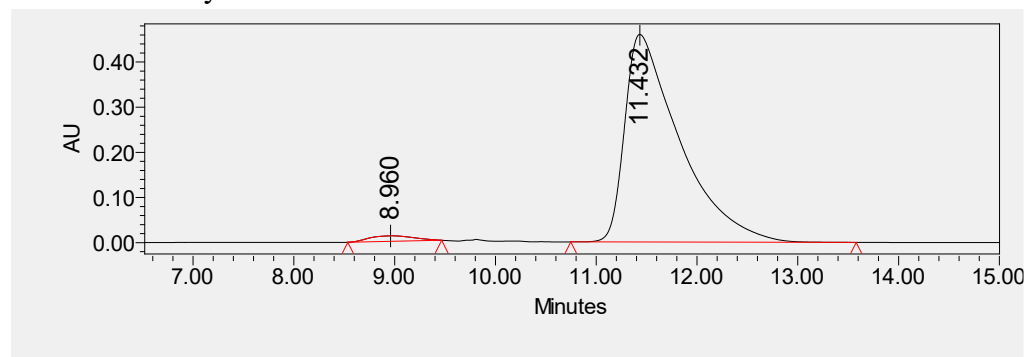
	Retention Time	Area	% Area	Height
1	8.860	9733897	49.23	485571
2	11.145	10037814	50.77	376866

Enantiomeric synthesis in-batch HPLC Traces:



	Retention Time	Area	% Area	Height
1	9.139	602716	3.36	30525
2	11.109	17360800	96.64	621444

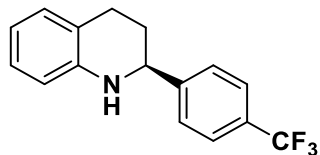
Enantiomeric synthesis in-flow HPLC Traces:



	Retention Time	Area	% Area	Height
1	8.960	374846	2.11	12219

2	11.432	17384075	97.89	459865
---	--------	----------	-------	--------

(S)-2-(4-(trifluoromethyl)phenyl)-1,2,3,4-tetrahydroquinoline (3-2i)



Known compound³⁷, yellowish solid, 19.1 mg, 69% yield, 94% NMR conv. in-flow(2.0 mL/min), 94% ee (batch), 98% ee (in-flow)

¹H NMR (500 MHz, Chloroform-*d*) δ 7.62 (d, $J = 8.1$ Hz, 2H), 7.52 (d, $J = 8.1$ Hz, 2H), 7.08 – 6.99 (m, 2H), 6.69 (td, $J = 7.4, 1.2$ Hz, 1H), 6.58 (dd, $J = 7.9, 1.2$ Hz, 1H), 4.53 (dd, $J = 8.9, 3.4$ Hz, 1H), 4.06 (s, 1H), 2.92 (ddd, $J = 15.9, 10.2, 5.4$ Hz, 1H), 2.72 (dt, $J = 16.4, 5.0$ Hz, 1H), 2.20 – 2.10 (m, 1H), 2.00 (dddd, $J = 13.0, 10.2, 8.9, 5.0$ Hz, 1H).

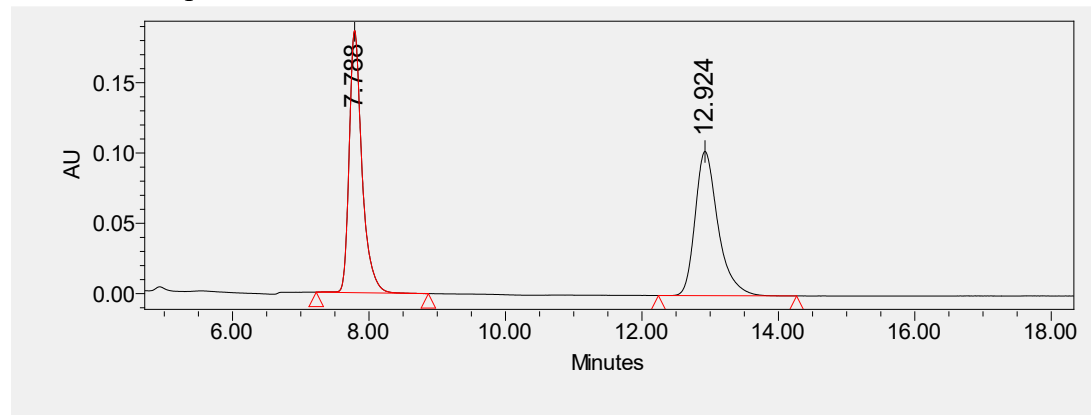
¹³C NMR (126 MHz, Chloroform-*d*) δ 148.94 (d, $J = 1.2$ Hz), 144.24, 129.68 (q, $J = 32.2$ Hz), 129.37, 127.06, 126.89, 125.55 (q, $J = 3.8$ Hz), 124.19 (q, $J = 272.0$ Hz), 120.79, 117.59, 114.15, 55.80, 30.88, 25.96.

HRMS (ESI+) (m/z): $[M+H]^+$ calcd for C₁₆H₁₄NF₃H⁺ 278.1151, found 278.1151;

$[\alpha]^{24}_D = -47.2^\circ$ ($c = 0.32M$, CH₃Cl).

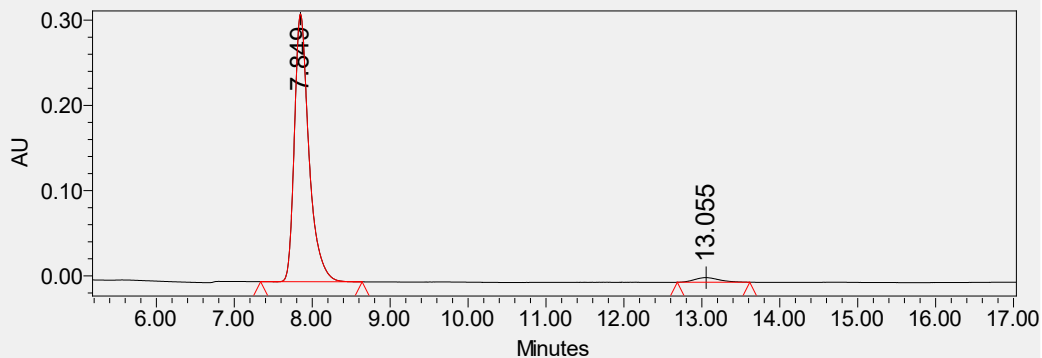
HPLC: Chiralpak OD-H column, 80:20 hexanes/isopropanol, 1.0 ml/min, tr = 7.8 min (major, *S*), 12.9 min (minor, *R*)

Racemic compound HPLC Traces:



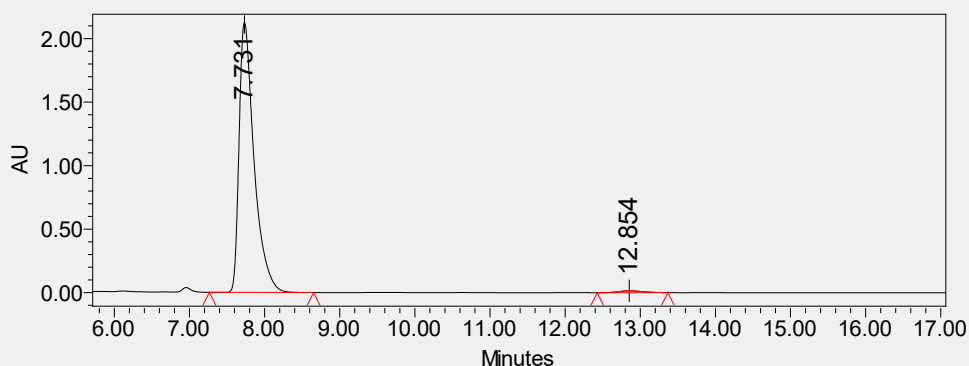
	Retention Time	Area	% Area	Height
1	7.788	2418717	50.29	186486
2	12.924	2390599	49.71	102565

Enantiomeric synthesis in-batch



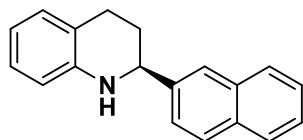
	Retention Time	Area	% Area	Height
1	7.849	4062463	96.97	314057
2	13.055	127043	3.03	5533

Enantiomeric synthesis in-flow HPLC Traces:



	Retention Time	Area	% Area	Height
1	7.731	29436872	98.92	2124855
2	12.854	320108	1.08	14683

(S)-2-(naphthalen-2-yl)-1,2,3,4-tetrahydroquinoline (3-2j)



Known compound³³, white solid, 20.5 mg, 79% yield, >95% NMR conv. in-flow(2.0 mL/min), 93% ee (batch), 92% ee (in-flow).

¹H NMR (500 MHz, Chloroform-d) δ 7.92 – 7.80 (m, 4H), 7.60 – 7.40 (m, 3H), 7.06 (td, J = 7.4, 5.1 Hz, 2H), 6.70 (td, J = 7.4, 1.2 Hz, 1H), 6.61 (dd, J = 7.8, 1.1 Hz, 1H), 4.62 (dd, J = 9.3, 3.4 Hz, 1H), 4.15 (s, 1H), 2.98 (ddd, J = 16.2, 10.7, 5.4 Hz, 1H), 2.79 (dt, J = 16.3, 4.8 Hz, 1H), 2.21 (dtd, J = 13.2, 5.1, 3.5 Hz, 1H), 2.11 (dddd, J = 12.9, 10.6, 9.2, 5.0 Hz, 1H).

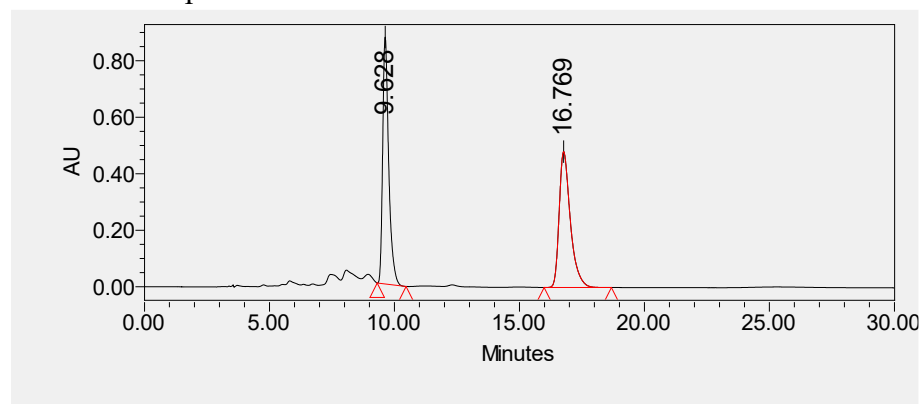
¹³C NMR (126 MHz, Chloroform-d) δ 144.73, 142.25, 133.45, 133.00, 129.36, 128.38, 127.88, 127.71, 126.99, 126.19, 125.80, 125.13, 124.90, 121.00, 117.27, 114.07, 56.39, 30.98, 26.46.

HRMS (ESI+) (m/z): $[M+H]^+$ calcd for $C_{19}H_{17}NH^+$ 260.1434, found 260.1442;

$[\alpha]^{24}_D = -25.4^\circ$ ($c = 0.43M$, CH_3Cl).

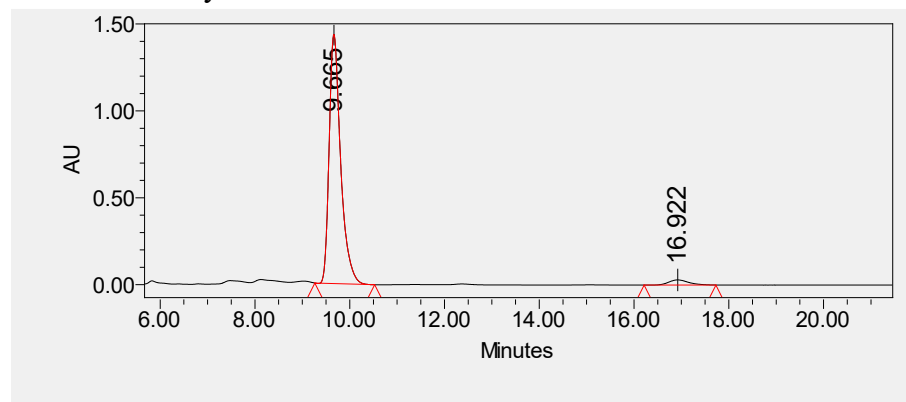
HPLC: Chiralpak OD-H column, 80:20 hexanes/isopropanol, 1.0 ml/min, $t_r = 9.6$ min (major, *S*), 16.8 min (minor, *R*)

Racemic compound HPLC Traces:



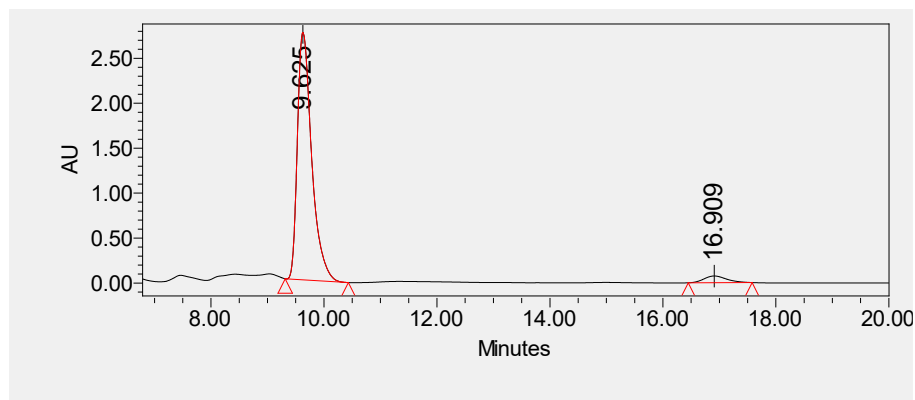
	Retention Time	Area	% Area	Height
1	9.628	14643169	49.50	873890
2	16.769	14937727	50.50	481024

Enantiomeric synthesis in-batch HPLC Traces:



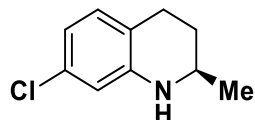
	Retention Time	Area	% Area	Height
1	9.665	24167946	96.52	1434126
2	16.922	872036	3.48	29717

Enantiomeric synthesis in-flow HPLC Traces:



	Retention Time	Area	% Area	Height
1	9.625	48383915	95.99	2751197
2	16.908	2021402	4.01	73688

(R)-7-chloro-2-methyl-1,2,3,4-tetrahydroquinoline (3-2k)



Known compound³⁴, yellowish solid, 17.8 mg, 98% yield, >95% NMR conv. in-flow (2.5 mL/min), 84% ee (batch), 90% ee (in-flow)

¹H NMR (500 MHz, Chloroform-d) δ 6.85 (d, J = 8.0 Hz, 1H), 6.54 (dd, J = 8.0, 2.1 Hz, 1H), 6.44 (d, J = 2.0 Hz, 1H), 3.75 (s, 1H), 3.39 (dq, J = 9.4, 6.3, 3.0 Hz, 1H), 2.81 – 2.64 (m, 2H), 1.92 (ddt, J = 12.5, 5.5, 3.3 Hz, 1H), 1.55 (dddd, J = 12.9, 11.2, 9.7, 5.3 Hz, 1H), 1.21 (d, J = 6.3 Hz, 3H).

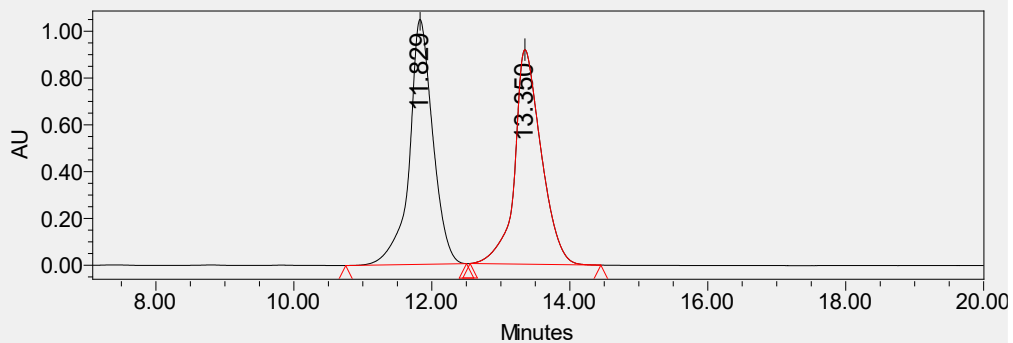
¹³C NMR (126 MHz, Chloroform-d) δ 145.84, 132.02, 130.29, 119.44, 116.68, 113.37, 77.41, 77.16, 76.91, 47.11, 29.89, 26.19, 22.59.

HRMS (ESI+) (m/z): $[M+H]^+$ calcd for C₁₀H₁₂ClNH⁺ 182.0731, 184.0702, found 182.0732(100%), 184.0701(33%);

$[\alpha]^{24}_D = +77.9^\circ$ (c = 0.035M, CH₃Cl).

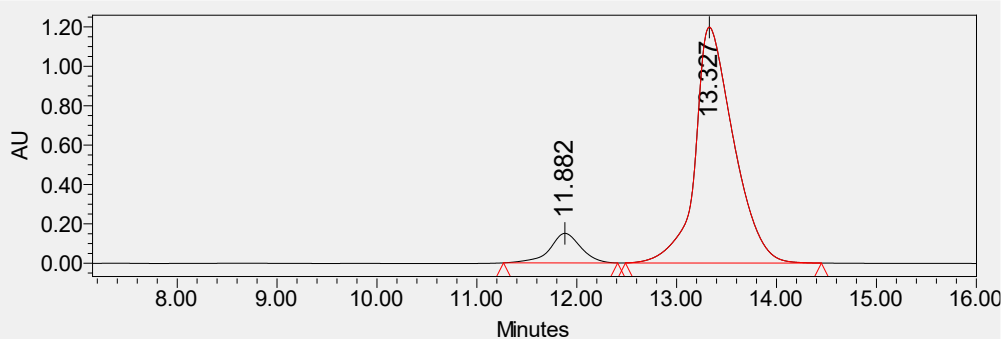
HPLC: Chiralpak OJ-H column, 92:8 hexanes/isopropanol, 1.0 ml/min, t_r = 11.8 min (minor, *S*), 13.4 min (major, *R*)

Racemic compound HPLC Traces:



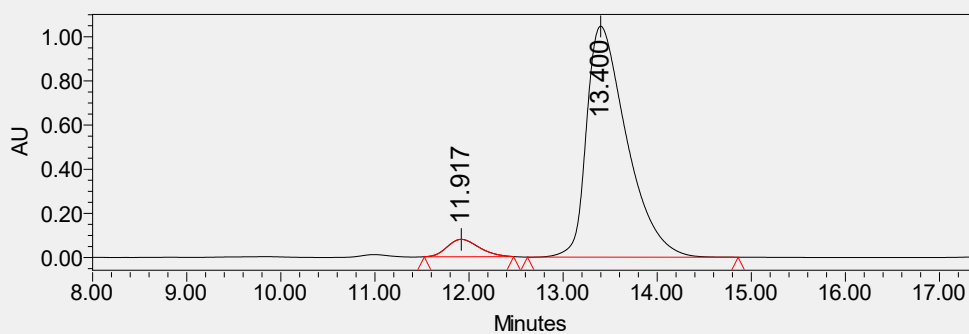
	Retention Time	Area	% Area	Height
1	11.829	24643975	50.07	1047445
2	13.350	24573701	49.93	917174

Enantiomeric synthesis in-batch HPLC Traces:



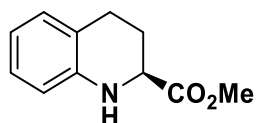
	Retention Time	Area	% Area	Height
1	11.882	3246986	9.19	150044
2	13.327	32095153	90.81	1197412

Enantiomeric synthesis in-flow HPLC Traces:



	Retention Time	Area	% Area	Height
1	11.917	1843389	5.60	78547
2	13.400	31083843	94.40	1046459

Methyl (S)-1,2,3,4-tetrahydroquinoline-2-carboxylate (3-2l)



Known compound³⁸, white solid, 14.1 mg, 74% yield, 89% ee (batch).

¹H NMR (500 MHz, Chloroform-d) δ 7.01 (td, $J = 7.8, 1.6$ Hz, 1H), 6.96 (dd, $J = 7.5, 1.5$ Hz, 1H), 6.65 (td, $J = 7.4, 1.2$ Hz, 1H), 6.59 (dd, $J = 8.0, 1.2$ Hz, 1H), 4.37 (s, 1H), 4.05 (dd, $J = 8.8, 3.8$ Hz, 1H), 3.78 (s, 3H), 2.84 (ddd, $J = 15.1, 9.3, 5.4$ Hz, 1H), 2.76 (dt, $J = 16.3, 5.5$ Hz, 1H), 2.29 (dtd, $J = 12.9, 5.6, 3.8$ Hz, 1H), 2.01 (dtd, $J = 13.0, 9.1, 5.2$ Hz, 1H).

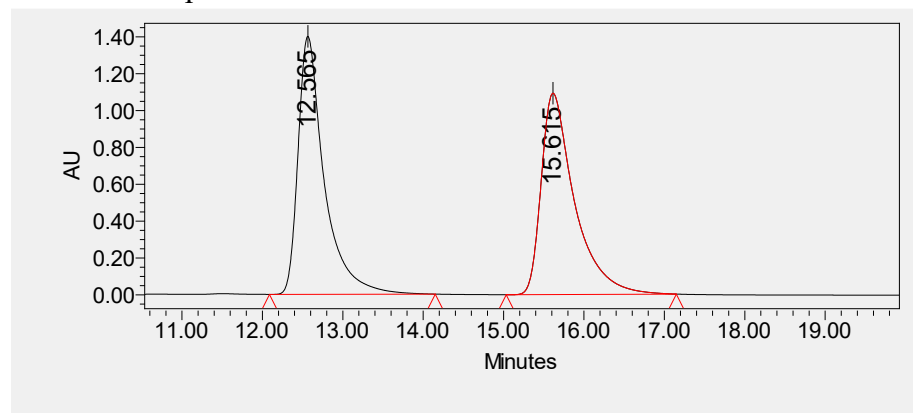
¹³C NMR (126 MHz, Chloroform-d) δ 173.73, 142.96, 129.14, 127.07, 120.55, 117.68, 114.60, 77.32, 77.07, 76.81, 53.92, 52.37, 25.83, 24.72.

HRMS (ESI+) (m/z): $[M+H]^+$ calcd for C₁₁H₁₃NO₂H⁺ 192.1019, found 192.1015;

$[\alpha]^{24}_D = +27.8^\circ$ ($c = 0.048M$, CH₃Cl), [lit: $[\alpha]^{20}_D = -37.9^\circ$ ($c = 1.05 M$, CH₃Cl) for R-enantiomer.]

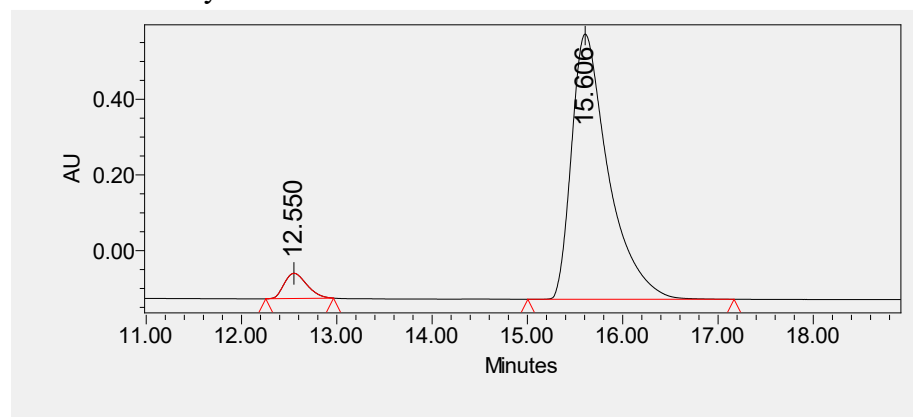
HPLC: Chiralpak IA column, 80:20 hexanes/isopropanol, 0.5 ml/min, $t_r = 12.5$ min (minor, R), 15.6 min (major, S)

Racemic compound HPLC Traces:



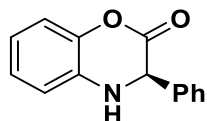
	Retention Time	Area	% Area	Height
1	12.565	31588130	50.14	1399414
2	15.615	31411703	49.86	1092092

Enantiomeric synthesis in-batch HPLC Traces:



	Retention Time	Area	% Area	Height
1	12.550	1100314	5.53	66595
2	15.606	18784418	94.47	701203

(R)-3-phenyl-3,4-dihydro-2H-benzo[b][1,4]oxazin-2-one (3-2m)



Known compound³³, yellow solid, 15.3 mg, 68% yield, 92% ee (batch).

¹H NMR (500 MHz, Chloroform-d) δ 7.39 (dq, $J = 17.1, 5.0, 2.1$ Hz, 5H), 7.04 (ddd, $J = 13.8, 7.8, 1.4$ Hz, 2H), 6.87 (td, $J = 7.8, 1.5$ Hz, 1H), 6.82 (dd, $J = 7.8, 1.5$ Hz, 1H), 5.07 (d, $J = 2.0$ Hz, 1H), 4.25 (s, 1H).

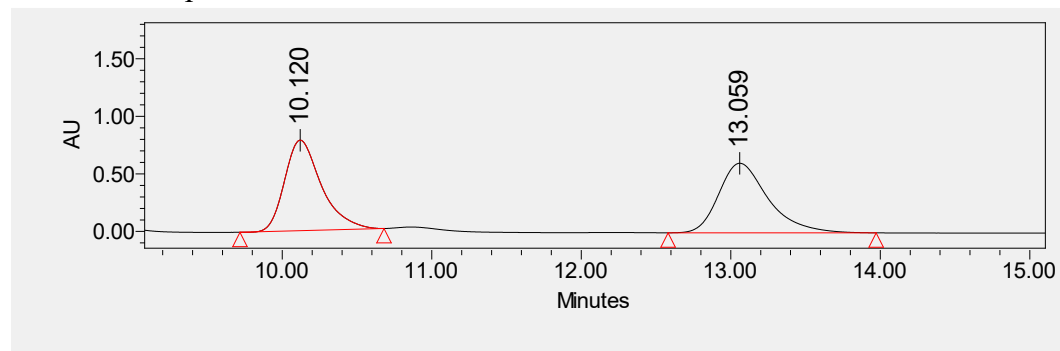
¹³C NMR (126 MHz, Chloroform-d) δ 165.20, 140.94, 136.38, 132.38, 129.03, 129.02, 127.51, 125.21, 120.44, 117.02, 114.89, 77.30, 77.05, 76.79, 59.31.

HRMS (ESI+) (m/z): [M+H]⁺ calcd for C₁₄H₁₁NO₂H⁺ 226.0863, found 226.0869;

$[\alpha]^{24}_D = +101.4^\circ$ ($c = 0.069M$, CH₃Cl).

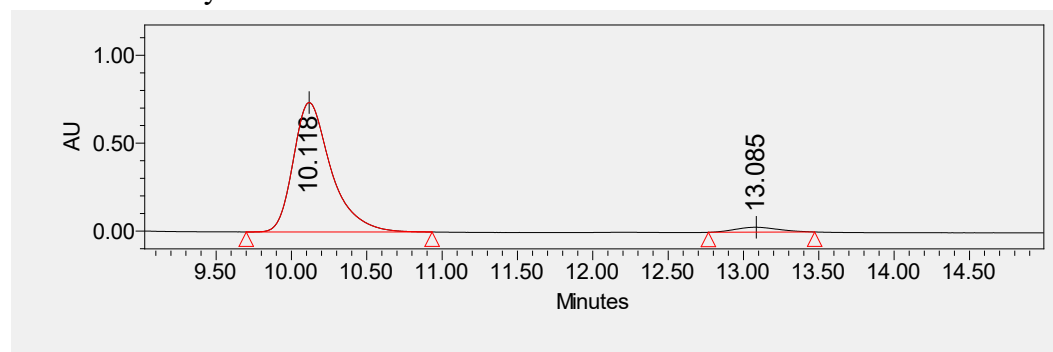
HPLC: Chiralpak OD-H column, 70:30 hexanes/isopropanol, 0.7 ml/min, $t_r = 10.1$ min (major, *R*), 13.1 min (minor, *S*)

Racemic compound HPLC Traces:



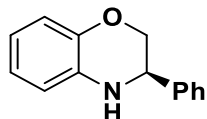
	Retention Time	Area	% Area	Height
1	10.120	13430049	49.16	786801
2	13.059	13887861	50.84	604505

Enantiomeric synthesis in-batch HPLC Traces:



	Retention Time	Area	% Area	Height
1	10.118	12820604	95.87	735294
2	13.085	552125	4.13	27868

(R)-3-phenyl-3,4-dihydro-2H-benzo[b][1,4]oxazine (3-2a)



Known compound³³, white solid, 19.2 mg, 91% yield, >95% NMR conv. in-flow(2.5 mL/min), 90% ee (batch), 95% ee (in-flow)

¹H NMR (500 MHz, Chloroform-d) δ 7.45 – 7.37 (m, 4H), 7.35 (ddd, J = 7.4, 4.1, 2.1 Hz, 1H), 6.87 (dd, J = 8.0, 1.4 Hz, 1H), 6.83 (td, J = 7.6, 1.5 Hz, 1H), 6.75 – 6.66 (m, 2H), 4.52 (dd, J = 8.6, 3.0 Hz, 1H), 4.30 (ddd, J = 10.6, 3.2, 1.4 Hz, 1H), 4.01 (dd, J = 10.7, 8.5 Hz, 2H).

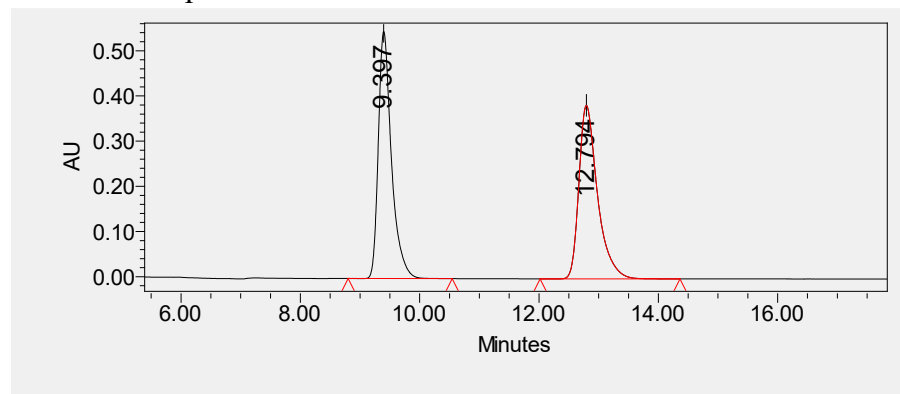
¹³C NMR (126 MHz, Chloroform-d) δ 143.65, 139.27, 134.03, 128.96, 128.47, 127.32, 121.62, 119.06, 116.73, 115.50, 71.11, 54.35.

HRMS (ESI+) (m/z): $[M+H]^+$ calcd for C₁₄H₁₃NOH⁺ 212.1070, found 212.1073;

$[\alpha]^{24}_D = -137.1^\circ$ ($c = 0.52M$, CH₃Cl).

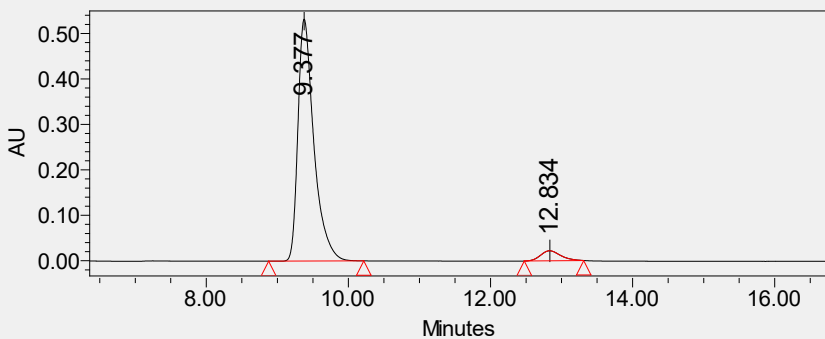
HPLC: Chiralpak OD-H column, 80:20 hexanes/isopropanol, 1.0 ml/min, $t_r = 9.4$ min (major, *R*), 12.8 min (minor, *S*)

Racemic compound HPLC Traces:



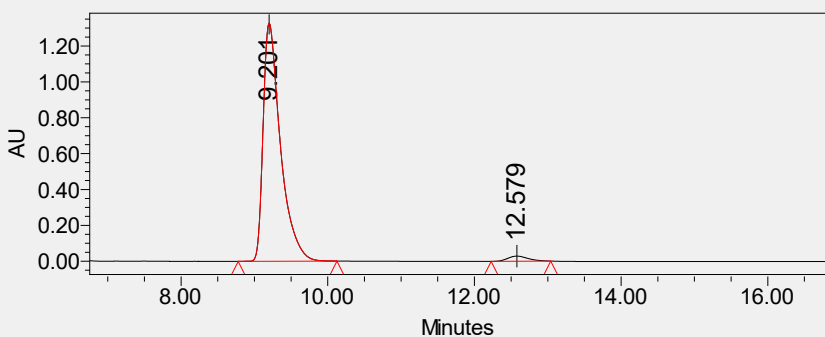
	Retention Time	Area	% Area	Height
1	9.397	8355846	50.14	546871
2	12.794	8309660	49.86	383788

Enantiomeric synthesis in-batch HPLC Traces:



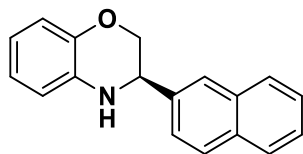
	Retention Time	Area	% Area	Height
1	9.377	8297971	95.01	532171
2	12.834	436198	4.99	22119

Enantiomeric synthesis in-flow HPLC Traces:



	Retention Time	Area	% Area	Height
1	9.201	21777045	97.51	1327256
2	12.579	557032	2.49	28817

(R)-3-(naphthalen-2-yl)-3,4-dihydro-2H-benzo[b][1,4]oxazine (3-2n)



Known compound³³, white solid, 18.3 mg, 70% yield, 90% ee (batch).

¹H NMR (500 MHz, Chloroform-d) δ 7.91 – 7.83 (m, 4H), 7.56 – 7.48 (m, 3H), 6.93 – 6.82 (m, 2H), 6.78 – 6.70 (m, 2H), 4.68 (dd, J = 8.7, 3.0 Hz, 1H), 4.37 (dd, J = 10.8, 3.0 Hz, 1H), 4.14 – 4.06 (m, 2H).

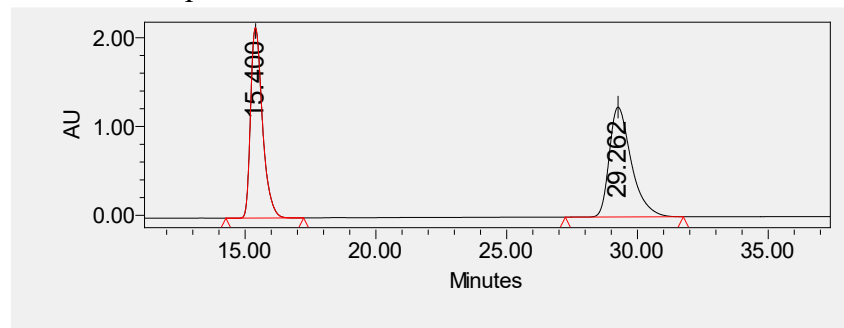
¹³C NMR (126 MHz, Chloroform-d) δ 143.71, 136.61, 134.01, 133.49, 133.43, 128.76, 128.05, 127.87, 126.54, 126.36, 126.31, 125.08, 121.68, 119.14, 116.78, 115.56, 71.06, 54.43.

HRMS (ESI+) (m/z): $[M+H]^+$ calcd for C₁₈H₁₅NOH⁺ 262.1226, found 262.1231;

$[\alpha]^{24}_D$ = -146.0° (c = 0.035M, CH₃Cl).

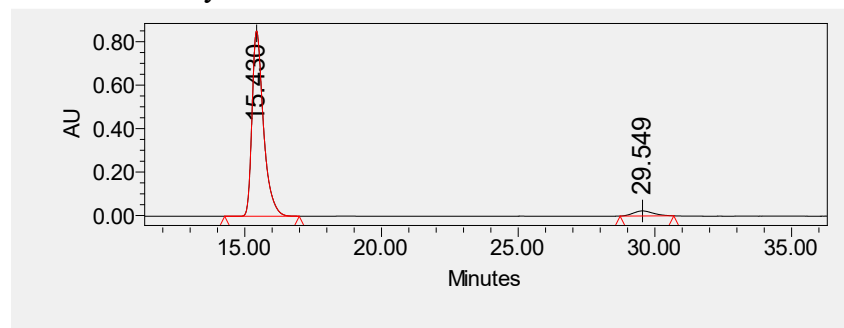
HPLC: Chiralpak OD-H column, 80:20 hexanes/isopropanol, 1.0 ml/min, t_r = 15.4 min (major, *R*), 29.3 min (minor, *S*)

Racemic compound HPLC Traces:



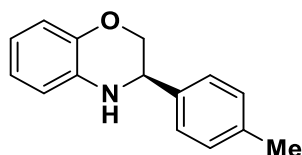
	Retention Time	Area	% Area	Height
1	15.400	67325447	48.22	2143614
2	29.262	72301524	51.78	1236831

Enantiomeric synthesis in-batch HPLC Traces:



	Retention Time	Area	% Area	Height
1	15.430	24715039	95.48	853323
2	29.549	1170655	4.52	23161

(R)-3-(p-tolyl)-3,4-dihydro-2H-benzo[b][1,4]oxazine (3-2o)



Known compound³³, colorless oil, 21.6 mg, 96% yield, 92% ee (batch).

¹H NMR (500 MHz, Chloroform-d) δ 7.38 – 7.27 (m, 2H), 7.20 (d, J = 7.8 Hz, 2H), 6.86 (dd, J = 8.0, 1.4 Hz, 1H), 6.81 (td, J = 7.6, 1.5 Hz, 1H), 6.74 – 6.65 (m, 2H), 4.48 (dd, J = 8.7, 3.0 Hz, 1H), 4.27 (dd, J = 10.6, 3.0 Hz, 1H), 3.99 (dd, J = 10.6, 8.7 Hz, 1H), 3.97 (s, 1H), 2.37 (s, 3H).

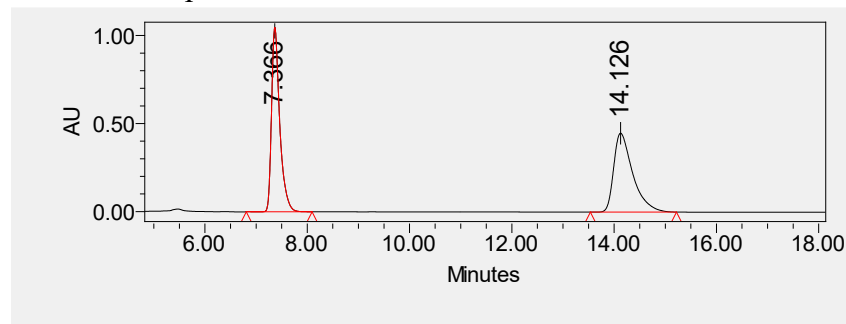
¹³C NMR (126 MHz, Chloroform-d) δ 143.65, 138.27, 136.25, 134.11, 129.63, 127.22, 121.57, 118.99, 116.70, 115.47, 71.19, 54.07, 21.28.

HRMS (ESI+) (m/z): $[M+H]^+$ calcd for $C_{15}H_{15}NOH^+$ 226.1226, found 226.1228;

$[\alpha]^{24}_D = -121.9^\circ$ ($c = 0.064M$, CH_3Cl).

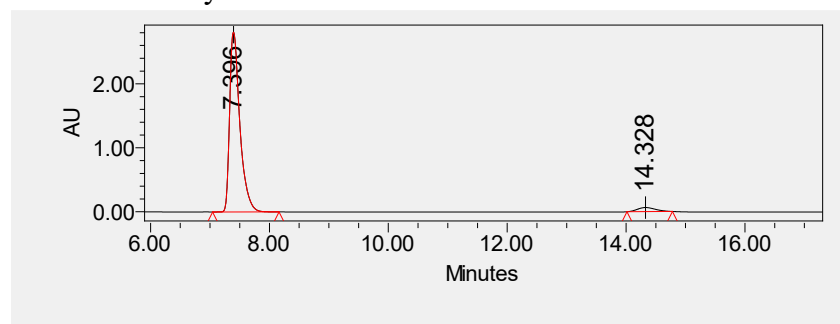
HPLC: Chiralpak OD-H column, 80:20 hexanes/isopropanol, 1.0 ml/min, $t_r = 7.4$ min (major, *R*), 14.1 min (minor, *S*)

Racemic compound HPLC Traces:



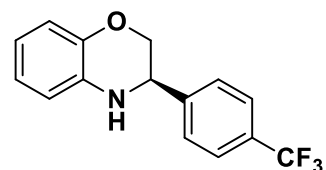
	Retention Time	Area	% Area	Height
1	7.366	11649402	50.17	1046875
2	14.126	11570313	49.83	448218

Enantiomeric synthesis in-batch HPLC Traces:



	Retention Time	Area	% Area	Height
1	7.396	33505534	96.10	2812243
2	14.328	1358085	3.90	64063

(R)-3-(4-(trifluoromethyl)phenyl)-3,4-dihydro-2H-benzo[b][1,4]oxazine (3-2p)



Known compound³⁹, white solid, 21.5 mg, 77% yield, 93% ee (batch).

¹H NMR (500 MHz, Chloroform-d) δ 7.65 (d, $J = 8.1$ Hz, 2H), 7.54 (d, $J = 8.0$ Hz, 2H), 6.90 – 6.81 (m, 2H), 6.73 (ddd, $J = 17.0, 7.7, 1.6$ Hz, 2H), 4.60 (dd, $J = 8.2, 3.0$ Hz, 1H), 4.29 (dd, $J = 10.7, 3.0$ Hz, 1H), 4.06 – 3.97 (m, 2H).

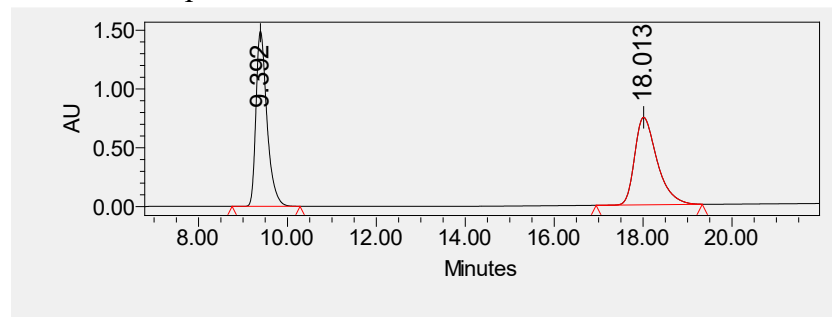
¹³C NMR (126 MHz, Chloroform-d) δ 143.51, 143.37 (q, $J = 1.4$ Hz), 133.37, 130.58 (q, $J = 32.5$ Hz), 127.57, 125.80 (q, $J = 3.8$ Hz), 124.02 (q, $J = 272.2$ Hz), 121.75, 119.31, 116.76, 115.54, 70.53, 53.92.

HRMS (ESI+) (m/z): $[M+H]^+$ calcd for C₁₅H₁₂F₃NOH⁺ 280.0948, found 280.0944;

$[\alpha]^{24}_{\text{D}} = -99.5^\circ$ ($c = 0.38\text{M}$, CH_3Cl).

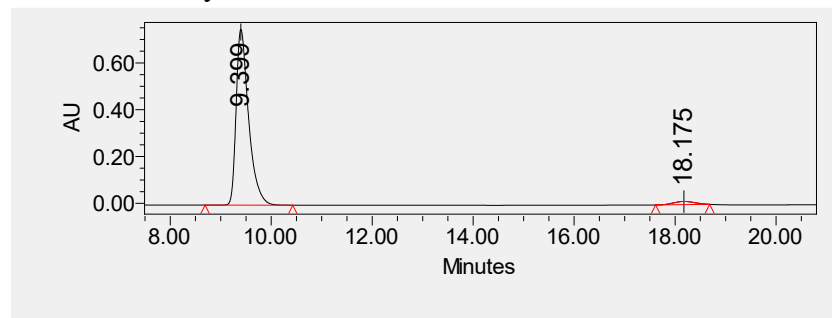
HPLC: Chiralpak IA column, 80:20 hexanes/isopropanol, 1.0 ml/min, $t_r = 9.4$ min (major, *R*), 18.1 min (minor, *S*)

Racemic compound HPLC Traces:



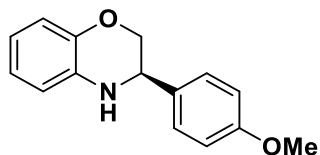
	Retention Time	Area	% Area	Height
1	9.392	25450180	49.42	1490003
2	18.013	26042877	50.58	744461

Enantiomeric synthesis in-batch HPLC Traces:



	Retention Time	Area	% Area	Height
1	9.399	12865027	96.95	751056
2	18.175	404802	3.05	13887

(R)-3-(4-methoxyphenyl)-3,4-dihydro-2H-benzo[b][1,4]oxazine (3-2q)



Known compound³³, yellow oil, 18.8 mg, 78% yield, 92% ee (batch).

$^1\text{H NMR}$ (500 MHz, Chloroform- d) δ 7.36 – 7.29 (m, 2H), 6.96 – 6.89 (m, 2H), 6.86 (dd, $J = 8.0$, 1.4 Hz, 1H), 6.81 (td, $J = 7.6$, 1.5 Hz, 1H), 6.70 (td, $J = 7.6$, 1.6 Hz, 1H), 6.67 (dd, $J = 7.8$, 1.6 Hz, 1H), 4.46 (dd, $J = 8.7$, 3.0 Hz, 1H), 4.25 (dd, $J = 10.6$, 3.0 Hz, 1H), 4.01 – 3.94 (m, 2H), 3.82 (s, 3H).

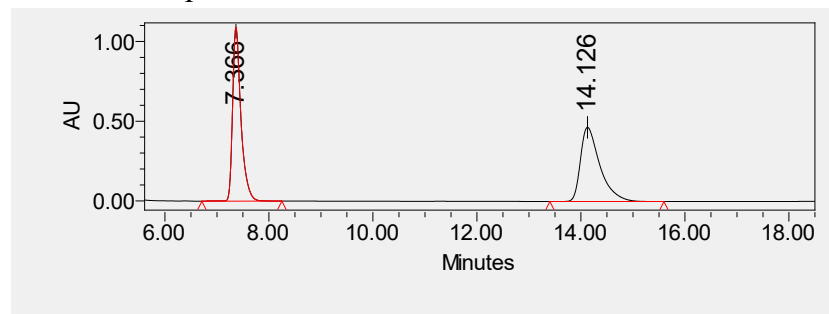
$^{13}\text{C NMR}$ (126 MHz, Chloroform- d) δ 159.75, 143.63, 134.13, 131.27, 128.45, 121.55, 118.99, 116.68, 115.46, 114.33, 71.23, 55.47, 53.71.

HRMS (ESI+) (m/z): $[\text{M}+\text{H}]^+$ calcd for $\text{C}_{15}\text{H}_{15}\text{NO}_2\text{H}^+$ 242.1163, found 242.1176;

$[\alpha]^{24}_{\text{D}} = -108.5^\circ$ ($c = 0.040\text{M}$, CH_3Cl).

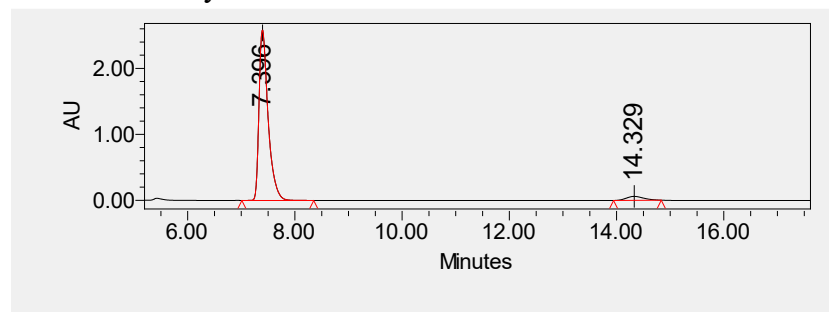
HPLC: Chiralpak OD-H column, 80:20 hexanes/isopropanol, 1.0 ml/min, tr = 7.4 min (major, *R*), 14.1 min (minor, *S*)

Racemic compound HPLC Traces:



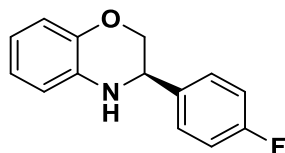
	Retention Time	Area	% Area	Height
1	7.366	12165659	50.31	1088602
2	14.126	12013668	49.69	464854

Enantiomeric synthesis in-batch HPLC Traces:



	Retention Time	Area	% Area	Height
1	7.396	30329029	95.76	2583461
2	14.329	1343353	4.24	60122

(*R*)-3-(4-fluorophenyl)-3,4-dihydro-2H-benzo[*b*][1,4]oxazine (3-2r)



Known compound³³, white solid, 20.1 mg, 88% yield, 89% ee (batch).

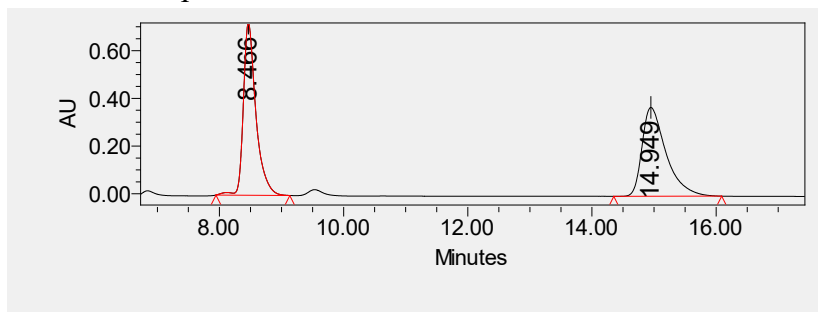
¹H NMR (500 MHz, Chloroform-*d*) δ 7.42 – 7.34 (m, 2H), 7.12 – 7.04 (m, 2H), 6.89 – 6.79 (m, 2H), 6.75 – 6.65 (m, 2H), 4.50 (dd, *J* = 8.6, 3.0 Hz, 1H), 4.26 (dd, *J* = 10.7, 3.0 Hz, 1H), 4.00 – 3.94 (m, 2H).

¹³C NMR (126 MHz, Chloroform-*d*) δ 162.67 (d, *J* = 246.8 Hz), 143.51, 134.96 (d, *J* = 3.1 Hz), 133.71, 128.83 (d, *J* = 8.2 Hz), 121.57, 119.12, 116.65, 115.75 (d, *J* = 21.5 Hz), 115.44, 70.94, 70.93, 53.55.

HRMS (ESI+) (*m/z*): [M+H]⁺ calcd for C₁₄H₁₂FNOH⁺ 230.0980, found 230.0976;

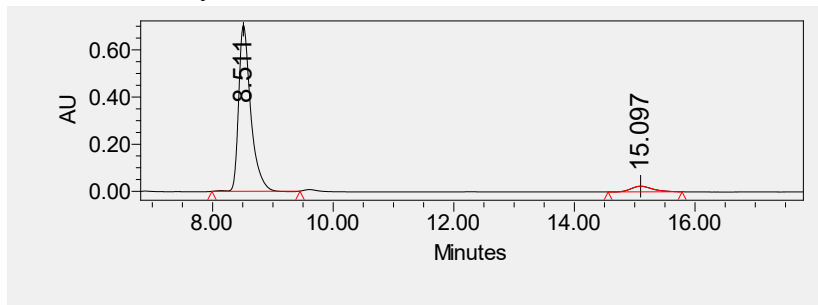
[α]_D²⁴ = -103.5° (c = 0.044M, CH₃Cl).

HPLC: Chiralpak OD-H column, 80:20 hexanes/isopropanol, 1.0 ml/min, tr = 8.5 min (major, *R*), 14.9 min (minor, *S*)
 Racemic compound



	Retention Time	Area	% Area	Height
1	8.466	10099134	50.30	720904
2	14.949	9977195	49.70	372156

Enantiomeric synthesis in-batch



	Retention Time	Area	% Area	Height
1	8.511	9779760	94.23	704108
2	15.097	598583	5.77	24060

3.6 References

- (1) Kerru, N.; Gummidi, L.; Maddila, S.; Gangu, K. K.; Jonnalagadda, S. B. A Review on Recent Advances in Nitrogen-Containing Molecules and Their Biological Applications. *Molecules*. MDPI AG April 1, 2020. <https://doi.org/10.3390/molecules25081909>.
- (2) Vitaku, E.; Smith, D. T.; Njardarson, J. T. Analysis of the Structural Diversity, Substitution Patterns, and Frequency of Nitrogen Heterocycles among U.S. FDA Approved Pharmaceuticals. *J Med Chem* **2014**, *57* (24), 10257–10274. <https://doi.org/10.1021/JM501100B>.
- (3) Taylor, A. P.; Robinson, R. P.; Fobian, Y. M.; Blakemore, D. C.; Jones, L. H.; Fadeyi, O. Modern Advances in Heterocyclic Chemistry in Drug Discovery. *Org Biomol Chem* **2016**, *14* (28), 6611–6637. <https://doi.org/10.1039/C6OB00936K>.
- (4) Wang, D. S.; Chen, Q. A.; Lu, S. M.; Zhou, Y. G. Asymmetric Hydrogenation of Heteroarenes and Arenes. *Chem Rev* **2012**, *112* (4), 2557–2590. https://doi.org/10.1021/CR200328H/ASSET/IMAGES/MEDIUM/CR-2011-00328H_0068.GIF.
- (5) Lückemeier, L.; Pierau, M.; Glorius, F. Asymmetric Arene Hydrogenation: Towards Sustainability and Application. *Chem Soc Rev* **2023**, *52* (15), 4996–5012. <https://doi.org/10.1039/D3CS00329A>.
- (6) Mattson, B.; Foster, W.; Greimann, J.; Hoette, T.; Le, N.; Mirich, A.; Wankum, S.; Cabri, A.; Reichenbacher, C.; Schwanke, E. Heterogeneous Catalysis: The Horiuti-Polanyi Mechanism and Alkene Hydrogenation. *J Chem Educ* **2013**, *90* (5), 613–619. https://doi.org/10.1021/ED300437K/SUPPL_FILE/ED300437K_SI_002.DOCX.
- (7) Wang, P. Z.; Chen, J. R.; Xiao, W. J. Hantzsch Esters: An Emerging Versatile Class of Reagents in Photoredox Catalyzed Organic Synthesis. *Org Biomol Chem* **2019**, *17* (29), 6936–6951. <https://doi.org/10.1039/C9OB01289C>.
- (8) Kim, A. N.; Stoltz, B. M. Recent Advances in Homogeneous Catalysts for the Asymmetric Hydrogenation of Heteroarenes. *ACS Catalysis*. American Chemical Society December 4, 2020, pp 13834–13851. <https://doi.org/10.1021/acscatal.0c03958>.
- (9) Rueping, M.; Antonchick, A. P.; Theissmann, T. A Highly Enantioselective Brønsted Acid Catalyzed Cascade Reaction: Organocatalytic Transfer Hydrogenation of Quinolines and Their Application in the Synthesis of Alkaloids. *Angew Chem Int Ed Engl* **2006**, *45* (22), 3683–3686. <https://doi.org/10.1002/ANIE.200600191>.
- (10) Rueping, M.; Sugiono, E.; Azap, C.; Theissmann, T.; Bolte, M. Enantioselective Brønsted Acid Catalyzed Transfer Hydrogenation: Organocatalytic Reduction of Imines. *Org Lett* **2005**, *7* (17), 3781–3783. <https://doi.org/10.1021/ol0515964>.
- (11) Ouellet, S. G.; Walji, A. M.; Macmillan, D. W. C. Enantioselective Organocatalytic Transfer Hydrogenation Reactions Using Hantzsch Esters. *Acc Chem Res* **2007**, *40* (12), 1327–1339. https://doi.org/10.1021/AR7001864/ASSET/IMAGES/MEDIUM/AR-2007-001864_0043.GIF.
- (12) Zhu, C.; Saito, K.; Yamanaka, M.; Akiyama, T. Benzothiazoline: Versatile Hydrogen Donor for Organocatalytic Transfer Hydrogenation. *Acc Chem Res* **2015**, *48* (2), 388–398. https://doi.org/10.1021/AR500414X/ASSET/IMAGES/LARGE/AR-2014-00414X_0028.JPEG.
- (13) Chen, Q. A.; Chen, M. W.; Yu, C. Bin; Shi, L.; Wang, D. S.; Yang, Y.; Zhou, Y. G. Biomimetic Asymmetric Hydrogenation: In Situ Regenerable Hantzsch Esters for Asymmetric Hydrogenation of Benzoxazinones. *J Am Chem Soc* **2011**, *133* (41), 16432–16435. https://doi.org/10.1021/JA208073W/SUPPL_FILE/JA208073W_SI_001.PDF.

- (14) Aillerie, A.; Gosset, C.; Dumont, C.; Skrzypczak, V.; Champetter, P.; Pellegrini, S.; Bousquet, T.; Pélinski, L. In Situ Generation of Dihydropyridine for the Enantioselective Transfer Hydrogenation of 1,4-Benzoxazines. *RSC Adv* **2016**, *6* (59), 54185–54188. <https://doi.org/10.1039/C6RA04930C>.
- (15) Zhou, Q.; Ei Meng, W.; Ing Yang, J.; Du, H.; Zhou, J Q; Meng, W; Du, H; Zhou, Q.; Yang, J. A Continuously Regenerable Chiral Ammonia Borane for Asymmetric Transfer Hydrogenations. *Angewandte Chemie International Edition* **2018**, *57* (37), 12111–12115. <https://doi.org/10.1002/ANIE.201806877>.
- (16) Pálvölgyi, Á. M.; Scharinger, F.; Schnürch, M.; Bica-Schröder, K. Chiral Phosphoric Acids as Versatile Tools for Organocatalytic Asymmetric Transfer Hydrogenations. *European Journal of Organic Chemistry*. John Wiley and Sons Inc October 14, 2021, pp 5367–5381. <https://doi.org/10.1002/ejoc.202100894>.
- (17) Shugrue, C. R.; Miller, S. J. Phosphothreonine as a Catalytic Residue in Peptide-Mediated Asymmetric Transfer Hydrogenations of 8-Aminoquinolines. *Angewandte Chemie International Edition* **2015**, *54* (38), 11173–11176. <https://doi.org/10.1002/ANIE.201505898>.
- (18) Parmar, D.; Sugiono, E.; Raja, S.; Rueping, M. Complete Field Guide to Asymmetric BINOL-Phosphate Derived Brønsted Acid and Metal Catalysis: History and Classification by Mode of Activation; Brønsted Acidity, Hydrogen Bonding, Ion Pairing, and Metal Phosphates. *Chemical Reviews*. American Chemical Society September 24, 2014, pp 9047–9153. <https://doi.org/10.1021/cr5001496>.
- (19) Rueping, M.; Sugiono, E.; Steck, A.; Theissmann, T. Synthesis and Application of Polymer-Supported Chiral Brønsted Acid Organocatalysts. *Adv Synth Catal* **2010**, *352* (2–3), 281–287. <https://doi.org/10.1002/adsc.200900746>.
- (20) Bleschke, C.; Schmidt, J.; Kundu, D. S.; Blechert, S.; Thomas, A. A Chiral Microporous Polymer Network as Asymmetric Heterogeneous Organocatalyst. *Adv Synth Catal* **2011**, *353* (17), 3101–3106. <https://doi.org/10.1002/adsc.201100674>.
- (21) Kundu, D. S.; Schmidt, J.; Bleschke, C.; Thomas, A.; Blechert, S. A Microporous Binol-Derived Phosphoric Acid. *Angewandte Chemie - International Edition* **2012**, *51* (22), 5456–5459. <https://doi.org/10.1002/anie.201109072>.
- (22) Zhang, X.; Kormos, A.; Zhang, J. Self-Supported BINOL-Derived Phosphoric Acid Based on a Chiral Carbazolic Porous Framework. *Org Lett* **2017**, *19* (22), 6072–6075. <https://doi.org/10.1021/acs.orglett.7b02887>.
- (23) Monterde, C.; Navarro, R.; Iglesias, M.; Sánchez, F. Adamantyl-BINOL as Platform for Chiral Porous Polymer Aromatic Frameworks. Multiple Applications as Recyclable Catalysts. *J Catal* **2019**, *377*, 609–618. <https://doi.org/10.1016/J.JCAT.2019.07.059>.
- (24) Chen, X.; Jiang, H.; Li, X.; Hou, B.; Gong, W.; Wu, X.; Han, X.; Zheng, F.; Liu, Y.; Jiang, J.; Cui, Y. Chiral Phosphoric Acids in Metal–Organic Frameworks with Enhanced Acidity and Tunable Catalytic Selectivity. *Angewandte Chemie International Edition* **2019**, *58* (41), 14748–14757. <https://doi.org/10.1002/ANIE.201908959>.
- (25) Chen, X.; Qiao, Z.; Hou, B.; Jiang, H.; Gong, W.; Dong, J.; Li, H. Y.; Cui, Y.; Liu, Y. Chiral Metal-Organic Frameworks with Tunable Catalytic Selectivity in Asymmetric Transfer Hydrogenation Reactions. *Nano Res* **2021**, *14* (2), 466–472. <https://doi.org/10.1007/S12274-020-2905-7/METRICS>.
- (26) Li, S.; Zhang, J.; Chen, S.; Ma, X. Semi-Heterogeneous Asymmetric Organocatalysis: Covalent Immobilization of BINOL-Derived Chiral Phosphoric Acid (TRIP) to

- Polystyrene Brush Grafted on SiO₂ Nanoparticles. *J Catal* **2022**, *416*, 139–148. <https://doi.org/10.1016/J.JCAT.2022.10.021>.
- (27) Rueping, M.; Bootwicha, T.; Sugiono, E. Continuous-Flow Catalytic Asymmetric Hydrogenations: Reaction Optimization Using FTIR Inline Analysis. *Beilstein Journal of Organic Chemistry* **2012**, *8*, 300–307. <https://doi.org/10.3762/bjoc.8.32>.
- (28) Clot-Almenara, L.; Rodríguez-Escrich, C.; Osorio-Planes, L.; Pericas, M. A. Polystyrene-Supported TRIP: A Highly Recyclable Catalyst for Batch and Flow Enantioselective Allylation of Aldehydes. *ACS Catal* **2016**, *6* (11), 7647–7651. https://doi.org/10.1021/ACSCATAL.6B02621/SUPPL_FILE/CS6B02621_SI_001.PDF.
- (29) Lai, J.; Fianchini, M.; Pericas, M. A. Development of Immobilized Spinol-Derived Chiral Phosphoric Acids for Catalytic Continuous Flow Processes. Use in the Catalytic Desymmetrization of 3,3-Disubstituted Oxetanes. *ACS Catal* **2020**, *10* (24), 14971–14983. https://doi.org/10.1021/ACSCATAL.0C04497/SUPPL_FILE/CS0C04497_SI_002.CIF.
- (30) Chaudhari, M. B.; Gupta, P.; Llanes, P.; Pericàs, M. A. Polymer-Supported Phosphoric-Acid Catalysed Enantioselective Pictet-Spengler Cyclisation for the Synthesis of Quaternary Tryptolines in Batch/Continuous Flow. *Adv Synth Catal* **2023**, *365* (4), 527–534. <https://doi.org/10.1002/ADSC.202201275>.
- (31) Chen, Q. A.; Wang, D. S.; Zhou, Y. G.; Duan, Y.; Fan, H. J.; Yang, Y.; Zhang, Z. Convergent Asymmetric Disproportionation Reactions: Metal/Bronsted Acid Relay Catalysis for Enantioselective Reduction of Quinoxalines. *J Am Chem Soc* **2011**, *133* (16), 6126–6129. https://doi.org/10.1021/JA200723N/SUPPL_FILE/JA200723N_SI_001.PDF.
- (32) Saito, K.; Shibata, Y.; Yamanaka, M.; Akiyama, T. Chiral Phosphoric Acid-Catalyzed Oxidative Kinetic Resolution of Indolines Based on Transfer Hydrogenation to Imines. *J Am Chem Soc* **2013**, *135* (32), 11740–11743. https://doi.org/10.1021/JA406004Q/SUPPL_FILE/JA406004Q_SI_006.CIF.
- (33) Chen, Q.; Gao, K.; Duan, Y.; Ye, Z.; Shi, L.; Yang, Y.; Zhou, Y. Dihydrophenanthridine: A New and Easily Regenerable NAD(P)H Model for Biomimetic Asymmetric Hydrogenation. *J Am Chem Soc* **2012**, *134* (4), 2442–2448.
- (34) Sun, S.; Nagorny, P. Exploration of Chiral Diastereomeric Spiroketal (SPIROL)-Based Phosphinite Ligands in Asymmetric Hydrogenation of Heterocycles. *Chemical Communications* **2020**, *56* (60), 8432–8435. <https://doi.org/10.1039/d0cc03088k>.
- (35) Rueping, M.; Antonchick, A. P.; Theissmann, T. A Highly Enantioselective Bronsted Acid Catalyzed Cascade Reaction: Organocatalytic Transfer Hydrogenation of Quinolines and Their Application in the Synthesis of Alkaloids. *Angewandte Chemie - International Edition* **2006**, *45* (22), 3683–3686. <https://doi.org/10.1002/anie.200600191>.
- (36) Saito, K.; Miyashita, H.; Akiyama, T. Chiral Phosphoric Acid Catalyzed Oxidative Kinetic Resolution of Cyclic Secondary Amine Derivatives Including Tetrahydroquinolines by Hydrogen Transfer to Imines. *Chemical Communications* **2015**, *51* (93), 16648–16651. <https://doi.org/10.1039/c5cc06436h>.
- (37) Han, Z. Y.; Xiao, H.; Chen, X. H.; Gong, L. Z. Consecutive Intramolecular Hydroamination/Asymmetric Transfer Hydrogenation under Relay Catalysis of an Achiral Gold Complex/Chiral Bronsted Acid Binary System. *J Am Chem Soc* **2009**, *131* (26), 9182–9183. <https://doi.org/10.1021/ja903547q>.
- (38) Zhao, Z. B.; Wang, J.; Zhu, Z. H.; Chen, M. W.; Zhou, Y. G. Enantioselective Synthesis of 2-Functionalized Tetrahydroquinolines through Biomimetic Reduction. *Org Lett* **2021**, *23* (23), 9112–9117. <https://doi.org/10.1021/acs.orglett.1c03430>.

(39) Qin, J.; Chen, F.; He, Y. M.; Fan, Q. H. Asymmetric Hydrogenation of 3-Substituted 2H-1,4-Benzoxazines with Chiral Cationic Ru-MsDPEN Catalysts: A Remarkable Counteranion Effect. *Organic Chemistry Frontiers* **2014**, *1* (8), 952–955. <https://doi.org/10.1039/c4qo00188e>.

Chapter 4 Photochemical Alkynylation of Aziridinoquinoxalines Through the Intermediacy of Azomethine Ylides³

4.1 Introduction to aziridine chemistry

Aziridines are the smallest nitrogen-containing molecules and as other three-membered rings (cyclopropanes, epoxides) they also have significant ring strain. Due to this ring strain, aziridine synthesis is not an easy task and this along with their stability poses limitations to the applications of aziridine-containing molecules. Despite this, molecules containing aziridine heterocycles found a wide application in various fields including drug discovery.^{1,2}

Ring strain of aziridines may significantly impact their physical and chemical properties. Mostly, the high ring strain of aziridines means that the three-membered ring will undergo ring-opening processes under relatively mild conditions in comparison to other heterocycles. Due to this, aziridines are excellent building blocks to access valuable products that include 1,2-diamines, amino alcohols, chiral amines, and new ring systems.² Similar to their epoxide analogs, aziridines can undergo a direct nucleophilic ring opening with strong nucleophiles (Scheme 4.1A). In the case of “activated” aziridines that contain electron-withdrawing substituents (EWG) on nitrogen, these compounds will react via a classical S_N2 mechanism that involves a nucleophilic attack on the most sterically accessible carbon atom. However, aziridines with alkyl substituents on the

³ Authors and Contributions:

This chapter is partially adapted from: **O. Zhelavskiy**, S. Parikh, Y.-J. Jhang, R. J. Staples, P. M. Zimmerman, P. Nagorny, *Angew. Chem. Int. Ed.* **2024**, 63, e202318876

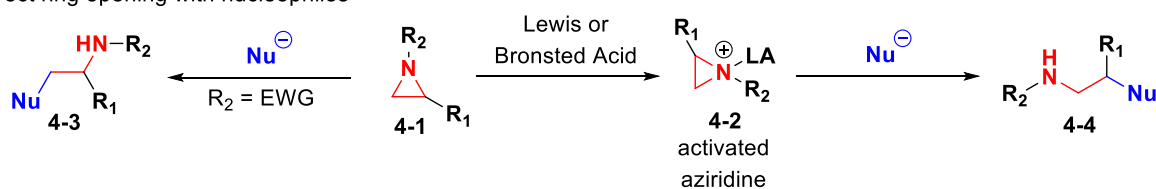
Y.-J. Jhang contributed to the synthesis of starting materials for the substrate scope screening
S. Parikh assisted in reaction conditions screening

nitrogen atom are not electrophilic enough and their activation via Lewis or Brønsted acid catalysis is needed. In this case, the nucleophilic attack will happen in the position of the most stable carbocation formation.³

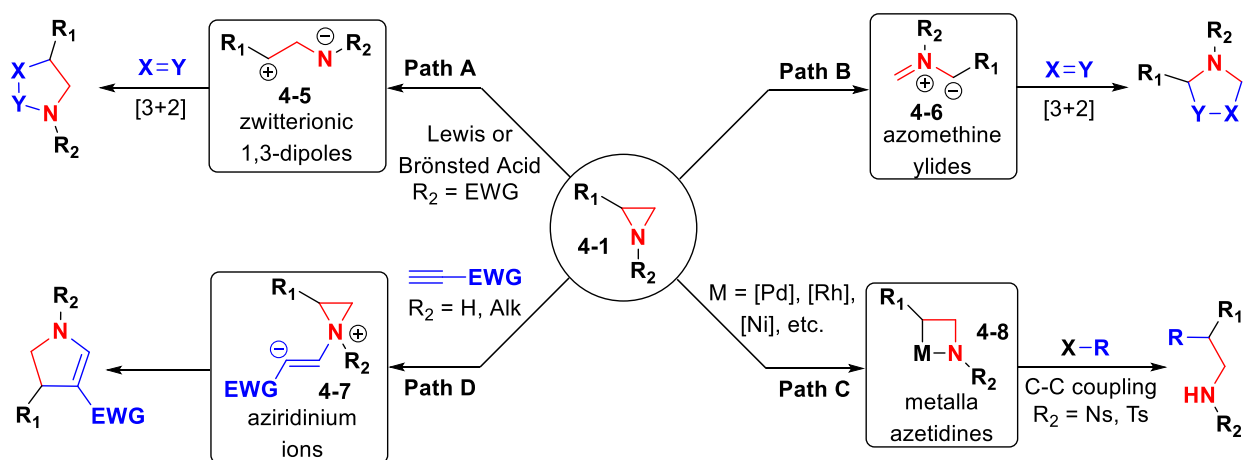
Ring-opening of aziridines can also proceed with the formation of reactive intermediates typically used for the cycloaddition reactions (Scheme 4.1B). Under Lewis or Brønsted acid catalysis aziridines can undergo C-N bond cleavage to form zwitterionic 1,3-dipoles **4-5** that are widely used in [3+2] cycloaddition reactions (Path A). Electron withdrawing groups at nitrogen significantly facilitate ring-opening.⁴

Scheme 4.1. Reactivity trends of aziridines

A. Direct ring opening with nucleophiles



B. Aziridine-based intermediates



On the other hand, in contrast to epoxides, a direct 4π -ring opening (under photochemical or thermal activation) of three-membered rings via C-C bond cleavage is possible for aziridines with the formation of relatively stable azomethine ylides **4-6** (Path B). This transformation is not

strongly dependent on substituents; however, R_1 substituents that can stabilize the negative charge formation on carbon atom will lower the energy barrier of the C-C bond cleavage.⁴

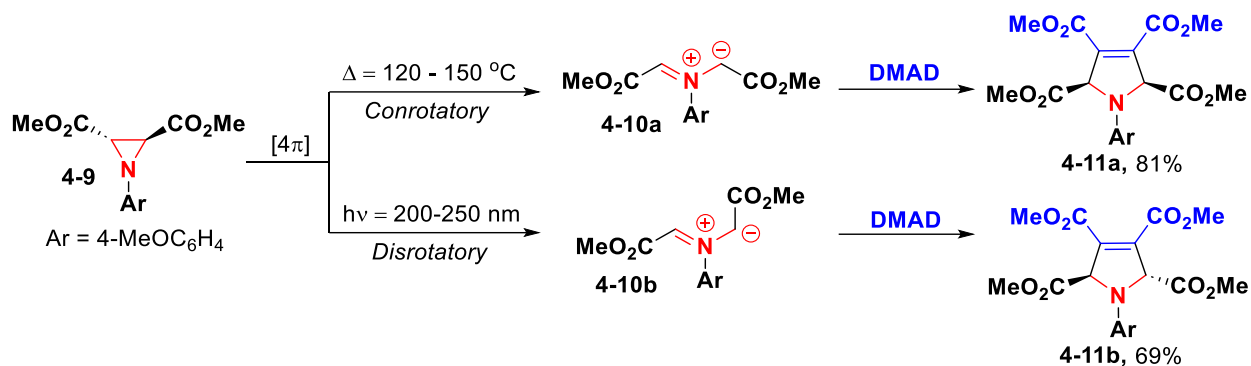
The increased s-character of the aziridine nitrogen, which reduces its π -donor abilities, greatly reduces the basicity of the nitrogen ($pK_a \sim 8$ in water) when compared with regular amines ($pK_a \sim 11$ in water). Despite its lower basicity, aziridine nitrogen may have significant nucleophilicity. For example, aziridines can perform Michael-type addition to electron-deficient alkynes (Scheme 4.1B, path C) to form aziridinium ions **4-7** as intermediates for the subsequent former [3+2] cycloaddition leading to 5-membered heterocycles as the reaction products.⁴

Finally, aziridines serve as useful reagents for C-C cross-coupling reactions (path D). Oxidative addition of transition-metal catalysts, such as Rh(I), Ni(0), Pd(0), etc. to aziridines could generate metallo-azetidines **4-8**. This complexes then can react with nucleophiles to produce amino derivatives, with alkenes and alkynes to form cyclic heterocycles via [3+2] or [5+2] cycloadditions. More importantly, metal in metallo-azetidines **4-8** can be transmetalated with various alkyl- and aryl-halides or boronic acids and then perform classical cross-coupling reactions via reductive elimination to form new C-C bonds.^{5,6}

As it is evident from the overview above, aziridines may serve as extremely useful building blocks for organic synthesis due to their versatile reactivity and multiple reactive intermediate formation. Among all reviewed pathways (Scheme 4.2), the direct 4π -electrocyclic ring opening still remains the most under-explored area in aziridine chemistry. Azomethine ylides derived from aziridines were first postulated as intermediates by Heine in 1965 who first reported cycloaddition of azirine **4-9** with dimethyl acetylene dicarboxylate (DMAD) via C-C bond cleavage under thermal conditions (Scheme 4.2).⁷ Stereochemical control of the reaction was explained by

Huisgen, who demonstrated that the same cycloaddition can be performed under UV irradiation (Scheme 4.2).⁸

Scheme 4.2. Stereochemical control of aziridine ring-opening.

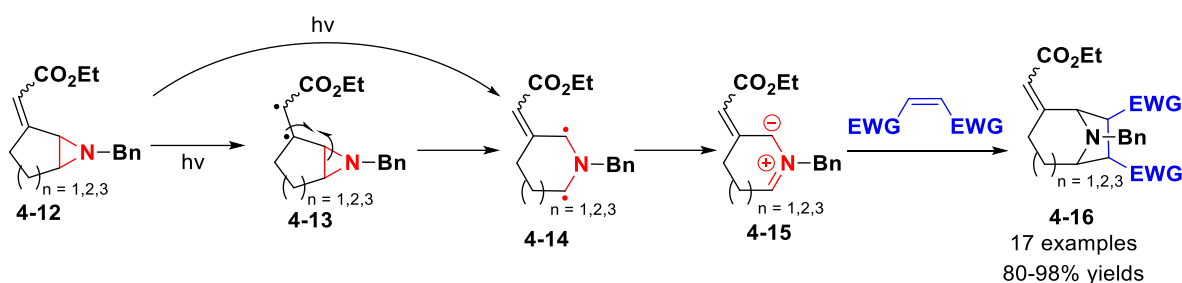


According to the Woodward–Hoffmann theory, thermal ring opening proceeds via a conrotatory C–C bond-breaking process, while the photochemical reaction leads to ylides **4-10b** generated via a disrotatory process. Ylide configuration dependence on the reaction activation will dictate the relative stereochemistry of the final product. Since these publications, a lot of cycloaddition reactions of aziridine ylides with alkenes and alkynes were reported resulting in the formation of valuable unsaturated *N*-heterocycles such as pyrrole and azepine.

However, such cycloadditions have been mostly performed under thermal activation. This can be explained by the harsh photochemical conditions required to excite an aziridine ring (UV-C region, 200-250 nm), which are not compatible with complex organic molecules or functional groups. For example, Sugiyama and co-workers⁹ reported aziridines **4-12** [3+2] cycloaddition with electron-deficient alkenes (Scheme 4.3) using 60 W low-pressure mercury lamp (184–254 nm). Authors postulate that this reaction happens through the formation of biradical species **4-14** that then relaxes to ylide **4-15**. Transformation proceeds with high yields (80-98%), which could be contribute to effective generation of ylides **4-15** in stark contrast to the previous publications where the yields of photochemical transformations were much lower.⁴ The effective photoexcitation

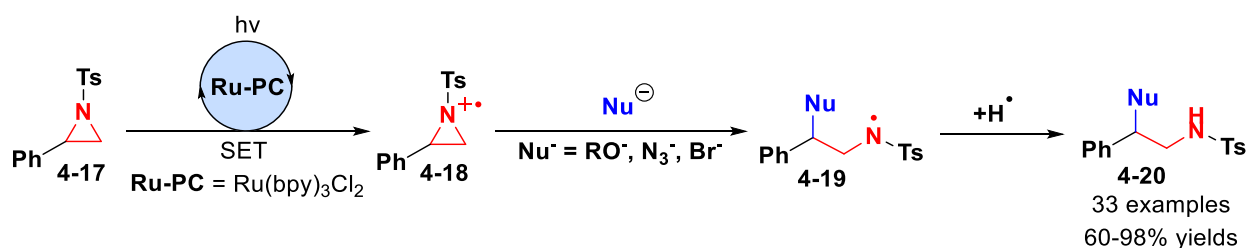
leading to ylides **4-15** in this case happens due to the presence of a conjugated alkene serving as a chromophore group. The excitation of the alkene is possible with UV-C irradiation leading first to triplet bi-radical **4-13** which only then facilitates ring opening via a radical mechanism.

Scheme 4.3. Aziridine ring opening via a direct photoexcitation with UV-C light.



Mild photochemical activation of aziridines could be achieved by using photocatalysts to perform SET processes, usually involving oxidation of nitrogen atoms to a radical-cation. For example, the reaction method developed by the Xia group (Scheme 4.4)¹⁰ involves a SET oxidation of aziridine **4-17** by Ru(II) photocatalyst under visible light irradiation (Blue LED). This leads to radical-cation **4-18**, which is much more electrophilic and reacts with various nucleophiles to produce ring-opened radical product **4-19**. Further H-abstraction (from methanol as the solvent) generates final 1,2-bifunctional amine **4-20**. In this case, photoredox catalysis promotes nucleophilic ring opening via C-N bond breaking and does not lead to ylide intermediates.

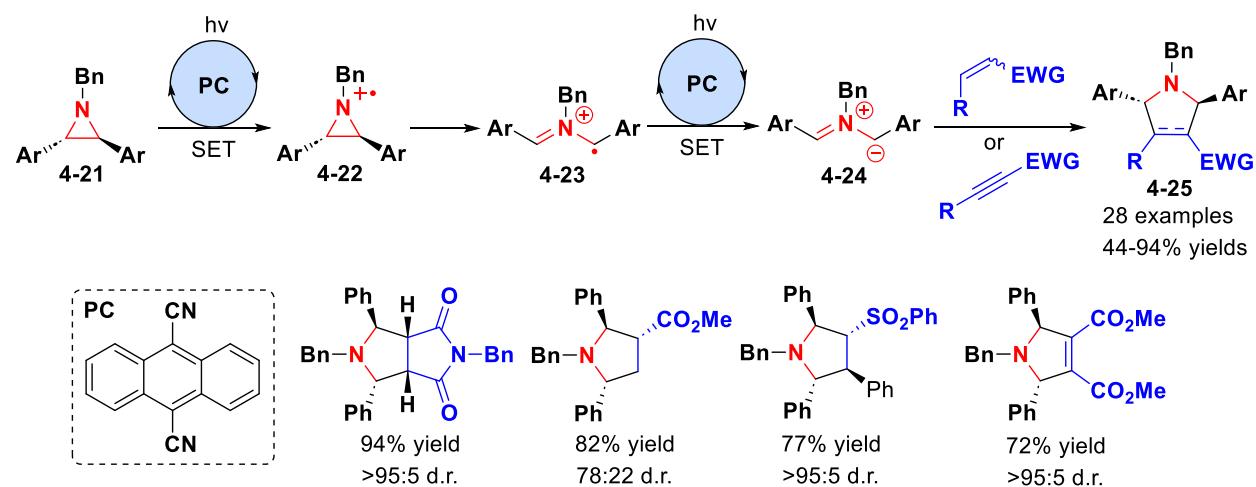
Scheme 4.4. SET oxidation of aziridine for activating ring for nucleophilic substitution.



Until recently, no mild photocatalytic protocol for ylide generation existed. However, in 2024, contemporaneously with our work described in this chapter, Dell'Amico researcher group

described photoredox catalytic generation of ylides from aziridines (Scheme 4.5).¹¹ Aziridines **4-21** were oxidized via a SET-process with excited state of dicyanoanthracene (DCA) catalyst under Blue LED irradiation (427 nm) to generate radical-cations **4-22** that undergo further ring-opening via a C-C bond cleavage. This acyclic radical-cation **4-23** then abstracts an electron from the reduced DCA photocatalyst to form the target ylide **4-24**. Then, the generated ylide is intercepted with alkenes or alkynes to produce 5-membered pyrrole rings **4-25**. The reaction proceeds with high levels of stereocontrol, as the cycloaddition is a stereospecific process, and the diastereoselectivity is being controlled by the configurations of alkene and aziridine. Despite the large number of included substrates (28 examples), the method had limited scope and only *bis*-aryl substituted aziridines **4-21** (Ar = Ph, 4-BrC₆H₄ and 4-MeC₆H₄) were used to react with electro-deficient alkenes.

Scheme 4.5. Photoredox generation of aziridine ylides and their [3+2] cycloaddition reactions.



The photoredox reactions like the one described above could be strongly sensitive to the substrate scope as the changes in the substrate structure may result in significantly mismatched substrate/catalyst redox potentials, thus resulting in reduced catalytic activity. Therefore, a method

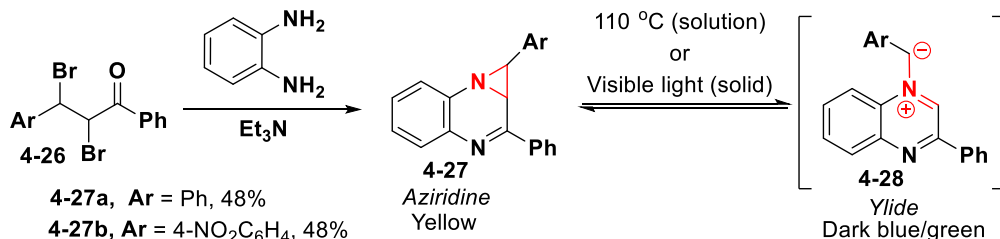
for aziridine excitation via an energy transfer process may hold great potential due to its potentially wider applicability.

4.2 Fused aziridinoquinoxalines as potential precursors for ylides generation

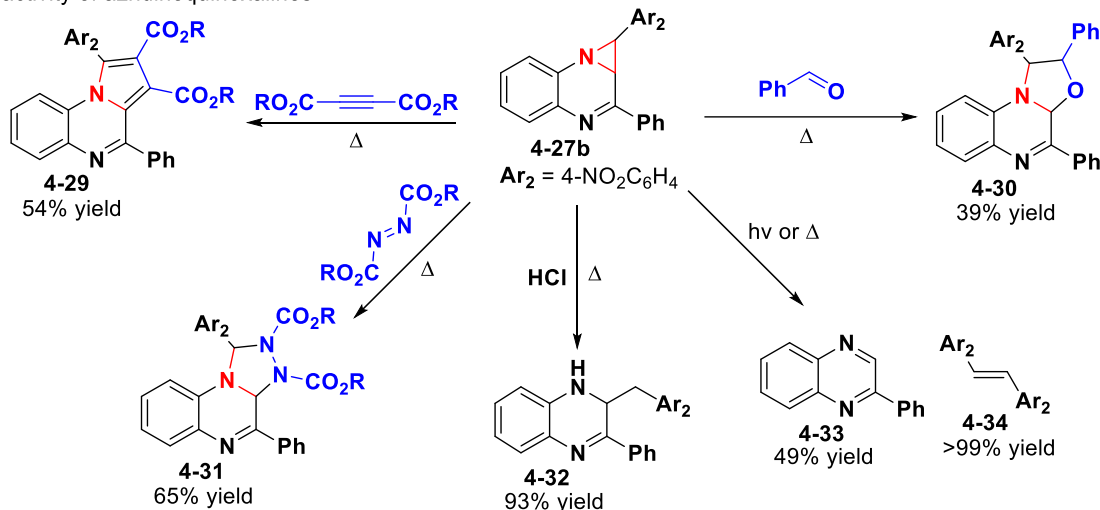
In 1965 Heine and co-workers demonstrated the utility of aziridines in thermal- and photochemically-activated cycloaddition reactions. The same researchers also performed the synthesis of novel fused aziridinoquinoxaline scaffold **4-27** with unique photochromic properties. Starting from easily accessible dibromo ketones **4-26** (dibromo chalcones), a condensation with aryldiamines, such as phenylene diamine, could be employed to produce aziridinoquinoxalines **4-27** in moderate yields (48%).¹² The following work by Orlov also demonstrated that freshly obtained compounds **4-27** are yellow; however, their exposure to visible light may reversibly change the compounds' color to dark blue or green. That can be attributed to the reversible ring-opening of aziridines by C-C bond cleavage with the formation of deeply colored aziridine ylides **4-28** (Scheme 4.6A). Notably, this photochromic transformation is reversible and was observed only in the solid state.¹³

Scheme 4.6. Synthesis and reactivity of aziridinoquinoxalines

A. Synthesis of aziridinoquinoxalines



B. Reactivity of aziridinoquinoxalines



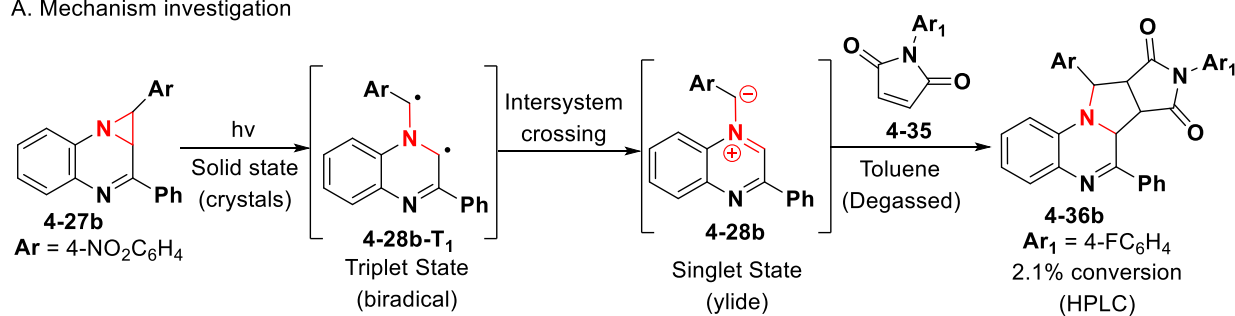
Since their discovery, various reactions have been reported for aziridinoquinoxalines (Scheme 4.6B). Most of them utilize thermal ring opening of aziridine fragment and generation of ylide to perform cycloaddition reactions with alkenes, alkynes, aldehydes, and diazocarbonylates. Treatment of compound **4-27b** with HCl leads to ring opening and unusual generation of compound **4-32**. Heating or irradiating compound **4-27b** with UV light leads to decomposition to 2-phenylquinoxaline **4-33** and generation of trans-stilbene.¹²

Interested in exploring aziridinoquinoxaline photochromic properties, Desenko and Chebanov performed various mechanistic studies to investigate the process of the aziridine ring opening of compound **4-27b** and its analogs.¹⁴ Compound **4-27b** does not have any strong absorbance bands in the UV/Vis spectrum, however, irradiation with a $\lambda_{\text{max}}=365$ nm light source leads to observable colorization of compound **4-27b** in a polystyrene film, and the formation of a

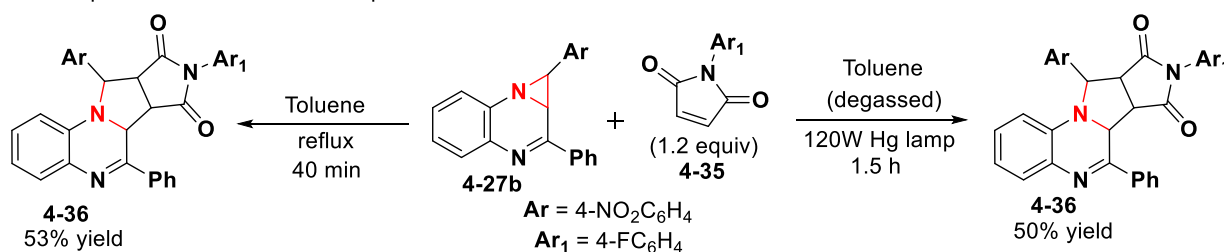
strong absorbance band at 570 nm. After keeping the irradiated sample in the dark, a new absorbance band around 420 nm appeared in parallel with a decrease of 570 nm peak. The above-mentioned results denote a two-step photoinduced transformation of aziridine. On the other hand, in organic solvents the appearance of only a 420 nm absorption band was observed, indicating either instability of the first transformation product or its fast interconversion into more stable intermediate. Authors postulated the formation of a bi-radical triplet state of the open form of aziridine **4-28b-T₁** upon irradiation of compound **4-27b** which then undergoes an intersystem crossing (relaxation) to the singlet state of ylide **4-28b**. Performed EPR studies indicated the formation of bi-radical triplet species both in the solid state and in solution (Scheme 4.7A).

Scheme 4.7. Investigation of photochemical properties of aziridinoquinoxalines.

A. Mechanism investigation



B. Direct photoexcitation of aziridinoquinoxaline



Finally, the studies of selective photo transformations in the chemically inert liquid crystalline medium were performed in cholesteric phase with compound **4-27b** was used as dopant.¹⁴ Upon irradiation of the liquid crystals, it was found that all these transformations were accompanied by a short-wavelength shift of the selective reflection peak from 540 to 495 nm, indicating a change in the geometrical properties of the dopant compound **4-27b**. As the dopant

molecule becomes closer in properties to the liquid crystal structure, it undergoes a smaller long-wavelength shift. In this case, the formation of a planar-type compound was concluded based on the observations, giving the evidence of plain azomethine ylides **4-28b** formation as a second photo transformation product.

On the other hand, the degree of photochemical ylide generation was not significant. Dissolving the irradiated powder of compound **4-27b** in a degassed toluene solution of *N*-(4-fluorophenyl)maleimide **4-35** resulted in full discoloration of the compound and 2.1 % conversion (by HPLC analysis) of the initial aziridine to cycloaddition product **4-36**. Thus, the photoconversion degree and the amount of the ylide photoproduct in irradiated powders did not exceed 2–3%. However, it was possible to obtain the cycloaddition product **4-36** in 50% yield while irradiating the reaction mixture in a quartz tube with a 120 W Hg lamp for 1.5 hours. Comparable yield was also achieved by a thermal activation of compound **4-27b** (reflux) in toluene (Scheme 4.7B).

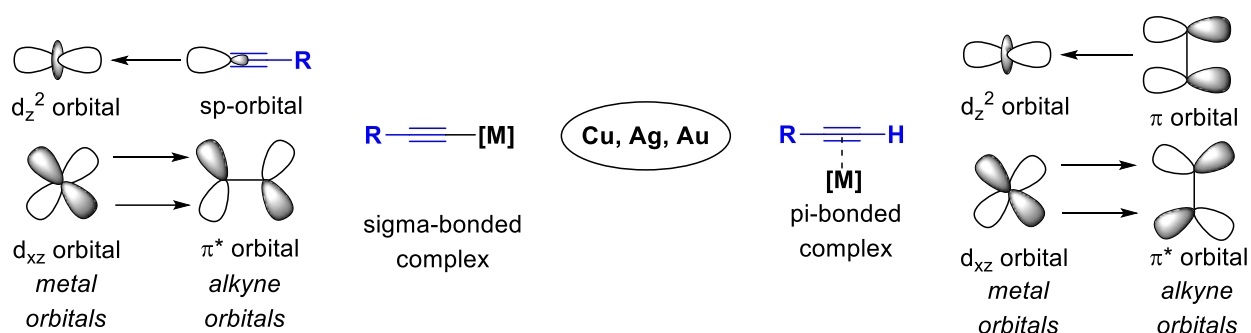
Therefore, azridinoquinoxalines possess unique photochromic properties and C-C bond cleavage leads to ring-opening and the formation of ylides can happen under visible light irradiation. These compounds may serve as the precursors for ylide generation under mild photochemical conditions. Surprisingly, only few transformations involving ylides **4-28** were reported, and the available reports rely on using thermal activation to achieve the ring-opening processes. Therefore, we envision that additional studies of these compounds may lead to the development of new protocols for the aziridine-derived ylide generation.

4.3 Overview of copper(I)-catalyzed asymmetric addition reactions of alkynes

4.3.1 Overview of mechanistic principles

Alkyne is one of the fundamentally important functional groups in organic chemistry due to its versatile reactivity allowing direct transformations into a diverse set of other functional groups. Among these transformations, the alkyne functionalization with transition metal catalysts has received significant attention.¹⁵ Unlike other unsaturated systems with π -orbitals, alkynes exhibit two distinct bonding modes with transition metals, and the formation of both σ - and π -bonded metal complexes is possible (Scheme 4.8). Deprotonation of terminal alkynes ($\text{pK}_a = 25\text{--}26$) can lead to the formation of σ -bonded complexes. In these complexes, the sp -orbital of the alkyne anion donates its electron density to d_z^2 -orbital of the metal, and, at the same time, the complex is stabilized by a π -back donation of the occupied d -orbital of the metal to the empty π^* -orbital of the acetylide. Transition metals capable of being π -acid can also coordinate to alkynes via d_z^2 -orbital bonding to occupied alkyne π -orbital. π -bonding of metals to alkynes lowers the pK_a of the C-H bond and deprotonation can occur even with moderate bases, such as tertiary amines leading to the formation of sigma-bonded complexes.¹⁶

Scheme 4.8. Two modes of metal-alkyne complexes formation.

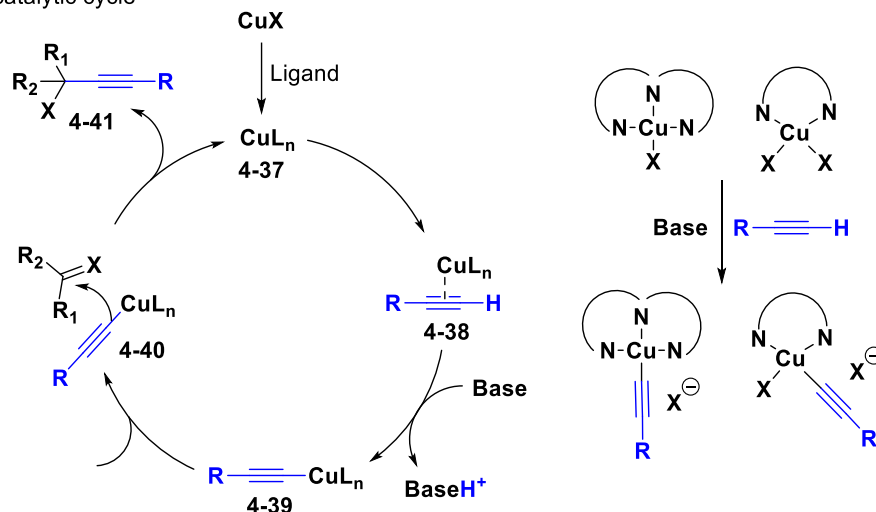


Only a few transition metals, especially a triad of coinage metals (Copper, Silver, and Gold) can enable the dual activation of alkynes. Among them, an enormous number of studies were dedicated towards copper-catalyzed alkyne reactions.¹⁷ A catalytic system consisting of copper (I) or copper (II) salt, weak non-nucleophilic base (such as tertiary amines) and optional achiral or

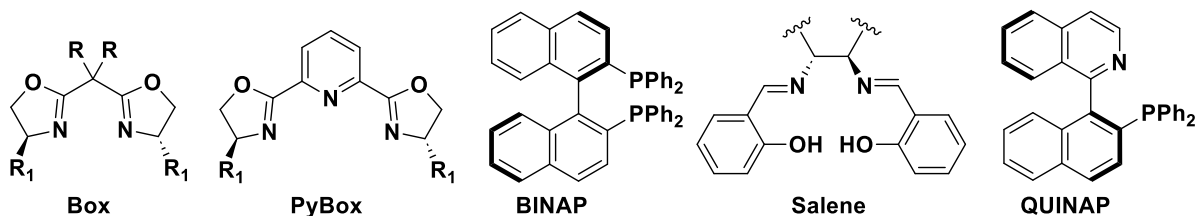
chiral ligand is generally employed for the majority of copper-catalyzed alkyne reactions (Scheme 4.9A). First, copper salt is complexed with the ligand to form copper(I) complex **4-37**, which then coordinates to terminal alkyne via π -bonding (complex **4-38**). This facilitates the alkyne deprotonation by base and formation of σ -bonded copper-acetylide complex **4-39**. Then, this complex **4-39** performs a nucleophilic attack on electrophiles, usually on electrophilic C=X double bonds.

Scheme 4.9. General mechanism of a copper(I)-catalyzed alkyne addition to electrophilic π -bonds.

A. General Cu(I) catalytic cycle



B. Examples of the common chiral ligands for Cu(I) catalysis



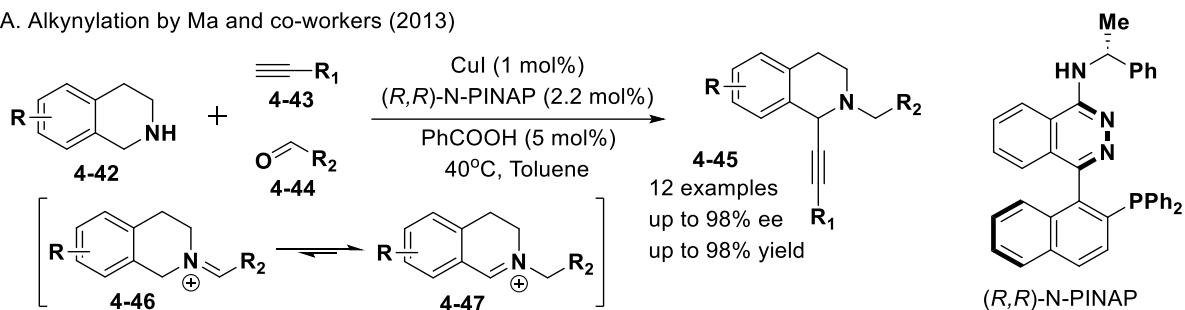
This generates reaction product **4-41** of alkyne addition to electrophilic centers. This reaction cycle can be performed with copper(I) salts only (CuI , CuCl , CuOTf , etc.); however, usually a ligand is used to enhance the solubility of the copper salt in organic solvents or to perform the alkynylation in an enantioselective manner. Copper(I) and (II) cations prefer to form square-planar tetra-

coordinated complexes with ligands (Scheme 4.9A). In the case of the bi- or tri-dentate ligands, the rest of the coordination sphere is taken up by the copper salt counteranions that are further replaced with an acetylide anion. Therefore, tetra-coordinated ligands usually demonstrate lower catalytic activity as all 4 positions of the copper cation are taken up by the ligand donor atoms. For the asymmetric variants of these reactions, catalytic or stoichiometric amounts of copper salts can be combined with different chiral ligands, such as Box, PyBox, BINAP, Salen, PINAP, PHOS, PHIM, etc. (Scheme 4.9B).¹⁸ These transformations usually require mild conditions (no heating or even cooling) and suitable for alkylation of aldehydes, ketones, imines, iminium and oxocarbenium cations, activated alkenes (with electron-withdrawing groups or conjugated to carbonyls), epoxides, etc.¹⁵

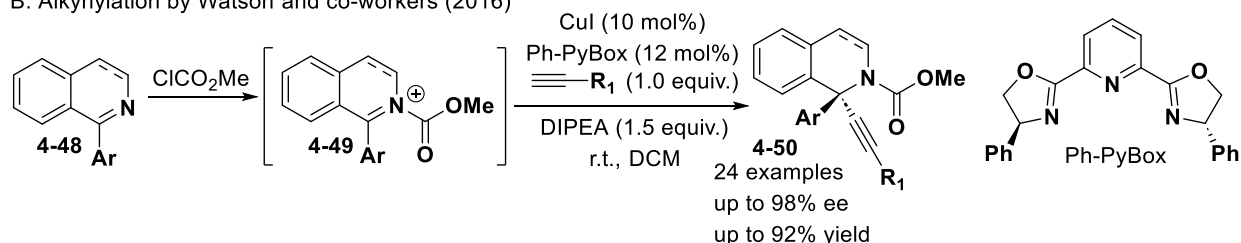
The asymmetric copper-catalyzed alkynylations have been extensively employed to achieve modification of various heterocyclic systems to produce valuable chiral building blocks. The selected precedents that are important for the studies in this chapter are discussed below. One of such key transformations was developed by Ma and coworkers in 2013 (Scheme 4.11A). In this work, the Ma group employed CuI complex with (*R,R*)-*N*-PINAP to perform an enantioselective C-C coupling of tetrahydroisoquinolines **4-42** and terminal alkynes.¹⁹ The electrophile was generated via a heterocycle condensation with an aldehyde that produced an iminium ion that further rearranged to a more stable conjugated cation that subsequently underwent a C1-alkynylation leading to the addition product **4-45**.

Scheme 4.10. Asymmetric alkylation of isoquinolinium and quinolinium-based cations.

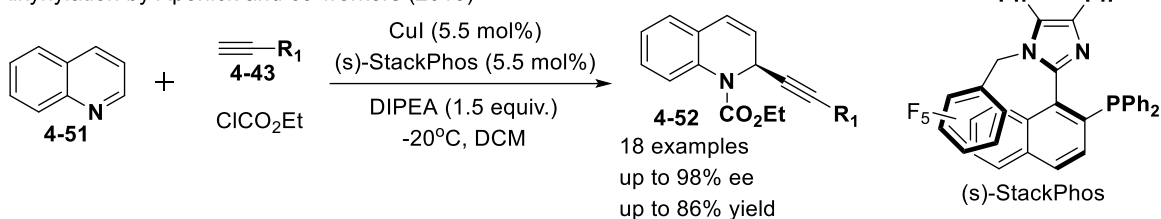
A. Alkylation by Ma and co-workers (2013)



B. Alkylation by Watson and co-workers (2016)



C. Alkylation by Aponick and co-workers (2015)



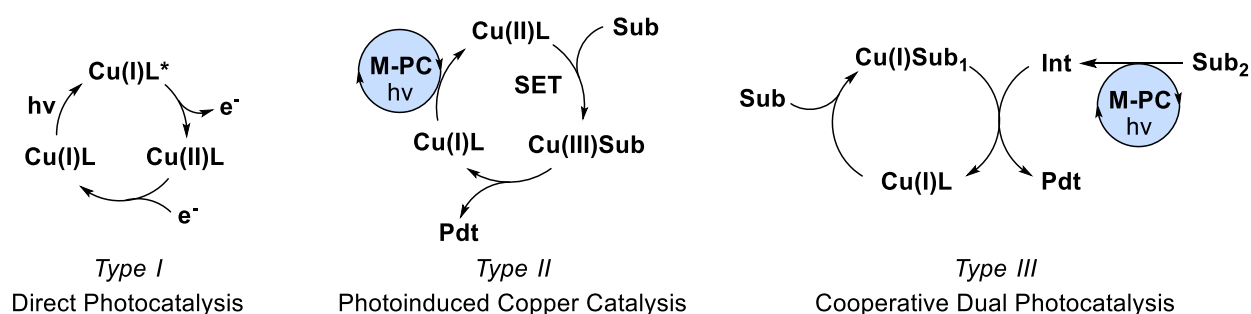
Aromatic heterocycles are also important synthetic building blocks, as it is possible to dearomatize them with enantioselective alkyne installation. Watson et al. in 2016 used methyl chloroformate to generate isoquinolinium salts **4-49** to perform an asymmetric C1-alkynylation using chiral $\text{Ph-PyBox}\cdot\text{CuI}$ complex (Scheme 4.10B).²⁰ Same approach can be used to achieve dearomative C2-alkynylation of quinoline **4-51** as demonstrated by Aponick (Scheme 4.10C).²¹ In both cases, aromatic heterocycles were acylated to produce highly electrophilic intermediates similar to well-known pyridinium cations (Katritzky Salts).

4.3.2 Photoinduced copper-catalyzed enantioselective alkynylations

Visible-light photoredox catalysis has become a powerful tool in organic synthesis. Although the field of photocatalysis is dominated by noble metal complexes (Ru, Ir), the

applications of less expensive copper-based catalysts are also known. The reactions involving metal photocatalysts (i.e. copper) can be classified into three types based on their mechanisms (Scheme 4.11). Type I is the classical direct catalysis of photoredox processes, where copper serves as a SET oxidant or reductant after being excited by the visible light. Despite being a cheaper and more abundant alternative to more common octahedral Ir and Ru complexes, copper-based photocatalysts have not yet found broad applications for several reasons. Primarily, the non-emissive nature and poor photostability of the electronic excited states of the first-row transition metals limit the application of the copper complexes.²²

Scheme 4.11. Three types of copper catalysis in photochemical transformations.



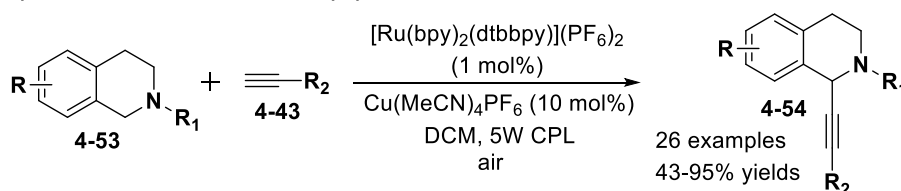
Type II is the photoinduced copper catalysis, where copper complexes are involved in the catalysis of chemical transformation, but are not directly excited by light. Different photocatalytic cycles (for example with Ir photocatalysts) provide oxidation or reduction of copper cation during the reaction thus changing the oxidation state for more effective interaction with the substrate. For example, photoredox catalysis promotes the Cu(I)/Cu(III) catalytic cycle used for many cross-coupling reactions. In this type of catalysis, copper complexes compete with well-established Ni(I)/Ni(III) and Ni(I)/Ni(II) catalytic cycles.²³ Finally, Type III catalysis represents cooperative dual photocatalysis, in which both metals activate substrates independently. The photoredox cycle generates intermediates from one substrate while copper catalysts activate another substrate for their further reactions. In this case, both the photocatalyst and copper catalyst perform the

transformation independently. Due to the high synergy of copper with other metals, the reaction scope that can be developed while applying dual catalysis is almost unlimited.^{17,24}

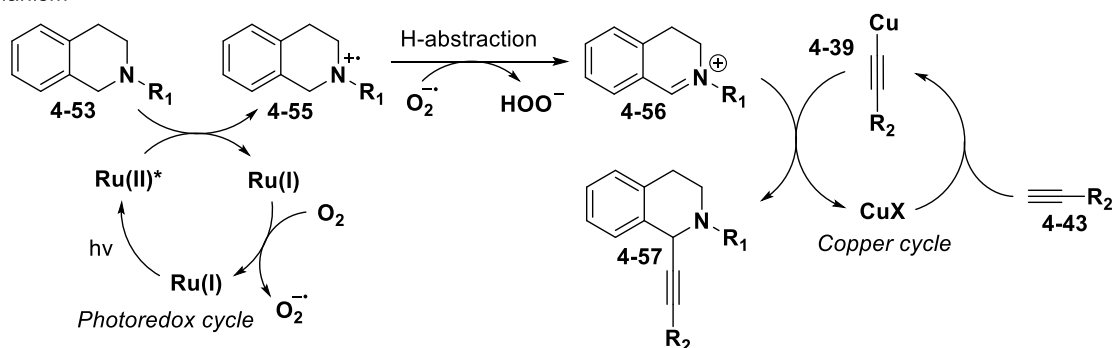
Alkynylation of heterocycles can be performed without preforming the iminium cations (as it was described in Chapter 5.3.1) by coupling the copper acetylide addition with the photoredox cycle to generate an electrophile. Using this approach, Rueping and co-workers developed an effective protocol for a direct C-C cross-coupling of alkynes and C-H group in tetrahydroisoquinolines **4-53** (Scheme 4.12A).²⁵

Scheme 4.12. Photocatalyzed C-C cross-coupling with alkynes.

A. Photocatalyzed aerobic oxidation and alkynylation



B. Mechanism

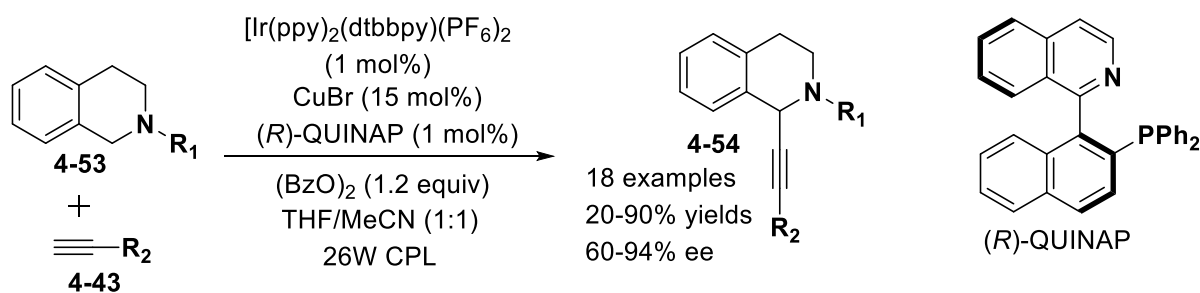


From the mechanistic side (Scheme 4.12B), Ru(II) photocatalyst was applied to perform an oxidation of nitrogen in tertiary amine. After Ru(II) gets excited by the visible light, it oxidizes nitrogen to radical-cation **4-55** and becomes Ru(I). Catalyst regeneration happened through the oxidation by air oxygen in the reaction vial, and under an inert atmosphere the authors reported no conversion. Generated peroxide radical-anion abstracts H atom from the amine radical-cation **4-55** to produce iminium cation **4-56** that further reacts with copper acetylide **4-39** generated via the Cu(I) catalytic cycle. In this case, no ligand was needed for Cu(I) complex formation. Despite the

reaction protocol allowing to produce of 26 examples of alkynylated isoquinolines **4-54**, the reaction was used to produce racemic products.

The further development of the described protocol was done by Li in 2015 by introducing chiral ligands to the catalytic system to generate chiral Cu-acetylide complexes (Scheme 4.13). After screening various chiral ligands, the authors discovered that (*R*)-QUINAP ligand provides the best enantioselectivity for the acetylide addition to the generated iminium cation. Another difference from the Rueping protocol consisted in using benzoyl peroxide as an oxidant for Ru(II) regeneration and H-abstraction from the radical-cation intermediates.²⁶

Scheme 4.13. Asymmetric photocatalyzed alkylation of tetrahydroisoquinolines.



There are numerous related methods utilizing Cu(I) catalysis combined with transition metal photoredox catalysis (TMPRCs) to achieve enantioselective alkylation or other transformations involving Cu-Substrate complexes formation. However, there are no examples of coupling copper catalysis and ring opening of aziridines via direct excitation or energy transfer process leading to ylide generation.

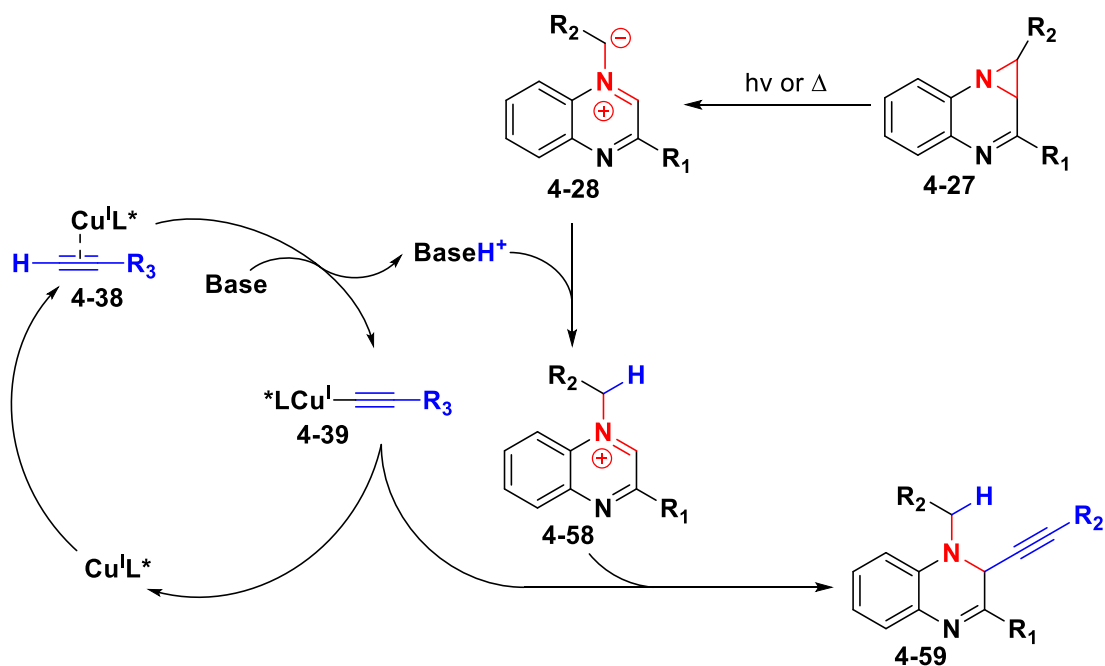
4.4 Generation and alkylation of ylides from aziridinoquinoxalines under thermal conditions

The prior studies exploring the reactivity of aziridinoquinoxalines and related compounds suggest that these compounds may undergo a thermal 4π -electrocyclic ring-opening reaction to

provide azomethine ylides that could be intercepted in various [3+2] cycloaddition reactions. Despite existing phenomena of photochromism of aziridinoquinoxalines indicating that this process has a low barrier for ring-opening, the reactivity of such compounds under photochemical conditions has not been explored in detail.

Based on the previous literature data and mechanistic studies described in Chapter 4.2, we surmised that azomethine ylides derived from aziridinoquinoxalines **4-27** might be intercepted with copper(I) acetylides through a catalytic cycle summarized in Scheme 4.14. The initial ring opening of aziridine can be performed either by well-documented thermal activation or by visible light activation which was our primary research interest. The copper catalytic cycle will involve generating Cu(I)-acetylide complex **4-39** by π -acid-promoted deprotonation of alkynes with tertiary amines.

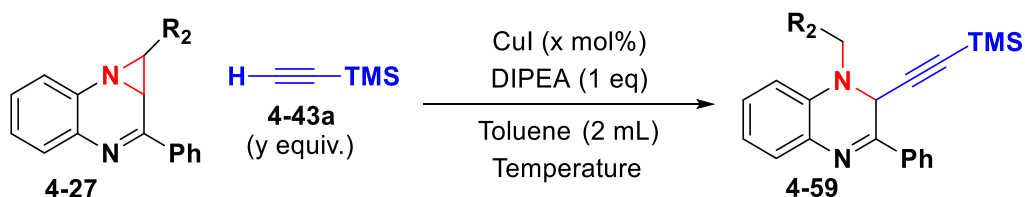
Scheme 4.14. Proposed reaction design based on copper-catalyzed alkylation of azomethine ylides.



Importantly, the protonated base will transfer proton to the ylide resulting in the formation of a high electrophilic quinoxalinium cation **4-58**, which will then be trapped by copper(I) acetylide to produce the desired product **4-59**. We also envisioned performing this transformation asymmetrically by using an appropriate chiral ligand for Cu(I) complex.

Our studies commenced with exploring the proposed in Scheme 4.14 catalytic cycle under the thermal activation conditions that were previously observed to convert substrate **4-27a** ($R_1, R_2 = \text{Ph}$) into the corresponding ylide. The reaction conditions were based on using copper(I) iodide and diisopropylethylamine (DIPEA) as a base to catalyze the addition of ethynyltrimethylsilane **4-43a** to generate ylides. The reaction did not show any conversion at room temperature; however, the desired product formation was observed in 91% yield after the reaction mixture was heated to 60°C for 24 hours (Table 4.1). The initial optimization involved selecting the optimal reaction temperature, stoichiometry, and catalyst loading. The efficient formation of product **4-59** (93% yield) was observed under the optimized conditions after heating the substrate for 18 h at 80 °C using 5 mol% of Cu(I) iodide and stoichiometric DIPEA. Further elevation of the temperature led to shorter reaction times; however, the formation of a side-product and decomposition impurities lowering the product yield was observed. As expected, excluding the copper catalyst from the reaction resulted in completely diminished reactivity. Unfortunately, our attempts to extend this method to other substrates such as the *t*-butyl-substituted aziridinoquinoxaline **4-27d** did not lead to the formation of the desired product, even at 110 °C, and only starting materials were isolated.

Table 4.1. Reaction conditions optimization for thermal activation of aziridinoquinoxalines.

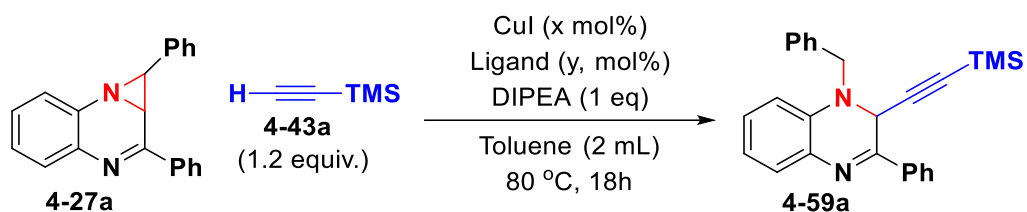


Entry	R ₂	T, °C	t, hours ^a	x, mol%	y, eq	Yield ^b , %
1	Ph	r.t.	24	10	2	N.R.
2	Ph	60	24	10	2	91
3	Ph	80	18	10	2	94
4	Ph	110	8	10	2	84
5	Ph	80	18	10	1	91
6	Ph	80	18	5	1	93
7	Ph	80	18	0	1	N.R.
8	tBu	80	18	5	1	N.R.
9	tBu	110	48	5	1	N.R.

^aReaction progress was monitored by TLC until full starting material consumption; ^bIsolated yield.

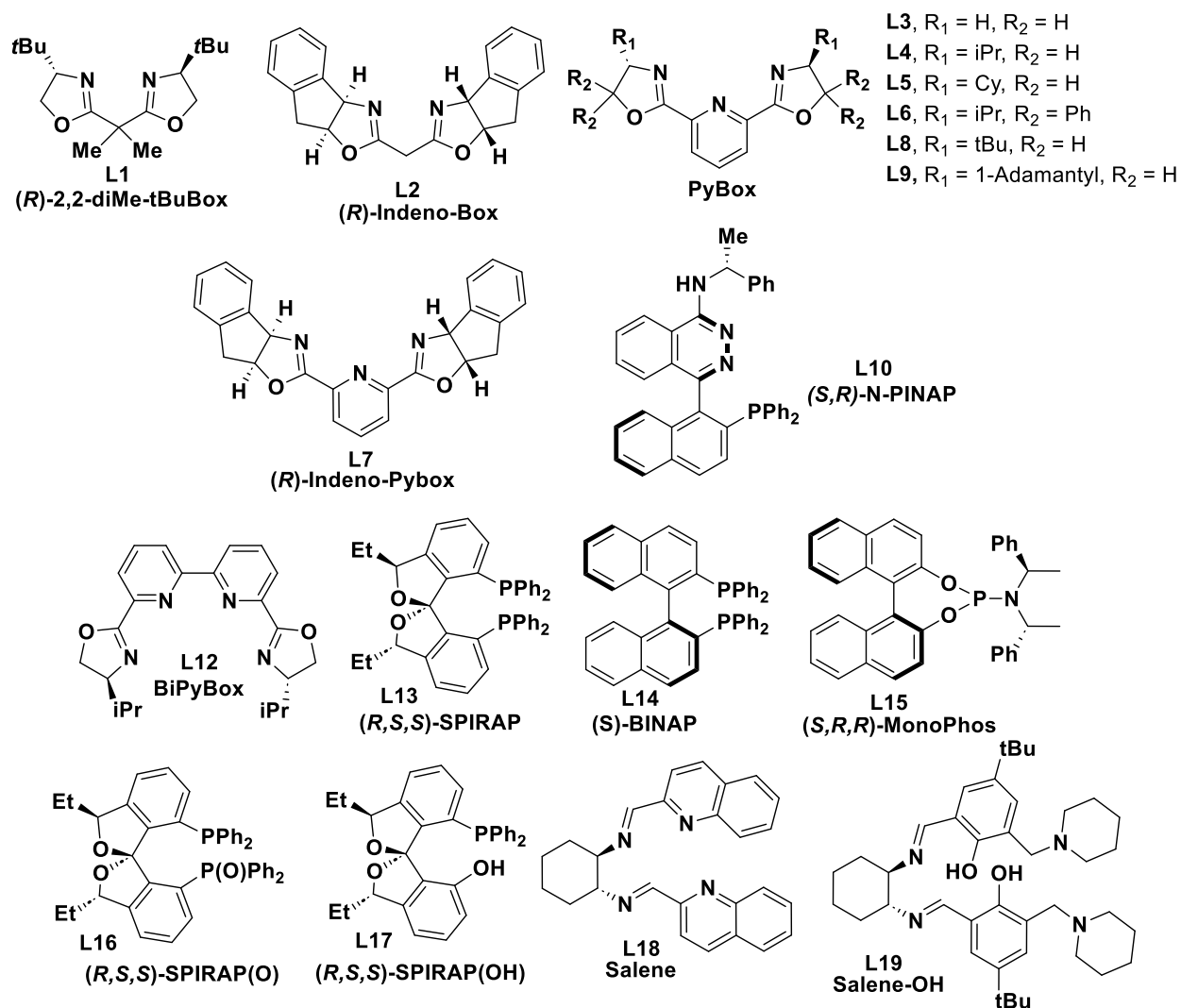
Based on the optimal conditions, we tried to search for the best chiral ligand to achieve an enantioselective formation of product **4-59a** (Table 4.2, Scheme 4.15). We started catalytic tests with broadly used for Cu(I) catalysis Box ligands; however, all tested Box ligands (Entries 1 and 2) demonstrated product generation with no enantioselective control (50:50 er). In contrast, tridentate PyBox ligands allowed generating product in moderate enantioselectivities (Entries 3-9) where the use of *t*-butyl- (**L8**) and 1-adamantyl- (**L9**) derived PyBox ligands resulted in 82:18 er. In all cases, the product yield was high (>80%). We also observed that the ligand to copper salt ratio impacted the reaction enantioselectivity. While using 5:6 and 5:2.5 copper/ligand ratio (mol%) generated the product with an approximately similar ~80:20 enantiomeric ratio, the excess of ligand (entry 11) diminished it to 69:31 er. Tetradentate PyBox ligand **L12** decreased the yield of the product (entry 12), and the same was observed with Salene-based ligands (entries 18 and 19). This suggests that Cu(I) deactivation was happening by forming stable tetra-coordinated complexes. Finally, using phosphorous-based ligands (entries 13-17) did not impact the reaction yield, but resulted in products with low enantioselectivity.

Table 4.2. Chiral ligand screening for thermal alkylation of aziridinoquinoxalines.

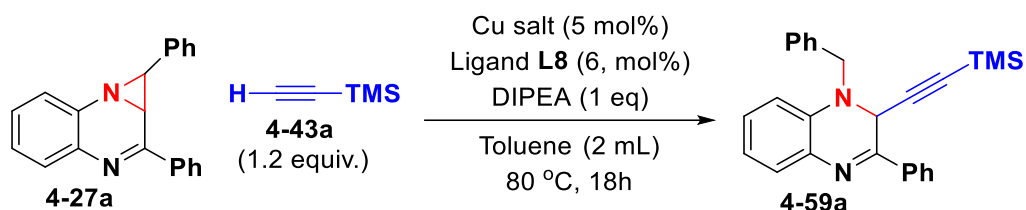


Entry	Ligand	x, mol%	y, mol%	Yield, %	<i>er</i>
1	L1	5	6	85	50:50
2	L2	5	6	94	50:50
3	L4	5	6	80	60:40
4	L5	5	6	78	63:37
5	L6	5	6	97	57.5:42.5
6	L7	5	6	90	69.5:31.5
7	L8	5	6	96	79.5:21.5
8	L9	5	6	86	82:18
9	L10	5	6	91	60:40
10	L8	5	2.5	93	82:18
11	L8	5	10	78	68:31
12	L12	5	6	26	62:38
13	L13	5	6	82	53:47
14	L14	5	6	87	54:46
15	L15	5	6	78	47:53
16	L16	5	6	89	51:49
17	L17	5	6	88	52:48
18	L18	5	6	<10	76:24
19	L19	5	6	<10	74:26

Scheme 4.15. Chiral ligands used for conditions screening in Table 4.2.



Finally, we attempted to screen different copper salts to observe if there is any counter-anion effect that could help to increase the reaction enantioselectivity (Table 4.3). Using 6 mol% of *t*-Bu-PyBox ligand **L8** that demonstrated the best catalytic activity, Cu(I) and Cu(II) salts were screened using 5 mol% catalyst loading. Cu(I) hexafluorophosphate tetra-acetonitrile complex (entry 1) did not promote the reaction, and only starting reagents were isolated. Lower product yields were also observed when both Cu(I) and Cu(II) acetates were employed (entries 3 and 6).

Table 4.3. Copper source screening for enantioselective alkylation

Entry	Cu salt	Yield, %	<i>er</i>
1	Cu(ACN) ₄ PF ₆	N.R.	-
2	Cu-thiophene-2-carboxylate	86	62.5:37.5
3	CuOAc	78	50:50
4	Cu(OTf) ₂	88	60:40
5	Cu(I)-diphenylphosphinate	95	65:35
6	Cu(OAc) ₂	63	53:47
7	CuCl	92	65:35
8	CuCl ₂	90	54.5:45.5
9	CuBr ₂	92	62:38

In general, we did not observe any significant impact of the counterion on reaction enantioselectivity; however, the salts with less coordinating anions, such as triflate, bromide and diphenyl phosphinate (entries 4, 5 and 9) performed slightly better than chlorides and acetate (entries 6–8). Unfortunately, no other copper salts could outperform the initially employed Cu(I) iodide.

Considering that the substrate scope for the thermal aziridinoquinoxalines activation was limited to aryl substituted substrates, and moderate enantioselectivities were observed despite extensive conditions optimization prompted us to pursue the development of a photochemical reaction variant next.

4.5 Photochemical activation and alkylation of aziridinoquinoxalines

The possibility of photochemical pathway was evaluated by density-functional theory (DFT) computations (B3LYP/6-31+G** for TS search and structure optimization and SMD(Toluene)/wb97x-D3/cc-pVTZ for electronic energy calculation) where the Growing String

Method (GSM) was used to compute the ring-opening energy barriers (Figure 4.1) in both the ground singlet state (S_0) as well as the excited triplet state (T_1).

Figure 4.1. Computed energy barriers (electronic energy) for photoinduced ring-opening of aziridinoquinoxalines.

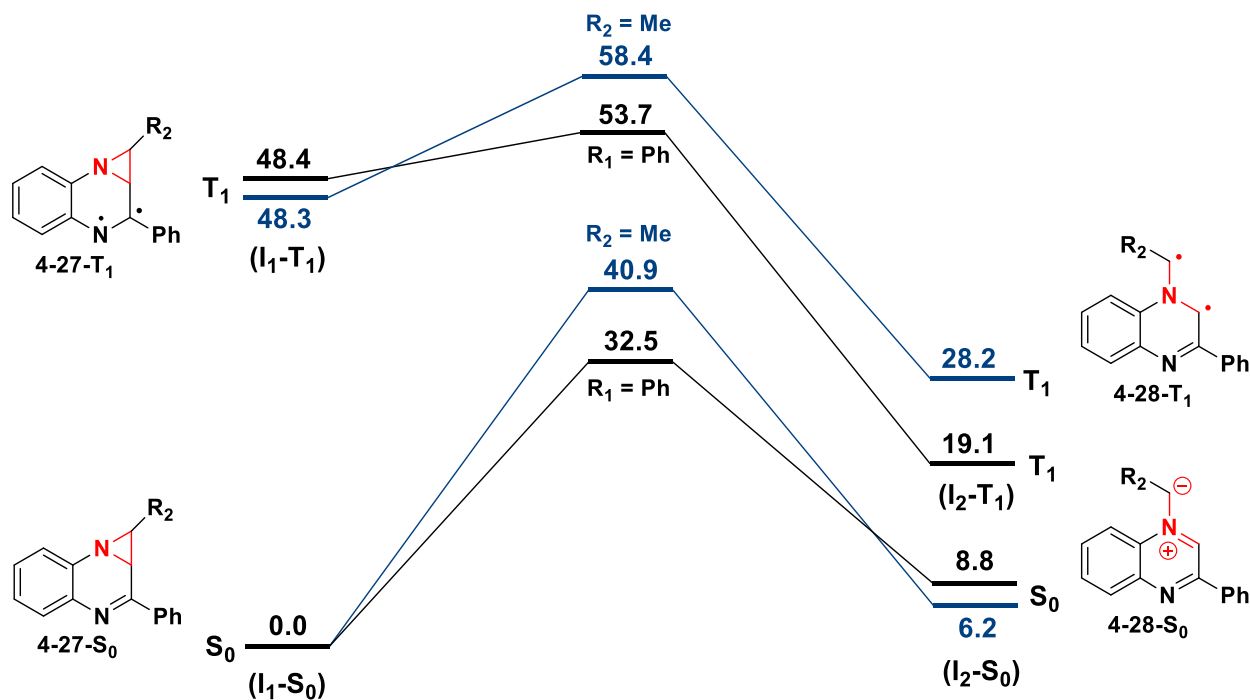
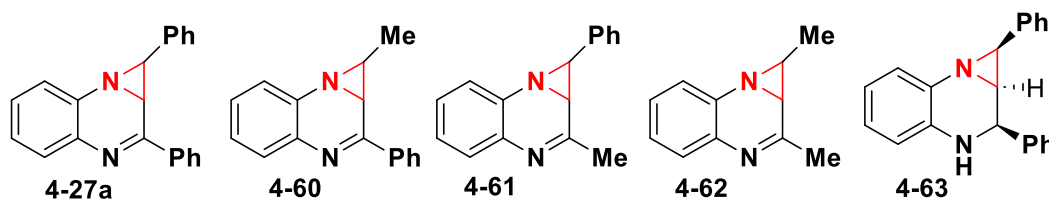


Table 4.4. Computed data for aziridinoquinoxaline substrate models.

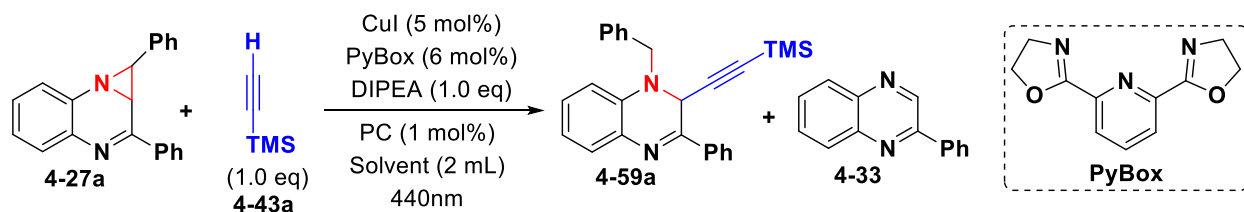


E (kcal/mol)	4-27a	4-60	4-61	4-62	4-63
$\Delta G^\ddagger(S_0)$	32.5	40.9	34.5	42.8	44.0
I_2-S_0	8.8	6.2	8.3	6.4	29.2
I_1-T_1	48.4	48.3	57.3	57.5	82.9
$\Delta G^\ddagger(T_1)$	4.7 (53.7)	10.1 (58.4)	1.0 (63.6)	6.1 (63.6)	4.4 (87.3)
I_2-T_1	19.1	28.2	19.1	29.4	46.6

For aziridine **4-27a**, the activation energy was found to be $\Delta G^\ddagger = 32.5$ kcal/mol for ring-opening in the S_0 -state, which is in good agreement with the observed reactivity under the thermal

activation conditions. However, the computed energy barrier for ring-opening in the T₁ state is only 4.7 kcal/mol, and the formation of ylide **4-28a-T₁** in the triplet state is also more thermodynamically favored by 29.3 kcal/mol. The triplet state (**I₁-S₀**) for compound **4-27a** is photochemically accessible at 48.4 kcal/mol above S₀. Results from these simulations also explain the low reactivity of alkyl-substituted aziridines such as **4-27d** in thermally activated ring-opening. The predicted thermal activation energy barrier from the S₀ state (**I₁-S₀**) is much higher for the alkyl-substituted substrates such as **4-60** and **4-62** (about 40.9 and 42.8 kcal/mol, correspondingly); however, the photochemically induced ring-opening of alkyl aziridines is more feasible from T₁ (**I₁-T₁**) state due to significantly lower barriers (10.1 and 6.1 kcal/mol, correspondingly). It is noteworthy that changing the C₂-phenyl substituent in the aziridinoquinoxaline ring to a methyl group (models **4-61** and **4-62**) results in a significant increase of the T₁-state energies (**I₁-T₁**) by ~9 kcal/mol due to the weaker radical stabilization. Finally, replacing the imine (C=N) chromophore with the CH–NH moiety present in **4-63** renders the photochemical process not feasible due to the highly unstable triplet state **4-63-T₁** (82.9 kcal/mol).

Based on the modeling results of Table 4.4, our subsequent studies focused on exploring the direct excitation of aziridinoquinoxaline **4-27a** with Blue LED ($\lambda_{\text{max}} = 440 \text{ nm}$) (Table 4.5). Achiral pyridine-bis-oxazoline (PyBox, **L3**) ligand was used to solubilize copper(I) iodide. After 6 h, complete consumption of **4-27a** was observed in both toluene and THF leading to the ylide decomposition product 2-phenylquinoxaline **4-33** (entries 1 and 2). Introducing Ir(III) photocatalysts (entries 3 and 4) didn't significantly improve the reaction outcome, and only with Ir(4-CF₃ppy)₃ the formation of minor amounts of **4-59a** was observed along with **4-33** in 22:78 ratio.

Table 4.5. Initial screening of photochemical conditions

Entry	Solvent	Time, hours ^a	PC	Conversion (% ^c , NMR) ^b	Ratios 4-59a : 4-33
1	Toluene	6	-	>95	0:100
2	THF	6	-	>95	0:100
3	THF	6	Ir(dFppy) ₃	>95	0:100
4	THF	6	Ir(4-CF ₃ -ppy) ₃	>95	22:78

^aReaction progress was monitored by TLC until full starting material consumption; ^b. Conversion is determined by the consumption of starting material by NMR; ^c. Ratio between product **4-59a** and decomposition product **4-33** is determined by NMR.

To understand the reasons behind the nonproductive decomposition leading to substrate **4-33** and to identify better conditions for the photochemical activation, time-dependent DFT calculations (TD-DFT, SMD(Toluene)/wB97x-D3/cc-pVTZ (SG-2) used to optimize geometries and excited states analysis) were performed to characterize the excited states of compounds **4-27** and their ylides (Figure 4.2). For compound **4-27a**, the first excited state S_1 was found to have a vertical excitation energy of 92.1 kcal/mol (313 nm) and an oscillator strength of 0.35. Geometry optimization gives the lowest point of the S_1 PES at 79.7 kcal/mol (359 nm). This implies that a direct excitation of **4-27a** is possible with the Kessil Blue LED source (Chapter 4.8). Computational results are also in good agreement with the experimental UV-VIS spectra of **4-27a** (Chapter 4.8) and fluorescence spectroscopy measurements that helped to identify the emission at 337 nm and absorption at 305 nm for the S_0 - S_1 transition (Figure 4.3). The fluorescence emission spectrum, obtained by exciting compound **4-27a** with light at 305 nm also showed a weak emission band at 515 nm that can be attributed to light emission of T_1 state of compound **4-27a-T₁**.

Figure 4.2. Excited states of aziridine 4-27a calculated via TD-DFT

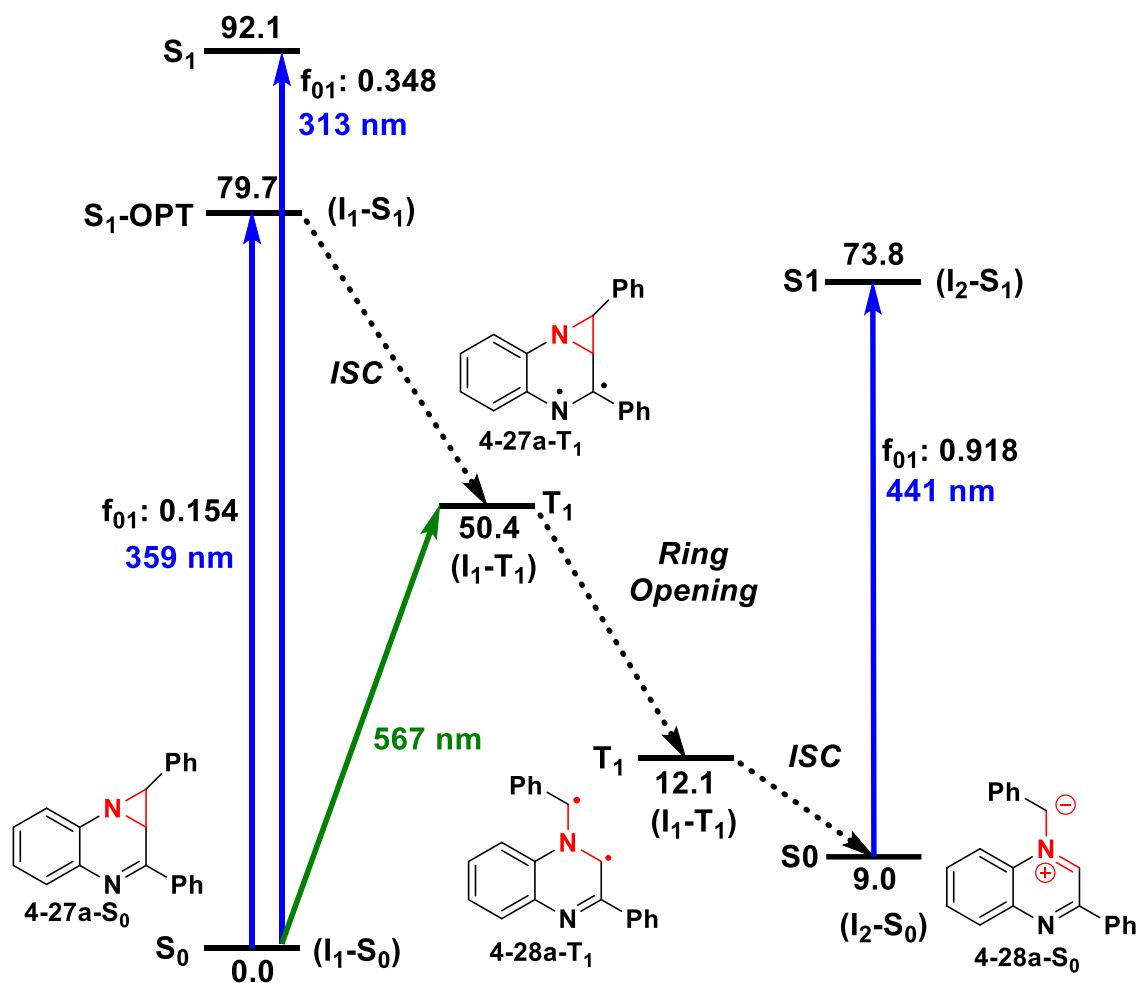


Figure 4.3. Fluorescence spectrum for S_0 - S_1 transition of compound 4-27a

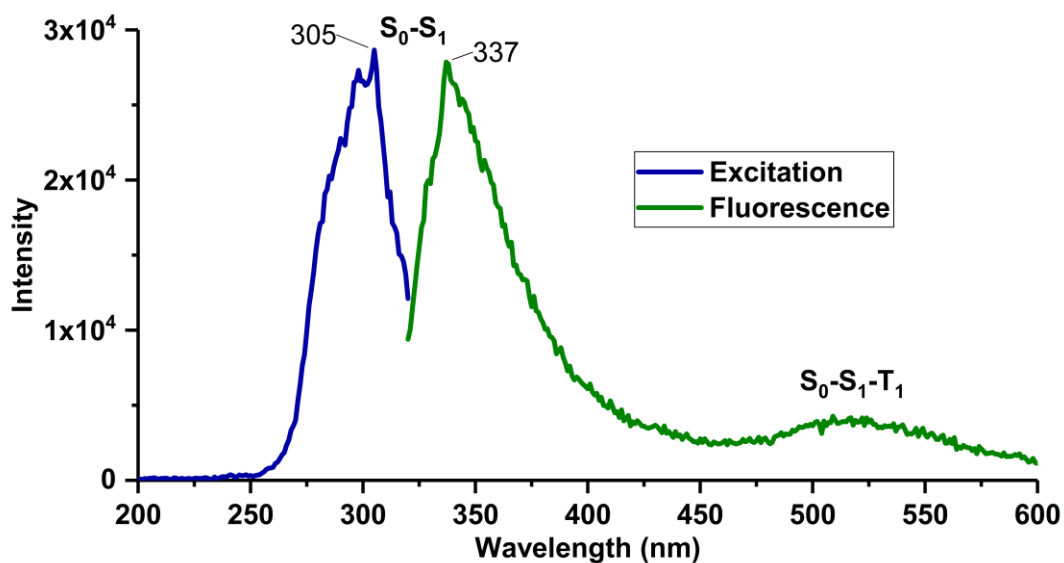
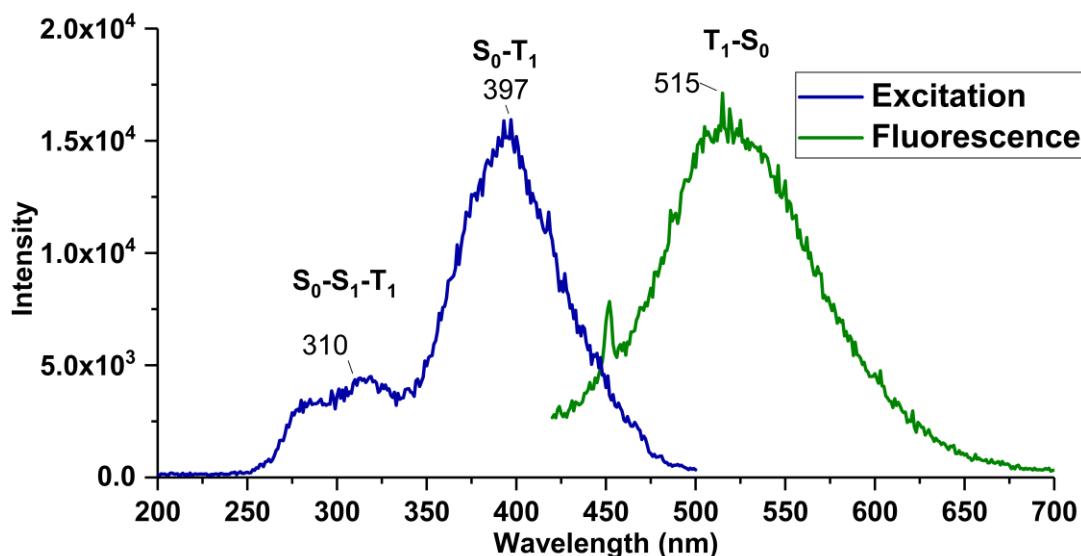


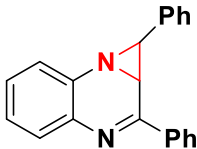
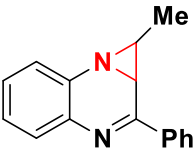
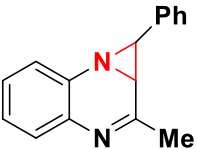
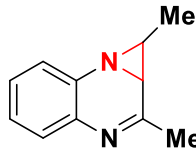
Figure 4.4. Fluorescence spectrum for S_0 - T_1 transition of compound **4-27a**

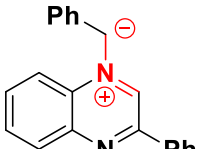
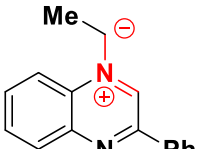
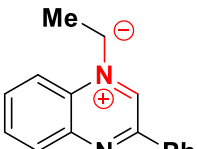
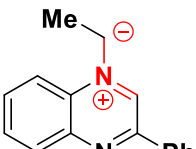


This can be explained by singlet-excited compound **4-27a** (S_1) undergoing an intersystem crossing to its triplet state **4-27a-T₁**, which has a computed energy of 50.4 kcal/mol (567 nm). The T_1 state is close to the detected fluorescence emission peak at 515 nm. Further fluorescence experiment demonstrated that the excited state emitting at 515 nm has two absorbance bands—the major one at 397 nm, which may correspond to the direct S_0 - T_1 excitation, and a small absorption band at 310 nm (Figure 4.4). This small absorption band at 310 nm is in the same region as the absorption peak of **4-27a** arising due to the S_0 - S_1 transition (Figure 4.3). This leads to conclusion that the excited state T_1 can be also accessed through S_0 - S_1 excitation of **4-27a** with the following rapid intersystem crossing. Therefore, the T_1 state could be involved in the photoactivation of **4-27a** under the tested conditions. In particular, the aziridine ring opening transforms the initial triplet geometry of **4-27a** (T_1) (50.4 kcal/mol) to a much lower energy structure (**4-28a-T₁**) (12.1 kcal/mol), as shown in Figure 4.2. **4-28a-T₁** then can nonradiatively relax to the ring-opened, ground **4-28a-S₀** state. From that point, TD-DFT analysis of the ylide intermediate **4-28a-S₀** indicated an S_0 - S_1 excitation at 73.8 kcal/mol (441 nm) with a substantial oscillator strength of 0.92. The ylide's S_0 - S_1 energy gap is well within the diapason of the Blue LED, and its high

oscillator strength suggests that the ylide intermediate **4-28a-S₀** is strongly photoactive. The obtained data for the ylide intermediate is also consistent with previously obtained data by Desenko and Chebanov¹⁴ who reported a 420 nm absorption band for one of the intermediates of aziridinoquinoxaline photoexcitation. As a result, low yields of the desired product **4-59a** can be explained by an undesired pathway that involves the excitation of intermediate **4-28a-S₀** by Blue LED at 440 nm, which leads to its decomposition.

Scheme 4.16. Summary of the excited state analysis for aziridine forms and ylides of compounds 4-27a, 4-60-4-62.

Aziridine				
	4-27a	4-60	4-61	4-62
S ₁ (kcal/mol)	91.2	91.2	104.9	105.5
λ (S ₀ -S ₁ , nm)	313	313	272	271
f ₀₁ (S ₀ -S ₁)	0.35	0.32	0.10	0.08
T ₁ (kcal/mol)	50.4	50.2	60.0	60.2
λ (S ₀ -T ₁ , nm)	567	569	476	474

Ylide				
	4-28a-S₀	4-64-S₀	4-65-S₀	4-66-S₀
S ₁ (kcal/mol)	64.6	78.3	68.9	82.7
λ (S ₀ -S ₁ , nm)	442	363	414	345
f ₀₁ (S ₀ -S ₁)	0.91	0.41	0.84	0.43
T ₁ (kcal/mol)	12.1	24.7	12.5	25.1

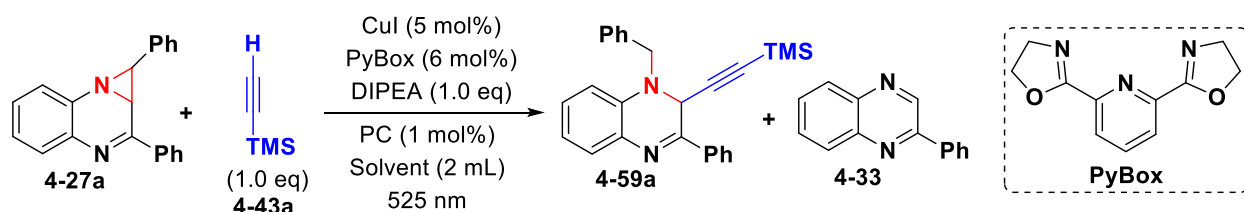
*S₁ – the first excited singlet state, λ – wavelength of the corresponding excitation transition, f₀₁ – oscillator strength for the S₀-S₁ transition, T₁ – the first excited triplet state.

In general, all other model substrates **4-60-4-62** (Scheme 4.16) produce photoactive ylides with accessible S₀-S₁ transitions. The photoexcited states are reachable due to the greater extent of conjugation in the open forms of aziridines. Methyl substituents at the C₁-position of aziridines **4-**

60 and **4-62** do not have any impact on the energies of the triplet states T_1 (**I1-T1**), while making the corresponding ylides **4-64-S₀** and **4-66-S₀** less stable and photoactive due to the absence of the additional aromatic conjugation such as the one that is present in compound **4-27a**. It is worth noting that the ylide (**I2-S₀**) derived from the C₂-phenyl-containing substrate **4-60** absorbs a shorter wavelength due to the alkyl substituent in the aziridine ring and should be more stable to decomposition under the photochemical conditions. In contrast, switching the phenyl substituent at the C₂-position of the quinoxalinium core to the methyl group (substrates **4-61** and **4-62**) destabilizes both excited singlet (S_1) and triplet (T_1) states of **4-65-S₀** and **4-66-S₀**. In summary, avoiding the excitation of the ylide intermediates under the reaction conditions should eliminate decomposition pathways. This can be achieved by switching to light sources with a longer wavelength (>475 nm) and establishing energy triplet transfer (EnT) through a photocatalyst that selectively promotes the S_0 - T_1 transitions.

Guided by the considerations above, we implemented a less energetic light source by switching to Green LED (525 nm, emission spectrum is provided in Chapter 4.8) to avoid the excitation of the ylide intermediates (Table 4.6).

Table 4.6. Photochemical conditions screening under activation by Green LED



Entry	Solvent	Time, hours ^a	PC	PC (T_1 -state), kcal/mol	τ (PC- T_1), ns ^b	Conversion (%; NMR) ^c	Ratio ^d 4-59a : 4-33
1	THF	24	-	-	-	<5	0:trace
2	THF	24	Ir(4-CF ₃ -ppy) ₃	56.4	2160	68	64:36
3	Toluene	24	-	-	-	26	84:16
4	Toluene	24	Ir(4-CF ₃ -ppy) ₃	56.4	2160	>95	93:7
5	Toluene	24	Ir(ppy) ₃	55.2	1900	>95	84:16
6	Toluene	24	Ir(ppy) ₂ (4,4'-dtbbpy)	49.2	557	11	65:35
7	Toluene	24	[Ir(dF(CF ₃)ppy) ₂ (dtbbpy)] PF ₆	60.1	2300	21	0:trace
8	Toluene	24	Eosin Y	53.2	172000	0	0:0

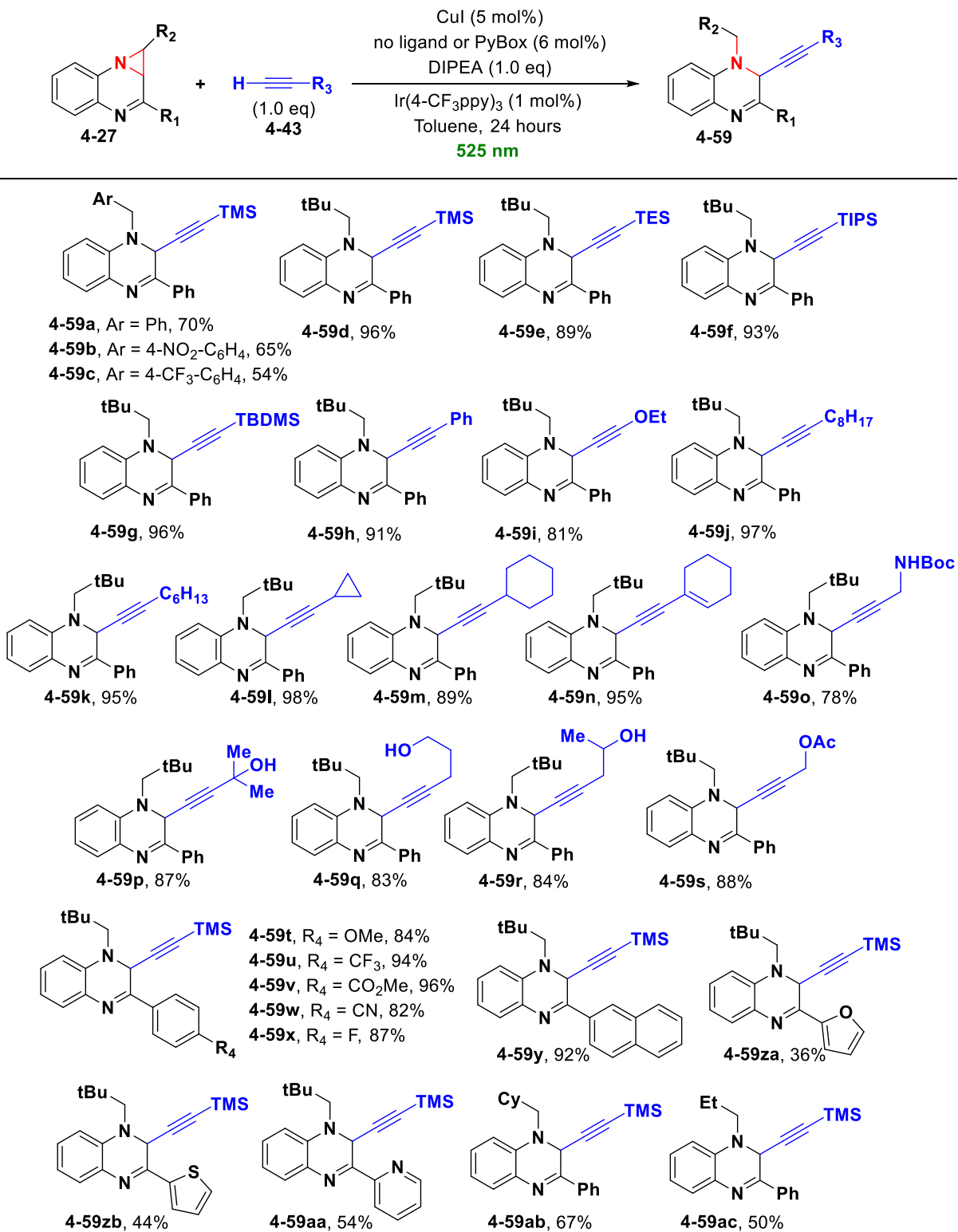
a. Reaction progress was monitored by TLC until full starting material consumption; b. Lifetime of the photocatalyst triplet state; c. Conversion determined by the consumption of the starting material by NMR; d. Ratio between product **4-59a** and decomposition product **4-33** determined by NMR.

As expected, we do not observe any reaction of **4-27a** in THF when exposed to Green LED alone (entry 1) as the light with $\lambda_{\max} = 525$ nm cannot effectively excite aziridinoquinoxalines such as **4-27a**. Introducing Ir(III) photocatalyst Ir(4-CF₃-ppy)₃ allowed us to achieve higher conversion in THF (entry 2) with a much better product **4-59a** to **4-33** ratio of 64:36. The reaction in toluene without photocatalyst was also not effective albeit provided some observable product (entry 3). However, the reaction progression was significantly improved when Ir(4-CF₃-ppy)₃ was used as the photocatalyst, and the reaction reached full conversion in 24 hours resulting in almost pure product **4-59a** (Entry 4). Further photocatalyst screening did not lead to improvement (entries 5-8) although the observed results were in good agreement with the proposed EnT mechanism. Ir(ppy)₃ both matches the triplet state energy and has a relatively long T_1 lifetime, and this catalyst was found to have a similar catalytic activity to Ir(4-CF₃-ppy)₃ (entry 5). Ir(ppy)₂(4,4'-dtbbpy)

photocatalyst in entry 6 has too low triplet energy (49.2 kcal/mol) while [Ir(dF(CF₃)ppy)₂(dtbbpy)]PF₆ catalyst in entry 7 is probably mismatched with the triplet gap of compound **4-27a** or cannot be excited by the light with $\lambda_{\text{max}}=525$ nm. Eosin Y is similar to Ir(4-CF₃ppy)₃ in terms of its triplet state energy, but it has a shorter excited state lifetime to promote the EnT mechanism. Using organic dye, Eosin Y, (entry 8) with the absorption at 520 nm that matches well the employed light source with $\lambda_{\text{max}} = 525$ nm neither lead to the formation of product nor to decomposition. This may be attributed to the low triplet state energy of Eosin Y or to the low solubility of Eosin Y in toluene.

With the optimized protocol in hand, the substrate scope evaluation was performed next by exploring the variations in alkynes **4-33** and aziridinoquinoxalines **4-27** (Scheme 4.17). As expected, the introduction of the electronwithdrawing substituents to the phenyl ring attached to the aziridine moiety had a minor effect on the reaction yield and substrates **4-59b** and **4-59c** were obtained in 65% and 54%, correspondingly. Due to a much lower energy barrier for ring-opening in the T₁ triplet state, *t*-Bu-substituted aziridinoquinoxaline **4-27d**, previously unreactive under the thermal activation conditions, was successfully converted to product **4-59d** in 96% yield using the green LED/Ir(III) activation protocol. In general, compound **4-27d** was significantly more stable under the photochemical conditions than **4-27a** (that provided product **4-59a** in only 70% yield) and other aryl-substituted aziridines such as **4-59b** and **4-59c**. Reaction proceeds with excellent yields (>90%) with a wide range of alkynes including various silyl-protected alkynes **4-59e-4-59g**, phenylacetylene **4-59h**, ethoxyacetylene **4-59i**, alkyl substituted acetylene **4-59j** and **4-59k**, and cyclohexyl-substituted **4-59m**. Alkynes with photolabile groups such as cyclohexene group (13n) and cyclopropyl group (**4-59l**) that can form radicals under photochemical excitation are well tolerated under the green LED radiation with $\lambda_{\text{max}}=525$ nm.

Scheme 4.17. The substrate scope of Green LED promoted alkylation of aziridinoquinoxalines.^a



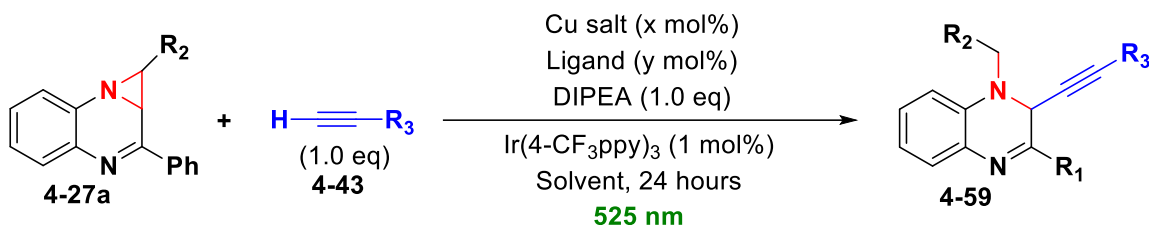
a. The reactions were carried on 0.1 mmol scale described in Chapter 4.8. Reactions leading to **4-59d–4-59z** were performed without **PyBox** Ligand (**L3**), and the formation of substrates **4-59a-4-59c**, **4-59aa-4-59ab** were carried with 6 mol% of **PyBox**.

The presence of the potentially nucleophilic groups such as amines and hydroxyls (**4-59o–4-59r**) did not lead to the formation of side products of competitive addition to quinoxalinium cations demonstrating high catalytic differentiation of Cu(I) catalysis towards alkyne addition. Similarly, the reaction proceeded smoothly with propargyl acetate to provide product **4-59s** in 88% yield. The variation in the C2-substituent of aziridinoquinoxalines was explored next (**4-59t-4-59z**). The introduction of both electron-withdrawing (**4-59u-4-59x**) and electron-donating (**4-59t**) substituents at the *para*-position of the C2-phenyl ring did not impact the yield and the corresponding adducts were obtained in 82-96% yield. Similarly, the C2-naphthyl-substituted product **4-59y** was formed in excellent 88% yield. At the same time, the 2-furanyl substituted product **4-59za** was isolated in only 36% yield due to significant decomposition presumably due to the side reactions of furan under the photochemical conditions. In the case of the C2-thiophene-substituted substrate **4-27l**, the reaction proceeded without any signs of decomposition with 51% conversion by NMR resulting in 44% yield of **4-59zb** and recovered starting material. Low conversion can be attributed to Ir(III) photocatalyst poisoning by the sulfur heterocycle. In addition, pyridine-substituted substrate **4-59aa** was also obtained in 47% yield without any signs of the decomposition of the starting material. The reaction rate retardation due to the copper(I) complexation with two molecules of the starting material **4-27p** was noted in this case in HRMS spectrum. Finally, the substrates containing the cyclohexyl- and ethyl-substituents at the aziridine ring, **4-27m** and **4-59n** were subjected to reaction with acetylene **4-33a** to provide products **4-59ab** and **4-59ac** in 67% and 50% yield, correspondingly.

After establishing the optimal conditions for green LED-induced alkyne addition to aziridinoquinoxalines, our subsequent studies focused on developing the asymmetric variant of

this reaction (Table 4.7). Various PyBox ligands (**L4-L9**) demonstrated low-to-moderate enantioselectivities (entries 1-6), while the best enantiomeric ratio (e.r.) of 82:18 was obtained using either tertbutyl (**L8**) or adamantly (**L9**) derivative of PyBox (entries 5-8). Further reaction optimization by reducing the catalytic loading of ligand **L8** to 2.5 mol% (Cu/L = 2:1 ratio) helped to increase the e.r. to 87:13 for product **4-59a** (entry 8). Excellent enantioselectivity (95:5) can be obtained using (*S,R*)-N-PINAP ligand **L10** (entries 9-10) albeit product **4-59a** was isolated in only 25% yield due to significant decomposition to 2-phenylquinoxaline **4-33**. As aziridinoquinoxaline **4-27d** previously exhibited higher stability than **4-27a**, we tested it with ligand **L10** in THF and the resultant isolated product **4-59d** was formed in 81% yield and 93:7 er. Further attempts to optimize the reaction conditions by evaluating copper(I) chloride, copper(I) or copper(II) trifluoromethanesulfonates as the catalysts did not lead to improved yields or selectivities (entries 12-14). Finally, we tried to use solvent mixtures of Toluene and THF to improve the solubility and complexation of copper(I) to ligand (entries 15-16) however, as in case of only THF usage, significant amounts of side-product **4-33** were observed.

Table 4.7. Development of the enantioselective alkyne addition under photochemical conditions.



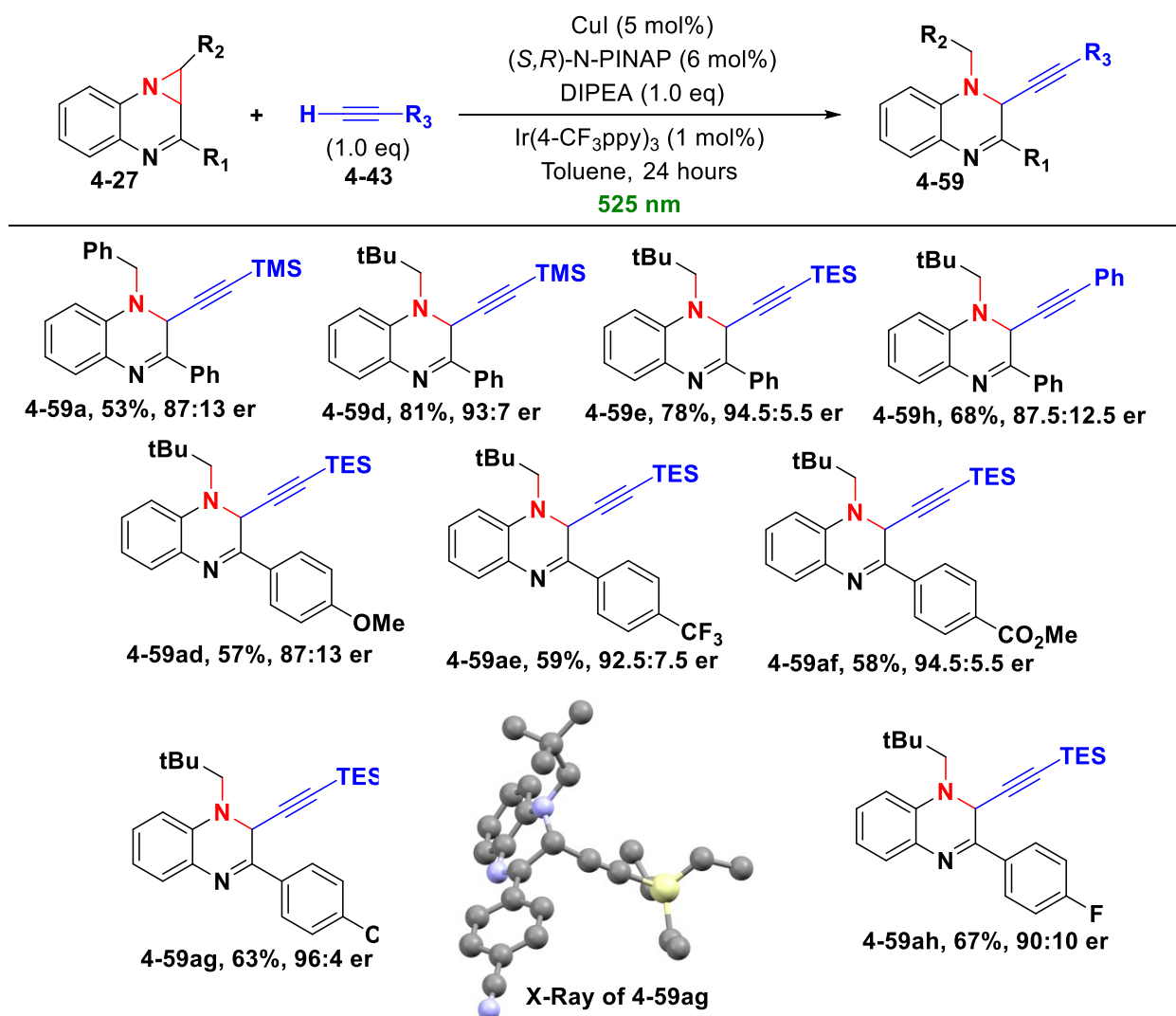
Entry	R ₂	Ligand	Cu Salt	Solvent	x	y	Conversion (%; NMR) ^a	Ratio ^b 4-59a:4-33	er ^c
1	Ph	L4	CuI	Toluene	5	6	>95	93:7	72:28
2	Ph	L5	CuI	Toluene	5	6	>95	89:11	55:45
3	Ph	L6	CuI	Toluene	5	6	>95	90:10	62.5:37.5
4	Ph	L7	CuI	Toluene	5	6	>95	67:33	57:43
5	Ph	L8	CuI	Toluene	5	6	>95	83:17	82:18
6	Ph	L9	CuI	Toluene	5	6	>95	87:13	82:18
7	Ph	L9	CuI	Toluene	5	2.5	>95	78:22	86.5:13.5
8	Ph	L8	CuI	Toluene	5	2.5	>95 (64) ^d	81:19	87:13
9	Ph	L10	CuI	Toluene	5	6	>95 (28) ^d	55:45	93:7
10	Ph	L10	CuI	THF	5	6	>95 (25) ^d	49:51	95:5
11	tBu	L10	CuI	THF	5	6	>95 (81) ^d	98:2	93:7
12	Ph	L10	CuCl	Toluene	5	6	70 (19)	71:29	94:6
13	Ph	L10	CuOTf	Toluene	5	6	60	78:22	88:12
14	Ph	L10	Cu(OTf) ₂	Toluene	5	6	68	68:32	96:4
15	Ph	L10	CuI	Toluene/THF (5:1)	5	6	>95	76:24	91:9
16	Ph	L10	CuI	Toluene/THF (4:1)	5	6	>95	61:39	91:9

a. Conversion determined by consumption of starting material by NMR; b. Ratio between product **4-59a** and decomposition product **4-33** determined by NMR; c. Enantiomeric ratio was determined by chiral HPLC/SFC analysis; d. Isolated yield after FCC.

Therefore, the conditions for the formation of **4-59d** with PINAP ligand **L10** (entry 11) were selected for further evaluation. Using the optimized conditions with ligand **L10** for the formation of chiral **4-59a** and **4-59d**, we explored the scope of this transformation using *tert*-butyl-substituted aziridinoquinoxalines next (Scheme 4.18). Changing trimethylsilyl-substituted alkyne **4-43a** to bulkier triethylsilyl-protected alkyne **4-43b** resulted in more enantioselective formation of the product **4-59e** (94.5:5.5 e.r.). However, the use of phenylacetylene lowered both the

selectivity and the yield for the formation of product **4-59h** (68% yield, 87.5:12.5 e.r.). The subsequent reactions with TES-substituted alkyne **4-43b** produced chiral substrates **4-59ad-4-59ah**. In general, introduction of an electron withdrawing substituent at the *para*-position of the C₂-phenyl ring resulted in similar e.r. values, but lower yield. Thus, *p*-CF₃-substituted substrate **4-27f** provided the corresponding product in 59% yield and 92.5:7.5 e.r., *p*-CO₂Me-substituted substrate **4-27g** led to product **4-59af** in 58% yield and 94.5:5.5 e.r., and the use of *p*-CN-substituted **4-27h** resulted in **4-59ag** in 63% yield and 96:4 e.r.

Scheme 4.18. Substrate scope for enantioselective alkyne addition.



The configuration of **4-59af** was determined via X-ray crystallographic analysis and was assigned as (*R*). At the same time, substitution with *p*-methoxy, and *p*-fluoro groups resulted in enantioselectivity erosion, and products **4-59ad** and **4-59ah** were obtained in 57% yield, 87:13 e.r. and 67% yield, 90:10 e.r., correspondingly.

4.5.1 Functionalization of alkynylated aziridines

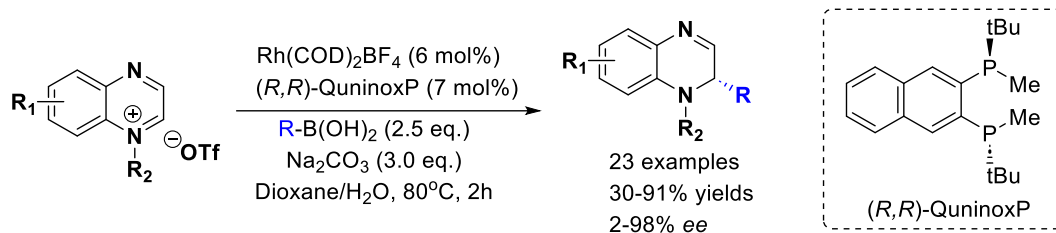
As discussed in Chapter 4.1 synthesis of chiral heterocyclic compounds remains a top priority for the modern pharmaceutical industry. Among various heterocycles, significant efforts have been focused on achieving the synthesis of substituted tetrahydroquinoxalines. These heterocyclic motifs are present in a variety of bioactive compounds and prospective drugs.^{27,28} The standard approaches to chiral tetrahydroquinoxalines involve hydrogenation or transfer hydrogenation of quinoxalines (similar to the method described in Chapter 3), which poses limitations to the types of products that could be accessed through these reductive methods.²⁹ For example, protocols published by the Du group resulted in *cis*-selective hydrogenation of 2,3-disubstituted quinoxalines.^{30,31}

Recently, Karimov and co-workers³² presented the method of asymmetric functionalization of quinoxalinium salts (Scheme 4.19A). Quinoxalinium salts generated via alkylation with alkyl triflates were used as strong electrophiles for Rhodium-catalyzed cross-coupling reactions with boronic acids. Functionalization of the reaction products, dihydroquinoxaline, allows the preparation of tetrahydroquinoxalines with various substitution patterns. Despite this, reaction protocol requires the preparation of alkylated quinoxalines which is usually done under harsh conditions. For example, pyridines can be easily alkylated with methyl iodide (Scheme 4.19B) at room temperature, while quinolinium salts require elevated temperatures. However, as we found out, direct alkylation of quinoline and quinoxalines didn't proceed with sterically hindered

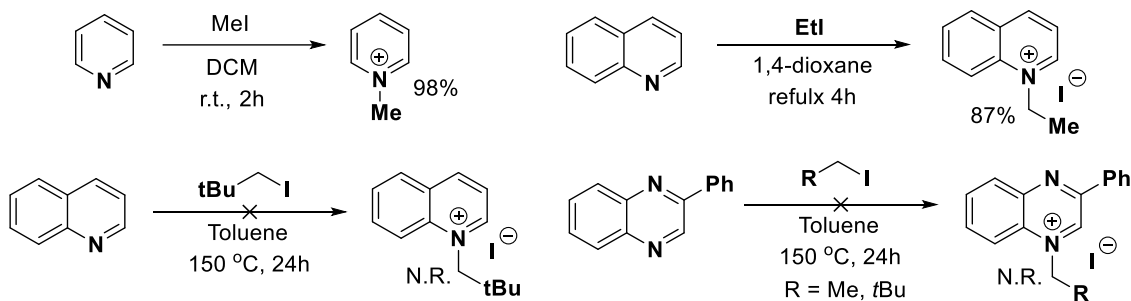
alkylation agents, such as neopentyl iodide even though reactions were performed in neat at 150 °C. This is consistent with the low basicity (pKa of the protonated form in water = 0.56) and nucleophilicity previously observed for quinoxalines.³³ These results also suggest that the described herein indirect method is unique for providing quinoxalinium ions and azomethine ylides, in particular, for the substrates containing other basic nitrogen groups such as **4-59aa** (Scheme 4.17).

Scheme 4.19. Asymmetric functionalization of quinoxalinium salts by Karimov and heteroarenum salts synthesis via alkylation reactions.

A. Rhodium-Catalyzed Asymmetric Functionalization of Quinoxalinium Salts by Karimov



B. Generation of heteroarenum salts via alkylation reactions

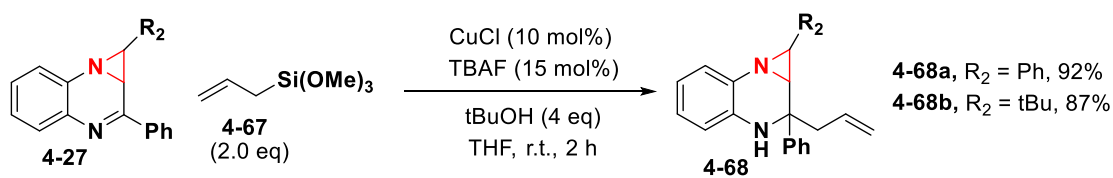


Initial aziridinoquinoxalines **4-27** as well as their product functionalization have multiple functional groups that can be further modified via other reactions. Therefore, our subsequent studies focused on demonstrating the versatility of the developed photochemical alkynylation in the synthesis of complex heterocyclic molecules. First, aziridinoquinoxalines can undergo imine group allylation with allyltrimethoxysilane **4-67** and Cu(I) catalysis to produce compounds **4-68** in high yields (Scheme 4.20A). The same transformation of the C=N moiety is also possible for

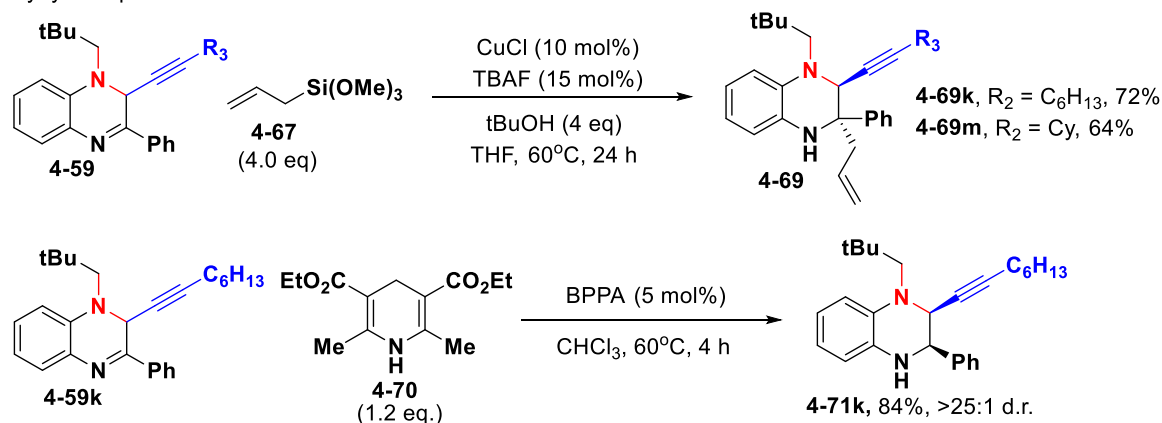
alkynylated products **4-59** to provide **4-69k** and **4-69m** in 72% and 64% yield as *anti*-diastereomers only (Scheme 4.20B). Following our previous research in the area of the C=N bonds reduction using CPA catalysis (Chapter 3) we also subjected **4-59k** to the reaction with stoichiometric Hantzsch ester **4-70** resulted in *syn*-diastereomer **4-71k** in 84% yield and >25:1 d.r. It is noteworthy that tetrahydroquinoxalines **4-68** and **4-69** cannot be easily derived by other methods such as the hydrogenation of quinoxalines due to presence of more reactive double bond.

Scheme 4.20. Further modifications of aziridinoquinoxalines and alkynylated aziridines.

A. Imine group allylation of aziridinoquinoxaline



B. Alkynylated products modifications

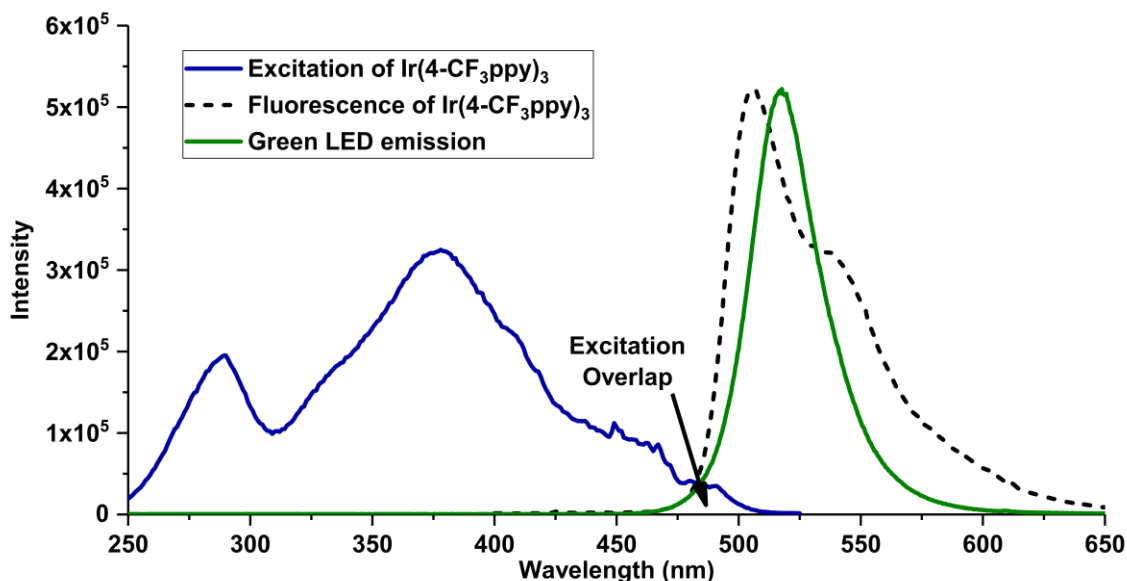


4.6 Mechanistic studies of photocatalytic aziridinoquinoxalines alkylation

With the aforementioned results in hand, our next studies were focused on getting further insights into the mechanism of these photochemical transformations. The entire transformation involves cooperative catalysis of Ir(III) and Cu(I) and consists of three stages 1) photocatalysis with Ir(III) leading to the formation of azomethine ylide; 2) formation of copper(I) acetylide; 3) reaction of copper(I) acetylide and azomethine ylide.

Our computational and fluorescence studies helped to shed some light on the possible role of the initial stages of the photochemical cascade leading to the formation of azomethine ylide. Ir(III) photocatalysts usually are excited by Blue LEDs (400-440 nm) and we are not aware of using light with longer wavelengths such as Green LED ($\lambda_{\text{max}}=525$ nm) to promote either photoredox or energy transfer reactions with Ir(III). The recorded fluorescent spectrum of Ir(4-CF₃-ppy)₃ demonstrates typical wide absorption in the 250-450 nm range that matches perfectly the spectrum of typical Blue LEDs; however, the absorption of Ir(III) and emission of Green LED spectra have minor overlap near 490-500 nm region (Figure 4.5). The emission of the employed Green LED light source seems to be sufficient to perform EnT mechanism in studied reaction. The emission of the photocatalyst also perfectly matches the energy of the computed and measured triplet state (Chapter 4.5, Figure 4.2).

Figure 4.5. Absorption (blue line) and fluorescence (dotted line) of Ir(4-CF₃-ppy)₃ photocatalyst and used Green LED emission (green line)



While the photoexcited Ir(III) catalyst may facilitate **4-27-T₁** formation via energy transfer mechanism (Scheme 4.21, Mechanism A), another possibility to consider is the photoredox

mechanism proceeding through radical cation intermediates **4-72** and **4-73** (Scheme 4.21, Mechanism B). Mechanism A has already been investigated computationally (Chapter 4.5). However, to gain a better understanding of Mechanism B, DFT computations (DFT, SMD/wB97x-D3/cc-pVTZ) were carried out. At the first step, aziridinoquinoxaline **4-27** may undergo a single-electron transfer (SET) oxidation to form cation radical **4-72**, for which the oxidation potential is estimated to be around $E_1 = 2.0$ V in toluene for both phenyl- and methyl-substituted aziridinoquinoxalines **4-27** and **4-60**. In THF and acetonitrile, this potential is lowered to 1.5 V and 1.3 V, respectively. The subsequent ring-opening of radical-cation **4-72** has a low energy barrier for $R_2 = \text{Ph}$ (8.7 kcal/mol) and slightly higher barrier for $R_2 = \text{Me}$ (16.0 kcal/mol), but in both cases this step should be feasible.

Scheme 4.21. Two photochemical mechanisms of ylide generation.

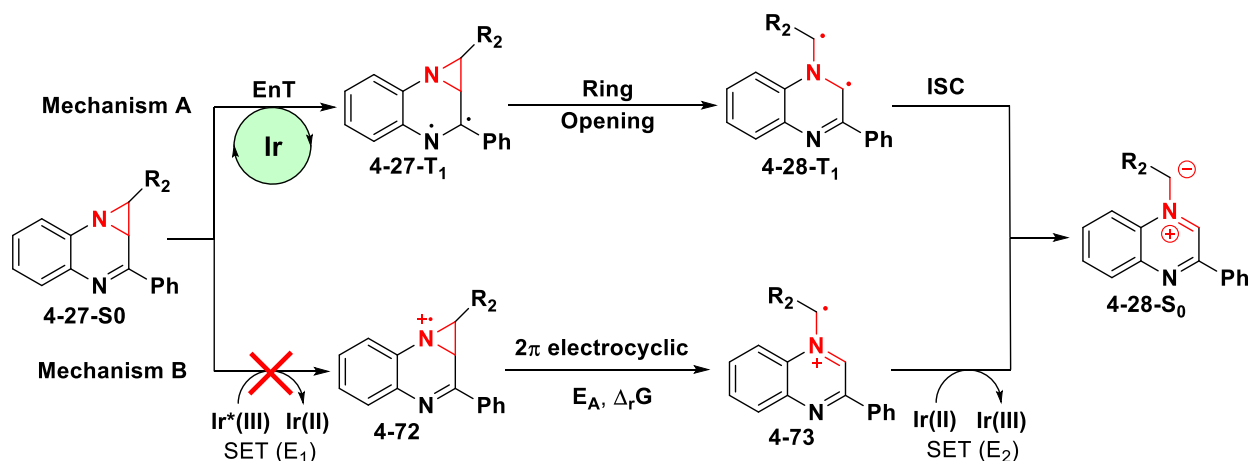


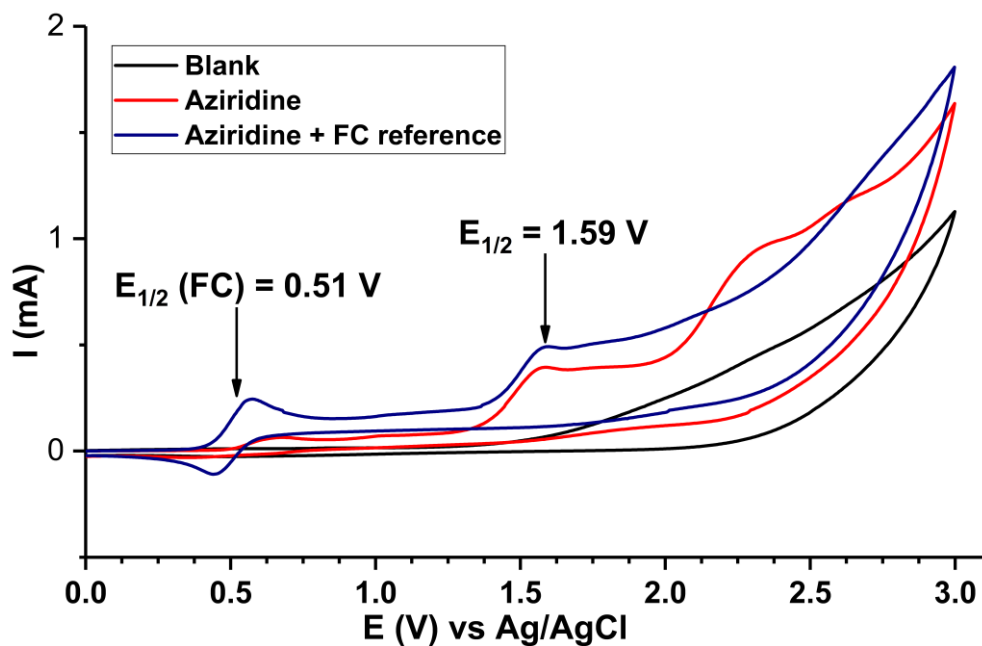
Table 4.8. Thermodynamic data for elementary steps of Mechanism B.

R_2	E_1 , V (Toluene)	E_1 , V (THF)	E_1 , V (MeCN)	E_A , kcal/mol	$\Delta_r G$, kcal/mol	E_2 , V (Toluene)	E_2 , V (THF)	E_2 , V (MeCN)
Ph (4-27)	2.08	1.52	1.36	8.7	-22.1	0.73	0.16	-0.01
Me (4-60)	2.04	1.47	1.30	16.0	-20.4	0.89	0.25	0.05

In addition, the ring-opening of radical-cation **4-72** is thermodynamically favored by approximately 20 kcal/mol (Gibbs Free Energy). Finally, the generation of ylide **4-28-S₀** should also proceed easily due to low reduction potential of open radical-cation **4-73** ($E_2 = 0.7$ to 0.9 V). For this alternative mechanism B, there are two key steps involving SET process, first is the oxidation of aziridinoquinoxalines **4-27**, and second is the final reduction of the open form of radical-cation **4-73** to ylide **4-28-S₀**. The reduction of **4-73** to ylide **4-28-S₀** should be possible by any Ir(II) photocatalyst present in the reaction mixture as for Ir(III)/Ir(II) redox reaction potentials are in range of -1.3 to -2.2 V (Chapter 4.8.2). However, the first oxidation step of **4-27-S₀** may have a potential mismatch with the oxidation potential of the excited Ir(III) photocatalyst (highest potential $E = 1.21$ V, Chapter 4.8.2).

To confirm our theoretical investigations, a cyclic voltammetry study was performed on aziridinoquinoxaline **4-27a** in acetonitrile (Figure 4.6, and experimental details in Chapter 4.8.2) demonstrating irreversible oxidation of **4-27a** with half wave at 1.49 V (vs SCE, corrected with ferrocene). The measured potential matches the computed in the DFT studies potential of 1.36 V in MeCN. Based on this, we can conclude that the proposed SET mechanism B cannot be operational under current photochemical conditions since Ir(4-CF₃-ppy)₃ is not a sufficiently strong oxidant to generate radical-cation **4-72**.

Figure 4.6. Cyclic voltammety measurements of compound 4-27a in acetonitrile

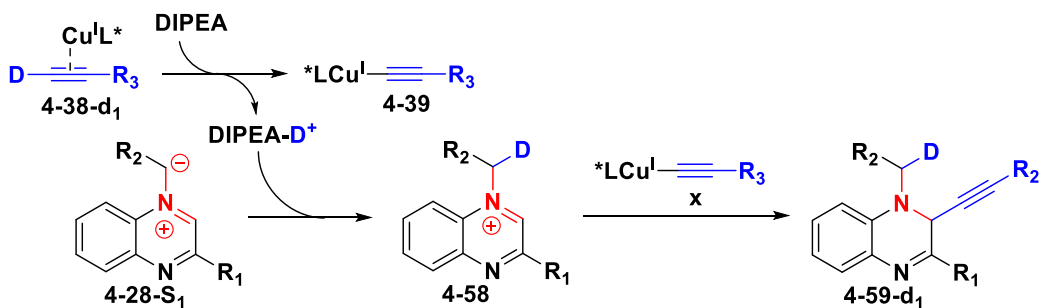


After proving that our initial mechanistic hypothesis with EnT ring opening is more plausible than the alternative photoredox pathway, we decided to probe the last step of the mechanism involving the reaction of copper(I) acetylide and ylide (Scheme 4.22A). The reaction of **4-27d** and D-labeled alkyne **4-43k-d₁** was investigated using the standard protocol to probe both the deprotonation step by DIPEA as well as the following H/D transfer to ylide **4-28**. If this mechanistic hypothesis is correct, then we should observe D-incorporation in final product **4-59d**. While the reaction with D-labeled **4-43k-d₁** proceeded as usual, the resultant product **4-49k** was isolated in 89% yield with no deuterium incorporation (Scheme 4.22B). As the deuterated toluene (d_8 -toluene) was used in the reaction, only DIPEA may serve as the source of hydrogen atoms that protonate the ylides instead of alkyne. This process may involve the oxidation of intermediate ylide **4-28** with Ir(III) to form intermediate **4-73** that subsequently undergoes HAT reaction with DIPEA (or protonated/deuterated DIPEA) to form protonated quinoxalium ion **4-58** that undergoes a

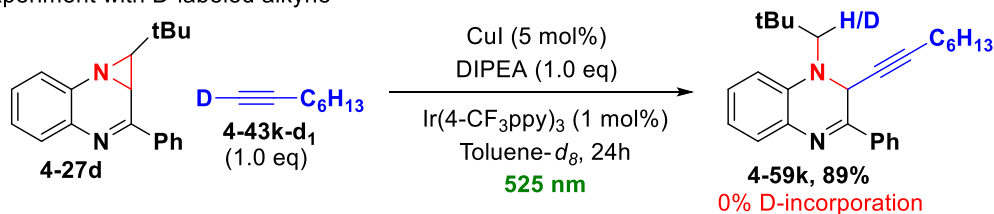
reaction with copper(I) acetylide (Scheme 4.22C). Generated DIPEA-radical further can be reduced by Ir(II) and protonated to regenerate DIPEA molecule.

Scheme 4.22. Mechanistic studies of alkyne addition to ylides

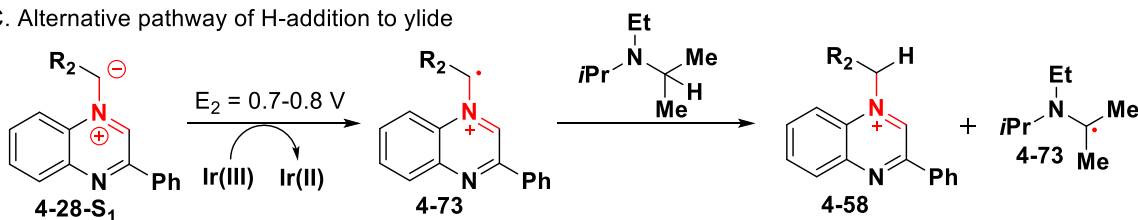
A. Mechanism of alkyne addition to ylides



B. Control experiment with D-labeled alkyne



C. Alternative pathway of H-addition to ylide



Finally, we were seeking to explain consistently observed decomposition of aziridinoquinoxaline to 2-phenylquinoxaline **4-33** (Scheme 4.23). The product-to-decomposition ratio depended on the solvent used as well as chiral ligand and copper(I) salt. This led us to the hypothesis that there is a competitive decomposition mechanism(s) to product formation and the reaction conditions may regulate the favoring pathway. We envisioned that the generated quinoxalinium intermediates **4-58** should have similar properties to *N*-alkylpyridinium (Katrizky's) salts, which are well-known to undergo radical extrusion after the SET reduction.

Scheme 4.23. Potential decomposition pathway through SET reduction.

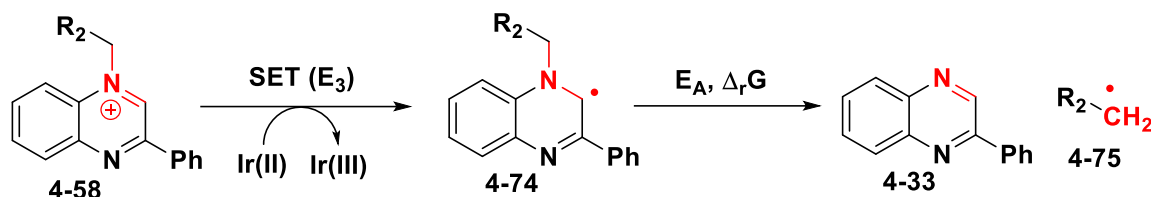


Table 4.9 Thermodynamic data for potential decomposition pathway on Scheme 4.22

R ₂	E ₁ , V (Toluene)	E ₁ , V (THF)	E ₁ , V (MeCN)	E _A , kcal/mol	Δ _r G, kcal/mol
Ph (4-27a)	-0.46	-0.39	-0.56	29.1	13.1
Me (4-60)	-0.44	-0.37	-0.55	37.9	27.4
t-Bu (4-27d)	-0.44	-0.37	-0.55	42.4	27.2

Similarly, the reduction of quinoxalium ion intermediates **4-58** to radical **4-74** followed by radical extrusion will lead to 2-phenylquinoxaline **4-33**. Therefore, we calculated the reduction potential for intermediates **4-58** to radical **4-74** (Scheme 4.23). DFT calculations at ωB97X-D3/cc-pVTZ level of theory and SMD solvation model (for Toluene, Acetonitrile and THF) provided values ranging from -0.35 to -0.65 V (Table 4.9). Therefore, the reduction of **4-58** can be accomplished with Ir(II) species generated by Ir(III) reduction with DIPEA. The subsequent step involving the C-N bond dissociation leading to **4-33** has high barriers (Table 4.9), but phenyl-substituted aziridinoquinoxaline **4-27a** (R₂ = Ph) decomposition proceeds with lower activation energy (29.1 kcal/mol) in comparison to the methyl (37.9 kcal/mol) and *tert*-butyl (42.4 kcal/mol) derivatives **4-60** and **4-27d**. Such difference in activation energy can be explained by the formation of a more stable benzyl radical, and it is consistent with our prior observations of lower photochemical stability of phenyl-substituted substrates **4-27a-c** in comparison to **4-27d** and related compounds.

4.7 Conclusions

In summary, this chapter describes a new method for accessing dihydroquinoxalines from readily available aziridinoquinoxalines. While aziridinoquinoxalines can undergo C=N addition reaction with nucleophiles as well as possessing photochromic properties, no prior literature data demonstrated successful photochemical activation of the heterocyclic core to produce and trap azomethine ylides from such compounds.

We have discovered a photochemical method that enables alkyne addition to the aziridine, rather than imine, a moiety of the aziridinoquinoxalines. While the attempts to accomplish this transformation using thermal activation or direct photolysis with Blue LED as the light source were not successful, the computational studies helped to discover a dual Ir(III)/Cu(I) catalytic system that promotes alkyne addition under green LED photolysis ($\lambda_{\text{max}} = 525 \text{ nm}$). This mild method features high levels of chemo- and regioselectivity and was used to generate 29 highly functionalized substituted dihydroquinoxalines (**4-59a-4-59ab**) in 44-98% yield. This transformation was also carried asymmetrically using (*S,R*)-N-PINAP (**L10**) as the chiral ligand to provide 9 chiral addition products in 96:4 to 86:14 e.r. These dihydroquinoxaline products may serve as the substrates for further functionalization to provide highly functionalized tetrahydroquinoxalines that cannot be easily obtained using other methods. The experimental and theoretical explorations of this photochemical reaction suggest a mechanism that involves Ir(III)-catalyzed triplet energy transfer mechanism followed by a ring-opening reaction ultimately leading to the formation of azomethine ylide intermediates. These azomethine intermediates undergo sequential protonation to provide quinoxalinium ion intermediates that undergo copper(I) acetylide addition. To the best of our knowledge, this is the first example of successful generation and trapping of azomethine ylides with visible light under mild conditions via energy transfer process.

4.8 Experimental information

Methods and reagents: Unless otherwise noted, all reagents were purchased from commercial suppliers and used without further purification. Solvents used for reactions (Toluene, THF) were filtered through a column (Solvent system Innovative Technology PS-MD-5) of activated alumina under nitrogen atmosphere. All reactions were carried out under an atmosphere of nitrogen in oven-dried glassware with magnetic stirring. Heating was achieved by use of a metal heating block with heating controlled by electronic contact thermometer. Reactions were monitored by nuclear magnetic resonance (NMR) or thin layer chromatography (TLC) on silica gel precoated glass plates (0.25 mm, SiliCycle, SiliaPlate). TLC plate visualization was accomplished by irradiation with UV light at 254 nm or by staining with a cerium ammonium molybdate (CAM) solution. Deionized water was used in the preparation of all aqueous solutions and for all aqueous extractions. Solvents used for chromatography were ACS or HPLC grade. Purification of reactions mixtures was performed by flash column chromatography on SiO₂ using SiliCycle SiliaFlash P60 (230-400 mesh) to pack the columns for Teledyne ISCO CombiFlash Rf+ purification system. Enantiomeric excess was determined by HPLC analysis using a Waters e2695 Separations Module with a Waters 2998 photodiode array detector and the Waters Investigator SFC system (supercritical CO₂/Methanol) with a Waters 2998 photodiode array detector.

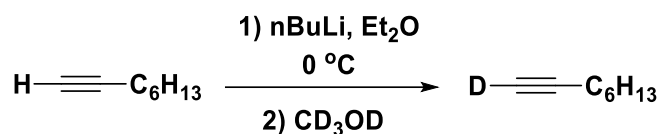
Instrumentation: All spectra were recorded on Bruker Avance Neo 500 (500 MHz) spectrometer and chemical shifts (δ) are reported in parts per million (ppm) and referenced to the ¹H signal of the internal tetramethylsilane according to IUPAC recommendations. Data are reported as (br = broad, s = singlet, d = doublet, t = triplet, q = quartet, qn = quintet, sext = sextet, m = multiplet; coupling constant(S) in Hz; integration). High resolution mass spectra (HRMS) were recorded on MicromassAutoSpecUltima or VG (Micromass) 70-250-S Magnetic sector mass spectrometers in

the University of Michigan mass spectrometry laboratory. Optical rotations were measured at room temperature in a solvent of choice on a JASCO P-2000 digital polarimeter at 589 nm (D-line).

4.8.1 General procedures

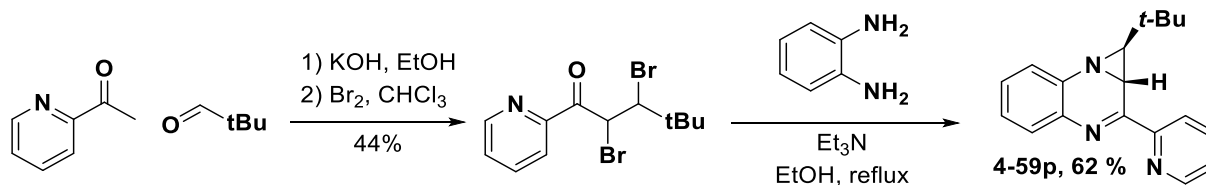
Synthesis of aziridines **4-59a-4-59p** and characterization data were previously reported in our previous publication.³⁴ Ligand **L9** is a known compound and was synthesized according to protocol.³⁵

Synthesis of oct-1-yne-1-d (**4-43-d1**)



To the solution of oct-1-yne (2.95 mL, 20 mmol) in 15 mL of dry Et₂O in a flame-dried round bottom flask, a solution of nBuLi (9.2 mL, 2.72 M in hexanes, 25 mmol) was added dropwise at 0 °C. White precipitate started forming immediately, and the reaction was stirred for 15 minutes. Then flask was warmed to r.t., and reaction mixture was quenched with 10 mL of CD₃OD, leading to clear solution. Water (15 mL) was added, and the reaction mixture was extracted with Et₂O (3x5 mL), organic layers were combined, dried with Na₂SO₄, and evaporated leading to 953 mg (43% yield, 99% D-incorporation by ¹H NMR) of oct-1-yne-1-d as a pale yellow liquid that can be used without further purification.

Synthesis of 1-(tert-butyl)-2-(pyridin-2-yl)-1,1a-dihydroazirino[1,2-a]quinoxaline (**4-27p**)



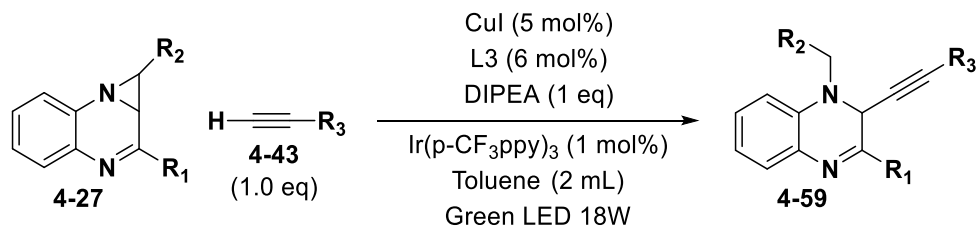
Aziridine **4-59p** was prepared according to the previously published protocol in 3 steps.³⁴ 2,3-dibromo-4,4-dimethyl-1-(pyridin-2-yl)pentan-1-one was prepared on 20 mmol scale. Aziridine **4-59p** cyclization was performed on 2.5 mmol scale to produce product in 62% yield (429 mg) as yellow solid.

¹H NMR (500 MHz, Chloroform-d) δ 8.60 (ddd, $J = 4.9, 1.8, 1.0$ Hz, 1H), 8.26 (dt, $J = 8.0, 1.1$ Hz, 1H), 7.69 (td, $J = 7.8, 1.8$ Hz, 1H), 7.33 (dd, $J = 7.6, 1.6$ Hz, 1H), 7.26 (ddd, $J = 7.5, 4.8, 1.2$ Hz, 1H), 7.17 (dd, $J = 7.4, 1.6$ Hz, 1H), 7.08 (td, $J = 7.5, 1.7$ Hz, 1H), 7.06 – 7.00 (m, 1H), 3.77 (d, $J = 3.6$ Hz, 1H), 1.73 (d, $J = 3.6$ Hz, 1H), 0.98 (s, 9H).

¹³C NMR (126 MHz, Chloroform-d) δ 162.1, 155.1, 149.1, 140.5, 136.6, 136.1, 129.6, 129.1, 125.5, 124.9, 124.9, 121.0, 83.8, 67.5, 48.0, 37.2, 30.8, 26.4.

HRMS (ESI+) (m/z): $[M+H]^+$ 278.1652 calcd for C₁₈H₂₀N₃⁺, found 278.1649;

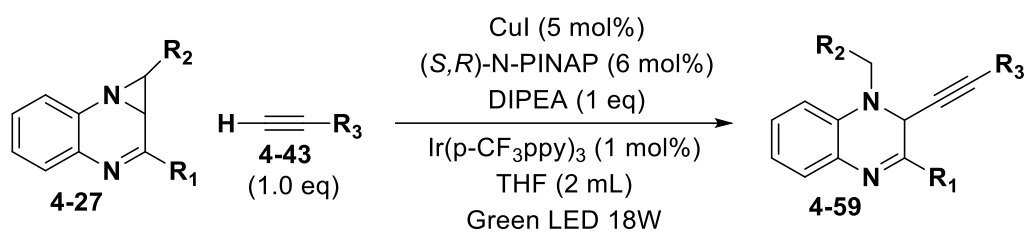
Photochemical copper-catalyzed Alkynylation (Protocol A)



The reaction was performed in 2-dram (8 mL) oven-dried (for 24 hours) glass vials. Dry toluene (from solvent system) was degassed prior reaction using freeze-pump-thaw method (3 times). Glass vial with a stir bar was charged with Ir(4-CF₃ppy)₃ photocatalyst (0.9 mg, 0.001 mmol, 1 mol%), copper (I) iodide CuI (1.0 mg, 0.005 mmol, 5 mol%) and *optionally ligand L3* (0.006 mmol, 6 mol%) then closed with cap with septum and covered with rubber septum which was fixed with electrical tape. The vial was vacuumed and refilled with nitrogen (3 times, under Shlenk line) and 1 mL of degassed toluene was injected into it, followed by alkyne **4-43** (0.1 mmol, 1.0 eq) and DIPEA (0.1 mmol, 17.4 μ L, 1.0 eq). The reaction mixture was stirred at r.t. for 1.5 hours and then

a solution (prepared in a separate vial under oxygen-free conditions) of aziridine **4-27** (0.1 mmol) in 1 ml of degassed toluene was injected to the vial. The reaction mixture was stirred under Green LED irradiation (18 W Hypatochem EVOLUCHEM LED 525PF) for 24 hours. After that vial was uncapped and the reaction mixture was filtered through a short plug of Fluorosil (Magnesium silicate) to remove copper(I) salts and photocatalyst and then evaporated under reduced pressure to result in yellow to orange oil of crude product **4-59**. Compounds were purified using CombiFlash Chromatograph system on SiO₂ using Hexane and EtOAc as solvents and gradient from 95:5 to 80:20 over 15 minutes.

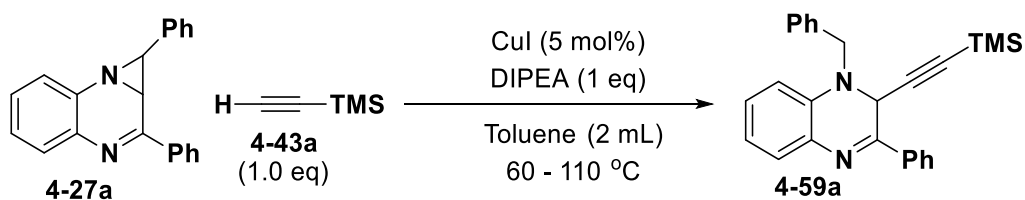
Asymmetric Photochemical copper-catalyzed Alkynylation (Protocol B)



The reaction was performed in 2-dram (8 mL) oven-dried (for 24 hours) glass vials. Dry THF (from the solvent system) was degassed prior to the reaction using the freeze-pump-thaw method (3 times). A Glass vial with a stir bar was charged with Ir(p-CF₃ppy)₃ photocatalyst (0.9 mg, 0.001 mmol, 1 mol%), copper (I) iodide CuI (1.0 mg, 0.005 mmol, 5 mol%), (S,R)-N-PINAP ligand **L10** (2.8 mg, 0.005 mmol, 6 mol%) then closed with cap with septum and covered with rubber septum which was fixed with electrical tape. Vial was vacuumed and refilled with nitrogen (3 times, under Shlenk line) and 1 mL of degassed toluene was injected into it, followed by alkyne **4-43** (0.1 mmol, 1.0 eq) and DIPEA (0.1 mmol, 17.4 μL, 1.0 eq). Reaction mixture was stirred at r.t. for 1.5 hours and then solution (prepared in separate vial under oxygen-free conditions) of aziridine **4-27** (0.1 mmol) in 1 ml of degassed THF was injected to vial. Reaction mixture was stirred under Green LED irradiation (18 W Hypatochem EVOLUCHEM LED 525PF) for 24 hours. After that vial was

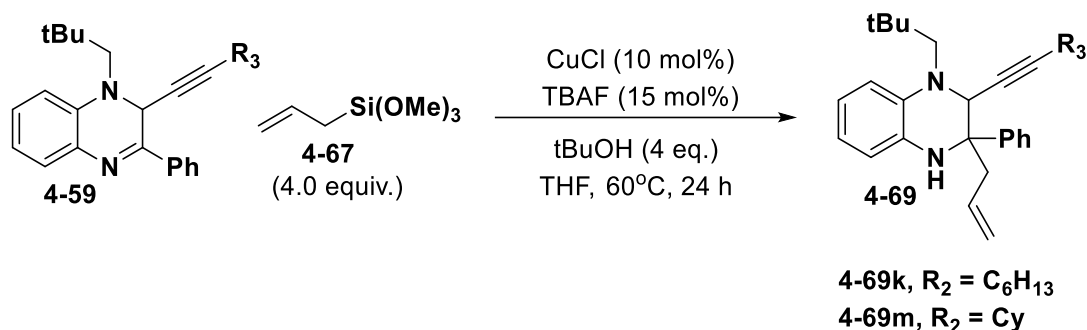
uncapped and reaction mixture filtered through short plug of Fluorosil (Magnesium silicate) to remove copper(I) salt and photocatalyst and then evaporated under reduced pressure to result in yellow to orange oil of crude product **4-59**. Purification was performed using CombiFlash Chromatograph system on SiO₂ using Hexane and EtOAc as solvents and gradient from 95:5 to 80:20 over 15 minutes.

Thermal activation of compound **4-27a** for copper-catalyzed Alkynylation (Protocol C)



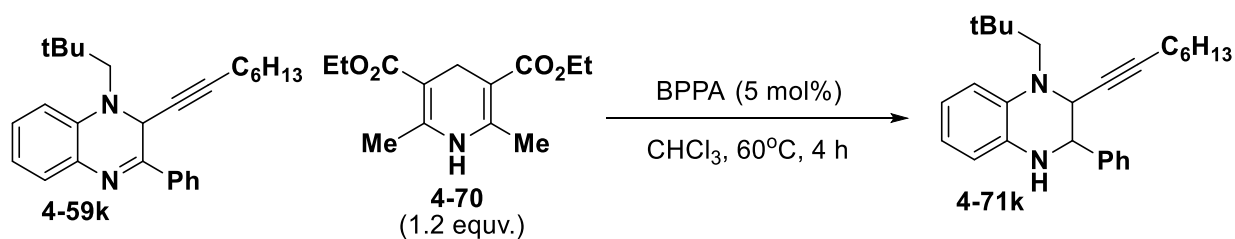
The reaction was performed in 2-dram (8 mL) oven-dried (for 24 hours) glass vials. Glass vial with a stir bar was charged with copper (I) iodide CuI (1.0 mg, 0.005 mmol, 5 mol%) and *optionally ligand L* (0.006 mmol, 6 mol%) then closed with cap with septum. Vial was vacuumed and refilled with nitrogen (3 times, under Shlenk line) and 1 mL of toluene was injected into it, followed by alkyne **4-43a** (0.1 mmol, 14.2 μ L, 1.0 eq) and DIPEA (0.1 mmol, 17.4 μ L, 1.0 eq). Reaction mixture was stirred at r.t. for 1.5 hours and then solution of aziridine **4-27a** (0.1 mmol, 29.6 mg) in 1 ml of toluene was injected to vial. Reaction mixture was stirred at 110 °C for 6 hours (reaction progress monitored by TLC). After that reaction mixture filtered through short plug of Fluorosil (Magnesium silicate) to remove copper(I) salts and then evaporated under reduced pressure to result in yellow oil of crude product **4-59a** (35.9 mg, 91% yield) that doesn't require purification.

Imine allylation of products **4-59** (Protocol C)



An oven-dried glass vial was charged with a stir bar, CuCl (1.0 mg, 0.01 mmol, 1 mol%), and closed with a septum cap. The vial was vacuumed and refilled with nitrogen (3 times, under Shlenk line) and 1 mL of dry THF was added into it, followed by 15 μ L TBAF solution in THF (1.0 M solution, 0.01 mmol, 15 mol%). The reaction mixture was stirred for 1 hour. After that solution of compound **4-59** (0.1 mmol), trimethoxyallylsilane **4-67** (67 μ L, 0.4 mmol, 4.0 eq.) and tBuOH (50 μ L) in 1 mL of THF was added to the vial and the reaction mixture stirred at 60 °C for 24 hours (monitored by TLC). Then the vial was cooled down to r.t. and the reaction mixture was filtered through a short pad of silica gel and evaporated under reduced pressure. Purification was performed using CombiFlash Chromatograph system on SiO₂ using Hexane and EtOAc as solvents and gradient from 100:0 to 90:10 over 15 minutes to give the final product **4-69**.

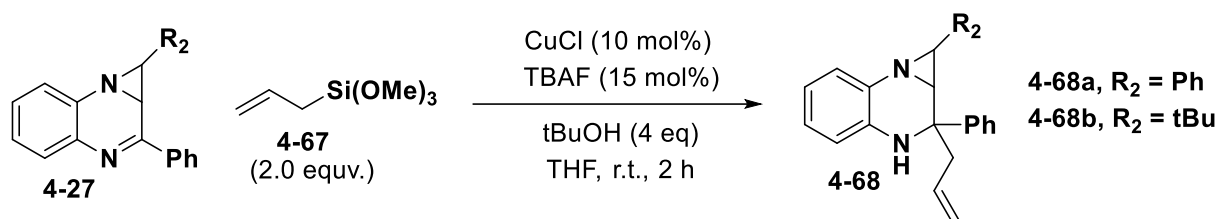
Imine hydrogenation of products **4-59** (Protocol D)



An oven-dried 2-dram vial with a magnetic stir bar and a septum containing corresponding substrate **4-59k** (0.1 mmol, 1 equiv), biphenylphosphoric acid BPPA (1.2 mg, 0.005 mmol, 5 mol%) and diethyl 2,6-dimethyl-1,4-dihydropyridine-3,5-dicarboxylate **4-70** (30.4 mg, 0.12 mmol, 1.2 equiv) was vacuumed for 2 minutes. The whole system was backfilled with N₂, and then 2.0 mL

of CHCl_3 was added to the vial. The resulting mixture was then stirred at 60 °C for 4 hours (monitored by TLC) and quenched by evaporating the solvent under reduced pressure. Purification was performed using CombiFlash Chromatograph system on SiO_2 using Hexane and EtOAc as solvents and gradient from 100:0 to 90:10 over 15 minutes to get 32.4 mg (84%) of **4-59k** as pale-yellow oil.

Imine allylation of starting aziridinoquinoxalines **4-27** (Protocol E)



An oven-dried glass vial was charged with a stir bar, CuCl (1.0 mg, 0.01 mmol, 1 mol%), and closed with a septum cap. The vial was vacuumed and refilled with nitrogen (3 times, under Shlenk line) and 1 mL of dry THF was added into it, followed by 15 μL TBAF solution in THF (1.0 M solution, 0.01 mmol, 15 mol%). The reaction mixture was stirred for 1 hour. After that solution of compound **4-27** (0.1 mmol), trimethoxyallylsilane **4-67** (34 μL , 0.2 mmol, 2.0 eq.), and tBuOH (50 μL) in 1 mL of THF was added to the vial and the reaction mixture stirred at r.t. for 2 hours (monitored by TLC). Then the vial was cooled down to r.t. and the reaction mixture was filtered through a short pad of silica gel and evaporated under reduced pressure. Purification was performed using CombiFlash Chromatograph system on SiO_2 using Hexane and EtOAc as solvents and gradient from 100:0 to 90:10 over 15 minutes to get the final product **4-68**.

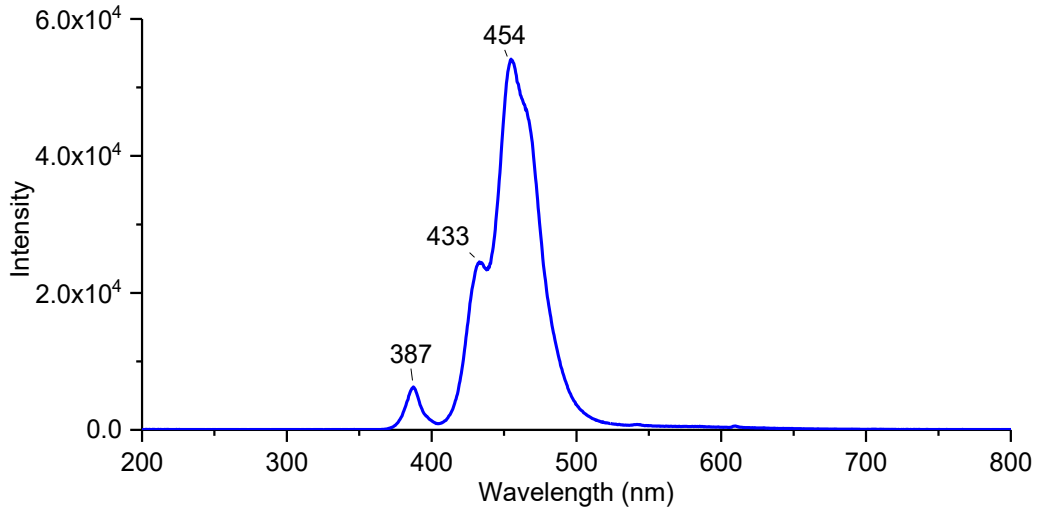
4.8.2 Mechanistic studies experimental details

4.8.2.1 Light sources emission spectra

a. A160WE Series Controllable Tuna Blue LED (Blue LED)

Peak Wavelength: 454 nm (Main)

Figure 4.7. Emission Spectrum of Blue LED

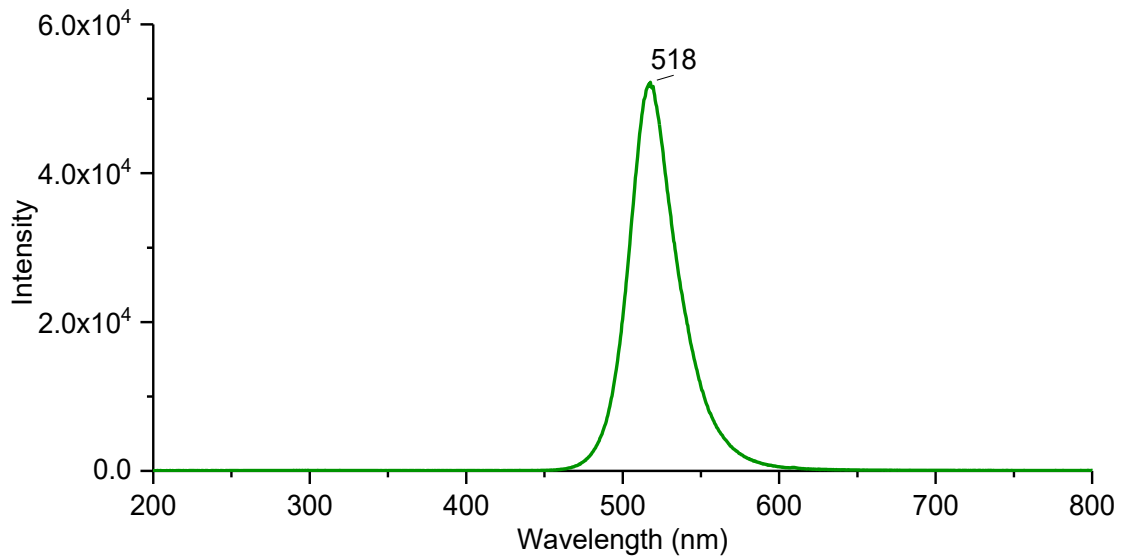


b. Hypatochem EVOLUCHEM LED 525PF (Green LED)

18W 525 nm 25 degrees

Peak Wavelength: 518 nm

Figure 4.8. Emission Spectrum of Green LED



4.8.2.2 UV-Vis absorption spectra of aziridine compounds

Spectra were recorded using Varian Cary 50 Bio UV-Visible Spectrophotometer in glass vial (10 mm; 2 Optical Windows; Volume: 3.0 ml, Spectral Range: 220-1100 nm). Solutions of compounds **4-27a** and **4-27b** was prepared in THF ($c = 0.00005$ M).

Figure 4.9. UV-Vis absorption spectrum of compound **4-27a**

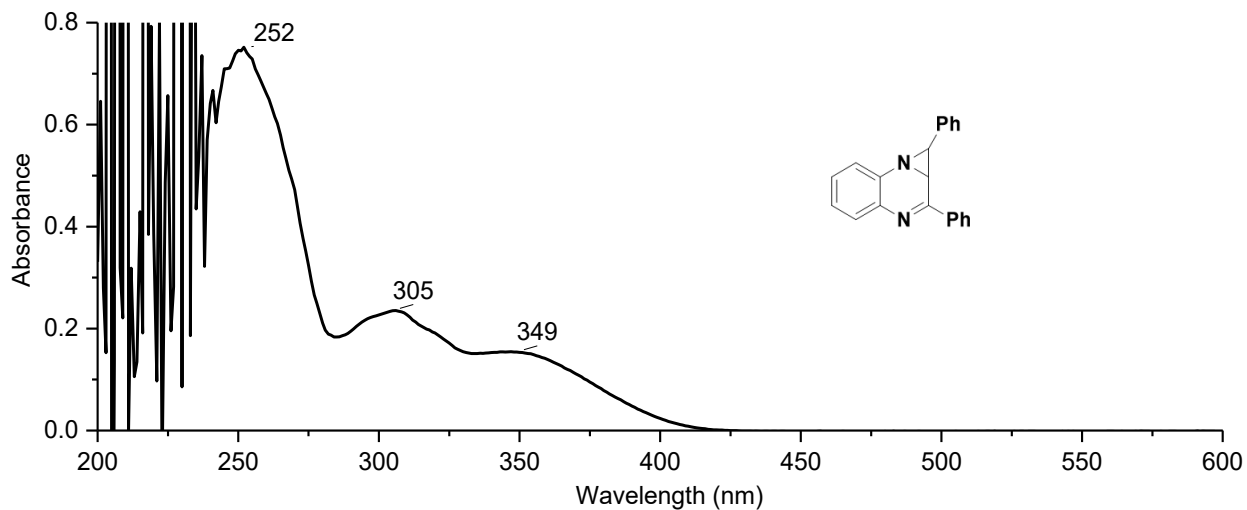
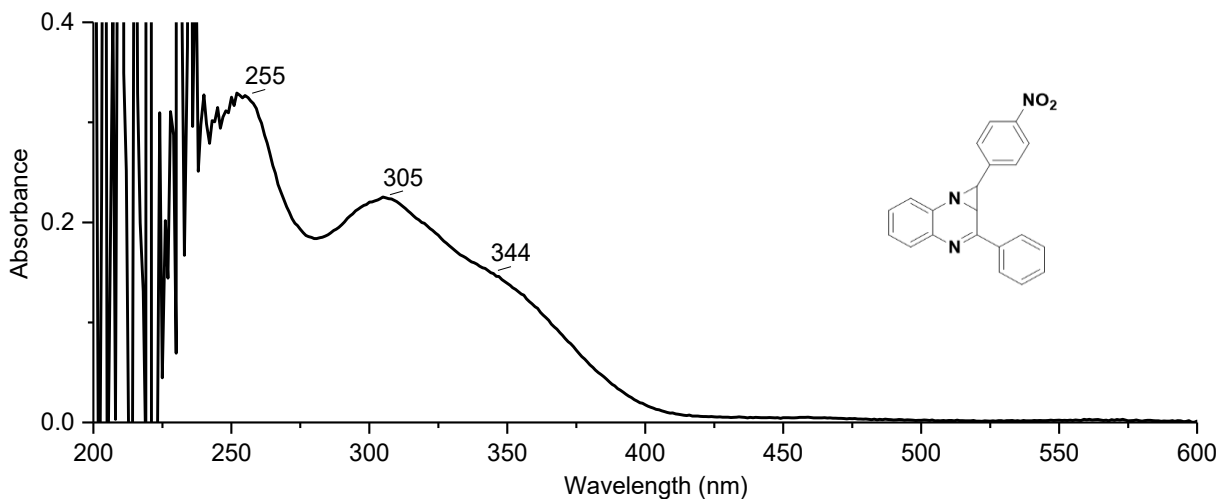


Figure 4.10. UV-Vis absorption spectrum of compound **4-27b**



4.8.2.3 Fluorescence measurements

Fluorescence measurements were performed in Alpha Nanotech UV Quartz Cuvettes with Screw Cap and Septum (Pathlength: 10 mm; 4 Optical Windows; Volume: 3.5 ml, Spectral Range: 190-2500 nm) under nitrogen atmosphere using Horiba PTI QuantaMaster 8000 fluorimeter.

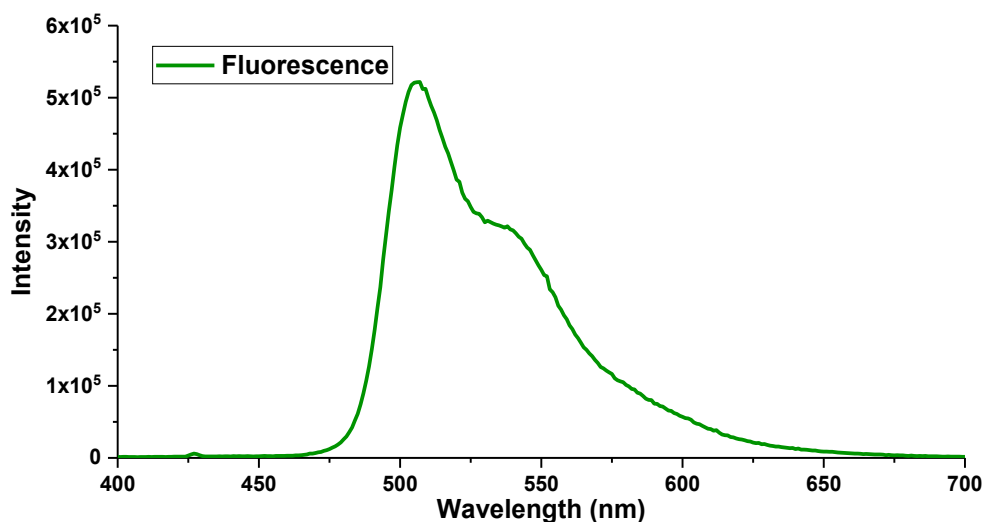
a) Ir(4-CF₃-ppy)₃ photocatalyst, c = 0.00005 M in THF (degassed)

Emission scan (Fluorescence):

λ (excitation) = 378 nm

Emission range scan = 400 – 700 nm

Figure 4.11. Fluorescence spectrum of Ir(4-CF₃-ppy)₃

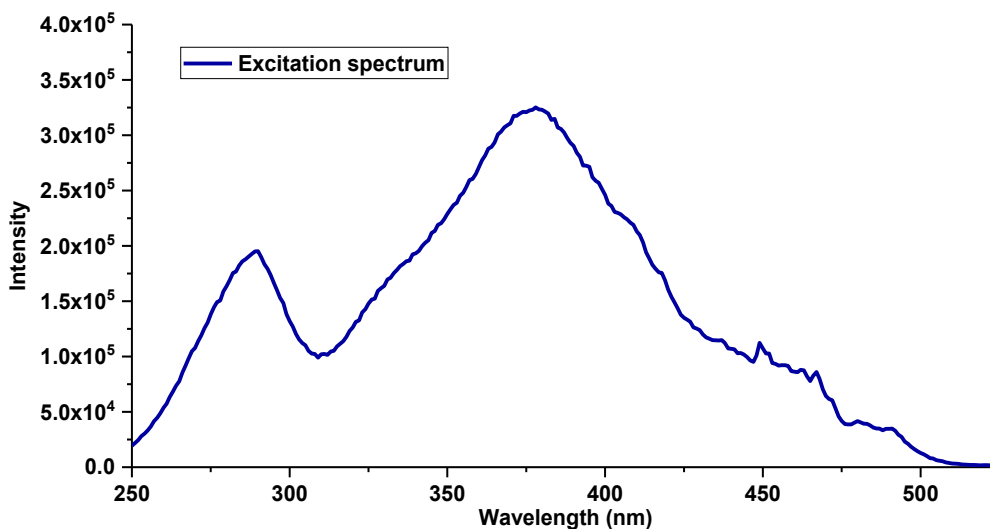


Excitation scan:

λ (emission detection) = 540 nm

Excitation range scan = 250 – 525 nm

Figure 4.12. Excitation (absorption) spectrum of Ir(4-CF₃-ppy)₃



b) Compound **4-27a**, $c = 0.00005$ M in THF (degassed)

S₀ – S₁ transition

Emission scan (Fluorescence):

λ (excitation) = 305 nm

Emission range scan = 320 – 600 nm

Excitation scan (Absorption):

λ (emission detection) = 337 nm

Excitation range scan = 200 – 320 nm

S₀ – T₁ transition

Emission scan (Fluorescence):

λ (excitation) = 397 nm

Emission range scan = 420 – 700 nm

Excitation scan (Absorption):

λ (emission detection) = 515 nm

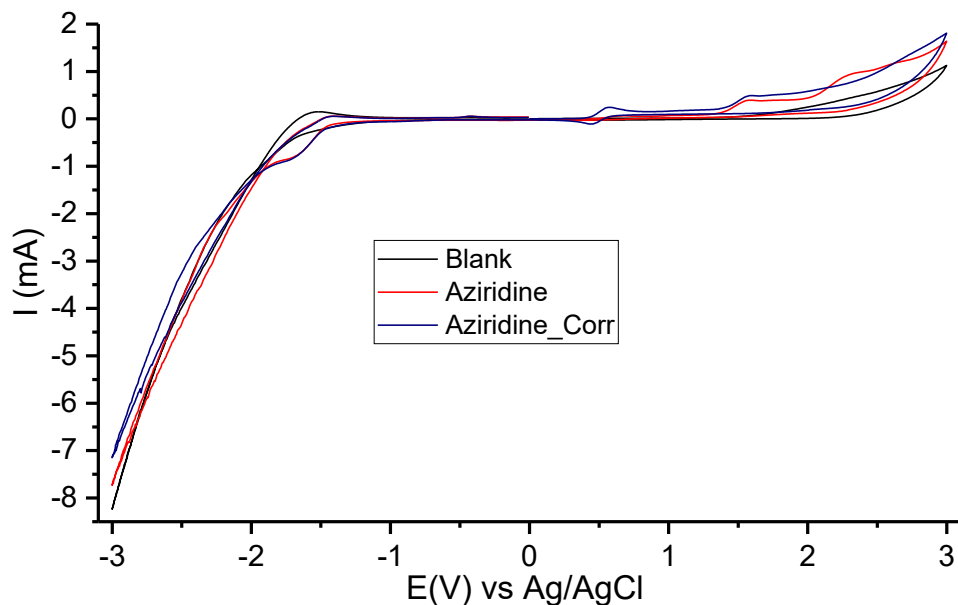
Excitation range scan = 200 – 500 nm

4.8.2.4 Cyclic voltammetry studies

Cyclic voltammetry studies were performed with the Pine WaveNowXV Potentiostat/Galvanostat. All experiments were measured under a slight argon stream. Electrodes were polished with 1000-grit sandpaper and cleaned by sonicating in acetone, and they were dried under high vacuum before use. All electrolytes were dried under a high vacuum before use. Dry acetonitrile was purchased from Alfa Aesar. All solvents were degassed with argon sparging before use.

Substrate: **4-27a**, (20 mM)
 Scan range: -3.0 V to 3.0 V
 Scan rate: 50 mV/s
 Electrolyte: TBABF₄ (0.1 M) / Solvent: acetonitrile (10 mL)
 Working electrode: 0.635 mm diameter Pt wire (0.5 cm submerged)
 Counter electrode: 0.635 mm diameter Pt wire (0.5 cm submerged)
 Reference electrode: Ag/AgCl
 Potential correction of reference electrode was performed by adding Ferrocene (10 mM)

Figure 4.13. Cyclic voltammetry scan of compound 4-27a, range -3.0 V to 3.0 V, 50 mV/s



Reference value (literature) of Ferrocene vs Ag/AgCl electrode:

$$E^{\text{lit}}(\text{Fc})_{\text{SCE}} = 0.4030 \text{ V}^{36-38}$$

Measured value of Ferrocene vs used Ag/AgCl electrode: $E(\text{Fc})_{\text{Ag/AgCl}} = 0.5056 \text{ V}$, $\Delta E = 66 \text{ mV}$

Correction to potential:

$$E(\text{Fc})_{\text{Ag/AgCl}} = \phi_{\text{Fc}} - \phi_{\text{Ag/AgCl}} = 0.5056 \text{ V}; E^{\text{lit}}(\text{Fc})_{\text{SCE}} = \phi_{\text{Fc}} - \phi_{\text{SCE}} = 0.4030 \text{ V}$$

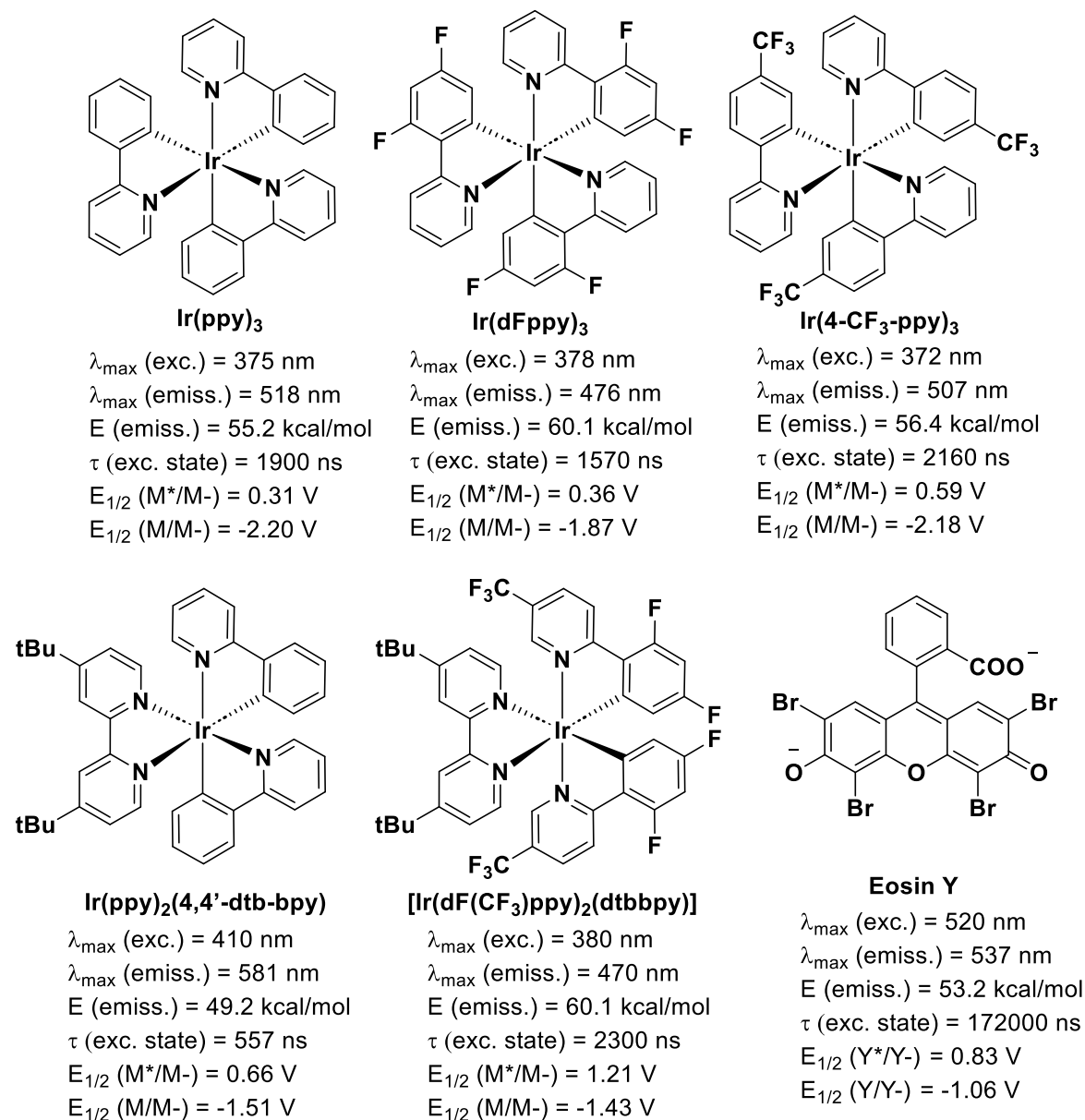
$$E^{\text{corr}}(\text{Fc})_{\text{SCE}} = \phi_{\text{Ag/AgCl}} - \phi_{\text{SCE}} = 0.4030 - 0.5056 = -0.1026 \text{ V}$$

Measured potential of aziridine **4-27a**: $E^{1/2\text{ox}}(\mathbf{4-27a})_{\text{Ag/AgCl}} = 1.5932 \text{ V}$

Corrected potential to SCE of aziridine **4-27a**: $E(\mathbf{4-27a})_{\text{Ag/AgCl}} = \phi_{6a} - \phi_{\text{Ag/AgCl}} = 1.5932 \text{ V}$

$E(\mathbf{4-27a})_{\text{SCE}} = E(\mathbf{4-27a})_{\text{Ag/AgCl}} + E^{\text{corr}}(\text{Fc})_{\text{SCE}} = 1.4906 \text{ V}$ (vs SCE electrode)

Scheme 4.24. Structures and the properties of used photocatalyst



4.8.3 Computational details

All quantum chemical computations were performed using QChem 5.2.0.³⁹ Reaction pathways were optimized using the growing string method (GSM) developed by Zimmerman group^{40,41}, using density functional theory (DFT) to represent the underlying potential energy surfaces. After each GSM run, transition state (TS) structures were further refined using an eigenvector TS optimizer. DFT simulations used the B3LYP⁴² functional and 6-31+G** basis set⁴³ for geometry

optimization and transition state search via GSM method. Enthalpic (Hvib) and entropic (Svib) corrections were applied under the rigid rotor/harmonic oscillator model, which includes translational, rotational, and vibrational contributions to these quantities (298.15K) at B3LYP/6-31+G** level of theory. The ω B97X-D3/cc-pVTZ^{44,45} level of theory was used for performing single-point energy calculations of optimized structures with SMD solvation correction.⁴⁶ Time-dependent DFT analysis of excited states (TD-DFT with Tamm–Dancoff approximation)⁴⁷ was performed on reoptimized structures at ω B97X-D3/cc-pVTZ (SG-2 grid) level of theory.

Computational data (XYZ files, energies breakdown of the all computed structures and transition states) available in Supplementary Information of paper published by Nagorny et. al.⁴⁸ <https://doi.org/10.1002/anie.202318876>

4.8.3.1 Growing string computations

For the double-ended growing string (DE-GSM) runs, 15 nodes were set as maximum limit. Starting structures (closed form of aziridine) and products (ylide, open form of aziridine) were optimized using B3LYP/6-31+G** level of theory prior to the GSM run. During the growth phase, new nodes were added when the RMS gradient was less than 0.005 Hartree/Å. An initial maximum optimization step size of 0.1 was used. When the total perpendicular gradient magnitude over all nodes, F , reached $F < 0.3$, the climbing image search was initiated. When $F < 0.1$, or when the highest energy node had an RMS gradient below double the nodal convergence criterion and $F < 0.2$, the exact transition state search was initiated within the string. The string is considered completely converged when an RMS gradient < 0.0003 Hartree/Å was obtained for the transition state node. After string optimization, the TSs were further optimized to higher tolerances (0.0015 gradient tolerance, 0.0002 energy tolerance). Further computational details can be found in references.^{49,50}

4.8.3.2 Redox potentials calculations

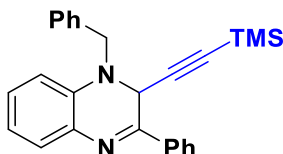
The reduction potential with respect to the reference electrode was calculated using the equation:

$$E_{calc}(V \text{ vs } ref) = E_{calc}^{abs}(V) - E_{exp,ref}^{abs}(V) = \frac{-\Delta G_{solv,calc}}{nF} - E_{exp,ref}^{abs}(V),$$

where $\Delta G_{solv,calc}$ is the Gibbs free energy change for a single electron process calculated with the ω B97X-D3/cc-pVTZ level of theory and SMD solvation model. Reference absolute potential according to the literature $E_{exp,ref}^{abs}(V) = 4.522 \text{ V vs SCE}$.⁵¹

4.8.4 Compounds characterization data

1-benzyl-3-phenyl-2-((trimethylsilyl)ethynyl)-1,2-dihydroquinoxaline (4-59a)



Yellow oil, 27.6 mg, 70% yield, obtained according to **Protocol A** (with adding ligand **L3**).

Yellow oil, 19.7 mg, 50% yield, 86:14 e.r., obtained according to **Protocol B**.

¹H NMR (500 MHz, Chloroform-d) δ 7.92 (dd, $J = 6.7, 3.1$ Hz, 2H), 7.48 (dd, $J = 7.7, 1.6$ Hz, 1H), 7.42 – 7.36 (m, 4H), 7.34 – 7.27 (m, 3H), 6.95 – 6.86 (m, 1H), 6.81 (d, $J = 8.0$ Hz, 1H), 5.07 (s, 1H), 4.72 (d, $J = 14.5$ Hz, 1H), 4.28 (d, $J = 14.5$ Hz, 1H), 0.02 (s, 9H)

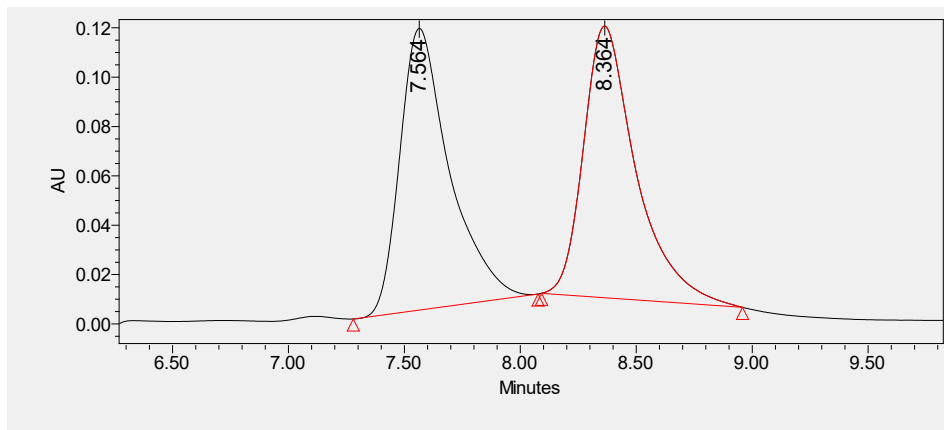
¹³C NMR (126 MHz, Chloroform-d) δ 154.4, 137.2, 136.5, 136.3, 135.2, 130.6, 128.9, 128.7, 128.3, 128.3, 128.3, 127.9, 127.1, 119.6, 112.8, 99.2, 91.8, 51.9, 47.4, 0.0.

HRMS (ESI+) (m/z): $[M+H]^+$ 395.1938 calcd for $C_{26}H_{27}N_2Si^+$, found 395.1941;

$[\alpha]^{24}_D = +55.40$ ($c = 0.01$ g/mL, CH_2Cl_2);

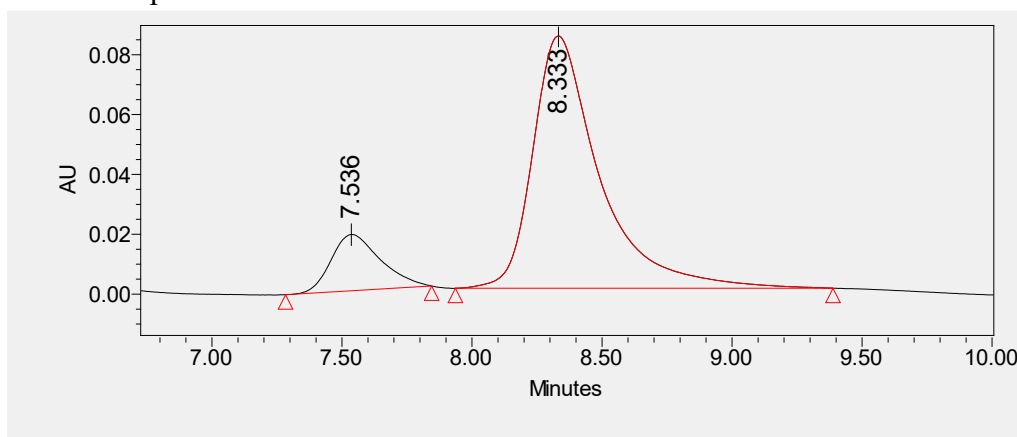
HPLC: (Chiralpak IA column, 95:5 hexanes/isopropanol, 0.5 mL/min, $I = 254$ nm): $t_r = 7.5$ min (minor), 8.4 min (major).

Racemic compound HPLC traces



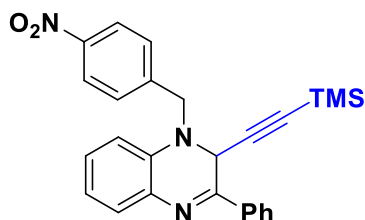
	Retention Time	Area	% Area	Height
1	7.564	1699271	49.46	114144
2	8.364	1736701	50.54	110100

Chiral compound HPLC traces



	Retention Time	Area	% Area	Height
1	7.536	228053	13.09	18799
2	8.333	1526206	86.91	84297

1-(4-nitrobenzyl)-3-phenyl-2-((trimethylsilyl)ethynyl)-1,2-dihydroquinoxaline (4-59b)



Orange oil, 28.5 mg, 65% yield, obtained according to **Protocol A** (with adding ligand **L3**).

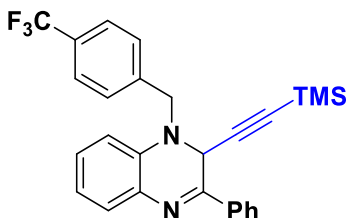
$^1\text{H NMR}$ (500 MHz, Chloroform- d) δ 8.19 – 8.12 (m, 2H), 7.99 – 7.91 (m, 2H), 7.55 – 7.50 (m, 2H), 7.48 (dd, $J = 7.7, 1.5$ Hz, 1H), 7.45 – 7.38 (m, 3H), 7.09 (td, $J = 7.7, 1.5$ Hz, 1H), 6.91 (td, J

= 7.5, 1.2 Hz, 1H), 6.60 (dd, $J = 8.1, 1.2$ Hz, 1H), 5.09 (s, 1H), 4.74 (d, $J = 15.9$ Hz, 1H), 4.45 (d, $J = 15.9$ Hz, 1H), 0.00 (s, 9H).

^{13}C NMR (126 MHz, Chloroform- d) δ 154.4, 147.8, 144.7, 136.2, 136.0, 135.3, 131.0, 128.9, 128.8, 128.6, 128.6, 127.1, 124.3, 120.4, 112.9, 98.8, 92.6, 52.2, 48.9, 0.0.

HRMS (ESI+) (m/z): $[\text{M}+\text{H}]^+$ 440.1789 calcd for $\text{C}_{26}\text{H}_{26}\text{N}_3\text{O}_2\text{Si}^+$, found 440.1781;

3-phenyl-1-(4-(trifluoromethyl)benzyl)-2-((trimethylsilyl)ethynyl)-1,2-dihydroquinoxaline (4-59c)



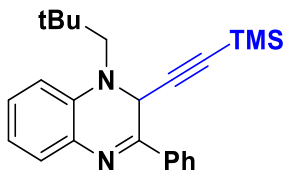
Yellow oil, 24.5 mg, 54% yield, obtained according to **Protocol A** (with adding ligand **L3**)

^1H NMR (500 MHz, Chloroform- d) δ 7.98 – 7.90 (m, 2H), 7.56 (d, $J = 8.1$ Hz, 2H), 7.47 (dd, $J = 7.7, 1.5$ Hz, 3H), 7.42 (dd, $J = 5.1, 1.9$ Hz, 3H), 7.10 (td, $J = 7.7, 1.6$ Hz, 1H), 6.90 (td, $J = 7.5, 1.2$ Hz, 1H), 6.68 (d, $J = 8.1$ Hz, 1H), 5.07 (s, 1H), 4.72 (d, $J = 15.4$ Hz, 1H), 4.38 (d, $J = 15.4$ Hz, 1H), 0.00 (s, 9H).

^{13}C NMR (126 MHz, Chloroform- d) δ 154.4, 141.0, 136.6, 136.1, 135.2, 130.9, 130.16 (q, $J = 32.5$ Hz), 128.8, 128.5, 128.3, 127.1, 125.96 (q, $J = 3.8$ Hz), 124.17 (q, $J = 271.9$ Hz), 120.1, 112.9, 99.0, 92.3, 52.0, 48.4, 0.0.

HRMS (ESI+) (m/z): $[\text{M}+\text{H}]^+$ 463.1812 calcd for $\text{C}_{27}\text{H}_{26}\text{F}_3\text{N}_2\text{Si}^+$, found 463.1807;

1-neopentyl-3-phenyl-2-((trimethylsilyl)ethynyl)-1,2-dihydroquinoxaline (4-59d)



Yellow oil, 35.9 mg, 96% yield, obtained according to **Protocol A**.

Yellow oil, 30.2 mg, 91% yield, 93:7 e.r., obtained according to **Protocol B**.

^1H NMR (500 MHz, Chloroform- d) δ 8.06 – 8.00 (m, 2H), 7.52 – 7.43 (m, 4H), 7.15 (ddd, $J = 8.6, 7.3, 1.6$ Hz, 1H), 6.93 – 6.87 (m, 1H), 6.84 (td, $J = 7.5, 1.2$ Hz, 1H), 5.20 (s, 1H), 3.55 (d, $J = 15.2$ Hz, 1H), 2.99 (d, $J = 15.3$ Hz, 1H), 0.95 (s, 9H), 0.01 (s, 9H).

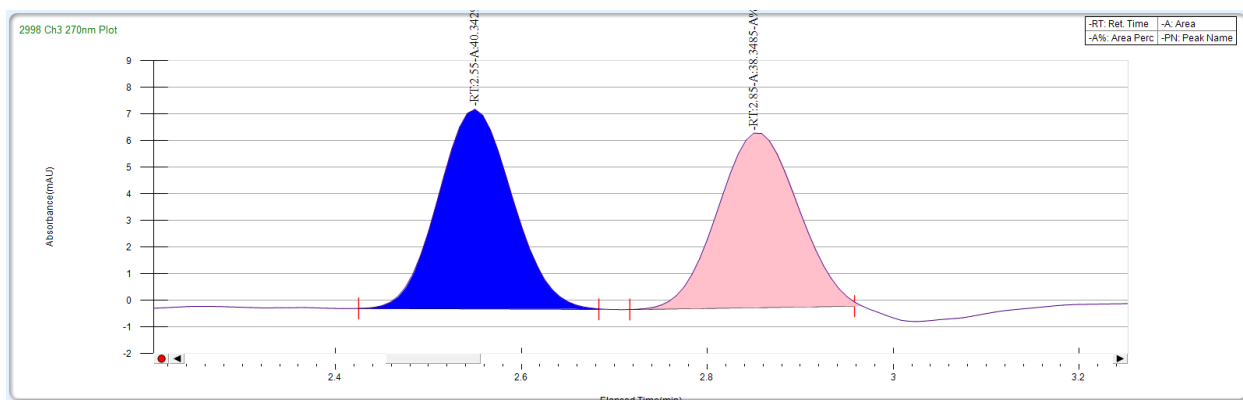
^{13}C NMR (126 MHz, Chloroform- d) δ 153.0, 137.7, 136.3, 135.0, 130.5, 128.7, 128.6, 128.3, 127.0, 118.3, 112.6, 100.7, 90.5, 58.4, 50.7, 34.4, 27.9, -0.1

HRMS (ESI+) (m/z): $[\text{M}+\text{H}]^+$ 375.2251 calcd for $\text{C}_{24}\text{H}_{31}\text{N}_2\text{Si}^+$, found 375.2245;

$[\alpha]^{24}_{\text{D}} = +132.83$ ($c = 0.01$ g/mL, CH_2Cl_2);

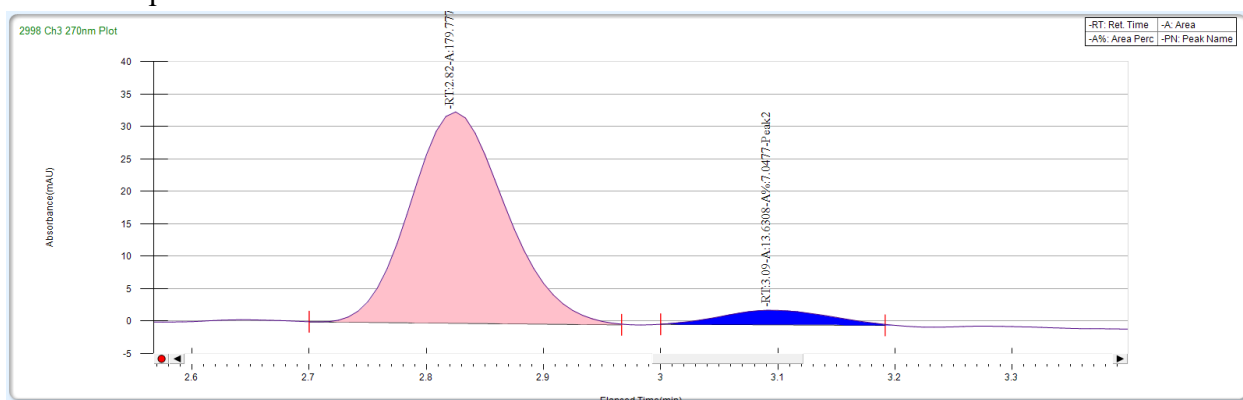
SFC (Chiralpak ODH column, 95:5 carbon dioxide/methanol, 3.5 mL/min, $I = 270$ nm): $t_r = 2.6$ min (major), 2.9 min (minor).

Racemic compound SFC traces



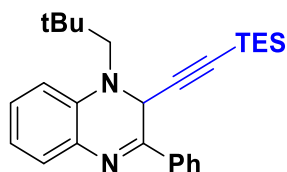
Peak Name	Area Percent	Area	Retention Time	Height
Peak1	51.2672	40.3429	2.55 min	7.4961
Peak2	48.7328	38.3485	2.85 min	6.5589

Chiral compound SFC traces



Peak Name	Area Percent	Area	Retention Time	Height
Peak1	92.9523	179.7775	2.82 min	32.5378
Peak2	7.0477	13.6308	3.09 min	2.238

1-neopentyl-3-phenyl-2-((triethylsilyl)ethynyl)-1,2-dihydroquinoxaline (4-59e)



Yellow oil, 37.0 mg, 89% yield, obtained according to **Protocol A**.

Yellow oil, 32.4 mg, 78% yield, 94.5:5.5 e.r., obtained according to **Protocol B**.

$^1\text{H NMR}$ (500 MHz, Chloroform- d) δ 8.05 – 8.00 (m, 2H), 7.51 – 7.42 (m, 4H), 7.13 (ddd, J = 8.6, 7.4, 1.6 Hz, 1H), 6.89 (d, J = 8.2 Hz, 1H), 6.83 (td, J = 7.5, 1.1 Hz, 1H), 5.15 (s, 1H), 3.54 (d, J = 15.1 Hz, 1H), 2.99 (d, J = 15.2 Hz, 1H), 0.95 (s, 9H), 0.78 (t, J = 7.9 Hz, 9H), 0.42 (q, J = 7.9 Hz, 6H).

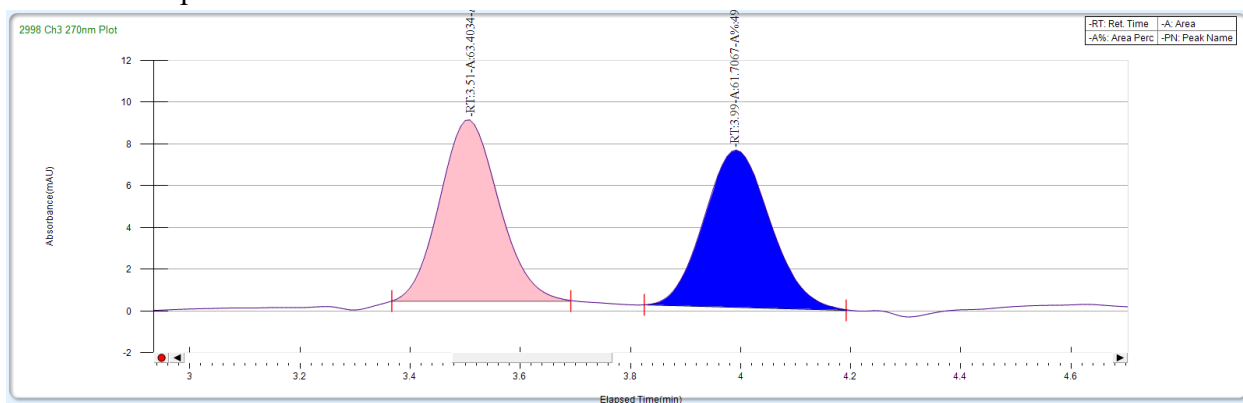
^{13}C NMR (126 MHz, Chloroform-d) δ 153.5, 137.8, 136.3, 135.2, 130.5, 128.7, 128.4, 128.3, 126.9, 118.4, 112.6, 102.1, 88.2, 58.5, 50.9, 34.3, 27.9, 7.4, 4.3

HRMS (ESI+) (m/z): $[\text{M}+\text{H}]^+$ 417.2721 calcd for $\text{C}_{27}\text{H}_{37}\text{N}_2\text{Si}^+$, found 417.2720;

$[\alpha]^{24}_{\text{D}} = +138.83$ ($c = 0.018$ g/mL, CH_2Cl_2);

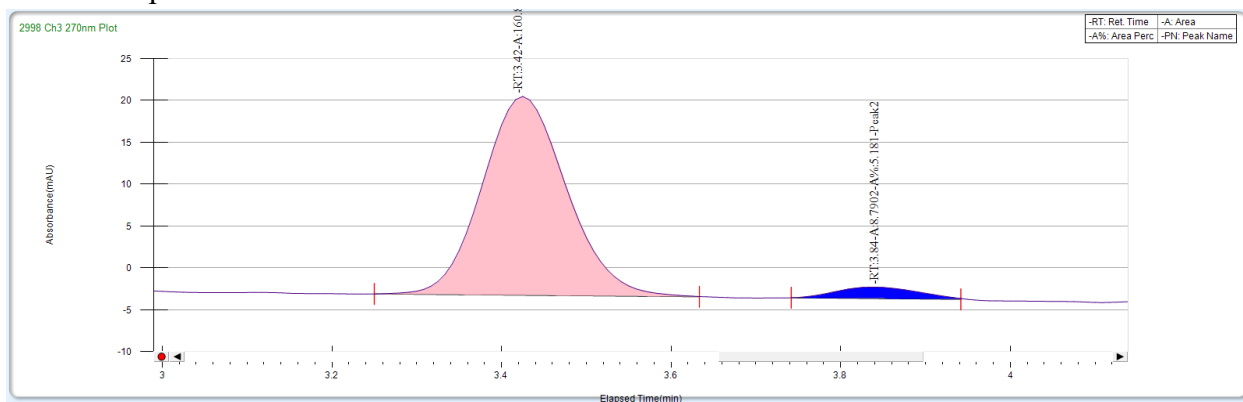
SFC (Chiralpak ODH column, 95:5 carbon dioxide/methanol, 3.5 mL/min, $I = 270$ nm): $t_r = 3.5$ min (major), 4.0 min (minor).

Racemic compound SFC traces



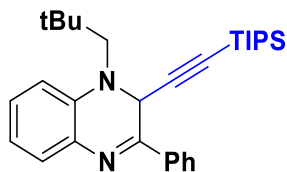
Peak Name	Area Percent	Area	Retention Time	Height
Peak1	50.6781	63.4034	3.51 min	8.6813
Peak2	49.3219	61.7067	3.99 min	7.5405

Chiral compound SFC traces



Peak Name	Area Percent	Area	Retention Time	Height
Peak1	94.819	160.8715	3.42 min	23.7585
Peak2	5.181	8.7902	3.84 min	1.3637

1-neopentyl-3-phenyl-2-((triisopropylsilyl)ethynyl)-1,2-dihydroquinoxaline (4-59f)



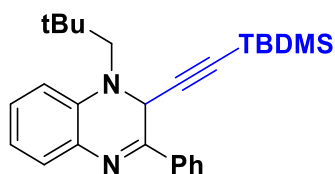
Yellow oil, 42.6 mg, 93% yield, obtained according to **Protocol A**.

$^1\text{H NMR}$ (500 MHz, Chloroform- d) δ 7.97 – 7.89 (m, 2H), 7.43 – 7.33 (m, 4H), 7.04 (ddd, J = 8.6, 7.3, 1.6 Hz, 1H), 6.82 (d, J = 8.2 Hz, 1H), 6.74 (td, J = 7.5, 1.2 Hz, 1H), 5.02 (s, 1H), 3.46 (d, J = 15.1 Hz, 1H), 2.91 (d, J = 15.1 Hz, 1H), 1.01 (tt, J = 5.2, 2.4 Hz, 3H), 0.88 (s, 9H), 0.78 (d, J = 1.6 Hz, 18H).

$^{13}\text{C NMR}$ (126 MHz, Chloroform- d) δ 152.7, 136.8, 135.3, 134.2, 129.3, 127.6, 127.2, 127.1, 125.8, 117.4, 111.5, 101.5, 86.3, 57.5, 49.9, 33.1, 26.7, 17.3, 17.3, 9.9.

HRMS (ESI+) (m/z): $[\text{M}+\text{H}]^+$ 459.3190 calcd for $\text{C}_{30}\text{H}_{43}\text{N}_2\text{Si}^+$, found 459.3197;

2-((tert-butyltrimethylsilyl)ethynyl)-1-neopentyl-3-phenyl-1,2-dihydroquinoxaline (4-59g)



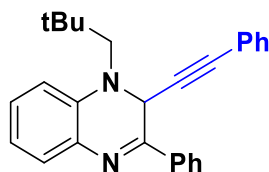
Yellow oil, 40.0 mg, 96% yield, obtained according to **Protocol A**.

$^1\text{H NMR}$ (500 MHz, Chloroform- d) δ 8.04 – 7.99 (m, 2H), 7.51 – 7.42 (m, 4H), 7.13 (ddd, J = 8.7, 7.3, 1.6 Hz, 1H), 6.90 (d, J = 8.2 Hz, 1H), 6.83 (td, J = 7.5, 1.2 Hz, 1H), 5.14 (s, 1H), 3.55 (d, J = 15.1 Hz, 1H), 2.98 (d, J = 15.2 Hz, 1H), 0.95 (s, 9H), 0.70 (s, 9H), -0.04 (s, 3H), -0.07 (s, 3H).

$^{13}\text{C NMR}$ (126 MHz, Chloroform- d) δ 153.4, 137.8, 136.3, 135.2, 130.5, 128.8, 128.4, 128.3, 127.0, 118.5, 112.6, 101.3, 89.2, 58.6, 50.8, 34.4, 27.9, 25.9, 16.6, -4.7, -4.8.

HRMS (ESI+) (m/z): $[\text{M}+\text{H}]^+$ 417.2721 calcd for $\text{C}_{27}\text{H}_{37}\text{N}_2\text{Si}^+$, found 417.2715;

1-neopentyl-3-phenyl-2-(phenylethynyl)-1,2-dihydroquinoxaline (4-59h)



Brown oil, 34.3 mg, 91% yield, obtained according to **Protocol A**.

$^1\text{H NMR}$ (500 MHz, Chloroform- d) δ 8.00 (dd, J = 7.5, 2.3 Hz, 2H), 7.41 (qd, J = 5.8, 2.6 Hz, 4H), 7.20 – 7.04 (m, 6H), 6.86 (d, J = 8.2 Hz, 1H), 6.77 (t, J = 7.5 Hz, 1H), 5.37 (s, 1H), 3.55 (d, J = 15.1 Hz, 1H), 3.01 (d, J = 15.2 Hz, 1H), 0.91 (s, 9H).

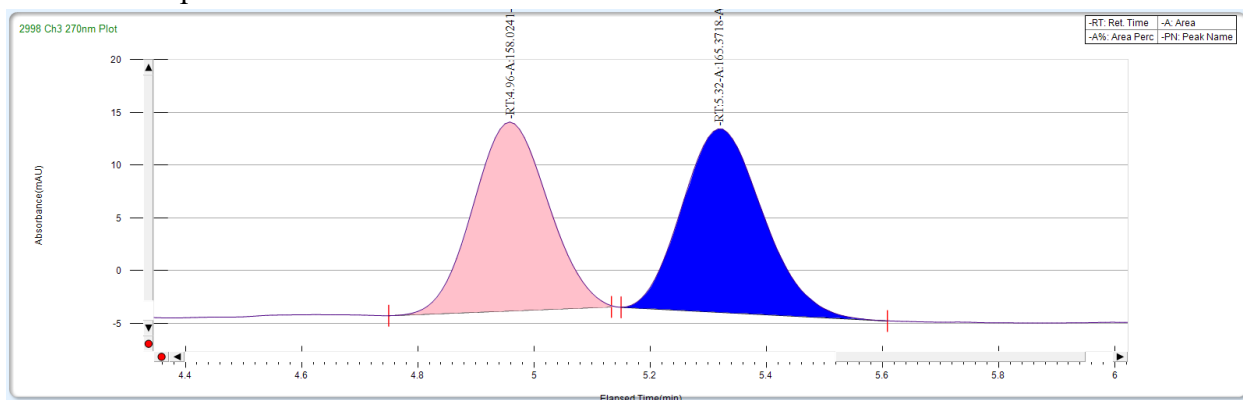
$^{13}\text{C NMR}$ (126 MHz, Chloroform- d) δ 152.9, 137.7, 136.1, 134.9, 132.0, 130.5, 128.7, 128.6, 128.4, 128.4, 128.1, 126.9, 122.3, 118.4, 112.5, 85.0, 84.5, 58.5, 50.4, 34.4, 27.8.

HRMS (ESI+) (m/z): $[\text{M}+\text{H}]^+$ 379.2169 calcd for $\text{C}_{27}\text{H}_{27}\text{N}_2^+$, found 379.2160;

$[\alpha]^{24}_{\text{D}}$ = +159.07 (c = 0.015 g/mL, CH_2Cl_2);

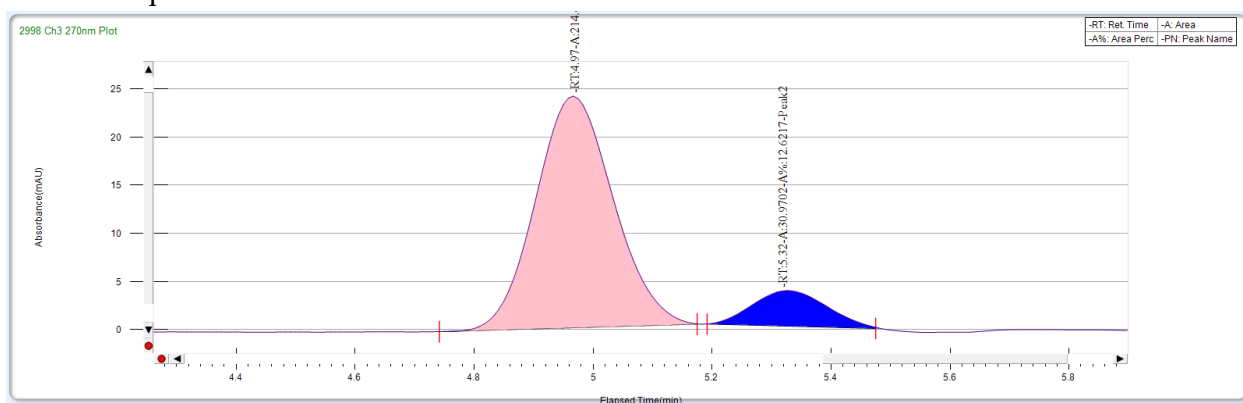
SFC (Chiralpak ODH column, 90:10 carbon dioxide/methanol, 3.5 mL/min, I = 270 nm): t_r = 5.0 min (major), 5.3 min (minor).

Racemic compound SFC traces



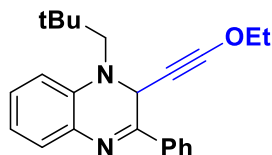
Peak Name	Area Percent	Area	Retention Time	Height
Peak1	48.864	158.0241	4.96 min	17.9036
Peak2	51.136	165.3718	5.32 min	17.3656

Chiral compound SFC traces



Peak Name	Area Percent	Area	Retention Time	Height
Peak1	87.3783	214.4019	4.97 min	24.0483
Peak2	12.6217	30.9702	5.32 min	3.6824

2-(ethoxyethynyl)-1-neopentyl-3-phenyl-1,2-dihydroquinoxaline (4-59i)



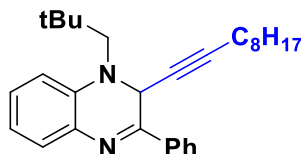
Yellow oil, 28.0 mg, 81% yield, obtained according to **Protocol A**.

$^1\text{H NMR}$ (500 MHz, Chloroform- d) δ 7.98 – 7.93 (m, 2H), 7.43 – 7.34 (m, 4H), 7.06 (td, J = 7.8, 1.6 Hz, 1H), 6.82 (d, J = 8.2 Hz, 1H), 6.75 (td, J = 7.5, 1.1 Hz, 1H), 5.10 (s, 1H), 3.81 (q, J = 7.1 Hz, 2H), 3.45 (d, J = 15.2 Hz, 1H), 2.90 (d, J = 15.1 Hz, 1H), 1.06 (t, J = 7.1 Hz, 3H), 0.87 (s, 9H).

^{13}C NMR (126 MHz, Chloroform-*d*) δ 154.2, 138.0, 136.3, 135.0, 130.3, 128.6, 128.3, 128.1, 126.9, 118.0, 112.5, 93.2, 74.6, 58.1, 49.3, 34.2, 33.8, 27.8, 14.0.

HRMS (ESI+) (*m/z*): $[\text{M}+\text{H}]^+$ 347.2118 calcd for $\text{C}_{23}\text{H}_{27}\text{N}_2\text{O}^+$, found 347.2115;

2-(dec-1-yn-1-yl)-1-neopentyl-3-phenyl-1,2-dihydroquinoxaline (4-59j)



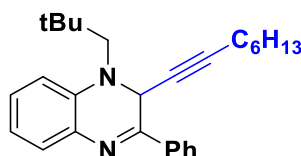
Yellow oil, 40.1 mg, 97% yield, obtained according to **Protocol A**.

^1H NMR (500 MHz, Chloroform-*d*) δ 7.99 – 7.91 (m, 2H), 7.38 (ddd, $J = 5.6, 3.5, 1.5$ Hz, 4H), 7.06 (ddd, $J = 8.4, 7.4, 1.6$ Hz, 1H), 6.81 (d, $J = 8.2$ Hz, 1H), 6.75 (td, $J = 7.5, 1.2$ Hz, 1H), 5.09 (t, $J = 2.1$ Hz, 1H), 3.46 (d, $J = 15.1$ Hz, 1H), 2.91 (d, $J = 15.2$ Hz, 1H), 1.93 (td, $J = 7.0, 2.0$ Hz, 2H), 1.21 (dt, $J = 24.6, 6.9$ Hz, 4H), 1.15 – 1.02 (m, 8H), 0.87 (s, 9H), 0.80 (t, $J = 7.2$ Hz, 3H).

^{13}C NMR (126 MHz, Chloroform-*d*) δ 153.8, 137.9, 136.2, 134.9, 130.3, 128.6, 128.4, 128.2, 126.8, 118.1, 112.4, 86.0, 75.3, 58.3, 50.0, 34.3, 31.8, 29.2, 29.0, 28.6, 28.4, 27.8, 22.7, 18.7, 14.1.

HRMS (ESI+) (*m/z*): $[\text{M}+\text{H}]^+$ 415.3108 calcd for $\text{C}_{29}\text{H}_{39}\text{N}_2^+$, found 415.3112;

1-neopentyl-2-(oct-1-yn-1-yl)-3-phenyl-1,2-dihydroquinoxaline (4-59k)



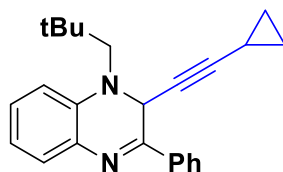
Yellow oil, 36.6 mg, 95% yield, obtained according to **Protocol A**.

^1H NMR (500 MHz, Chloroform-*d*) δ 8.00 – 7.91 (m, 2H), 7.39 (tt, $J = 5.3, 3.2$ Hz, 4H), 7.06 (ddd, $J = 8.7, 7.3, 1.6$ Hz, 1H), 6.81 (d, $J = 8.2$ Hz, 1H), 6.75 (td, $J = 7.5, 1.2$ Hz, 1H), 5.09 (t, $J = 2.1$ Hz, 1H), 3.46 (d, $J = 15.2$ Hz, 1H), 2.91 (d, $J = 15.1$ Hz, 1H), 1.94 (td, $J = 7.0, 2.1$ Hz, 2H), 1.24 (p, $J = 6.9$ Hz, 2H), 1.18 – 1.00 (m, 6H), 0.88 (s, 9H), 0.75 (t, $J = 7.1$ Hz, 3H).

^{13}C NMR (126 MHz, Chloroform-*d*) δ 153.8, 137.9, 136.2, 134.9, 130.3, 128.6, 128.4, 128.2, 126.8, 118.1, 112.4, 86.0, 75.3, 58.2, 49.9, 34.3, 31.2, 28.3, 28.2, 27.8, 22.5, 18.7, 14.0.

HRMS (ESI+) (*m/z*): $[\text{M}+\text{H}]^+$ 387.2795 calcd for $\text{C}_{27}\text{H}_{35}\text{N}_2^+$, found 387.2787;

2-(cyclopropylethynyl)-1-neopentyl-3-phenyl-1,2-dihydroquinoxaline (4-59l)



Yellow oil, 33.6 mg, 98% yield, obtained according to **Protocol A**.

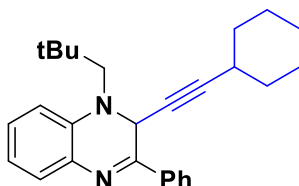
^1H NMR (500 MHz, Chloroform-*d*) δ 7.98 – 7.90 (m, 2H), 7.38 (ddt, $J = 7.3, 5.2, 3.1$ Hz, 4H), 7.06 (ddd, $J = 8.7, 7.4, 1.6$ Hz, 1H), 6.81 (d, $J = 8.2$ Hz, 1H), 6.75 (td, $J = 7.5, 1.2$ Hz, 1H), 5.07

(d, $J = 1.8$ Hz, 1H), 3.46 (d, $J = 15.1$ Hz, 1H), 2.89 (d, $J = 15.2$ Hz, 1H), 0.99 (tt, $J = 8.2, 5.0, 1.7$ Hz, 1H), 0.86 (s, 9H), 0.59 – 0.49 (m, 2H), 0.46 – 0.36 (m, 2H).

^{13}C NMR (126 MHz, Chloroform- d) δ 153.9, 138.2, 136.6, 135.2, 130.8, 129.0, 128.9, 128.6, 127.3, 118.5, 112.8, 89.3, 70.8, 58.6, 50.3, 34.7, 28.2, 8.9, 8.8, -0.0.

HRMS (ESI+) (m/z): $[\text{M}+\text{H}]^+$ 343.2169 calcd for $\text{C}_{24}\text{H}_{27}\text{N}_2^+$, found 343.2163;

2-(cyclohexylethynyl)-1-neopentyl-3-phenyl-1,2-dihydroquinoxaline (4-59m)



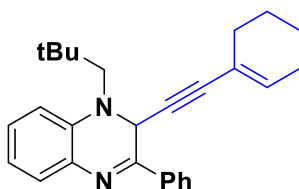
Yellow oil, 34.1 mg, 89% yield, obtained according to **Protocol A**.

^1H NMR (500 MHz, Chloroform- d) δ 7.95 (dd, $J = 7.4, 2.3$ Hz, 2H), 7.39 (tq, $J = 5.7, 2.7$ Hz, 4H), 7.09 – 7.02 (m, 1H), 6.81 (d, $J = 8.2$ Hz, 1H), 6.74 (td, $J = 7.5, 1.2$ Hz, 1H), 5.08 (d, $J = 1.9$ Hz, 1H), 3.46 (d, $J = 15.1$ Hz, 1H), 2.91 (d, $J = 15.1$ Hz, 1H), 2.16 (ddt, $J = 13.1, 7.5, 3.2$ Hz, 1H), 1.51 – 1.32 (m, 4H), 1.31 – 1.02 (m, 6H), 0.87 (s, 9H).

^{13}C NMR (126 MHz, Chloroform- d) δ 153.9, 137.9, 136.3, 135.0, 130.3, 128.6, 128.3, 128.1, 126.8, 118.1, 112.4, 90.1, 75.4, 58.2, 50.1, 34.3, 32.3, 32.2, 28.7, 27.8, 25.8, 24.2.

HRMS (ESI+) (m/z): $[\text{M}+\text{H}]^+$ 385.2638 calcd for $\text{C}_{27}\text{H}_{33}\text{N}_2^+$, found 385.2640;

2-(cyclohex-1-en-1-ylethynyl)-1-neopentyl-3-phenyl-1,2-dihydroquinoxaline (4-59n)



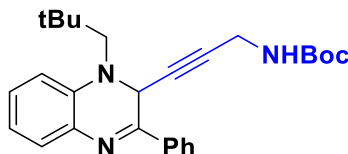
Yellow oil, 36.3 mg, 95% yield, obtained according to **Protocol A**.

^1H NMR (500 MHz, Chloroform- d) δ 7.99 – 7.93 (m, 2H), 7.43 – 7.34 (m, 4H), 7.06 (ddd, $J = 8.3, 7.4, 1.6$ Hz, 1H), 6.82 (d, $J = 8.2$ Hz, 1H), 6.75 (td, $J = 7.5, 1.2$ Hz, 1H), 5.86 (tt, $J = 4.0, 1.8$ Hz, 1H), 5.24 (s, 1H), 3.49 (d, $J = 15.1$ Hz, 1H), 2.93 (d, $J = 15.2$ Hz, 1H), 1.87 (ddq, $J = 26.5, 6.0, 3.0$ Hz, 4H), 1.47 – 1.35 (m, 4H), 0.88 (s, 9H).

^{13}C NMR (126 MHz, Chloroform- d) δ 153.2, 137.8, 136.2, 135.8, 134.8, 130.3, 128.6, 128.5, 128.2, 126.9, 119.9, 118.1, 112.5, 86.8, 81.6, 58.3, 50.3, 34.3, 29.0, 27.8, 25.5, 22.1, 21.3.

HRMS (ESI+) (m/z): $[\text{M}+\text{H}]^+$ 383.2482 calcd for $\text{C}_{27}\text{H}_{31}\text{N}_2^+$, found 383.2481;

tert-butyl (3-(1-neopentyl-3-phenyl-1,2-dihydroquinoxalin-2-yl)prop-2-yn-1-yl)carbamate (4-59o)



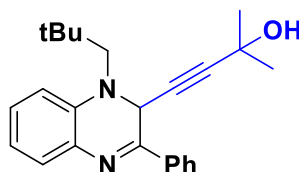
Yellow oil, 33.5 mg, 78% yield, obtained according to **Protocol A**.

$^1\text{H NMR}$ (500 MHz, Chloroform- d) δ 7.94 (dd, $J = 6.7, 3.0$ Hz, 2H), 7.44 – 7.36 (m, 4H), 7.08 (ddd, $J = 8.5, 7.3, 1.6$ Hz, 1H), 6.83 (d, $J = 8.2$ Hz, 1H), 6.80 – 6.72 (m, 1H), 5.17 (t, $J = 2.0$ Hz, 1H), 4.41 (s, 1H), 3.70 (s, 1.5H), 3.49 (d, $J = 15.1$ Hz, 1H), 2.89 (d, $J = 15.2$ Hz, 1H), 2.69 (s, 0.5H), 1.31 (s, 9H), 0.87 (s, 9H).

$^{13}\text{C NMR}$ (126 MHz, Chloroform- d) δ 155.1, 152.7, 137.5, 135.9, 134.7, 130.5, 128.7, 128.6, 128.4, 126.8, 118.4, 112.5, 81.0, 79.9, 78.3, 58.3, 49.6, 46.0, 34.3, 30.7, 28.3, 27.8.

HRMS (ESI+) (m/z): $[\text{M}+\text{H}]^+$ 432.2646 calcd for $\text{C}_{27}\text{H}_{34}\text{N}_3\text{O}_2^+$, found 432.2642;

2-methyl-4-(1-neopentyl-3-phenyl-1,2-dihydroquinoxalin-2-yl)but-3-yn-2-ol (4-59p)



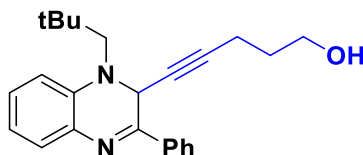
Yellow oil, 31.4 mg, 87% yield, obtained according to **Protocol A**.

$^1\text{H NMR}$ (500 MHz, Chloroform- d) δ 7.97 – 7.90 (m, 2H), 7.44 – 7.35 (m, 4H), 7.10 – 7.03 (m, 1H), 6.82 (d, $J = 8.2$ Hz, 1H), 6.75 (td, $J = 7.5, 1.2$ Hz, 1H), 5.15 (s, 1H), 3.47 (d, $J = 15.1$ Hz, 1H), 2.89 (d, $J = 15.2$ Hz, 1H), 1.80 (s, 1H), 1.24 (d, $J = 2.7$ Hz, 6H), 0.87 (s, 9H).

$^{13}\text{C NMR}$ (126 MHz, Chloroform- d) δ 152.8, 137.5, 136.0, 134.8, 130.5, 128.7, 128.5, 128.3, 126.8, 118.3, 112.5, 89.8, 77.2, 65.1, 58.3, 49.7, 34.3, 31.3, 31.2, 27.8.

HRMS (ESI+) (m/z): $[\text{M}+\text{H}]^+$ 361.2274 calcd for $\text{C}_{24}\text{H}_{29}\text{N}_2\text{O}^+$, found 361.2270;

5-(1-neopentyl-3-phenyl-1,2-dihydroquinoxalin-2-yl)pent-4-yn-1-ol (4-59q)



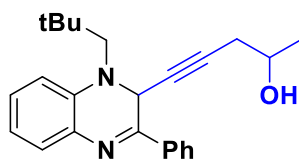
Yellow oil, 29.9 mg, 83% yield, obtained according to **Protocol A**.

$^1\text{H NMR}$ (500 MHz, Chloroform- d) δ 7.98 – 7.90 (m, 2H), 7.39 (ddd, $J = 5.0, 2.9, 1.3$ Hz, 4H), 7.07 (ddd, $J = 8.1, 7.3, 1.6$ Hz, 1H), 6.83 (d, $J = 8.2$ Hz, 1H), 6.76 (td, $J = 7.4, 1.2$ Hz, 1H), 5.07 (t, $J = 2.1$ Hz, 1H), 3.48 (d, $J = 15.1$ Hz, 1H), 3.39 (t, $J = 6.2$ Hz, 2H), 2.89 (d, $J = 15.1$ Hz, 1H), 2.06 (td, $J = 6.9, 2.0$ Hz, 2H), 1.47 (p, $J = 6.6$ Hz, 2H), 1.26 (s, 1H), 0.87 (s, 9H).

$^{13}\text{C NMR}$ (126 MHz, Chloroform- d) δ 153.7, 137.8, 136.1, 134.9, 130.5, 128.7, 128.4, 128.2, 126.8, 118.2, 112.5, 85.1, 76.0, 61.4, 58.3, 49.9, 34.3, 30.9, 27.8, 15.3.

HRMS (ESI+) (m/z): $[\text{M}+\text{H}]^+$ 361.2274 calcd for $\text{C}_{24}\text{H}_{29}\text{N}_2\text{O}^+$, found 361.2268;

5-(1-neopentyl-3-phenyl-1,2-dihydroquinoxalin-2-yl)pent-4-yn-2-ol (4-59r)



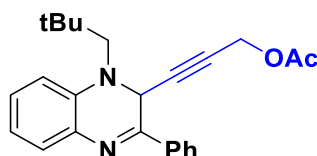
Yellow oil, 30.3 mg, 84% yield, obtained according to **Protocol A**.

¹H NMR (500 MHz, Chloroform-*d*) δ 7.98 – 7.90 (m, 2H), 7.44 – 7.35 (m, 4H), 7.08 (ddd, J = 8.5, 7.4, 1.6 Hz, 1H), 6.84 (d, J = 8.2 Hz, 1H), 6.81 – 6.75 (m, 1H), 3.63 (ddd, J = 11.7, 6.5, 5.4 Hz, 1H), 3.49 (d, J = 15.1 Hz, 1H), 2.89 (d, J = 15.1 Hz, 1H), 2.15 (dtd, J = 16.7, 5.0, 1.9 Hz, 1H), 2.07 (dtd, J = 16.7, 6.4, 1.8 Hz, 1H), 1.53 (s, 1H), 0.94 (t, J = 6.0 Hz, 3H), 0.87 (s, 9H).

¹³C NMR (126 MHz, Chloroform-*d*) δ 153.8, 153.7, 137.7, 137.7, 135.9, 135.0, 135.0, 130.5, 128.7, 128.4, 128.4, 126.8, 118.5, 112.5, 112.5, 82.3, 78.0, 66.1, 58.4, 49.9, 49.9, 34.3, 29.3, 29.2, 27.7, 22.0.

HRMS (ESI+) (m/z): $[M+H]^+$ 361.2274 calcd for $C_{24}H_{29}N_2O^+$, found 361.2273;

3-(1-neopentyl-3-phenyl-1,2-dihydroquinoxalin-2-yl)prop-2-yn-1-yl acetate (4-59s)



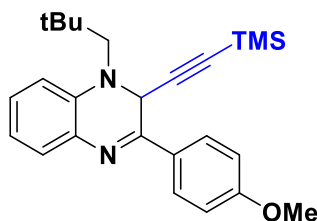
Yellow oil, 32.9 mg, 88% yield, obtained according to **Protocol A**.

¹H NMR (500 MHz, Chloroform-*d*) δ 7.98 – 7.90 (m, 2H), 7.40 (td, J = 5.2, 1.8 Hz, 4H), 7.08 (ddd, J = 8.6, 7.3, 1.6 Hz, 1H), 6.84 (d, J = 8.2 Hz, 1H), 6.78 (td, J = 7.5, 1.2 Hz, 1H), 5.22 (d, J = 1.9 Hz, 1H), 4.49 – 4.39 (m, 2H), 3.52 (d, J = 15.2 Hz, 1H), 2.90 (d, J = 15.2 Hz, 1H), 1.93 (s, 3H), 0.87 (s, 9H).

¹³C NMR (126 MHz, Chloroform-*d*) δ 170.1, 152.3, 137.4, 135.9, 134.7, 130.6, 128.7, 128.6, 128.4, 126.8, 118.5, 112.5, 82.0, 78.8, 58.3, 52.3, 49.7, 34.4, 27.8, 20.7.

HRMS (ESI+) (m/z): $[M+H]^+$ 375.2067 calcd for $C_{24}H_{27}N_2O_2^+$, found 375.2060;

3-(4-methoxyphenyl)-1-neopentyl-2-((trimethylsilyl)ethynyl)-1,2-dihydroquinoxaline (4-59t)



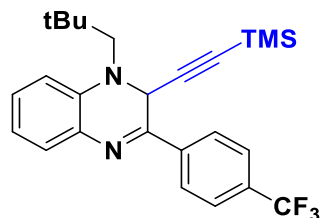
Yellow oil, 34.0 mg, 84% yield, obtained according to **Protocol A**.

¹H NMR (500 MHz, Chloroform-*d*) δ 8.01 – 7.94 (m, 2H), 7.42 (dd, J = 7.7, 1.6 Hz, 1H), 7.11 (td, J = 7.8, 1.6 Hz, 1H), 7.01 – 6.94 (m, 2H), 6.88 (d, J = 8.2 Hz, 1H), 6.81 (td, J = 7.5, 1.1 Hz, 1H), 5.17 (s, 1H), 3.86 (s, 3H), 3.54 (d, J = 15.2 Hz, 1H), 2.97 (d, J = 15.2 Hz, 1H), 0.94 (s, 9H), 0.00 (s, 9H).

^{13}C NMR (126 MHz, Chloroform- d) δ 161.7, 152.7, 137.6, 135.1, 129.1, 128.7, 128.2, 127.9, 118.3, 114.2, 112.6, 100.9, 90.4, 58.4, 55.6, 50.7, 34.5, 28.0, -0.0.

HRMS (ESI+) (m/z): $[\text{M}+\text{H}]^+$ 405.2357 calcd for $\text{C}_{25}\text{H}_{33}\text{N}_2\text{OSi}^+$, found 405.2351;

1-neopentyl-3-(4-(trifluoromethyl)phenyl)-2-((trimethylsilyl)ethynyl)-1,2-dihydroquinoxaline (4-59u)



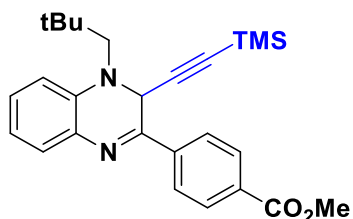
Orange oil, 41.6 mg, 94% yield, obtained according to **Protocol A**.

^1H NMR (500 MHz, Chloroform- d) δ 8.11 (d, $J = 8.2$ Hz, 2H), 7.71 (d, $J = 8.2$ Hz, 2H), 7.44 (dd, $J = 7.7, 1.6$ Hz, 1H), 7.15 (ddd, $J = 8.4, 7.3, 1.6$ Hz, 1H), 6.89 (d, $J = 8.2$ Hz, 1H), 6.83 (td, $J = 7.5, 1.2$ Hz, 1H), 5.17 (s, 1H), 3.55 (d, $J = 15.2$ Hz, 1H), 2.97 (d, $J = 15.2$ Hz, 1H), 0.93 (s, 9H), 0.00 (d, $J = 0.9$ Hz, 9H).

^{13}C NMR (126 MHz, Chloroform- d) δ 151.3, 139.5, 137.8, 134.8, 132.1 (q, $J = 32.5$ Hz), 129.2, 129.1, 127.3, 125.8 (q, $J = 3.8$ Hz), 124.3 (q, $J = 272.3$ Hz), 118.7, 112.9, 100.2, 91.2, 58.5, 50.7, 34.6, 28.0, 0.0.

HRMS (ESI+) (m/z): $[\text{M}+\text{H}]^+$ 443.2125 calcd for $\text{C}_{25}\text{H}_{30}\text{F}_3\text{N}_2\text{Si}^+$, found 443.2130;

methyl 4-(4-neopentyl-3-((trimethylsilyl)ethynyl)-3,4-dihydroquinoxalin-2-yl)benzoate (4-59v)



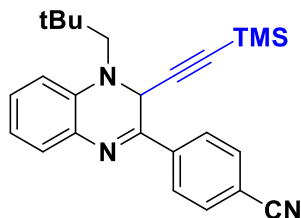
Orange oil, 41.5 mg, 96% yield, obtained according to **Protocol A**.

^1H NMR (500 MHz, Chloroform- d) δ 8.12 (d, $J = 8.3$ Hz, 2H), 8.07 (d, $J = 8.5$ Hz, 2H), 7.45 (dd, $J = 7.7, 1.6$ Hz, 1H), 7.15 (ddd, $J = 8.6, 7.3, 1.6$ Hz, 1H), 6.89 (d, $J = 8.2$ Hz, 1H), 6.86 – 6.80 (m, 1H), 5.20 (s, 1H), 3.94 (s, 3H), 3.55 (d, $J = 15.2$ Hz, 1H), 2.98 (d, $J = 15.2$ Hz, 1H), 0.94 (s, 9H), 0.00 (s, 9H).

^{13}C NMR (126 MHz, Chloroform- d) δ 167.0, 151.7, 140.2, 137.8, 134.9, 131.6, 130.1, 129.1, 129.1, 127.0, 118.6, 112.9, 100.4, 91.1, 58.5, 52.5, 50.7, 34.6, 28.0, 0.0.

HRMS (ESI+) (m/z): $[\text{M}+\text{H}]^+$ 433.2306 calcd for $\text{C}_{26}\text{H}_{33}\text{N}_2\text{O}_2\text{Si}^+$, found 433.2302;

4-(4-neopentyl-3-((trimethylsilyl)ethynyl)-3,4-dihydroquinoxalin-2-yl)benzotrile (4-59w)



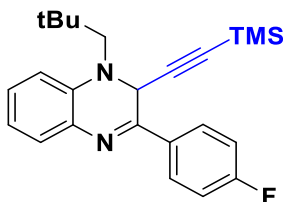
Orange solid, 32.8 mg, 82% yield, obtained according to **Protocol A**.

$^1\text{H NMR}$ (500 MHz, Chloroform- d) δ 8.10 (d, $J = 7.8$ Hz, 2H), 7.74 (d, $J = 8.0$ Hz, 2H), 7.43 (d, $J = 7.7$ Hz, 1H), 7.17 (t, $J = 7.9$ Hz, 1H), 6.91 – 6.80 (m, 2H), 5.15 (s, 1H), 3.55 (d, $J = 15.2$ Hz, 1H), 2.97 (d, $J = 15.3$ Hz, 1H), 0.93 (s, 9H), 0.00 (s, 9H).

$^{13}\text{C NMR}$ (126 MHz, Chloroform- d) δ 150.5, 140.2, 137.8, 134.7, 132.7, 129.6, 129.3, 127.5, 118.9, 118.8, 113.7, 113.0, 100.0, 91.5, 58.5, 50.6, 34.6, 28.0, 0.0.

HRMS (ESI+) (m/z): $[\text{M}+\text{H}]^+$ 400.2204 calcd for $\text{C}_{25}\text{H}_{30}\text{N}_3\text{Si}^+$, found 400.2205;

3-(4-fluorophenyl)-1-neopentyl-2-((trimethylsilyl)ethynyl)-1,2-dihydroquinoxaline (4-59x)



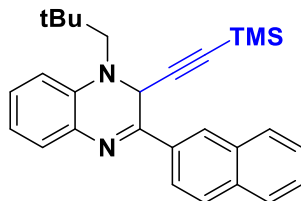
Yellow oil, 34.1 mg, 87% yield, obtained according to **Protocol A**.

$^1\text{H NMR}$ (500 MHz, Chloroform- d) δ 8.05 – 7.97 (m, 2H), 7.42 (dd, $J = 7.7, 1.6$ Hz, 1H), 7.18 – 7.09 (m, 3H), 6.88 (d, $J = 8.2$ Hz, 1H), 6.85 – 6.79 (m, 1H), 5.15 (s, 1H), 3.54 (d, $J = 15.2$ Hz, 1H), 2.96 (d, $J = 15.3$ Hz, 1H), 0.93 (s, 9H), 0.00 (s, 9H).

$^{13}\text{C NMR}$ (126 MHz, Chloroform- d) δ 164.42 (d, $J = 251.2$ Hz), 151.9, 137.6, 134.9, 132.6 (d, $J = 3.1$ Hz), 129.1 (d, $J = 8.6$ Hz), 128.5 (d, $J = 12.2$ Hz), 118.5, 116.0, 115.8, 112.7, 100.5, 90.9, 58.5, 50.8, 34.6, 28.0, -0.0.

HRMS (ESI+) (m/z): $[\text{M}+\text{H}]^+$ 393.2157 calcd for $\text{C}_{24}\text{H}_{30}\text{FN}_2\text{Si}^+$, found 393.2162;

3-(naphthalen-2-yl)-1-neopentyl-2-((trimethylsilyl)ethynyl)-1,2-dihydroquinoxaline (4-59y)



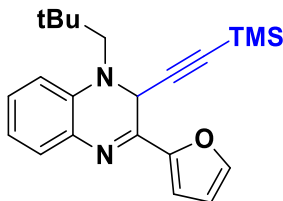
Yellow solid, 39.1 mg, 92% yield, obtained according to **Protocol A**.

$^1\text{H NMR}$ (500 MHz, Chloroform- d) δ 8.31 (d, $J = 7.9$ Hz, 2H), 7.97 – 7.83 (m, 3H), 7.57 – 7.47 (m, 3H), 7.15 (ddd, $J = 8.5, 7.3, 1.6$ Hz, 1H), 6.84 (td, $J = 7.5, 1.2$ Hz, 1H), 5.36 (s, 1H), 3.58 (d, $J = 15.2$ Hz, 1H), 3.03 (d, $J = 15.2$ Hz, 1H), 0.95 (s, 9H), 0.00 (s, 9H).

^{13}C NMR (126 MHz, Chloroform- d) δ 152.8, 137.8, 135.1, 134.6, 133.8, 133.3, 129.1, 128.7, 128.5, 128.5, 128.0, 127.4, 127.1, 126.7, 124.3, 118.5, 112.7, 100.9, 90.8, 58.5, 50.8, 34.6, 28.0, 0.0.

HRMS (ESI+) (m/z): $[\text{M}+\text{H}]^+$ 425.2408 calcd for $\text{C}_{28}\text{H}_{33}\text{N}_2\text{Si}^+$, found 425.2414;

3-(furan-2-yl)-1-neopentyl-2-((trimethylsilyl)ethynyl)-1,2-dihydroquinoxaline (4-59za)



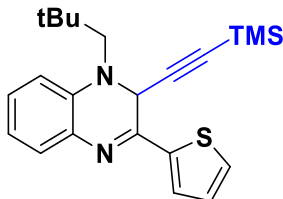
Brown oil, 13.1 mg, 36% yield, obtained according to **Protocol A**.

^1H NMR (500 MHz, Chloroform- d) δ 7.62 (d, $J = 1.8$ Hz, 1H), 7.45 (dd, $J = 7.7, 1.6$ Hz, 1H), 7.12 (ddd, $J = 8.6, 7.3, 1.6$ Hz, 1H), 6.97 (d, $J = 3.5$ Hz, 1H), 6.87 (d, $J = 8.2$ Hz, 1H), 6.82 (td, $J = 7.5, 1.2$ Hz, 1H), 6.56 (dd, $J = 3.6, 1.8$ Hz, 1H), 5.06 (s, 1H), 3.54 (d, $J = 15.1$ Hz, 1H), 2.95 (d, $J = 15.2$ Hz, 1H), 0.95 (s, 9H), 0.00 (s, 9H).

^{13}C NMR (126 MHz, Chloroform- d) δ 151.0, 145.4, 144.3, 137.9, 134.9, 128.5, 128.3, 118.6, 113.1, 112.8, 112.4, 100.3, 90.3, 58.4, 50.0, 34.6, 28.0, 0.0.

HRMS (ESI+) (m/z): $[\text{M}+\text{H}]^+$ 365.2044 calcd for $\text{C}_{22}\text{H}_{29}\text{N}_2\text{OSi}^+$, found 365.2036;

1-neopentyl-3-(thiophen-2-yl)-2-((trimethylsilyl)ethynyl)-1,2-dihydroquinoxaline (4-59zb)



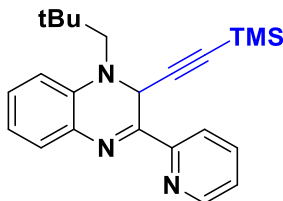
Yellow oil, 16.7 mg, 44% yield, obtained according to **Protocol A**.

^1H NMR (500 MHz, Chloroform- d) δ 7.49 – 7.47 (m, 1H), 7.44 (d, $J = 3.7$ Hz, 1H), 7.39 (dd, $J = 7.7, 1.6$ Hz, 1H), 7.14 – 7.07 (m, 2H), 6.86 (d, $J = 8.2$ Hz, 1H), 6.84 – 6.77 (m, 1H), 5.15 (s, 1H), 3.53 (d, $J = 15.2$ Hz, 1H), 2.94 (s, 0H), 0.95 (s, 9H), 0.00 (s, 9H).

^{13}C NMR (126 MHz, Chloroform- d) δ 148.4, 142.9, 137.8, 134.8, 130.1, 128.3, 128.1, 128.0, 127.7, 118.5, 112.7, 100.3, 90.6, 58.4, 51.2, 34.6, 28.0, 0.0.

HRMS (ESI+) (m/z): $[\text{M}+\text{H}]^+$ 381.1815 calcd for $\text{C}_{22}\text{H}_{29}\text{N}_2\text{SSi}^+$, found 381.1807;

1-neopentyl-3-(pyridin-2-yl)-2-((trimethylsilyl)ethynyl)-1,2-dihydroquinoxaline (4-59aa)



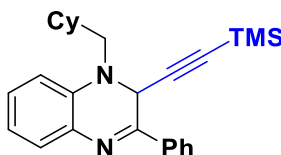
Yellow oil, 20.2 mg, 54% yield, obtained according to **Protocol A** (with adding ligand **L3**)

¹H NMR (500 MHz, Chloroform-*d*) δ 8.70 (dd, *J* = 4.9, 1.6 Hz, 1H), 8.47 (d, *J* = 8.0 Hz, 1H), 7.83 (td, *J* = 7.7, 1.7 Hz, 1H), 7.49 (dd, *J* = 7.7, 1.6 Hz, 1H), 7.36 (ddd, *J* = 7.3, 4.9, 1.3 Hz, 1H), 7.19 (ddd, *J* = 8.5, 7.3, 1.6 Hz, 1H), 6.94 (d, *J* = 8.2 Hz, 1H), 6.85 (td, *J* = 7.5, 1.2 Hz, 1H), 6.03 (s, 1H), 3.58 (d, *J* = 15.1 Hz, 1H), 3.09 (d, *J* = 15.1 Hz, 1H), 0.98 (s, 9H), 0.00 (s, 9H).

¹³C NMR (126 MHz, Chloroform-*d*) δ 153.5, 153.4, 149.1, 138.9, 136.5, 134.9, 128.9, 128.7, 124.6, 122.1, 118.1, 112.9, 101.3, 89.2, 58.3, 48.1, 34.3, 27.9, 0.0.

HRMS (ESI+) (*m/z*): [M+H]⁺ 376.2204 calcd for C₂₃H₃₀N₃Si⁺, found 376.2198;

1-(cyclohexylmethyl)-3-phenyl-2-((trimethylsilyl)ethynyl)-1,2-dihydroquinoxaline (4-59ab)



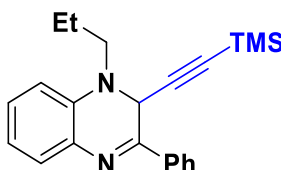
Yellow oil, 26.8 mg, 67% yield, obtained according to **Protocol B**.

¹H NMR (500 MHz, CD₂Cl₂) δ 8.04 – 7.98 (m, 2H), 7.48 – 7.42 (m, 3H), 7.35 (dd, *J* = 7.7, 1.6 Hz, 1H), 7.13 (ddd, *J* = 8.7, 7.5, 1.6 Hz, 1H), 6.79 (td, *J* = 7.5, 1.2 Hz, 1H), 6.75 (d, *J* = 8.1 Hz, 1H), 5.23 (s, 1H), 3.32 (dd, *J* = 14.2, 5.7 Hz, 1H), 3.00 (dd, *J* = 14.2, 8.1 Hz, 1H), 1.86 – 1.59 (m, 6H), 1.22 – 1.10 (m, 2H), 0.99 – 0.87 (m, 2H), 0.00 (s, 9H).

¹³C NMR (126 MHz, CD₂Cl₂) δ 154.0, 138.5, 137.5, 135.9, 131.9, 130.0, 129.7, 128.3, 119.7, 113.6, 101.8, 92.0, 56.5, 50.4, 37.5, 33.0, 32.4, 28.1, 27.5, 27.5, 0.9.

HRMS (ESI+) (*m/z*): [M+H]⁺ 401.2408 calcd for C₂₆H₃₃N₂Si⁺, found 401.2404;

3-phenyl-1-propyl-2-((trimethylsilyl)ethynyl)-1,2-dihydroquinoxaline (4-59ac)



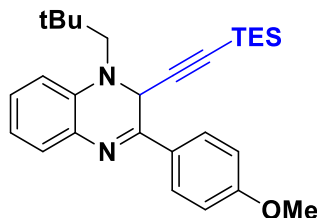
Yellow oil, 17.3 mg, 50% yield, obtained according to **Protocol B**.

¹H NMR (500 MHz, CD₂Cl₂) δ 8.06 – 7.98 (m, 2H), 7.46 (p, *J* = 3.5 Hz, 3H), 7.36 (dd, *J* = 7.6, 1.6 Hz, 1H), 7.15 (td, *J* = 7.7, 1.6 Hz, 1H), 6.85 – 6.79 (m, 1H), 6.77 (d, *J* = 8.1 Hz, 1H), 5.29 (s, 1H), 3.36 (dt, *J* = 14.5, 7.4 Hz, 1H), 3.24 (dt, *J* = 14.4, 7.6 Hz, 1H), 1.78 (hept, *J* = 7.1 Hz, 2H), 0.95 (t, *J* = 7.4 Hz, 3H), 0.00 (d, *J* = 0.8 Hz, 9H).

¹³C NMR (126 MHz, CD₂Cl₂) δ 154.4, 138.3, 137.5, 136.0, 132.0, 130.1, 130.1, 129.7, 128.4, 119.9, 113.6, 102.1, 92.3, 52.1, 49.4, 31.2, 21.7, 12.9, 0.9.

HRMS (ESI+) (*m/z*): [M+H]⁺ 347.1938 calcd for C₂₂H₂₇N₂Si⁺, found 347.1934;

3-(4-methoxyphenyl)-1-neopentyl-2-((triethylsilyl)ethynyl)-1,2-dihydroquinoxaline (4-59ad)



Yellow oil, 25.4 mg, 57% yield, 87:13 e.r., obtained according to **Protocol B**.

$^1\text{H NMR}$ (500 MHz, Chloroform- d) δ 8.01 – 7.94 (m, 2H), 7.41 (dd, $J = 7.7, 1.6$ Hz, 1H), 7.10 (ddd, $J = 8.5, 7.3, 1.6$ Hz, 1H), 7.01 – 6.95 (m, 2H), 6.88 (d, $J = 8.2$ Hz, 1H), 6.81 (td, $J = 7.5, 1.1$ Hz, 1H), 5.12 (s, 1H), 3.87 (s, 3H), 3.53 (d, $J = 15.1$ Hz, 1H), 2.97 (d, $J = 15.2$ Hz, 1H), 0.94 (s, 9H), 0.77 (t, $J = 7.9$ Hz, 9H), 0.41 (q, $J = 7.9$ Hz, 6H).

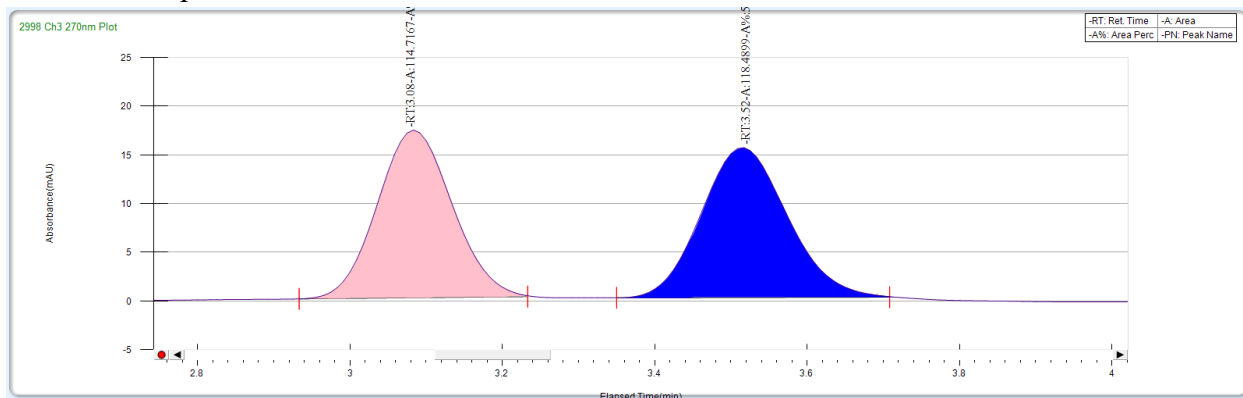
$^{13}\text{C NMR}$ (126 MHz, Chloroform- d) δ 161.5, 153.0, 137.5, 135.2, 129.0, 128.5, 127.9, 127.6, 118.3, 114.0, 112.4, 102.1, 87.9, 58.4, 55.4, 50.7, 34.2, 27.8, 7.2, 4.2.

HRMS (ESI+) (m/z): $[\text{M}+\text{H}]^+$ 447.2826 calcd for $\text{C}_{28}\text{H}_{39}\text{N}_2\text{OSi}^+$, found 447.2830;

$[\alpha]^{24}_{\text{D}}$ = +244.25 ($c = 0.012$ g/mL, CH_2Cl_2);

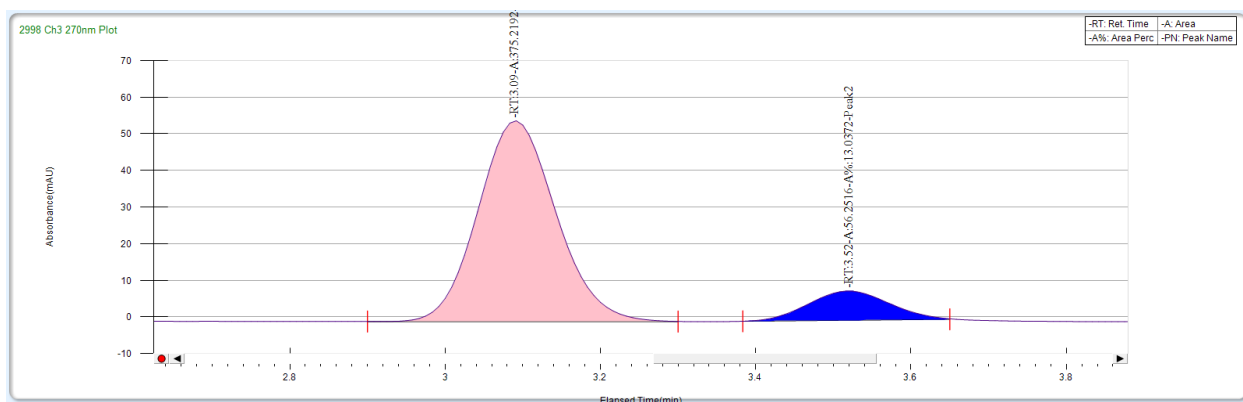
SFC (Chiralpak ODH column, 90:10 carbon dioxide/methanol, 3.5 mL/min, $I = 270$ nm): $t_r = 3.1$ min (major), 3.5 min (minor).

Racemic compound SFC traces



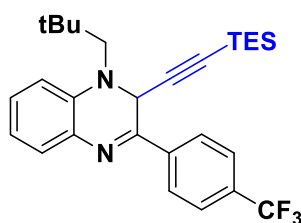
Peak Name	Area Percent	Area	Retention Time	Height
Peak1	49.191	114.7167	3.08 min	17.2245
Peak2	50.809	118.4899	3.52 min	15.3903

Chiral compound SFC traces



Peak Name	Area Percent	Area	Retention Time	Height
Peak1	86.9628	375.2192	3.09 min	54.8447
Peak2	13.0372	56.2516	3.52 min	7.9969

1-neopentyl-2-((triethylsilyl)ethynyl)-3-(4-(trifluoromethyl)phenyl)-1,2-dihydroquinoxaline (4-59ae)



Yellow oil, 28.5 mg, 59% yield, 92.5:7.5 e.r., obtained according to **Protocol B**.

¹H NMR (500 MHz, Chloroform-d) δ 8.12 (d, *J* = 8.1 Hz, 2H), 7.72 (d, *J* = 8.2 Hz, 2H), 7.45 (dd, *J* = 7.7, 1.6 Hz, 1H), 7.16 (ddd, *J* = 8.5, 7.3, 1.6 Hz, 1H), 6.90 (d, *J* = 8.2 Hz, 1H), 6.84 (td, *J* = 7.5, 1.2 Hz, 1H), 5.13 (s, 1H), 3.55 (d, *J* = 15.2 Hz, 1H), 2.99 (d, *J* = 15.5 Hz, 1H), 0.95 (s, 9H), 0.78 (t, *J* = 7.9 Hz, 9H), 0.42 (q, *J* = 8.0 Hz, 6H).

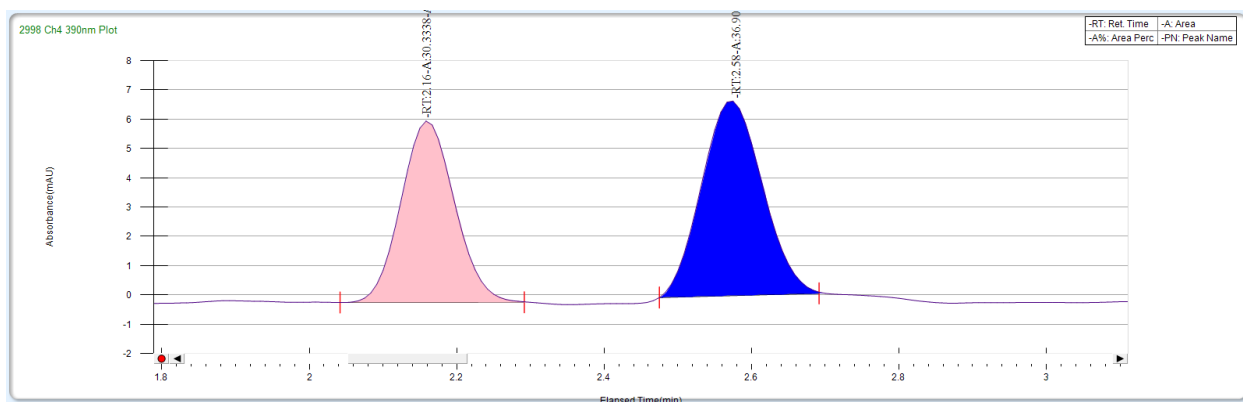
¹³C NMR (126 MHz, Chloroform-d) δ 151.5, 139.3, 139.3, 137.7, 134.8, 131.8 (q, *J* = 32.6 Hz), 128.9, 128.7, 127.0, 125.6 (q, *J* = 3.8 Hz), 123.9 (t, *J* = 273.2 Hz), 118.5, 112.7, 101.3, 88.7, 58.4, 50.7, 34.2, 27.7, 7.2, 4.2.

HRMS (ESI+) (*m/z*): [M+H]⁺ 485.2594 calcd for C₂₈H₃₆F₃N₂Si⁺, found 485.2591;

[α]²⁴_D = +333.41 (c = 0.011 g/mL, CH₂Cl₂);

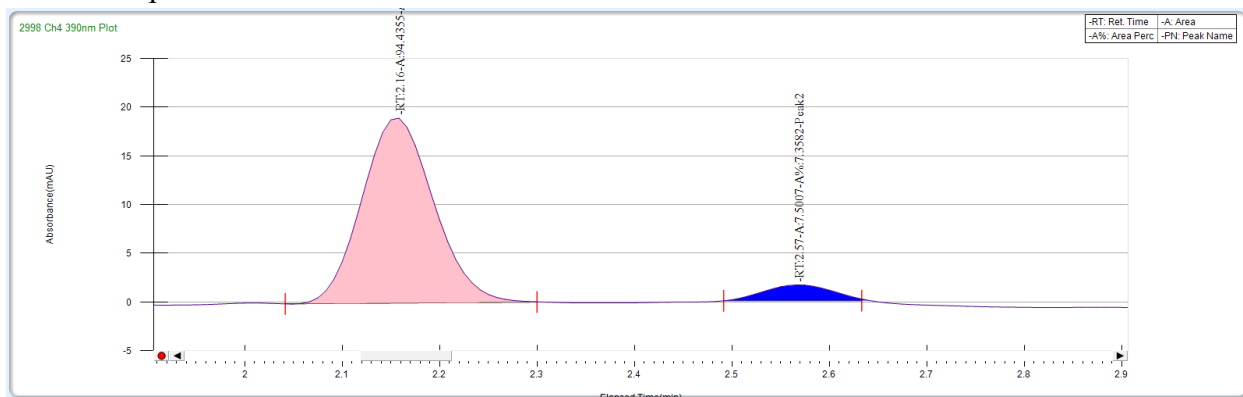
SFC (Chiralpak ODH column, 95:5 carbon dioxide/methanol, 3.5 mL/min, I = 270 nm): tr = 2.2 min (major), 2.6 min (minor).

Racemic compound SFC traces



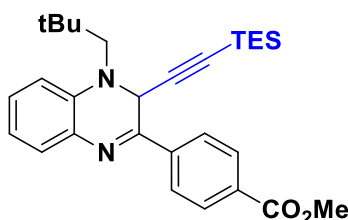
Peak Name	Area Percent	Area	Retention Time	Height
Peak1	45.1164	30.3338	2.16 min	6.1932
Peak2	54.8836	36.9007	2.58 min	6.6465

Chiral compound SFC traces



Peak Name	Area Percent	Area	Retention Time	Height
Peak1	92.6418	94.4355	2.16 min	18.9963
Peak2	7.3582	7.5007	2.57 min	1.6274

methyl 4-(4-neopentyl-3-((triethylsilyl)ethynyl)-3,4-dihydroquinoxalin-2-yl)benzoate (4-59af)



Yellow oil, 27.5 mg, 58% yield, 94.5:5.5 e.r., obtained according to **Protocol B**.

$^1\text{H NMR}$ (500 MHz, Chloroform- d) δ 8.13 (d, $J = 8.2$ Hz, 2H), 8.07 (d, $J = 8.6$ Hz, 2H), 7.45 (dd, $J = 7.8, 1.6$ Hz, 1H), 7.15 (ddd, $J = 8.6, 7.3, 1.6$ Hz, 1H), 6.89 (d, $J = 8.3$ Hz, 1H), 6.83 (td, $J = 7.5, 1.2$ Hz, 1H), 5.15 (s, 1H), 3.95 (s, 3H), 3.55 (d, $J = 15.2$ Hz, 1H), 2.99 (d, $J = 15.1$ Hz, 1H), 0.95 (s, 9H), 0.77 (t, $J = 7.9$ Hz, 9H), 0.41 (q, $J = 7.9$ Hz, 6H).

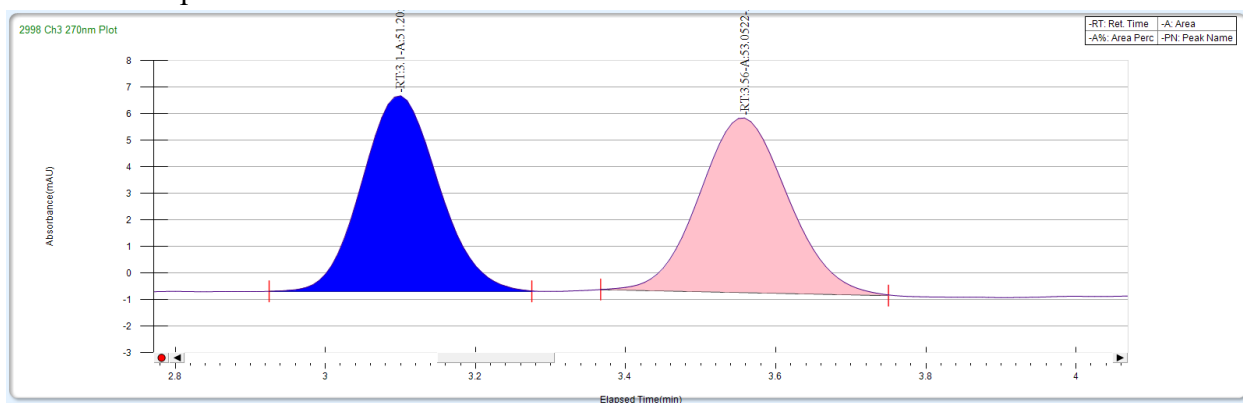
^{13}C NMR (126 MHz, Chloroform-d) δ 166.7, 152.0, 140.1, 137.7, 134.9, 131.4, 129.8, 128.8, 128.7, 126.7, 118.5, 112.6, 101.5, 88.6, 58.4, 52.3, 50.7, 34.2, 27.8, 7.2, 4.2.

HRMS (ESI+) (m/z): $[\text{M}+\text{H}]^+$ 475.2775 calcd for $\text{C}_{29}\text{H}_{39}\text{N}_2\text{O}_2\text{Si}^+$, found 475.2768;

$[\alpha]^{24}_{\text{D}} = +444.18$ ($c = 0.012$ g/mL, CH_2Cl_2);

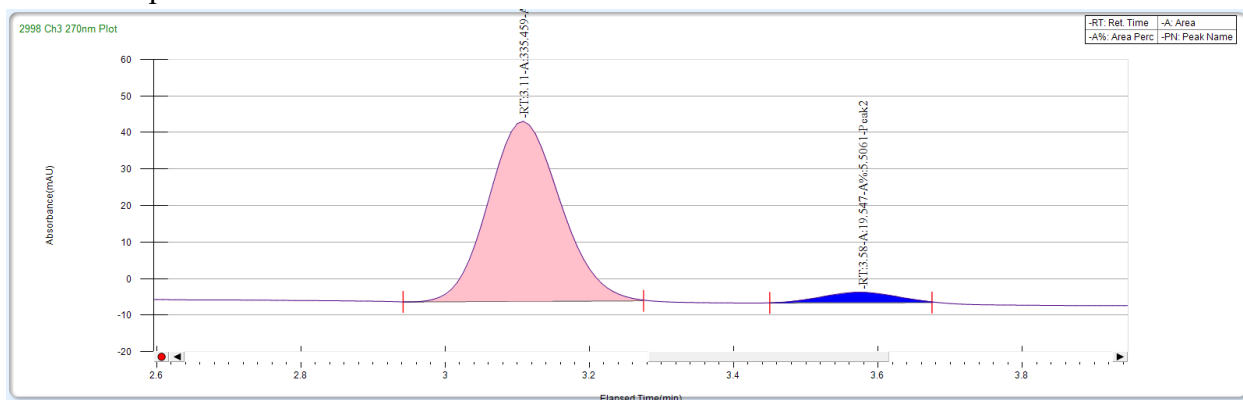
SFC (Chiralpak ODH column, 90:10 carbon dioxide/methanol, 3.5 mL/min, $I = 270$ nm): $t_r = 3.1$ min (major), 3.6 min (minor).

Racemic compound SFC traces



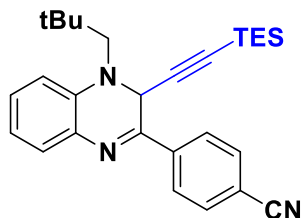
Peak Name	Area Percent	Area	Retention Time	Height
Peak1	49.1144	51.2056	3.1 min	7.3617
Peak2	50.8856	53.0522	3.56 min	6.5721

Chiral compound SFC traces



Peak Name	Area Percent	Area	Retention Time	Height
Peak1	94.4939	335.459	3.11 min	49.3102
Peak2	5.5061	19.547	3.58 min	2.8578

4-(4-neopentyl-3-((triethylsilyl)ethynyl)-3,4-dihydroquinoxalin-2-yl)benzotrile (4-59ag)



Yellow oil, 27.8 mg, 63% yield, 96:4 e.r., obtained according to **Protocol B**.

$^1\text{H NMR}$ (500 MHz, Chloroform- d) δ 8.04 (d, $J = 8.5$ Hz, 2H), 7.69 (d, $J = 8.5$ Hz, 2H), 7.37 (dd, $J = 7.8, 1.6$ Hz, 1H), 7.10 (ddd, $J = 8.6, 7.3, 1.6$ Hz, 1H), 6.83 (d, $J = 8.2$ Hz, 1H), 6.77 (td, $J = 7.5, 1.1$ Hz, 1H), 5.04 (s, 1H), 3.48 (d, $J = 15.1$ Hz, 1H), 2.91 (d, $J = 15.2$ Hz, 1H), 0.88 (s, 9H), 0.70 (t, $J = 7.9$ Hz, 8H), 0.35 (q, $J = 7.9$ Hz, 6H).

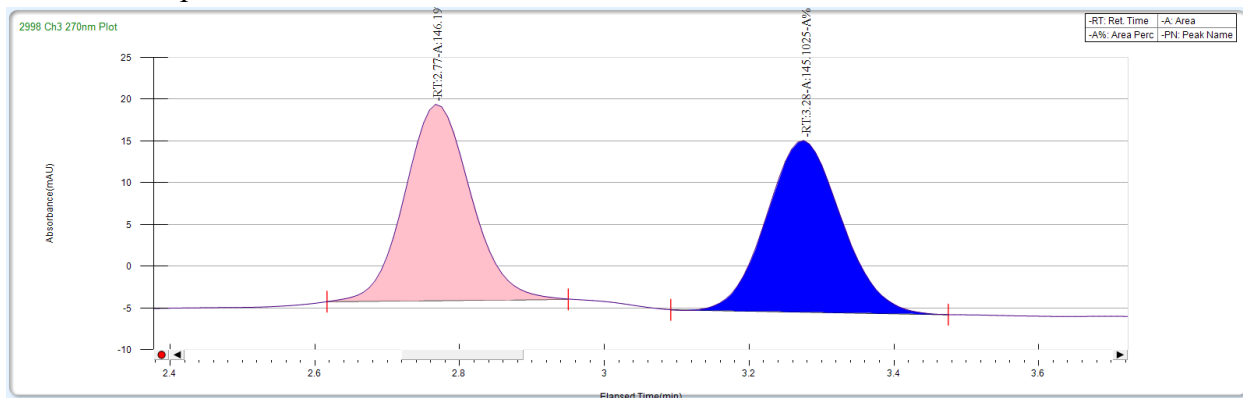
$^{13}\text{C NMR}$ (126 MHz, Chloroform- d) δ 150.8, 139.9, 137.7, 134.7, 132.4, 129.3, 128.9, 127.2, 118.7, 118.6, 113.4, 112.7, 101.1, 89.1, 58.4, 50.5, 34.3, 27.7, 7.2, 4.1.

HRMS (ESI+) (m/z): $[\text{M}+\text{H}]^+$ 442.2673 calcd for $\text{C}_{28}\text{H}_{36}\text{N}_3\text{Si}^+$, found 442.2681;

$[\alpha]^{24}_{\text{D}} = +585.73$ ($c = 0.011$ g/mL, CH_2Cl_2);

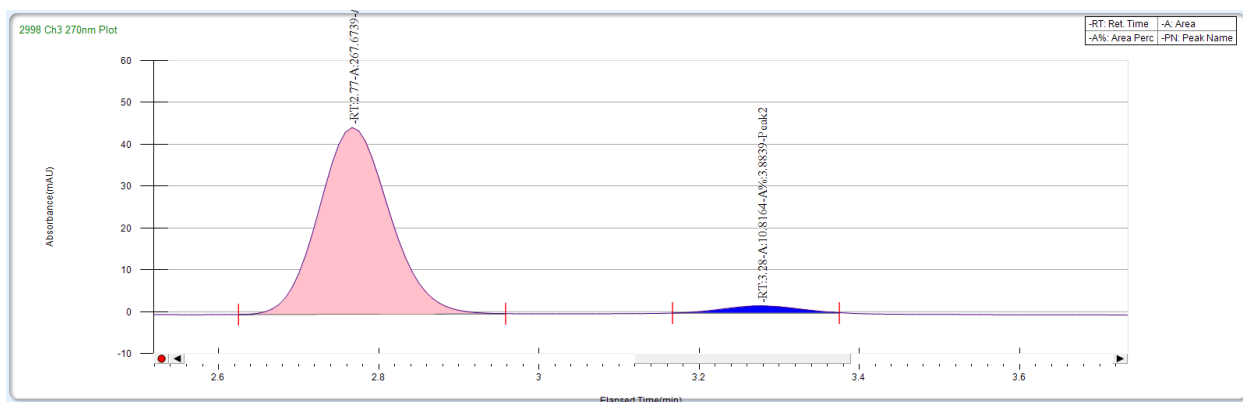
SFC (Chiralpak ODH column, 90:10 carbon dioxide/methanol, 3.5 mL/min, $I = 270$ nm): $t_r = 2.8$ min (major), 3.3 min (minor).

Racemic compound SFC traces



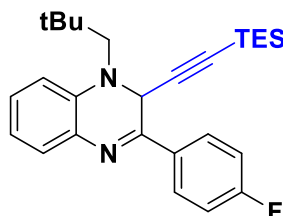
Peak Name	Area Percent	Area	Retention Time	Height
Peak1	50.1879	146.1973	2.77 min	23.5274
Peak2	49.8121	145.1025	3.28 min	20.5591

Chiral compound SFC traces



Peak Name	Area Percent	Area	Retention Time	Height
Peak1	96.1161	267.6739	2.77 min	44.6311
Peak2	3.8839	10.8164	3.28 min	1.7221

3-(4-fluorophenyl)-1-neopentyl-2-((triethylsilyl)ethynyl)-1,2-dihydroquinoxaline (4-59ah)



Yellow oil, 29.0 mg, 67% yield, 90:10 e.r., obtained according to **Protocol B**.

¹H NMR (500 MHz, Chloroform-d) δ 7.98 – 7.90 (m, 2H), 7.35 (dd, J = 7.7, 1.6 Hz, 1H), 7.13 – 6.99 (m, 3H), 6.81 (d, J = 8.2 Hz, 1H), 6.75 (td, J = 7.5, 1.2 Hz, 1H), 5.03 (s, 1H), 3.47 (d, J = 15.1 Hz, 1H), 2.90 (d, J = 15.2 Hz, 1H), 0.88 (s, 9H), 0.70 (t, J = 7.9 Hz, 9H), 0.34 (q, J = 7.9 Hz, 6H).

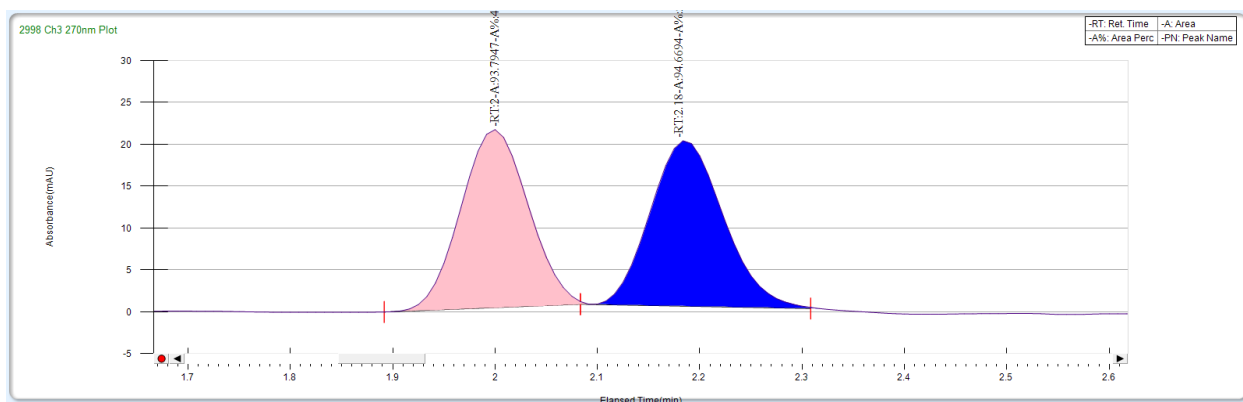
¹³C NMR (126 MHz, Chloroform-d) δ 164.2 (d, J = 251.1 Hz), 152.2, 137.5, 134.9, 132.5 (d, J = 3.1 Hz), 128.9 (d, J = 8.5 Hz), 128.2, 118.4, 115.66 (d, J = 21.8 Hz), 112.5, 101.7, 88.3, 58.4, 50.7, 34.2, 27.8, 7.2, 4.2.

HRMS (ESI+) (m/z): $[M+H]^+$ 435.2626 calcd for $C_{27}H_{36}FN_2Si^+$, found 435.2619;

$[\alpha]^{24}_D = +195.95$ (c = 0.013 g/mL, CH_2Cl_2);

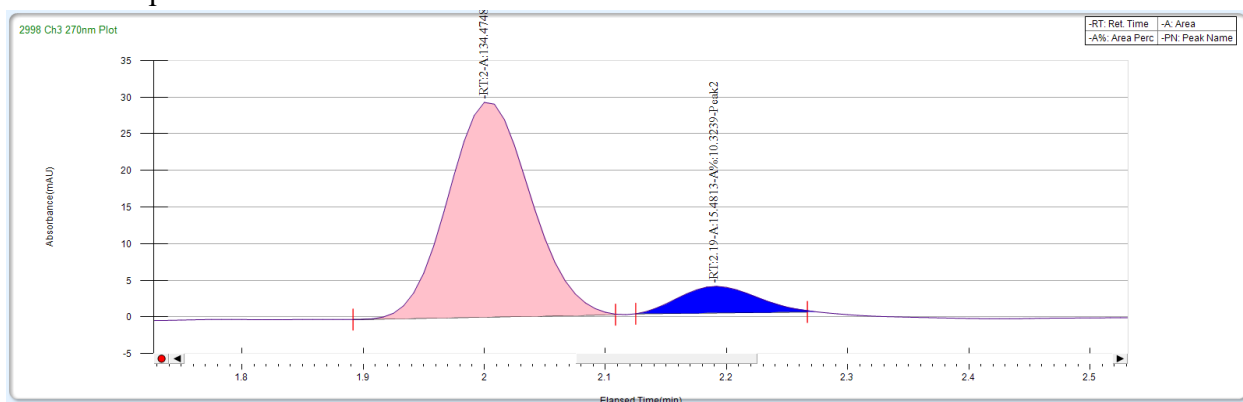
SFC (Chiralpak ODH column, 90:10 carbon dioxide/methanol, 3.5 mL/min, I = 270 nm): t_r = 2.0 min (major), 2.2 min (minor).

Racemic compound SFC traces



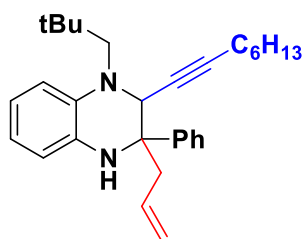
Peak Name	Area Percent	Area	Retention Time	Height
Peak1	49.768	93.7947	2 min	21.2976
Peak2	50.232	94.6694	2.18 min	19.7403

Chiral compound SFC traces



Peak Name	Area Percent	Area	Retention Time	Height
Peak1	89.6761	134.4748	2 min	29.3415
Peak2	10.3239	15.4813	2.19 min	3.6449

3-allyl-1-neopentyl-2-(oct-1-yn-1-yl)-3-phenyl-1,2,3,4-tetrahydroquinoxaline (4-69k)



Yellow oil, 30.9 mg, 72% yield, obtained according to **Protocol C**.

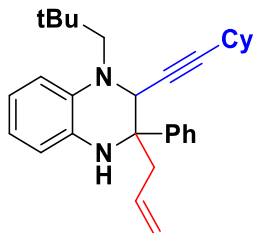
¹H NMR (500 MHz, Chloroform-d) δ 7.45 – 7.41 (m, 2H), 7.30 (t, *J* = 7.7 Hz, 2H), 7.22 – 7.19 (m, 1H), 6.65 (t, *J* = 3.5 Hz, 2H), 6.58 (dd, *J* = 3.8, 1.6 Hz, 2H), 5.38 – 5.26 (m, 1H), 4.90 (dd, *J* = 10.2, 2.2 Hz, 1H), 4.84 (dd, *J* = 17.3, 2.1 Hz, 1H), 4.05 (t, *J* = 2.1 Hz, 1H), 4.01 (s, 1H), 3.19 (d, *J* = 15.5 Hz, 1H), 2.97 (d, *J* = 15.5 Hz, 1H), 2.83 (dd, *J* = 13.5, 9.1 Hz, 1H), 2.73 (dd, *J* = 13.4, 5.7

Hz, 1H), 1.79 (td, $J = 6.9, 2.0$ Hz, 2H), 1.26 – 1.17 (m, 2H), 1.15 – 1.00 (m, 4H), 0.99 (s, 9H), 0.98 – 0.90 (m, 2H), 0.76 (t, $J = 7.3$ Hz, 3H).

^{13}C NMR (126 MHz, Chloroform- d) δ 142.2, 134.5, 133.3, 132.1, 128.1, 126.9, 126.2, 119.4, 118.9, 118.3, 115.9, 113.1, 85.1, 76.9, 61.3, 60.7, 58.8, 41.4, 34.3, 31.3, 31.3, 28.5, 28.5, 28.1, 22.5, 18.6, 14.1.

HRMS (ESI+) (m/z): $[\text{M}+\text{H}]^+$ 429.3264 calcd for $\text{C}_{30}\text{H}_{41}\text{N}_2^+$, found 429.3257;

3-allyl-2-(cyclohexylethynyl)-1-neopentyl-3-phenyl-1,2,3,4-tetrahydroquinoxaline (4-69m)



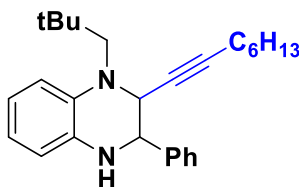
Yellow oil, 27.2 mg, 64% yield, obtained according to **Protocol C**.

^1H NMR (500 MHz, Chloroform- d) δ 7.55 – 7.48 (m, 2H), 7.36 (t, $J = 7.7$ Hz, 2H), 7.26 (t, 1H), 6.75 – 6.69 (m, 2H), 6.67 – 6.62 (m, 2H), 5.42 (dtd, $J = 16.1, 9.6, 5.7$ Hz, 1H), 4.97 (dd, $J = 10.2, 2.2$ Hz, 1H), 4.93 (d, $J = 17.3$ Hz, 1H), 4.11 (s, 1H), 4.10 (d, $J = 2.1$ Hz, 1H), 3.25 (d, $J = 15.4$ Hz, 1H), 3.03 (d, $J = 15.5$ Hz, 1H), 2.90 (dd, $J = 13.5, 9.1$ Hz, 1H), 2.81 (dd, $J = 13.6, 5.7$ Hz, 1H), 2.13 – 2.06 (m, 1H), 1.45 – 1.37 (m, 2H), 1.35 – 1.23 (m, 4H), 1.18 – 1.07 (m, 4H), 1.05 (s, 9H).

^{13}C NMR (126 MHz, Chloroform- d) δ 142.2, 134.5, 133.3, 132.3, 128.0, 126.9, 126.4, 119.5, 118.7, 118.2, 115.7, 113.1, 89.1, 77.2, 61.3, 60.8, 58.9, 41.4, 34.3, 32.3, 32.3, 29.7, 28.5, 25.9, 24.2.

HRMS (ESI+) (m/z): $[\text{M}+\text{H}]^+$ 427.3108 calcd for $\text{C}_{30}\text{H}_{39}\text{N}_2^+$, found 427.2998;

1-neopentyl-2-(oct-1-yn-1-yl)-3-phenyl-1,2,3,4-tetrahydroquinoxaline (4-69k)



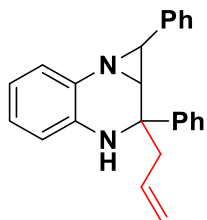
Yellow oil, 32.6 mg, 84% yield, obtained according to **Protocol D**.

^1H NMR (500 MHz, Chloroform- d) δ 7.45 (d, $J = 7.4$ Hz, 2H), 7.27 (dt, $J = 23.2, 7.3$ Hz, 3H), 6.68 – 6.59 (m, 2H), 6.54 (q, $J = 4.9$ Hz, 2H), 4.66 (d, $J = 2.8$ Hz, 1H), 4.04 (q, $J = 2.4$ Hz, 1H), 3.81 (s, 1H), 3.14 (d, $J = 15.3$ Hz, 1H), 2.91 (d, $J = 15.3$ Hz, 1H), 1.99 – 1.94 (m, 2H), 1.29 – 1.23 (m, 2H), 1.19 – 1.06 (m, 8H), 0.94 (s, 9H), 0.78 (t, $J = 7.1$ Hz, 3H).

^{13}C NMR (126 MHz, Chloroform- d) δ 139.9, 134.8, 133.9, 128.2, 128.1, 127.8, 118.9, 118.0, 114.6, 113.2, 85.9, 75.7, 61.3, 58.0, 57.5, 34.7, 31.4, 28.6, 28.4, 28.3, 22.6, 18.8, 14.1.

HRMS (ESI+) (m/z): $[\text{M}+\text{H}]^+$ 389.2951 calcd for $\text{C}_{27}\text{H}_{37}\text{N}_2^+$, found 389.2959;

2-allyl-1,2-diphenyl-1,1a,2,3-tetrahydroazirino[1,2-a]quinoxaline (4-68a)



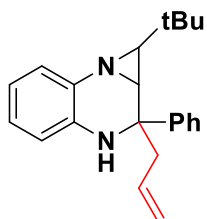
Colorless oil, 31.0 mg, 92% yield, obtained according to **Protocol E**.

¹H NMR (500 MHz, Chloroform-*d*) δ 7.54 – 7.49 (m, 2H), 7.32 (t, J = 7.7 Hz, 2H), 7.27 (dd, J = 7.7, 1.5 Hz, 1H), 7.21 (t, J = 7.4 Hz, 1H), 7.18 – 7.13 (m, 2H), 7.12 – 7.06 (m, 3H), 6.93 (td, J = 7.6, 1.5 Hz, 1H), 6.69 (td, J = 7.6, 1.4 Hz, 1H), 6.51 (dd, J = 7.9, 1.4 Hz, 1H), 5.45 (dtd, J = 16.8, 9.8, 5.2 Hz, 1H), 5.00 (dd, J = 10.3, 2.1 Hz, 1H), 4.92 (d, J = 17.1 Hz, 1H), 3.97 (s, 1H), 3.51 (d, J = 3.4 Hz, 1H), 2.99 (dd, J = 13.8, 5.3 Hz, 1H), 2.84 (d, J = 3.5 Hz, 1H), 2.68 (dd, J = 13.8, 9.4 Hz, 1H).

¹³C NMR (126 MHz, Chloroform-*d*) δ 142.7, 138.7, 137.4, 134.9, 132.5, 128.9, 128.3, 127.3, 127.1, 127.1, 126.4, 125.8, 125.7, 120.2, 119.3, 116.4, 57.8, 55.5, 44.8, 41.4.

HRMS (ESI+) (m/z): $[M+H]^+$ 339.1856 calcd for $C_{24}H_{23}N_2^+$, found 339.1850;

2-allyl-1-(tert-butyl)-2-phenyl-1,1a,2,3-tetrahydroazirino[1,2-a]quinoxaline (4-68b)



Colorless oil, 27.6 mg, 87% yield, obtained according to **Protocol E**.

¹H NMR (500 MHz, Chloroform-*d*) δ 7.50 – 7.45 (m, 2H), 7.32 (t, J = 7.8 Hz, 2H), 7.23 – 7.15 (m, 2H), 6.88 (td, J = 7.6, 1.5 Hz, 1H), 6.66 (td, J = 7.5, 1.4 Hz, 1H), 6.45 (dd, J = 7.8, 1.4 Hz, 1H), 5.44 (dtd, J = 17.1, 9.9, 5.1 Hz, 1H), 4.98 (dd, J = 10.3, 2.2 Hz, 1H), 4.93 – 4.86 (m, 1H), 3.90 – 3.86 (m, 1H), 3.00 – 2.92 (m, 1H), 2.60 (dd, J = 13.9, 9.7 Hz, 1H), 2.55 (dd, J = 4.0, 2.1 Hz, 1H), 2.24 (d, J = 3.9 Hz, 1H), 0.61 (s, 9H).

¹³C NMR (126 MHz, Chloroform-*d*) δ 143.4, 137.3, 132.9, 128.7, 128.4, 127.1, 126.5, 125.7, 125.1, 120.0, 119.1, 116.2, 55.2, 52.6, 51.7, 41.6, 30.3, 26.4.

HRMS (ESI+) (m/z): $[M+H]^+$ 319.2169 calcd for $C_{22}H_{27}N_2^+$, found 319.2176;

4.9 References

- (1) Singh, G. S. Synthetic Aziridines in Medicinal Chemistry: A Mini-Review. *Mini-Reviews in Medicinal Chemistry* **2016**, *16* (11), 892–904. <https://doi.org/10.2174/1389557515666150709122244>.
- (2) Dequina, H. J.; Jones, C. L.; Schomaker, J. M. Recent Updates and Future Perspectives in Aziridine Synthesis and Reactivity. *Chem* **2023**, *9* (7), 1658–1701. <https://doi.org/10.1016/J.CHEMPR.2023.04.010>.
- (3) Hu, X. E. Nucleophilic Ring Opening of Aziridines. *Tetrahedron*. March 15, 2004, pp 2701–2743. <https://doi.org/10.1016/j.tet.2004.01.042>.
- (4) Feng, J. J.; Zhang, J. Synthesis of Unsaturated N-Heterocycles by Cycloadditions of Aziridines and Alkynes. *ACS Catalysis*. American Chemical Society October 7, 2016, pp 6651–6661. <https://doi.org/10.1021/acscatal.6b02072>.
- (5) Takeda, Y.; Sameera, W. M. C.; Minakata, S. Palladium-Catalyzed Regioselective and Stereospecific Ring-Opening Cross-Coupling of Aziridines: Experimental and Computational Studies. *Acc Chem Res* **2020**, *53* (8), 1686–1702. <https://doi.org/10.1021/acs.accounts.0c00395>.
- (6) Chai, Z. Catalytic Asymmetric Transformations of Racemic Aziridines. *Synthesis (Germany)*. Georg Thieme Verlag June 17, 2020, pp 1738–1750. <https://doi.org/10.1055/s-0039-1690857>.
- (7) Heine, H. W.; Peavy, R. Aziridines XI. Reaction of 1,2,3-Triphenylaziridine with Diethylacetylene Dicarboxylate and Maleic Anhydride. *Tetrahedron Lett* **1965**, *6* (35), 3123–3126. [https://doi.org/10.1016/S0040-4039\(01\)89232-7](https://doi.org/10.1016/S0040-4039(01)89232-7).
- (8) Huisgen, R.; Scheer, W.; Huber, H. Stereospecific Conversion of Cis-Trans Isomeric Aziridines to Open-Chain Azomethine Ylides. *J Am Chem Soc* **1967**, *89* (7), 1753–1755. https://doi.org/10.1021/JA00983A052/ASSET/JA00983A052.FP.PNG_V03.
- (9) Ishii, K.; Kido, M.; Noji, M.; Sugiyama, S. Photoreactions of Bicyclic Aziridines with Alkenes and Alkynes: A Novel Synthetic Methodology for 8-Azabicyclo[3.2.1]Octane Derivatives. *Org Biomol Chem* **2008**, *6* (17), 3186–3195. <https://doi.org/10.1039/b805801f>.
- (10) Sun, H.; Yang, C.; Lin, R.; Xia, W. Regioselective Ring-Opening Nucleophilic Addition of Aziridines through Photoredox Catalyst. *Adv Synth Catal* **2014**, *356* (13), 2775–2780. <https://doi.org/10.1002/adsc.201400476>.
- (11) Mazzarella, D.; Bortolato, T.; Pelosi, G.; Dell'Amico, L. Photocatalytic (3 + 2) Dipolar Cycloadditions of Aziridines Driven by Visible-Light. *Chem Sci* **2023**, *15* (1), 271–277. <https://doi.org/10.1039/d3sc05997a>.
- (12) Heine, H. W.; Smith, A. B.; Bower, D.; Moureu, H.; Chovin, P.; Petit, L. Aziridines. XXI. The 1,4-Diazabicyclo[4.1.0]Hept-4-Enes and 1,1a-Dihydro-1,2-Diarylazirino[1,2-a]Quinoxalines. *Journal of Organic Chemistry* **1969**, *34* (1), 171–175. <https://doi.org/10.1021/JO00838A037>.
- (13) Orlov, V. D.; Vorob'eva, N. P.; Tishchenko, A. A.; Pikalev, O. M.; Popov, V. I.; Yagupol'skii, L. M. Aziridinyl Ketones and Their Cyclic Anils. 11. Fluorine-Containing Photochromes. *Chem Heterocycl Compd (N Y)* **1991**, *27* (9), 942–946. <https://doi.org/10.1007/BF00484355/METRICS>.
- (14) Zbruyev, A. I.; Shishkin, O. V.; Doroshenko, A. O.; Desenko, S. M.; Chebanov, V. A. Stepwise Photoinduced Transformation of Fused Aziridines via Stable Biradicals and Azomethine Ylides. *J Photochem Photobiol A Chem* **2018**, *353*, 469–476. <https://doi.org/10.1016/j.jphotochem.2017.11.053>.

- (15) Ramani, A.; Desai, B.; Patel, M.; Naveen, T. Recent Advances in the Functionalization of Terminal and Internal Alkynes. *Asian J Org Chem* **2022**, *11* (5), e202200047. <https://doi.org/10.1002/AJOC.202200047>.
- (16) Shah, S.; Das, B. G.; Singh, V. K. Recent Advancement in Copper-Catalyzed Asymmetric Reactions of Alkynes. *Tetrahedron* **2021**, *93*. <https://doi.org/10.1016/j.tet.2021.132238>.
- (17) Kim, U. Bin; Jung, D. J.; Jeon, H. J.; Rathwell, K.; Lee, S. G. Synergistic Dual Transition Metal Catalysis. *Chemical Reviews*. American Chemical Society December 23, 2020, pp 13382–13433. <https://doi.org/10.1021/acs.chemrev.0c00245>.
- (18) Babu, S. A.; Krishnan, K. K.; Ujwaldev, S. M.; Anilkumar, G. Applications of Pybox Complexes in Asymmetric Catalysis. *Asian Journal of Organic Chemistry*. Wiley-VCH Verlag June 1, 2018, pp 1033–1053. <https://doi.org/10.1002/ajoc.201800094>.
- (19) Lin, W.; Cao, T.; Fan, W.; Han, Y.; Kuang, J.; Luo, H.; Miao, B.; Tang, X.; Yu, Q.; Yuan, W.; Zhang, J.; Zhu, C.; Ma, S. Enantioselective Double Manipulation of Tetrahydroisoquinolines with Terminal Alkynes and Aldehydes under Copper(I) Catalysis. *Angewandte Chemie - International Edition* **2014**, *53* (1), 277–281. <https://doi.org/10.1002/anie.201308699>.
- (20) Dasgupta, S.; Liu, J.; Shoffler, C. A.; Yap, G. P. A.; Watson, M. P. Enantioselective, Copper-Catalyzed Alkynylation of Ketimines to Deliver Isoquinolines with α -Diaryl Tetrasubstituted Stereocenters. *Org Lett* **2016**, *18* (23), 6006–6009. https://doi.org/10.1021/ACS.ORGLETT.6B02787/SUPPL_FILE/OL6B02787_SI_003.CIF.
- (21) Pappoppula, M.; Cardoso, F. S. P.; Garrett, B. O.; Aponick, A. Enantioselective Copper-Catalyzed Quinoline Alkynylation. *Angewandte Chemie International Edition* **2015**, *54* (50), 15202–15206. <https://doi.org/10.1002/ANIE.201507848>.
- (22) Sandoval-Pauker, C.; Molina-Aguirre, G.; Pinter, B. Status Report on Copper (I) Complexes in Photoredox Catalysis; Photophysical and Electrochemical Properties and Future Prospects. *Polyhedron* **2021**, *199*, 115105. <https://doi.org/10.1016/J.POLY.2021.115105>.
- (23) Busch, J.; Knoll, D. M.; Zippel, C.; Bräse, S.; Bizzarri, C. Metal-Supported and -Assisted Stereoselective Cooperative Photoredox Catalysis. *Dalton Transactions*. Royal Society of Chemistry 2019, pp 15338–15357. <https://doi.org/10.1039/c9dt02094b>.
- (24) Song, L.; Cai, L.; Gong, L.; Van der Eycken, E. V. Photoinduced Copper-Catalyzed Enantioselective Coupling Reactions. *Chemical Society Reviews*. Royal Society of Chemistry March 14, 2023, pp 2358–2376. <https://doi.org/10.1039/d2cs00734g>.
- (25) Rueping, M.; Koenigs, R. M.; Poscharny, K.; Fabry, D. C.; Leonori, D.; Vila, C. Dual Catalysis: Combination of Photocatalytic Aerobic Oxidation and Metal Catalyzed Alkynylation Reactions-C-C Bond Formation Using Visible Light. *Chemistry - A European Journal* **2012**, *18* (17), 5170–5174. <https://doi.org/10.1002/chem.201200050>.
- (26) Perepichka, I.; Kundu, S.; Hearne, Z.; Li, C. J. Efficient Merging of Copper and Photoredox Catalysis for the Asymmetric Cross-Dehydrogenative-Coupling of Alkynes and Tetrahydroisoquinolines. *Org Biomol Chem* **2015**, *13* (2), 447–451. <https://doi.org/10.1039/c4ob02138j>.
- (27) Law, R. P.; Atkinson, S. J.; Bamborough, P.; Chung, C. W.; Demont, E. H.; Gordon, L. J.; Lindon, M.; Prinjha, R. K.; Watson, A. J. B.; Hirst, D. J. Discovery of Tetrahydroquinoxalines as Bromodomain and Extra-Terminal Domain (BET) Inhibitors with Selectivity for the Second Bromodomain. *J Med Chem* **2018**, *61* (10), 4317–4334. <https://doi.org/10.1021/ACS.JMEDCHEM.7B01666>.
- (28) Wilson, J. E.; Kurukulasuriya, R.; Reibarkh, M.; Reiter, M.; Zwicker, A.; Zhao, K.; Zhang, F.; Anand, R.; Colandrea, V. J.; Cumiskey, A. M.; Crespo, A.; Duffy, R. A.; Murphy, B. A.; Mitra,

K.; Johns, D. G.; Duffy, J. L.; Vachal, P. Discovery of Novel Indoline Cholesterol Ester Transfer Protein Inhibitors (CETP) through a Structure-Guided Approach. *ACS Med Chem Lett* **2016**, *7* (3), 261–265.

https://doi.org/10.1021/ACSMEDCHEMLETT.5B00404/SUPPL_FILE/ML5B00404_SI_001.PDF.

(29) Rueping, M.; Tato, F.; Schoepke, F. R. The First General, Efficient and Highly Enantioselective Reduction of Quinoxalines and Quinoxalinones. *Chemistry – A European Journal* **2010**, *16* (9), 2688–2691. <https://doi.org/10.1002/CHEM.200902907>.

(30) Zhang, Z.; Du, H. A Highly Cis-Selective and Enantioselective Metal-Free Hydrogenation of 2,3-Disubstituted Quinoxalines. *Angewandte Chemie International Edition* **2015**, *54* (2), 623–626. <https://doi.org/10.1002/ANIE.201409471>.

(31) Li, S.; Meng, W.; Du, H. Asymmetric Transfer Hydrogenations of 2,3-Disubstituted Quinoxalines with Ammonia Borane. *Org Lett* **2017**, *19* (10), 2604–2606. https://doi.org/10.1021/ACS.ORGLETT.7B00935/SUPPL_FILE/OL7B00935_SI_001.PDF.

(32) Ortiz, K. G.; Hammons, J. S.; Karimov, R. R. Rhodium-Catalyzed Asymmetric Functionalization of Quinoxalinium Salts. *Org Lett* **2023**, *25* (50), 8987–8991. https://doi.org/10.1021/ACS.ORGLETT.3C03555/SUPPL_FILE/OL3C03555_SI_001.PDF.

(33) Cheeseman, G. W. H.; Cookson, R. F. Condensed Pyrazines. **1979**.

(34) Jhang, Y.; Zhelavskiy, O.; Nagorny, P. Enantioselective Parallel Kinetic Resolution of Aziridine-Containing Quinoxalines via Chiral Phosphoric Acid-Catalyzed Transfer Hydrogenation. **2023**. <https://doi.org/10.1021/acs.orglett.3c03072>.

(35) Comelles, J.; Pericas, A.; Moreno-Mañas, M.; Vallribera, A.; Drudis-Solé, G.; Lledos, A.; Parella, T.; Roglans, A.; García-Granda, S.; Roces-Fernández, L. Highly Enantioselective Electrophilic Amination and Michael Addition of Cyclic β -Ketoesters Induced by Lanthanides and (S,S)-Ip-Pybox: The Mechanism. *Journal of Organic Chemistry* **2007**, *72* (6), 2077–2087. https://doi.org/10.1021/JO0622678/SUPPL_FILE/JO0622678SI20070119_045826.PDF.

(36) Paul, A.; Borrelli, R.; Bouyanfif, H.; Gottis, S.; Sauvage, F. Tunable Redox Potential, Optical Properties, and Enhanced Stability of Modified Ferrocene-Based Complexes. *ACS Omega* **2019**, *4* (12), 14780–14789. https://doi.org/10.1021/ACSOMEGA.9B01341/ASSET/IMAGES/MEDIUM/AO9B01341_M003.GIF.

(37) Hwang, B.; Park, M. S.; Kim, K. Ferrocene and Cobaltocene Derivatives for Non-Aqueous Redox Flow Batteries. *ChemSusChem* **2015**, *8* (2), 310–314. <https://doi.org/10.1002/CSSC.201403021>.

(38) Cardona, C. M.; Li, W.; Kaifer, A. E.; Stockdale, D.; Bazan, G. C.; Cardona, C. M.; Li, W.; Kaifer, A. E.; Stockdale, D.; Bazan, G. C. Electrochemical Considerations for Determining Absolute Frontier Orbital Energy Levels of Conjugated Polymers for Solar Cell Applications. *Advanced Materials* **2011**, *23* (20), 2367–2371. <https://doi.org/10.1002/ADMA.201004554>.

(39) Shao, Y.; Gan, Z.; Epifanovsky, E.; Gilbert, A. T. B.; Wormit, M.; Kussmann, J.; Lange, A. W.; Behn, A.; Deng, J.; Feng, X.; Ghosh, D.; Goldey, M.; Horn, P. R.; Jacobson, L. D.; Kaliman, I.; Khaliullin, R. Z.; Kus, T.; Landau, A.; Liu, J.; Proynov, E. I.; Rhee, Y. M.; Richard, R. M.; Rohrdanz, M. A.; Steele, R. P.; Sundstrom, E. J.; Woodcock, H. L.; Zimmerman, P. M.; Zuev, D.; Albrecht, B.; Alguire, E.; Austin, B.; Beran, G. J. O.; Bernard, Y. A.; Berquist, E.; Brandhorst, K.; Bravaya, K. B.; Brown, S. T.; Casanova, D.; Chang, C. M.; Chen, Y.; Chien, S. H.; Closser, K. D.; Crittenden, D. L.; Diedenhofen, M.; Distasio, R. A.; Do, H.; Dutoi, A. D.; Edgar, R. G.; Fatehi, S.; Fusti-Molnar, L.; Ghysels, A.; Golubeva-Zadorozhnaya, A.; Gomes, J.;

- Hanson-Heine, M. W. D.; Harbach, P. H. P.; Hauser, A. W.; Hohenstein, E. G.; Holden, Z. C.; Jagau, T. C.; Ji, H.; Kaduk, B.; Khistyayev, K.; Kim, J.; Kim, J.; King, R. A.; Klunzinger, P.; Kosenkov, D.; Kowalczyk, T.; Krauter, C. M.; Lao, K. U.; Laurent, A. D.; Lawler, K. V.; Levchenko, S. V.; Lin, C. Y.; Liu, F.; Livshits, E.; Lochan, R. C.; Luenser, A.; Manohar, P.; Manzer, S. F.; Mao, S. P.; Mardirossian, N.; Marenich, A. V.; Maurer, S. A.; Mayhall, N. J.; Neuscamman, E.; Oana, C. M.; Olivares-Amaya, R.; O'Neill, D. P.; Parkhill, J. A.; Perrine, T. M.; Peverati, R.; Prociuk, A.; Rehn, D. R.; Rosta, E.; Russ, N. J.; Sharada, S. M.; Sharma, S.; Small, D. W.; Sodt, A.; Stein, T.; Stück, D.; Su, Y. C.; Thom, A. J. W.; Tsuchimochi, T.; Vanovschi, V.; Vogt, L.; Vydrov, O.; Wang, T.; Watson, M. A.; Wenzel, J.; White, A.; Williams, C. F.; Yang, J.; Yeganeh, S.; Yost, S. R.; You, Z. Q.; Zhang, I. Y.; Zhang, X.; Zhao, Y.; Brooks, B. R.; Chan, G. K. L.; Chipman, D. M.; Cramer, C. J.; Goddard, W. A.; Gordon, M. S.; Hehre, W. J.; Klamt, A.; Schaefer, H. F.; Schmidt, M. W.; Sherrill, C. D.; Truhlar, D. G.; Warshel, A.; Xu, X.; Aspuru-Guzik, A.; Baer, R.; Bell, A. T.; Besley, N. A.; Chai, J. Da; Dreuw, A.; Dunietz, B. D.; Furlani, T. R.; Gwaltney, S. R.; Hsu, C. P.; Jung, Y.; Kong, J.; Lambrecht, D. S.; Liang, W.; Ochsenfeld, C.; Rassolov, V. A.; Slipchenko, L. V.; Subotnik, J. E.; Van Voorhis, T.; Herbert, J. M.; Krylov, A. I.; Gill, P. M. W.; Head-Gordon, M. Advances in Molecular Quantum Chemistry Contained in the Q-Chem 4 Program Package. *Mol Phys* **2015**, *113* (2), 184–215. <https://doi.org/10.1080/00268976.2014.952696>.
- (40) Zimmerman, P. M. Growing String Method with Interpolation and Optimization in Internal Coordinates: Method and Examples. *J Chem Phys* **2013**, *138* (18). <https://doi.org/10.1063/1.4804162>.
- (41) Zimmerman, P. M. Automated Discovery of Chemically Reasonable Elementary Reaction Steps. *J Comput Chem* **2013**, *34* (16), 1385–1392. <https://doi.org/10.1002/JCC.23271>.
- (42) Becke, A. D. Density-functional Thermochemistry. III. The Role of Exact Exchange. *J Chem Phys* **1993**, *98* (7), 5648–5652. <https://doi.org/10.1063/1.464913>.
- (43) Hehre, W. J.; Ditchfield, R.; Pople, J. A.; Wall, F. T.; Hiller, L. A.; Wheeler, D. J.; Chern Phys, J.; Hammersley, J. M.; Morton, K. W.; Roy Stat Soc, J.; Herre, W. J.; Ditchfield, R. Self-Consistent Molecular Orbital Methods. XII. Further Extensions of Gaussian-Type Basis Sets for Use in Molecular Orbital Studies of Organic Molecules. *J Chem Phys* **1972**, *56* (5), 2257–2261. <https://doi.org/10.1063/1.1677527>.
- (44) Lin, Y. S.; Li, G. De; Mao, S. P.; Chai, J. Da. Long-Range Corrected Hybrid Density Functionals with Improved Dispersion Corrections. *J Chem Theory Comput* **2013**, *9* (1), 263–272. https://doi.org/10.1021/CT300715S/SUPPL_FILE/CT300715S_SI_001.PDF.
- (45) Kendall, R. A.; Dunning, T. H.; Harrison, R. J. Electron Affinities of the First-row Atoms Revisited. Systematic Basis Sets and Wave Functions. *J Chem Phys* **1992**, *96* (9), 6796–6806. <https://doi.org/10.1063/1.462569>.
- (46) Marenich, A. V.; Cramer, C. J.; Truhlar, D. G. Universal Solvation Model Based on Solute Electron Density and on a Continuum Model of the Solvent Defined by the Bulk Dielectric Constant and Atomic Surface Tensions. *Journal of Physical Chemistry B* **2009**, *113* (18), 6378–6396. <https://doi.org/10.1021/jp810292n>.
- (47) Hirata, S.; Head-Gordon, M. Time-Dependent Density Functional Theory within the Tamm-Dancoff Approximation. *Chem Phys Lett* **1999**, *314* (3–4), 291–299. [https://doi.org/10.1016/S0009-2614\(99\)01149-5](https://doi.org/10.1016/S0009-2614(99)01149-5).
- (48) Zhelavskiy, O.; Parikh, S.; Jhang, Y. J.; Staples, R. J.; Zimmerman, P. M.; Nagorny, P. Green Light Promoted Iridium(III)/Copper(I)-Catalyzed Addition of Alkynes to

Aziridinoquinoxalines Through the Intermediacy of Azomethine Ylides. *Angewandte Chemie International Edition* **2024**, *63* (12), e202318876. <https://doi.org/10.1002/ANIE.202318876>.

(49) Zimmerman, P. M. Single-Ended Transition State Finding with the Growing String Method. *J Comput Chem* **2015**, *36* (9), 601–611. <https://doi.org/10.1002/JCC.23833>.

(50) Zimmerman, P. Reliable Transition State Searches Integrated with the Growing String Method. *J Chem Theory Comput* **2013**, *9* (7), 3043–3050. <https://doi.org/10.1021/CT400319W>.

(51) Isse, A. A.; Gennaro, A. Absolute Potential of the Standard Hydrogen Electrode and the Problem of Interconversion of Potentials in Different Solvents. *J Phys Chem B* **2010**, *114* (23), 7894–7899. <https://doi.org/10.1021/JP100402X>.

Chapter 5 Closing Remarks and Future Directions

Since the process of industrialization growth at the beginning of the 20th century, the chemical industry has become the main provider of new types of materials and compounds that are essential for the rapid development of other industrial fields, such as construction, common household goods production, agricultural supplies, and pharmaceutical drugs. The development of catalysis has played an important role in creating new efficient routes for the synthesis of previously inaccessible targets. Starting with the famous Haber-Bosch process and reaching modern catalytic systems developed by D. MacMillan and B. List catalysis dominates the field of chemical synthesis. However, such achievements in the chemical industry came at a cost as it became one of the industrial fields with the most significant waste generation. Among the other challenges associated with the application of modern catalytic methods are the high cost and low availability of many of the newly developed catalysts. Despite this, catalysts such as Chiral Phosphoric Acids (CPAs) may be used for highly efficient catalysis of asymmetric reactions, but most of them are available only in small quantities. This limitation forces chemical manufacturers to use old and less efficient methods leading to waste generation, higher energy consumption, etc. Since P. Anastas and J. Warner postulated 12 principles of “green” chemistry, they started to be actively used or at least considered during the development of new catalytic systems. Synthetic routes developed according to “green” chemistry postulates are not only more environmentally friendly but also more economically effective as minimizing waste generation leads to cost reduction of its utilization.

This dissertation has summarized some of our achievements in developing new sustainable catalytic methods for diastereoselective and enantioselective synthesis of carbohydrates and heterocyclic molecules. Developing a new catalytic system always faces the problem of screening an very large set of different reaction conditions. However, the recent developments in quantum chemistry calculations have significantly improved the availability of theoretical methods for catalytic reaction exploration. In the current dissertation, we successfully implemented *ab initio* methods such as DFT calculations to assist the process of developing experimental reaction protocols. DFT computations can be effectively used now to quantify the physical properties of interest, search for the reaction transition states, or even predict reaction mechanisms. The Zimmerman group has developed state-of-the-art tools for rapid potential energy surface exploration to find the reaction pathways and transition states that were used to assist and drive the research projects described in this thesis.

Chapter 2 of this thesis is dedicated to the development of immobilized CPAs and their applications for regioselective monosaccharide acetalizations. (*R*)-BINOL-based CPA catalysis enabled highly selective acetalizations of carbohydrates at the C₂-positions (with >25:1 r.r.) while (*S*)-SPINOL CPA reverted the selectivity and provided regioisomeric C₃-protected monosaccharides with high yields and good regioselectivity. Immobilized CPAs demonstrated higher catalytic activity at low catalyst loadings and in many cases resulted in increased regioselectivity in comparison to the homogeneous catalysts. Computational studies were performed using the developed QM/MM model and growing string method for the exploration of potential reaction mechanisms and factors controlling the selectivity. Computed results were essential for developing NMR experiments to prove our hypothesis of two competitive mechanisms controlling regioselectivity.

In Chapter 3 we continued to explore the potential applications of the developed immobilized CPA catalysts. We have discovered that valuable quinoline derivatives (2-Aryl and carboxylates) as well as 2H-benzo[b][1,4]oxazines and benzo[b][1,4]oxazine-2-ones can be effectively reduced with high yields and enantioselectivity (80-98% ee) using the immobilized catalyst (*R*)-PS-AdTRIP and Hantzsch ester. Subsequently, the immobilized CPA was then used to prepare a packed-bed reactor and to perform the synthesis in continuous flow. Impressively, we have discovered that asymmetric transfer hydrogenations could be achieved at high flow rates (2.5 mL/min) without erosion in the reaction yields and with consistent improvements in the reaction enantioselectivities.

During the studies of the asymmetric transfer hydrogenation (Chapter 3), we discovered unique photochromic properties of the fused aziridinoquinoxalines, and DFT computations were performed to gain a better understanding of their photochemical properties and reactivity. Detailed computational analysis using the TD-DFT method provided details about the excitation profiles of the studied aziridines and provided mechanistic insight that assisted the development of the most optimal reaction conditions for azomethine ylide generation. Subsequently, we implemented the green LED activation of aziridinylquinoxalines with Ir(III) photocatalyst combined with Cu(I) catalysis to provide the alkyne addition products to generate azomethine ylides with excellent yields. This transformation can also be carried out enantioselectivity with (*S,R*)-*N*-PINAP ligand to obtain target compounds with up to 96:4 e.r. (Chapter 4).

Our studies of the aziridinoquinoxalines also described in Appendix A where (*R*)-TRIP CPA catalyzed the reduction of imine bond with Hantzsch ester were successfully used to perform parallel kinetic resolution of aziridinoquinoxalines. Obtained chiral diastereomers can be further

functionalized via nucleophilic aziridine ring-opening to produce tetrahydroquinoxalines containing three contiguous stereocenters with excellent enantioselective excess (up to 99% ee).

Even though this dissertation described three projects dedicated to the development of the new catalytic methods guided by “green” chemistry principles, it is only a small fraction of all research work done today to address current industrial issues and challenges. With the growing demand for novel pharmaceutical drugs to address current and future diseases, inventing more efficient synthetic routes and protocols will be always one of the most important research directions in the future. We envision that our contributions to the scientific community are achieved due to productive collaboration between the Nagorny and Zimmerman groups and can serve as a good starting point for future researchers. Developed immobilized CPA catalysts demonstrated great catalytic activity and recyclability in regioselective protection of carbohydrates and enantioselective reduction of aromatic heterocycles. However, the true potential of immobilized CPA application was barely touched and utilized in Chapter 3. As heterogeneous CPA catalysts implementation in batch conditions simplify the catalyst preservation and recovery, the flow chemistry field should benefit the most from using immobilized CPAs in packed-bed reactors. Even though flow system design for new reactions can be challenging as described in Appendix B, enantioselective transfer hydrogenation of six-membered heterocycles already demonstrated synthetic applicability for the large-scale synthesis. In addition to our protocols allowing the enantioselective synthesis of tetrahydroquinolines and benzoxazines, we assume that the same method of CPA-catalyzed reduction using Hantzsch esters can be applied broadly to other heterocyclic systems, such as seven-membered benzodiazepines or for asymmetric reduction of imine-type double bonds in both cyclic and non-cyclic molecules.

Another promising direction is photochemically-promoted aziridine ring opening leading to *in-situ* generation of azomethine ylides. Photochemical activation already was broadly used for promoting organic reactions. While photoredox reactions are well-known to perform single-electron reductive or oxidative reactions, our collaborative work contributes to the less explored field of energy transfer catalysis. Energy triplet catalysis allowed to perform undirect excitation and ring-opening process of otherwise photolabile aziridinoquinoxalines. Generated azomethine ylides served as precursors for the quinoxalinium salts preparation. We assume, that our mechanistic investigations and developed protocol for Green LED promoted photochemical transformation of aziridines can be further applied to other aziridine-containing molecules. Even though the potential application of EnT catalysis principle for azomethine ylide generation via aziridine ring-opening can be a useful tool for performing [3+2] reactions, we envision that future work in this area can be also focused on iminium cation generation from azomethine ylides. Such protocol if developed on the broader substrate scope can serve as an alternative synthetic route towards iminium cations that are usually generated via condensation reactions of carbonyl groups and secondary amines or alkylation of nitrogen-containing aromatic heterocycles.

Finally, we hope that our mechanistic studies using QM/MM methods of CPA-directed acetalization reactions can be useful for the future development of the site-selective modification of polyol molecules. Besides carbohydrates, there are plenty of other important classes of polyol-containing molecules that can benefit from developing new regioselective CPA-catalyzed reactions. As presented in Chapter 2, computational methods can be used for systematic studies of catalyst-controlled hydroxyl group protections as there are no previously reported stereochemical models allowing the prediction of regioselective protection of polyols molecules.

Appendices

Appendix A: Studies of Enantioselective Kinetic Resolution of Aziridine-Containing Quinoxalines¹

A.1 Introduction

Nitrogen-containing heterocycles have been of great importance to drug discovery, their preparation and exploration have been a driving force for numerous studies in asymmetric synthesis and catalysis as we described in previous chapters. The aziridine-containing substrates are key to the synthesis of nitrogen-containing compounds including cyclic and bicyclic nitrogen-containing heterocycles, and numerous recent efforts have been focused on addressing various aspects associated with the synthesis and activation of the aziridine rings.¹ Both the aziridine-containing compounds such as mitomycin C, and compounds with tetrahydroquinoxaline motifs, such as the Merck CETP inhibitor x and Glaxo-Smith-Klaine BET bromodomain inhibitor GSK340, have been extensively explored in drug discovery (Scheme A.1).²⁻⁴

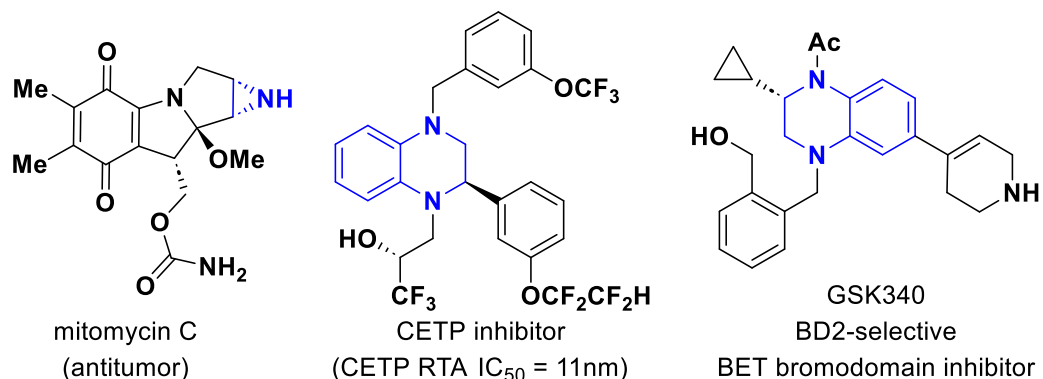
¹ Authors and Contributions:

This Appendix is based on: Jhang Y.-J., Zhelavskiy O., Nagorny P. *Organic Letters* 2023, 25 (42), 7721-7726

Y.-J. Jhang contributed to the synthesis of starting materials, reaction conditions development, and substrate scope screening

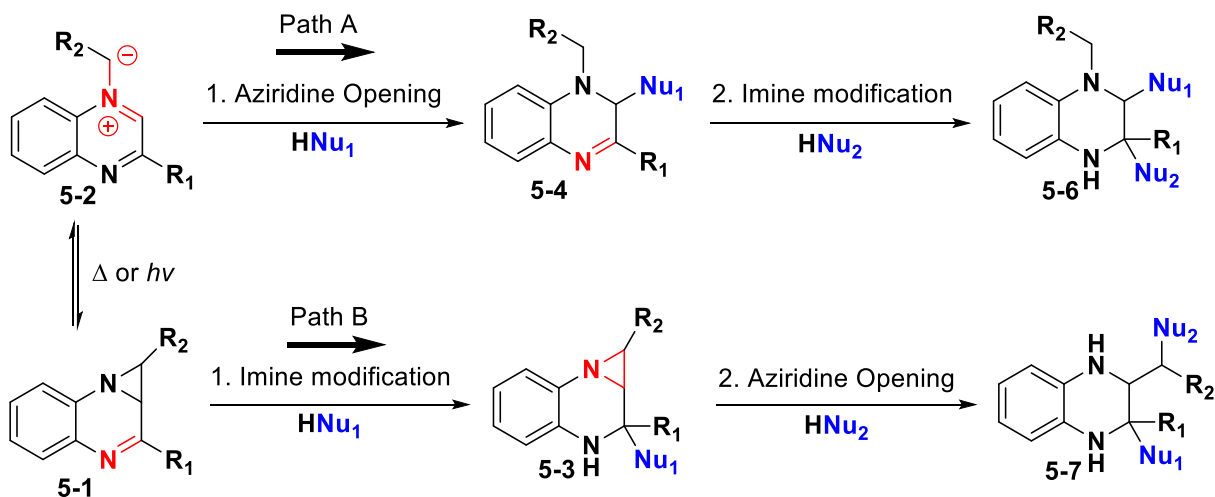
My contribution is preliminary studies and developing conditions for nucleophilic ring-opening reaction

Appendix Scheme A.1. Examples of aziridine-containing and quinoxaline-based pharmaceuticals.



In contrast to simple aziridines, only a few asymmetric methods are available for the synthesis of the heterocyclic systems containing fused aziridine rings such as aziridinoquinoxaline **5-1** (Scheme A.2). The seminal studies by Gaunt and coworkers⁵ have resulted in a streamlined synthesis of fused aziridines via sp^3 -CH functionalization; however, no similar asymmetric methods are available for the synthesis of benzene ring-containing heterocycles such as **5-1**.

Appendix Scheme A.2. Regiodivergent modifications of aziridinoquinoxalines.

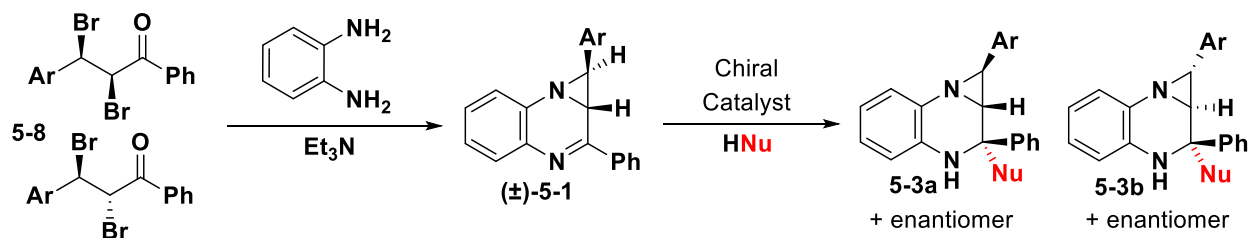


Chapter 4 describes a new aziridine ring functionalization that was accomplished via a photoinduced C-C bond cleavage followed by ylide capturing to obtain a modified quinoxaline core (Scheme A.2, Path A). Obtained quinoxalines **5-4** could then be further modified via

nucleophile addition to the C=N bond to result in complex heterocyclic core **5-6** with multiple stereocenters. As we demonstrated, these steps can be performed enantioselectively (aziridine opening) and diastereoselectively (following addition to C=N). Alternatively, the aziridinoquinoxaline core **5-1** can be first modified via imine modification (Scheme A.2, Path B) to produce compounds **5-3** while the aziridine ring is preserved. In this case, the absence of the imine double bond will make it impossible to generate ylides from the aziridine ring as no strong chromophore group is present to produce a stable triplet state. However, ring opening can still be achieved via the classical S_N2 reaction leading to a different quinoxaline scaffold **5-7**. For pathway B, the first step already represents a challenging transformation as the initial aziridine contains two stereocenters and can exist as different diastereomers resulting in various stereochemical outcome of the nucleophilic addition step. Therefore, stereocontrol is needed to produce desired diastereomers during the first step of the transformation.

Aziridinoquinoxalines can be easily synthesized via a double nucleophilic addition of diamines to di-bromo ketone derivatives (Scheme A.3) as it was firstly reported by Heine⁶. Despite such transformations leaving almost no room for the implementation of stereocontrol via chiral catalysis, previous publications confirmed the formation of a single diastereomer during phenylenediamine cyclization with dibromochalcone **5-8**. Formed diastereomer **5-1** has a *trans*-configuration of the aziridine ring hydrogens, and its structure was previously confirmed via X-ray crystallography.⁷ Therefore, a nucleophilic addition to imine double bond of compound (±)-**5-1** can produce two possible diastereomers (and 4 enantiomers in total) and to achieve stereocontrol we should develop a method for the chiral resolution of two enantiomers of compound (±)-**5-1** (Scheme A.3).

Appendix Scheme A.3. Synthesis of racemic aziridinoquinoxalines 5-1 with following chiral resolution during nucleophilic addition.



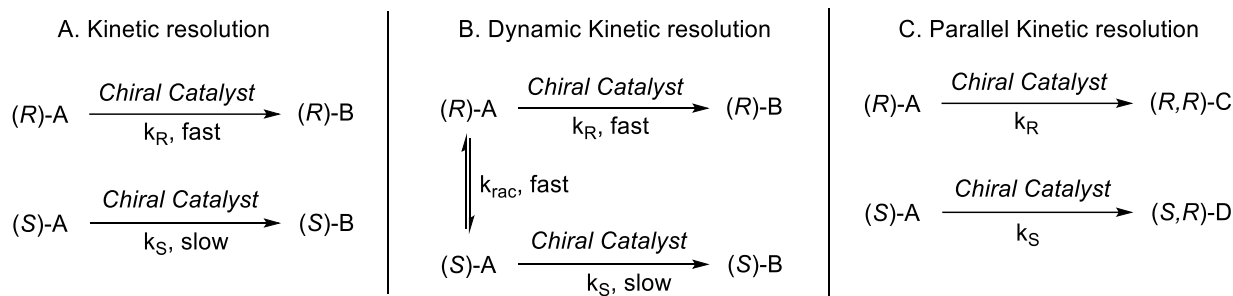
A.2 Chiral Phosphoric Acid catalyzed kinetic resolution.

Chiral phosphoric acids are among the most powerful chiral organocatalysts in asymmetric catalysis, and a wide array of CPA catalysts has been developed and is available for use. CPAs have been extensively used for enantioselective transformations to obtain enantiomerically enriched products from non-chiral starting materials. Even though enantioselective catalysis is the most preferred way for producing chiral molecules, in some cases more classical approaches such as the kinetic resolution of racemic mixtures can be more feasible. Kinetic resolution is particularly useful for obtaining enantiopure materials from inexpensive racemic substrates obtained from feedstock or through simple synthesis.⁸

The main principle of kinetic resolution is that two different enantiomers will have different reaction rates upon association with a chiral reagent or catalyst. Preferably, chiral resolution conditions should be established using chiral catalysts rather than stoichiometric amounts of chiral reagents. There are several types of kinetic resolution processes that could be grouped based on the reaction mechanism (Scheme A.4). First is the classical kinetic resolution (KR), where the chiral catalyst differentiates two enantiomers of the starting material. When the chirality of compound A matches the chirality of the catalyst, a reaction will occur much faster than when the opposite enantiomer is used (Scheme A.4A). Selectivity factor (S) has been used to describe the

efficiency of a KR reaction, which is defined as the ratio of the rate constant of the fast-reacting and slow-reacting enantiomers ($s=k_R/k_S$). Practically, to obtain the product and the starting material with high optical purities, the reaction conversion should be around 50% and the selectivity factor should be above 20.⁹

Appendix Scheme A.4. Types of kinetic resolutions.

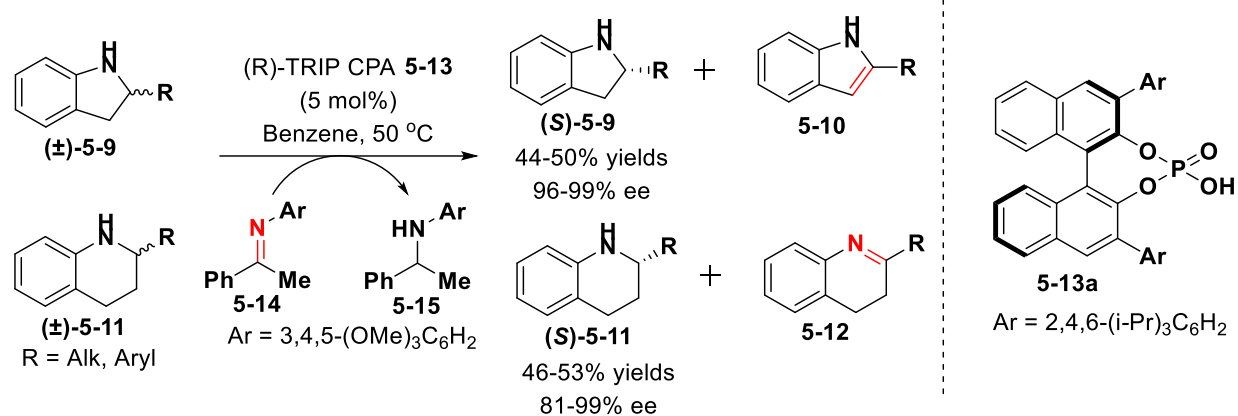


Another strategy to obtain the desired product with a maximum 100% recovery is dynamic kinetic resolution (DKR, Scheme A.4B). This resolution is possible in case of fast epimerization equilibrium existing between (*R*)-A and (*S*)-A molecules. While the (*R*)-enantiomer reacts faster than the (*S*) enantiomer, the quantity of (*R*)-enantiomer is constantly replenished by (*S*) enantiomer epimerization according to the Curtin-Hammett principle.⁹ In this case, 100% conversion of racemic substrate to enantiopure material is possible.

Finally, the third type of kinetic resolution allows the separation of the initial racemate in the form of two new isomeric compounds (Scheme A.4C). It is termed parallel kinetic resolution (PKR) and is based on the principle that two enantiomers are transformed into two diastereomers or regioisomers by reacting with another chiral compound or under chiral catalysis. As diastereomers or regioisomers may have significantly different physical and chemical properties, they can be then separated via physical purification methods (column chromatography, recrystallization, etc.).¹⁰

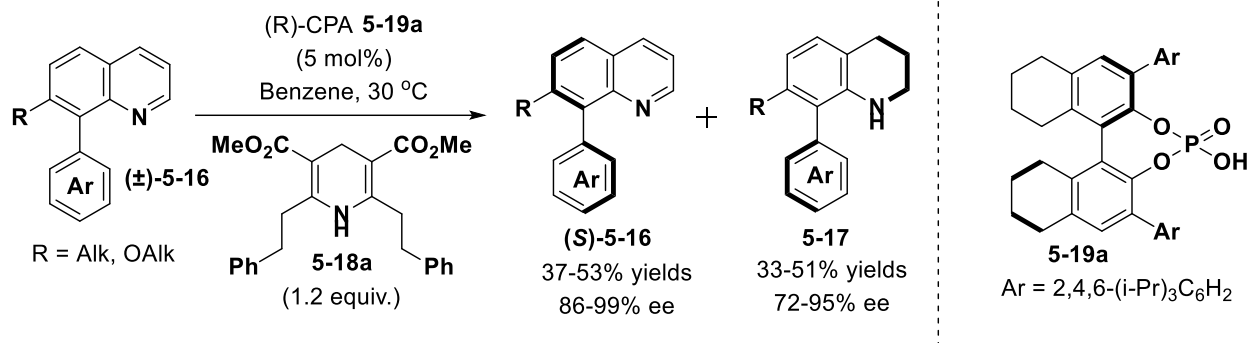
CPAs are extensively used as catalysts for performing kinetic resolutions.⁹ In the field of heterocyclic chemistry, Akiyama and co-workers pioneered the development of methods for oxidative kinetic resolution of indolines **5-9** with sacrificial imine using the CPA catalyst to differentiate enantiomers of the initial substrate (Scheme A.5). Acetophenone-derived imine **5-14** performed selective oxidation of (*R*)-enantiomer of **5-9** resulting in indole **5-10** as a side-product and remained indoline was isolated in 44-50% yields with excellent enantiomeric excess (96-99% ee). In 2015, the same group extended this protocol for chiral resolution of 2-substituted tetrahydroquinolines **5-11**.^{11,12}

Appendix Scheme A.5. Kinetic resolution of indolines and tetrahydroquinolines.



Reductive conditions were used by the Zhou group to perform kinetic resolution of 5- and 8-substituted quinoline atropoisomers (Scheme A.6). H₈-BINOL CPA **5-19a** was used to selectively reduce the quinoline core of one of the atropoisomers **5-16** with Hantzsch esters. It was reported that 2,6-diphenethyl Hantzsch ester **5-18a** was the most effective in producing both compounds in the expected 30-50% yield range and with high levels of enantiomeric enrichment. It is worth noting that Hantzsch ester was used in approximately 1:1 molar ratio to product to prevent reaction conversion exceeding 50% and to achieve the best enantiomeric resolution.¹³

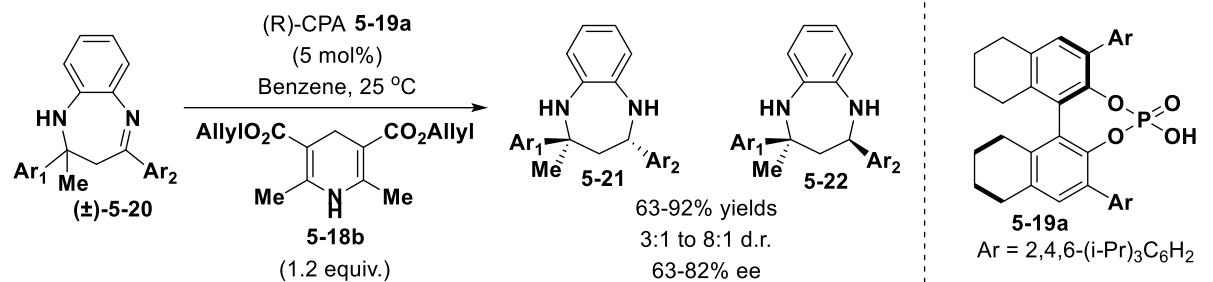
Appendix Scheme A.6. Kinetic resolution of atropoisomers.



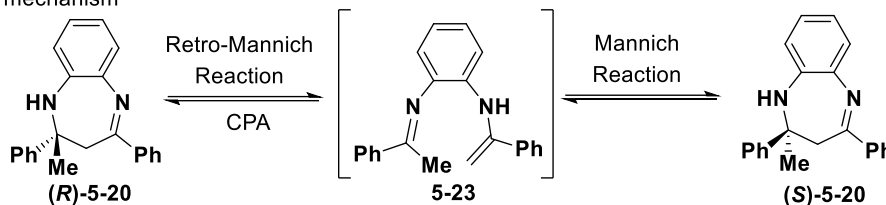
While a number of studies have explored CPA-catalyzed KR reactions, the CPA-catalyzed dynamic kinetic resolutions were significantly less developed, probably, due to the limited number of systems that can undergo fast substrate epimerization. Nevertheless, in 2017 Gong and co-workers¹⁴ presented the method of DKR reductive resolution of 2,4-diaryl-2,3-dihydrobenzo[b][1,4]diazepines catalyzed by CPA **5-19a** with Hantzsch ester **5-18b** as the reducing agent (Scheme A.7A). Starting racemic heterocycle (\pm) -**5-20** was converted to reduced diastereomers **5-21** and **5-22** in 63-92% yields and 3:1 to 8:1 diastereomer ratio, correspondingly. Each diastereomer was also isolated with moderate to excellent levels of enantiomeric enrichment (63 to 92% ee). Racemization of the starting diazepine was achieved through a retro-Mannich reaction catalyzed by CPA with the formation of ring-opened intermediate **5-23**, which then underwent Mannich reaction to form the opposite enantiomer (Scheme A.7).

Appendix Scheme A.7. Example of DKR reaction catalyzed by CPA.

A. Dynamic kinetic resolution

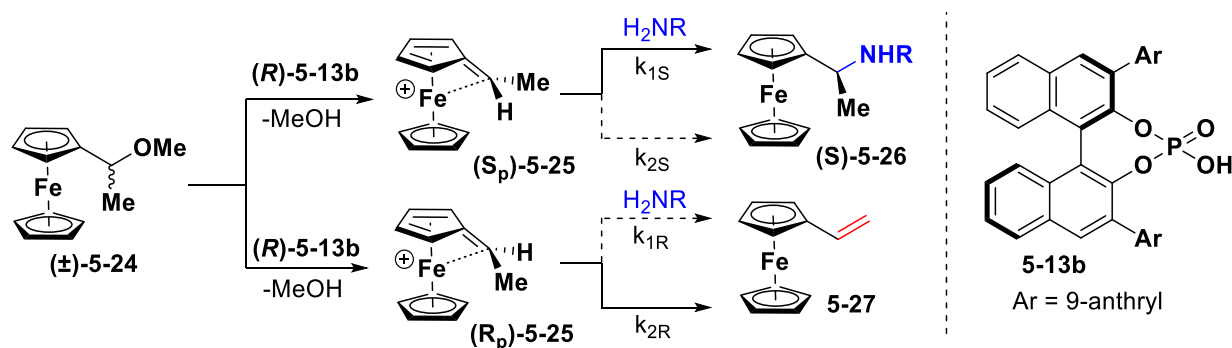


B. Racemization mechanism



To the best of our knowledge, there are no literature precedents of Parallel Kinetic resolution applications in the area of heterocyclic chemistry. However, recently, the Terada group¹⁵ published a method for PKR resolution of ferrocene derivatives under CPA catalysis (Scheme A.8). CPA promotes methanol elimination from compounds **5-24** and the formation of two stereoisomers of cations **5-25**. The formed cation then can undergo either a nucleophilic addition reaction with primary amines to form product (S)-**5-26** or an elimination reaction leading to alkene **5-27**.

Appendix Scheme A.8. PKR resolution of ferrocene derivatives.

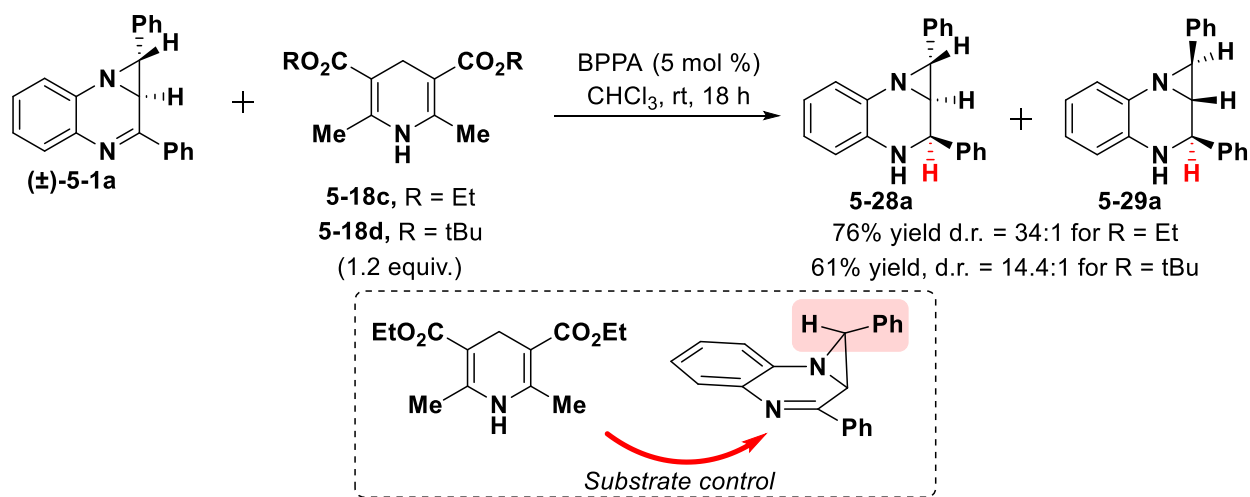


Performing DFT studies of transition states demonstrated that the CPA-anion controls the stability of the transition states which leads to either an addition or elimination reaction. While for one of the carbocations (S_p -isomer) nucleophilic addition was the favored pathway, its stereoisomer underwent deprotonation facilitated by CPA-counter anion that resulted in elimination product **5-27**.

A.3 Chiral resolution of aziridinoquinoxalines

Our studies focused on developing chiral resolution of aziridinoquinoxalines commenced with subjecting the substrate to reduction with achiral catalyst. Aziridinoquinoxaline **5-1a** was reduced using ethyl-substituted Hantzsch ester **5-18c** and 5 mol% of Biphenyl Phosphoric Acid (BPPA) as non-chiral Bronsted acid (Scheme A.9). The reaction was carried out using our standard conditions developed for enantioselective reduction of quinolines in Chapter 3.

Appendix Scheme A.9. Reduction under non-chiral conditions.

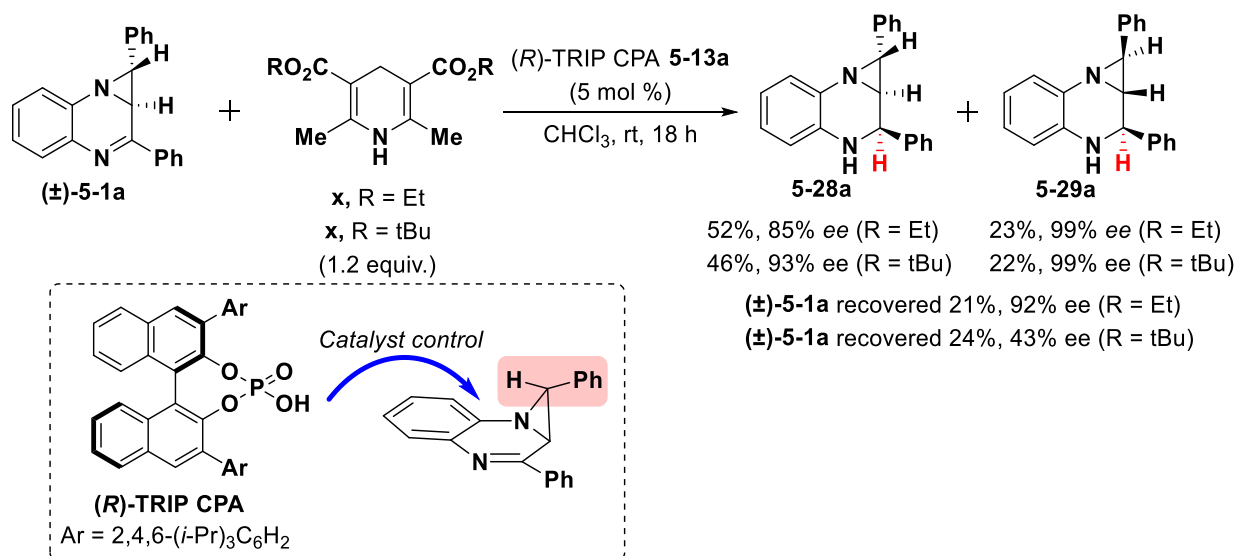


Reaction conditions led to highly diastereoselective reduction of (\pm) -**5-1a**, providing **5-28a** as the major product along with only trace amounts of **5-29a** (76% yield, 34:1 d.r.). When a bulkier Hantzsch ester **5-18d** (R = tBu) was employed, the reaction yield dropped to 61% and the

diastereomer ratio decreased to 14.4:1. These results demonstrate strong substrate control imposed by the substituted aziridine moiety on the diastereoselectivity of the reduction. Accounting for the non-planar structure of the 3-membered ring situated next to the imine functionality, we can conclude that the reduction is inherently preferred from the face opposite to the aziridine moiety. In this case, we can achieve the formation of only one specific diastereomer of the reduced product, however, due to non-chiral catalyst usage, it still exists as a racemic mixture.

Our subsequent studies were focused on exploring various chiral phosphoric acids as catalysts that may override this inherent substrate bias and dictate the reduction selectivity. Substrate (\pm)-**5-1** was subject to the reduction under the same conditions but with (*R*)-TRIP CPA **5-13a** as a chiral catalyst (Scheme A.10).

Appendix Scheme A.10. CPA-catalyzed reduction of aziridinoquinoxaline **5-1a**.

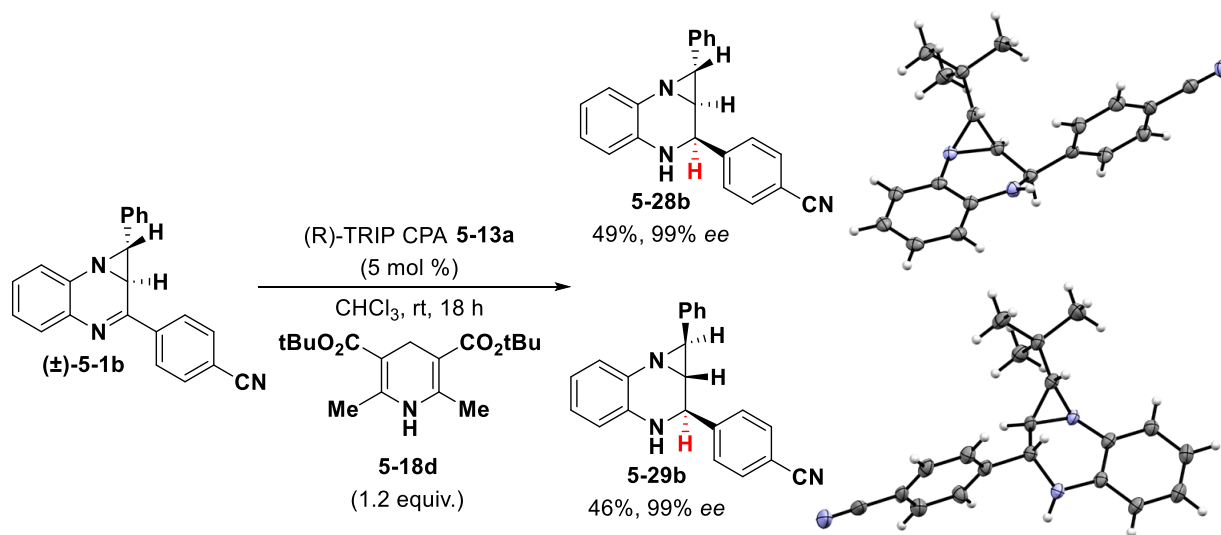


The reaction resulted in the formation of both diastereomers **5-28a** and **5-29a** in approximate 2.9:1 ratio and 75% total yield. Major diastereomer **5-28a** was formed in 85% enantiomeric excess while minor one was isolated almost in pure enantiomeric form (99% ee). The use of *tert*-butyl (instead of ethyl) Hantzsch ester **5-18d** has resulted in a slower, but more selective

reaction yielding 46% of **5-28a** in 93% ee and 22% of **5-29a** in 99% ee (2.1:1 d.r. for a mixture). Observed results indicate that catalyst control overrides the substrate control of aziridine resulting in poor diastereoselective ratios, but selective addition to imine dictated by catalyst provides high enantioselectivity of both diastereomers. As we can see, initial racemic enantiomers of (\pm)-**5-1a** under chiral reductive conditions resulted in formation of two different compounds which is exact example of parallel chiral resolution reaction. The observed results for the (*R*)-TRIP-catalyzed reduction suggest that not only product **5-28a** but also diastereomer **5-29a** and starting material **5-1a** may undergo enantioenrichment. Indeed, a more detailed analysis of the reaction mixture indicated that the reduction with ethyl substituted Hantzsch ester (1.2 equiv.) resulted in enantioenriched **5-1a** (21% yield, 92% ee). Similarly, the use of the *t*-butyl substituted Hantzsch ester **5-18d** (1.2 equiv.) also resulted in enantioenriched **5-1a** (24% yield, 43% ee).

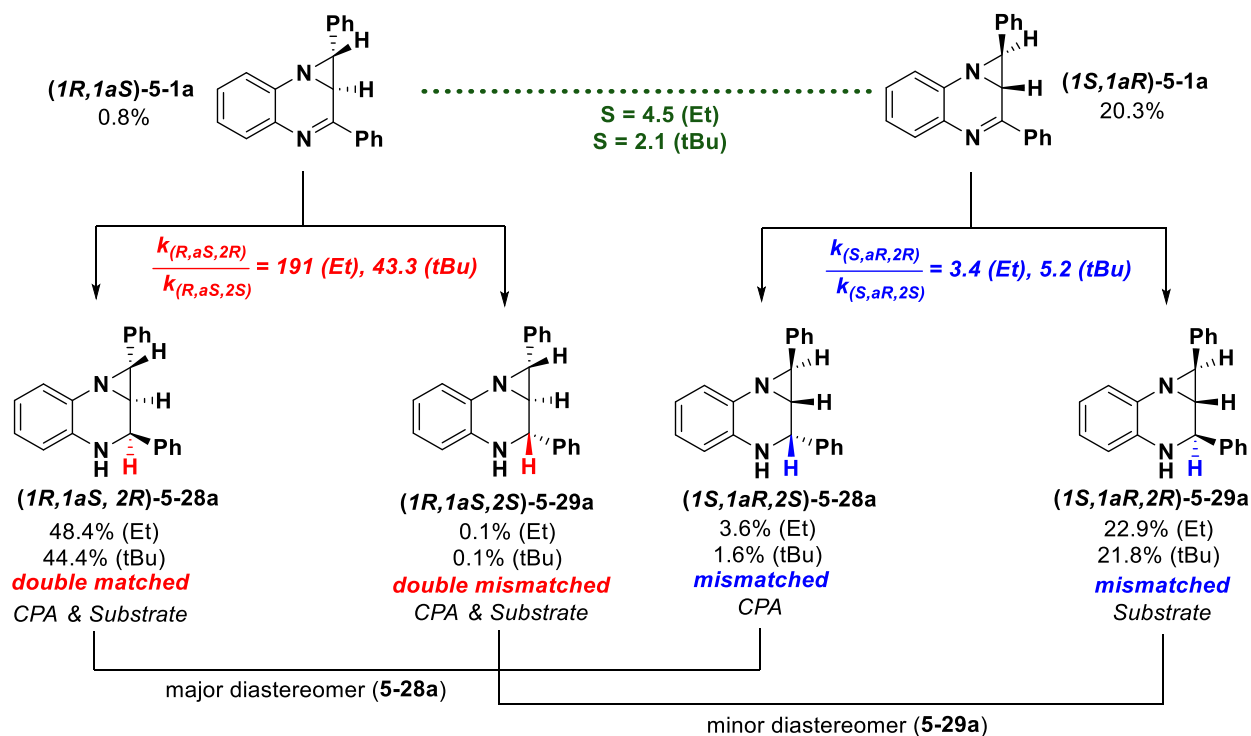
Based on the X-ray crystallographic analysis of the derivatives **5-28b** and **5-29b** synthesized by Yin-Jia Jhang (Scheme A.11) the absolute stereoisomer configurations were determined and the distribution summarized in Scheme A.12 was calculated.

Appendix Scheme A.11. Synthesis of reduced aziridinoquinoxalines and X-Ray characterization performed by Yin-Jia Jhang.



(*R*)-TRIP favors the formation of the (*R*)-configuration at the newly formed stereocenter. In the case of the substrate (*1R,1aS*)-**5-1a**, the selectivity imposed by (*R*)-TRIP could be matched with the selectivity imposed by the aziridine ring, and the resultant product (*1R,1aS,2R*)-**5-28a** is expected to be the most favored product among the four potential stereoisomers formed in this reaction.

Appendix Scheme A.12. Detailed analysis of the parallel kinetic resolution reduction of **5-1a.**

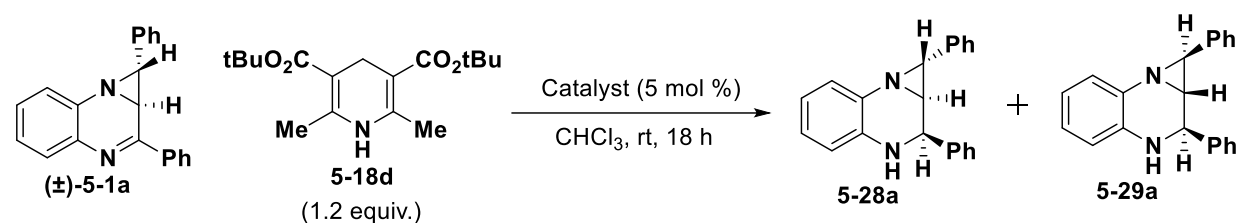


In contrast, the reduction from the *Si*-face would provide a double mismatched product (*1R,1aS,2S*)-**5-29a**, which is observed in only trace quantities in both cases. Therefore, the formation of (*1R,1aS,2R*)-**5-28a** and (*1R,1aS,2S*)-**5-29a** from (*1R,1aS*)-**5-1a** proceeds with significant rate differences ($k_{(1R,1aR,2R)}/k_{(1R,1aR,2S)} = 191$ for ethyl and 43.3 for *t*-butyl Hantzsch esters). In contrast, the reduction of the enantiomer (*1S,1aR*)-**5-1a** has a mismatch between the catalyst-imposed and substrate-imposed selectivities. The observed selectivities suggest that the catalyst-controlled product (*1S,1aS,2R*)-**5-29a** formation is favored over the substrate-controlled

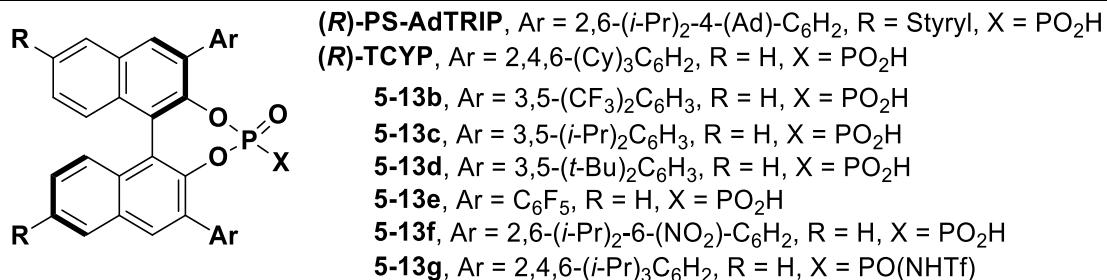
formation of **(1*S*,1*aS*,2*S*)-5-28a** ($k_{(1*S*,1*aS*,2*S*)/k_{(1*S*,1*aS*,2*Rt*-butyl Hantzsch esters). Consistent with this model, the **(1*R*,1*aS*)-5-1a** enantiomer is more reactive than **(1*S*,1*aR*)-5-1a**, and kinetic resolution of these enantiomers is also observed under the reduction conditions ($S = 4.5$ for ethyl Hantzsch ester, and $S = 2.1$ for *t*-butyl Hantzsch ester).$

The subsequent studies on CPA catalyst optimization for the reaction were performed by current graduate student Yin-Jia Jhang (Table A.1).

Appendix Table A.1. Chiral Phosphoric Acid catalyst optimization performed by Yin-Jia Jhang



Entry	Catalyst	d.r.	Yield (11a), %	ee (11a), %
1	(<i>R</i>)-5-13b	1:0	49	19
2	(<i>R</i>)-5-13c	1:0	54	8
3	(<i>S</i>)-5-13d	1:0	36	-12
4	(<i>S</i>)-5-13e	9.5:1	58	-36
5	(<i>R</i>)-TCYP	2.5:1	40	89
6	PS-AdTRIP	2.0:1	55	81
7	(<i>R</i>)-5-13f	2.3:1	42	78
8	(<i>R</i>)-5-13g	6.6:1	53	49



The exploration of (*R*)-BINOL-based CPAs containing *meta*-substituted 3,3'-aryl groups with *t*-butyl substituted Hantzsch ester resulted in slow, but selective formation of **5-28a** and no diastereomer **5-29a** was observed (entries 1-3). The moderate enantioselectivities (19% ee for Ar

= 3,5-(CF₃)₂C₆H₃, 8% ee for Ar = 3,5-(*i*-Pr)₂C₆H₃, and -12% ee for Ar = 3,5-(*t*-Bu)₂C₆H₃ coupled with the exclusive formation of **5-28a** indicate that these reductions proceed under substrate control and the catalyst chirality has little impact on the facial selectivity of the reduction. Similarly, the reaction with pentafluorophenyl substituted catalyst **5-13e** (entry 4) favored the formation of **5-28a** (9.5:1 d.r., 58% yield, -36% ee). As the conditions utilizing TRIP CPA catalyst remained the most efficient, evaluating variants of TRIP (entries 5-8) were performed that included using **TCYP**, **PS-AdTRIP**, 6,6'-dinitrosubstituted TRIP (**5-13f**) as well as *N*-triflyl phosphoramidate catalyst **5-13g**. These further attempts did not lead to improvements in the enantioselectivity of this reaction and subsequent studies were carried out with standard TRIP catalysts. With established conditions, Yin-Jia Jhang also performed substrate scope screening, resulting in the parallel kinetic resolution of 16 different aziridinoquinoxalines that led to obtaining both diastereomers with moderate yields and high enantioselectivity (32-61% yield, 64-99% ee, for the (*S,S,R*)-diastereomers **5-28** and 7-45% yield, 97-99% ee for the (*R,R,S*)-diastereomers **5-28**). Details can be found in the publication by Jhang et. al.¹⁶

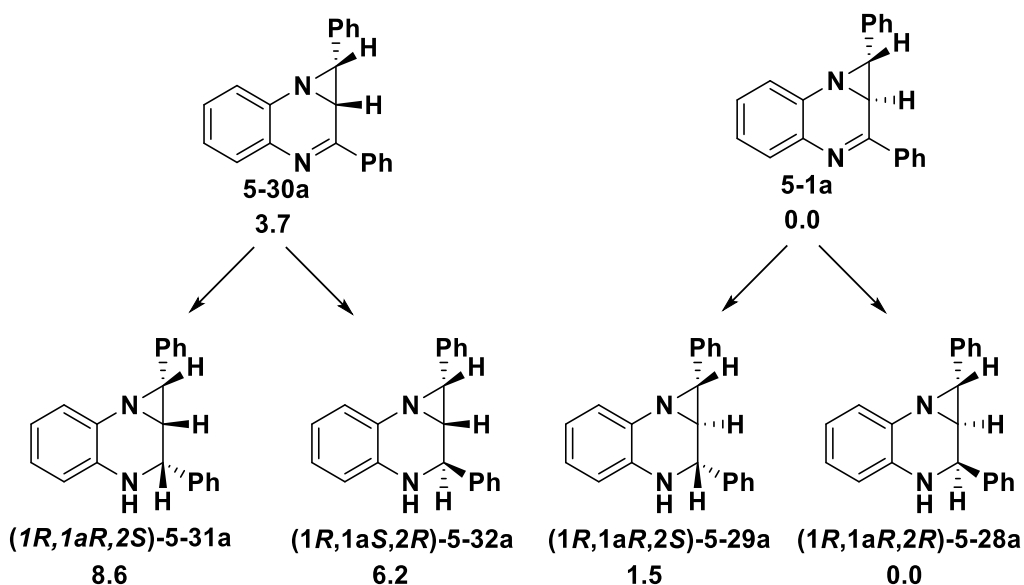
A.4 Ring-opening of the tetrahydroazirino[1,2-a]quinoxalines

Based on the results of the previous chapter we established the method of enantioselective parallel kinetic resolution of the aziridinoquinoxalines as the first step of the proposed sequence of the two-step modifications (Scheme A.2). Our next step is to develop ring-opening of the reduced aziridinoquinoxalines to produce chiral tetrahydroquinoxalines with three contiguous stereocenters.

First, we computed a relative stability (based on Gibbs free energies) of all possible diastereomers of the reduced products using DFT (Scheme A.13). Structures were optimized at B3LYP/6-31+G** (also used for entropy factor calculations) and the electronic energy component

was evaluated at ω B97X-D3/cc-pVTZ level of theory. We also computed reduced products **5-31a** and **5-32a** with *cis*-ring junction that could be theoretically generated from aziridinoquinoxaline **5-30a**. As expected, *cis*-configuration of the aziridine moiety brings significant ring strain to both the initial aziridine (3.7 kcal/mol destabilization) and to its reduced products **5-31a** and **5-32a**, which are 8.6 and 6.2 kcal/mol less stable than diastereomer **5-28a**, correspondingly. That aligns well with the fact that no *cis*-configured stereoisomers were formed from the mixture of *cis*- and *trans*-dibromo chalcones **5-8** during the aziridinoquinoxaline synthesis. For both pairs of diastereomers the molecule with the same facial orientation of phenyl rings bears excessive ring strain energy of ~ 1.5 kcal/mol.

Appendix Scheme A.13. Relative stabilities of all possible diastereomers of tetrahydroazirino[1,2-a]quinoxalines

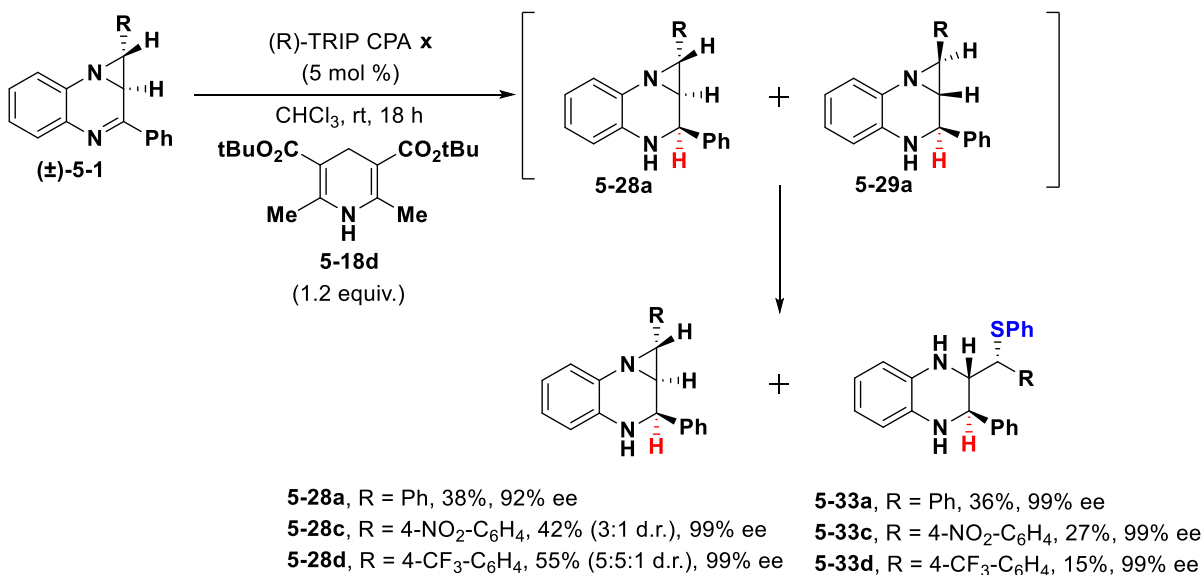


We surmised that this feature might be used to selectively functionalize diastereomer **5-29a** to perform parallel kinetic resolution of diastereomer mixture of **5-28a** and **5-29a**, especially in cases where the direct separation of them via column chromatography was not possible. Indeed, the aryl-substituted aziridines **5-29a**, **5-29c**, and **5-29d** were found to be significantly more reactive with

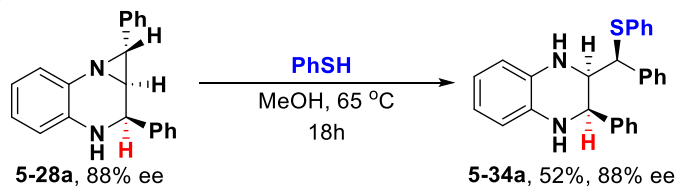
thiophenol than their diastereomers **5-28a**, **5-28c**, and **5-28d** (Scheme A.14A). Thus, simple addition of thiophenol to the reaction mixture at the end of the reduction leads to quantitative and selective formation of the ring-opened product **5-33a** in 99% ee after stirring the reaction mixture for 24 hours at room temperature. The resulting reaction mixture could be conveniently purified to separate **5-28a** from **5-33a**. In this case, we observe classical S_N2 reaction resulting in ring-opening via C-N bond cleavage and with full transfer of the enantiomeric excess from diastereomers **5-29** (isolated before with 99% ee)¹⁶ to the reaction products (also isolated as single diastereomer and 99% ee).

Appendix Scheme A.14. Nucleophilic ring-opening of tetrahydroazirino[1,2-a]quinoxalines

A. Parallel resolution of the diastereomers *in-situ*



B. Ring-opening of the major diastereomer



It is also noteworthy that major diastereomer **5-28a** could also undergo a ring-opening reaction with thiophenol to produce diastereomeric product **5-34a** (Scheme A.14B). However, as predicted

by the computations (Scheme A.13), the major diastereomer has less ring strain and is more stable than minor diastereomer **5-29**. Therefore, the ring-opening process is much slower and requires elevated temperature (65 °C) to achieve the reaction.

A.5 Results and conclusions

In summary, a highly selective parallel kinetic resolution leading to valuable and previously unknown aziridinoquinoxalines **5-28** and **5-29** from readily available racemic fused heterocycles **5-1** has been developed. This resolution was achieved using transfer hydrogenation conditions with a Hantzsch ester and commercially available (*R*)-TRIP CPA as the catalyst. The use of (*R*)-TRIP CPA was essential for overcoming the selectivity imposed by the aziridine ring. The detailed analysis of the product and starting material distribution suggests a complex interplay of the catalyst- and substrate-imposed factors affecting the enantio- and diastereoselectivities. Thus, a highly enantioselective formation of the diastereomer **5-29a** (97-99% ee) was observed in all cases as the enantiomer (*1R,1aR,2S*)-**5-29a** would result from a double mismatched reaction. Similarly, high enantioselectivities for **5-28a** (34-99% ee) are due to the faster formation of the double-matched enantiomer (*1R,1aR,2R*)-**5-29a** in comparison to the mismatched enantiomer (*1S,1aS,2S*)-**5-28a**, which suffers from the opposing catalyst and substrate-dictated selectivities. The chiral aziridinoquinoxalines could be readily functionalized by reactions with thiophenol to produce previously inaccessible tetrahydroquinoxalines **5-33** and **5-34** containing three contiguous stereocenters. To the best of our knowledge, this is the first example of the formation of chiral quinoxalines such as **5-33** or **5-34** containing three contiguous stereocenters, and our protocol offers a streamlined synthesis of such compounds from the readily available materials and catalysts.

A.6 Experimental information

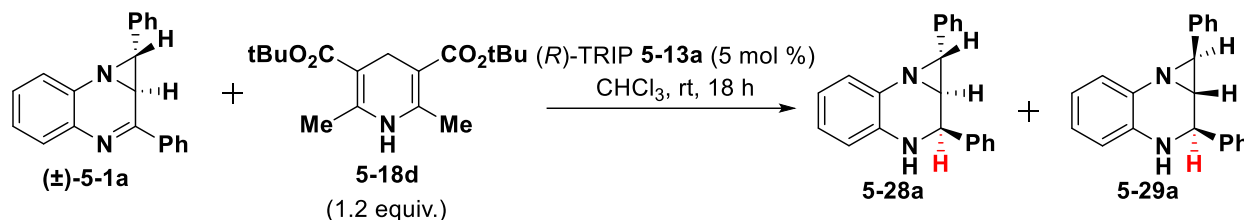
Methods and Reagents: Unless otherwise stated, all reagents and solvents (ACS grade) were purchased and used as received without further purification. Dichloromethane (CH_2Cl_2) was first purged with nitrogen and then dried over activated alumina using a solvent purification system. All reactions were carried out in oven-dried glassware with magnetic stirring under a positive nitrogen (N_2) atmosphere with the standard Schlenk line technique. Heating was achieved by use of a silicone bath with heating controlled by an electronic contact thermometer. Reactions were monitored by thin layer chromatography (TLC) on silica gel precoated glass plates (0.25 mm, SiliCycle, SiliaPlate), visualized by UV (254 nm) and cerium ammonium molybdate (CAM) staining solution. Deionized water was used in the preparation of all aqueous solutions and for all aqueous extractions. Flash column chromatography (FCC) was performed on SiliCycle SilicaFlash P60 (230-400 mesh). Enantiomeric excess was determined by HPLC analysis using a Waters e2695 Separations Module with a Waters 2998 photodiode array detector and The Waters Investigator SFC system (supercritical CO_2 /Methanol) with a Waters 2998 photodiode array detector.

Instrumentation: All ^1H , ^{13}C NMR spectra were measured on Bruker Avance Neo 500 (500 MHz) spectrometer, and chemical shifts (δ) were denoted in parts per million (ppm) with residual solvent signals as internal standard (chloroform at 7.26 ppm for ^1H spectra; chloroform at 77.16 ppm for ^{13}C spectra). All ^{19}F NMR spectra were measured on a Varian NMR (600 MHz) spectrometer and chemical shifts (δ) were denoted in parts per million (ppm) and are referenced to CFCl_3 at 0 ppm. The following abbreviations were used to explain the multiplicities: s = singlet, br = broad, d = doublet, t = triplet, q = quartet, dd = doublet of doublets, td = triple of doublets, dt = double of triplets, m = multiplet. Coupling constants (J) are reported in Hertz (Hz). High-resolution mass spectroscopy (HRMS) was performed on Micromass AutoSpec Ultima or VG

(Micromass) 70-250-S Magnetic sector mass spectrometers in the University of Michigan mass spectrometry laboratory. Melting points were measured using MEL-TEMP® 3.0 instrument and borosilicate glass capillary tubes (1.5x90 mm).

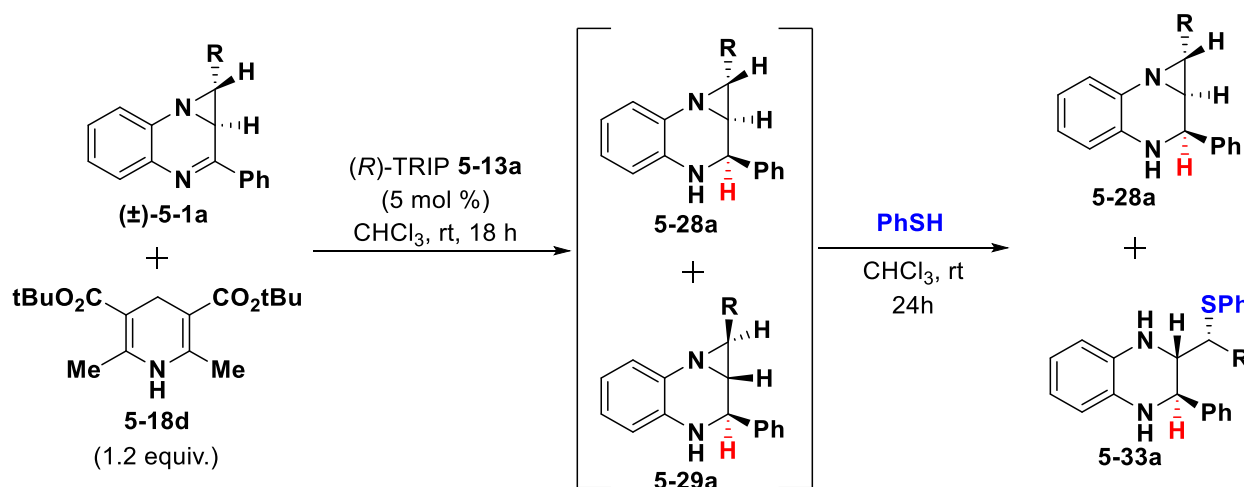
General procedure for enantioselective parallel kinetic resolution by transfer hydrogenation

(Procedure A)



An oven-dried 2-dram vial with a magnetic stir bar and a septum containing corresponding substrate (\pm)-**5-1a** (0.1 mmol, 1 equiv), (*R*)-TRIP **5-13a** (3.8 mg, 0.005 mmol, 5 mol%) and *tert*-butyl 2,6-dimethyl-1,4-dihydropyridine-3,5-dicarboxylate **5-18d** (37 mg, 0.12 mmol, 1.2 equiv) was vacuumed for 2 minutes. The whole system was backfilled with N_2 , and then 2.0 mL of anhydrous CHCl_3 was added to the vial. The resulting mixture was then stirred at room temperature for 18 h and quenched by evaporating the solvent under reduced pressure. The crude residue thus obtained was purified by FCC.

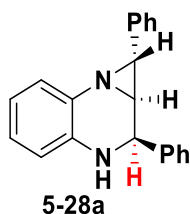
General procedure for one-pot functionalization (Procedure B)



An oven-dried 2-dram vial with a magnetic stir bar and a septum containing corresponding substrate (\pm)-**5-1** (0.1 mmol, 1 equiv), (*R*)-TRIP **5-13a** (3.8 mg, 0.005 mmol, 5 mol%) and di-*tert*-butyl 2,6-dimethyl-1,4-dihydropyridine-3,5-dicarboxylate **5-18d** (37 mg, 0.12 mmol, 1.2 equiv) was vacuumed for 2 minutes. The whole system was backfilled with N₂, and then 2 mL of anhydrous CHCl₃ was added to the vial. The resulting mixture was stirred at room temperature. After 18 hours, PhSH (10.2 μ L, 0.1 mmol, 1 equiv) was added and stirred for another 24 hours. The resulting mixture was then quenched by evaporating the solvent under reduced pressure. The crude residue thus obtained was purified by FCC.

A.7 Characterization data

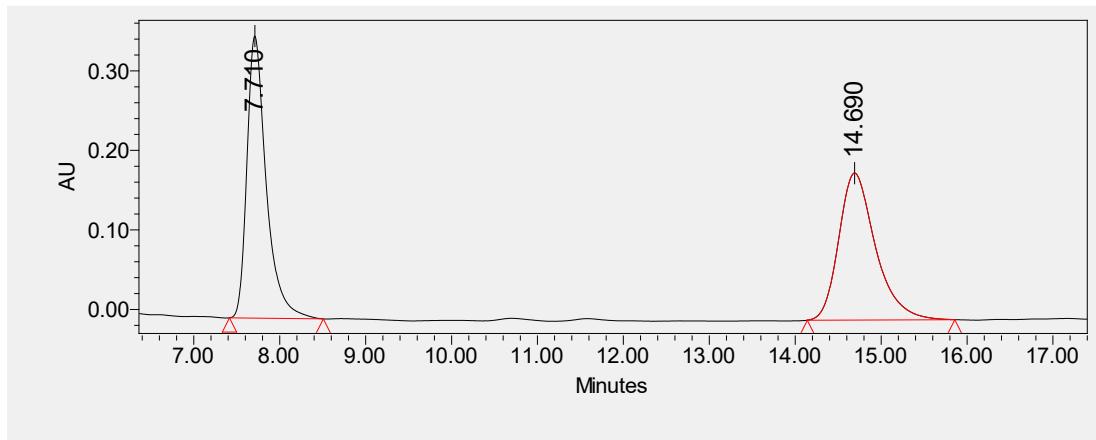
(1*R*,1*aR*,2*R*)-1,2-diphenyl-1,1*a*,2,3-tetrahydroazirino[1,2-*a*]quinoxaline (**5-28a**)



The reaction was conducted with 0.1 mmol of (\pm)-**5-1a** following the general procedure A. The crude product was purified by FCC (2.5% EtOAc in hexanes \rightarrow 15% EtOAc in hexanes) to afford **5-28a** (14 mg, 46% yield, 93% ee) as yellow solid, (mp 100.2-101.4 $^{\circ}$ C). Large scale experiment was performed according to general procedure A with reaction scale up to 1 mmol (296 mg) of (\pm)-**5-1a**, (*R*)-TRIP (38 mg, 0.05 mmol, 5 mol%) and di-*tert*-butyl-2,6-dimethyl-1,4-dihydropyridine-3,5-dicarboxylate (371 mg, 1.2 mmol, 1.2 equiv) in 20 mL of CHCl₃ to afford **5-28a** after FCC (101 mg, 34% yield, 88% ee). ¹H NMR (500 MHz, CDCl₃): δ 7.53 – 7.49 (m, 2H), 7.41 – 7.37 (m, 3H), 7.35 – 7.27 (m, 5H), 7.24 – 7.20 (m, 1H), 6.99 (td, *J* = 7.6, 1.5 Hz, 1H), 6.77 (td, *J* = 7.6, 1.4 Hz, 1H), 6.60 (dd, *J* = 7.9, 1.4 Hz, 1H), 4.65 (d, *J* = 2.5 Hz, 1H), 3.94 (d, *J* = 3.5 Hz, 1H), 3.82 (br s, 1H), 3.05 – 3.01 (m, 1H); ¹³C NMR (126 MHz, CDCl₃): δ 140.8, 139.7, 138.8, 135.3, 129.1, 128.5, 128.5, 127.7, 127.5, 127.3, 126.6, 125.6, 119.6, 115.3, 54.8, 53.4, 43.3; HRMS (ESI-TOF) (*m/z*): [M+H]⁺ for C₂₁H₁₉N₂ calcd: 299.1543, found: 299.1540; [α]_D²⁵ = -

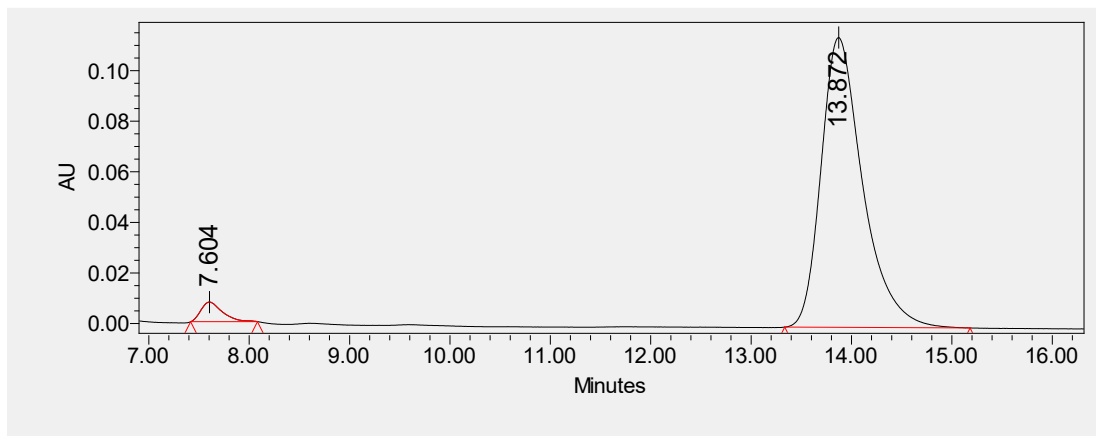
287.04 (c = 0.024, CH₂Cl₂) ; **HPLC**: (Chiralpak IA column, 80:20 hexanes/ isopropanol, 1 mL/min, I = 254 nm), tr = 7.7 min (minor), 14.7 min (major).

Racemic compound HPLC Traces:



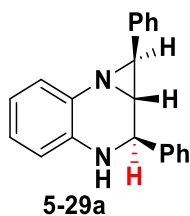
	Retention Time	Area	% Area
1	7.710	5542749	50.26
2	14.690	5484347	49.74

Chiral HPLC Traces:



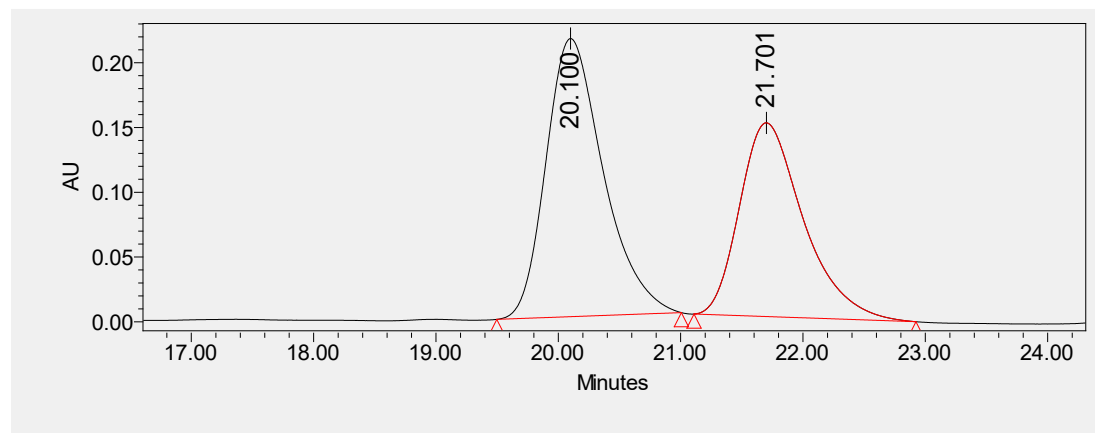
	Retention Time	Area	% Area
1	7.604	115241	3.37
2	13.872	3299609	96.63

(1*S*,1*aS*,2*R*)-1,2-diphenyl-1,1*a*,2,3-tetrahydroazirino[1,2-*a*]quinoxaline (5-29a)



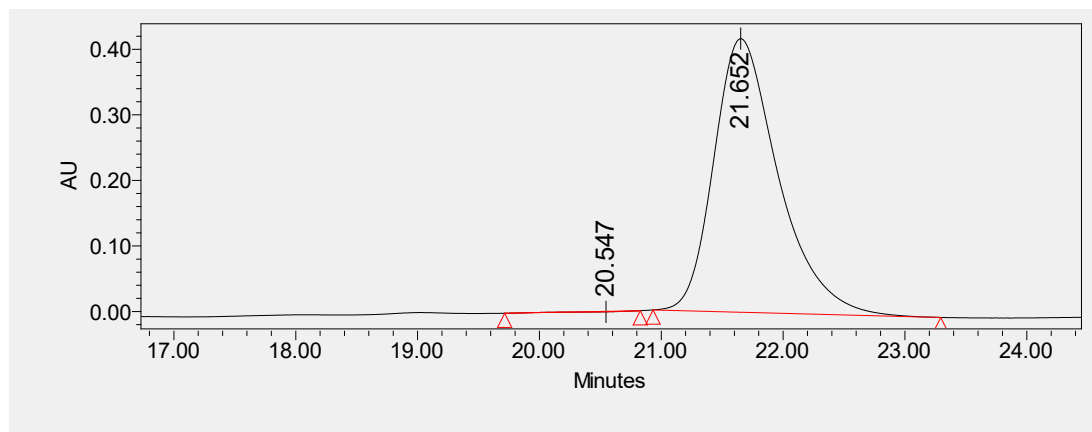
The reaction was conducted with 0.1 mmol of (\pm)-**5-1a** following the general procedure A. The crude product was purified by FCC (2.5% EtOAc in hexanes \rightarrow 15% EtOAc in hexanes) to afford **5-29a** (7 mg, 22% yield, 99% ee) as yellow oil. Large scale experiment was performed according to general procedure A with reaction scale up to 1 mmol (296 mg) of (\pm)-**5-1a**, (*R*)-TRIP (38 mg, 0.05 mmol, 5 mol%) and di-*tert*-butyl-2,6-dimethyl-1,4-dihydropyridine-3,5-dicarboxylate (371 mg, 1.2 mmol, 1.2 equiv) in 20 mL of CHCl₃ to afford **5-29a** after FCC (56 mg, 19% yield, 99% ee). ¹H NMR (500 MHz, CDCl₃): δ 7.47 – 7.43 (m, 2H), 7.38 – 7.27 (m, 9H), 6.93 (td, *J* = 7.6, 1.5 Hz, 1H), 6.78 (td, *J* = 7.6, 1.4 Hz, 1H), 6.62 (dd, *J* = 7.8, 1.4 Hz, 1H), 4.33 (d, *J* = 3.7 Hz, 1H), 3.88 (br s, 1H), 3.26 (d, *J* = 3.0 Hz, 1H), 2.88 (t, *J* = 3.4 Hz, 1H); ¹³C NMR (126 MHz, CDCl₃): δ 142.6, 139.0, 138.3, 136.1, 129.1, 128.5, 128.2, 127.5, 127.3, 126.4, 125.7, 124.6, 119.8, 115.6, 55.3, 50.7, 49.7; HRMS (ESI-TOF) (*m/z*): [M+H]⁺ for C₂₁H₁₉N₂ calcd: 299.1543, found: 299.1536; [α]_D²⁵ = +47.52 (*c* = 0.011, CH₂Cl₂); HPLC: (Chiralpak IA column, 90:10 hexanes/isopropanol, 0.5 mL/min, I = 254 nm), *t*_r = 20.1 min (minor), 21.7 min (major).

Racemic compound HPLC Traces:



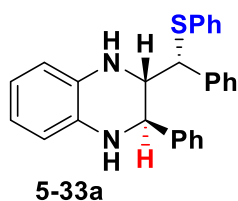
	Retention Time	Area	% Area
1	20.100	6992769	56.33
2	21.701	5421770	43.67

Chiral HPLC Traces:



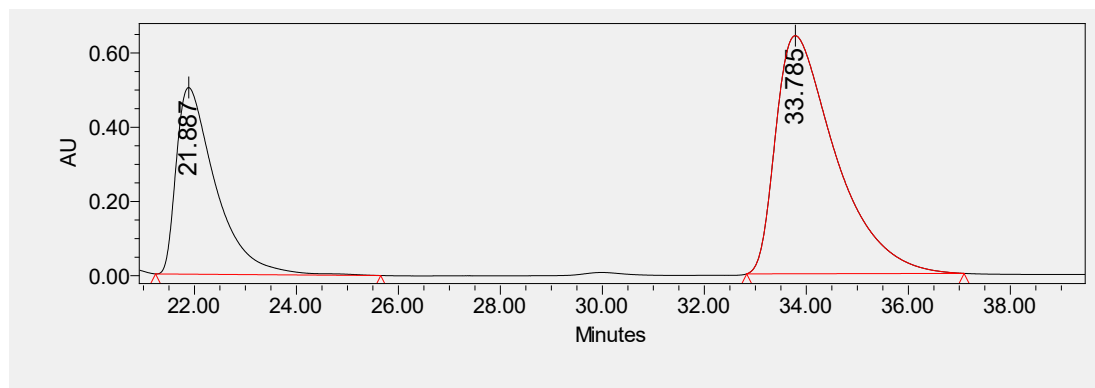
	Retention Time	Area	% Area
1	20.547	20778	0.13
2	21.652	15378969	99.87

(2*R*,3*S*)-2-phenyl-3-((*R*)-phenyl(phenylthio)methyl)-1,2,3,4-tetrahydroquinoxaline (5-33a)



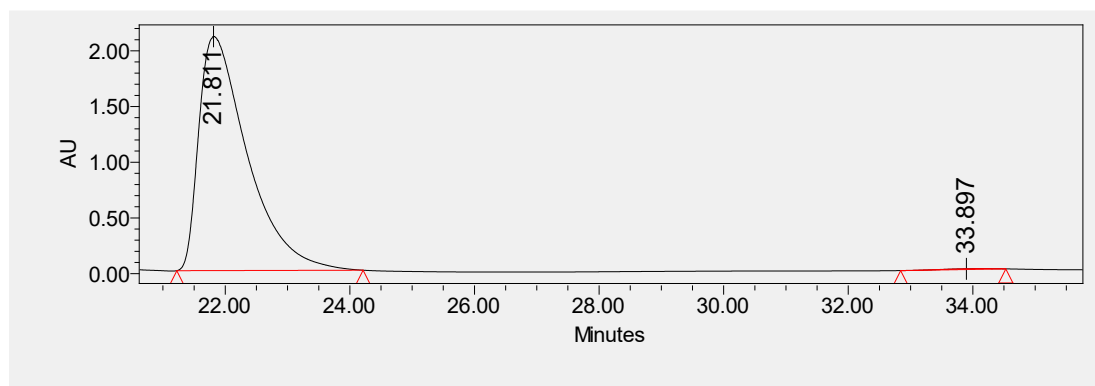
The reaction was conducted with 0.1 mmol of (\pm)-**5-1a** following the general procedure A. The crude product was purified by FCC (2.5% EtOAc in hexanes \rightarrow 15% EtOAc in hexanes) to afford **5-33a** (15 mg, 36% yield, 99% ee) as yellow oil. $^1\text{H NMR}$ (500 MHz, CDCl_3): δ 7.34 – 7.26 (m, 6H), 7.26 – 7.23 (m, 4H), 7.23 – 7.17 (m, 5H), 6.64 (td, $J = 7.5, 1.5$ Hz, 1H), 6.59 (td, $J = 7.5, 1.6$ Hz, 1H), 6.54 (dd, $J = 7.5, 1.6$ Hz, 1H), 6.39 (dd, $J = 7.7, 1.5$ Hz, 1H), 4.71 (d, $J = 4.5$ Hz, 1H), 4.28 (d, $J = 7.4$ Hz, 1H), 4.05 (br s, 1H), 3.93 (br s, 1H), 3.64 (dd, $J = 7.4, 4.5$ Hz, 1H); $^{13}\text{C NMR}$ (126 MHz, CDCl_3): δ 142.8, 138.6, 134.3, 133.1, 132.1, 131.4, 129.1, 129.1, 128.6, 128.5, 127.9, 127.8, 127.4, 127.3, 119.0, 118.5, 114.9, 113.4, 58.1, 55.7, 54.9; **HRMS (ESI-TOF)** (m/z): $[\text{M}+\text{H}]^+$ for $\text{C}_{27}\text{H}_{25}\text{N}_2\text{S}$ calcd: 409.1733, found: 409.1727; $[\alpha]_D^{25} = -19.12$ ($c = 0.018$, CH_2Cl_2); **HPLC**: (Chiralpak ODH column, 95:5 hexanes/ isopropanol, 0.5 mL/min, $I = 254$ nm), $t_r = 21.9$ min (major), 33.8 min (minor).

Racemic compound HPLC Traces:



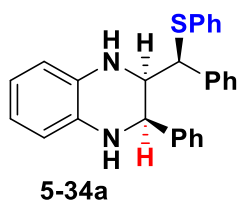
	Retention Time	Area	% Area
1	21.887	27050974	34.06
2	33.785	52369905	65.94

Chiral HPLC Traces:



	Retention Time	Area	% Area
1	21.811	113719463	99.68
2	33.897	363833	0.32

(2R,3R)-2-phenyl-3-((S)-phenyl(phenylthio)methyl)-1,2,3,4-tetrahydroquinoxaline (5-34a)

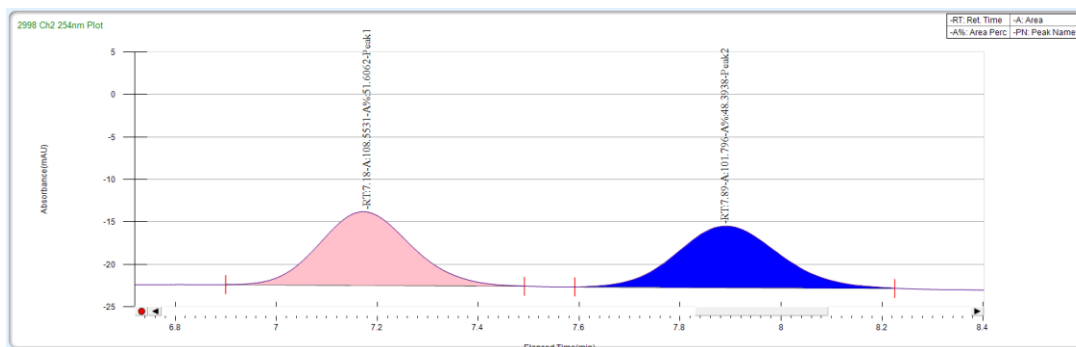


The reaction was carried out using enantiomerically enriched substrate **5-34a** (88% ee) as the starting material. Compound **5-28a** (0.1 mmol, 29.8 mg) was placed in an oven-dried vial and capped with a septum. The vial was vacuumed for 2 minutes and refilled with nitrogen. 2 mL of methanol was added followed by thiophenol (0.12 mmol, 15 μ L). The reaction mixture was heated to 65 $^{\circ}$ C with stirring for 18 hours. After that, the solvent was evaporated under reduced pressure,

and crude material was subjected to FCC (5% EtOAc in hexanes → 20% EtOAc in hexanes) to give 21.1 mg (52% yield, 88% ee) of compound **5-34a** as a yellow oil.

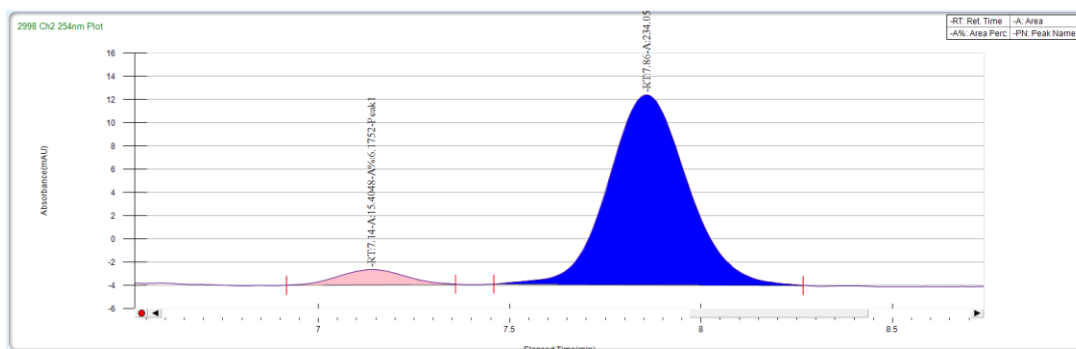
¹H NMR (500 MHz, CD₂Cl₂): δ 7.54 – 7.49 (m, 2H), 7.32 (dd, J = 5.2, 2.0 Hz, 3H), 7.22 (dd, J = 4.5, 2.0 Hz, 3H), 7.15 – 7.05 (m, 5H), 6.99 – 6.92 (m, 2H), 6.62 – 6.56 (m, 1H), 6.48 (dd, J = 8.9, 6.9 Hz, 2H), 6.27 (dd, J = 7.6, 1.4 Hz, 1H), 5.17 (d, J = 3.1 Hz, 1H), 4.39 (s, 1H), 4.06 (dd, J = 10.9, 3.1 Hz, 1H), 3.38 (d, J = 10.9 Hz, 1H), 3.33 (s, 1H); ¹³C NMR (126 MHz, CD₂Cl₂): δ 141.8, 138.5, 133.1, 132.9, 132.6, 132.1, 128.8, 128.6, 128.6, 128.5, 128.4, 128.1, 127.8, 127.5, 127.5, 119.7, 117.7, 114.3, 113.4, 56.5, 55.6, 55.4; [α]_D²⁵ = +179.08 (c = 0.025, CH₂Cl₂); HRMS (ESI-TOF) (m/z): [M+H]⁺ for C₂₇H₂₅N₂S calcd: 409.1733, found: 409.1730; SFC: (Chiralpak ODH column, 80:20 carbon dioxide/methanol, 3.5 mL/min, I = 254 nm), tr = 7.1 min (minor), 7.9 min (major).

Racemic compound SFC Traces:



Peak Name	Area Percent	Area	Retention Time	Height
Peak1	51.6062	108.5531	7.18 min	8.6717
Peak2	48.3938	101.796	7.89 min	7.2539

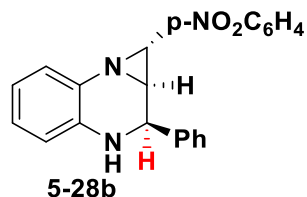
Chiral SFC Traces:



Peak Name	Area Percent	Area	Retention Time	Height
Peak1	15.4488	7.52	7.52 min	~4
Peak2	84.5512	7.93	7.93 min	~13

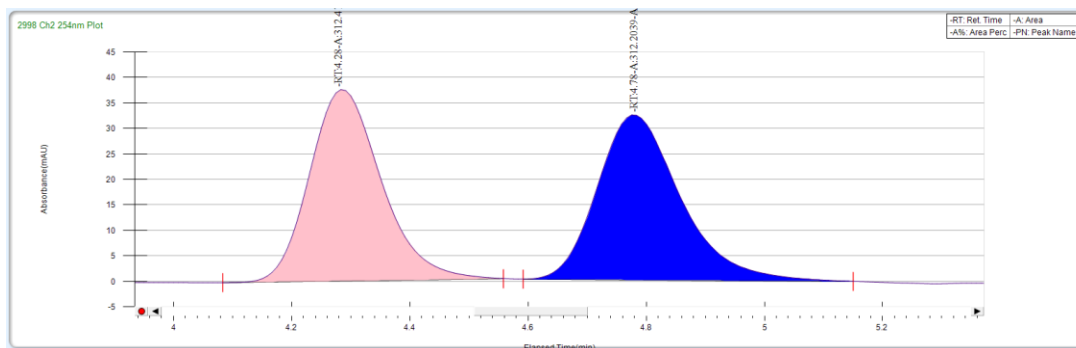
Peak1	6.1752	15.4048	7.14 min	1.3099
Peak2	93.8248	234.0585	7.86 min	16.3674

(1*R*,1*aR*,2*R*)-1-(4-nitrophenyl)-2-phenyl-1,1*a*,2,3-tetrahydroazirino[1,2-*a*]quinoxaline (5-28b)



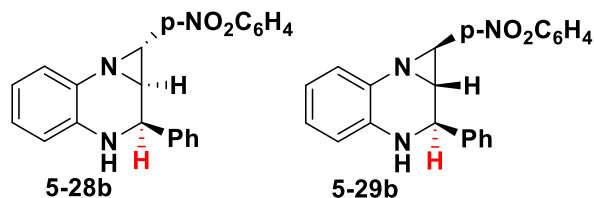
The reaction was conducted with 0.1 mmol of (\pm)-**5-1b** following the general procedure B using BPPA as a catalyst. The crude product was purified by FCC (5% EtOAc in hexanes \rightarrow 20% EtOAc in hexanes) to afford **5-28b** (29 mg, 85% yield, racemic compound) as yellow solid (mp 98.6-99.4 °C). **¹H NMR** (500 MHz, CDCl₃): δ 8.19 – 8.13 (m, 2H), 7.52 (s, 2H), 7.48 (d, J = 8.7 Hz, 2H), 7.45 – 7.37 (m, 4H), 7.05 (td, J = 7.6, 1.5 Hz, 1H), 6.82 (td, J = 7.6, 1.4 Hz, 1H), 6.65 (dd, J = 7.8, 1.4 Hz, 1H), 4.72 – 4.68 (m, 1H), 4.07 (d, J = 3.3 Hz, 1H), 3.88 (s, 1H), 3.02 (q, J = 2.7 Hz, 1H); **¹³C NMR** (126 MHz, CDCl₃): δ 147.1, 146.6, 140.2, 139.6, 134.3, 129.1, 128.6, 127.4, 127.4, 127.1, 126.0, 123.7, 119.7, 115.3, 55.9, 53.3, 42.1; **HRMS (ESI-TOF)** (m/z): [M+H]⁺ for C₂₁H₁₈N₃O₂ calcd: 344.1394, found: 344.1385; **SFC**: (Chiralpak ASH column, 80:20 carbon dioxide/methanol, 3.5 mL/min, I = 254 nm), t_r = 4.3 min (minor), 4.8 min (major).

Racemic compound SFC Traces:



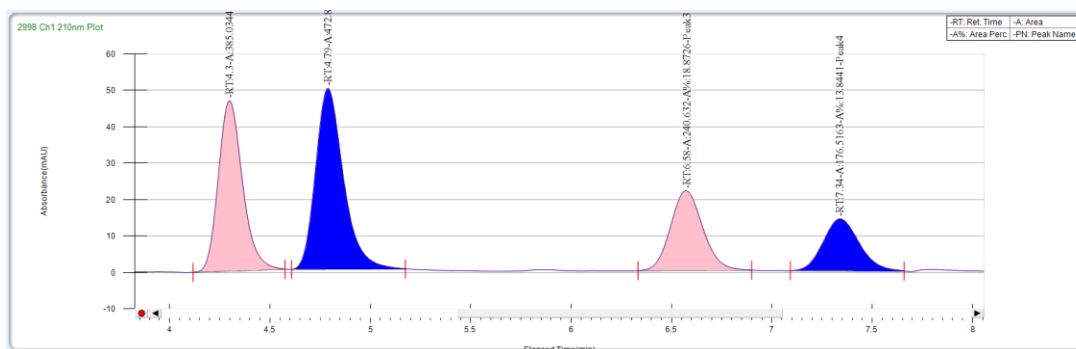
Peak Name	Area Percent	Area	Retention Time	Height
Peak1	50.0166	312.4107	4.28 min	37.5867
Peak2	49.9834	312.2039	4.78 min	32.377

(1*R*,1*aR*,2*R*)-1-(4-nitrophenyl)-2-phenyl-1,1*a*,2,3-tetrahydroazirino[1,2-*a*]quinoxaline and (1*S*,1*aS*,2*R*)-1-(4-nitrophenyl)-2-phenyl-1,1*a*,2,3-tetrahydroazirino[1,2-*a*]quinoxaline (5-28b+5-29b)



The reaction was conducted with 0.1 mmol of (\pm)-**5-1b** following the general procedure B. The crude product was purified by FCC (5% EtOAc in hexanes \rightarrow 20% EtOAc in hexanes) to afford mixture of **5-28b** and **5-29b** (26 mg, 76%, yield, 1.5:1 dr, 94% and 99 % ee before resolution with thiophenol; and 14.5 mg, 42%, yield, 3:1 dr, 94% and 99% ee after resolution with thiophenol) as yellow solid (mp 80.7-82.4 °C). **¹H NMR** (500 MHz, CDCl₃): δ 8.15 – 8.09 (m, 2H), 8.10 – 8.03 (m, 3H), 7.48 – 7.42 (m, 5H), 7.40 – 7.21 (m, 14H), 6.96 (td, $J = 7.6$, 1.5 Hz, 2H), 6.89 (td, $J = 7.6$, 1.5 Hz, 1H), 6.72 (tdd, $J = 7.4$, 5.5, 1.3 Hz, 2.5H), 6.55 (ddd, $J = 7.9$, 2.9, 1.3 Hz, 2.5H), 4.63 – 4.59 (m, 1.5H), 4.35 (d, $J = 3.3$ Hz, 1H), 3.97 (d, $J = 3.3$ Hz, 1.5H), 3.84 (s, 1.5H), 3.78 (s, 1H), 3.35 (d, $J = 2.8$ Hz, 1H), 2.92 (q, $J = 2.7$ Hz, 1.5H), 2.82 (t, $J = 3.1$ Hz, 1H); **¹³C NMR** (126 MHz, CDCl₃): δ 147.2, 147.1, 146.6, 146.6, 142.1, 140.2, 139.6, 137.8, 135.0, 134.3, 129.1, 129.1, 128.6, 128.3, 127.4, 127.4, 127.1, 127.0, 126.0, 125.8, 125.2, 123.7, 123.7, 119.8, 119.7, 115.6, 115.3, 55.9, 54.6, 53.3, 51.8, 47.9, 42.1; **HRMS (ESI-TOF)** (m/z): [M+H]⁺ for C₂₁H₁₈N₃O₂ calcd: 344.1394, found: 344.1398; **SFC**: (Chiralpak ASH column, 80:20 carbon dioxide/methanol, 3.5 mL/min, I = 210 nm), $t_r = 4.3$ min (**5-28b**, minor), 4.8 min (**5-28b**, major), $t_r = 6.6$ min (**5-29b**, major), 7.3 min (**5-29b**, minor).

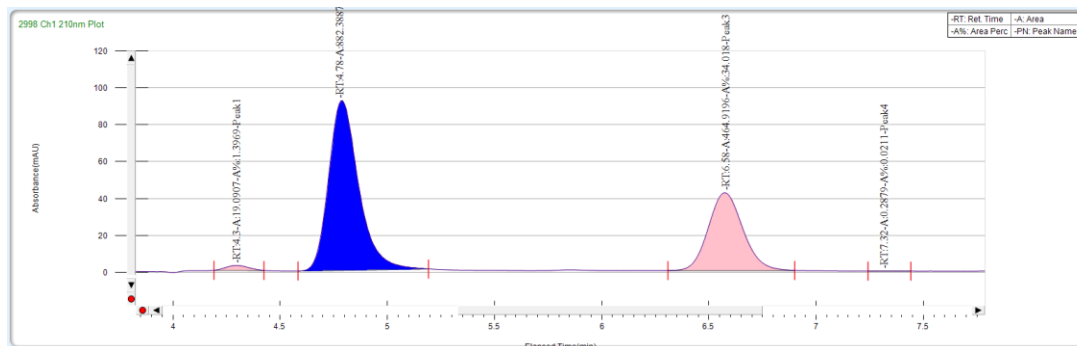
Racemic compound SFC Traces:



Peak Name	Area Percent	Area	Retention Time	Height
-----------	--------------	------	----------------	--------

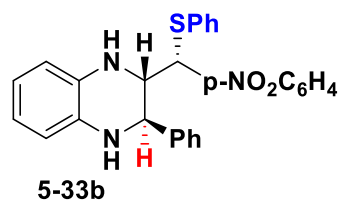
Peak1	30.198	385.0344	4.3 min	46.8922
Peak2	37.0853	472.8505	4.79 min	49.7065
Peak3	18.8726	240.632	6.58 min	21.9191
Peak4	13.8441	176.5163	7.34 min	14.3112

Chiral SFC Traces:



Peak Name	Area Percent	Area	Retention Time	Height
Peak1	1.3969	19.0907	4.3 min	2.7102
Peak2	64.5641	882.3887	4.78 min	92.051
Peak3	34.018	464.9196	6.58 min	42.2155
Peak4	0.0211	0.2879	7.32 min	0.0612

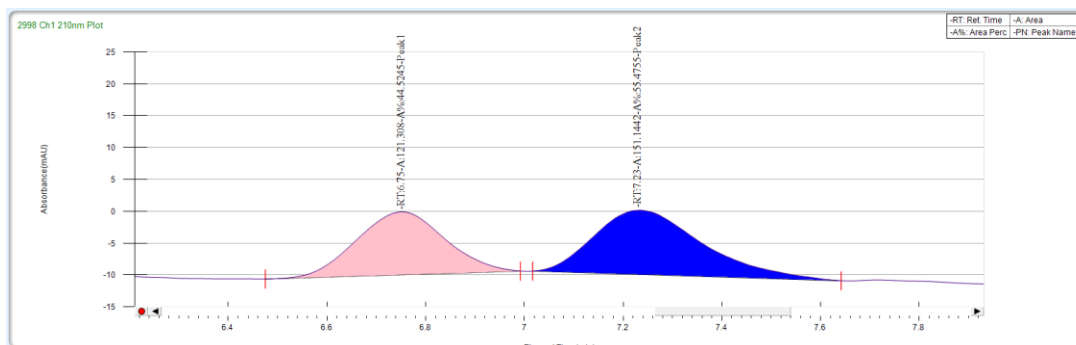
(2*S*,3*R*)-2-((*R*)-(4-nitrophenyl)(phenylthio)methyl)-3-phenyl-1,2,3,4-tetrahydroquinoxaline (5-33b).



The reaction was conducted with 0.1 mmol of (\pm)-**5-1b** following the general procedure B. The crude product was purified by FCC (5% EtOAc in hexanes \rightarrow 20% EtOAc in hexanes) to afford **5-33b** (12.2 mg, 27% yield, 99% ee) as yellow oil. $^1\text{H NMR}$ (500 MHz, CDCl_3): δ 8.02 (d, $J = 8.7$ Hz, 2H), 7.34 (d, $J = 8.7$ Hz, 2H), 7.29 – 7.21 (m, 3H), 7.18 – 7.09 (m, 7H), 6.60 (td, $J = 7.5, 1.4$ Hz, 1H), 6.54 (td, $J = 7.5, 1.5$ Hz, 1H), 6.50 (dd, $J = 7.6, 1.5$ Hz, 1H), 6.33 (dd, $J = 7.6, 1.4$ Hz, 1H), 4.62 (d, $J = 4.6$ Hz, 1H), 4.27 (d, $J = 7.3$ Hz, 1H), 3.92 (s, 1H), 3.64 (dd, $J = 7.3, 4.6$ Hz, 1H), 2.75 (s, 1H); $^{13}\text{C NMR}$ (126 MHz, CDCl_3): δ 147.3, 146.5, 142.0, 132.9, 132.7, 132.5, 130.7, 130.0, 129.2, 128.7, 128.1, 128.0, 127.1, 123.5, 119.5, 118.7, 115.0, 113.6, 57.7, 55.6, 54.8.; **HRMS (ESI-TOF)** (m/z): $[\text{M}+\text{H}]^+$ for $\text{C}_{27}\text{H}_{24}\text{N}_3\text{O}_2\text{S}^+$ calcd: 454.1584, found: 454.1590; $[\alpha]_D^{25} =$

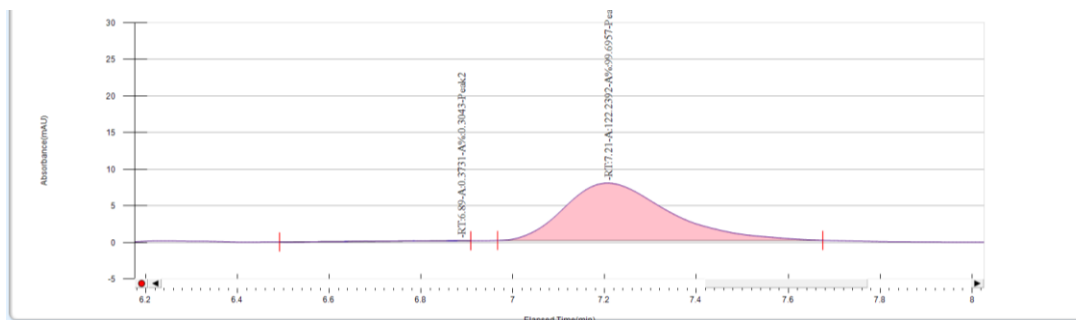
-54.50 (c = 0.013, CH₂Cl₂); **SFC**: (Chiralpak ASH column, 80:20 carbon dioxide/methanol, 3.5 mL/min, I = 210 nm), tr = 4.3 min (minor), 4.8 min (major).

Racemic compound HPLC Traces:



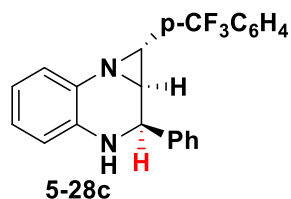
Peak Name	Area Percent	Area	Retention Time	Height
Peak1	44.5245	121.308	6.75 min	9.9024
Peak2	55.4755	151.1442	7.23 min	10.0862

Chiral compound HPLC Traces:



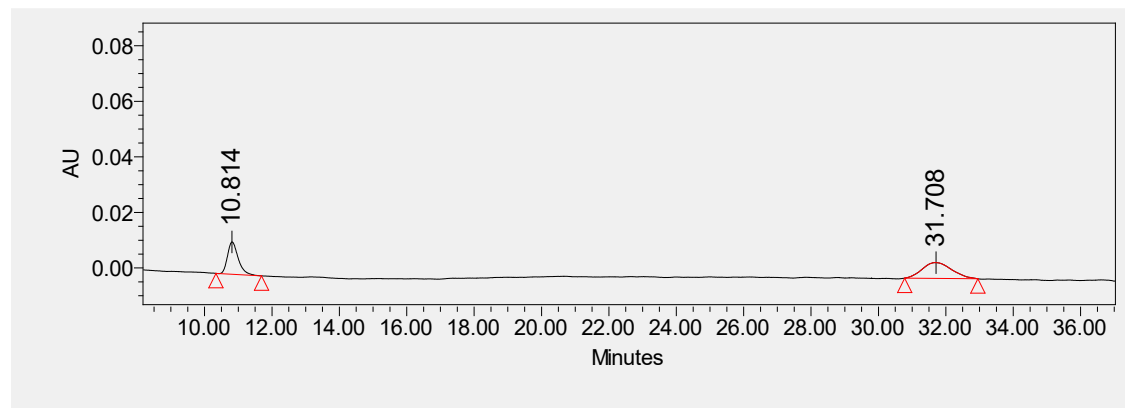
Peak Name	Area Percent	Area	Retention Time	Height
Peak1	0.3043	0.3731	6.89 min	0.0314
Peak2	99.6957	122.2392	7.21 min	7.8431

(1R,1aR,2R)-2-phenyl-1-(4-(trifluoromethyl)phenyl)-1,1a,2,3-tetrahydroazirino[1,2-a]quinoxaline (5-28c).



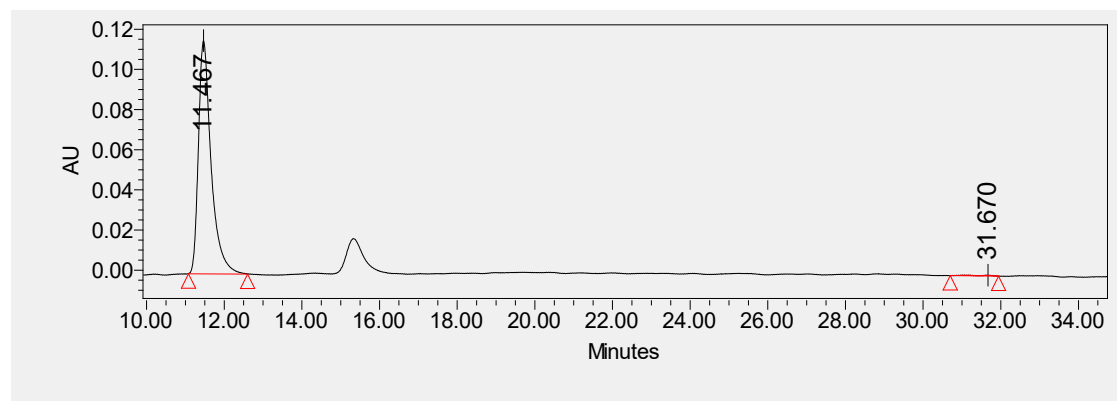
The reaction was conducted with 0.1 mmol of (\pm)-**5-1c** following the general procedure B. The crude product was purified by FCC (5% EtOAc in hexanes \rightarrow 20% EtOAc in hexanes) to afford **5-28c** (20.1 mg, 55% yield, 5.5:1 d.r., 99% ee) as yellow solid (mp 87.1-88.5 °C). **^1H NMR** (500 MHz, CDCl_3): δ 7.56 – 7.49 (m, 5H), 7.44 – 7.31 (m, 8H), 7.02 (td, $J = 7.6, 1.5$ Hz, 1H), 6.79 (td, $J = 7.6, 1.4$ Hz, 1H), 6.62 (dd, $J = 7.8, 1.5$ Hz, 1H), 4.66 (d, $J = 2.6$ Hz, 1H), 4.00 (d, $J = 3.4$ Hz, 1H), 3.85 (s, 1H), 3.00 (q, $J = 2.5$ Hz, 1H); **^{13}C NMR** (126 MHz, CDCl_3): 143.0, 143.0, 140.5, 139.7, 134.8, 129.5 (q, $J = 32.4$ Hz), 129.2, 128.7, 128.3, 127.6, 127.5, 127.3, 126.8, 126.7, 125.9, 125.8, 125.42 (q, $J = 3.8$ Hz), 119.8, 115.4, 55.4, 53.4, 42.5. δ ; **HRMS (ESI-TOF)** (m/z): $[\text{M}+\text{H}]^+$ 367.1417 for calcd: $\text{C}_{22}\text{H}_{18}\text{F}_3\text{N}_2^+$, found: 367.1421; **HPLC**: (Chiralpak ODH column, 95:5 hexanes/ isopropanol, 0.5 mL/min, $I = 254$ nm), $t_r = 10.8$ min (major), 31.7 min (minor).

Racemic compound HPLC Traces:



	Retention Time	Area	% Area
1	10.814	257327	42.62
2	31.708	346414	57.38

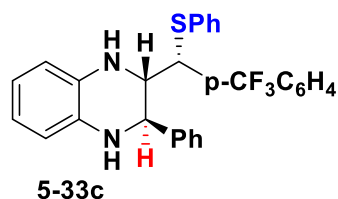
Chiral compound HPLC Traces:



	Retention Time	Area	% Area
1	11.467	257327	42.62
2	31.670	346414	57.38

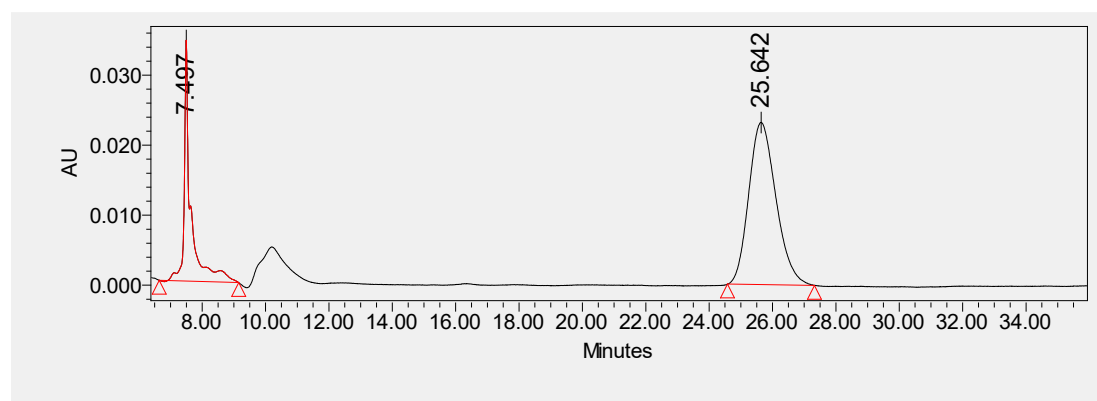
1	11.467	2632623	99.51
2	31.670	12992	0.49

(2R,3S)-2-phenyl-3-((R)-(phenylthio)(4-(trifluoromethyl)phenyl)methyl)-1,2,3,4-tetrahydroquinoxaline (5-33c)



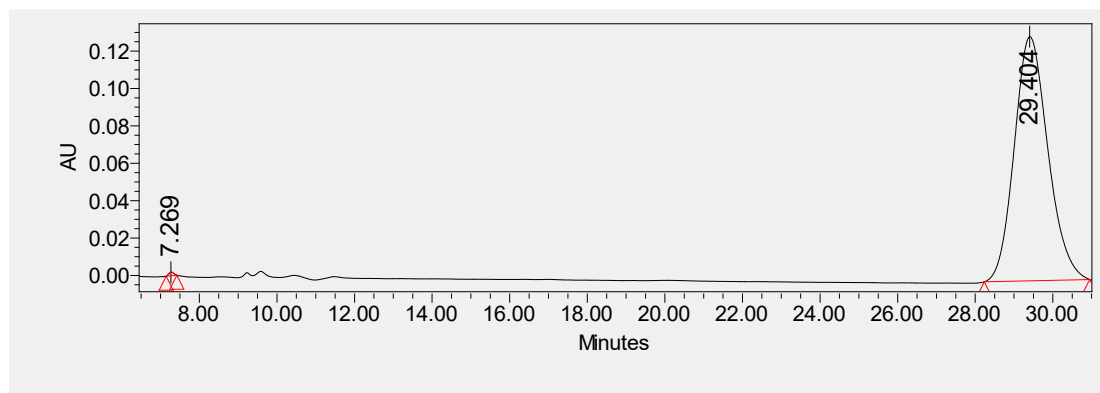
The reaction was conducted with 0.1 mmol of (\pm)-**5-1c** following the general procedure B. The crude product was purified by FCC (5% EtOAc in hexanes \rightarrow 20% EtOAc in hexanes) to afford **5-33c** (7 mg, 15% yield, 99% ee) as yellow oil. **$^1\text{H NMR}$** (500 MHz, CDCl_3): δ 7.51 (d, $J = 8.1$ Hz, 2H), 7.38 (d, $J = 8.1$ Hz, 2H), 7.35 – 7.30 (m, 3H), 7.28 – 7.26 (m, 1H), 7.26 – 7.24 (m, 1H), 7.24 – 7.15 (m, 5H), 6.63 (dtd, $J = 23.0, 7.5, 1.5$ Hz, 2H), 6.55 (dd, $J = 7.5, 1.6$ Hz, 1H), 6.41 (dd, $J = 7.6, 1.5$ Hz, 1H), 4.66 (d, $J = 4.7$ Hz, 1H), 4.30 (d, $J = 7.1$ Hz, 1H), 4.04 (s, 1H), 3.96 (s, 1H), 3.68 (dd, $J = 7.2, 4.8$ Hz, 1H); **$^{13}\text{C NMR}$** (126 MHz, CDCl_3): δ 142.9, 142.3, 133.4, 133.1, 132.4, 131.1, 130.10 (q, $J = 32.5$ Hz), 129.6, 129.2, 128.8, 128.1, 127.9, 127.3, 125.38 (q, $J = 3.7$ Hz), 124.17 (q, $J = 272.1$ Hz), 119.3, 118.7, 115.0, 113.6, 57.8, 55.8, 54.7; **HRMS (ESI-TOF)** (m/z): $[\text{M}+\text{H}]^+$ 477.1607 for calcd: $\text{C}_{28}\text{H}_{24}\text{F}_3\text{N}_2\text{S}^+$, found: 477.1601; $[\alpha]_D^{25} = -27.55$ ($c = 0.007$, CH_2Cl_2); **HPLC**: (Chiralpak ODH column, 95:5 hexanes/ isopropanol, 0.5 mL/min, $I = 254$ nm), $t_r = 7.5$ min (minor), 25.6 min (major).

Racemic compound HPLC Traces:



	Retention Time	Area	% Area
1	7.497	484699	25.97
2	25.642	1381591	74.03

Chiral compound HPLC Traces:



	Retention Time	Area	% Area
1	7.269	16872	0.21
2	29.404	7858858	99.79

A.8 Computational details

All quantum (QM) computations were performed using the development version of QChem 5.2.0¹⁷

The optimization of structures and entropy corrections were performed using B3LYP¹⁸ DFT functional double- ζ -quality basis set 6-31+G**¹⁹. Single point energies were evaluated at ω B97X-D3/cc-pVTZ^{20,21} level of theory with SMD²² solvation model (Chloroform as a solvent).

Computational data (XYZ files, energies breakdown of all computed structures available in Supplementary Information of a paper published by Zhang et. al¹⁶

A.9 References

- (1) Salimi, F.; Karbakhshzadeh, A.; Salehi, N. A Review on Recent Approaches to the Asymmetric Synthesis of Aziridines Derivatives. *Journal of Chemistry Letters* **2021**, 2 (2), 56–63. <https://doi.org/10.22034/JCHEMLETT.2021.301693.1037>.
- (2) Ismail, F. M. D.; Levitsky, D. O.; Dembitsky, V. M. Aziridine Alkaloids as Potential Therapeutic Agents. *Eur J Med Chem* **2009**, 44 (9), 3373–3387. <https://doi.org/10.1016/J.EJMECH.2009.05.013>.
- (3) Wilson, J. E.; Kurukulasuriya, R.; Reibarkh, M.; Reiter, M.; Zwicker, A.; Zhao, K.; Zhang, F.; Anand, R.; Colandrea, V. J.; Cumiskey, A. M.; Crespo, A.; Duffy, R. A.; Murphy, B. A.; Mitra, K.; Johns, D. G.; Duffy, J. L.; Vachal, P. Discovery of Novel Indoline Cholesterol Ester Transfer Protein Inhibitors (CETP) through a Structure-Guided Approach. *ACS Med Chem Lett* **2016**, 7 (3), 261–265.

- https://doi.org/10.1021/ACSMEDCHEMLETT.5B00404/ASSET/IMAGES/LARGE/ML-2015-00404J_0007.JPEG.
- (4) Law, R. P.; Atkinson, S. J.; Bamborough, P.; Chung, C. W.; Demont, E. H.; Gordon, L. J.; Lindon, M.; Prinjha, R. K.; Watson, A. J. B.; Hirst, D. J. Discovery of Tetrahydroquinoxalines as Bromodomain and Extra-Terminal Domain (BET) Inhibitors with Selectivity for the Second Bromodomain. *J Med Chem* **2018**, *61* (10), 4317–4334. https://doi.org/10.1021/ACS.JMEDCHEM.7B01666/SUPPL_FILE/JM7B01666_SI_002.CSV.
- (5) Smalley, A. P.; Cuthbertson, J. D.; Gaunt, M. J. Palladium-Catalyzed Enantioselective C-H Activation of Aliphatic Amines Using Chiral Anionic BINOL-Phosphoric Acid Ligands. *J Am Chem Soc* **2017**, *139* (4), 1412–1415. https://doi.org/10.1021/JACS.6B12234/SUPPL_FILE/JA6B12234_SI_002.CIF.
- (6) Heine, H. W.; Peavy, R. Aziridines XI. Reaction of 1,2,3-Triphenylaziridine with Diethylacetylene Dicarboxylate and Maleic Anhydride. *Tetrahedron Lett* **1965**, *6* (35), 3123–3126. [https://doi.org/10.1016/S0040-4039\(01\)89232-7](https://doi.org/10.1016/S0040-4039(01)89232-7).
- (7) Zbruyev, A. I.; Vashchenko, V. V.; Andryushchenko, A. A.; Desenko, S. M.; Musatov, V. I.; Knyazeva, I. V.; Chebanov, V. A. Synthesis of Polyarene Derivatives of Fused Aziridines by Suzuki–Miyaura Cross-Coupling. *Tetrahedron* **2007**, *63* (20), 4297–4303. <https://doi.org/10.1016/J.TET.2007.03.060>.
- (8) Parmar, D.; Sugiono, E.; Raja, S.; Rueping, M. Complete Field Guide to Asymmetric BINOL-Phosphate Derived Brønsted Acid and Metal Catalysis: History and Classification by Mode of Activation; Brønsted Acidity, Hydrogen Bonding, Ion Pairing, and Metal Phosphates. *Chemical Reviews*. American Chemical Society September 24, 2014, pp 9047–9153. <https://doi.org/10.1021/cr5001496>.
- (9) Liu, W.; Yang, X. Recent Advances in (Dynamic) Kinetic Resolution and Desymmetrization Catalyzed by Chiral Phosphoric Acids. *Asian J Org Chem* **2021**, *10* (4), 692–710. <https://doi.org/10.1002/AJOC.202100091>.
- (10) Vedejs, E.; Chen, X. Parallel Kinetic Resolution. *J Am Chem Soc* **1997**, *119* (10), 2584–2585. https://doi.org/10.1021/JA963666V/SUPPL_FILE/JA2584.PDF.
- (11) Saito, K.; Shibata, Y.; Yamanaka, M.; Akiyama, T. Chiral Phosphoric Acid-Catalyzed Oxidative Kinetic Resolution of Indolines Based on Transfer Hydrogenation to Imines. *J Am Chem Soc* **2013**, *135* (32), 11740–11743. https://doi.org/10.1021/JA406004Q/SUPPL_FILE/JA406004Q_SI_006.CIF.
- (12) Saito, K.; Miyashita, H.; Akiyama, T. Chiral Phosphoric Acid Catalyzed Oxidative Kinetic Resolution of Cyclic Secondary Amine Derivatives Including Tetrahydroquinolines by Hydrogen Transfer to Imines. *Chemical Communications* **2015**, *51* (93), 16648–16651. <https://doi.org/10.1039/C5CC06436H>.
- (13) Wang, J.; Chen, M. W.; Ji, Y.; Hu, S. B.; Zhou, Y. G. Kinetic Resolution of Axially Chiral 5- or 8-Substituted Quinolines via Asymmetric Transfer Hydrogenation. *J Am Chem Soc* **2016**, *138* (33), 10413–10416. https://doi.org/10.1021/JACS.6B06009/SUPPL_FILE/JA6B06009_SI_003.CIF.
- (14) Han, Z. Y.; Xiao, H.; Gong, L. Z. Dynamic Kinetic Asymmetric Transfer Hydrogenation of Racemic 2,4-Diaryl-2,3-Dihydrobenzo[b][1,4]Diazepines Catalyzed by Chiral Phosphoric Acids. *Bioorg Med Chem Lett* **2009**, *19* (14), 3729–3732. <https://doi.org/10.1016/J.BMCL.2009.05.039>.

- (15) Toda, Y.; Korenaga, T.; Obayashi, R.; Kikuchi, J.; Terada, M. Dynamic Parallel Kinetic Resolution of α -Ferrocenyl Cation Initiated by Chiral Brønsted Acid Catalyst. *Chem Sci* **2021**, *12* (30), 10306–10312. <https://doi.org/10.1039/D1SC02122B>.
- (16) Jhang, Y.; Zhelavskiy, O.; Nagorny, P. Enantioselective Parallel Kinetic Resolution of Aziridine-Containing Quinoxalines via Chiral Phosphoric Acid-Catalyzed Transfer Hydrogenation. **2023**. <https://doi.org/10.1021/acs.orglett.3c03072>.
- (17) Shao, Y.; Gan, Z.; Epifanovsky, E.; Gilbert, A. T. B.; Wormit, M.; Kussmann, J.; Lange, A. W.; Behn, A.; Deng, J.; Feng, X.; Ghosh, D.; Goldey, M.; Horn, P. R.; Jacobson, L. D.; Kaliman, I.; Khaliullin, R. Z.; Kuš, T.; Landau, A.; Liu, J.; Proynov, E. I.; Rhee, Y. M.; Richard, R. M.; Rohrdanz, M. A.; Steele, R. P.; Sundstrom, E. J.; Woodcock, H. L.; Zimmerman, P. M.; Zuev, D.; Albrecht, B.; Alguire, E.; Austin, B.; Beran, G. J. O.; Bernard, Y. A.; Berquist, E.; Brandhorst, K.; Bravaya, K. B.; Brown, S. T.; Casanova, D.; Chang, C. M.; Chen, Y.; Chien, S. H.; Closser, K. D.; Crittenden, D. L.; Diedenhofen, M.; Distasio, R. A.; Do, H.; Dutoi, A. D.; Edgar, R. G.; Fatehi, S.; Fusti-Molnar, L.; Ghysels, A.; Golubeva-Zadorozhnaya, A.; Gomes, J.; Hanson-Heine, M. W. D.; Harbach, P. H. P.; Hauser, A. W.; Hohenstein, E. G.; Holden, Z. C.; Jagau, T. C.; Ji, H.; Kaduk, B.; Khistyayev, K.; Kim, J.; Kim, J.; King, R. A.; Klunzinger, P.; Kosenkov, D.; Kowalczyk, T.; Krauter, C. M.; Lao, K. U.; Laurent, A. D.; Lawler, K. V.; Levchenko, S. V.; Lin, C. Y.; Liu, F.; Livshits, E.; Lochan, R. C.; Luenser, A.; Manohar, P.; Manzer, S. F.; Mao, S. P.; Mardirossian, N.; Marenich, A. V.; Maurer, S. A.; Mayhall, N. J.; Neuscammen, E.; Oana, C. M.; Olivares-Amaya, R.; Oneill, D. P.; Parkhill, J. A.; Perrine, T. M.; Peverati, R.; Prociuk, A.; Rehn, D. R.; Rosta, E.; Russ, N. J.; Sharada, S. M.; Sharma, S.; Small, D. W.; Sodt, A.; Stein, T.; Stück, D.; Su, Y. C.; Thom, A. J. W.; Tsuchimochi, T.; Vanovschi, V.; Vogt, L.; Vydrov, O.; Wang, T.; Watson, M. A.; Wenzel, J.; White, A.; Williams, C. F.; Yang, J.; Yeganeh, S.; Yost, S. R.; You, Z. Q.; Zhang, I. Y.; Zhang, X.; Zhao, Y.; Brooks, B. R.; Chan, G. K. L.; Chipman, D. M.; Cramer, C. J.; Goddard, W. A.; Gordon, M. S.; Hehre, W. J.; Klamt, A.; Schaefer, H. F.; Schmidt, M. W.; Sherrill, C. D.; Truhlar, D. G.; Warshel, A.; Xu, X.; Aspuru-Guzik, A.; Baer, R.; Bell, A. T.; Besley, N. A.; Chai, J. Da; Dreuw, A.; Dunietz, B. D.; Furlani, T. R.; Gwaltney, S. R.; Hsu, C. P.; Jung, Y.; Kong, J.; Lambrecht, D. S.; Liang, W.; Ochsenfeld, C.; Rassolov, V. A.; Slipchenko, L. V.; Subotnik, J. E.; Van Voorhis, T.; Herbert, J. M.; Krylov, A. I.; Gill, P. M. W.; Head-Gordon, M. Advances in Molecular Quantum Chemistry Contained in the Q-Chem 4 Program Package. *Mol Phys* **2015**, *113* (2), 184–215. <https://doi.org/10.1080/00268976.2014.952696>.
- (18) Grimme, S.; Ehrlich, S.; Goerigk, L. Effect of the Damping Function in Dispersion Corrected Density Functional Theory. *J Comput Chem* **2011**, *32* (7), 1456–1465. <https://doi.org/10.1002/JCC.21759>.
- (19) Hehre, W. J.; Ditchfield, K.; Pople, J. A. Self—Consistent Molecular Orbital Methods. XII. Further Extensions of Gaussian—Type Basis Sets for Use in Molecular Orbital Studies of Organic Molecules. *J Chem Phys* **1972**, *56* (5), 2257–2261. <https://doi.org/10.1063/1.1677527>.
- (20) Lin, Y. S.; Li, G. De; Mao, S. P.; Chai, J. Da. Long-Range Corrected Hybrid Density Functionals with Improved Dispersion Corrections. *J Chem Theory Comput* **2013**, *9* (1), 263–272. https://doi.org/10.1021/CT300715S/SUPPL_FILE/CT300715S_SI_001.PDF.
- (21) Kendall, R. A.; Dunning, T. H.; Harrison, R. J. Electron Affinities of the First-row Atoms Revisited. Systematic Basis Sets and Wave Functions. *J Chem Phys* **1992**, *96* (9), 6796–6806. <https://doi.org/10.1063/1.462569>.
- (22) Marenich, A. V.; Cramer, C. J.; Truhlar, D. G. Universal Solvation Model Based on Solute Electron Density and on a Continuum Model of the Solvent Defined by the Bulk Dielectric

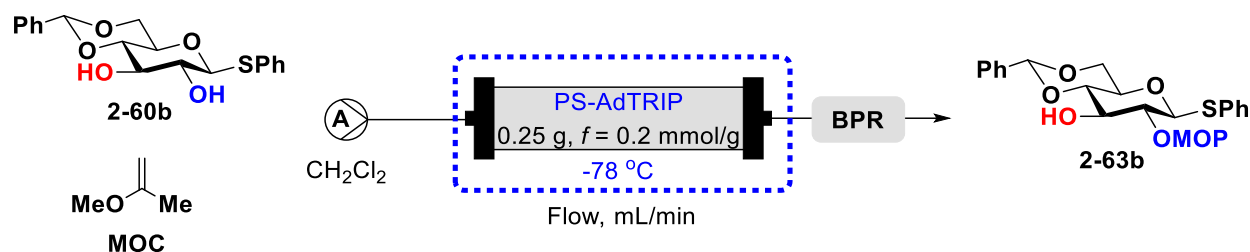
Constant and Atomic Surface Tensions. *Journal of Physical Chemistry B* **2009**, *113* (18), 6378–6396. <https://doi.org/10.1021/jp810292n>.

Appendix B: Regioselective Acetalization of Carbohydrates in a Continuous Flow

B.1 Continuous flow conditions development

We established conditions for regioselective acetalization of monosaccharides in Chapter 2 using immobilized CPAs. (*R*)-BINOL-based immobilized CPA PS-AdTRIP resulted in high-selective C2-protection, while (*S*)-SPINOL-based CPA reverts selectivity and allowed to achieve C3-protection with moderate selectivities (up to 10:1 r.r.). Our next step was to implement the developed protocol for continuous flow systems. Immobilized CPA **PS-AdTRIP** (250 mg) was packed into the stainless steel HPLC column (4.6 mm I.D., 100 mm length) and then connected to the Dual Piston pump (Table B.1). Solution containing substrate **2-60b** and protecting group (**MOC**) was then pumped through the system. Colling to -78 °C was achieved by submerging the HPLC column in Neslab Cryocool immersion cooler. The low flow rate (Entry 1) was not sufficient for the effective solution pumping through the system. An increase of flow rate to 0.2 mL/min led to unstable flow and high pressure in the system (Entry 2). Product **2-63b** was formed in 40% yield and diminished regioselectivity ratio of 12:1. Further conditions screening (entries 3 and 4) demonstrated the ineffectiveness of the protocol for the continuous flow applications as low temperatures significantly increased the density of the dichloromethane used as a solvent. As a result, significant pressure build-up happened in the tubing and packed-bed reactor in the flow system.

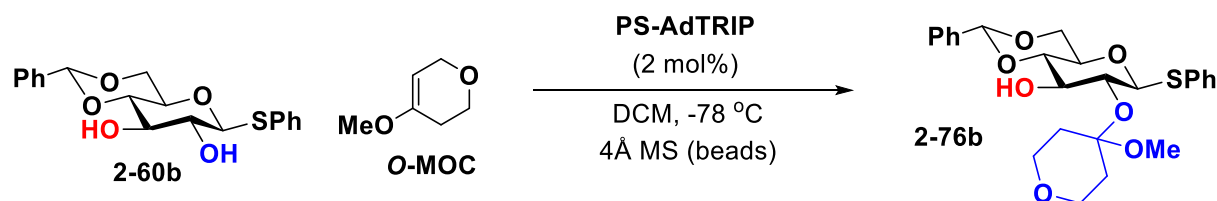
Appendix Table B.1. Optimization of regioselective acetalization in continuous flow



Entry	Flow (mL/min)	Pressure (psi)	Concentration (M)	Conversion (NMR, %)	r.r.
1	0.05	-	0.05	-	-
2	0.2	3500	0.05	40	12:1
3	0.1	>4000	0.05	-	-
4	0.1	>4000	0.025	-	-

Subsequently, we decided to optimize acetalization conditions to perform reactions at higher temperatures and potentially address the issue of the high viscosity of solvent at -78°C . In Chapter 2 we described that the MOP protection group requires -78°C for achieving high regioselectivity of the reaction, while MOC allows the synthesis of acetalized products at -55°C . Following this trend, we tested 4-methoxy-3,6-dihydro-2H-pyran (*O*-MOC) as enol ether for carbohydrate protection (Table B.2). We observed no reaction conversion at -78°C and only 45% conversion to product **2-76b** after 24 hours at -15°C . Prolonging reaction time to 48 hours increased the conversion to 70% and resulted in product **2-76b** formation with 15:1 r.r. Although using *O*-MOC at -15°C resulted in product formation, the reaction time was quite long for flow chemistry application. Increasing the temperature to 4°C led to decreasing the regioselectivity to 3:1 r.r. (entry 4).

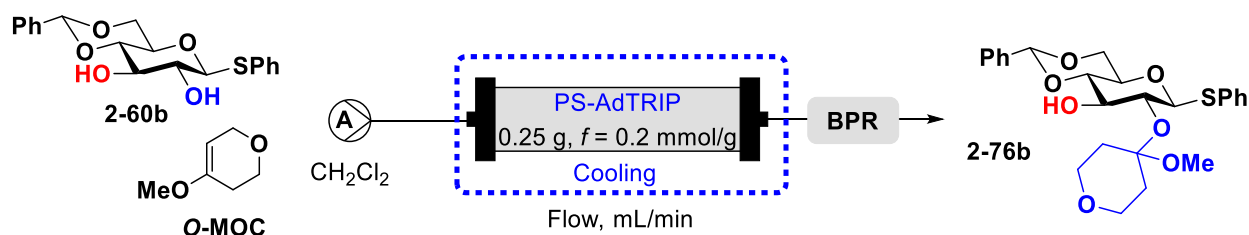
Appendix Table B.2. Conditions screening for the *O*-MOC protection group installation



Entry	T °C	Time (h)	Conversion (NMR, %)	r.r (C2:C3)
1	-78	24	N.R.	N.R.
2	-15	24	45	15:1
3	-15	48	70	15:1
4	4	24	77	3:1

Finally, after establishing the new conditions for acetalization with O-MOC, we decided to test the flow conditions with a new protecting group (Table B.3). Unfortunately, no attempts to develop the continuous flow conditions were successful. Low flow rates (entries 1-2) were not sufficient to create any flow to overcome the back pressure of the packed-bed reactor. Assuming that low temperatures are still a main factor creating obstacles for a stable flow rate, we further increased temperature to -5 °C and 4 °C (entries 3 and 4). Even though some quantities of product **2-76b** were isolated, the regioisomer ratio of the product was low (3:1 r.r.). Considering our previous work in flow chemistry transfer hydrogenation (Chapter 3) we can assume that high catalytic loading of PS-AdTRIP in the packed-bed reactor can promote product decomposition to starting reagents as acetal groups are acid-labile. Therefore, at higher temperatures due to CPA-promoted equilibration, we observe low regioselectivity. Future studies can be focused on testing higher flow rates to minimize equilibration between C2- and C3- C3-protected products.

Appendix Table B.3. Optimization of regioselective acetalization in a continuous flow using O-MOC enol as a protecting group.



Entry	Flow (mL/min)	T (°C)	Result	Conversion (NMR, %)	r.r.
1	0.05	-15	No flow	-	-
2	0.05	-15	No flow	-	-
3	0.05	-5	Unstable	20	3:1
4	0.05	4	Unstable	50	3:1

B.2 Summary

Despite our efforts to optimize developed conditions for regioselective acetalization from Chapter 2, we didn't manage to generate the desired products in continuous flow with the same regioisomer ratios and yields as in batch conditions. Several potential problems are causing low yields and selectivity. Higher catalytic loading in comparison to batch conditions and elevated temperatures may cause product decomposition during the reaction in a packed-bed reactor. Higher temperatures may also cause a decrease in the regioisomeric selectivity of the reaction. At the same time, a decrease in temperature leads to increased solvent viscosity causing unstable flow and excessive pressure build-up in the system. We envision that additional studies can be performed in the future to address the issues described above and create a sustainable protocol for the regioselective synthesis of protected carbohydrates in continuous flow.